3D lens-free imaging of 3D cell culture

Anthony Berdeu

Communauté
UNIVERSITÉ Grenoble Alpes

THÈSE

Pour obtenir le grade de

DOCTEUR DE LA COMMUNAUTÉ UNIVERSITÉ GRENOBLE ALPES

Spécialité : Biotechnologie, instrumentation, signal et imagerie pour la biologie, la médecine et l'environnement

Arrêté ministériel : 25 mai 2016

Présentée par

Anthony Berdeu

Thèse dirigée par **Nathalie Picollet-D'hahan**
et co-encadrée par **Cédric Allier**

rattachée au laboratoire de **Biologie à Grande Échelle**
de **l'École Doctorale Ingénierie pour la Santé, la Cognition et l'Environnement (EDISCE)**
et préparée au sein du **Laboratoire Imagerie et Systèmes d'Acquisition – CEA Leti**

Imagerie sans lentille 3D pour la culture cellulaire 3D

3D lens-free imaging of 3D cell culture

Thèse soutenue publiquement le **16 novembre 2017**,
devant le jury composé de :

Mme. Nathalie Picollet-D'hahan
Chargée de Recherche, Université Grenoble Alpes, Directrice de thèse
Institut de Biosciences et Biotechnologies de Grenoble – CEA – Grenoble

Mr. Olivier Haeberlé
Professeur des Universités, Université de Haute-Alsace, Rapporteur
Laboratoire Modélisation Intelligence Processus Systèmes

Mr. Francesco Pampaloni
Directeur de Recherche, Goethe University of Frankfurt, Rapporteur
Buchmann Institute of Molecular Life Sciences

Mme. Corinne Fournier
Maître de Conférences, Université Jean Monnet, Examinatrice
Laboratoire Hubert Curien

Mme. Françoise Peyrin, présidente du jury
Directeur de Recherche, Université Claude Bernard Lyon 1, Examinatrice
Laboratoire Creatis

Mr. Éric Thiébaut
Astronome, Université Claude Bernard Lyon 1, Examinateur
Centre de Recherche Astrophysique de Lyon

Mr. Cédric Allier
Ingénieur de Recherche, Université Grenoble Alpes, Invité
Laboratoire Imagerie et Systèmes d'Acquisition – CEA – Grenoble

Mr. Fabien Momey
Maître de Conférences, Université Jean Monnet, Invité
Laboratoire Hubert Curien

Table of contents

Acknowledgment **v**

Acronyms and notations **ix**

Introduction **1**

I Context and state of the art **5**
1 Overview of the development of 3D cell culture 5
1.1 A brief history 5
1.2 Access to new phenomena 6
2 Standard 3D imaging of biological sample 7
2.1 Standard microscopy 7
2.2 Fluorescence microscopy 7
2.3 Coherent microscopy 11
2.4 Lens-free microscopy: a complementary tool 14
3 Development of lens-free time-lapse microscopy 14
3.1 Principle and potential 14
3.2 2D in-line holography overview 17
3.3 First work in 3D lens-free microscopy 21

II 3D diffraction physics **25**
1 3D diffraction model of low scattering objects 25
1.1 Equation of wave propagation 25
1.2 The Born approximation 28
2 The Fourier diffraction theorem 30
2.1 Demonstration 31
2.2 Geometrical interpretation 34
2.3 A diffractive version of the Fourier slice theorem 35
3 3D numerical simulations 37
3.1 Reformulation of the Born approximation and the Fourier diffraction theorem 37
3.2 Comparison of the two models 45
3.3 Consistency with the 2D models 49
3.4 Conclusion and discussion 54

III A versatile prototype and first reconstruction algorithms 57
1 Overview of the experimental bench 57
1.1 Design and functioning 57
1.2 First acquisitions 59
2 A first 3D reconstruction method based on the Radon transform . . . 63
2.1 Overview of the method 63
2.2 Adding a 2D pre-focusing step 65
2.3 3D reconstructions 67
3 A second method based on z-stack acquisitions 73
3.1 Motivation of the method 75
3.2 Few tests of deconvolution 76
3.3 Toward iterative inverse problem approaches 78
4 A third method based on the Fourier diffraction theorem 85
4.1 Overview of the method: a Fourier mapping 85
4.2 A phase ramp to compensate the lack of phase 86
4.3 3D reconstruction and comments 88
5 A few thoughts on the lighting angles... 94
5.1 Method and experiment 95
5.2 Results 98
5.3 Conclusion and discussion 100

IV A second design and new reconstruction methods 103
1 Overview of the experimental bench 103
1.1 Design motivations 103
1.2 First acquisitions and reconstructions 111
2 Iterative phase retrieval 114
2.1 Inverse problem formulation 115
2.2 Numerical simulations 118
2.3 3D reconstructions on experimental data 121
3 3D inverse problem approach 124
3.1 Inverse problem formulation 125
3.2 Numerical simulations 131
3.3 3D reconstructions on experimental data 137
4 Regularized Gerchberg–Saxton algorithm 139
4.1 A modified Gerchberg–Saxton algorithm 139
4.2 Numerical simulations 142
4.3 3D reconstructions on experimental data 145
5 Comparison of the algorithms 151
5.1 Biological samples 153
5.2 3D reconstructions 155
5.3 Comparison with a standard microscope 164
5.4 Conclusion, discussion and perspectives 169

V Towards 3D time-lapse microscopy in incubator **175**
1 Toward an improved and incubator-proofed prototype . . . 175
2 3D+t reconstructions . . . 178
2.1 Access to 3D large scale phenomena . . . 178
2.2 Study of the extracellular matrix . . . 186
3 Characterization . . . 191
3.1 Experiment and data processing . . . 192
3.2 Accuracy . . . 198
3.3 Resolution and xyz-sizing . . . 201
3.4 Conclusion and discussion . . . 208

Conclusion and perspectives **213**

Communications **221**

A Green's functions to solve linear differential equations **223**
1 Overview . . . 223
2 Solution of the wave equation . . . 224

B Weyl's integral for harmonic spherical waves **227**
1 Reformulation of the problem . . . 227
2 Holomorphic functions and residue theorem to calculate integrals . . 229
3 Proof of Weyl's integral . . . 231

C Data registration methods and z_s estimation **235**
1 Data registration methods . . . 235
1.1 Registration algorithms . . . 236
1.2 Raw *versus* reconstructed holograms . . . 237
1.3 Discussion . . . 238
2 z_s estimation . . . 239
2.1 Simple 2D back-propagation . . . 239
2.2 Simple 3D back-propagation . . . 240

D Gradient of $J(f)$ **241**
1 Data fidelity . . . 241
2 L_1-norm . . . 243
3 ∇-norm . . . 243

E 3D chemotaxis simulations **247**
1 Experiments . . . 247
1.1 RWPE1: Prostate Epithelial Cells . . . 247
1.2 HUVEC: Human Umbilical Vein Endothelial Cells . . . 249
2 Mathematical model . . . 249
2.1 The model . . . 252
2.2 Static diffusers . . . 253
2.3 Mobile diffusers . . . 253

2.4 Boundary conditions 254
3 Results and discussion 255
3.1 RWPE1: tumorous prostatic cells 256
3.2 HUVEC: Epithelial cells 258
3.3 Discussion 259

F Résumé en Français **261**

Bibliography **287**

Acknowledgement

First of all, I would like to naturally thank all the jury members who agreed to evaluate my work. I enjoyed to get your feedback during my PhD defense and I had a great pleasure to exchange about my results and the perspectives of my work. I hope that we will meet and work together in the future to continue these discussions.

I sincerely hope that this thesis will draw the reader's attention. I would also like to apologize on my English which may sometimes look a bit approximate or too French and hope that this thesis is nevertheless understandable.

Continuing this remark, the rest of the acknowledgments being addressed to the people of my team, it will benefit from being written in French.

Je tiens à remercier Jean-Marc puis plus récemment Sophie grâce à qui j'ai pu être hébergé au LISA au cours de ces trois dernières années.

Mes remerciements se tournent ensuite naturellement vers l'équipe encadrante. D'abord à Nathalie ma directrice de thèse qui m'a permis de faire mes premiers pas en biologique, ce qui ne fut pas toujours une mince affaire. Promis, je vais continuer de compléter mes connaissances et arrêter de confondre les cellules épithéliales avec des cellules endothéliales. Ensuite à Cédric, dont je sais que le rôle d'encadrant n'a pas été facile tous les jours et qui fut disponible à tout moment pour répondre à mes interrogations ou venir m'aider à (des)souder mes différents prototypes. Nous avons souvent eu des débats animés dans l'openspace mais toujours intéressants et au final sincères et constructifs. Merci pour tes nombreux avis sur la rédaction des papiers et la présentation des résultats, mais surtout merci de m'avoir forcé à sortir la tête de mes codes à plusieurs reprises pour m'encourager à aller faire des manips. Parce que sinon, « on reste d'accord avec soi-même... Et donc : So what ? »

Ensuite, je tiens à remercier les personnes sans qui cette présente thèse aurait été impossible :

Thomas, pour le temps bien trop important que je lui ai demandé de me consacrer pour m'apprendre à souder, coder en Labview, allumer une LED avec un capteur CMOS, usiner des pièces en impression 3D et j'en passe... Sans toi, les prototypes auraient eu bien plus de mal à tourner aussi rapidement (ou à tourner tout court).

Fabien, qui m'a mis le pied (voire les deux) à l'étrier concernant les codes de reconstructions et le théorème de diffraction de Fourier ainsi que la bibliographie associée. Nos échanges en début de thèse m'ont fait gagner un temps considérable. Plus la peine de m'énumérer tous les avantages des approches par problème inverse, tu m'as largement convaincu ! Désolé toutefois de t'avoir un peu trahi avec mon dernier code de reconstruction...

Bastien, dont j'admire le doigté de chirurgien en ce qui concerne les pipettes et autres instruments de torture des paillasses de biologie. Merci d'avoir su concocter de très belles cultures cellulaires pour tester mes prototypes et mes algorithmes et d'avoir su mettre en œuvre les différentes idées qu'on a pu avoir en ce qui concerne des expériences originales.

Merci ensuite à Véronique, puis surtout Laurence, nos mamans au LISA, qui m'ont bien soulagé dès qu'il s'agissait de parler de démarches administratives, de l'envoi de courrier à la réservation des hôtels et autres moyens de transport pour se rendre en conférence à l'autre bout du monde. Mention spéciale à Laurence qui a su être patiente quand je revenais pour poser une question que j'avais déjà posée la veille mais dont j'avais oublié toutes les réponses.

Merci à Frédérique, Stéphanie et Caterina pour les échantillons biologiques que vous avez pu fournir au cours de ce travail de thèse. Merci à Mathilde pour ta patience dans le L2 pour m'apprendre à entretenir un incubateur.

Merci bien sûr aux membres de l'équipe du LISA, permanents ou juste de passage, de m'avoir bien intégré dans leurs rangs durant ces années, en particulier Olivier, Lionel, Pierre J. et Ondrej de l'équipe sans lentille avec qui j'ai pu échanger sur les subtilités de Matlab et l'expérimentation. Merci à Pierre B. pour tes retours avisés sur mon manuscrit et les coquilles mathématiques qui s'y sont glissées et à Romaric pour le temps que tu as consacré à la relecture d'un de mes papiers ainsi que de tes conseils de rédaction avisés que j'ai bien eu du mal à mettre en œuvre pour ma rédaction de thèse. Mais j'y travaille ! Un grand merci aussi à Charlotte pour ton animation avec une bonne humeur sans faille de la vie du labo, des repas et des sorties.

D'un point de vue moins professionnel, merci à toute l'équipe des gens qui mangeaient à H1 dans la bonne ambiance le midi, ce fut un plaisir de partager ces moments de détente avec vous et de penser à autre chose : Camille, Justin, Damien, Samy, Émeric, avec une petite pensée émue pour mes partenaires de combat en thèse Valentin et Nils ainsi que les vétéranes Judy, Veronica et Sophie (tu m'avais demandé de prendre soin de Cédric, j'ai fait ce que j'ai pu) et les petits nouveaux Isaure et David : bon courage à vous pour la suite.

Et de manière plus personnelle, je tiens à remercier ma famille, en particulier mes parents qui m'ont donné le goût des sciences dès mon plus jeune âge et qui ont toujours été là pour répondre à mes nombreuses questions existentielles. Merci de m'avoir toujours apporté (et de continuer à le faire) vos encouragements, vos avis éclairés et votre soutien indéfectible dans mes choix et décisions quelles qu'aient pu en être les conséquences. Merci à Armelle pour tes retours et avis sur la clarté de mon manuscrit et surtout sur mon anglais. Merci aussi d'avoir été là ces trois années malgré la distance pour m'encourager et me soutenir dans les moments difficiles.

Enfin, je ne peux pas ne pas avoir une pensée pour ma grand-mère dont je me souviendrai des débats sur l'origine et la composition de l'Univers (oui, je te promets de rester passionné par les sciences et l'astronomie et tout ce qu'on peut trouver dans le ciel) et pour Nacha dont les traces de pattes sur mes cours de maths resteront à jamais la preuve de tes encouragements jusque tard dans la nuit quand nous n'étions

que les deux seuls encore éveillés dans la maison (à moins que tu ne cherchais juste que des genoux pour dormir ?).

Acronyms and notations

Acronyms

2D	Two Dimensions
3D	Three Dimensions
BiOS 2017	SPIE Photonics West, Biomedical optics, and imaging conference, SF, US 01/28-02/02/2017
BFGS algorithm	Broyden–Fletcher–Goldfarb–Shanno algorithm: method to iteratively solve unconstrained nonlinear optimization problems
CMOS	Complementary Metal Oxide Semiconductor
CT	Computed tomography
DMEM	Dulbecco's Modified Eagle's medium
ECBO 2017	European Conferences on Biomedical Optics, Munich, Germany, 06/25-06/29/2017
ECM	Extracellular Matrix
FFT	Fast Fourier Transform
FSB	Fetal Serum Bovin
FWHM	Full Width at Half Maximum
GPU	Graphics Processing Unit
HUVEC	Human Umbilical Vein Endothelial Cells
LED	Light Emitting Diode
MEM	Minimum Essential Medium
pix	Pixel
RGB	Red Green Blue
ROI	Region of interest
RWPE1	Prostate Epithelial Cells
t	Time
vox	Voxel

Notations

III.4	Fourier mapping method introduced in chapter III, section 4 with a phase ramp approximation for the unmeasured phase.
IV.4	Regularized Gerchberg-Saxton algorithm introduced in chapter IV, section 4
IV.3	3D inverse problem approach introduced in chapter IV, section 3
IV.2	Iterative 2D phase retrieval method introduced in chapter IV, section 2
dx, dy, dz	Elementary length on the x, y and z-directions
d_{pix}	Sensor pixel pitch
ds	Elementary surface of a 2D grid
dv	Elementary volume of a 3D grid
nb_{it}^{GS}	Number of iterations of the global loop in the regularized Gerchberg-Saxton algorithm IV.4without the regularization step 3.2.
$nb_{it}^{GS,r}$	Number of iterations of the global loop in the regularized Gerchberg-Saxton algorithm IV.4with the regularization step 3.2.
nb_{it}^{IP}	Number of iterations in the inverse problem approach IV.3
nb_{it}^{PR}	Number of iterations in the phase retrieval method IV.2
nb_{reg}^{GS}	Number of iterations in the regularization step 3.2 in the regularized Gerchberg-Saxton algorithm IV.4
$nb_{x,y}^{p}$	Number of pixels in a 2D grid on the x and y-directions
$nb_{x,y,z}^{v}$	Number of voxels in a 3D gird on the x, y and z-directions
$\mathcal{R}(c)$	Real part of the complex number c
$\%\ v/v$	percentage dilution volume per volume
$\%\ w/v$	percentage dilution weight per volume
λ	Wavelength of the light source
φ	In the context of the first prototype: the angle of the rotation stage of the φ-axis compared to a normal lighting. Otherwise: the azimuthal angle of the lighting direction.
φ-axis	Axis of the rotation stage in the φ-mode
φ-mode	Modality of the first prototype in which the sample and the sensor plane are fixed and only the light source is rotated.
θ	In the context of the first prototype: the angle of the rotation stage of the θ-axis. Otherwise: the polar angle of the lighting direction compared to the normal to the sensor.

θ-axis	Axis of the rotation stage in the θ-mode
θ-mode	Modality of the first prototype in which the light source and the sensor are fixed. The lighting remains orthogonal to the sensor plane. Only the sample is rotated.
$\cdots$	The equation continues on the next line.

Introduction

In biology, since the first attempts to grow cell cultures in laboratories in the late XIX$^{\text{th}}$ century [1], 2D cultures in plastic and glass dishes have been the reference. Once scientists understood how to maintain cells alive, it became possible to grow them over several days to perform experiments. In the forties and fifties, cell culture protocols greatly improved leading to breakthroughs in many fields of biology such as fundamental life science research, genetics, oncology, pharmaceutics, toxicology and virology [2, Chapter 20].

But recent years developments show that such culture conditions create strong observational biases. In many ways, nature is three-dimensional and at some points, 2D cultures reach their limits [3]. For instance, multicellular organisms, embryos and organs evolve in 3D. Their development and study can hardly be reproduced in the realm of 2D biology. Moreover it has been shown that even a single cell behaves differently and has a different genetic expression if it adheres on a 2D surface or if it lies in a 3D extracellular matrix [4].

Since the early 2000s, new protocols are being developed to grow cells in 3D gel matrices [5]. Such cultures open new fields of research at a scale between standard 2D cultures and small animal experiments that raise ethical concerns [6]. Many advances are expected in cancer biology, regenerative medicine and fundamental biology [7, 8].

New microscopes are consequently needed to help realizing the full potential of these 3D cell culture studies by gathering large quantitative and systematic data over extended period of time while preserving the integrity of the living sample [9].

In microscopy, optical light microscopes [10] have been the standard tool in biology for several centuries since its systematic introduction in the field by Leeuwenhoek in the late XVII$^{\text{th}}$ century [11]. Ever since, optical microscopes became more and more complex in order to achieve better magnification, contrast and resolution [12]. An increasing resolution is generally accompanied with a small field of view. Nevertheless, the basics did not change: a light source, a sample and multiple lenses to focus [9]. But this increasing complexity leads to increasing costs and a need of trained biologists. Moreover, putting these microscopes in incubator conditions is challenging and usually the biological samples need to be prepared, sometimes with toxic labeling agents, and they are consequently not observed in their natural state.

Some work is done to introduce new physics developments in the context of biological microscopy, trying to find cost-effective, easy to use and robust technologies.

The development of lens-free microscopy [13, 14], based on the in-line holography theory introduced by Denis Gabor in 1948 [15] is addressing these needs in the context of 2D cell culture, providing label-free and non-phototoxic acquisition of large datasets.

This thesis is at the interface of these two new fields. It aims at creating a lens-free microscope to reconstruct large volumes of 3D cell cultures while preserving the ability to catch every single cell. At the beginning of this work, the laboratory expertise was focused on lens-free microscopy of 2D cell cultures both in terms of experimentation and computer-based reconstruction. From this knowledge in the realm of 2D cell cultures, lens-free diffractive tomography microscopes performing multi-angle acquisitions are designed and built. In parallel, an intensive work is done on implementing dedicated 3D holographic reconstruction algorithms. Reconstructions are finally performed both on simulations and real samples embedded in Matrigel®, fixed or living.

This manuscript begins with an overview of the 3D cell culture context and its standard microscopy before focusing on the lens-free imaging development applied to 2D cell cultures.

Then, the second chapter is devoted to an introduction of the 3D diffraction physics and the formalism used all along this manuscript. This chapter is not essential for the reader already familiar with the concepts of 3D diffraction physics.

Afterwards, this thesis follows globally chronologically the work done during this PhD work. It introduces the different choices for the design and the associated algorithms. A first bench is built to get in touch with the 3D imaging and its constraints while giving the opportunity to reconstruct the first 3D volumes. From this first experience, a second design is made to overcome the limitations of the first prototype and the associated codes.

The conception of prototypes, parallel to the development of the reconstruction codes allows to simultaneously develop these two sides of this PhD work, leading to an overall improvement of the 3D reconstruction techniques and imaging.

Thus, the third chapter focuses on the first prototype and its associated reconstruction codes. It is mainly composed of designs or methods whose developments are not pursued because of their limitations and drawbacks. It is needed in order to fully understand the reasoning which leads to the choices made in terms of prototypes and algorithms for the following. It introduces the basics for the algorithms later developed. As a consequence, an in-depth comprehension by the reader is not compulsory to understand this PhD work and the following of the thesis.

The fourth chapter constitutes the core of this thesis. It presents the chosen solutions in terms of design for a 3D lens-free microscope as well as the dedicated fully 3D reconstruction algorithms which are implemented.

The final chapter focuses on the adaptation of the 3D lens-free microscope to incubator conditions. It introduces time-lapse results obtained on cell cultures which are followed during several weeks as well as the characterization of the proposed 3D tomographic lens-free microscope.

The following figure is a schematic summary of this thesis. The left column

presents the different diffraction models from the literature which are used in this PhD work. The central column summarizes the reconstruction algorithms adapted to lens-free microscopy which are developed and implemented in this thesis. The right column introduces the three different lens-free prototypes which are designed, built and tested.

The green lines link the algorithms to their corresponding physical model used to reconstruct the 3D objects. The blue lines link the different prototypes with the algorithms used to reconstruct their acquisitions. The faint black arrows indicate the genealogical dependence of the methods, algorithms and designs.

The red frames highlight the models, algorithms and designs, mainly presented in the third chapter, which are finally abandoned in this thesis.

The dates indicate the time frame of the development of the corresponding algorithm or prototype in the format *year/month*.

Finally, Roman and Arabic numerals indicate the chapter and the section in which each model, algorithm or prototype is introduced in this thesis.

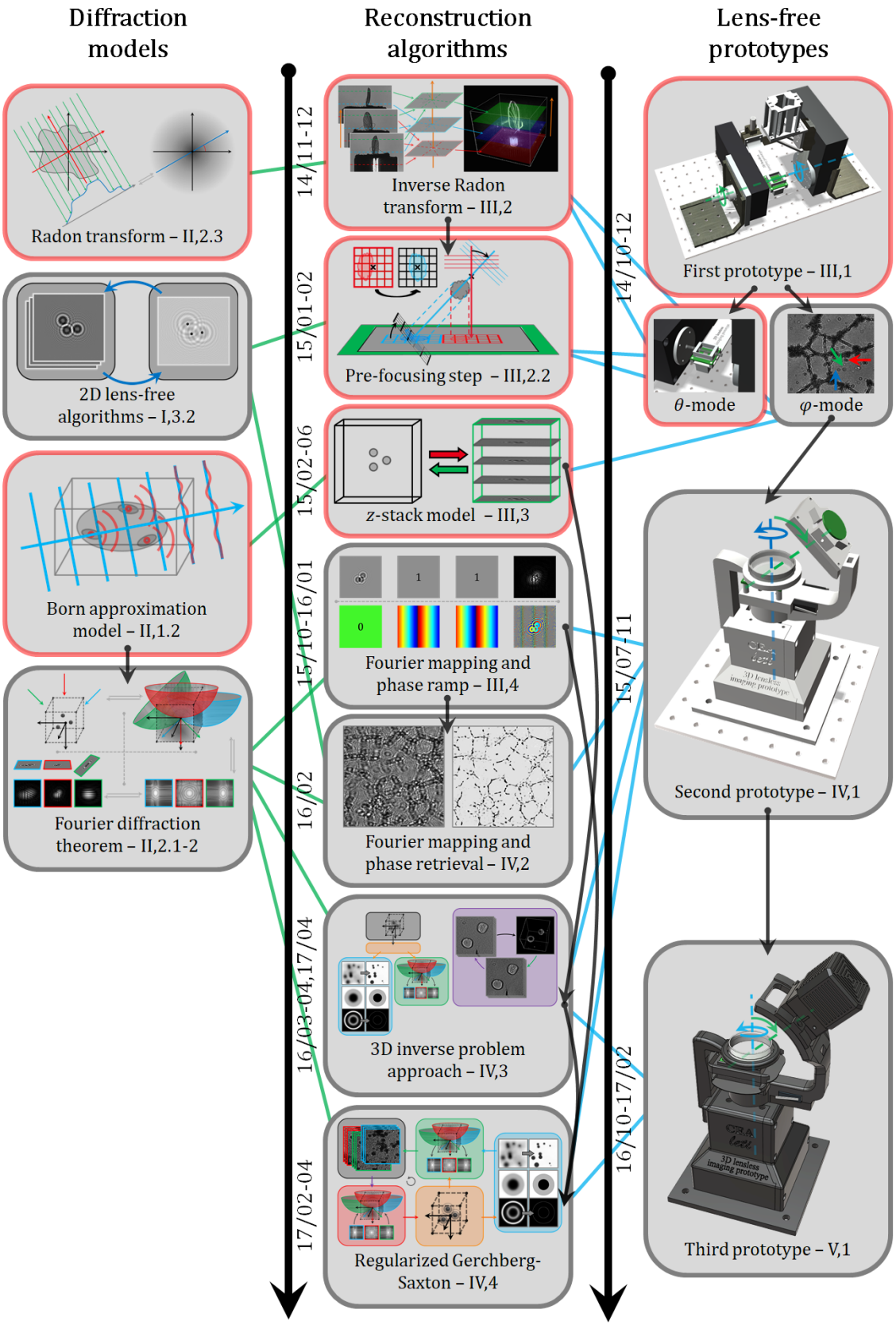
Diffraction models
Reconstruction algorithms
Lens-free prototypes
Radon transform – II,2.3
2D lens-free algorithms – I,3.2
Born approximation model – II,1.2
Fourier diffraction theorem – II,2.1-2
14/11-12
15/01-02
15/02-06
15/10-16/01
16/02
16/03-04,17/04
17/02-04
Inverse Radon transform – III,2
Pre-focusing step – III,2.2
z-stack model – III,3
Fourier mapping and phase ramp – III,4
Fourier mapping and phase retrieval – IV,2
3D inverse problem approach – IV,3
Regularized Gerchberg-Saxton – IV,4
14/10-12
15/07-11
16/10-17/02
First prototype – III,1
θ-mode
φ-mode
Second prototype – IV,1
Third prototype – V,1

Chapter I

Context and state of the art

This chapter sets the biological context of 3D cell culture and its standard imaging tools. It also introduces the development of lens-free microscopy in the field of 2D biology and its first adaptations to 3D samples.

1 Overview of the development of 3D cell culture

1.1 A brief history

Since its beginning, standard of cell biology has been 2D cultures in Petri dishes. Lots of standardized protocols emerged to perform biological research at large scale in several domains, from fundamental biology to drug screening.

But nowadays, it is commonly admitted that such a simplified model introduces important observational biases in the experiments and hides lots of biological phenomena [4]. Animal experimentations became the standard method to perform biological studies in a more realistic 3D environment but raise ethical and repeatability concerns.

3D cell cultures are considered as an alternative tool to animal models to perform experiments on complex samples or small artificially grown organs in a more controlled environment [3, 6].

The missing of standardized 3D cell culture was due to the lack of methods to grow cells in three dimensions and leading to a abscence of imaging tools to study them because of the unexisting of demand [9].

For a few years, new techniques have emerged based on extracellular matrices in the form of gels, such as Matrigel®[1], that allowed growing the first 3D cultures on small scale (few hundreds of microns). New protocols are being developed to overcome the technological challenges of 3D cell culture and new fields of biology are being opened [6, 8].

[1] It is a gel composed of a gelatinous protein mixture secreted by Engelbreth-Holm-Swarm (EHS) mouse sarcoma cells [16]. It resembles the complex extracellular environment found in many tissues and is used by cell biologists as a substrate for culturing cells, especially in a 3D environment.

New microscopes and imaging tools are consequently needed to explore the full potential of 3D organoid culture studies.

1.2 Access to new phenomena

As mentioned above, 3D cell cultures provide a new access to biological phenomena which cannot be observed in standard 2D biology. Even if these experiments are not the scope of this thesis, it can be interesting to keep in mind what will be the type of samples that a new 3D microscope will have to deal with.

The following non-exhaustive list gives an idea of the potential applications, both in fundamental biology and pharmaceutics research. It is mainly inspired from the reviews [4], [7] and [8] where the interested reader can find all the details and references.

Cell adhesion, 3D motility and chemotaxis - Adherent cells on 2D subtract and cells evolving in three dimensions do not present the same migration strategies. In 2D conditions, the migration is mainly driven by the strength of the cell-surface adhesion, and cells adapt their shape according to a specific distribution of transmembrane adhesion proteins. In 3D, cells adopt different strategies according to the extracellular matrix and the biological situation (individual or collective migrations, clusters or multicellular sheets). The use of extracellular gel matrix provides also a new tool to study chemotaxis [17]. Indeed, the liquid culture medium in standard 2D experiments hides the local effects as it quickly mixes the proteins possibly produced by the cells, preventing to study their effect. A gel matrix will lead to a spreading of these potential chemo-attractants based on diffusion responsible for heterogeneities in the gel.

Gene expression - As for the cell motility, the culture conditions influence the gene expression of the cells [4, 7, 8]. Studies show that it is more complex in a 3D environment, leading to similar expression as in real tumors for example.

Epithelial and endothelial cell morphogenesis - In 3D, such cells present a highly different phenotype than their 2D equivalent [4, 7]. The first ones are able to differentiate to create polarized and organized structures. The second ones shape stable cellular networks and allow studying angiogenesis.

Embryogenesis and developmental biology - 3D cell culture gives access to the early stages of an embryo formation. Studies showed that it is an intrinsic 3D phenomenon since the mechanical forces play a role in the cell differentiation [4, 7].

Oncology - As mentioned above, the gene expression presents a more realistic pattern in three dimensions. Moreover, small tumors derived from real tumorous cells can be grown in 3D culture in a more realistic situation [3]. Co-cultures, in which different kinds of cells are simultaneously grown, lead to a more complex simulation of how a tumor can interact with its environment. Such a model coupled with angiogenesis experiments can help to better understand tumor formation and growth and to look for new cures [5].

Drug screening and toxicology - Beyond oncology, deficient organs (for example in autoimmune diseases) could be reproduced at small scale through 3D cell culture techniques. It provides a new tool to test and select drugs prior to an animal test, lowering the costs and the needs in laboratory specimens or patients [3, 5, 18].

2 Standard 3D imaging of biological sample

The rise of three dimensional cell cultures created a need for new imaging technique adapted to this new culture modality. In specific conditions, a prepared sample can be imaged with classical microscopes. Nevertheless, fluorescence microscopy remains the most commonly used techniques to study 3D samples at high resolution and different scales. This powerful tool needs to label the sample, which raises concerns about its toxicity. To overcome these limitations, new techniques based on coherent illuminations begin to emerge and provide complementary tool to study these 3D cultures.

2.1 Standard microscopy

Only needing a classical microscope, optical projection tomography techniques take benefit from the tools of the computed tomography [19] initially developed in the context of X-ray imaging [20].

In this technique, the sample is firstly fixed into a transparent hydrogel such as agarose. If the illuminating parallel rays pass though the sample with negligible refraction or scattering, one can record the absorption map of the 3D sample at different angles (see figure I.1.a). Using a filtered back-propagation algorithm [20], the 3D volume can be reconstructed 2D slice by 2D slice (the red slice in the figure).

Optical clearing [21] of biological tissue allows extending the application of this technique. It is well adapted to mesoscopic scale and is routinely applied in developmental biology on embryos (chick, mouse, zebrafish, drosophila, ...) or isolated organs of developed specimens (limb, brain for instance) [22]. Nonetheless the admissible wavelengths for the illumination are limited in the infrared window which can go through several centimeters of biological tissue and consequently limit the resolution.

It is very important that the sample remains unchanged during the rotation to perform the acquisition. It requires a specific preparation in which the sample is killed and immersed in a transparent hydrogel. Even if some live optical projection tomography experiments have been implemented [22], this technique is hardly applicable to living cultures in Petri dishes.

2.2 Fluorescence microscopy

Fluorescence microscopy remains the standard technique to study 3D biological cell cultures [23]. The principle of fluorescence microscopy [24] is based on the fluorescence of specific molecules, the fluorophores, spread among the 3D sample.

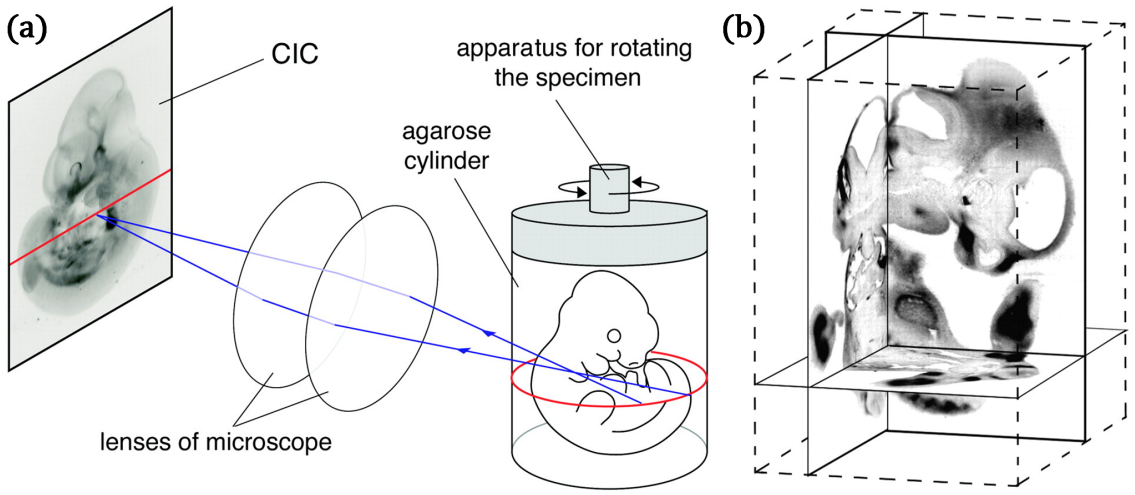

Figure I.1: (a) Scheme of an optical projection tomographic microscope. The specimen is rotated within a cylinder of agarose while held in position for imaging by a microscope. Light transmitted from the specimen (blue lines) is focused by the lenses onto the camera-imaging chip (CIC). The apparatus is adjusted so that light emitted from a section that is perpendicular to the axis of rotation (red ellipse) is focused onto a single row of pixels on the CIC (red line). (b) The 3D reconstruction of the embryo shown in (a). Virtual sections in three orthogonal planes are shown, within the context of the full 3D block of voxel data. Courtesy of [19].

These molecules can for instance be fixed on microbeads or antibodies or can be directly expressed by genetically modified cells. Illuminated with a specific exciting wavelength λ_{ex}, a fluorophore absorbs the light and re-emits it in a different wavelength λ_{em}. Using a filter, this light can be imaged by standard microscopy to give a repartition map of the fluorophores.

The principal advantage of this technique is its high signal to noise ratio.

The three main techniques are the confocal microscopy, the light-sheet microscopy and the multi-photon microscopy (and their derivatives).

Confocal microscopy - In confocal microscopy [25], apertures after the light sources and before the sensor conjugate a point in the 3D sample on the focal plane of the microscope and the light detector (see figure I.2). The 3D volume is scanned by translating either the sample or the optical parts along the three directions. This modality of acquisition presents an important photo-toxicity for the sample since at each acquisition of a point in the volume, the exciting light passes through the whole culture.

Light-sheet microscopy - Light-sheet microscopy [26] partly solves this issue by shaping the exciting beam with a cylindrical lens into a thin plane orthogonal to the acquisition tool (see figure I.3) or into a line scanning this plane. This allows reducing the acquisition time as a whole plane is acquired at a time and the photo-toxicity since the sample is illuminated once per acquisition.

Multiphoton microscopy - Multiphoton microscopy [27] is an evolution of

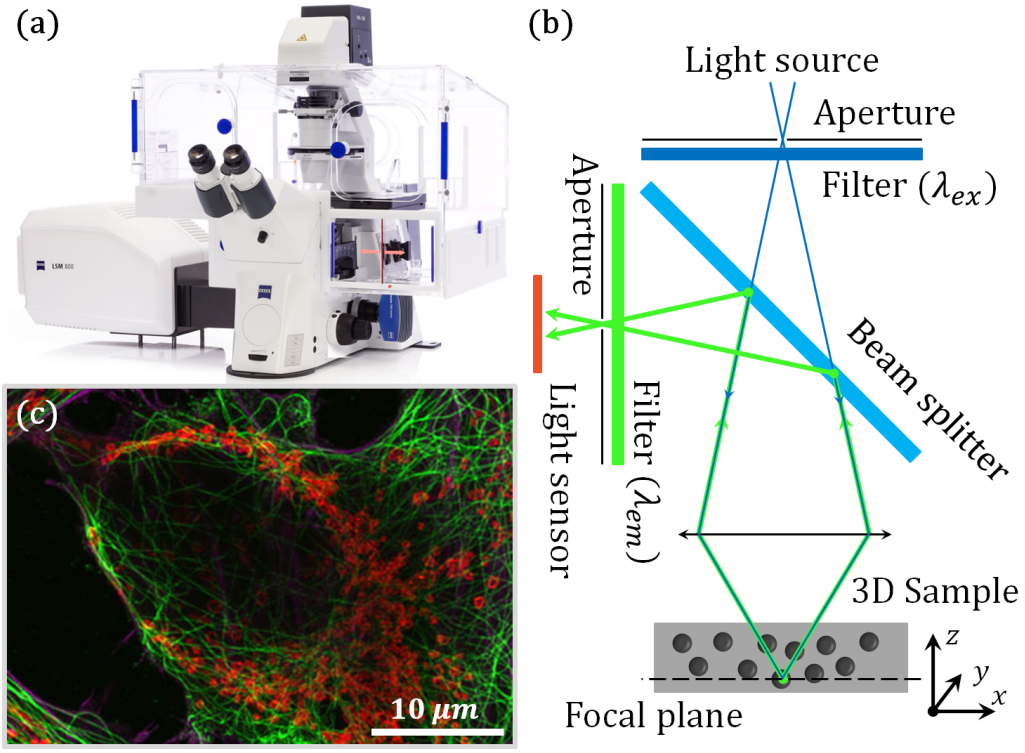

Figure I.2: (a) An example of a confocal microscope: the ZEISS LSM 800. (b) Schematic principle of confocal microscopy. (c) HeLa cells, red: mitochondria membrane, green: microtubuli, magenta: actin fibers. Sample: courtesy of Arne Seitz, EPFL, Lausanne, Switzerland.

confocal microscopy where the exciting wavelength is set to λ_{ex}. It takes benefit from the fact that a fluorophore can either absorb a photon with a wavelength of λ_{ex} or two photons with a wavelength of $2\lambda_{ex}$ if they arrive at the same time at the same location. Because of this strong constraint, fluorescence can only occur at the focal point of the laser beam where the density of photons is the highest. This leads to three major improvements. Firstly, for a given illumination intensity, the efficiency of the microscope is increased since less photons are lost in out-of-focus absorption. Limiting background fluorescence, this also increases the resolution. Secondly, this kind of microscope is less sensitive to the scattering of the re-emitted light in the sample since it physically comes mainly from the focal point. There is no need any more of the aperture before the sensor to conjugate the focal point with the detector. This increases the sensibility of the method. As a lower intensity is needed, this strongly decreases the photo-toxicity of the confocal technology. And finally, the use of longer wavelengths makes possible to probe the sample more deeply as such wavelengths are less scattered and absorbed by biological tissues. This technique is consequently well suited for the study of *in vivo* tissues. Moreover, for some biological samples with specific geometrical and polarization properties, the

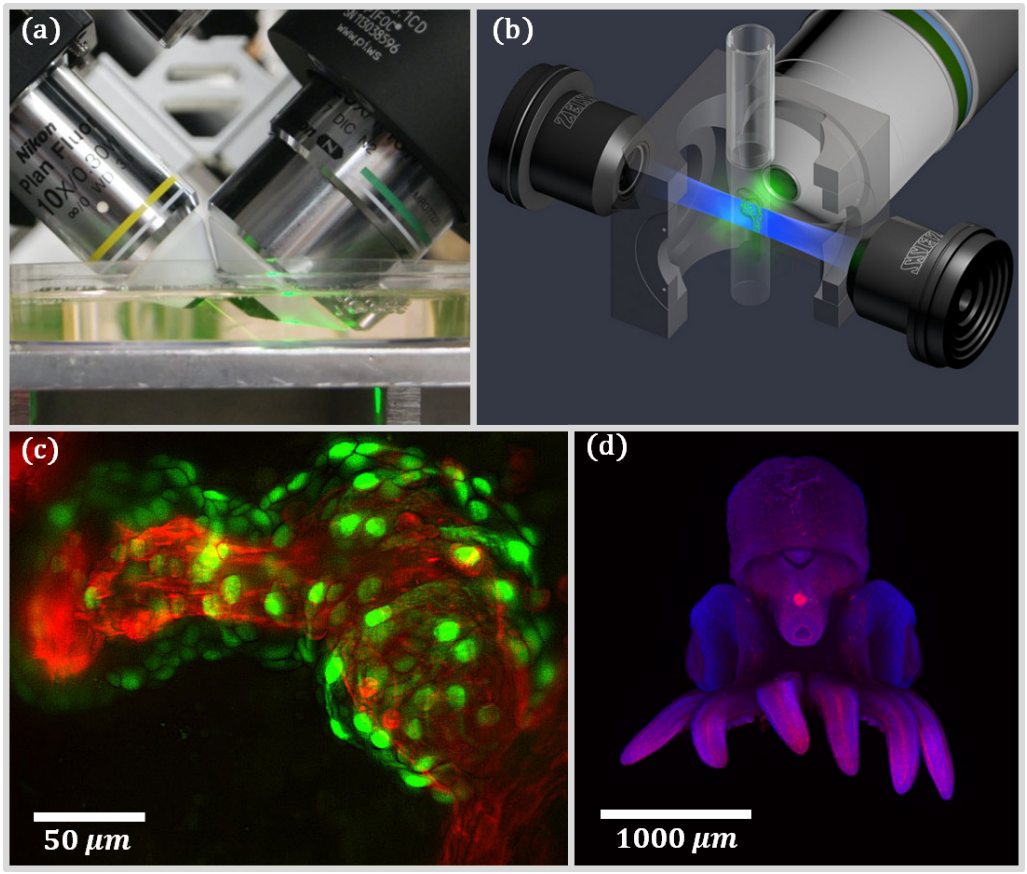

Figure I.3: (a) An example of a light-sheet microscope: courtesy of Cambridge Advanced Imaging Centre. (b) Detailed view of the ZEISS Lightsheet Z.1. (c) Light sheet fluorescence microscopy images the beating heart of a 2 days old zebrafish embryo over extended periods of time, delivering maximal frame rates (80 to 100 fps) with only minimal light exposure. The 2-channel fluorescence image dataset shows blood vessels and the endocardium labeled in red, the myocardium in green. Sample: courtesy of M. Weber and J. Huisken, MPI-CBG Dresden, Germany. (d) Octopus bimaculoides, age approx 1 month. Light Sheet Fluorescence Microscopy with fluorochromes Alexa 546 phalloidin - actin/muscle and To-Pro3 Alexa 642 - DNA. 5x (0.6 zoom) Maximum Intensity Projection. Sample courtesy of Eric Edsinger and Daniel S. Rokhsar, Okinawa Institute of Science and Technology.

second [28] or third [29, 30] harmonic generation[2] can provide a label-free tool which does not suffer the effects of phototoxicity or photobleaching.

These different techniques achieve very good optical resolution and can even go beyond the diffraction limit if super-resolution techniques are implemented, such as PALM (PhotoActivation Localization Microscopy [31]), STORM (Stochastic Optical Reconstruction Microscopy [32]) or STED (Stimulated-Emission-Depletion fluorescence microscopy [33]) for example. Fluorescence labeling provides a unique and

[2]These non-linear effects are nevertheless not strictly based on fluorescence phenomena.

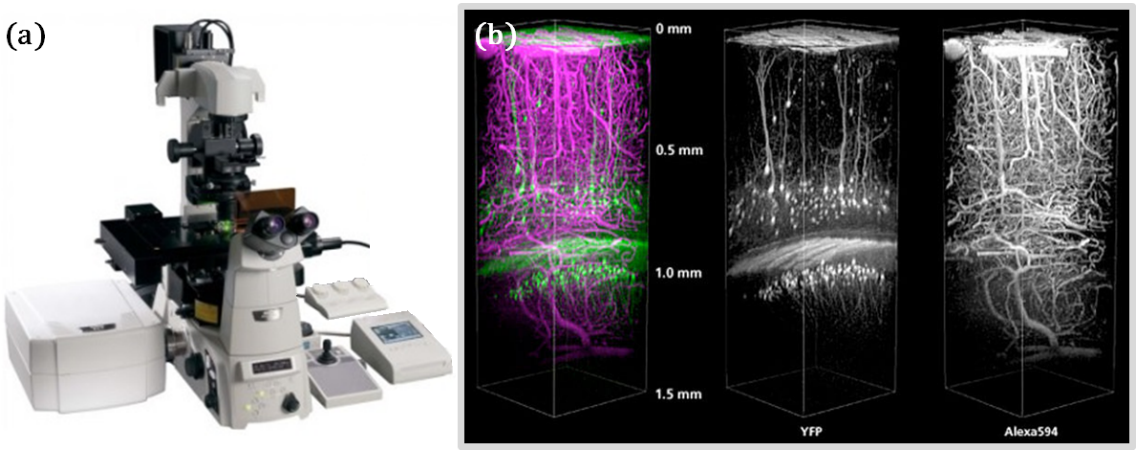

Figure I.4: (a) An example of a multiphoton microscope: the Nikon's A1R MP+. (b) The cerebral cortex of an anesthetized YFP-H mouse (4-week-old) studied with the open skull method. Alexa594 was injected into the tail vein to visualize the blood vessel. Courtesy of: Drs. Ryosuke Kawakami, Terumasa Hibi and Tomomi Nemoto, Research Institute for Electronic Science, Hokkaido University.

powerful tool to identify and trace specific molecules in a large range of scales in a sample, from the whole cell itself to its internal nanoscopic structures via the expression of fluorescent proteins in genetically modified cells. In addition biological fluorescent dyes became a standard tool in biology in the study of cell cultures both for 2D and 3D applications.

Nevertheless, fluorescence microscopy has inherent drawbacks. Only a few endogenous fluorophores are already present in biological samples [34] and generally have an excitation wavelength in the ultraviolet, harmful to the cells. There is consequently a need to either label or genetically modify the cells, which means that the cell culture is never observed in its natural state. This also means that the sample must be specifically prepared and labeled within an adapted culture protocol, a step which is time consuming. Furthermore, despite some examples in specific configurations [28, 35], fluorescence is generally not quantitative and some fluorophores may induce toxicity, either because their activation degrades the molecules or releases toxic agents for the cell. Adding the fact that some may see their performance degrades along time, it makes hard to study a given sample for extended periods of time. Finally, the analysis of a sample via fluorescence microscopy is limited to the parts which can be fluorescently labeled, the other parts being not observable.

2.3 Coherent microscopy

To overcome the limitations of fluorescence microscopy listed above and in order to provide complementary tools to analyze cell culture, new tools emerged based on coherent imaging. The resulting signal depends on the optical path traveled by the light rays and is directly linked to the local complex refractive index of the sample. It is a very powerful and label-free mean to probe the physical features of a biological

sample [36].

Optical coherence tomography - Optical coherence tomography is an efficient tool to scan deeply into tissues [23, 37, 38]. It consists of a Michelson type interferometer (see figure I.5.a) with a low coherence light source (blue). Light is split into two arms. One arm (red) travels through the sample and ballistic photons are reflected on the discontinuities. They interfere with the reference arm (green) and the resulting signal is recorded by a sensor. As the coherence is low, there is interference only if the depth of reflection matches the length of the reference arm. The scan in depth is then either performed by translating the mirror or via a frequency shaping of the illumination and the frequency analysis of the resulting interference. This geometry is very efficient to detect surface discontinuities and makes it an adapted tool to study the retina or the skin (to detect cancers or analyze burns for instance). It can also be applied to embryos or brain tissues or small animals such as the zebrafish.

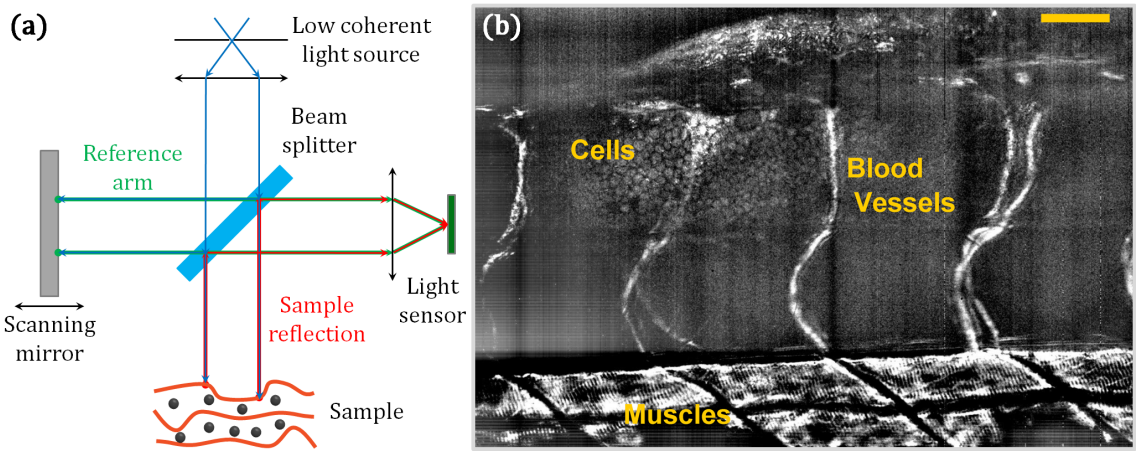

Figure I.5: (a) Schematic principle of the optical coherence tomography: a Michelson type interferometer. (b) *In vivo* dynamic FF-OCT in a 2 days post fertilization zebrafish larva. Despite strong phase variations caused by the blood flow, which generates a strong dynamic signal, some cells can still be revealed in between the capillaries. The scale bar represents 40 μm. Courtesy of [38].

Optical diffractive tomography - Optical diffractive tomography emerged with the development of the digital holographic microscopy [39]. This kind of microscope allows recording the wave diffracted by a sample illuminated by a coherent source (see figure I.6.a). Different configurations exist. The most common configuration uses a reference arm to produce off-axis holograms. This allows retrieving full information on the diffracted wave both in terms of amplitude and phase. This type of microscope does not need any labeling or staining of the sample which can be studied in its natural state. It is directly sensitive to the sample local complex refractive index which provides complementary information compared with the fluorescence microscopy. The sample can be segmented according to its absorption (the imaginary part of the complex refractive index) or its refractive index (the real part

of the complex refractive index) [40, 41]. The 3D lens-free microscope developed during this PhD belongs to this kind of microscopy.

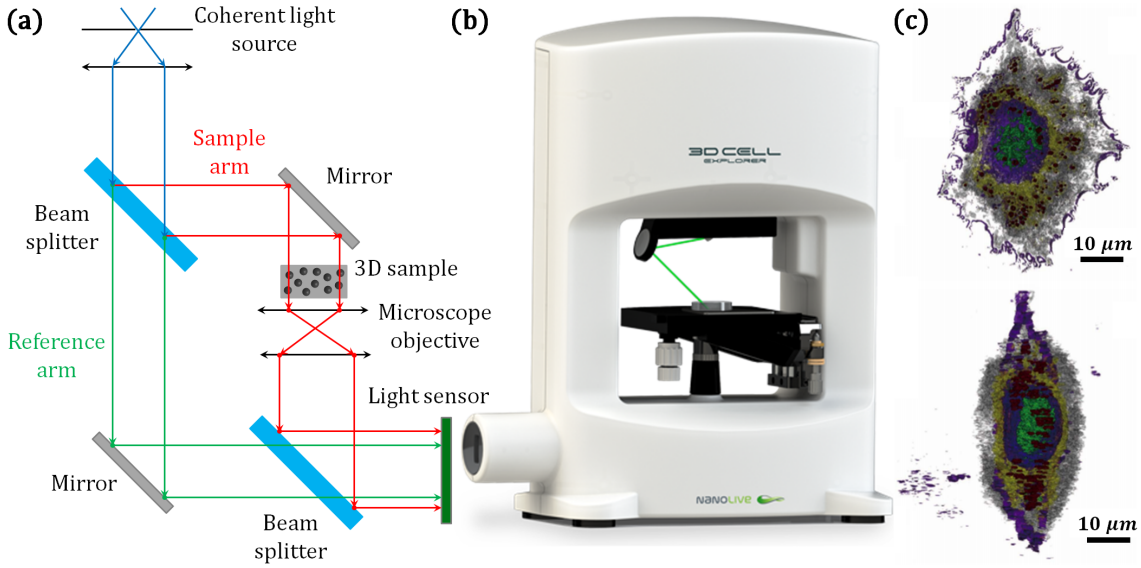

Figure I.6: (a) Schematic principle of optical diffractive tomography: the result of the diffraction of a coherent light through the 3D sample is recorded. The use of a reference arm which interferes with the diffracted wave allows retrieving the phase information of the complex wave which is lost otherwise. (b) An example of an optical diffractive tomographic microscope: the 3D Cell Explorer (Nanolive). (c) 3D rendering of a HepG2 cell with a 3D Cell Explorer, top view and side view. Each color represents a different refractive index range. Courtesy of [42].

Since the first works in tomography with digital holographic microscopes, the technique evolved. At first, the retrieved 2D pictures at each illumination angle were interpreted as overall phase delay introduced by the sample in the optical path, directly linked to the integral of the refractive index along the line of sight [43]. They were consequently processed similarly to the absorption maps produced in X-ray tomography and the volume was retrieved via Radon transforms in a filtered back-propagation algorithm [20]. It showed the potential of digital holographic microscopes to retrieve information on 3D cell cultures. Assuming that the propagation inside the sample follows straight lines, this model nevertheless does not take into account the diffraction inside the sample. Indeed, in optical wavelengths, the sample scatters the incoming illumination.

New works are taking into account this diffraction using either the Fourier diffraction theorem[3] [44, 45, 46] or multi-slices models in which the diffraction is simulated in a volume numerically cut slice after slice approximated by 2D diffracting planes [47].

These techniques generally require multiplying the viewing angles around the sample to obtain the 3D information. The solution is either to rotate the sample in

[3]See chapter II, section 2

the microscope or, to avoid any complex sample preparation, rotate the illumination itself, for example by tilting the mirror in the sample arm in the figure I.6.a.

Some recent works try to remove any moving parts in the system to reduce the cost of such microscopes. Some of them uses a LED array to change the illumination angle [47, 48], or to retrieve phase contrast and bright-field images [49][4]. Some others replace the tilted illumination by structured illuminations to retrieve similar information [50, 51].

All these techniques nevertheless work on sample limited in size. Indeed, the general framework assumes low scattering objects[5]. Researches then focus on achieving the best resolution on small volumes (cubes with sides of few tens of microns).

2.4 Lens-free microscopy: a complementary tool

As shown above, the study of *in vitro* cell populations remains a challenging task if one needs to gather large quantitative and systematic data over extended periods of time while preserving the integrity of the living sample. Most of the techniques introduced above also have a limited field of view, raising the issue of missing isolated events if a cell culture presents multiphenotypes at the same time.

As discussed in [9], there is a need for a new microscopy technique that must be label-free and non-phototoxic to be as "gentle" as possible with the sample, and "smart" enough to observe the sample exhaustively at a variety of scales both in space and time. Lens-free video microscopy is addressing these needs in the context of 2D cell culture (see [13, 14, 52, 53]).

The main objective of this PhD work is to investigate if this technology can be adapted to 3D cell cultures in order to provide a complementary tool from the ones presented above.

Figure I.7 gives a quick overview of these different techniques and their pros and cons as well as the expectations awaited from a 3D lens-free microscope.

3 Development of lens-free time-lapse microscopy

This section gives a brief overview of the 2D lens-free microscopy and introduces some tools and notions that will be used in the 3D problem.

3.1 Principle and potential

The 2D lens-free microscopy is based on the in-line holography principle introduced by Denis Gabor in 1948 [15]: a coherent illumination is scattered by a 2D sample, leading to interference patterns which are recorded by a photographic plate. If a coherent light, so-called reference field, is then diffracted back through this hologram, an image of the original 2D transmissive plane is created.

[4]This work [49] does not remove all moving parts since a translation stage is used to scan the sample along the z-direction.

[5]See chapter II, section 1.2

	Labeling (staining, fluorescence)	**Sample-friendly** (toxicity, fixing)	**Resolution**	**Field of view**	**Time-lapse**	Biological sample
Optical projection tomography	No fluorescence staining possible	Clearing, fixing	$> 10\ \mu m$	$\sim cm^3$	Hardly adapted to incubator	Embryo, zebrafish, transparent tissues...
Confocal microscopy	Fluorescence	Strong light toxicity	$< 1\ \mu m$	$\sim 0.1\ mm^3$	Specially adapted incubator	Cell culture, Petri dishes
Light sheet microscopy	Fluorescence	Light toxicity	$< 1\ \mu m$	$\sim 0.1\ mm^3$	Specially adapted incubator	Cell culture, Petri dishes
Multiphoton microscopy	Fluorescence	Reduced light toxicity	$< 1\ \mu m$	$\sim mm^3$	Specially adapted incubator, *in-vivo* imaging	Cell culture, Petri dishes, tissues, brain, ...
Optical coherence tomography	No fluorescence staining possible	Biological infrared window, label free	$\sim \mu m$	$\sim 10\ mm^3$	*In-vivo* imaging	Skin, brain, retina, tissues, ...
Optical diffractive tomography	No fluorescence staining possible	Low power visible light, label free	$< 0{,}1\ \mu m$	$\sim 0.001\ mm^3$	Adapted incubator	Cell culture, Petri dishes
Lens-free microscopy	No fluorescence staining possible	Low power visible light, label free	$> 5\ \mu m$	$\sim 40\ mm^3$	Compact, standard incubator	Cell culture, Petri dishes

Figure I.7: Table comparing the standard 3D microscopy techniques. A lens-free microscope would complete the panel of possibilities: not competitive in terms of resolution, it gives a label-free imaging tool on large volumes and allows easy time-lapse microscopy in incubator conditions.

Figure I.8 presents a schematic view of the technique in the realm of biological microscopy. To avoid parasitic interferences, the illumination in visible light is only partially coherent. It is obtained by placing a LED behind a pinhole, creating a spherical wave[6]. The sample being placed a few centimeters away, this wave can be approximated by a semi-coherent plane wave. The photographic plate is replaced by a CMOS sensor located a few millimeters behind the sample. It records the resulting interference of the light scattered by the sample: the hologram.

The recovery of the sample image from this hologram is then performed numerically, based on the knowledge of wave propagation physics between the sample and the sensor (see 3.2).

Figure I.8 presents simulations based on the Fresnel propagator[7] h_z, with three opaque discs of radius $r_d = 10\ \mu m$ and a lighting wavelength of $\lambda = 630\ nm$, the sensor being placed at $z_s = 2\ mm$.

Such a compact and minimalistic technology leads to numerous advantages. For instance:

- The absence of lenses or moving parts means robustness and ease of use.
- Such a device can handle incubator conditions, while being user-friendly for the experimenter.

[6]The diffuser in the figure aims to produce a uniform lighting on the pinhole. This is particularly useful in the case of multi-wavelength illumination.

[7]Which will be introduced in the following section 3.2.

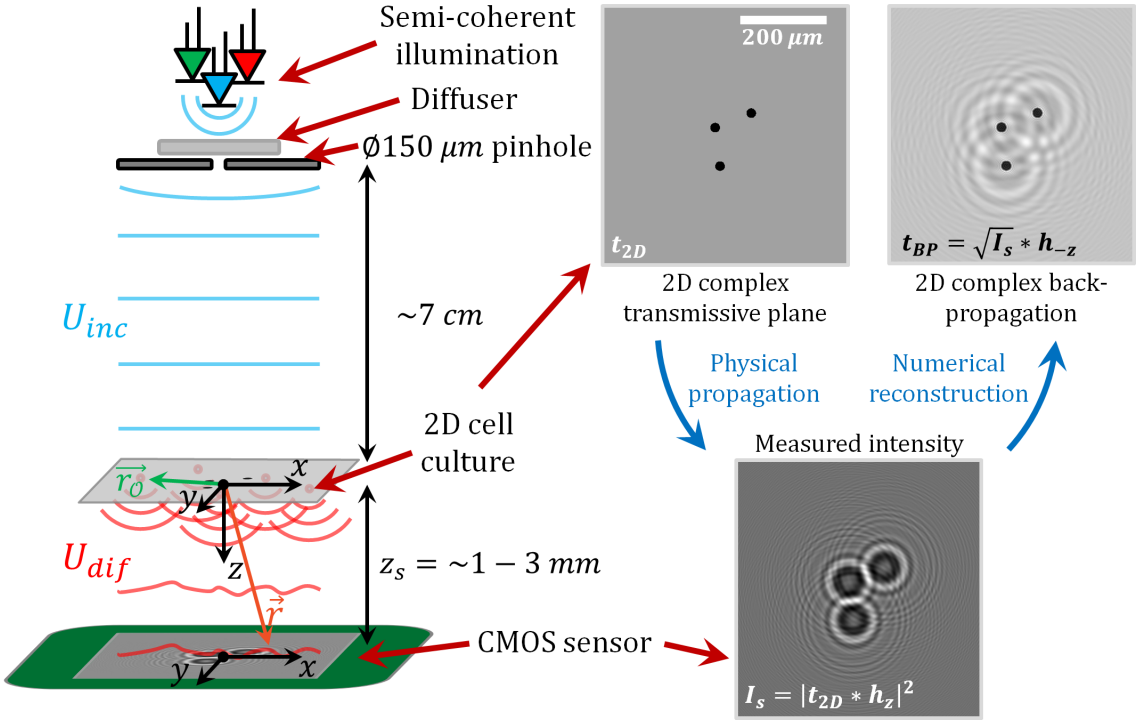

Figure I.8: Schematic diagram of the 2D lens-free imaging. A semi-coherent wave front U_{inc} is generated with a LED placed behind a pinhole: a few centimeters from the pinhole, the spherical wave can be approximated by a plane wave. This incident plane wave diffracts through the 2D biological sample. The resulting diffracted wave U_{dif} propagates in free space toward a CMOS sensor placed a few millimeters away. The sensor measures the produced interference patterns: only the intensity of the wave front is registered, the phase information is lost. A numerical reconstruction is then performed to retrieve the 2D object.

- The field of view is larger than with conventional methods since it is directly the sensor surface and one can think of statistic experiments on large data set, for example for new drug screening applications.
- The method is also label-free and is not toxic for the biological sample, allowing video-microscopy on large periods of time without killing or modifying the sample, which does not need any specific preparation.

But this method also has its drawbacks. For example, as there is no magnification, the resolution is directly linked to the pixel pitch of the sensors which are currently not competitive with classical optical microscopes[8].

One of the main pitfalls of this optical design is the lack of reference beam, leading to the loss of the wave front phase in the recording step. The numerical reconstruction techniques will consequently have to take into account this lack of information to reduce the resulting artifacts, such as the rings on the simulated

[8] $d_{pix} = 1 \sim 2\ \mu m$

back-propagation in the figure, the so-called "twin image" [54].

3.2 2D in-line holography overview

As previously explained, in a 2D lens-free microscope, there is no lens to perform any magnification or focusing. As a consequence, the hologram recorded by the sensor appears as a "blurred" picture. For example on the simulation of figure I.8, the three spheres appear as unfocused concentric rings.

Even if quantitative and relevant information can be retrieved directly from the holograms without the need of a proper reconstruction (see [55] for example), many applications need a more classical rendering comparable with what can be obtained with a classical microscope. To do so, numerical computation replace the role of the lenses in a lens-free setup by back-focusing the recorded holograms using a physical model of light propagation. The quality of the reconstructions will consequently depend on the quality and accuracy of this model.

In the context of 2D lens-free microscopy, the model is based on the Rayleigh-Sommerfeld diffraction formula [56]. Using the notation of figure I.8, it states that for a monochromatic incident wave U_{inc} with a wavelength of λ_0, the wave U_{dif} diffracted by a 2D complex transmissive plane t_{2D} at $z = 0$ is given at a given point $\vec{r} = (x, y, z > 0)$ by:

$$\boxed{U_{dif}\left(\overrightarrow{r}\right) = \frac{z}{i\lambda_0} \iint\limits_{\overrightarrow{r_\mathcal{O}} \in \mathcal{O}} t_{2D}\left(\overrightarrow{r_\mathcal{O}}\right) U_{inc}\left(\overrightarrow{r_\mathcal{O}}\right) \frac{e^{ik_0 \left\| \overrightarrow{r} - \overrightarrow{r_\mathcal{O}} \right\|}}{\left\| \overrightarrow{r} - \overrightarrow{r_\mathcal{O}} \right\|^2} d^2\overrightarrow{r_\mathcal{O}}} \tag{I.1}$$

where $k_0 = 2\pi/\lambda_0$ is the wave number of the field in free space and $\mathcal{O}$ stands for the 2D object. Using the convolution symbol $\star$, equation (I.1) becomes:

$$U_{dif}\left(\overrightarrow{r}\right) = \left(U_{inc}.t_{2D}\right) \star \left(\frac{z}{i\lambda_0} \frac{e^{ik_0 r}}{r^2}\right) \tag{I.2}$$

The convolution kernel $\frac{z}{i\lambda_0}\frac{e^{ik_0 r}}{r^2}$ corresponds to the equation of a propagating spherical complex wave $\frac{e^{ik_0 r}}{r}$ normalized by the pre-factor $\frac{z}{ir\lambda_0}$. Looking closer, it appears that $z/r = \cos\,\theta$ where θ is the angle between the direction normal to the diffracting plane and the position pointed by $\vec{r}$: the pre-factor gives the "efficiency" of the diffraction according to the angle at which is seen the diffracting 2D object. Equation (I.2) is consequently the mathematical formulation of the well-known Huygens-Fresnel principle: the diffracted wave is composed of the summation of the spherical waves emitted at each point $\overrightarrow{r_\mathcal{O}}$ of the sample, the amplitude of these waves being modulated by the local transmission of the object $t_{2D}\left(\overrightarrow{r_\mathcal{O}}\right)$ and the local value of the incident wave $U_{inc}\left(\overrightarrow{r_\mathcal{O}}\right)$.

This equation gives a tool to propagate a complex field from the object at $z = 0$ to the sensor plane at $z = z_s$, using a convolution. But it does not provide a straightforward tool to perform the reverse operation to retrieve a 2D view of a sample given its hologram on the sensor plane. Indeed, deconvolution can be

complex when the problem is ill-posed[9] or in the presence of noise, two drawbacks which are encountered in the case of the presented in-line holographic microscope.

To overcome these limitations, equation (I.2) can be expressed in a paraxial context: the Fresnel formulation [56]. It is motivated by the facts that the illumination is normal to the sample and the sensor, and that the spatial extension of the holograms is in the order of magnitude of a few tens of microns whereas the distance between the object and the sensor is higher than a millimeter. With $z_s \gg (x, y, x_\mathcal{O}, y_\mathcal{O})$ one gets:

$$\overrightarrow{r} - \overrightarrow{r_\mathcal{O}} = \sqrt{(x - x_\mathcal{O})^2 + (y - y_\mathcal{O})^2 + z_s^2} \simeq z_s + \frac{(x - x_\mathcal{O})^2 + (y - y_\mathcal{O})^2}{2z_s} \tag{I.3}$$

and equation (I.2) becomes:

$$U_{dif}\left(\overrightarrow{r}\right) = (U_{inc}.t_{2D}) \star \left(\frac{e^{ik_0 z_s}}{i\lambda_0 z_s} e^{\frac{ik_0}{2}\frac{r_{2D}^2}{z_s}}\right) = (U_{inc}.t_{2D}) \star \left(h_{z_s}^{\lambda_0}\right) \tag{I.4}$$

where $r_{2D}^2 = x^2 + y^2$ and where the convolution kernel $h_z^{\lambda_0} = \frac{e^{ik_0 z}}{i\lambda_0 z} e^{\frac{ik_0}{2}\frac{r_{2D}^2}{z}}$ is the Fresnel propagator.

This formulation has two main advantages. First of all, the expression of the Fourier transform of the Fresnel propagator can be obtained analytically [57], allowing to perform the convolution in equation (I.4) directly into the Fourier domain with a good numerical precision:

$$\boxed{h_z^{\lambda_0}(x, y) = \frac{e^{ik_0 z}}{i\lambda_0 z} e^{\frac{ik_0}{2}\frac{x^2+y^2}{z}} \Leftrightarrow \hat{h}_z^{\lambda_0}(u, v) = e^{ik_0 z} e^{-i\pi\lambda_0 z\left(u^2+v^2\right)}} \tag{I.5}$$

Secondly, from this equation (I.5), one gets that the inverse propagator of $h_z^{\lambda_0}$ is directly $h_{-z}^{\lambda_0}$ as $\hat{h}_z^{\lambda_0} \times \hat{h}_{-z}^{\lambda_0} = 1$ [57]. With $\left|\hat{h}_z^{\lambda_0}\right| = 1$, it comes that the Fresnel propagator $h_{-z}^{\lambda_0}$ can directly be used to back-propagate the complex field U_{dif} in the sensor plane without any amplification of the noise as in standard deconvolution where the high frequencies diverge.

In addition, for a normal incident plane wave $U_{inc} = U_0.e^{i(k_0 z+\varphi)}$ on the sample, ignoring a complex constant factor of $U_0.e^{i\varphi}$, one can assume that the incident wave is normalized to $U_{inc} = 1$. The 2D transmissive plane is then retrieved by:

$$\boxed{t_{2D} = (U_{dif}) \star \left(h_{-z_s}^{\lambda_0}\right)} \tag{I.6}$$

This method has as a prerequisite the knowledge of the totality of the complex wave U_{dif} both in terms of amplitude and phase. But the sensor is only sensitive to the intensity of this complex field:

$$\boxed{I_s = |U_{dif}|^2 = \left|t_{2D} \star h_{z_s}^{\lambda_0}\right|^2} \tag{I.7}$$

[9] Here the phase information on the diffracted wave is unknown.

As previously mentioned, the problem is consequently ill-posed, leading to the recurrent problem of phase retrieval since the simplicity of the system leads to a lack of a reference beam to get the absolute phase. If nothing is done to retrieve some information on the phase, the reconstructions suffer from artifacts as in figure I.8 where the diffracted wave was approximated by $U_{dif} \simeq \sqrt{I_s}$. The resulting unfocused rings surrounding the reconstructed objects correspond to the "twin-image" artifact [54]. These are the images of the same objects but defocused at $z = 2z_s$. The information on on which side of the sensor the object was supposed to focus is in the phase of the diffracted wave which is lost during the acquisition.

Several phase retrieval techniques can be implemented and are generally based on a Gerchberg-Saxton type algorithm [58, 59] in which back and forth propagations between the experimental data and the reconstructions are iterated to ensure data fidelity on the first side and apply constraints on the second part. Presented in figure I.9.a, this type of algorithm works as follows:

- Step 1: At the first iteration of the algorithm, the complex wave on the sensor is initialized with a modulus corresponding to the recorded intensity and its phase is set to 0. In the next iterations, step 1 insures the data fidelity by replacing in the modulus of the complex wave simulated in step 4 with the square root of the recorded intensity.
- Step 2: Back-propagation of the complex wave from the sensor plane to the reconstruction plane.
- Step 3: Application of *a priori* constraints on the object.
- Step 4: Forward propagation of the complex field from the object to the sensor plane.

This general framework leads to a large variety of algorithms depending on the solutions implemented for the data acquisition or for the constraints application or both and are successfully applied in the context of 2D lens-free microscopy.

Concerning the object plane, the use of a mask remains the most straightforward technique by either spatially limiting the object via an *a priori* knowledge of its shape and position or by constraining its value in a specific domain, for example via non-negativity enforcement when the object must physically be real and positive [60]. This masking technique can be replaced or complemented by regularization on the object [61].

To improve the available information on the object without requiring *a priori* information, the data acquisition process can also be modified: for example with acquisition planes at different distances z_s [61, 62], by multiplying the holograms to perform super-resolution [63] or with multi-wavelength acquisitions [64, 65].

Figure I.9.b presents an algorithm which is used during this PhD work. It was developed during a previous PhD done by Sophie Morel [66, 67] and is based on a RGB acquisition process. The three wavelengths are combined in the object plane as follows:

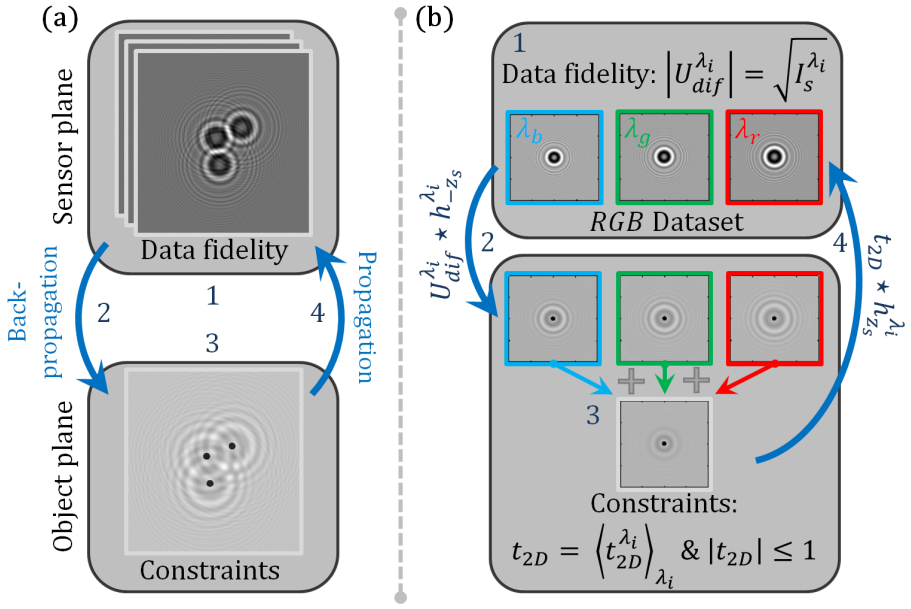

Figure I.9: (a) Schematic diagram of a Gerchberg-Saxton algorithm [58]: in a back and forth loop between the acquisition plane and the object plane, data fidelity is enforced on the first one and constraints are applied on the second one. (b) Scheme of the *RGB* phase retrieval developed for a lens-free *RGB* microscope by Sophie Morel during her PhD. Courtesy of [57].

- Step 1: At the first iteration of the algorithm, each of the complex waves on the sensor at the different illumination $\lambda_j \in \{R, G, B\}$ is initialized with a modulus corresponding to the recorded intensities and a phase set to 0: $U_{dif,0}^{j} = \sqrt{I_s^j}$. In the next iterations, step 1 insures the data fidelity. The simulated complex waves simulated in step 4 are updated to match the recorded dataset: $U_{dif,it}^{j} = \frac{U_{dif,it-1}^{j}}{\left|U_{dif,it-1}^{j}\right|}\sqrt{I_s^j}$.

- Step 2: Each complex wave $U_{dif,it}^{j}$ on the sensor plane is back-propagated using the Fresnel kernel (I.6) $h_{-z_s}^{\lambda_j}$.

- Step 3: The object t_{2D} is then retrieved by averaging the three obtained complex fields t_{2D}^{j}: $t_{2D} = \left\langle t_{2D}^{\lambda_j} \right\rangle_{\lambda_j}$. As the object cannot emit light in the presented model, a constraint of domain is applied by forcing its modulus to be lower than 1: $|t_{2D}| \leq 1$.

- Step 4: The object t_{2D} is propagated in the three wavelengths using the Fresnel kernel (I.7) $h_{z_s}^{\lambda_j}$ to simulate intensities for the next loop: $I_s^j = \left|t_{2D} \star h_{z_s}^{\lambda_j}\right|^2$

This algorithm is simple to implement and runs fast, providing good results within only a few iterations.

3.3 First work in 3D lens-free microscopy

Inspired from the techniques and algorithms developed for microscopes with lenses, some works were published in the field of 3D lens-free microscopy. But this still remains a marginal technology in optical diffractive tomography.

Ozcan's team at UCLA in the US, very prolific in 2D lens-free microscopy, developed an experimental bench to perform 3D tomography [68, 69]. Figure I.10 presents some results on C. Elegans. "The partially coherent light source with spectral bandwidth of, *e.g.*, approximately $1-10\ nm$, is filtered through a large aperture with diameter approximately $0.05-0.1\ mm$. The light source is rotated to record lens-free holograms of the micro-objects from multiple viewing angles. The device also includes the work developed by the team to perform digital super-resolution: 9 holograms are recorded, at each angle, by translating the aperture in the plane parallel to the sensor within a 3×3 grid with discrete shifts of $< 70\ \mu m$ (see the inset in figure I.10.c)."

The tomographic algorithm uses standard 2D lens-free reconstruction. "A scaling factor is used to correct the deformation of the holograms acquire with an angle. Once each of the holograms is reconstructed, a filtered back-propagation algorithm [20] based on the Radon transform is used to retrieve the 3D volume. And finally, image deconvolution is applied to all the presented microscope images and tomograms in figure I.10 to further improve their image quality." As mentioned earlier for [43], this model does not strictly take into account the 3D diffraction in the sample and is consequently limited on objects with a small extension along the axial axis.

Figure I.11 presents the results from Chen's Chinese team [70]. There is no moving part in the system: the multi-angle viewing is performed with a LED array. Using *RGB* illumination, a 2D phase retrieval is performed for each angle to extract the complex diffracted waves both in terms of amplitude and phase. These are used to map the 3D Fourier transform of the 3D sample via the Fourier diffraction theorem[10], commonly used in optical diffractive tomography. To compensate the missing information due to the limited angular coverage, iterative algorithm with non-negativity constraint is applied, inspired from [44]. This work presents techniques and algorithms very similar from the ones developed in this thesis[11].

[10] See chapter II, section 2

[11] See chapter III, section 4 and chapter IV, section 2.

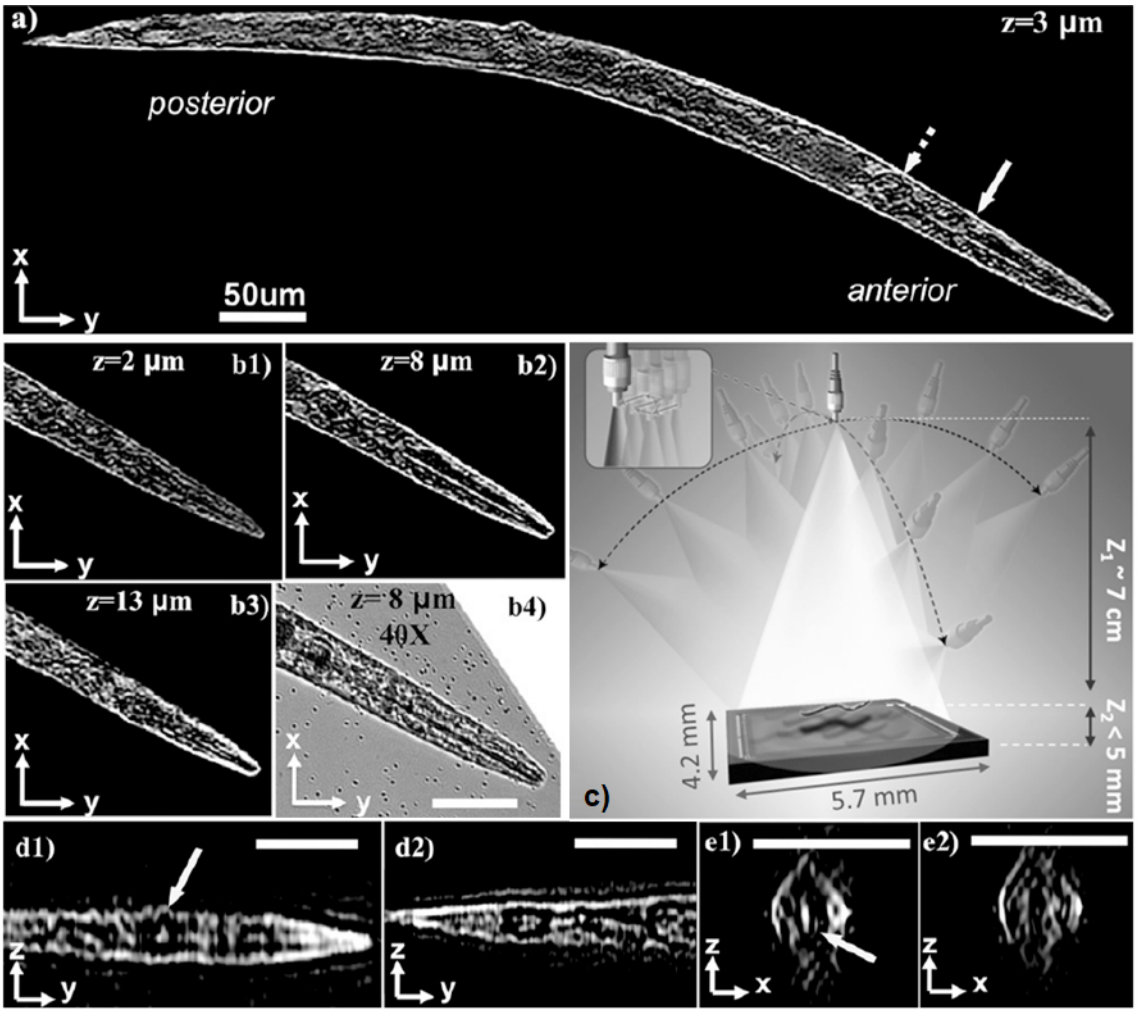

Figure I.10: Application of lens-free on-chip tomography toward 3D imaging of C. Elegans. (a) A tomogram for the entire worm corresponding to a plane that is 3 μm above the center of the worm. (b.1–3) Tomograms at different layers for the anterior of the worm. The pharyngeal tube of the worm, which is a long cylindrical structure with < 5 μm outer diameter, is clearly visible at $z = 8$ μm plane, and disappears at outer layers. (b.4) A microscope image (40X, 0.65NA) for comparison. (c) Schematic diagram of the lens-free tomography setup. The sample is placed directly on the sensor array with < 5 mm distance to the active area. (d.1-2) $y - z$ orthogonal slices from the anterior and posterior regions of the worm, respectively. (e.1-2) $x - z$ orthogonal slices along the direction of the solid and dashed arrow in (a), respectively. The 3D structure of the anterior bulb of the worm, pointed by the solid arrows, can be probed by inspecting (a) and (d.1). Scale bars, 50 μm. Courtesy of [68].

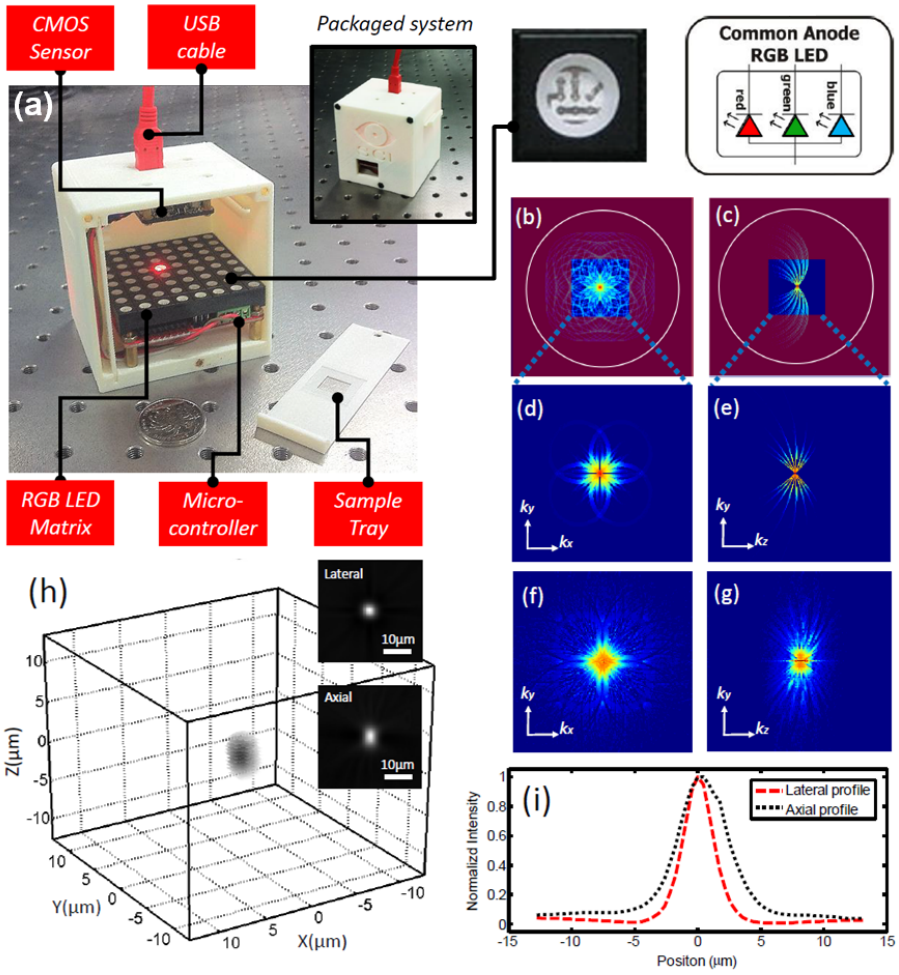

Figure I.11: (a) Picture of the microscope. The system consists of a CMOS imaging sensor and a LED matrix controlled by a MCU, where each LED can provide RGB narrow-band illumination. The whole device is powered through the USB connection. (b-i) Tomographic reconstruction of a 2 μm silica bead. The LED array sequentially illuminates the sample with different LED elements. (b-c) The retrieved complex fields are mapped in 3D Fourier space according to Fourier diffraction theory. (d-e) Due to the limited pixel resolution abilities, the actual detectable frequencies of the platform only occupy a limited portion of the 3D Ewald sphere, while the information in the red shaded region is unrecoverable. (f-g) An iterative non-negative constraint processing method is implemented for filling the rest of 3D space. (h) Finally a 3D inverse Fourier transform yields 3D tomogram of the bead. (i) The FWHM value for the lateral line-profile is 3.41 μm, while the axial FWHM shrinks to 5 μm. Courtesy of [70].

Chapter II

3D diffraction physics

The objective of this chapter is to give a brief overview of the 3D diffractive physics needed in this thesis while introducing the notations and formulations that will be used all along the manuscript.

A first section focuses on the global problem of 3D in-line holography and gives a first simplification of the equations. A second section introduces the Fourier diffraction theorem and its mathematical derivation as well as a geometrical interpretation. A last section compares the different models with real acquisitions and with 2D models and discusses the limitations of the different methods.

1 3D diffraction model of low scattering objects

This section and its notations are mainly inspired from the chapter 6 "Tomographic Imaging with Diffracting Sources" of [20] and from [44]. They are themselves based on the founding work of Emil Wolf [71] published in 1969, for his demonstration of the Fourier diffraction theorem (see section 2).

The objective is to find a relation linking the 3D sample refractive index to the wave front at a given point beyond the sample for a given incident wave.

1.1 Equation of wave propagation

Let's consider a scattering object $\mathcal{O}$ with a complex refractive index n immersed in a homogeneous medium of refractive index n_0 as illustrated in figure II.1. A frame centered on O is arbitrary set in the object, giving the three axes x, y and z.

By convention, the position vectors pointing toward a point in the surrounding space around the object will be noted $\vec{r} = (x, y, z)$ whereas inside the object they will be noted $\overrightarrow{r_{\mathcal{O}}} = (x_{\mathcal{O}}, y_{\mathcal{O}}, z_{\mathcal{O}})$.

The complex refractive index n of the scattering object depends on the position inside the object: $n\left(\overrightarrow{r_{\mathcal{O}}}\right)$. Its real part is the standard refractive index while its imaginary part represents the object absorption [40, 41]. The aim here is to work out

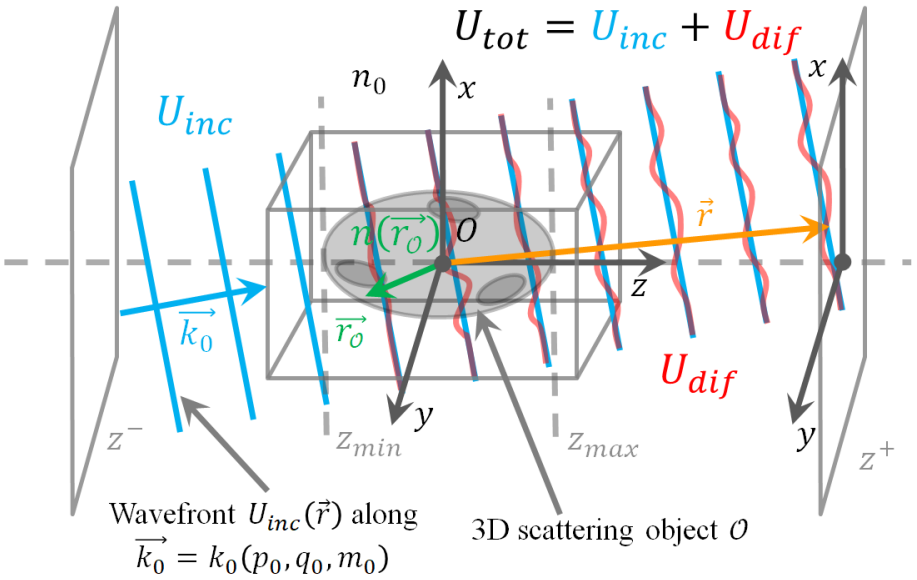

Figure II.1: Illustration of an incident plane wave U_{inc} (in blue) with a wave vector $\vec{k_0}$ scattering through an object $\mathcal{O}$. The resulting total wave U_{tot} is composed of the incident wave and the scattered field U_{dif} diffracted by the object (in red). The direction of the incident wave propagation is given by the unit vector (p_0, q_0, m_0), oriented toward increasing z. z_{min} and z_{max} are the minimal and maximal object's coordinates on the z-axis. The object is immersed in a medium with a constant refractive index n_0.

the total field[1] $U_{tot}(\overrightarrow{r})$ of an incident wave $U_{inc}(\overrightarrow{r})$ propagating trough $\mathcal{O}$ toward increasing z. It can be shown[2] that the field can be decomposed in monochromatic fields with wavelength λ_0, and that such a field must satisfy the following wave equation:

$$\Delta U_{tot}(\overrightarrow{r}) + k^2(\overrightarrow{r})\, U_{tot}(\overrightarrow{r}) = 0 \tag{II.1}$$

where $k(\overrightarrow{r}) = k_0.n(\overrightarrow{r})$ is the local wave number, $k_0 = 2\pi/\lambda_0$ being the wave number of the field in free space. $\Delta. = \nabla^2. = \overrightarrow{\nabla}.\overrightarrow{\nabla}.$ is the Laplacian operator.

Replacing k by its expression in equation (II.1):

$$\Delta U_{tot}(\overrightarrow{r}) = -k_0^2 n^2(\overrightarrow{r})\, U_{tot}(\overrightarrow{r})$$

and introducing the refractive index n_0 of the surrounding medium, equation (II.1) becomes by adding $k_0^2 n_0^2 U_{tot}(\overrightarrow{r})$ on both sides:

$$\Delta U_{tot}(\overrightarrow{r}) + k_0^2 n_0^2 U_{tot}(\overrightarrow{r}) = -k_0^2\left(n^2(\overrightarrow{r}) - n_0^2\right) U_{tot}(\overrightarrow{r}) \tag{II.2}$$

As presented in figure II.1, the total field U_{tot} can be expressed as a sum of two sub-wave fronts: the incident wave U_{inc} and the diffracted wave U_{dif}. U_{inc} is

[1] As there is no polarization effect in the considered situation, a scalar formulation for the field is adapted to the mathematical development.

[2] In details in the chapter 6 "Tomographic Imaging with Diffracting Sources" of [20]. It also deals with the time dependence which can be ignored in the current problem.

the incident field present in the medium without any inhomogeneities. U_{dif}, the remaining field to get U_{tot} from U_{inc}, is considered as being the field scattered by the object $\mathcal{O}$. It comes then:

$$\boxed{U_{tot} = U_{inc} + U_{dif}} \tag{II.3}$$

According to its definition, U_{inc} is thus solution of the simplified wave equation in a homogeneous medium of refractive index n_0:

$$\Delta U_{inc}\left(\overrightarrow{r}\right) + k_0^2 n_0^2 U_{inc}\left(\overrightarrow{r}\right) = 0 \tag{II.4}$$

Using this equality (II.4) and the expression (II.3) of the total wave in equation (II.2), one gets the following equation for the diffracted wave:

$$\Delta U_{dif}\left(\overrightarrow{r}\right) + k_0'^2 U_{dif}\left(\overrightarrow{r}\right) = f_0\left(\overrightarrow{r}\right) U_{tot}\left(\overrightarrow{r}\right) \tag{II.5}$$

with $k_0' = k_0 n_0$ the wave number normalized to a propagation medium with a refractive index n_0 and f the scattering potential of the object $\mathcal{O}$ for a given wavelength λ_0:

$$\boxed{f_0\left(\overrightarrow{r}\right) = -k_0'^2 \left(\left(\frac{n\left(\overrightarrow{r}\right)}{n_0}\right)^2 - 1\right)} \tag{II.6}$$

Thereafter, it will be more convenient to work on a normalized scattering potential that does not depend on the wavelength[3]:

$$\boxed{f\left(\overrightarrow{r}\right) = -\frac{f_0\left(\overrightarrow{r}\right)}{k_0'^2} = \left(\left(\frac{n\left(\overrightarrow{r}\right)}{n_0}\right)^2 - 1\right)} \tag{II.7}$$

Equation (II.5) cannot be solved for U_{dif} directly in the general case. But this equation can be considered as a linear operator according to U_{dif} on the left-hand side while the right-hand side is a forcing term. Thus if Green's functions $g\left(\overrightarrow{r_1}, \overrightarrow{r_2}\right)$ exist for the differential equation[4]:

$$\Delta g\left(\overrightarrow{r_1}, \overrightarrow{r_2}\right) + k_0'^2 g\left(\overrightarrow{r_1}, \overrightarrow{r_2}\right) = \delta\left(\overrightarrow{r_1} - \overrightarrow{r_2}\right) \tag{II.8}$$

one can express the diffracted wave U_{dif} as a convolution[5] on the total 3D space $\mathbb{R}^3$:

$$U_{dif}\left(\overrightarrow{r}\right) = -k_0'^2 \iiint\limits_{\overrightarrow{r_\mathcal{O}} \in \mathbb{R}^3} f\left(\overrightarrow{r_\mathcal{O}}\right) U_{tot}\left(\overrightarrow{r_\mathcal{O}}\right) g\left(\overrightarrow{r}, \overrightarrow{r_\mathcal{O}}\right) d^3\overrightarrow{r_\mathcal{O}} \tag{II.9}$$

In 3D space, an expression of g, solution of equation(II.8) is[6]:

$$g\left(\overrightarrow{r}, \overrightarrow{r_\mathcal{O}}\right) = \frac{-1}{4\pi} \frac{e^{ik_0' \left\| \overrightarrow{r} - \overrightarrow{r_\mathcal{O}} \right\|}}{\left\| \overrightarrow{r} - \overrightarrow{r_\mathcal{O}} \right\|} \tag{II.10}$$

[3] If one assumes that the refractive index n does not depend on the wavelength either.
[4] δ stands for the Dirac delta function.
[5] See appendix A, section 1 for more details.
[6] See appendix A, section 2 for more details.

One may notice that this is the expression of a spherical wave at $\overrightarrow{r}$ emitted from $\overrightarrow{r_{\mathcal{O}}}$. This is consistent with equation (II.8) where the forcing term on the right-hand side can be seen as a point inhomogeneity located at $\overrightarrow{r_{\mathcal{O}}}$ due to the Dirac delta function. One may consequently expect that a solution of the wave equation with such a forcing is indeed a spherical wave propagating from this point $\overrightarrow{r_{\mathcal{O}}}$.

Let's also note that according to the expression (II.7) of the scattering potential, $f = 0$ outside the object $\mathcal{O}$. The integral in equation (II.9) can then be expressed only on the object.

Finally, the expression of the total wave U_{tot} is:

$$\boxed{U_{dif}\left(\overrightarrow{r}\right) = \frac{k_0'^2}{4\pi} \iiint\limits_{\overrightarrow{r_{\mathcal{O}}} \in \mathcal{O}} f\left(\overrightarrow{r_{\mathcal{O}}}\right) U_{tot}\left(\overrightarrow{r_{\mathcal{O}}}\right) \frac{e^{ik_0' \left\| \overrightarrow{r} - \overrightarrow{r_{\mathcal{O}}} \right\|}}{\left\| \overrightarrow{r} - \overrightarrow{r_{\mathcal{O}}} \right\|} d^3\overrightarrow{r_{\mathcal{O}}}} \tag{II.11}$$

1.2 The Born approximation

One could think that the formula (II.11) is a good solution to express the diffracted field U_{dif} according to the scattering potential f of the object. But looking closer, one must notice that U_{dif} depends on itself since it appears in the expression of U_{tot} (II.3).

A solution is to restrict to a low scattering object. If it produces a perturbation on the field which can be considered negligible compared to the incident wave U_{inc} inside the object, $\left|U_{dif}\left(\overrightarrow{r_{\mathcal{O}}}\right)\right| \ll \left|U_{inc}\left(\overrightarrow{r_{\mathcal{O}}}\right)\right|$, then $U_{tot}\left(\overrightarrow{r_{\mathcal{O}}}\right) \simeq U_{inc}\left(\overrightarrow{r_{\mathcal{O}}}\right)$ and the solution (II.11) can be written:

$$\boxed{U_{dif}^{B}\left(\overrightarrow{r}\right) \simeq \frac{k_0'^2}{4\pi} \iiint\limits_{\overrightarrow{r_{\mathcal{O}}} \in \mathcal{O}} f\left(\overrightarrow{r_{\mathcal{O}}}\right) U_{inc}\left(\overrightarrow{r_{\mathcal{O}}}\right) \frac{e^{ik_0' \left\| \overrightarrow{r} - \overrightarrow{r_{\mathcal{O}}} \right\|}}{\left\| \overrightarrow{r} - \overrightarrow{r_{\mathcal{O}}} \right\|} d^3\overrightarrow{r_{\mathcal{O}}}} \tag{II.12}$$

This is called the Born approximation. It gives a first order estimation of U_{dif}. To get an approximation of higher degree $U_{dif}^{B_2}$, one must use the first order approximation of $U_{tot} \simeq U_{inc} + U_{dif}^{B}$ in equation (II.11):

$$U_{dif}^{B_2}\left(\overrightarrow{r}\right) \simeq \frac{k_0'^2}{4\pi} \iiint\limits_{\overrightarrow{r_{\mathcal{O}}} \in \mathcal{O}} f\left(\overrightarrow{r_{\mathcal{O}}}\right) \left(U_{inc} + U_{dif}^{B}\right)\left(\overrightarrow{r_{\mathcal{O}}}\right) \frac{e^{ik_0' \left\| \overrightarrow{r} - \overrightarrow{r_{\mathcal{O}}} \right\|}}{\left\| \overrightarrow{r} - \overrightarrow{r_{\mathcal{O}}} \right\|} d^3\overrightarrow{r_{\mathcal{O}}} \tag{II.13}$$

And one can similarly increase the order of the approximation iteratively, going from the i-th to the $i+1$-th using $U_{tot} \simeq U_{inc} + U_{dif}^{B_i}$:

$$U_{dif}^{B_{i+1}}\left(\overrightarrow{r}\right) \simeq \frac{k_0'^2}{4\pi} \iiint\limits_{\overrightarrow{r_{\mathcal{O}}} \in \mathcal{O}} f\left(\overrightarrow{r_{\mathcal{O}}}\right) \left(U_{inc} + U_{dif}^{B_i}\right)\left(\overrightarrow{r_{\mathcal{O}}}\right) \frac{e^{ik_0' \left\| \overrightarrow{r} - \overrightarrow{r_{\mathcal{O}}} \right\|}}{\left\| \overrightarrow{r} - \overrightarrow{r_{\mathcal{O}}} \right\|} d^3\overrightarrow{r_{\mathcal{O}}} \tag{II.14}$$

This work will focus on the first order approximation. Equation (II.12) can also

be expressed as a convolution:

$$U_{dif}^{B} = (f.U_{inc}) \star \underbrace{\left(\frac{k_0'^2}{4\pi} \frac{e^{ik_0' \|\overrightarrow{r}\|}}{\|\overrightarrow{r}\|} \right)}_{\text{Convolution kernel}} \tag{II.15}$$

It clearly appears that the incident wave, weighted by the scattering potential, is convolved with a spherical propagator. This is the 3D equivalent of the Huygens-Fresnel principle (see section 3.2): each point in the scattering medium reemits a secondary wave, propagating spherically from this point, with an amplitude depending on the incident primary wave amplitude and the local medium characteristics. All these spherical waves interfere to create the diffracted field U_{dif}, as illustrated in figure II.2.

A significant difference with the 2D model is that U_{dif} is not directly the total field behind the object but only the scattered part. One needs to add the incident field U_{inc}.

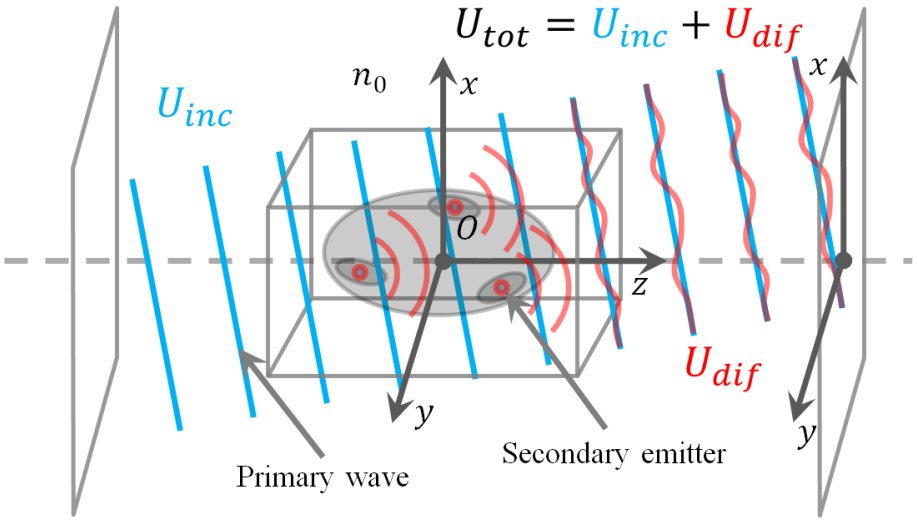

Figure II.2: Illustration of the Huygens-Fresnel principle in three dimensions. The incident wave U_{inc} acts as a primary wave while getting through the scattering object $\mathcal{O}$. Each points of this object then behaves as a secondary emitter of spherical waves directly depending on the primary wave. All this components finally merge to create the diffracted wave U_{dif}. The global resulting field adds these two parts: $U_{tot} = U_{inc} + U_{dif}$.

One can also mention a problem of energy conservation since U_{inc} is not affected while going through the object, whereas its amplitude should decrease as it scatters in the object. Thus the energy carried by U_{dif} is not taken from U_{inc} but nonetheless added in the total field U_{tot}. It appears clearly then that this model is a strong approximation.

In the same spirit, the secondary emitters are not diffracting the total incoming wave U_{tot} which reaches their location but only the incident wave U_{inc}. Indeed, in a

scattering volume, the wave which is diffracted at the back of the object has crossed the whole object and should be containing the information of all the diffractions it has undergone. In this model, one keeps only the incident wave, the undergone diffractions being considered as negligible. That is why this model is named the first Born approximation and is valid only at the first order.

It is briefly mentioned earlier that equation (II.12) is valid only for low scattering objects. Several works studied its domain of validity such as [20], [44] and [72]. They show that for biological samples composed of several cells, such as 3D cell cultures, the total phase shift introduced by the sample is too important and the Born approximation breaks down as soon as the objects are larger than a few tens of microns. For a cell with a typical refractive index of 1.36 in water [44, 73], the relative refractive index is $\delta n = 0.03$. With a typical cell length of $l = 20\ \mu m$ and in the visible light $\lambda \simeq 550\ nm$ the overall introduced phase delay is $2\pi l \delta n/\lambda > 2\pi$ which is not negligible.

Nonetheless, this formulation will still be used as this is the only one applicable in practical use. The future reconstructions are consequently not expected to be phase quantitative. But it can be expected that it will allow determining morphological information on the biological sample, such as positions, dimensions and shapes.

Let's also mention another formulation, the Rytov approximation, well described in [72]. In this model, the total field is expressed as:

$$U_{tot}\left(\overrightarrow{r}\right) = U_{inc}\left(\overrightarrow{r}\right).e^{\psi\left(\overrightarrow{r}\right)} \tag{II.16}$$

In the Rytov approximation, the complex phase ψ is equal to:

$$\psi\left(\overrightarrow{r}\right) = \frac{U^B_{dif}\left(\overrightarrow{r}\right)}{U_{inc}\left(\overrightarrow{r}\right)} \tag{II.17}$$

where U^B_{dif} is the diffracted wave given by the Born approximation (II.12).

This approximation is valid for bigger objects than the Born approximation as soon as the refractive index varies softly in space[7]. However, even with this extended domain of validity, the 3D biological objects studied in this thesis fall outside these limits. Moreover, its formulation is more complicated to put into practice. Consequently it will not be used in the following models.

2 The Fourier diffraction theorem

This section is mainly based on [71] and aims at finding a simple relation between the 3D object $\mathcal{O}$ to retrieve and the 2D wave front measured on different planes.

Using the notation introduced in figure II.1, such a relation exists for a monochromatic incident wave $U_{inc}\left(\overrightarrow{r}\right) = e^{i\overrightarrow{k_0}.\overrightarrow{r}}$, where the wave vector $\overrightarrow{k'_0}$ indicates the direction of propagation. Its norm is $k'_0 = \frac{2\pi n_0}{\lambda_0}$ and its direction is given by the unit vector (p_0, q_0, m_0). This relation links the 3D Fourier transform of the scattering

[7] See [44] and [72].

potential f with the 2D Fourier transform of the diffracted field U_{dif} on a given plane at $z = z^+$ and is called the Fourier diffraction theorem:

$$\boxed{\hat{f}(\alpha,\beta,\gamma) = \frac{4\pi}{ik_0'^2} w e^{-2i\pi w z^+} \hat{U}_{dif}\left(u,v;z^+\right)} \tag{II.18}$$

where (u,v) and (α,β,γ) are respectively the coordinates in the 2D Fourier space of the plane $z = z^+$ and in the 3D Fourier space of the object. These coordinates satisfy the following relations:

$$\boxed{\begin{cases} \alpha = u - \frac{n_0.p_0}{\lambda_0} \\ \beta = v - \frac{n_0.q_0}{\lambda_0} \\ \gamma = w - \frac{n_0.m_0}{\lambda_0} \end{cases} \text{ and } w = \sqrt{\frac{n_0^2}{\lambda_0^2} - u^2 - v^2}} \tag{II.19}$$

Note that the Fourier transform[8] and its inverse transform are defined for a given function g as:

$$\begin{aligned} \mathcal{F}(g)(u) = \hat{g}(u) &= \int_{-\infty}^{\infty} g(x) e^{-2i\pi u x} dx \\ \mathcal{F}^{-1}(\hat{g})(x) &= \int_{-\infty}^{\infty} \hat{g}(u) e^{2i\pi x u} du \end{aligned} \tag{II.20}$$

2.1 Demonstration

Let's demonstrate this theorem by highlighting the main steps. Using the monochromatic incident plane wave expression introduced above for U_{inc}, the expression (II.12) for the diffracted wave becomes:

$$U_{dif}(\overrightarrow{r}) = \frac{k_0'^2}{4\pi} \iiint_{\overrightarrow{r_\mathcal{O}} \in \mathcal{O}} f(\overrightarrow{r_\mathcal{O}}) e^{i\overrightarrow{k_0'}.\overrightarrow{r_\mathcal{O}}} \frac{e^{ik_0' \| \overrightarrow{r} - \overrightarrow{r_\mathcal{O}} \|}}{\| \overrightarrow{r} - \overrightarrow{r_\mathcal{O}} \|} d^3\overrightarrow{r_\mathcal{O}} \tag{II.21}$$

Using $\overrightarrow{r} = (x,y,z)$ and $\overrightarrow{r_\mathcal{O}} = (x_\mathcal{O}, y_\mathcal{O}, z_\mathcal{O})$, it can be shown[9] that the spherical wave can be decomposed in a summation of plane waves:

$$\frac{e^{ik_0' \| \overrightarrow{r} - \overrightarrow{r_\mathcal{O}} \|}}{\| \overrightarrow{r} - \overrightarrow{r_\mathcal{O}} \|} = \frac{ik_0'}{2\pi} \iint_{-\infty}^{\infty} \frac{1}{m} e^{ik_0'[p(x-x_\mathcal{O}) + q(y-y_\mathcal{O}) + m|z-z_\mathcal{O}|]} dp dq \tag{II.22}$$

where $m = (1 - p^2 - q^2)^{1/2}$. Then, one gets:

$$m = \begin{cases} \sqrt{1-p^2-q^2} & \text{when} \quad p^2+q^2 < 1 \\ i\sqrt{p^2+q^2-1} & \text{when} \quad p^2+q^2 > 1 \end{cases} \tag{II.23}$$

[8] This definition extends naturally to higher dimensions.

[9] See appendix B.

Let's consider now the semi-space beyond z_{max} as defined in figure II.1: $\forall\,(z_{\mathcal{O}}, z^+) \in \mathcal{O} \times [z_{max}, +\infty[$, one has: $|z^+ - z_{\mathcal{O}}| = z^+ - z_{\mathcal{O}}$. It comes from equations (II.21) and (II.22):

$$\begin{aligned} U_{dif}\left(\overrightarrow{r}\right) &= \frac{k_0'^2}{4\pi} \iiint_{\overrightarrow{r_{\mathcal{O}}}\in\mathcal{O}} f\left(\overrightarrow{r_{\mathcal{O}}}\right) e^{i\overrightarrow{k_0'}.\overrightarrow{r_{\mathcal{O}}}} \times \cdots \\ &\qquad \left(\frac{ik_0'}{2\pi} \iint_{-\infty}^{\infty} \frac{1}{m} e^{ik_0'\left[p(x-x_{\mathcal{O}})+q(y-y_{\mathcal{O}})+m\left(z^+-z_{\mathcal{O}}\right)\right]} dpdq \right) d^3\overrightarrow{r_{\mathcal{O}}} \\ &= \iiint_{\overrightarrow{r_{\mathcal{O}}}\in\mathcal{O}} \left(\iint_{-\infty}^{\infty} \frac{ik_0'^3}{8\pi^2} \frac{1}{m} f\left(\overrightarrow{r_{\mathcal{O}}}\right) e^{ik_0'(p_0x_{\mathcal{O}}+q_0y_{\mathcal{O}}+m_0z_{\mathcal{O}})} \times \cdots \right. \\ &\qquad \left. e^{ik_0'\left[p(x-x_{\mathcal{O}})+q(y-y_{\mathcal{O}})+m\left(z^+-z_{\mathcal{O}}\right)\right]} dpdq \right) dx_{\mathcal{O}}dy_{\mathcal{O}}dz_{\mathcal{O}} \end{aligned} \tag{II.24}$$

then by developing the scalar product $\overrightarrow{k_0'}.\overrightarrow{r_{\mathcal{O}}}$ and inverting the integration order:

$$\begin{aligned} U_{dif}\left(\overrightarrow{r}\right) = \iint_{-\infty}^{\infty} \frac{ik_0'^3}{8\pi^2} \frac{1}{m} e^{ik_0'\left(px+qy+mz^+\right)} &\left(\iiint_{\overrightarrow{r_{\mathcal{O}}}\in\mathcal{O}} f\left(\overrightarrow{r_{\mathcal{O}}}\right) \times \cdots \right. \\ &\left. e^{-ik_0'[(p-p_0)x_{\mathcal{O}}+(q-q_0)y_{\mathcal{O}}+(m-m_0)z_{\mathcal{O}}]} dx_{\mathcal{O}}dy_{\mathcal{O}}dz_{\mathcal{O}} \right) dpdq \end{aligned} \tag{II.25}$$

and finally with the following change of variables:

$$\begin{array}{ll} \frac{n_0}{\lambda_0}p = \frac{k_0'}{2\pi}p \leftrightarrow u & \frac{n_0}{\lambda_0}q = \frac{k_0'}{2\pi}q \leftrightarrow v \\ dpdq \leftrightarrow \left(\frac{2\pi}{k_0'}\right)^2 dudv & \frac{n_0}{\lambda_0}m \leftrightarrow w \end{array} \tag{II.26}$$

it comes from equation (II.25):

$$\begin{aligned} U_{dif}\left(\overrightarrow{r}\right) &= \iint_{-\infty}^{\infty} \frac{ik_0'^3}{8\pi^2} \frac{k_0'}{2\pi w} e^{2i\pi\left(ux+vy+wz^+\right)} \left(\iiint_{\overrightarrow{r_{\mathcal{O}}}\in\mathcal{O}} f\left(\overrightarrow{r_{\mathcal{O}}}\right) \times \cdots \right. \\ &\qquad e^{-2i\pi\left[x_{\mathcal{O}}\left(u-\frac{n_0}{\lambda_0}p_0\right)+y_{\mathcal{O}}\left(v-\frac{n_0}{\lambda_0}q_0\right)+z_{\mathcal{O}}\left(w-\frac{n_0}{\lambda_0}m_0\right)\right]} \times \cdots \\ &\qquad \left. dx_{\mathcal{O}}dy_{\mathcal{O}}dz_{\mathcal{O}} \right) \left(\frac{2\pi}{k_0'}\right)^2 dudv \\ &= \iint_{-\infty}^{\infty} \frac{ik_0'^2 e^{2i\pi wz^+}}{4\pi w} \left(\iiint_{\overrightarrow{r_{\mathcal{O}}}\in\mathcal{O}} f\left(\overrightarrow{r_{\mathcal{O}}}\right) \times \cdots \right. \\ &\qquad e^{-2i\pi\left[x_{\mathcal{O}}\left(u-\frac{n_0}{\lambda_0}p_0\right)+y_{\mathcal{O}}\left(v-\frac{n_0}{\lambda_0}q_0\right)+z_{\mathcal{O}}\left(w-\frac{n_0}{\lambda_0}m_0\right)\right]} \times \cdots \\ &\qquad \left. dx_{\mathcal{O}}dy_{\mathcal{O}}dz_{\mathcal{O}} \right) e^{2i\pi(ux+vy)} dudv \end{aligned} \tag{II.27}$$

where:

$$w = \begin{cases} \sqrt{\left(\frac{n_0}{\lambda_0}\right)^2 - u^2 - v^2} & \text{when} \quad u^2+v^2 < \left(\frac{n_0}{\lambda_0}\right)^2 \\ i\sqrt{u^2+v^2-\left(\frac{n_0}{\lambda_0}\right)^2} & \text{when} \quad u^2+v^2 > \left(\frac{n_0}{\lambda_0}\right)^2 \end{cases}$$

Noticing that at a given plane $z = z^+$:

$$U_{dif}\left(\overrightarrow{r}\right) = \mathcal{F}_{2D}^{-1}\left(\hat{U}_{dif}\right)\left(\overrightarrow{r}\right) = \iint_{-\infty}^{\infty} \hat{U}_{dif}\left(u, v; z^+\right) e^{2i\pi(ux+vy)} du dv \tag{II.28}$$

it comes from equation (II.27) that:

$$\begin{aligned}\hat{U}_{dif}\left(u, v; z^+\right) = \frac{ik_0'^2 e^{2i\pi w z^+}}{4\pi w} \iiint_{\overrightarrow{r_{\mathcal{O}}} \in \mathcal{O}} f\left(\overrightarrow{r_{\mathcal{O}}}\right) \times \cdots \\ e^{-2i\pi\left[x_{\mathcal{O}}\left(u-\frac{n_0}{\lambda_0}p_0\right)+y_{\mathcal{O}}\left(v-\frac{n_0}{\lambda_0}q_0\right)+z_{\mathcal{O}}\left(w-\frac{n_0}{\lambda_0}m_0\right)\right]} dx_{\mathcal{O}} dy_{\mathcal{O}} dz_{\mathcal{O}}\end{aligned} \tag{II.29}$$

The form of this equation is:

$$\hat{U}_{dif}\left(u, v; z^+\right) = \frac{ik_0'^2 a\left(u, v\right)}{4\pi w} e^{2i\pi w z^+} \tag{II.30}$$

with:

$$a\left(u, v\right) = \iiint_{\overrightarrow{r_{\mathcal{O}}} \in \mathcal{O}} f\left(\overrightarrow{r_{\mathcal{O}}}\right) e^{-2i\pi\left[x_{\mathcal{O}}\left(u-\frac{n_0}{\lambda_0}p_0\right)+y_{\mathcal{O}}\left(v-\frac{n_0}{\lambda_0}q_0\right)+z_{\mathcal{O}}\left(w-\frac{n_0}{\lambda_0}m_0\right)\right]} dx_{\mathcal{O}} dy_{\mathcal{O}} dz_{\mathcal{O}}$$

It can be then noticed that for $u^2 + v^2 > \left(\frac{n_0}{\lambda_0}\right)^2$, w is strictly imaginary and $\hat{U}_{dif}\left(u, v; z^+\right)$ is an evanescent wave as a function of z^+:

$$\left|\hat{U}_{dif}\left(u, v; z^+\right)\right| = \frac{k_0'^2 \left|a\left(u, v\right)\right|}{4\pi} \frac{e^{-2\pi\sqrt{u^2+v^2-\left(\frac{n_0}{\lambda_0}\right)^2} z^+}}{\sqrt{u^2+v^2-\left(\frac{n_0}{\lambda_0}\right)^2}} \xrightarrow[z^+ \to +\infty]{} 0 \tag{II.31}$$

Consequently, this means that any information carried by these frequencies (u, v) will be lost if one gets too far from the object $\mathcal{O}$ since the absolute value of the coefficient becomes too small to be recorded.

On the other hand, when $u^2 + v^2 < \left(\frac{n_0}{\lambda_0}\right)^2$, w is real. Moreover, using the previously mentioned remark that integrating on the object $\mathcal{O}$ and on the whole space is identical since $f\left(\overrightarrow{r_{\mathcal{O}}}\right) = 0$ outside the object, it follows that $a\left(u, v\right)$ has the shape of the 3D Fourier transform of the scattering potential f:

$$\begin{aligned} a\left(u, v\right) &= \iiint_{-\infty}^{\infty} f\left(\overrightarrow{r_{\mathcal{O}}}\right) \times \cdots \\ &\qquad e^{-2i\pi\left[x_{\mathcal{O}}\left(u-\frac{n_0}{\lambda_0}p_0\right)+y_{\mathcal{O}}\left(v-\frac{n_0}{\lambda_0}q_0\right)+z_{\mathcal{O}}\left(w-\frac{n_0}{\lambda_0}m_0\right)\right]} dx_{\mathcal{O}} dy_{\mathcal{O}} dz_{\mathcal{O}} \\ &= \mathcal{F}_{3D}\left(f\right)\left(u - \frac{n_0}{\lambda_0}p_0, v - \frac{n_0}{\lambda_0}q_0, w - \frac{n_0}{\lambda_0}m_0\right) \\ &= \hat{f}\left(u - \frac{n_0}{\lambda_0}p_0, v - \frac{n_0}{\lambda_0}q_0, w - \frac{n_0}{\lambda_0}m_0\right) \end{aligned} \tag{II.32}$$

And finally, one finds back the Fourier diffraction theorem (II.18) from equation (II.30):

$$\hat{U}_{dif}\left(u,v;z^{+}\right)=\frac{ik_0'^2\hat{f}\left(u-\frac{n_0}{\lambda_0}p_0,v-\frac{n_0}{\lambda_0}q_0,w-\frac{n_0}{\lambda_0}m_0\right)}{4\pi we^{-2i\pi wz^{+}}} \tag{II.33}$$

Let's insist here again on the fact that the Fourier diffraction theorem only holds for specific sets of frequencies (u,v) verifying $u^2+v^2<\left(\frac{n_0}{\lambda_0}\right)^2$. Thus, only a part of the 3D Fourier space of $\hat{f}$ is accessible.

2.2 Geometrical interpretation

Looking closer at the formulation of the Fourier diffraction theorem (II.18), one must notice that it links a 3D object, the 3D Fourier transform of the scattering potential $\hat{f}$, to a 2D entity, the 2D Fourier transform of the diffracted wave $\hat{U}_{dif}$ at a given distance z^+ from the object, or in another words a 2D surface to a 3D volume.

From expression (II.19), one gets that the three coordinates (α,β,γ) depend on the 2D coordinates (u,v). The resulting 2D surface in the 3D space lies on a sphere[10] with center $-n_0/\lambda_0\,(p_0,q_0,m_0)$ and radius n_0/λ_0, as pictured in scheme II.3. (p_0,q_0,m_0) being the unit vector in the direction of light propagation, the mentioned sphere passes through the origin, the center of the sphere being placed a radius apart from it.

As noticed in the previous section, only a part of this sphere is accessible, since the frequencies (u,v) must satisfy $u^2+v^2<\left(\frac{n_0}{\lambda_0}\right)^2$. Consequently, the 2D surface lies on a semi-sphere as drawn in figure II.3.

The position of these caps depends on the lighting direction. Indeed, if the plane $z=z^+$ rotates with the lighting direction, the cap also rotates accordingly in the 3D frequency domain[11]. If the coordinate system (x,y,z) remains still as the lighting rotates, the cap is then simply translated[12].

As illustrated in figure II.3, it is possible to go in two different ways leading to two different applications of this theorem. If one goes clockwise, from the object f to the diffracted waves U_{dif}, the Fourier diffraction theorem gives a tool to simulate data from a given object numerically designed. On the contrary, if one goes counter-clockwise, from the diffracted waves U_{dif} to the object f, the Fourier diffraction theorem gives a mean to retrieve an object from several diffracted waves acquisitions through a mapping of the 3D Fourier domain of f.

The main pitfall of this theorem is its numerical application. Indeed, one must keep in mind that its formulation is analytic. But the coordinates will have to be discretized to be processed numerically. For example, if one wants to use the Fast Fourier Transform algorithm to compute $\hat{f}$ from f, the scattering potential will be discretized on a homogeneous mesh, leading to a homogeneous mesh in the Fourier

[10] Indeed, $\left(\alpha+\frac{n_0.p_0}{\lambda_0}\right)^2+\left(\beta+\frac{n_0.q_0}{\lambda_0}\right)^2+\left(\gamma+\frac{n_0.m_0}{\lambda_0}\right)^2=u^2+v^2+w^2=\frac{n_0^2}{\lambda_0^2}$

[11] See the rotation of the cap from the red to the green position in figure.

[12] See the translation of the cap from the red to the blue position in figure.

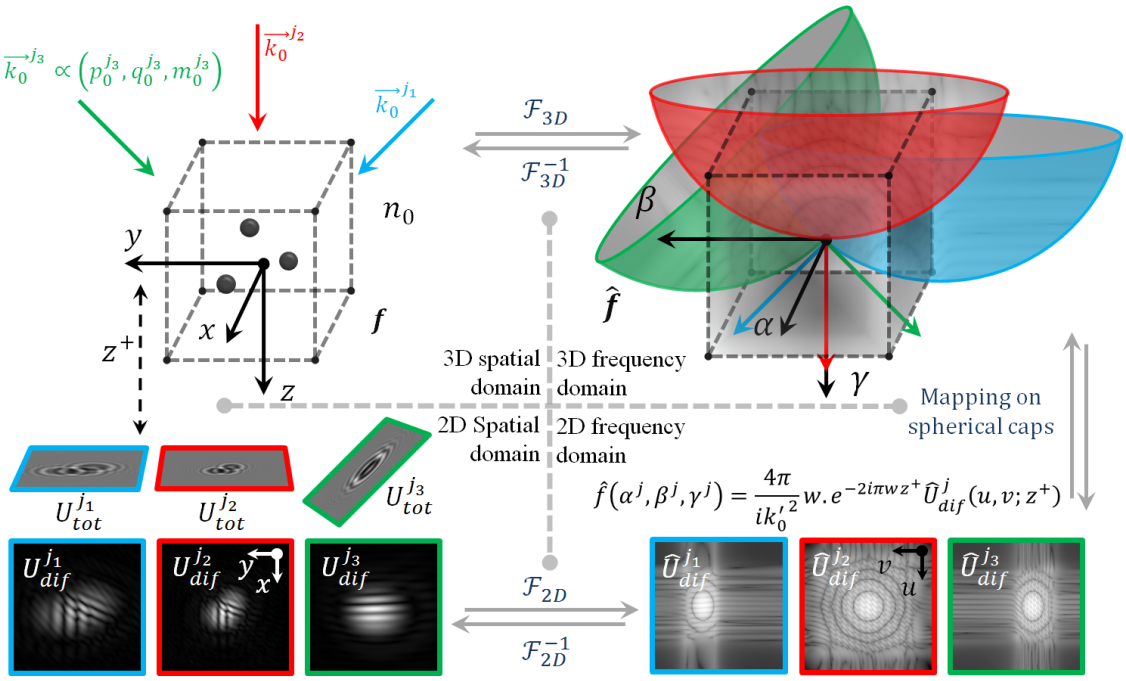

Figure II.3: Illustration of the geometrical interpretation of the Fourier diffraction theorem. A 3D Fourier transform links the 3D spatial and frequency domains of the scattering potential f. A 2D Fourier transform links the 2D spatial and frequency domains of the diffracted wave U_{dif}^j for each lighting situation j. A mapping on spherical caps links the 2D frequency domain of the diffracted wave and the 3D frequency domain of the object. The orientation and position of these caps directly depend on the lighting directions $\overrightarrow{k_0}^j \propto \left(p_0^j, q_0^j, m_0^j\right)$.

domain. On the other side, the same discretization of the 2D coordinates u and v will lead to discretized positions (α, β, γ) on the spherical caps which will not necessarily match with the homogeneous mesh.

One will consequently have to find a way to map the inhomogeneous positions on the spherical caps into the 3D Fourier homogeneous mesh.

2.3 A diffractive version of the Fourier slice theorem

This section aims at emphasizing the strong link which exists between the Fourier diffraction theorem and the Fourier slice theorem[13]. The latter is commonly used in classical computed tomography (CT) such as X-ray tomography and uses the Radon transform, notion introduced in 1917 by Johann Radon[14].

The radon transform $R_\alpha[f](s)$ of a compactly supported continuous function $f(x, y)$ on $\mathbb{R}^2$ is its projection (its integral along the straight lines $\Gamma_{\alpha,s}$) along a given direction (α, s), where α is the angle relative to the x-axis and s the distance

[13] See [74], entry "Tomography".
[14] See [74], entry "Radon transform". This subsection is also inspired from [75] and [76]

to the frame origin, as pictured in figure II.4:

$$\begin{aligned} R_\alpha[f](s) &= \int_{\Gamma_{\alpha,s}} f(\overrightarrow{\gamma}) \, \|d\overrightarrow{\gamma}\| \\ &= \int_{-\infty}^{+\infty} f((s\cos\alpha - z\sin\alpha), (s\sin\alpha + z\cos\alpha)) \, dz \end{aligned} \tag{II.34}$$

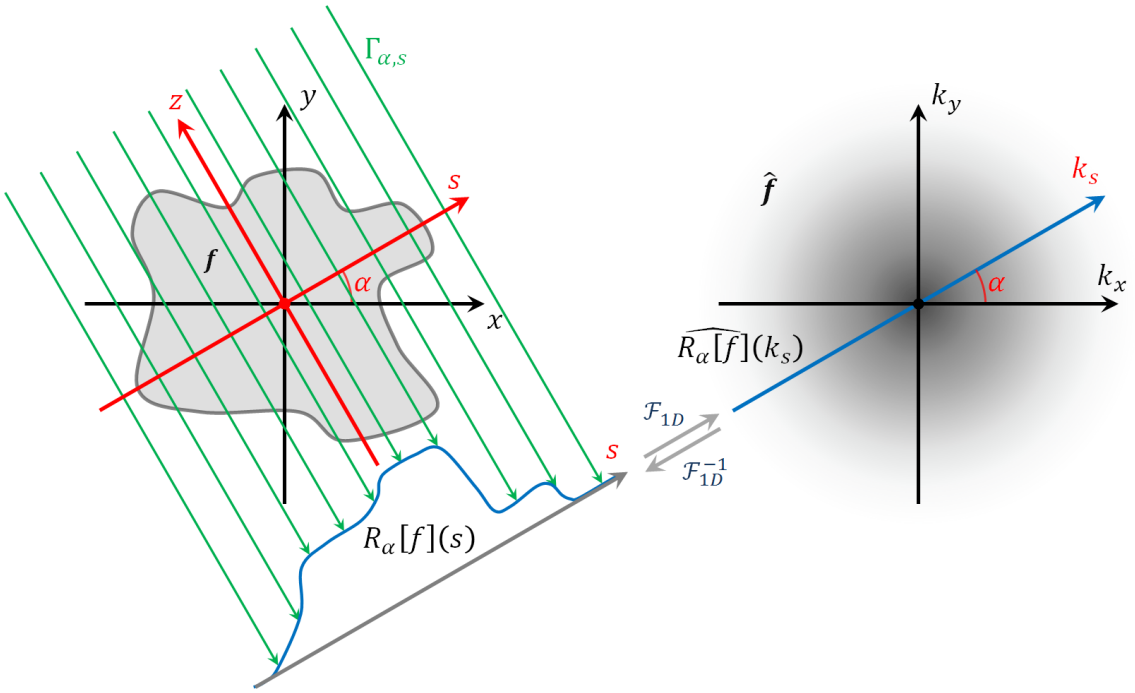

Figure II.4: Illustration of the geometrical interpretation of the Fourier slice theorem. On the left-hand side of the figure is represented the Radon transform $R_\alpha[f](s)$ of a function $f(x,y)$: it is its projection along a given axis s oriented with an angle α relative to the x-axis (in blue). On the right-hand side, its unidimensional Fourier transform $\widehat{R_\alpha[f]}(k_s)$ is a line in $\hat{f}$, the Fourier transform of f.

The Fourier slice theorem states that the unidimensional Fourier transform of $R_\alpha[f]$ is a slice in the Fourier domain of f, as schematically drawn in figure II.4.

$$\boxed{\widehat{R_\alpha[f]}(k_s) = \hat{f}(k_s\cos\alpha, k_s\sin\alpha)} \tag{II.35}$$

$$\begin{aligned} \widehat{R_\alpha[f]}(k_s) &= \int_{-\infty}^{+\infty} R_\alpha[f](s) \, e^{-2i\pi s k_s} ds \\ &= \int_{-\infty}^{+\infty} \int_{-\infty}^{+\infty} f((s\cos\alpha - z\sin\alpha), (s\sin\alpha + z\cos\alpha)) \, e^{-2i\pi s k_s} ds dz \\ &= \iint_{-\infty}^{+\infty} f(x,y) \, e^{-2i\pi(x k_s\cos\alpha + y k_s\sin\alpha)} dx dy \\ &= \hat{f}(k_s\cos\alpha, k_s\sin\alpha) \end{aligned}$$

via the following change of variables:

$$\begin{aligned} \begin{pmatrix} x \\ y \end{pmatrix} &= \begin{pmatrix} \cos\alpha & -\sin\alpha \\ \sin\alpha & \cos\alpha \end{pmatrix} \begin{pmatrix} s \\ z \end{pmatrix} \\ dxdy &= \left|\det \begin{pmatrix} \cos\alpha & -\sin\alpha \\ \sin\alpha & \cos\alpha \end{pmatrix}\right| dsdz = |1|\, dsdz = dsdz \end{aligned} \tag{II.36}$$

This theorem is expandable to higher dimensions: for a three-dimensional object, the 2D Fourier transform of its projection on a plane will be a planar slice of its 3D Fourier transform $\hat{f}$. Thus, one can retrieve the volume information of an object from different acquisitions of its absorbency along different directions, for example with X-ray projections, each acquisition giving a part of the Fourier transform of the object.

One consequently get something very close to the geometrical interpretation previously made for the Fourier diffraction theorem, replacing spherical caps by planes.

Let's remember that the caps radius r_c is inversely proportional to the lighting wavelength: $r_c = n_0/\lambda_0$. Moreover for X-rays, the wavelength λ_X gets far smaller than for the visible light λ_{vis}: $\lambda_X \ll \lambda_{vis}$, and $r_c \xrightarrow[\lambda_0 \to 0]{} +\infty$: the spherical caps tend toward planar surfaces.

Hence one can say that the Fourier slice theorem is the limit of the Fourier diffraction theorem when the lighting wavelength becomes shorter, or in other words when the diffraction tends to disappear and that rays propagate straight through the sample without being scattered.

3 3D numerical simulations

The objective of this section is to get familiar with the formulations introduced in the previous sections 1 and 2, but in their numerical forms. Indeed, some adaptations are needed to implement the analytic formulae into a numerical program.

Then, the Fourier diffraction theorem is compared with the Born approximation. To conclude this chapter, the consistency of the 3D models with the 2D lens-free reconstruction methods and real data are discussed.

3.1 Reformulation of the Born approximation and the Fourier diffraction theorem

The aim of the developed models is to give an approximation of the total wave front U_{tot} at a given position in space. In this work, these models are consequently used to link the 3D object and the wave front on the sensor plane.

Let's suppose that the origin of the reference frame is placed at the center of the object of interest as illustrated in figure II.5, the z-axis being oriented along the light propagation direction, normal to the sensor plane, placed at $z = z_s$.

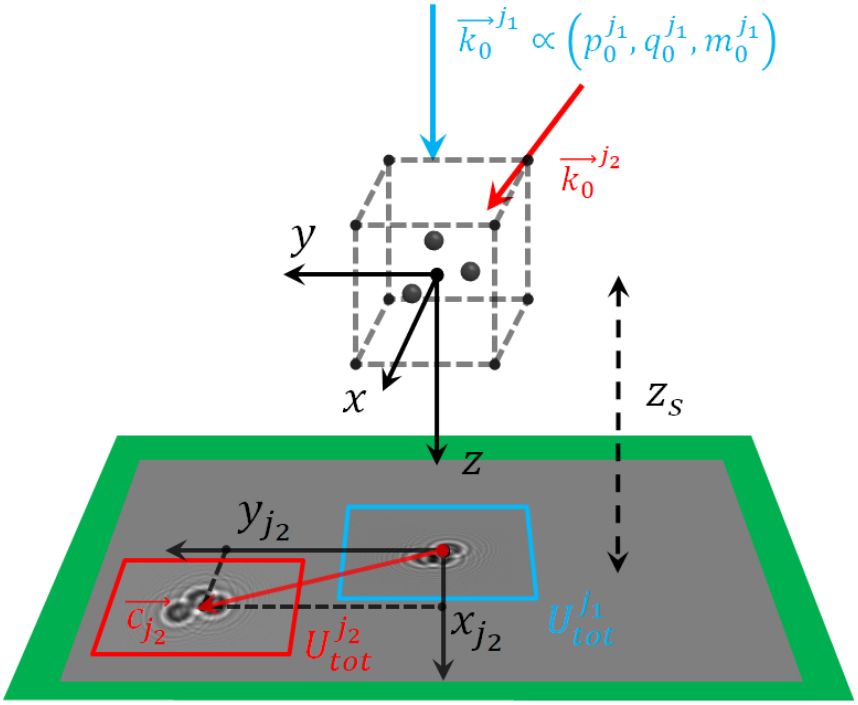

Figure II.5: Illustration of the displacement of the region of interest when the incident lighting is not normal to the sensor: according to the lighting position $\overrightarrow{k_0}^j \propto \left(p_0^j, q_0^j, m_0^j\right)$, the hologram produced by the object is shifted by $\overrightarrow{c_j}$ on the sensor plane $z = z_s$.

The first remark is that one does not need the entire plane, or in other words the whole sensor surface, to retrieve the object. Indeed, the most important part of the object's hologram is directly centered under the object at $(x, y) = (0, 0)$ for a normal lighting, as pictured in blue in the scheme. If the lighting remains orthogonal to the sensor plane during the different acquisitions or simulations, one can consequently work on a cropped part of the sensor plane, directly placed under the object.

If the lighting is not orthogonal to the sensor along the direction (p_0, q_0, m_0), one is in the situation pictured in red in the scheme: the hologram is shifted on the sensor plane to the position $\overrightarrow{c_0} = (x_0, y_0) = \frac{z_s}{m_0}(p_0, q_0)$. One can consequently work on a cropped picture centered on (x_0, y_0).

Working on centered cropped pictures drastically reduces the memory needs and the calculation times are greatly reduced. Moreover, working directly on centered holograms is easier for the user to understand and interpret the simulation and the acquired data.

Born approximation Let's find a numerical formulation of the Born approximation expressed in section 1.2. As mentioned, it can be expressed as a convolution,

equation (II.15). This is consequently convenient to express it in the Fourier domain:

$$\mathcal{F}_{3D}\left(U_{dif}\right) = \mathcal{F}_{3D}\left(f.U_{inc}\right) \times \mathcal{F}_{3D}\left(\frac{k_0'^2}{4\pi}\frac{e^{ik_0'\|\overrightarrow{r}\|}}{\|\overrightarrow{r}\|}\right) \tag{II.37}$$

To perform the computation numerically, one will have to work on a discrete bounded 3D space. The easiest model is a parallelepiped volume divided uniformly in parallelepiped voxels lying on a regular mesh of size $nb_x \times nb_y \times nb_z$. The sides of the voxel are dx, dy and dz. The analytic Fourier transforms are replaced by their discrete equivalent and computed by *Fast Fourier Transform* algorithms[15]. For unidimensional vectors of length n:

$$\begin{aligned}\mathcal{F}\left(f\right)\left(x\right) = y \leftrightarrow Y_k &= \mathrm{FFT}\left(f\left(X_j\right)_{j\in\{1,n\}}\right) = \sum_{j=1}^{n} f\left(X_j\right) e^{-\frac{2\pi i}{n}(j-1)(k-1)} \\ \mathcal{F}^{-1}\left(g\right)\left(y\right) = x \leftrightarrow X_j &= \mathrm{FFT}^{-1}\left(g\left(Y_k\right)_{k\in\{1,n\}}\right) = \frac{1}{n}\sum_{k=1}^{n} g\left(Y_k\right) e^{\frac{2\pi i}{n}(j-1)(k-1)}\end{aligned} \tag{II.38}$$

By using `fft` in Matlab®, one gets an output matrix of the same size as the input matrix.

Let's x_{3D}, y_{3D} and z_{3D} be the 3D matrices of the coordinates on a mesh as defined above, centered on $(0,0,0)$. Let's use the symbols $\times$ for the conventional matrix product and . for the term-by-term multiplication[16]. Under the Born approximation U_{dif} is numerically expressed as follows:

$$\begin{aligned}U_{dif} = \mathrm{FFT}_{3D}^{-1}\Bigg(&\mathrm{FFT}_{3D}\left(f\left(x_{3D},y_{3D},z_{3D}\right).U_{inc}\left(x_{3D},y_{3D},z_{3D}\right)\right).\cdots \\ &\mathrm{FFT}_{3D}\left(\frac{k_0'^2}{4\pi}\frac{e^{ik_0'\sqrt{\left(x_{3D}+x_0\right)^2+\left(y_{3D}+y_0\right)^2+\left(z_{3D}+z_s\right)^2}}}{\sqrt{\left(x_{3D}+x_0\right)^2+\left(y_{3D}+y_0\right)^2+\left(z_{3D}+z_s\right)^2}}\right)\Bigg)\,dv\end{aligned} \tag{II.39}$$

with $dv = dx.dy.dz$

Doing so, one gets a 3D matrix U_{dif} on a volume centered on (x_0, y_0, z_s): $U_{dif}\left(x_0 + x_{3D}, y_0 + y_{3D}, z_s + z_{3D}\right)$. To get only the field on the sensor, one has just to extract the slice of this 3D matrix corresponding to $z = z_s$ which is the slice on which $z_{3D} = 0$.

This method has the advantage of being suitable for all kind of incident waves U_{inc} and allows for example to test the approximation made for the wave front as being planar if the sample is placed far enough from a point source.

But its main disadvantage is that for each lighting situation, two 3D FFTs have to be performed. One on the spherical propagator $\frac{k_0'^2}{4\pi}\frac{e^{ik_0'r}}{r}$, and another one on $f.U_{inc}$. When the number of lighting angles increases, the running time will become a constraint.

[15] See the Matlab® "help" entry `fft`.

[16] Excepted if mentioned, the standard operation will also be applied coefficient by coefficient: $A^2 = A.A$, e^A will be the matrix composed of the exponential of the coefficients of A, $\frac{A}{B}$ the matrix composed of the coefficients of A divided by the coefficients of B and so on...

It is possible to get a simpler formulation in the case of plane wave illuminations $U_{inc} = e^{i\overrightarrow{k_0'}.\overrightarrow{r}}$. Indeed, from equation (II.12) one gets:

$$\begin{aligned} U_{dif}\left(\overrightarrow{r}\right) &= \frac{k_0'^2}{4\pi} \iiint\limits_{\overrightarrow{r_{\mathcal{O}}}\in\mathcal{O}} f\left(\overrightarrow{r_{\mathcal{O}}}\right) e^{i\overrightarrow{k_0'}.\overrightarrow{r_{\mathcal{O}}}} \frac{e^{ik_0'\left\|\overrightarrow{r}-\overrightarrow{r_{\mathcal{O}}}\right\|}}{\left\|\overrightarrow{r}-\overrightarrow{r_{\mathcal{O}}}\right\|} d^3\overrightarrow{r_{\mathcal{O}}} \\ &= \frac{k_0'^2 e^{i\overrightarrow{k_0'}.\overrightarrow{r}}}{4\pi} \iiint\limits_{\overrightarrow{r_{\mathcal{O}}}\in\mathcal{O}} f\left(\overrightarrow{r_{\mathcal{O}}}\right) e^{-i\overrightarrow{k_0'}.\left(\overrightarrow{r}-\overrightarrow{r_{\mathcal{O}}}\right)} \frac{e^{ik_0'\left\|\overrightarrow{r}-\overrightarrow{r_{\mathcal{O}}}\right\|}}{\left\|\overrightarrow{r}-\overrightarrow{r_{\mathcal{O}}}\right\|} d^3\overrightarrow{r_{\mathcal{O}}} \\ &= \frac{k_0'^2 e^{i\overrightarrow{k_0'}.\overrightarrow{r}}}{4\pi} \left(f\right) \star \underbrace{\left(e^{-i\overrightarrow{k_0'}.\overrightarrow{r}} \frac{e^{ik_0'\left\|\overrightarrow{r}\right\|}}{\left\|\overrightarrow{r}\right\|} \right)}_{\text{Convolution kernel}} \end{aligned} \tag{II.40}$$

This leads to the following numerical formulation:

$$\begin{aligned} U_{dif} = \frac{k_0'^2 e^{i\overrightarrow{k_0'}.(x_{3D}+x_0, y_{3D}+y_0, z_{3D}+z_s)}}{4\pi} . \mathrm{FFT}_{3D}^{-1}\Bigg(& \mathrm{FFT}_{3D}\left(f\right) . \cdots \\ & \mathrm{FFT}_{3D}\Bigg(e^{-i\overrightarrow{k_0'}.(x_{3D}+x_0, y_{3D}+y_0, z_{3D}+z_s)} . \cdots \\ & \frac{e^{ik_0'\sqrt{(x_{3D}+x_0)^2+(y_{3D}+y_0)^2+(z_{3D}+z_s)^2}}}{\sqrt{(x_{3D}+x_0)^2+(y_{3D}+y_0)^2+(z_{3D}+z_s)^2}} \Bigg) \Bigg) dv \end{aligned} \tag{II.41}$$

$$\begin{aligned} U_{dif} = \frac{k_0'^2 e^{i\overrightarrow{k_0'}.(x_{3D}, y_{3D}, z_{3D})}}{4\pi} . \mathrm{FFT}_{3D}^{-1}\Bigg(& \mathrm{FFT}_{3D}\left(f\right) . \cdots \\ & \mathrm{FFT}_{3D}\Bigg(e^{-i\overrightarrow{k_0'}.(x_{3D}, y_{3D}, z_{3D})} . \cdots \\ & \frac{e^{ik_0'\sqrt{(x_{3D}+x_0)^2+(y_{3D}+y_0)^2+(z_{3D}+z_s)^2}}}{\sqrt{(x_{3D}+x_0)^2+(y_{3D}+y_0)^2+(z_{3D}+z_s)^2}} \Bigg) \Bigg) dv \end{aligned} \tag{II.42}$$

Compared to the formulation (II.39), this latter reduces the number of needed FFTs. Indeed, $\mathrm{FFT}_{3D}\left(f\right)$ can be computed once for all, stored, and used for each lighting situation. Only the FFT of the kernel has to be computed for each situation since it depends on the position of the hologram (x_0, y_0, z_s).

One last remark must be done before using this numerical simulation and concerns the zero-padding of the object f. Indeed, if one performs directly the above formulation without any padding, one will get the situation of the figure II.6. The scheme is drawn for a lighting along the z-axis but remains valid along the other dimensions. The diffracting volume is in a cube on the left side, between z_{min} and z_{max} while the diffracted wave is computed in a cube on the right side around the sensor plane z_s. For each simulated plane, a whole volume on the object's side is used. To simulate the middle plane $z = z_s$ the red volume must be used and is sufficient.

The problems arise if one wants to simulate a wave front above or under this plane (or laterally for a lighting inclined relative to the sensor plane) like the purple or the green planes. Indeed, in these situations, two artefacts occur.

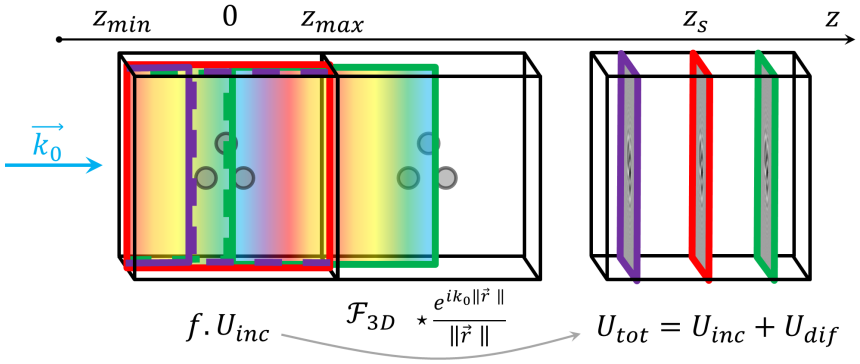

Figure II.6: Illustration of the volume wrapping if it is not correctly padded. The diffracting volume is in the cube on the left side and the simulated diffracted wave is in the cube on the right. For a given simulated plane, a whole cube around the object is used in the convolution. The red, green and purple colors indicate the needed volume to simulate a given plane. Absence of padding leads to two artefacts: the object, originally placed between z_{min} and z_{max} becomes periodic and the wave front is not consistent. The scheme only pictures the situation of a lighting direction along the z-axis but is valid for the three dimensions.

Firstly, the FFT makes the volume periodic. For example, to compute the green plane, one can see on the left in full line the volume that it is used (the dashed lines represents the wrapping) with an object that has been duplicated. Everything behaves as if a new object was diffracting and the diffracted pattern is consequently not consistent with the initial 3D object.

And secondly, there is a phase jump in the wrapping process. As one can see once again on the green volume, the rainbow pattern, symbolizing the phase evolution in space of the incident wave front U_{inc}, has a discontinuity at z_{max}: the phase jumps to its z_{min} value, creating this inconsistency. As seen later in this section, the phase value is very important since it is the part responsible for the interference between the incident wave front and the diffracted wave. The present wrapping creates a diffracted wave not consistent with the phase shift introduced by the propagation along the direction of the wave vector and which is carried by the incident wave.

Consequently, as this object duplication and phase inconsistency happen in all directions, one must zero-pad the object on a volume $\left(x_{3D}^{pad}, y_{3D}^{pad}, z_{3D}^{pad}\right)$ at least twice as big as the initial volume along all directions. This prevents the duplication of the object[17]. The kernel must also be computed on a bigger volume for the convolution step. This prevents the phase jumps. Noting *pad* the zero-padding operation and pad^{-1} the extraction of a volume with the initial size from a padded volume, the

[17] One has to be very careful on where is the zero-frequency in the used FFT definition. Using Matlab®, there must always be a 0 inside the kernel vectors: at the center if the pixel number nb_{pix} is odd and placed at $nb_{pix}/2$ if this number is even.

numerical formulations become:

$$\boxed{\begin{aligned} U_{dif} = pad^{-1}\Bigg(\mathrm{FFT}_{3D}^{-1}\Bigg(\mathrm{FFT}_{3D}\left(pad\left(f\left(x_{3D},y_{3D},z_{3D}\right)\cdot\cdots\right.\right. \\ \left.\left. U_{inc}\left(x_{3D},y_{3D},z_{3D}\right)\right)\right).\mathrm{FFT}_{3D}\left(\frac{k_0'^2}{4\pi}.\cdots \right. \\ \left.\left.\left.\frac{e^{ik_0'\sqrt{\left(x_{3D}^{pad}+x_0\right)^2+\left(y_{3D}^{pad}+y_0\right)^2+\left(z_{3D}^{pad}+z_s\right)^2}}}{\sqrt{\left(x_{3D}^{pad}+x_0\right)^2+\left(y_{3D}^{pad}+y_0\right)^2+\left(z_{3D}^{pad}+z_s\right)^2}}\right)\right)\Bigg)dv \end{aligned}} \tag{II.43}$$

for the general problem and

$$\boxed{\begin{aligned} U_{dif} = \frac{k_0'^2 e^{i\overrightarrow{k_0'}.\left(x_{3D},y_{3D},z_{3D}\right)}}{4\pi}.pad^{-1}\Bigg(\mathrm{FFT}_{3D}^{-1}\Bigg(\mathrm{FFT}_{3D}\left(pad\left(f\right)\right)\cdot\cdots \\ \mathrm{FFT}_{3D}\Bigg(e^{-i\overrightarrow{k_0'}.\left(x_{3D}^{pad},y_{3D}^{pad},z_{3D}^{pad}\right)}.\cdots \\ \left.\left.\frac{e^{ik_0'\sqrt{\left(x_{3D}^{pad}+x_0\right)^2+\left(y_{3D}^{pad}+y_0\right)^2+\left(z_{3D}^{pad}+z_s\right)^2}}}{\sqrt{\left(x_{3D}^{pad}+x_0\right)^2+\left(y_{3D}^{pad}+y_0\right)^2+\left(z_{3D}^{pad}+z_s\right)^2}}\right)\right)\Bigg)dv \end{aligned}} \tag{II.44}$$

for the plane wave situation.

Fourier diffraction theorem Let's now find a numerical approach of the Fourier diffraction theorem expressed in section 2. As mentioned previously, one will have to tackle with different pitfalls of the analytic formulation: the estimation of spherical caps into a Cartesian mesh as the one introduced above (x_{3D}, y_{3D}, z_{3D}) and the translation in the Fourier domain according to the relations (II.19). The aim is also to express the diffracted wave on the sensor plane $z = z_s$ centered on the hologram position (x_0, y_0).

Let's start by using the fact that a modulation in the spatial domain is a translation in the frequency domain[18]:

$$\mathcal{F}_{2D}\left[g\left(x,y\right)\right]\left(u+u_0,v+v_0\right) = \mathcal{F}_{2D}\left[g\left(x,y\right)e^{-2i\pi(xu_0+yv_0)}\right]\left(u,v\right) \tag{II.45}$$

and *vice versa* that a translation in the spatial domain is a modulation in the frequency domain:

$$\mathcal{F}_{2D}^{-1}\left[h\left(u,v\right)\right]\left(x+x_0,y+y_0\right) = \mathcal{F}_{2D}^{-1}\left[e^{2i\pi(x_0u+y_0v)}h\left(u,v\right)\right]\left(x,y\right) \tag{II.46}$$

[18]The variables of integration are explicitly enlightened: $\mathcal{F}_{2D}\left[g\left(x,y\right)\right]\left(u,v\right)$ means the 2D Fourier transform of the function g, of spatial variables (x, y), estimated at the frequencies (u, v). The integral is consequently along the x and y variables.

Using equality (II.45) for $g(x,y) = U_{dif}(x,y;z_s)$ and the Fourier diffraction theorem (II.18) by noting $(u_0,v_0,w_0) = \left(\frac{n_0.p_0}{\lambda_0}, \frac{n_0.q_0}{\lambda_0}, \frac{n_0.m_0}{\lambda_0}\right)$, it comes[19]:

$$\begin{aligned} U_{dif}(x,y;z_s) &= e^{2i\pi(xu_0+yv_0)}\mathcal{F}_{2D}^{-1}\Big[\cdots \\ &\qquad \mathcal{F}_{2D}\left[U_{dif}(x,y;z_s)\right](u+u_0,v+v_0;z_s)\Big](x,y;z_s) \\ &= e^{2i\pi(xu_0+yv_0)}\mathcal{F}_{2D}^{-1}\Bigg[\frac{ik_0'^2 e^{2i\pi w(u+u_0,v+v_0)z_s}}{4\pi w(u+u_0,v+v_0)}\times\cdots \\ &\qquad \mathcal{F}_{3D}[f](u,v,w(u+u_0,v+v_0)-w_0)\Bigg](x,y;z_s) \end{aligned} \tag{II.47}$$

with $w(u,v) = \sqrt{\frac{n_0^2}{\lambda_0^2} - u^2 - v^2}$. Applying this equality to $(x+x_0, y+y_0)$ and according to the equality (II.46) applied for:

$$h(u,v) = \frac{ik_0'^2 e^{2i\pi w(u+u_0,v+v_0)z_s}}{4\pi w(u+u_0,v+v_0)}\mathcal{F}_{3D}[f](u,v,w(u+u_0,v+v_0)-w_0)$$

it finally comes:

$$\begin{aligned} U_{dif}(x+x_0,y+y_0;z_s) = e^{2i\pi((x+x_0)u_0+(y+y_0)v_0)}\mathcal{F}_{2D}^{-1}\Big[\cdots \\ e^{2i\pi(x_0u+y_0v)}\times\frac{ik_0'^2 e^{2i\pi w(u+u_0,v+v_0)z_s}}{4\pi w(u+u_0,v+v_0)}\cdots \\ \mathcal{F}_{3D}[f](u,v,w(u+u_0,v+v_0)-w_0)\Big](x,y;z_s) \end{aligned} \tag{II.48}$$

This formulation directly gives the expression of the diffracted wave centered on (x_0,y_0) and based on the 3D Fourier transform of the object f expressed in the natural frequency coordinates: $\mathcal{F}_{3D}[f](u,v,w)$. Before giving its numerical form, the problem of the estimation of the spherical surface $(u,v,w(u+u_0,v+v_0)-w_0)$ remains. Indeed, as previously mentioned, in the numerical formulation, u and v will be discrete, leading to points placed in the 3D Fourier space, but not necessary lying on the nodes of the Cartesian mesh on which the Fourier transform of f is computed, as one can see in figure II.7.

Finding a good estimate of their value is not trivial in the Fourier space. Let's nevertheless focus on the two simplest ones that can be implemented in standard spatial domain: a nearest-neighbor technique and a linear interpolation.

The nearest-neighbor interpolation consists in approximating that the value of the Fourier transform on the discrete caps is equal to the value of the closest voxel. For example in the figure, the value on $\left(u_{i_p}, w\left(u_{i_p}\right)\right)$ will be approximated by the one on (u_{i_v}, w_{k_v}):

$$f\left(u_{i_p}, w\left(u_{i_p}\right)\right) \simeq f(u_{i_v}, w_{k_v}) \tag{II.49}$$

[19]It is implied here that: $\mathcal{F}_{3D}[f](u,v,w) = \mathcal{F}_{3D}[f(x,y,z)](u,v,w)$

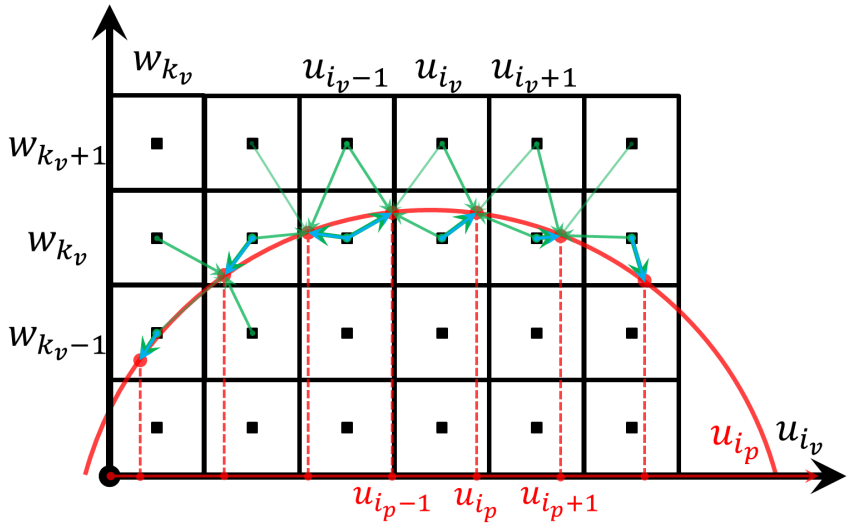

Figure II.7: Illustration of a discrete spherical cap (in red) not lying on the discrete Cartesian mesh (in black) for a given function f. To ease the reading, the scheme is drawn in two dimension but easily adaptable to the 3D problem. The value on each of the red dots is either estimated as being equal to the value of its nearest-neighbor (in blue) or being a linear interpolation of the values of its four (eight in 3D) neighbors (in green), weighted by the involved distances. u_{i_p} and u_{i_v} are the discrete abscissae of the frequency axis along x for the pixels and the voxels. w_{k_v} are the discrete coordinates of the frequency axis along z for the voxels.

This is a strong approximation. For example both the points indexed by u_{i_p-2} and u_{i_p-1} will have the value on (u_{i_v-1}, w_{k_v}):

$$f\left(u_{i_p-2}, w\left(u_{i_p-2}\right)\right) \simeq f\left(u_{i_p-1}, w\left(u_{i_p-1}\right)\right) \simeq f\left(u_{i_v-1}, w_{k_v}\right)$$

Another solution is to perform a linear interpolation with the neighboring voxel values. The attributed value is then an average on the neighboring values, weighted with the relative distances. Still in figure II.7, the value on $\left(u_{i_p}, w\left(u_{i_p}\right)\right)$ is:

$$\begin{aligned} f\left(u_{i_p}, w\left(u_{i_p}\right)\right) \simeq\ & t_u t_w f\left(u_{i_v+1}, w_{k_v+1}\right) + t_u\left(1-t_w\right) f\left(u_{i_v+1}, w_{k_v}\right) + \cdots \\ & \left(1-t_u\right) t_w f\left(u_{i_v}, w_{k_v+1}\right) + \cdots \\ & \left(1-t_u\right)\left(1-t_w\right) f\left(u_{i_v}, w_{k_v}\right) \end{aligned} \tag{II.50}$$

with $t_u = \frac{u_{i_p}-u_{i_v}}{u_{i_v+1}-u_{i_v}}$ and $t_w = \frac{w\left(u_{i_p}\right)-w_{k_v}}{w_{k_v+1}-w_{k_v}}$. This formula naturally extends to three dimensions by adding a weighting factor on the v-axis and therefore has eight terms.

Thus this method is more time and memory consuming than the nearest-neighbor approach since eight indices must be found instead of one and the linear distances must also be computed to estimate the eight weights.

Now let $interp\left(f, (u, v, w)\right)$ be the function giving the approximation on (u, v, w) of a function f known on a Cartesian mesh either using the nearest-neighbor technique or the linear interpolation. It is possible now to give a discrete formulation of the Fourier diffraction theorem.

Keeping the notation introduced above, let's (x_{3D}, y_{3D}, z_{3D}) be the 3D mesh centered on $(0,0,0)$ on which the object is defined and be dx^v, dy^v and dz^v the voxel side lengths. And let's (x_{2D}, y_{2D}) be the 2D mesh centered on $(0,0)$ modeling the sensor and dx^p, dy^p the pixel pitches along the two directions x and y. As written above, (x_{3D}, y_{3D}) and (x_{2D}, y_{2D}) can be different and do not have to overlap.

u_{2D} and v_{2D} will be the coordinates in the Fourier space corresponding to x_{2D} and y_{2D}. With these notations, the discrete formulation of the Fourier diffraction theorem is:

$$\begin{aligned} U_{dif} = e^{2i\pi((x_{2D}+x_0)u_0+(y_{2D}+y_0)v_0)} pad^{-1}\Bigg[\mathrm{FFT}_{2D}^{-1}\Bigg[\cdots \\ e^{2i\pi\left(x_0 u_{2D}^{pad}+y_0 v_{2D}^{pad}\right)} . \frac{ik_0'^2 e^{2i\pi w\left(u_{2D}^{pad}+u_0, v_{2D}^{pad}+v_0\right) z_s}}{4\pi w\left(u_{2D}^{pad}+u_0, v_{2D}^{pad}+v_0\right)} . \cdots \\ interp\Big[\mathrm{FFT}_{3D}\left[pad\left(f\left(x_{3D}, y_{3D}, z_{3D}\right)\right)\right], \cdots \\ \left(u_{2D}^{pad}, v_{2D}^{pad}, w\left(u_{2D}^{pad}+u_0, v_{2D}^{pad}+v_0\right) - w_0\right)\Big]\Bigg]\Bigg] \frac{dv}{ds} \end{aligned} \tag{II.51}$$

with $w(u,v) = \sqrt{\frac{n_0^2}{\lambda_0^2} - u^2 - v^2}$, $(u_0, v_0, w_0) = \left(\frac{n_0.p_0}{\lambda_0}, \frac{n_0.q_0}{\lambda_0}, \frac{n_0.m_0}{\lambda_0}\right)$, $ds = dx^p.dy^p$ the elementary pixel surface and $dv = dx^v.dy^v.dz^v$ the elementary voxel volume.

3.2 Comparison of the two models

To test and compare the different models, simulations were performed on a numerical object $\mathcal{O}$ composed of cubic voxels v with a side of $d_{pix} = 1.67\ \mu m$. It is composed of three identical spheres of radius $r_c = 10\ \mu m$ which present a difference of refractive index $\delta n = 0.005i$ with their surrounding medium of refractive index $n_0 = 1$. The three spheres are placed at different heights: $z_1 = 14.d_{pix} = 23.38\ \mu m$, $z_2 = -16.d_{pix} = -26.72\ \mu m$ and $z_3 = d_{pix} = 1.67\ \mu m$ (see figure II.8.a). The holograms are simulated for a wavelength of $\lambda_0 = 630\ nm$ with a distance between the hologram plane and the center of the volume of $z_s = 1.5\ mm$. Two lighting positions are tested: a normal illumination orthogonal to the sensor plane and a tilted illumination. The tilted illumination is tilted by an angle $\theta = 35°$ compared to the axis orthogonal to the sensor and rotated of an angle $\varphi = 125°$ around this axis.

Four direct models are compared:

- Volume integration: the reference hologram is given by the integral (II.12), numerically performed in the real space by a discrete integration, voxel by

voxel:

$$U_{dif} \simeq \frac{k_0'^2}{4\pi} \sum_{v \in \mathcal{O}} f_v\left(x_v, y_v, z_v\right) . U_{inc}\left(x_v, y_v, z_v\right) . \cdots \\ \frac{e^{ik_0' \sqrt{(x_{2D}+x_0-x_v)^2+(y_{2D}+y_0-y_v)^2+(z_s-z_v)^2}}}{\sqrt{\left(x_{2D}+x_0-x_v\right)^2+\left(y_{2D}+y_0-y_v\right)^2+\left(z_s-z_v\right)^2}} d_{pix}^3 \tag{II.52}$$

- Fourier convolution: the integral (II.12) is performed in the Fourier domain using the formulation (II.43)
- Linear interpolation: Fourier diffraction theorem (II.51) with a linear interpolation in the Fourier domain by the function *interp*.
- Nearest-neighbor: Fourier diffraction theorem (II.51) with a nearest-neighbor interpolation in the Fourier domain by the function *interp*.

For the convolution, the volume is composed of $512 \times 512 \times 128$ voxels. To improve the coverage of the spherical caps, the Fourier diffraction theorem is used on a $512 \times 512 \times 256$ voxels[20]. For all the situations, both the 2D and the 3D domains are zero-padded.

Figure II.8 compares the intensities given by the different models for a normal illumination. Their phase are compared in figure II.9 as well as the intensities for a tilted lighting.

The convolution in the Fourier domain and the Fourier diffraction theorem with a linear interpolation present a good agreement with the reference hologram, their maximal divergence being less than $3.5\ 10^{-3}$ for the two intensities (arbitrary unit for an incident wave normalized to one, $|U_{inc}| = 1$) and the phase (rad) (see table [II.1] and figures II.8.c,d and figures II.9.b,c,f,g.).

For the normal illumination, the nearest-neighbor interpolation gives worse results on the two beads which are further from the median plane $z = 0$ in the simulated object, both for the amplitude and the phase (figures II.8.e and II.9.d.). The situation degrades even more for the tilted illumination with lots of artifacts appearing in the background of the simulated picture in figure II.9.h. Nevertheless, the amplitude of the divergence remains low, three orders of magnitude below the reference hologram intensity (see table [II.1]).

Some tests, not presented here, show that this is related to both the interpolation method and the number of planes nb_z. Indeed, if the simulated volume is not thick enough compared to its width on the xy-plane, a part of the spherical caps in the Fourier diffraction theorem may fall outside the accessible Fourier domain and cannot be extracted to simulate the diffracted wave. It appears that the linear interpolation is more robust to this effect.

[20]Simulation with $nb_z = 128$ (not presented here) showed that the two interpolations methods fail to correctly simulate the hologram because a too important part of the spherical caps falls outside the simulated Fourier domain.

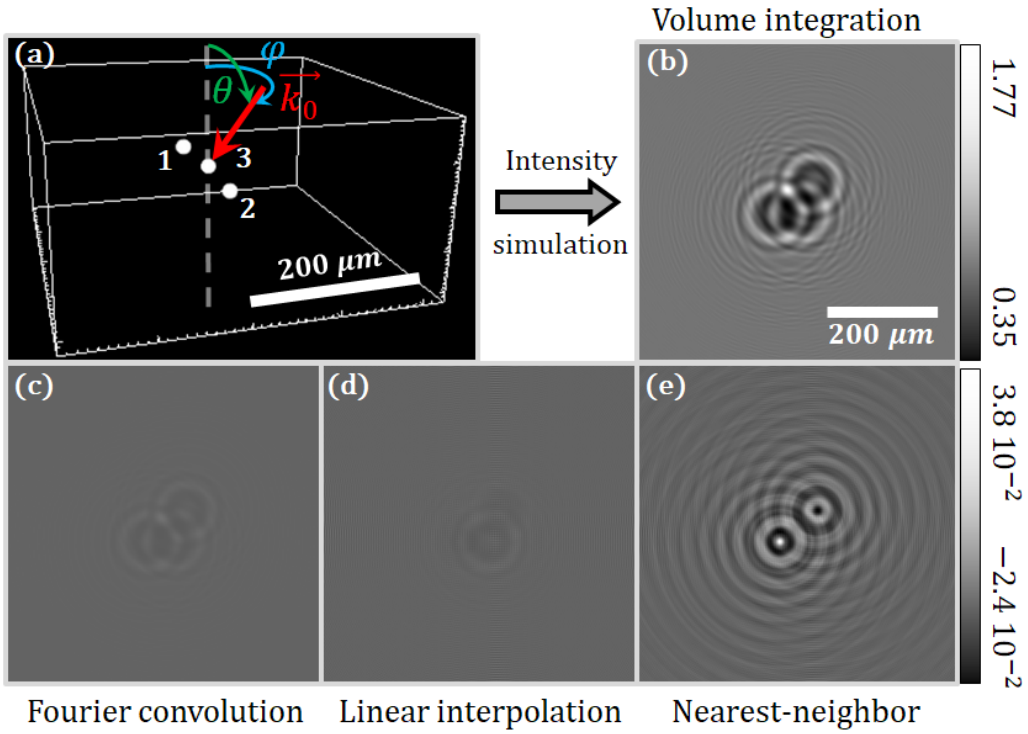

Figure II.8: Comparison of the different models on a numerical object composed of three identical beads (a) with a normal incidence. Differences between the different results and the reference hologram intensity obtained by integration voxel by voxel (b), for the convolution in the Fourier domain (c) and the Fourier diffraction theorem with a linear (d) or nearest-neighbor (e) interpolation in the Fourier domain.

		Volume integration	Fourier convolution	Linear interpolation	Nearest-neighbor
$\lvert U_{tot}\rvert$ (normal)	*min*	0.35	$-1.9\ 10^{-3}$	$-3.2\ 10^{-3}$	$-2.4\ 10^{-2}$
	max	1.77	$3.4\ 10^{-3}$	$3.0\ 10^{-3}$	$3.8\ 10^{-2}$
$\arg(U_{tot})$ (normal)	*min*	−0.62	$-1.6\ 10^{-3}$	$-1.8\ 10^{-3}$	$-1.5\ 10^{-2}$
	max	0.07	$1.6\ 10^{-3}$	$1.7\ 10^{-3}$	$1.5\ 10^{-2}$
$\lvert U_{tot}\rvert$ (tilted)	*min*	0.41	$-1.8\ 10^{-3}$	$-1.3\ 10^{-3}$	$-1.8\ 10^{-3}$
	max	1.72	$3.2\ 10^{-3}$	$1.9\ 10^{-3}$	$2.9\ 10^{-3}$

Table II.1: Table of the minimal and maximal gray values of the reference hologram (volume integration) and of the differences of the different models (Fourier convolution, Fourier diffraction theorem with linear or nearest-neighbor interpolation) with this reference hologram (see figures II.8 and II.9) for the normal and the tilted illuminations.

In addition to this comparison, it is also interesting to use the ability of the convolution formulation (II.43) to work with any incident plane wave U_{inc} to test

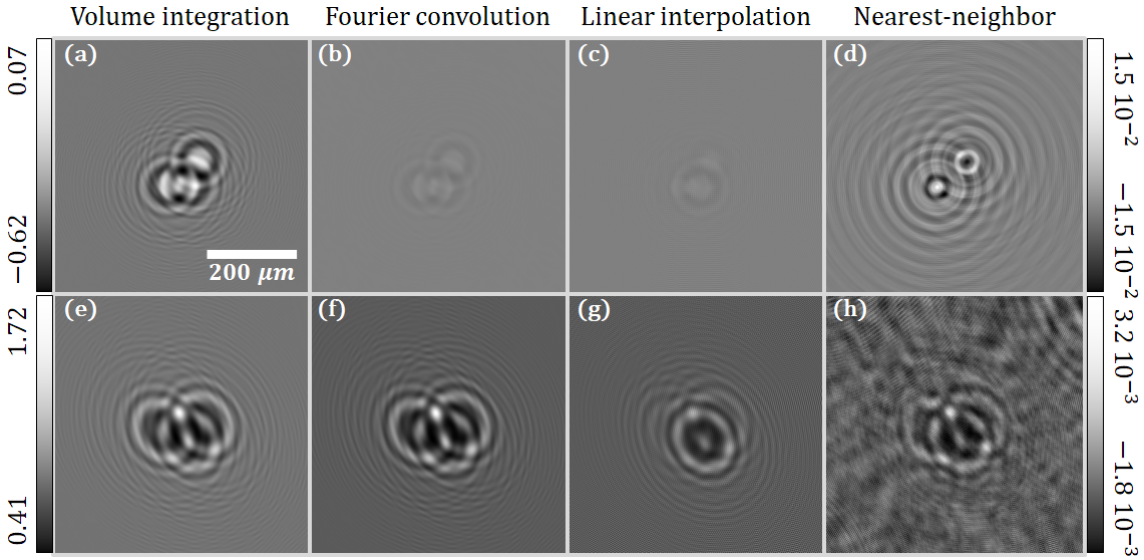

Figure II.9: Comparison of the different models on a numerical object composed of three identical beads. Differences between the different models and the reference holograms phase (a-d) and intensity (e-h) obtained by integration voxel by voxel for a normal incidence (a) and a tilted lighting (e) for the convolution in the Fourier domain (b,f), the Fourier diffraction theorem with a linear (c,g) or nearest-neighbor (d,h) interpolation in the Fourier domain. The calibration bars on the left give the gray values of the reference holograms. The calibration bars on the right give the gray values of the three comparisons with the same dynamics.

the assumption that the spherical wave produced by the source can be approximated by a plane wave because of its large distance d to the sample.

To do so, the spherical wave is simulated for a normal illumination by:

$$U_{inc}(x,y,z) = d.\frac{e^{ik_0'\sqrt{x^2+y^2+(z+d)^2}}}{\sqrt{x^2+y^2+(z+d)^2}} \tag{II.53}$$

The factor d is used to normalize the amplitude of the wave so that it equals 1 at the center $O = (0,0,0)$ of the sample.

Different distances $d \in \{1\ m, 10\ cm, 7\ cm5\ cm\}$ were tested and their differences with the reference hologram obtained for an incident plane wave are presented in figure II.10.

The holograms seem dilated, an effect which increases when the distance to the source diminishes and which is used in standard in-line holography to perform magnification [77]. This dilation affects the rings of the interference patterns which are shifted of several microns. It would be necessary to quantify this effect on the reconstructions which use the assumption that the incident wave is plane.

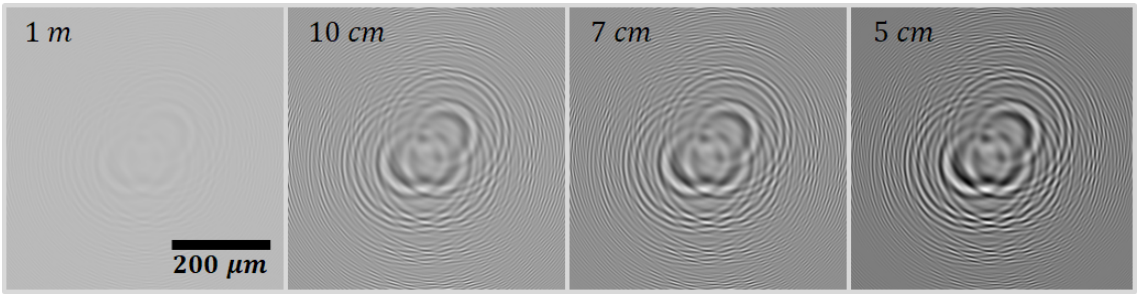

Figure II.10: Comparison of the effect of the distance of the light source d on a numerical object composed of three identical beads. Differences between the intensities at different distances $d \in \{1\ m, 10\ cm, 7\ cm, 5\ cm\}$ and the reference hologram obtained with a plane wave (source placed at infinity) for a normal incidence with the same gray values dynamics.

3.3 Consistency with the 2D models

After comparing the 3D propagation models, studying their consistency with the 2D model is interesting to know if some 2D algorithms can be used in the 3D reconstruction processes.

The main difference between the models using 2D propagators introduced in chapter I, section 3 and the ones given by the 3D equations in this chapter is that the former can directly work on the total complex wave front whereas the latter model only works on the diffracted wave. More steps are consequently needed to retrieve the unknown sample from the recording of the intensity of the wave front by the sensor.

The phase information of the wave front being lost, the quality of the reconstruction will depend on how the algorithms will deal with this loss, as one can see in figure II.11 where the holograms of the previous section are reconstructed using the 2D Fresnel propagator introduced in I, section 3 with a distance $-z_s$. The convolution (I.6) is performed in the zero-padded Fourier domain using the Fourier transform of the Fresnel kernel (I.5). To do so, the amplitudes of the holograms to back-propagate are initialized with the square root of the simulated intensities (and eventually the simulated phase) and then one-padded.

All the propagated holograms are composed of 512×512 pixels.

To back-propagate the tilted complex waves, the phase is first corrected by a phase ramp characteristic of the tilted illumination and equal to the incident plane wave on the sensor U_{inc}. Indeed, the Fresnel propagator assumes paraxial propagation normal to the sensor. Then, the propagation distance z_s is corrected by the tilt angle θ to get the effective propagation distance[21] $z_s^{eff} = z_s / \cos\theta$.

The back-propagations correspond to the effective 2D complex transmissive planes which would give the same holograms.

First, the 2D and the 3D propagation distances are coherent as the beads are in focus in the 2D reconstructions.

[21] For distance $z_s = 1.5\ mm$ and an angle $\theta = 35°$, the effective distance is $z_s^{eff} \simeq 1.83\ mm$

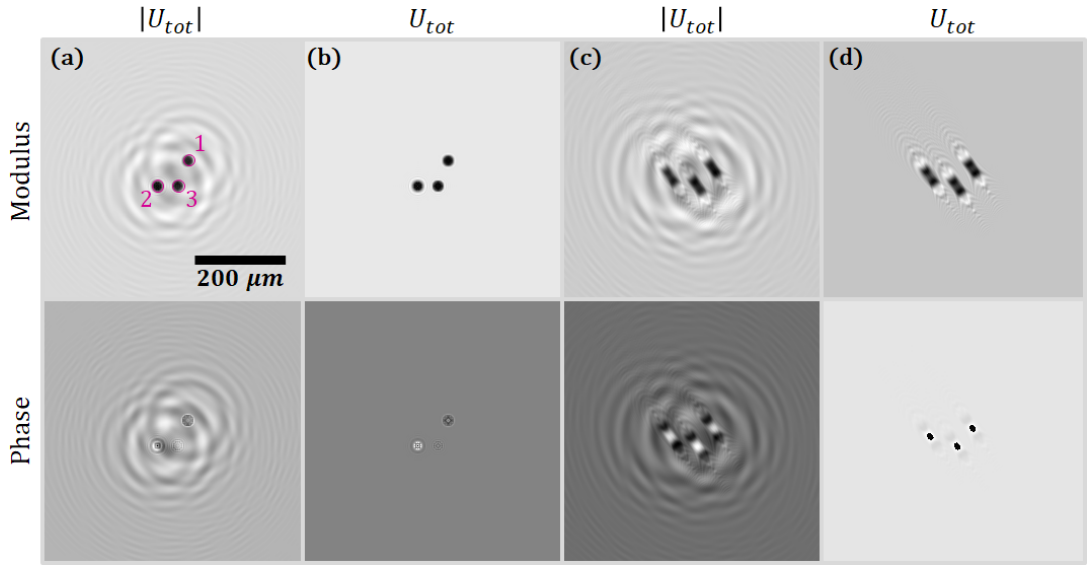

Figure II.11: Modulus and phase of the 2D back-propagations of the simulated holograms of figures II.8 and II.9 for a normal incident light (a,b) and a tilted lighting (c,d) without (a,c) and with (b,d) the knowledge of the phase in the hologram plane. The dynamics of each picture was maximized.

When only the intensity is back-propagated, twin image artifacts surround the focused beads even for the tilted illumination (figures II.11.a,c).

Then, the phase produced by the 3D model is coherent with a 2D propagation as the twin-image disappears when the full information of the complex wave is used for the back-propagation (figures II.11.b,d).

Looking at the phase of the three beads, one can notice the phase inversion phenomenon [78] at the focal plane for the absorbent objects. The two beads 1 and 2 which are on both sides of the focal plane present a positive (bead 2) and negative phase (bead 1) whereas the bead 3 which is placed closed to the focal plane $z = 0$ disappears in the phase pictures (figures II.11.a,b). This is coherent with the fact that a purely imaginary complex index is interpreted as a 2D absorbent object.

Looking at the back-propagation for the tilted illumination (figures II.11.c,d), one can see that the 2D Fresnel propagator fails to precisely reconstruct the beads. This is an expected result as this paraxial kernel can only propagate circles and cannot focus ellipses.

To continue testing the coherence of the refractive index interpretation, holograms were simulated for a purely dephasing object with $\delta n = 0.005$ and then back-propagated for a normal incident plane wave.

The results in figure II.12 show that the information is now mainly present in the phase images[22]. But unlike the previous case of an absorbent object, a part of the

[22]Note here that the dynamics of the gray values calibration bar were maximized for each view and can consequently lead to misinterpretation. But comparing the intensity of the beads with the intensity of the twin-image artifacts, it clearly appears that the information is concentrated on the phase images.

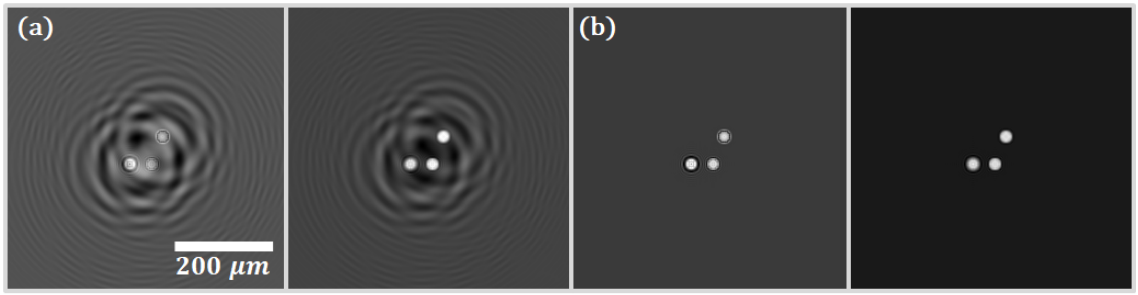

Figure II.12: Modulus and phase of the 2D back-propagations of the simulated holograms of a phase object for a normal incident light without (a) and with (b) the knowledge of the phase in the hologram plane. The dynamics of each picture was maximized.

signal here is reconstructed into the modulus of the equivalent transmissive plane.

Figure II.13 compares the back-propagations of the holograms for different distances of the source with the hologram obtained for a plane wave illumination. As for the holograms, the reconstructions are dilated, with an effect visible even at 10 cm. The focal distance to get the beads into focus is also slightly changed: ~ 1520 μm for $d = 10$ cm, ~ 1530 μm for $d = 7$ cm and ~ 1550 μm for $d = 5$ cm.

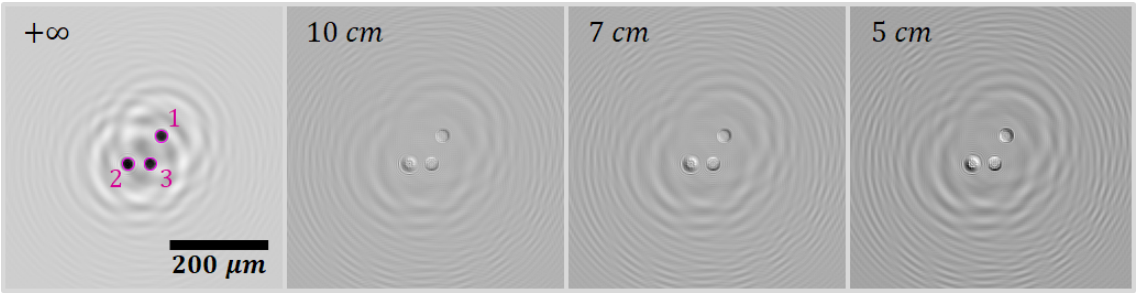

Figure II.13: Effect of the light source distance d on the modulus of the 2D back-propagations of the intensity holograms introduced in figure II.10. Differences of the 2D back-propagations for three different distances $d \in \{10\ cm, 7\ cm, 5\ cm\}$ with the plane wave incident light reconstructions $(+\infty)$. The three differences are given with the same gray values dynamic. The positions of the three reconstructed beads were measured for each 2D reconstruction (purple circles for the plane wave situation).

To better quantify the dilation effect, the positions of the reconstructed beads are extracted using the `trackmate` plug-in in `ImageJ` [79]. These positions are used to compute the relative distances of the three beads. Dilation ratios are computed by dividing these distances by their corresponding counterpart for the plane wave illumination (see table [II.2]). The scaling factors are obtained by averaging these ratios.

The approximation of the incident spherical wave by a plane wave leads to a scaling factor on the xy-plane which is constrained in a range from 1 to 3 % for

d	Beads distances (μm)			Ratios			
	$1 \leftrightarrow 2$	$2 \leftrightarrow 3$	$1 \leftrightarrow 3$	$1 \leftrightarrow 2$	$2 \leftrightarrow 3$	$1 \leftrightarrow 3$	Average
$+\infty$	65.37	33.66	44.30	-	-	-	-
10 cm	66.22	34.08	44.92	1.013	1.012	1.014	1.013
7 cm	66.59	34.26	45.18	1.019	1.018	1.020	1.019
5 cm	67.09	34.52	45.54	1.026	1.026	1.028	1.027

Table II.2: Computation of the scaling factor due to the finite distance of the light source d. The positions of the three beads are measured for the different distances d and the reference situation of the plane wave illumination ($+\infty$) to compute their relative distances (see figure II.13.a). Ratios of these distances with the distances for the plane wave situation are averaged to determine the order of magnitude of the scaling factor.

a distance $d \in [5\ cm, 10\ cm]$ between the sample and the light source. As this is a geometrical effect on how the light source is seen by the scattering object, this ratio should not depend on the illumination wavelength or the distance between the sample and the sensor.

Then, the Born approximation is tested on real data. Emulsion of oil droplets of refractive index $n_{oil} = 1.38$ in water of refractive index $n_{H_2O} = 1.33$ are imaged with a standard 2D lens-free microscope for a red illumination $\lambda = 630\ nm$. A hologram is selected and back-propagated to estimate the droplet diameter (see figures II.14.a,b) by estimating the width of its profile. The back-propagation distance is $z_s = 1320\ \mu m$ in the air.

A numerical object is simulated accordingly by a sphere of diameter 9.5 μm placed in a volume of $nb_x^v = nb_y^v = 400$ and $nb_z^v = 256$ voxels of 1.67 μm^3 with refractive index $n_0 = 1.33$. The holograms of $nb_x^p = nb_y^p = 400$ pixels are simulated with the Fourier diffraction theorem with a linear interpolation in the Fourier domain, zero-padding both the 2D and the 3D domains with an effective propagating distance $z_s^{eff} = n_0.z_s = 1755.6\ \mu m$.

Two possible solutions for the difference of refractive index are tested. The expected situation of a phase object with a purely real refractive index $\delta n = 0.05$ (see figure II.14.d) and the opposite situation of an absorbent object with a purely imaginary difference of refractive index $\delta n = 0.05i$ (see figure II.14.c).

Surprisingly, it is the wrong situation which perfectly matches the data with a simulated absorbent object. It also shows the correctness of the effective propagating distance z_s^{eff} as the sizes of the holograms are equal.

This unexpected result comes from the non-validity of the Born approximation. As mentioned in section 1.2, the phase delay[23] introduced by the oil droplet is $2\pi l\delta n/\lambda \simeq 0.9\pi$ which is not negligible. The 2D reconstruction shows that even with the 2D Fresnel propagation the droplet is seen as an absorbent dot.

Having a purely imaginary δn is moreover the only way to match the simulations

[23]With $\delta n = 0.03$, $l = 9.5\ \mu m$ and $\lambda = 630\ nm$.

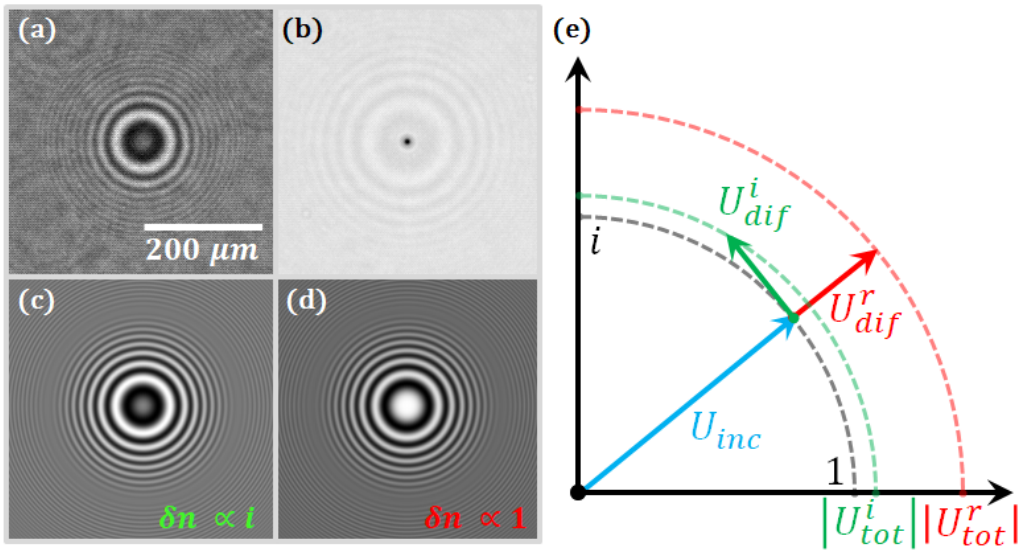

Figure II.14: Comparison of a real hologram acquired on an oil sphere immersed in water (a) and its 2D back-propagation intensity (b) with simulated holograms of an object of the same size with a purely imaginary (c) or purely real (d) difference of refractive index δn with its surrounding medium. (e) Scheme of the influence of the phase of the diffracted wave U_{dif} compared to the phase of the incident wave U_{inc} for a purely real (red) or purely imaginary (green) δn.

with the data: most of the holograms recorded during this PhD present a center with a gray value close from the background value. Looking back at the equations (II.7) and (II.12) and the figure II.14.e, the only possibility to keep a gray center with a homogeneous scattering object is to have a purely imaginary δn. Indeed, according to equation (II.12), because of the spherical propagator in the convolution, the phase of the diffracted wave U_{dif} at the center of the hologram[24] in the direction of $\overrightarrow{k'_0}$ is directly the phase of the incident plane wave U_{inc} modified by the phase of the scattering potential f.

And for a small refractive index δn one gets from equation (II.7):

$$\boxed{f\left(\overrightarrow{r}\right) \simeq 2\frac{\delta n}{n_0}} \tag{II.54}$$

This means that if the difference in the refractive index δn is real and positive, no phase shift is introduced in the diffracted wave whose complex representation is co-linear with the incident wave as for the red situation in figure II.14.e. Its interference with the incident wave is constructive and the total wave presents an intensity higher than the background as for the simulation in figure II.14.d. On the contrary, if the difference in the refractive index δn is purely imaginary, a $\pm\pi$ phase shift is introduced in the diffracted wave whose complex representation is

[24]Because for a position $\overrightarrow{r}$ in the direction of $\overrightarrow{k'_0}$, $U_{inc}\left(\overrightarrow{r_\mathcal{O}}\right) e^{ik'_0\|\overrightarrow{r}-\overrightarrow{r_\mathcal{O}}\|} = U_{inc}\left(\overrightarrow{r_\mathcal{O}}\right) e^{i\overrightarrow{k'_0}.\left(\overrightarrow{r}-\overrightarrow{r_\mathcal{O}}\right)} = U_{inc}\left(\overrightarrow{r}\right)$ and $1/\|\overrightarrow{r}-\overrightarrow{r_\mathcal{O}}\|$ does not introduced any phase.

now orthogonal to the incident wave as for the green situation in figure II.14.e. Its interference with the incident wave produces a total wave with an intensity similar with the incident wave, that is to say similar to the background as for the simulation in figure II.14.c.

Finally, let's show that it is impossible to retrieve the 3D information from a given 2D hologram with a reconstruction only based on a 2D back-propagation. Figure II.15 shows that back-propagating a hologram at different distances only produces a stack of focused and unfocused objects whose 3D rendering looks like columns with varying intensities. Each slice of the stack is moreover a transmissive plane which can produced the back-propagated hologram whereas in a real reconstructed volume, the hologram is a combination of all the information in the volume, some parts participating more than others in the hologram shaping.

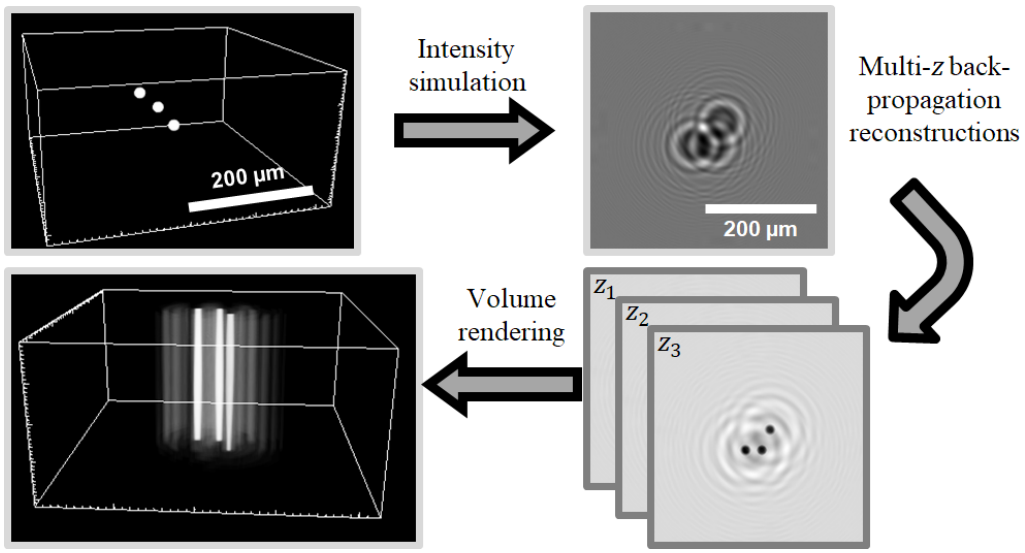

Figure II.15: Illustration of a multi-z reconstruction based on a simulated hologram ($z_s = 1.5\ mm$ and $\lambda_0 = 630\ nm$). *Top-right* - Intensity of the simulated hologram. *Bottom-right* - 2D back-propagations performed at different z. *Bottom-left* - 3D visualization of the obtained stack.

3.4 Conclusion and discussion

As a conclusion, the three tested direct models present a good agreement with the reference hologram for a plane wave illumination within a range of $4\ 10^{-2}$ from the reference hologram both for the intensity and the phase. As mentioned earlier, the Fourier diffraction theorem only needs one 3D Fourier transform to perform a simulation and is consequently the fastest. Nevertheless its accuracy depends on the interpolation technique. The linear interpolation gives the best results, but is longer and above all is not invertible if one wants to use the Fourier diffraction theorem

as a mapping tool of the Fourier domain of the reconstructed object[25]. This kind of reconstruction will be consequently based on nearest-neighbor interpolations. It has been shown that it gives lower quality results as a direct model and the same can be expected if it is used as a reconstruction tool.

To complete this study, more tests should be done. Indeed, it was mentioned that the number of planes nb_z has an effect on the numerical efficiency of the Fourier diffraction theorem. A better understanding of this effect can help to choose reconstruction parameters more wisely. In the tested situations, both the volume and the 2D grids are overlapping. It would be interesting to test the effect of a difference in the number of pixels nb_x^p and nb_y^p on the 2D plane and the number of voxels nb_x^v and nb_y^v in the 3D volume as well as a difference in the resolution dx^p, dy^p dx^v and dy^v, leading to a difference in the sampling and frequency in the Fourier domain.

On an other subject, it has been demonstrated that the finite distance between the sample and the light source leads to a spherical propagating wave which cannot be strictly assumed to be plane for distances lower than $d = 10\ cm$ generally used in lens-free microscopy. Working nevertheless under this assumption leads to a scaling factor in the range of 1 to 3 percent.

Once again, more studies are needed to better estimate this effect and to verify that it does not depend on the wavelength or the distance between the sample and the sensor and how it behaves with tilted illuminations.

Concerning the interpretation of the refractive index of the 3D numerical objects, it seems coherent for the very low diffracting objects which are simulated[26]. But it fails at explaining real data with a more realistic refractive index whose variation with the surrounding medium cannot be considered as weakly scattering. The interpretation even seems inverted: real holograms of phase objects are well simulated only for purely imaginary variations of refractive index which normally correspond to absorbent objects.

A more complete test on different objects of different sizes and refractive indices would be beneficial to really investigate the limit of the Born approximation and the induced effects in the reconstructions. Indeed, it does not hold in the case of a lens-free microscope for extended 3D cell cultures, as mentioned in the previous section 1.2.

[25]Indeed, the most intuitive solution would be to spread the values of the coefficients on the spherical caps in their surrounding voxels, weighted by the relative distances (see figure II.7 by reversing the arrows directions). This leads to a "dilution" of the coefficients. If one for example performs a mapping and then estimates back the diffracted wave, he will not find back its initial values. This prevents any stable reconstruction with a linear interpolation technique based on the mapping of the Fourier domain.

[26]$|\delta n| = 0.005$

Chapter III

A versatile prototype and first reconstruction algorithms

This chapter presents the work mainly done during the first year of the PhD program. A first prototype is developed from scratch to test different modalities and first ideas of reconstruction algorithms.

It allows having a first glance at 3D samples acquisition and the associated constraints, while giving an idea on the first algorithms performances and limitations. From these results, new directions are taken for the PhD work.

This work has led to a first publication in the Biomedical Optics Express journal [80].

1 Overview of the experimental bench

1.1 Design and functioning

Unlike 2D lens-free imaging, where only one image is required to retrieve the 2D object, one can expect that a reconstruction of a 3D object from lens-free acquisitions requires to multiply the viewing angles. For this purpose, a new experimental bench is developed, illustrated in figure III.1. It is composed of a semi-coherent illumination source and a CMOS sensor[1].

The semi-coherent illumination is composed of a 3λ LED[2]. To get a semi-coherent illumination, it is placed behind a 150 μm diameter pinhole. A diffuser is used to make the illumination on the pinhole uniform for the three wavelengths.

The spherical wave emitted by the pinhole can be considered as a plane wave if seen from far enough. That is why the sample is placed several centimeters away from the lighting ($\sim$ 7 cm)[3]. Since the lighting is not fully coherent, to record

[1]IDS - 29.4 mm^2, 3840×2748 monochromatic pixels, pixel pitch 1.67 μm - *ref.* UI-1492LE-M.

[2]LED CREE RGB, $\lambda_R = 630\ nm$, $\lambda_G = 520\ nm$, $\lambda_B = 450\ nm$ - *ref.* XLamp MC-E RGBW MCE4CT, with spectral widths of $\Delta\lambda_R \simeq 10\ nm$, $\Delta\lambda_G \simeq 40\ nm$, $\Delta\lambda_B \simeq 20\ nm$.

[3]A translational stage allows the user to change the distance of the illumination.

the produced hologram, the sensor is placed a few millimeters behind the sample, typically 1 to 3 mm.

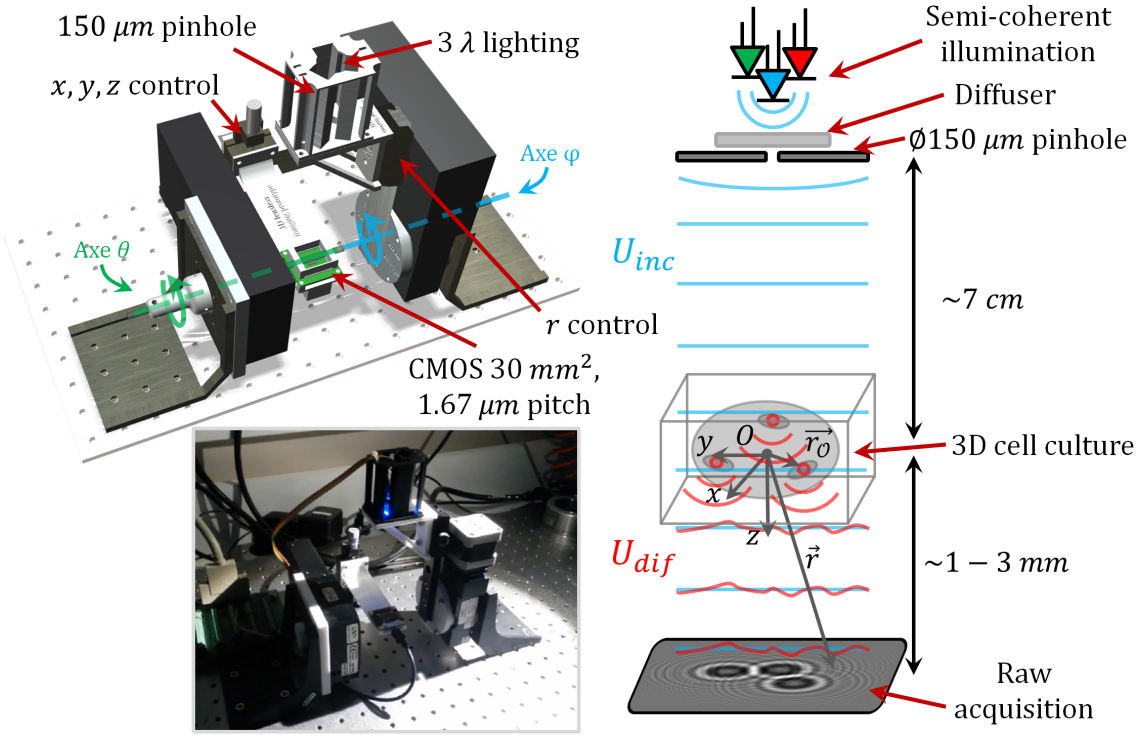

Figure III.1: *Left-hand side* - Experimental bench dedicated to lens-free diffractive tomography. *Right-hand side* - Optical scheme of the system. The semi-coherent incident plane wave U_{inc} passes through the sample volume. Each element of the volume diffracts the incident plane wave, behaving like secondary spherical sources, creating a diffracted wave U_{dif} as explained in chapter II, section 1. The sensor records the intensity of their summation: $I_{tot} = |U_{tot}|^2 = |U_{inc} + U_{dif}|^2$.

Two modes of acquisition are available on the setup:

- θ-mode: the illumination and the sensor are static. The object is rotated around an axis passing through its center with a rotation stage[4] about the θ-axis[5]. This geometry is similar to a X-ray tomographic scanner, where the light propagation remains orthogonal to the sensor. It can be used with samples trapped in capillary.

- φ-mode: the object and the sensor are static. The light source is rotated with a rotation stage [6] about the φ-axis[7]. The illumination direction is tilted relative to the sensor plane. This modality is the most adapted to 3D organoid culture in standard containers such as Petri dish or well plates.

[4]Newport - *ref.* URS75CC, controlled by a Newport universal motion controller - *ref.* ESP300
[5]See the green axis in figure II.4
[6]Newport - *ref.* M-URM80APP, controlled by a Newport universal motion controller - *ref.* ESP300
[7]See the blue axis in figure II.4

These two modes aim at different applications. The θ-mode pretends to be the simplest geometry as the lighting is always normally incident on the sensor, there is no problem of angle relative to the sensor or the different interfaces with different refractive indices. Moreover, all the angles around the object are theoretically available. Such a geometry is also the one commonly used in tomography and simplifies the preliminary studies of the possibility of a 3D lens-free microscope. This geometry could be used in a capsule cytometer, the capsules traveling in capillaries.

But this geometry is not adapted for 3D cell cultures in Petri dish which can only be fixed on the experimental bench. This is why the φ-mode is also designed in this bench to acquire the first biological data with tilted lighting. Nevertheless one can expect that this geometry will be harder to deal with since one will have to model the tilted propagation of the light. But its main disadvantage is the very limited angular coverage which is limited to roughly $\varphi \in [-45°, 45°]$. Such limitation is a huge problem in tomography that has to be dealt with. Moreover, on a more practical point of view, the more the lighting angle increases, the less the sensor gets energy and the holograms are harder to record.

1.2 First acquisitions

Inert and biological data are acquired with this prototype, both in θ-mode and φ-mode. Only the most informative data are presented here.

Inert data: a mosquito wing - A mosquito wing is imaged with the prototype. For the θ-mode it is fixed to a capillary inserted in the θ-motor stage whereas it is directly placed onto the sensor in the φ-mode.

The results are presented in figure III.2. It shows data acquired in both modes. The three dimensional shape and structure of the wing is clearly visible on both modes.

This figure emphasizes the differences between the two acquisition modes. On the left side, for the θ-mode, the dynamic remains identical for all angle while the object rotates about a well-defined vertical axis (not drawn in the figure). Some dust on the sensor is present at each angle at the same position on the picture which will lead to artefacts in the 3D reconstruction.

On the right side, the full frame representations of data acquired in the φ-mode show that there is no more a clearly identified rotation axis. It seems closer to a shadow projection during daytime, the shadow moving and spreading according to the lighting angle. This is due to the fact that in this geometry, the sensor stays still during the acquisitions. Nevertheless, 3D information can be retrieved from the data, since it is possible to see some parts of the wing moving above one another as the lighting rotates. Another side effect of the geometry is the loss of signal to noise ratio as the lighting tilts (for a constant lighting intensity and integration time), leading to a drop of the dynamic.

Biological data: Matrigel® - The main concern with the living sample is that they must be kept in the matrix providing their life support (culture medium

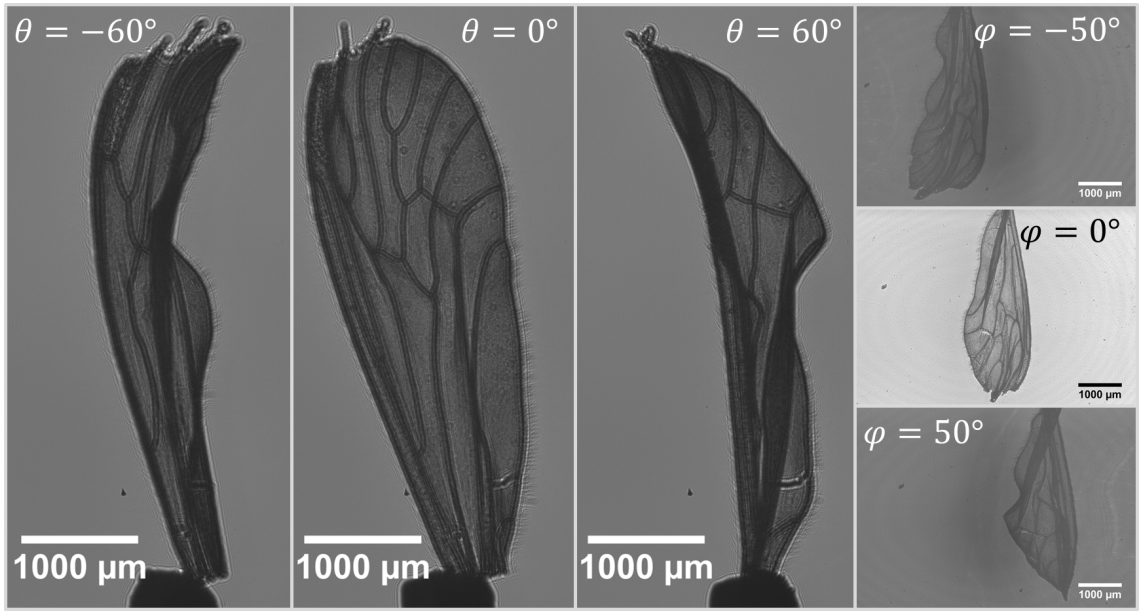

Figure III.2: *Left-hand side* - Cropped acquisitions in the θ-mode at different angles $\theta \in \{-60°, 0°, 60°\}$ of a mosquito wing in the blue channel $\lambda = 450\ nm$.
Right-hand side - Full frame acquisitions in the φ-mode at different angles $\varphi \in \{-50°, 0°, 50°\}$ of a mosquito wing in the red channel $\lambda = 630\ nm$.

or Matrigel® for instance). Its texture may raise some issues[8], especially in the θ-mode. If it is rigid enough, one can try to fix it on a spike, whereas if it is too liquid, it can be put in capillary. These two solutions are tested as presented in figure III.3.

The first thing that appears in the figure is that the gap of refractive index between the air $n_{air} = 1$ and the culture medium, close to the water refractive index $n_{H_20} \simeq 1.33$ is too big. In the air, the Matrigel® and the capillary behave like a lens and focus the light. The tubing inside the capillary is then not visible.

A pool is designed and 3D printed to perform index matching. The Matrigel® is now visible on the spike, but inside the capillary the refractive index gap between the capillary glass and the water is still too important. Replacing water by adapted immersion oil would not solve the problem since the tubing inside the capillary would still be filled with water and Matrigel®.

Acquisitions in φ-mode are easier to perform as the Petri dish has only to be laid on the sensor. Results on epithelial cells are presented in figure III.4. The arrows pointing at different cells at different angles show that the parallax effect is sufficient enough to record 3D information. The distortion at high angles of the hologram is also an important effect that one can see in the medallions.

To get such a culture, RWPE1 cells are grown in Matrigel® according to a no top coat protocol[9]. This means that the cells are seeded on the top of a Matrigel® bed and then culture media is slowly poured over the attached cells and is changed every

[8]For example, the Matrigel® has a viscosity which depends on the temperature.
[9]See chapter IV, section 5.1 for more details on the cells conditioning and the culture protocol.

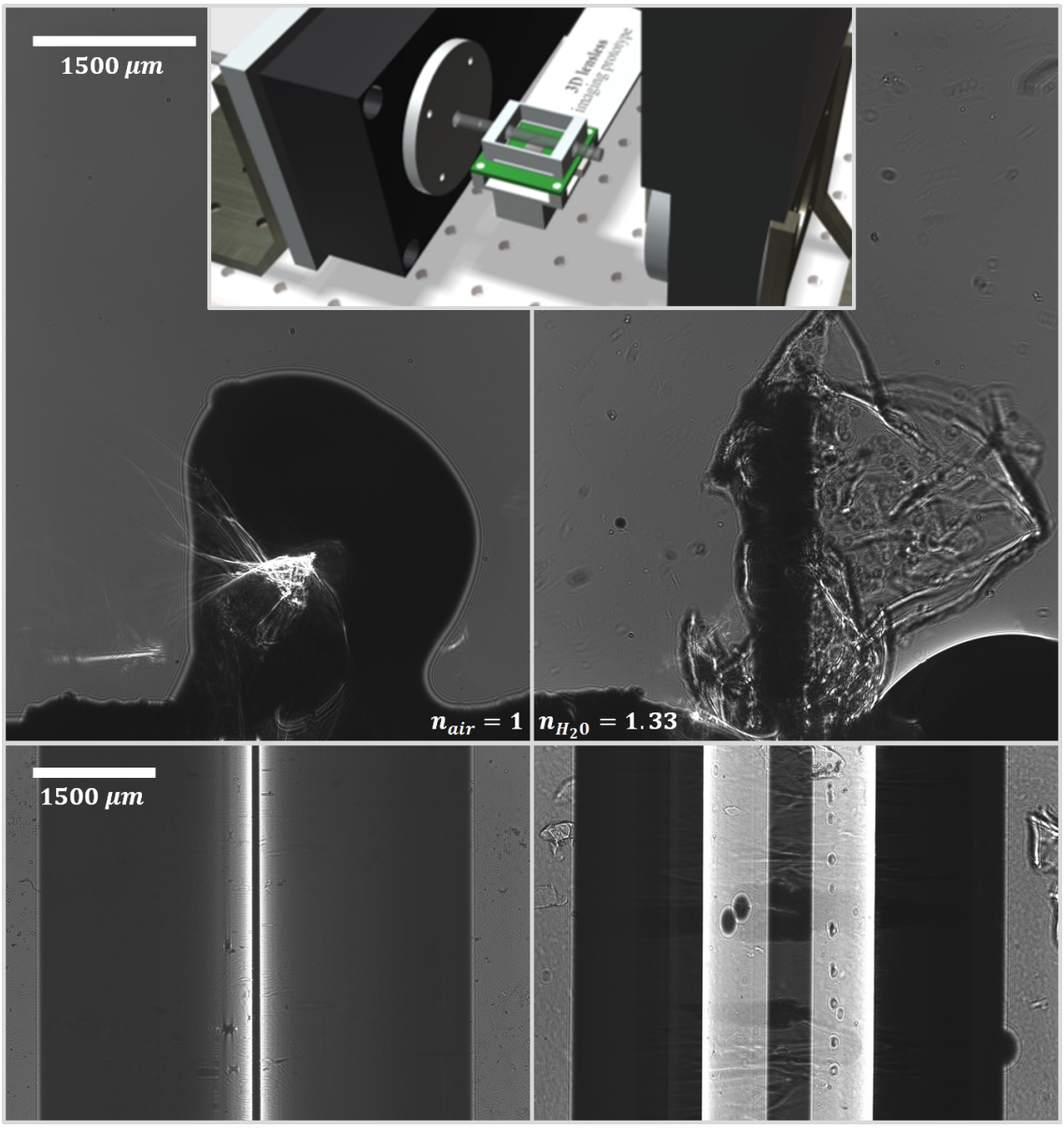

Figure III.3: Matrigel® culture acquired in θ-mode. To compensate the gap of refractive index between the air (on the left-hand side) and the culture, one must use a index matching pool as the one designed and presented at the top of the figure. On the right-hand side, the acquisition done in water show the limitation of this θ-mode used with Matrigel®. The sample fixed on a spike (top raw) is not rigid enough to rotate smoothly with the capillary. Inside the capillary (bottom raw), despite the water, the index matching is not sufficient and the glass highly distorts the holograms, behaving like a lens.

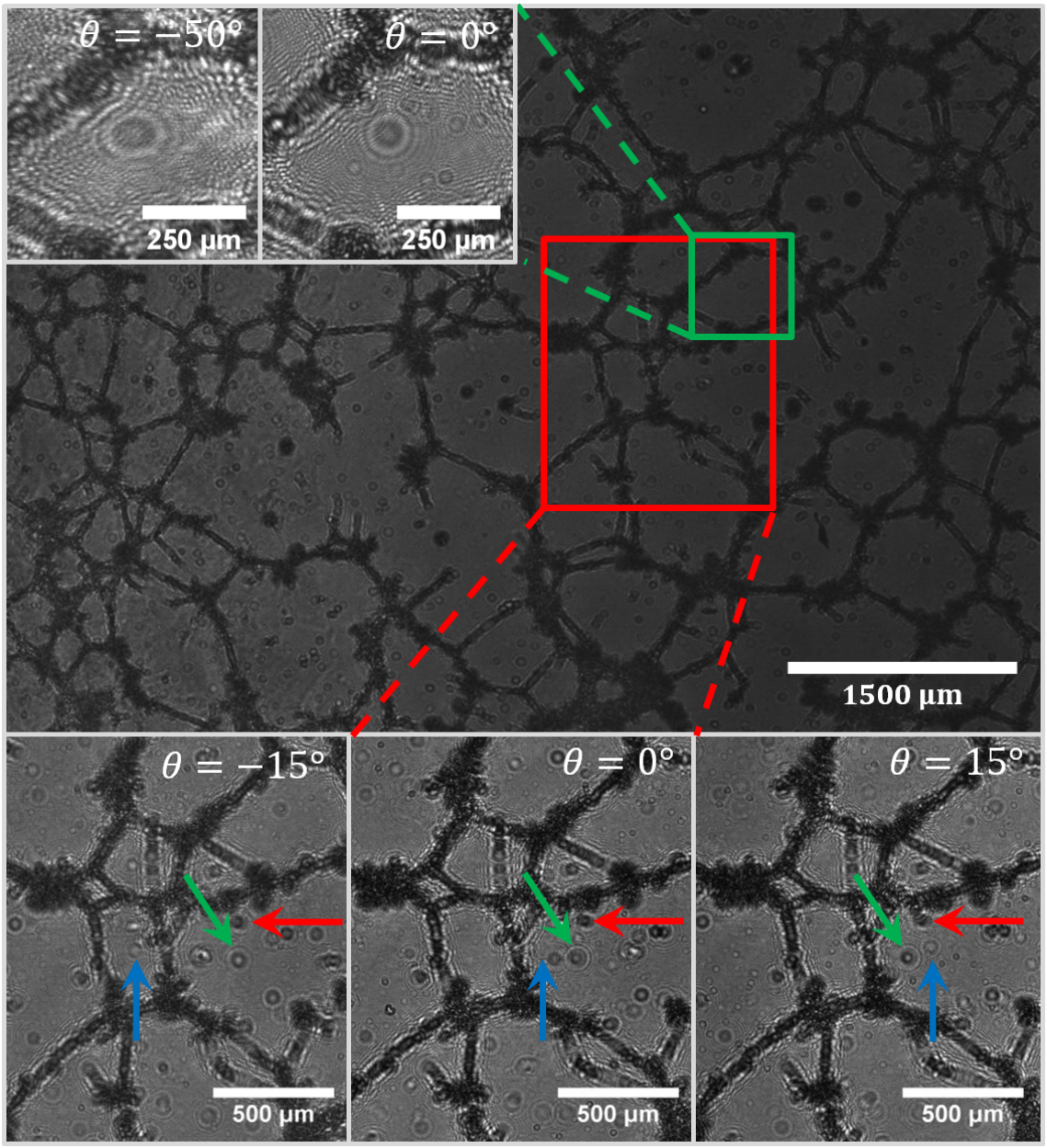

Figure III.4: *At the top* - Epithelial cells branching into a network on a Matrigel® bed. *At the bottom* - Three crops of the data acquired in φ-mode for $\varphi \in \{-15°, 0°, 15°\}$ in the blue channel $\lambda = 450$ *nm*. The colored arrows point at specific cells whose relative positions change according to the angle. The parallax effect shows that three dimensional information can be retrieved from this acquisition mode. *In the medallion* - Zoom on a hologram at $\varphi \in \{-50°, 0°\}$ in the red channel $\lambda = 630$ *nm*. The deformation of the circular shape to an ellipse with increasing angle is visible.

day. In this situation, these cells tend to develop networks[10].

2 A first 3D reconstruction method based on the Radon transform

The method, developed during the first months of the PhD work aims at proving the feasibility of a lens-free tomographic microscope. This method has independently been previously developed in other laboratories [68, 69] to perform lens-free diffractive tomography and is based on the inverse Radon transform.

2.1 Overview of the method

The idea is to get closer to the existing algorithms in the field of X-ray tomography. The filtered back projection algorithm [20] is commonly used to retrieve an object from its straight projection at different angles and works with limited angle coverage. It is moreover native in the programming tool used during this PhD work[11].

The approximation here is to consider a recorded hologram as a direct and straight projection of the sample at a given angle just as if it was a shadow. Doing so, each line on the z-axis in the dataset can be processed independently. As described in chapter II, section 2.3, each line gives information on a line in the Fourier domain of the object which can be consequently reconstructed slice by slice.

The reconstruction then works as schematically described in figure III.5: for the three chosen z, green, blue and red, the corresponding lines in the data set at different angles θ lead to the reconstruction of three different slices. Compiling all the reconstructed planes gives access to the whole volume of the object. The reconstruction is performed in the blue channel. Indeed, the holograms are the smallest in this wavelength, the diffraction being proportional to the wavelength. It limits the effects of the diffraction.

The figure presents the results on a real sample: a mosquito wing on which the 3D structure is clearly visible. Some small details as ribs and dust are visible. At the bottom left, one can notice that the sample moved during the acquisition since the top of the wing is doubled.

This method has numerous advantages. Dealing with the sample slice by slice instead of the whole volume at once is an optimal method in terms of memory consumption and large volumes can be processed[12] while the computing time is drastically reduced. Moreover, an important bibliography exists in this field, motivated by the medical domain with the X-ray computed tomography and this method is consequently easy to implement.

[10] Non published data. The dynamics of this process are later described in V, section 2.
[11] Command "`iradon`" in Matlab®.
[12] Up to 50 mm^3 in the example of the figure III.5

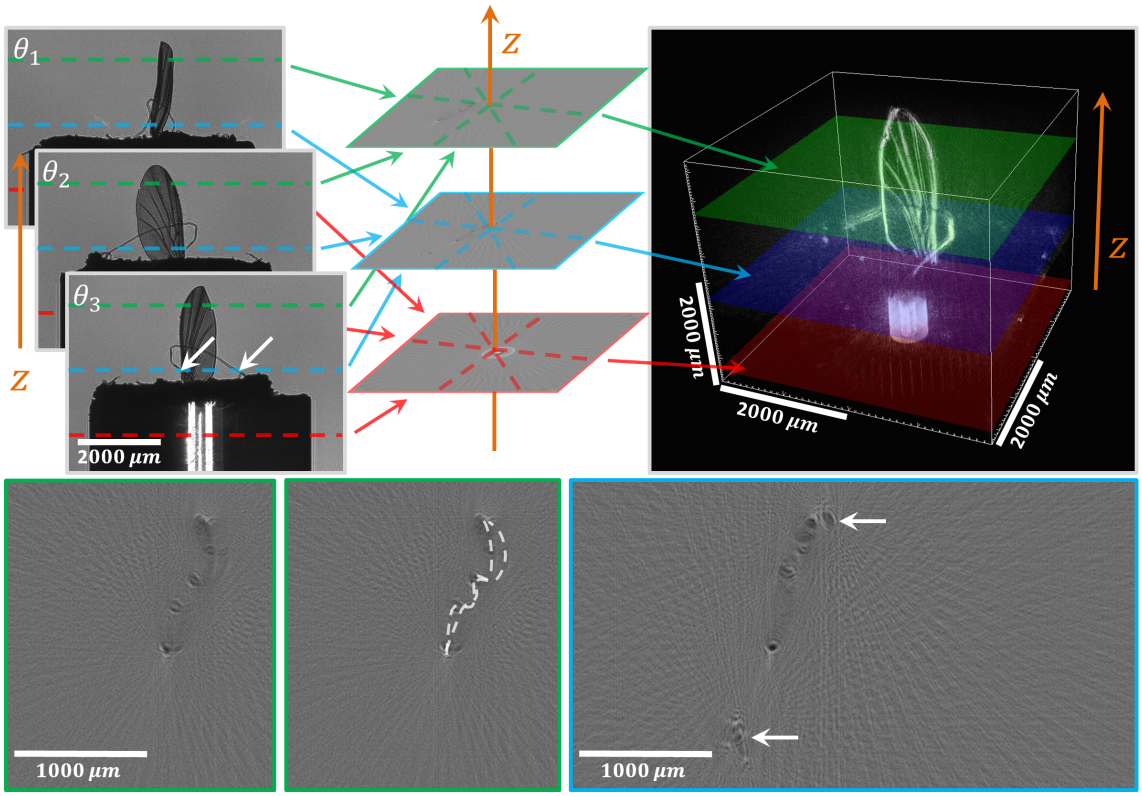

Figure III.5: *Top line* - Schematic view of a 3D reconstruction on real data in the θ-mode using the inverse Radon transform. Data at different angles are processed by going through the z-axis. At each z the lines extracted from each angle are processed to get a 2D slice of the 3D object. Assembling these slices at each z gives access to the whole volume. *Bottom line* - Zoom on the green and blue slices. On the green slice, one can notice a doubling of the wing's edge at its top due to its movement during the sample rotation (white dashed lines). On the blue slice, one can see the limit of this method: as the diffraction is not properly taken in account, the reconstruction seems unfocused with "tubes" instead of nicely shaped ribs. The straight lines are due to the lack of angle for a proper reconstruction with an inverse Radon transform. The white arrows point at the dust surrounding the wing. The global reconstructed volumes is: $4 \times 4 \times 3.34\ mm^3 = 53.44\ mm^3$ and is performed in the blue channel.

The main disadvantage of this method is that it does not take into account the diffraction phenomenon, which is a 3D effect. The holograms are consequently not focused by this algorithm, leading to tubes and spheres instead of lines and dots in the reconstructed volume as one can see in figure III.5.

This method is consequently a good solution to get the localization of the objects in the volume but will not provide detailed reconstructions at low scale.

One may notice that this method is not directly applicable to the φ-mode. Indeed, in this mode, there is not a well-defined rotation axis anymore and the data cannot be considered as direct projections as they are distorted with the tilted an-

gle φ. A solution is to add a straightening step as presented in figure III.6.

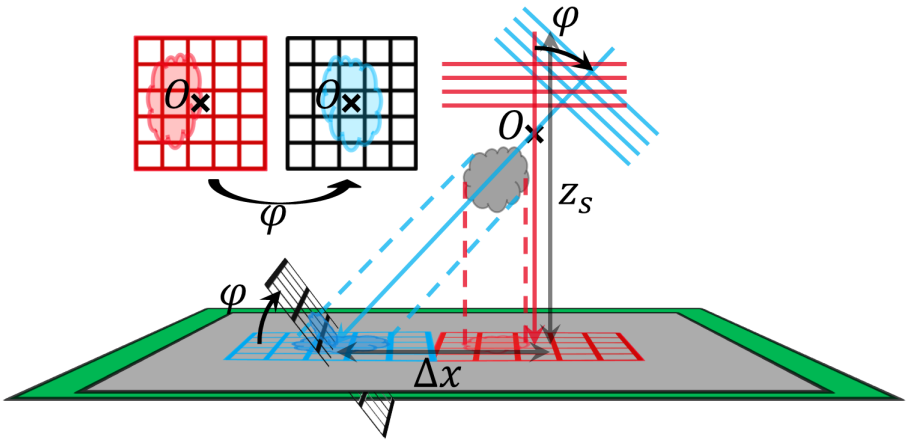

Figure III.6: In the φ-mode the data are straightened to get closer to the θ-mode. For an incident lighting normal to the sensor, the projection is directly the recorded hologram (red situation). When the lighting is tilted (blue situation), the region of interest in the blue area is extracted and straightened in the tilting direction to fit into the black frame, miming a hologram recorded with an angle φ with a lighting normal to the sensor.

If one knows the distance of the object to the sensor z_s, the center of the projection of the object at a given angle φ can be computed from its known position with a normal lighting. It is directly $\Delta x = z_s . \tan \varphi$.

This method is nevertheless not satisfactory. Indeed, with a tilted lighting, the light undergoes multiple refractions at the different interfaces such as between the air and the water from the culture medium or between the air and the glass of the sensor. Different methods are consequently developed to align the data to artificially create a rotation axis in the φ-mode[13]. The ones used in this section are the first two developed: the cross-correlation on the raw data and a least square minimization method on the raw data.

Before reconstructing the 3D volume, a last step is added to increase the reconstruction quality: a pre-focusing step.

2.2 Adding a 2D pre-focusing step

One of the previously mentioned disadvantages of this method is that it does not take into account the diffraction of the sample, leading to unfocused projections. A mean to reduce this effect is to perform a step of 2D back-propagation on the data set before the Radon reconstruction. At each angle, a 2D reconstruction of the object at a mean plane z_s is done, refocusing partially the object, as described in figure III.7.

[13]See appendix C.

Different 2D back-propagation methods exist, as introduced in chapter I, section 3.2. Using a *RGB* lighting, the reconstruction technique used here is the one developed by Sophie Morel during her PhD work [57].

This method does not pretend to give a perfectly focused object. Indeed, the same z_s is applied to the whole data set, consequently, if the sample is not on the rotation axis, its distance from the sensor will vary according to the angles θ, degrading the reconstruction quality. Moreover, even with an object placed at this distance z_s, the reconstruction will only accurately focus the regions at z_s. For 3D samples, the distance from this plane will vary according to the region of interest as presented of the figure III.7: only one of the three spheres is laying on the plane, the two others are consequently not reconstructed at the correct distance.

In the φ-mode, the 2D back-propagations are performed after the straightening step using the Fresnel propagator[14] h_z.

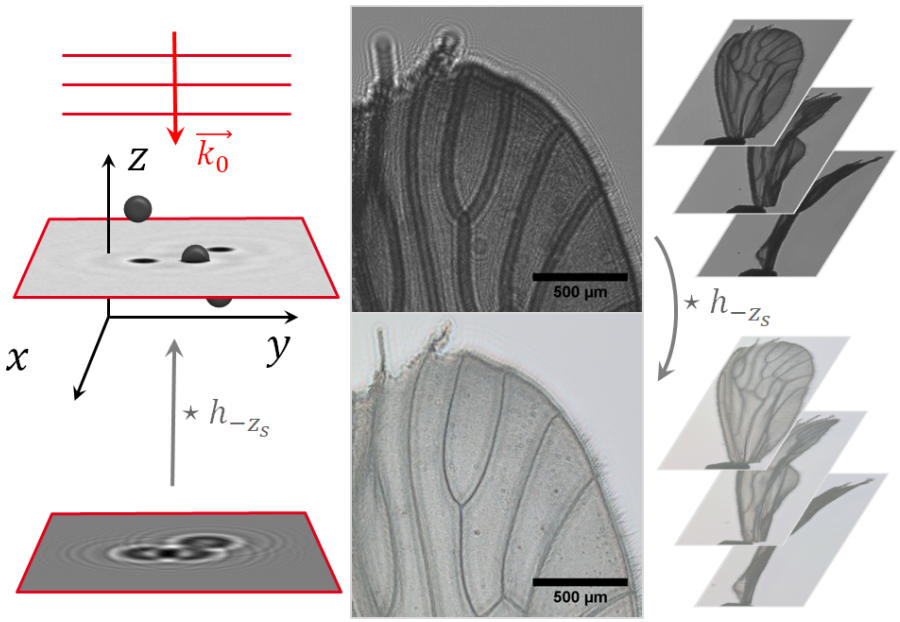

Figure III.7: *Left-hand side* - Scheme of the 2D back-propagation step performed before the 3D reconstruction. The object is refocused at an average plane leading to a more accurate approximation of the projection. h_{z_s} represents the Fresnel propagator introduced in 2D in-line holography, in chapter I, section 3.2. One can see on the ribs that the quality of the refocusing depends on the distance from the sensor: at the center of the reconstruction, they are sharp whereas they are blurred on the edges where the wing is folded and further from the sensor. Nevertheless, the global rendering is better. *Right-hand side* - This operation is performed on all the data set (on the right) for the different angles.

[14] A more rigorous model of 2D tilted back-propagation is developed later in this thesis and is introduced in chapter IV, section 2.1.

2.3 3D reconstructions

Figure III.8 presents the results of this method in θ-mode on a mosquito wing. It is based on a data set acquired every $\Delta\theta = 5°$ over 30 angles in the three RGB channels. The total reconstructed volume is $\sim 2.8 \times 2.8 \times 5\ mm^3 \simeq 40\ mm^3$ with visible details as small as $\sim 5\ \mu m$.

The zooms on the red boxes on the back propagated 2D data show that, as previously said, the focus quality depends on the region of interest because of the different heights in the object. For example, with $\theta = 40°$, unlike the ribs, the dots are not in focus (and consequently present hologram shapes), whereas with $\theta = 80°$ the dots are well focused while the ribs are not. The "white cloud" surrounding the reconstruction is due to the noise and the lack of angles to properly reconstruct the object.

Figures III.9 and III.10 present results on another mosquito wing directly placed on the sensor and imaged in the φ-mode. The data set is composed of acquisitions done every $\Delta\varphi = 1°$ from $\varphi = -50°$ to $\varphi = 50°$ in RGB. The data are aligned by the least square minimization method on the raw data and then back-propagated. The total reconstructed volume is $\sim 1.65 \times 1.65 \times 2.34\ mm^3 \simeq 6.10\ mm^3$ with visible details as small as $\sim 5\ \mu m$.

Nevertheless, unlike the reconstruction presented in the θ-mode, the resolution is not isotropic. On a plane parallel to the sensor (top-left view in figure III.10) the resolution is comparable to the resolution of the sensor whereas it gets worse on the orthogonal axis as one may see on the top-right view in the figure. It is due to the bow-shaped artifact that one can see on the bottom-left view and highlighted in blue.

These artifacts can have numerous causes such as the limited angular coverage, or alignment problems. But one can note that they are arched around the rotation axis. Consequently the main cause seems to be a problem with the straightening step, which is maybe not a good enough approximation of the projection that one could get with a normal lighting on the sensor. Moreover, it is possible that the angle used to straighten may actually not be strictly equal to the lighting angle due to refraction effects between the air and the glass above the sensor. More studies are needed to accurately conclude on this point.

Concerning biological data in the θ-mode, none of 3D reconstructions is relevant enough to be presented because of the reasons given in section 1.2. In the φ-mode, figure III.11 presents the 3D reconstruction of the data introduced in figure III.4. The data set is composed of acquisitions done every $\Delta\varphi = 1°$ from $\varphi = -50°$ to $\varphi = 50°$ in RGB. The data are aligned by the least square minimization method on the raw data and then back-propagated. The total reconstructed volume is $\sim 2.36 \times 2.36 \times 4.17\ mm^3 \simeq 32.9\ mm^3$.

The colored arrows point at the isolated single objects identified in figure III.4 and lying outside the network plane. The global structure of the network is visible. At first glance, it appears spread two-dimensionally: the cells mainly grew on the surface of the Matrigel®. Nevertheless, the side views show that the structure is not strictly planar, but slightly twisted, as emphasized by the red dashed lines.

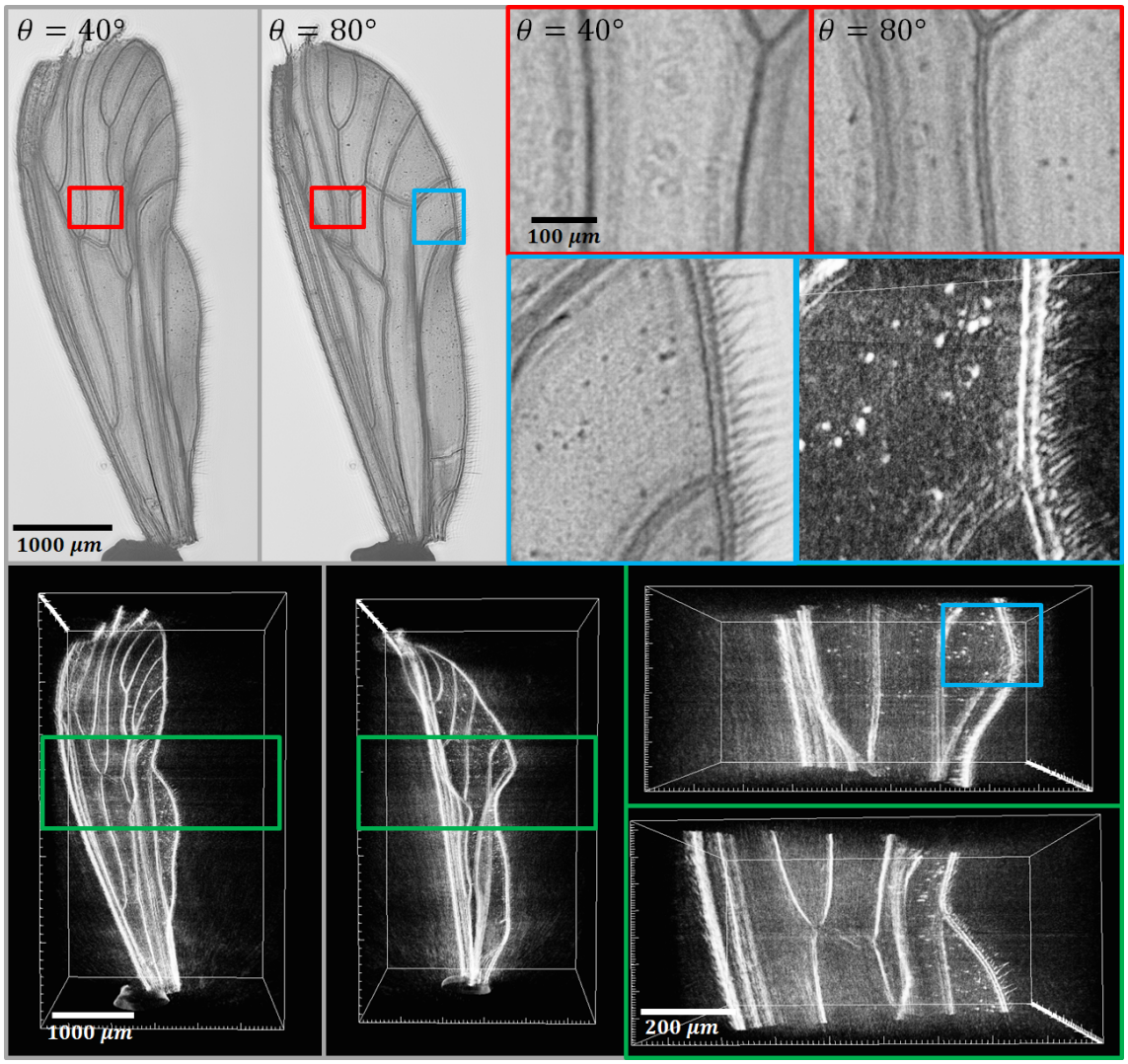

Figure III.8: Reconstruction of a mosquito wing with the θ-mode. Gray background pictures are 2D visualizations whereas black background pictures are 3D visualizations. The 2D visualizations present the data after the reconstruction step at two different acquisition angles. The red framed medallions are zooms on the 2D data whereas the green framed medallions present zoomed regions on the 3D visualization at full resolution. On the blue zoom, the dots on the wing are $\sim 5\ \mu m$ large while the small hair are $\sim 70\ \mu m$ long. Reconstructed volume: $\sim 2.8 \times 2.8 \times 5\ mm^3 \simeq 40\ mm^3$.

As noticed previously, the reconstruction quality appears much better in the plane parallel to the sensor than on the orthogonal direction. The bow-shaped artifacts are once again visible on the top view. They have a spatial extension of a magnitude bigger than 200 μm whereas a typical cell diameter is approximately $\sim$ 15 μm.

Figure III.11 also presents a 3D reconstruction performed directly on the raw

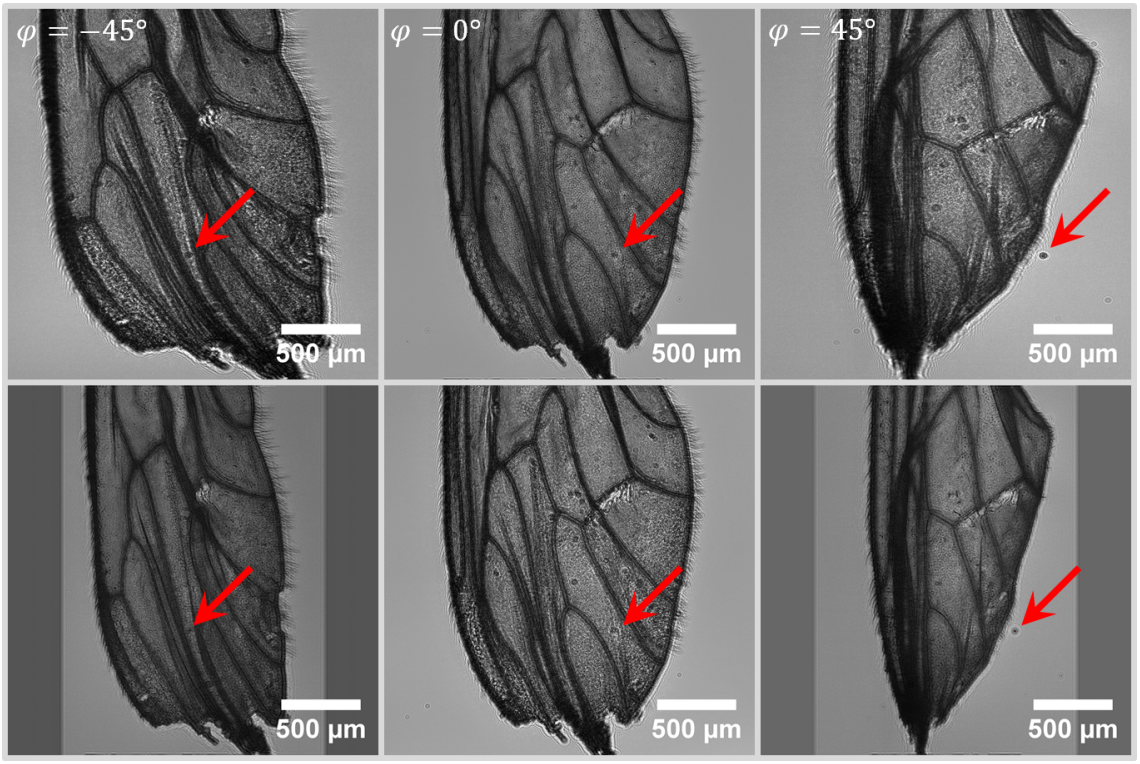

Figure III.9: *Top line* - Acquisition on a mosquito wing laid directly on the sensor in the φ-mode at three different angles. *Bottom line* - The corresponding 2D back propagation after the straightening step. The red arrows point at a speck of dust on the sensor.

data in the red channel[15]. On the red and green framed medallions, one can see the tubular reconstruction of the network and the spherical aspect of single objects due to the holograms shape. It shows the necessity of the focusing step by back-propagation to get resolved reconstructions.

Figure III.12 presents a 3D reconstruction on a smaller sample, giving a better idea of the reconstruction resolution and its artifacts. These are single isolated cells embedded in Matrigel® capsules[16]. The data set is composed of acquisitions done every $\Delta\varphi = 1°$ from $\varphi = -30°$ to $\varphi = 30°$ in RGB. The data are aligned by the least square minimization method on the raw data and then back-propagated. The total reconstructed volume is $\sim 942 \times 942 \times 1336\ \mu m^3 \simeq 1.2\ mm^3$. The cells are $\sim 20\ \mu m$ wide and the capsule at the center of the frame is 360 μm in diameter.

Once again, even if the distribution of the cells on the z-axis is clearly visible, the image quality remains better on the xy-plane. The objects pointed by the green arrows appear badly focused because they are not on the capsule plane, chosen as the distance for the back-projection step. This shows again the limitation of this

[15]Where the holograms are consequently the most spread.

[16]See chapter IV, section 5.1 for more details on the cells conditioning and the culture protocol to produce Matrigel® capsules.

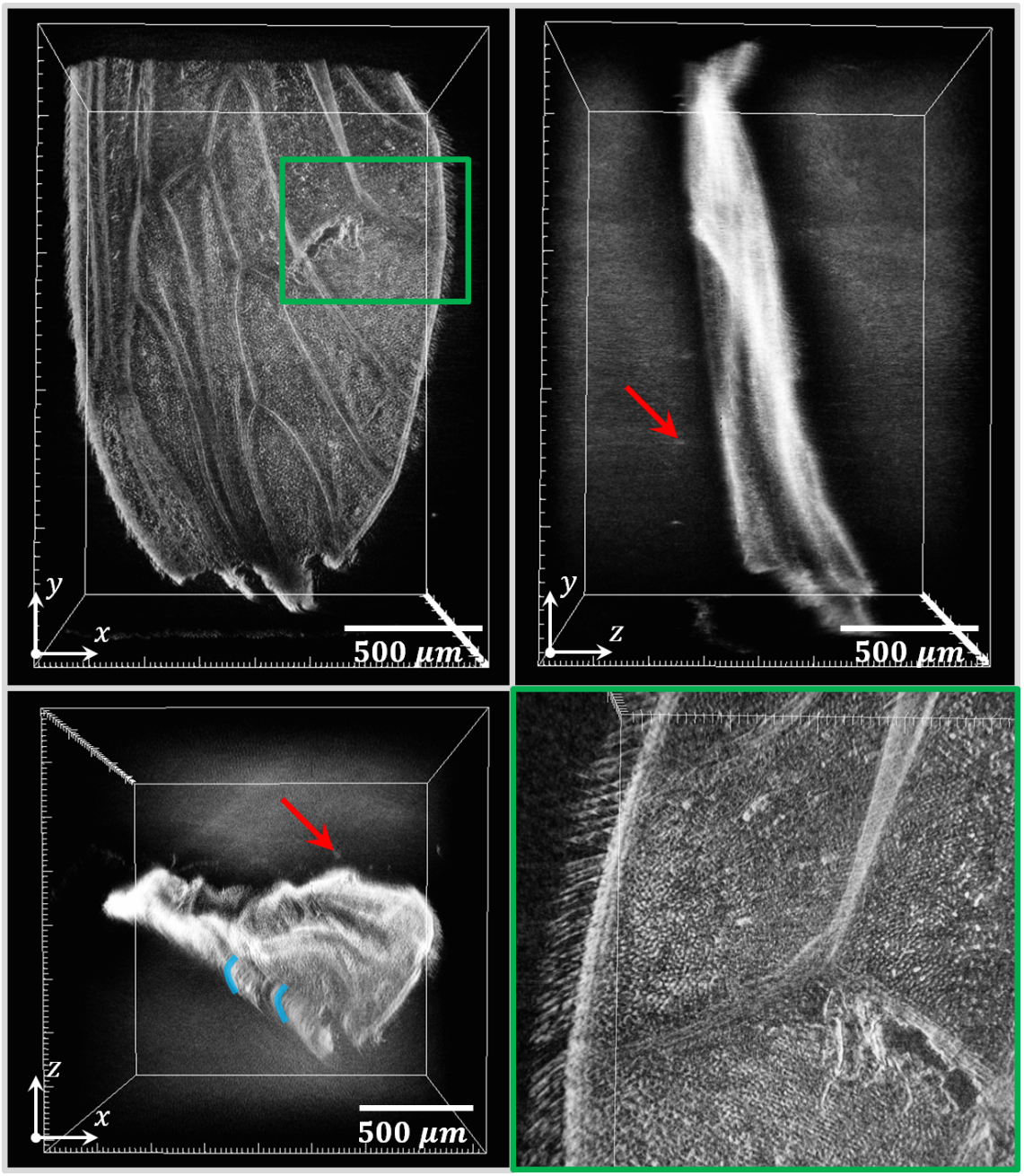

Figure III.10: The three orthogonal views of the 3D reconstruction of the data introduced in figure III.9. The green framed area is a zoom on a tear in the wing. The red arrows point at the dust on the sensor identified in figure III.9. The blue curves emphasize bow-shaped artifacts. Reconstructed volume: $\sim 1.65\times \sim 1.65\times \sim 2.34\ mm^3 \simeq 6.10\ mm^3$.

method.

The main observation is that only a ring surrounding the cells is reconstructed, although the capsules are roughly spherical. Once again, this can be assigned to the

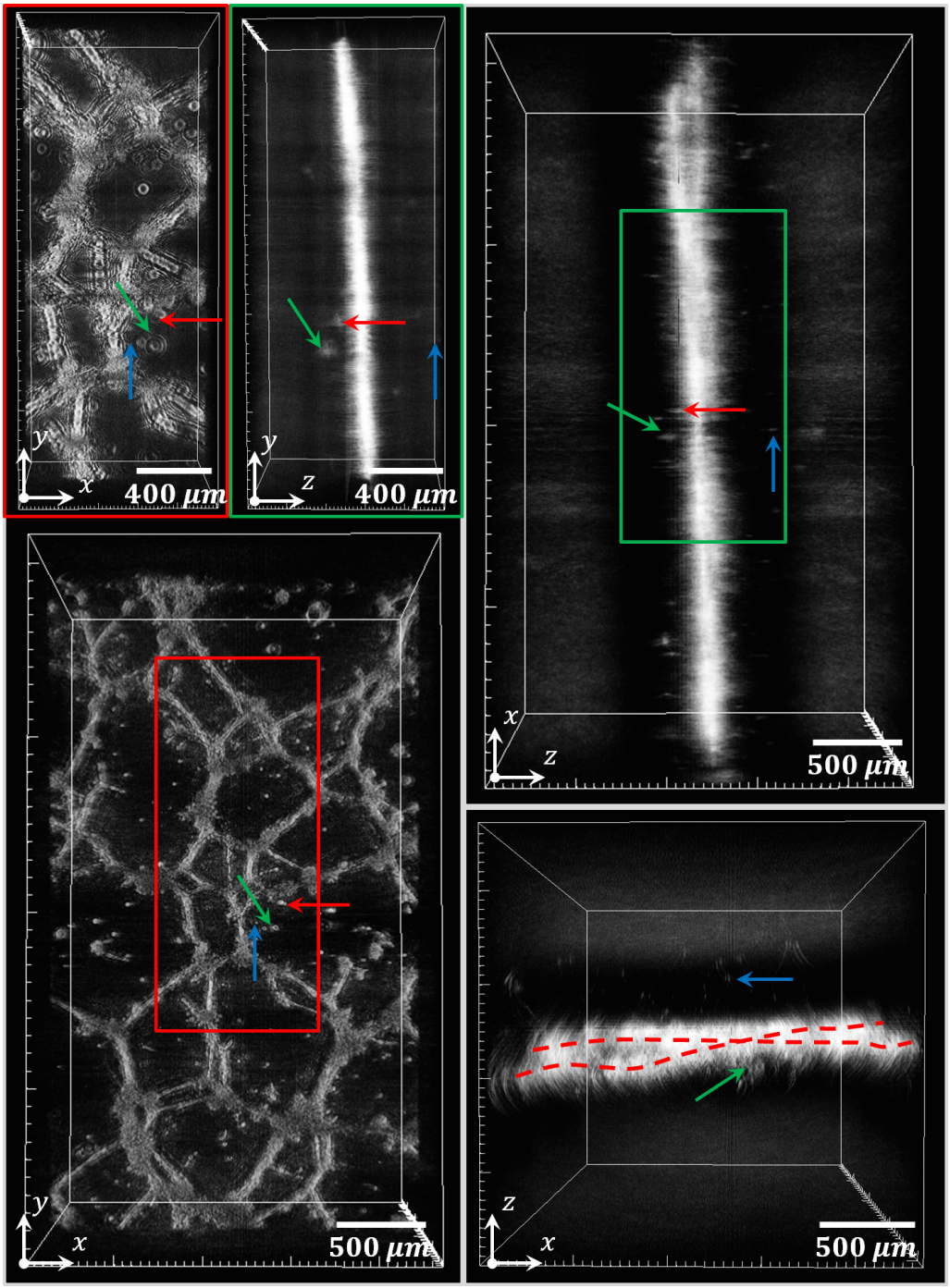

Figure III.11: The three orthogonal views of the 3D reconstruction of the data introduced in figure III.4. The green and red framed zooms are reconstructed with the same dataset but aligned by correlation and without the refocusing steps in the red channel. The arrows point at the features identified in figure III.4. The red dashed lines indicate the average 2D surface on which lies the cell culture. It is not strictly a plane and depends on the position in the culture. Reconstructed volume: $\sim 2.36 \times 2.36 \times 4.17\ mm^3 \simeq 32.9\ mm^3$.

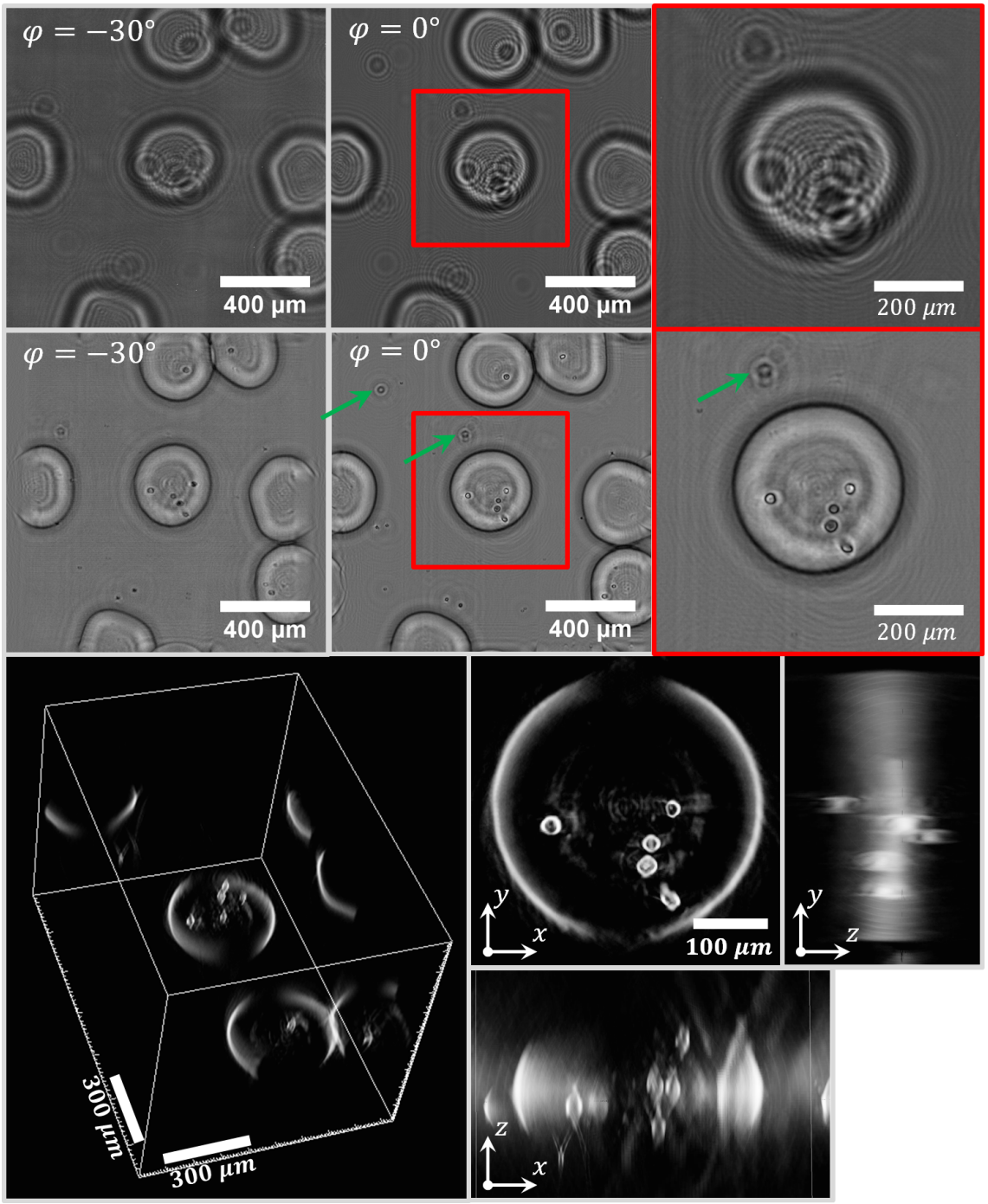

Figure III.12: 3D reconstruction of isolated cells embedded in Matrigel® capsules. The top line presents the raw data at $\varphi = -30°$ and $0°$ in the red channel and a zoom on a capsule. The associated back-propagations are on the middle line. The green arrows point at badly focused single objects which are not in the plane of the capsules. The bottom line presents the 3D visualization. Reconstructed volume: $\sim 942 \times 942 \times 1336\ \mu m^3 \simeq 1.2\ mm^3$.

limited angular coverage. This consequently gives a limitation on the objects one can expect to reconstruct.

A second observation is the non-uniformity of this ring. This comes from the fact that the lighting is fixed on a rotation axis[17], limiting the possibilities of points of view on the object. Consequently, the capsule surface is better reconstructed orthogonally to the rotation axis (left and right sides) than on the axis (at the top and the bottom).

Finally, figure III.13 presents a reconstruction of a culture grown in a top coat condition: the seeded cells are overlaid with Matrigel® instead of culture medium[18]. This prevents the cells from forming a network as previously presented in figure III.11 for example. The data set is composed of acquisitions done every $\Delta\varphi = 1°$ from $\varphi = -30°$ to $\varphi = 29°$ in RGB. The data are aligned by the least square minimization method on the raw data and then back-propagated. The total reconstructed volume is $\sim 1.77\times \sim 1.77\times \sim 3.0\ mm^3 \simeq 9.42\ mm^3$.

Once again, the culture presents an overall 2D structure because of the way the cells are initially spread on their Matrigel® bed. The interesting thing in this reconstruction is that a branch grew orthogonally to this plane on more than 600 μm as one can see on the side view of the 3D reconstruction. It appears to be an isolated behavior that one could easily miss with standard microscopy. It emphasizes the potential of the 3D lens-free microscopy to identify rare events thanks to the possibility to reconstruct large volumes.

To conclude, this section introduces the first 3D reconstructions obtained by the lens-free imaging setup. Performed with a basic algorithm developed with strong approximations, this algorithm can work fast (a few minutes) on large volumes, using the full potential of the large field of view allowed by the lens-free technology. The results show nevertheless the potential of the 3D lens-free tomography. Indeed, the global shape of the samples are retrieved and the position of the single objects isolated from the main structure can be determined. Lots of artifacts remain nonetheless and the future approaches need to correct them.

3 A second method based on z-stack acquisitions

This section presents an algorithm developed to be an alternative solution to traditional methods that use multi-angle acquisitions and the Fourier diffraction theorem.

As the results are not convincing, it will not be described in details. Nevertheless, it is important to mention it in this thesis as the negative results emphasize the need to multiply the viewing angles. Moreover it introduces the formalism of the iterative inverse problems. It is indeed the first implementation of such an approach in this PhD work.

[17] The rotation axis is vertical on the top view of the capsule.

[18] See chapter IV, section 5.1 for more details on the cells conditioning.

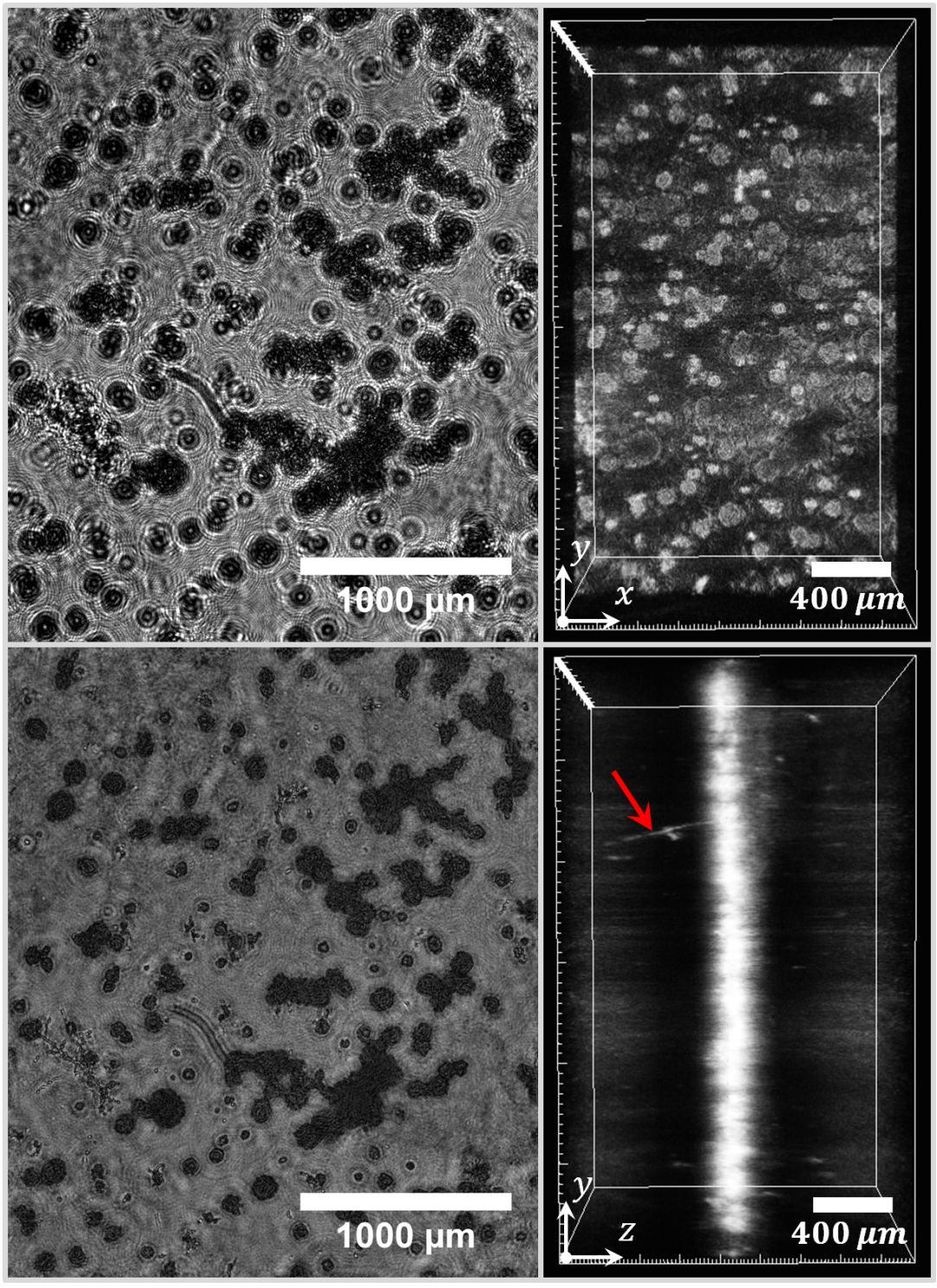

Figure III.13: *Left column* - Raw data of RWPE1 cells grown via a top coat protocol and the associated back-propagation for a normal incidence. *Right column* - 3D reconstruction of the cell culture. The reconstructed volume is $\sim 1.77 \times 1.77 \times 3.0\ mm^3 \simeq 9.42\ mm^3$. The arrow points at a branch which grew inside the Matrigel®.

3.1 Motivation of the method

As mentioned earlier, biological samples strongly limit the acquisitions possibilities. Multi-angle views on Petri dishes can only be achieved with the φ-mode and the angular coverage is constrained by the wall height. Things get worse if one considers cultures in multiwell plates in which the culture size on the xy-plane is in the same order of magnitude than the walls height.

The method described in this section is not based on multi-angle acquisitions, but on acquisitions done behind the sample for different distances of the sensor z_s, solving the problem raised by multiwell plates or other container with limited angular coverage.

Indeed, the hologram shape is characteristic of the distance of propagation: for a scattering sphere, the size of the resulting rings will increase with the distance of propagation. One can consequently speculate that having holograms at different distances could give some information about the distance of the object, thus how to retrieve it.

Moreover as mentioned in chapter II, section 3, one can get a simulated total wave on a volume[19], given a volume object correctly padded with zeros. This is the situation symbolized by the red arrow in figure III.14.

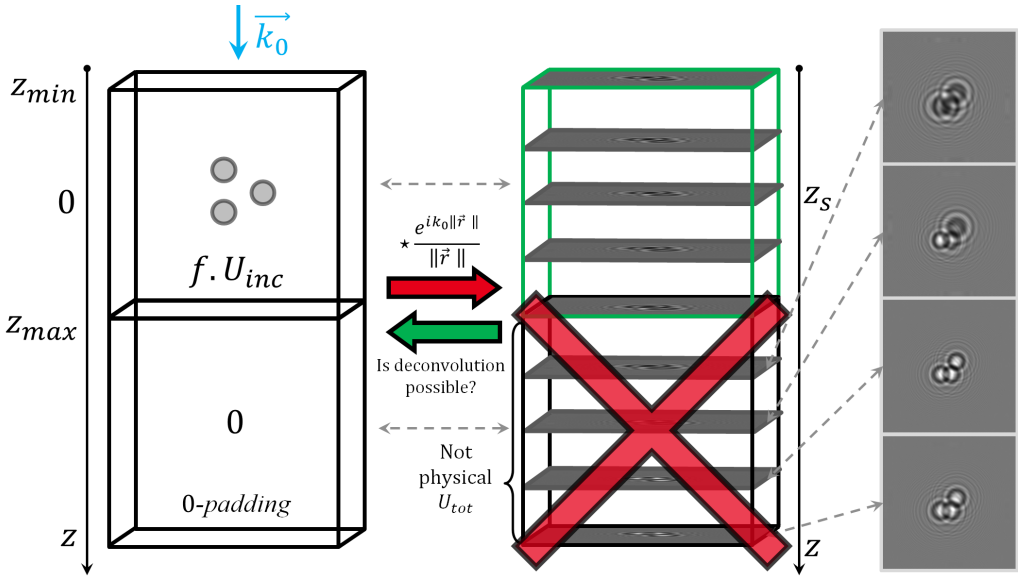

Figure III.14: Illustration of the simulation of the diffracted wave on a volume composed of three identical spheres given a correctly padded object (red arrow) according to equation (II.37) for an incident lighting normal to the sensor plane. The diffracted wave is computed on a volume. The counterpart of the zero-padding is that half of this volume is not physical (crossed out in red in the figure) and contains the wrapping artifacts of the FFT (see figure II.6). The green volume is the one physically reachable by acquisition.

[19]See the simulations based on the Born approximation and its convolution formulation (II.37).

One can consequently think of a reconstruction method based on the reverse way: knowing the diffracted wave on a volume behind the object (the green cube in the figure) could allow retrieving this 3D object using the convolution formulation. The main pitfall is that, as described in figure III.14, the counterpart of the zero-padding operation leads to a non-physical diffracted wave on the simulated volume which is not taken into account in the simulation process. But as one can see on the right side of the figure, these artifacts contain strong information on the position of the objects. When the wrapping effect loops on the spheres, the phase shift[20] introduced by this wrapping produces important changes in the holograms.

The aim of this section is to find a deconvolution method to retrieve the object from such a z-stack acquisition (the green arrow in the figure). It is mainly based on numerical simulations since such z-stack acquisitions cannot be captured with the developed prototype.

3.2 Few tests of deconvolution

The algorithm which is developed to retrieve the object is described in figure III.15 and is based on a Gerchberg–Saxton algorithm structure, as the ones developed for RGB phase retrieval and presented in chapter I, section 3.2.

The challenge here lies in the deconvolution step. Indeed, based on equation (II.37), one would like to retrieve f with:

$$\mathcal{F}_{3D}\left(f.U_{inc}\right) = \frac{\hat{D}}{\hat{H}} \tag{III.1}$$

where: $\hat{D} = \mathcal{F}_{3D}\left(U_{dif}\right)$ and $\hat{H} = \mathcal{F}_{3D}\left(\frac{k_0'^2}{4\pi}\frac{e^{ik_0'\|\overrightarrow{r}\|}}{\|\overrightarrow{r}\|}\right)$.

But this kind of method is very unstable, especially for noisy data and it diverges rapidly during iterations. Filters are needed to prevent this.

Different types of deconvolution filters are tested.

Wiener filter - In this situation [81], equation (III.1) becomes:

$$\mathcal{F}_{3D}\left(f.U_{inc}\right) = \frac{\overline{\hat{H}}}{\left|\hat{H}\right|^2 + \frac{N}{S}}\hat{D} \tag{III.2}$$

where N and S are the power spectral densities of the noise and the signal U_{dif}. $\overline{\hat{H}}$ is the complex conjugate of $\hat{H}$.

Low-pass filter - This filter selects the propagating frequencies according to the modulus of $\hat{H}$ if it gets to low compared to a given value τ:

$$\mathcal{F}_{3D}\left(f.U_{inc}\right) = \begin{cases} \frac{\hat{D}}{\hat{H}} & \text{if } \left|\hat{H}\right| > \tau \\ 0 & \text{if } \left|\hat{H}\right| \leq \tau \end{cases} \tag{III.3}$$

[20] See II.6 for more details.

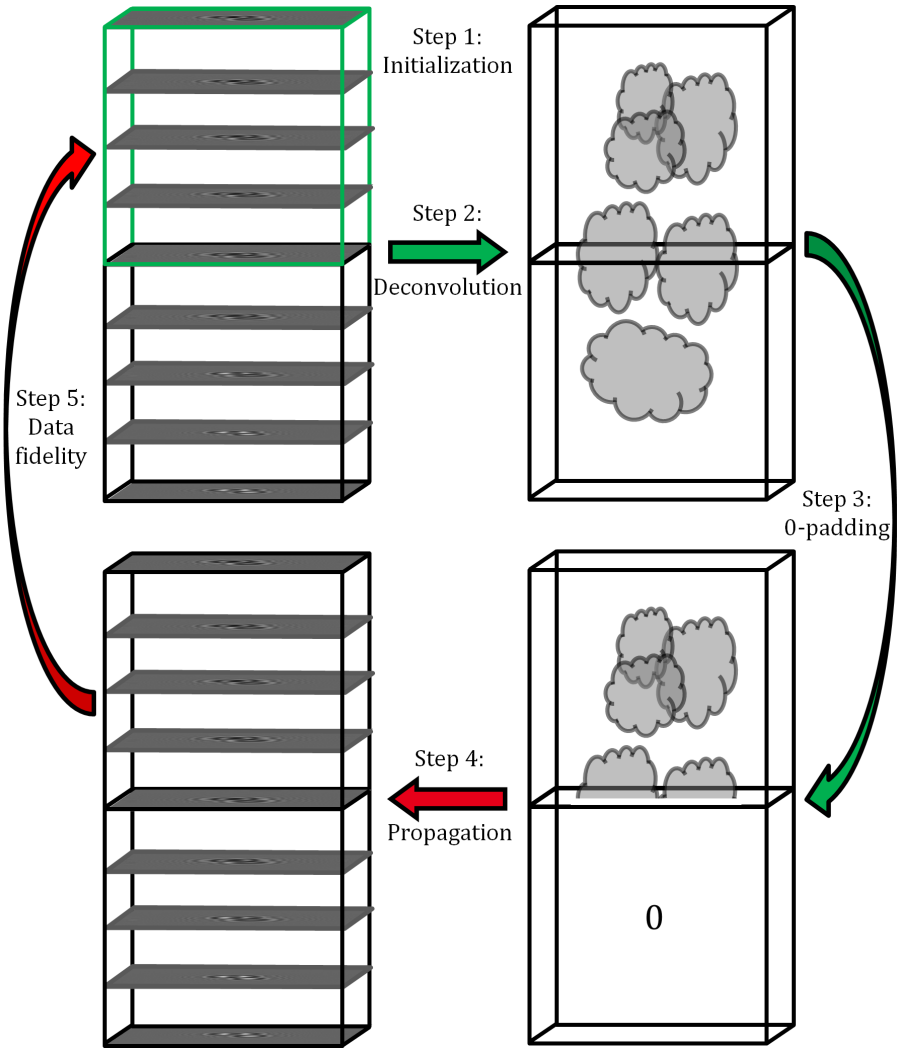

Figure III.15: Illustration of the iterative algorithm which is developed to retrieve the object. Step 1: the dataset, in green, is first initialized on the non-physical part due to the volume padding. Step 2: deconvolution of the diffracted volume towards the object. Step 3: forcing the 0-padding. Step 4: simulation of the diffracted wave due to this padded object. Step 5: to ensure data fidelity, the intensities in the green volume are replaced by the recorded intensities. The algorithm then loops over the steps 2 to 5 until convergence.

Adapted low-pass filter - This filter, inspired from [46], changes the modulus of $\hat{H}$ if it gets to low compared to a given value τ:

$$\mathcal{F}_{3D}\left(f.U_{inc}\right) = \frac{\hat{D}}{\tilde{\hat{H}}} \text{ with } \tilde{\hat{H}} = \begin{cases} \hat{H} & \text{if } \left|\hat{H}\right| > \tau \\ 1.e^{i\arg\left(\hat{H}\right)} & \text{if } \left|\hat{H}\right| \leq \tau \end{cases} \tag{III.4}$$

These filters prevent the amplification of the frequencies when $\hat{H}$ becomes too low and can consequently act as low-pass filters for the noise frequencies.

Different tests are performed on a simulated object composed of three identical spheres and all give results similar to the one presented in figure III.16. The reconstruction is accurately positioned on the xy-plane but fails to constrain the position on the z-axis, producing hourglass-shaped patterns. It can nevertheless be noticed that these hourglasses focus at the correct z of the objects.

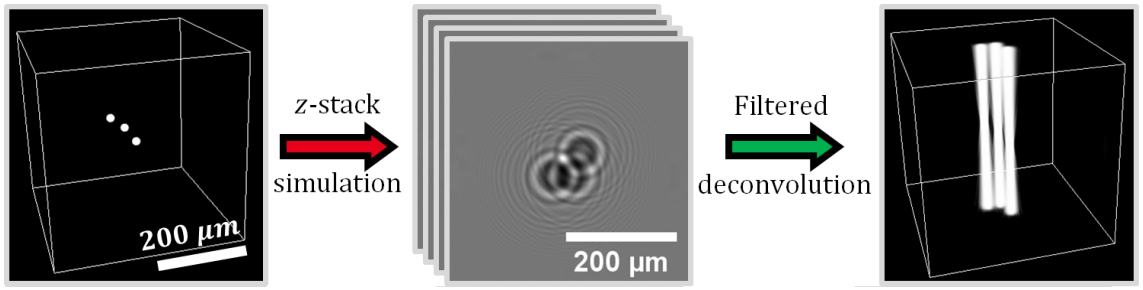

Figure III.16: Test of an iterative deconvolution on simulated data. The simulated volume is composed of $256 \times 265 \times 256$ cubic voxels with a side of 1.67 μm and contains three identical spheres of radius $r_c = 10$ μm and with $n_0 = 1$ and $\delta n = 0.005i$. The propagation distance is $z_s = 1.5$ mm and $\lambda_0 = 630$ nm. The reconstruction appears to be very good for the xy-positions but totally ineffective along the z-direction even if the hourglass-shape is more focused around the correct positions of the spheres on the z-axis.

Different values are tested for τ or N/S leading to either a divergence of the iterative reconstructions or these deformed hourglass-shaped reconstructions. It is also tested to initialize the algorithm with the targeted correct solution and it appears to be not stable: the simulated objects shifts also towards hourglass-shaped objects.

These solutions seem consequently not restrictive enough on the z-axis to be satisfactory. But looking closer to the results in figure III.16, one could expect that an algorithm forcing the object to be spatially limited would tend to focus the objects around their correct positions, where the hourglass-shape is narrower. This leads to the first inverse problem approach developed in this PhD work.

3.3 Toward iterative inverse problem approaches

An inverse problem approach to retrieve an object is based on the knowledge of the direct model which allows simulating data (here $|U_{tot}|^2$) for a given numerical object (here the scattering potential f).

Thus, for any object, one can estimate "how far" it is from the recorded data (here the intensities I_d) for a given choice of a "distance". Here, the "distance" will

be the Euclidean norm, or l_2-norm[21]:

$$\left\| |U_{tot}(f)|^2 - I_d \right\| = \sqrt{\sum_{pixels_{i,j}} \left(|U_{tot}(f)|^2_{i,j} - I_{d,i,j} \right)^2} \tag{III.5}$$

Retrieving f consequently becomes a minimization of this distance to best match the data. But this method also provides regularization tools if some of the object properties are known such as its sparsity, a possible bounded domain, and so on.

In this section, the retrieved f is then the solution of the following minimization:

$$\boxed{\tilde{f} = \underset{C(f)}{\operatorname{argmin}} \underbrace{\frac{1}{nb_x nb_y nb_{z,s} N} \sum_j \left\| \left| U^j_{tot,s}(f) \right|^2 - I^j_d \right\|^2}_{\text{data fidelity } J_d(f)} + \mu_{L_1} \underbrace{\frac{1}{nb_x nb_y nb_z} \|f\|_{L_1,\epsilon}}_{\text{sparsity constraint } J_{L_1,\epsilon}(f)}} \tag{III.6}$$

$\frac{1}{nb_x nb_y nb_{z,s} N}$ and $\frac{1}{nb_x nb_y nb_z}$ are normalizing factors, nb_x, nb_y and nb_z still being the voxels number in each direction of the reconstructed object f. The index s stands for "sampled". Indeed, one may work only on a limited number $nb_{z,s}$ of slices in the simulated volume U_{dif} which possesses nb_z slices.

The data fidelity is composed of a summation on j, standing for the N lighting directions and wavelength illuminations $\overrightarrow{k'^j_0}$ (several wavelengths can be used for a same lighting direction and *vice versa*).

As defined in appendix D, $\|f\|_{L_1,\epsilon}$ is the "relaxed" L_1-norm of the object:

$$\|f\|_{L_1,\epsilon} = \sum_{voxels_{i,j,k}} \sqrt{|f_{i,j,k}|^2 + \epsilon^2} \tag{III.7}$$

Minimizing this norm consequently tends to favor sparse reconstructions. μ_{L_1} is the hyperparameter weighting the sparsity constraint $J_{L_1}(f)$ compared to the data fidelity $J_d(f)$ in the global cost function:

$$\boxed{J(f) = J_d(f) + \mu_{L_1} J_{L_1,\epsilon}(f)} \tag{III.8}$$

It remains $C(f)$, the constraints on the definition domain of f. It can be for example the whole complex plane $C(f) = \left\{ f \in \mathcal{M}_{nb_x,nb_y,nb_z}(\mathbb{C}) \right\}$ or a limitation such as $C(f) = \{f / \mathcal{I}(f) < 0\}$.

Noting *samp* the sampling operator on the $nb_{z,s}$ kept slices in the simulated volume, $U^j_{inc,s}$ the matrix $e^{i\overrightarrow{k'^j_0}.(x_{3D},y_{3D},z_{3D})}$ sampled on these slices and $\hat{H^j_{z_s}}$ the matrix:

$$\hat{H^j_{z_s}} = dx.dy.dz.\mathrm{FFT}_{3D}\left(\frac{k'^{j2}_0}{4\pi} e^{-i\overrightarrow{k'^j_0}.\left(x^{pad}_{3D},y^{pad}_{3D},z^{pad}_{3D}\right)} . \dots \right.$$
$$\left. \frac{e^{ik'^j_0 \sqrt{\left(x^{pad}_{3D}+x^j_0\right)^2+\left(y^{pad}_{3D}+y^j_0\right)^2+\left(z^{pad}_{3D}+z_s\right)^2}}}{\sqrt{\left(x^{pad}_{3D}+x^j_0\right)^2+\left(y^{pad}_{3D}+y^j_0\right)^2+\left(z^{pad}_{3D}+z_s\right)^2}} \right) \tag{III.9}$$

[21] Here it matches the definition given in appendix D for $W = 1$. As mentioned in the appendix, it is possible to weight each pixel for example to minimize the influence of hot or dead pixels.

equation (II.44) becomes:

$$U^j_{dif,s} = U^j_{inc,s}.samp\left(pad^{-1}\left(\mathrm{FFT}^{-1}_{3D}\left(\hat{H^j_{z_s}}.\mathrm{FFT}_{3D}\left(pad\left(f\right)\right)\right)\right)\right) \tag{III.10}$$

All these operations are linear and one can use the matrix formalism as specified in the appendix D. f, $\hat{H^j_{z_s}}$, $U^j_{dif,s}$ and $U^j_{inc,s}$ are consequently unfolded in their vector shapes $\overrightarrow{f}$, $\overrightarrow{\hat{H^j_{z_s}}}$, $\overrightarrow{U}^j_{dif,s}$ and $\overrightarrow{U}^j_{inc,s}$, f being decomposed on its real and imaginary parts.

Let's note P, P^i, F, F^i and S the matrix representations of the linear operators *pad*, pad^{-1}, FFT_{3D}, FFT^{-1}_{3D} and *samp*, and $R2C$ the matrix to get the complex representation of a vector from its decomposition on the real and imaginary part. Let also be *diag* the function turning a vector into a diagonal matrix whose coefficients are the ones of the initial vector.

Equation (III.10) becomes:

$$\begin{aligned}\overrightarrow{U}^j_{dif,s} &= diag\left(\overrightarrow{U}^j_{inc,s}\right) \times S \times P^i \times F^i \times diag\left(\overrightarrow{\hat{H^j_{z_s}}}\right) \times F \times P \times R2C \times \overrightarrow{f} \\ &= O \times \overrightarrow{f}\end{aligned} \tag{III.11}$$

It comes from appendix D:

$$\nabla J_d\left(\overrightarrow{f}\right) = \frac{1}{nb_x nb_y nb_{z,s} N} \sum_j 4\mathcal{R}\left[O^\star \times \left[\overrightarrow{U}^j_{tot,s}\left(\overrightarrow{f}\right).\left(\left|\overrightarrow{U}^j_{tot,s}\left(\overrightarrow{f}\right)\right|^2 - \overrightarrow{I}^j_d\right)\right]\right] \tag{III.12}$$

with:

$$O^\star = R2C^\star \times P^\star \times F^\star \times diag\left(\overrightarrow{\hat{H^j_{z_s}}}\right)^\star \times F^{i\star} \times P^{i\star} \times S^\star \times diag\left(\overrightarrow{U}^j_{inc,s}\right)^\star \tag{III.13}$$

where the Hermitian adjoint of a matrix M is $M^\star = {}^t\overline{M}$. Looking closer at the matrix representation of each operation, it comes:

$$diag\left(\overrightarrow{V}\right)^\star = diag\left(\overrightarrow{\overline{V}}\right) \tag{III.14}$$

$$P = \left.\begin{pmatrix} 1 & & \\ & \ddots & \\ & & 1 \\ & 0 & \end{pmatrix}\right\}\text{padding} \quad \Rightarrow \begin{cases} P^\star = \begin{pmatrix} 1 & & & \\ & \ddots & & \underbrace{0}_{\text{cropping}} \\ & & 1 & \end{pmatrix} = P^i \\ P^{i\star} = P \end{cases} \tag{III.15}$$

$$S = \begin{pmatrix} 0\cdots010\cdots0 & & 0 \\ & \ddots & \\ 0 & & 0\cdots010\cdots0 \end{pmatrix} \Rightarrow S^\star = \begin{pmatrix} 0 & \\ \vdots & \\ 0 & \\ 1 & 0 \\ 0 & \\ \vdots & \\ 0 & \\ 0 & \ddots \end{pmatrix} \tag{III.16}$$

$$R2C = \begin{pmatrix} 1 & & i & & \\ & \ddots & & \ddots & \\ & & 1 & & i \end{pmatrix} \Rightarrow R2C^\star = \begin{pmatrix} 1 & & \\ & \ddots & \\ & & 1 \\ -i & & \\ & \ddots & \\ & & -i \end{pmatrix} \tag{III.17}$$

Thus the adjoint of the padding operation appears to be its "inverse", the cropping operation. The adjoint of the sampling operation $samp^\star$ consists in adding zeros in the matrix in the places of the volume slices which are not kept in the sampling operation. Moreover, it is known that the adjoint of the Fourier transform operation is its inverse function as it is a unitary operator [82]: $F^\star = F^i$ and $F^{i\star} = F$.

Looking closer at the equation (III.17), it comes for a complex vector $\overrightarrow{c}$:

$$\mathcal{R}\left[R2C^\star \times \overrightarrow{c}\right] = \mathcal{R}\left[\begin{pmatrix} \overrightarrow{c} \\ -i.\overrightarrow{c} \end{pmatrix}\right] = \begin{pmatrix} \mathcal{R}\left(\overrightarrow{c}\right) \\ \mathcal{I}\left(\overrightarrow{c}\right) \end{pmatrix} = C2R\left(\overrightarrow{c}\right) \tag{III.18}$$

This is the inverse operation $C2R$ to go from a complex representation of a vector to its decomposition on its real and imaginary parts.

Finally using the previous remarks and the matrix expression (III.13), it is possible to express the gradient of the data fidelity in terms of the complex volume f:

$$\boxed{\begin{aligned} \nabla J_d\left(f\right) = \frac{1}{nb_x nb_y nb_{z,s} N} \sum_j 4.pad^{-1}\Big(\mathrm{FFT}_{3D}^{-1}\Big(\bar{\hat{H}}_{z_s}^j.\mathrm{FFT}_{3D}\Big(\cdots \\ pad\left(samp^{-1}\left(\bar{U}_{inc,s}^j.U_{tot,s}^j\left(f\right).\left(\left|U_{tot,s}^j\left(f\right)\right|^2 - I_d^j\right)\right)\right)\Big)\Big)\Big) \end{aligned}} \tag{III.19}$$

Using the appendix D to get the gradient of $J_{L_1,\epsilon}\left(f\right)$, one has the numerical expression of the gradient of the cost function (III.8) at a given f:

$$\nabla J\left(f\right) = \nabla J_d\left(f\right) + \mu_{L_1} \nabla J_{L_1,\epsilon}\left(f\right) \tag{III.20}$$

The gradient of the cost function being numerically calculated, one can now iteratively solve the minimization problem (III.6) using descent gradient algorithms. In this section, a BFGS algorithm[22] adapted[23] to boundary constraints is used.

[22]The Matlab® code which is used in this section is implemented by Mark Schmidt [83] and runs a quasi-Newton strategy where the steps direction are computed with a limited-memory Broyden–Fletcher–Goldfarb–Shanno algorithm [84].

[23]Thanks to Éric Thiébaut and Fabien Momey for its interfacing with Matlab.

Figure III.17 presents different reconstructions obtained with different parameters. Noisy data are simulated to create a full volume of the diffracted wave surrounding the sensor plane $nb_{z,s} = nb_z$. The numerical object is composed of $256 \times 265 \times 128$ cubic voxels with a side of 1.67 μm and contains three identical spheres of radius $r_c = 10$ μm and with $n_0 = 1$ and $\delta n_c = 0.005i$. The propagation distance is $z_s = 1.5$ mm.

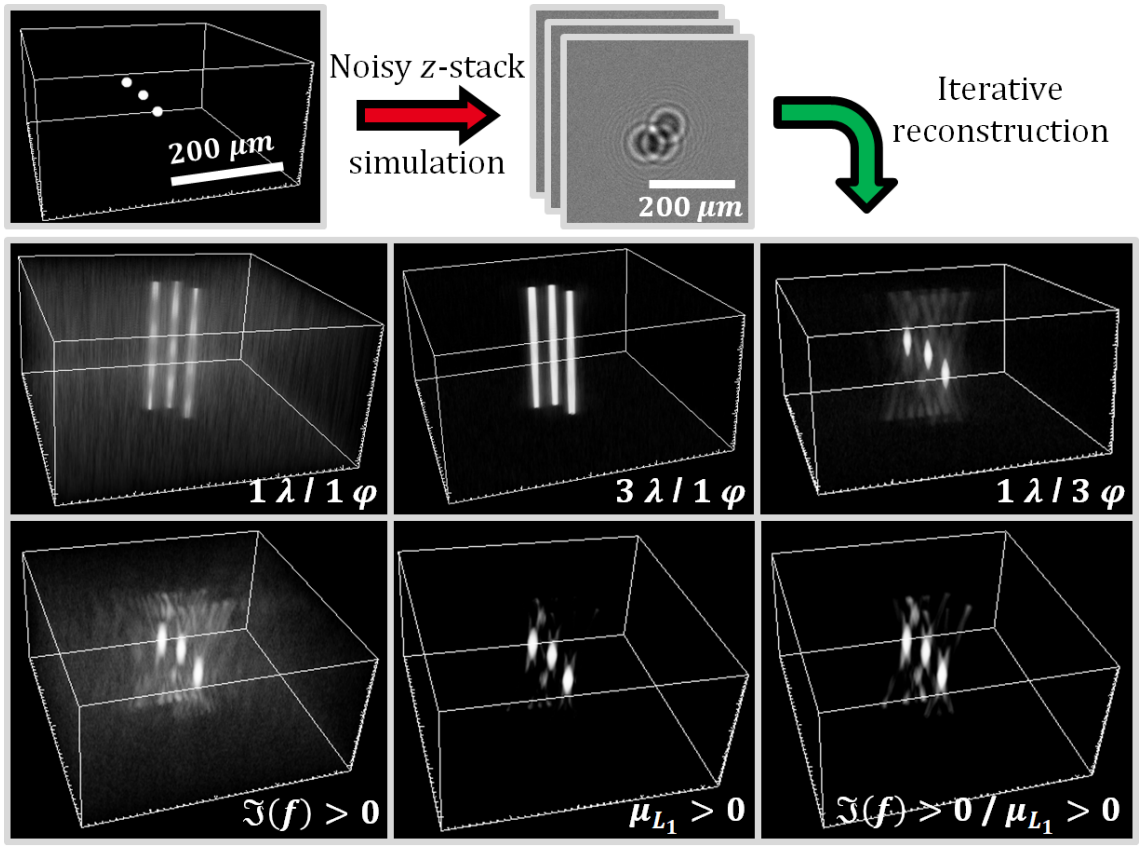

Figure III.17: The figure presents reconstructions obtained with different parameters. *First line* - Data simulation process. *Second line* - Reconstructions performed without regularization or constraint ($C(f) = \{f \in \mathbb{C}\}, \mu_{L_1} = 0$). It compares reconstructions in terms of number of wavelengths (red channel or RGB) and angles ($\varphi = 0°$ or $\varphi \in \{-15°, 0°, 15°\}$). *Third line* - Influence of the regularization and constraints for data in the red channel at three angles. The iteration number is $nb_{it} = 30$. All the 3D views are displayed with the same dynamics.

Multiplying the wavelengths does not appear critical when only a lighting angle is used. It helps to minimize the effect of the noise in the reconstruction as it acts as an averaging of several datasets (one per wavelength) but does not constraint the objects on the z-axis. Thus, the inverse problem approach and the deconvolution methods developed in 3.2 leads to similar results. Even if not plotted here, these conclusions remain valid if regularization is applied.

These reconstructions look very similar to a z-stack that one can obtain by a sim-

ple back-propagation at different distances from a given hologram (see figure II.15). These tubular shapes are consequently explained by the fact that a given hologram can be due to different transmissive planes at different distances z, exactly as any slice in the z-stack in figure II.15 produces the original hologram. Everything acts as if the method reconstructs at once all these slices which are all correct in regard of the simulated volume. It presents a similarity with X-ray tomography: it is not possible from one angle to get where on the z-axis is an absorbent point. The fact that the hologram changes along the diffracted volume is not enough restrictive.

Reintroducing angles in the method appears far more efficient to constraint the z-positions. The third line in figure III.17 presents different tests of constraint and regularization. It is tested to have a solution with a positive imaginary part $\mathcal{I}(f) > 0$ and the sparsity parameters are set to $\mu_{L_1} = 250$ and $\epsilon = 10^{-5}$. It appears that the sparsity regularization is efficient to reduce the reconstruction artifacts.

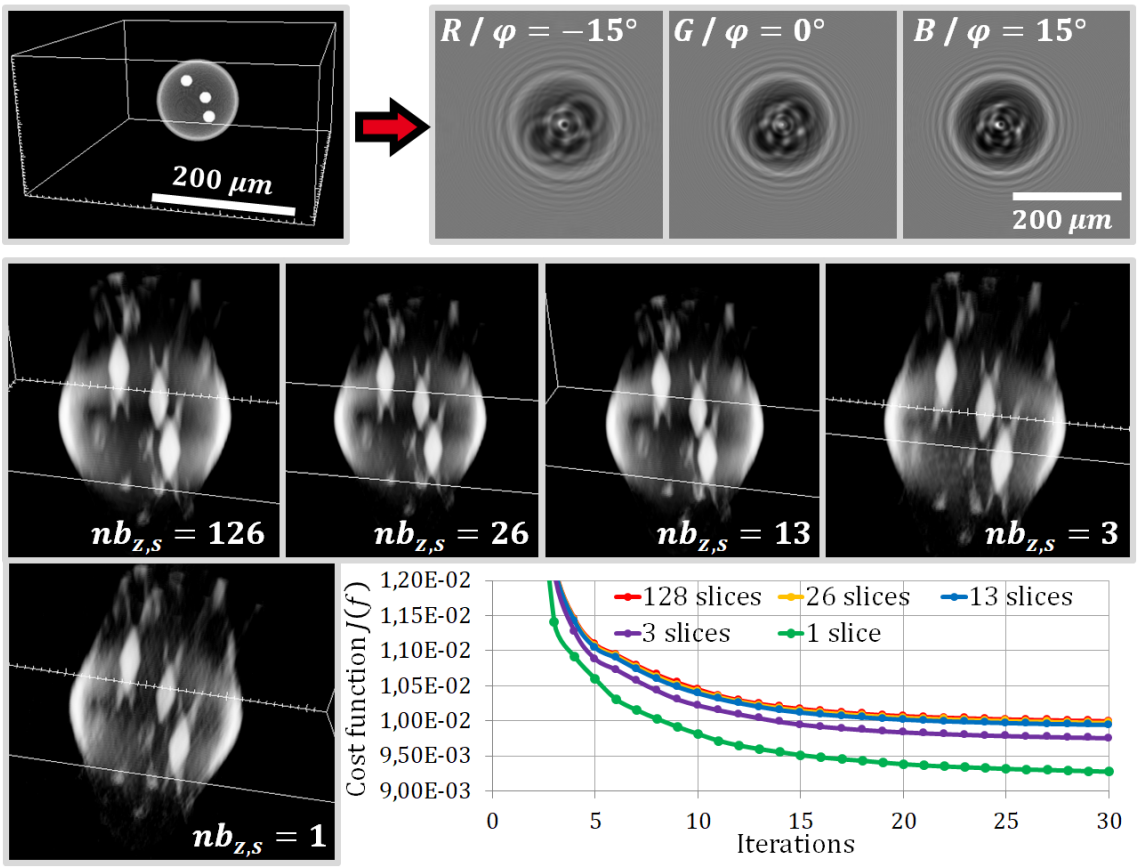

Figure III.18: Reconstruction of a simulated dataset for different slicing numbers $nb_{z,s}$. *First line* - Data simulation process for three lighting angle, one per channel R, G and B. *Second line* - Reconstructions performed for different slicing numbers $nb_{z,s} \in \{126, 26, 13, 3\}$. *Third line* - Reconstruction with $nb_{z,s} = 1$ and comparison of the evolution of the cost function during iterations.

As shown in figure III.18, one can evaluate the influence of the number of kept slices in the diffracted volume. The numerical object is the same as previously

described with a spherical membrane surrounding the three spheres to simulate cells embedded in a Matrigel® capsule. Its external radius is $r_{cap} = 70\ \mu m$ and its internal radius is $0.9 r_{cap}$. Its refractive index is $\delta n_{cap} = 0.2 \delta n_c$.

The reconstructions are similar, even if the more slices are kept, the smoother is the reconstruction. But $nb_{z,s}$ does not appear determinant in the objects separation or location. The comparison of the convergence curves of the cost function with these different slicing parameters shows that $nb_{z,s}$ does not influence the convergence rapidity.

This method is consequently considered as being a dead end. Indeed, it appears that multiplying the lighting angles is necessary, whereas the initial aim of the method to work on a unique z-stack obtained with a normal incidence does not seem to produce a better reconstruction than with only $nb_{z,s} = 1$ acquisition. According to equation (III.19), multiplying the lighting angles leads to increase by a factor of 2 the needs of 3D FFT, which is rapidly time consuming. This is a strong limitation in an iterative reconstruction method.

Nevertheless, a 3D reconstruction is performed on a real data set, presented in figure III.19, to show the feasibility of a first 3D object retrieval method taking into account the diffraction process, in opposition to the Radon method introduced in the previous section 2.

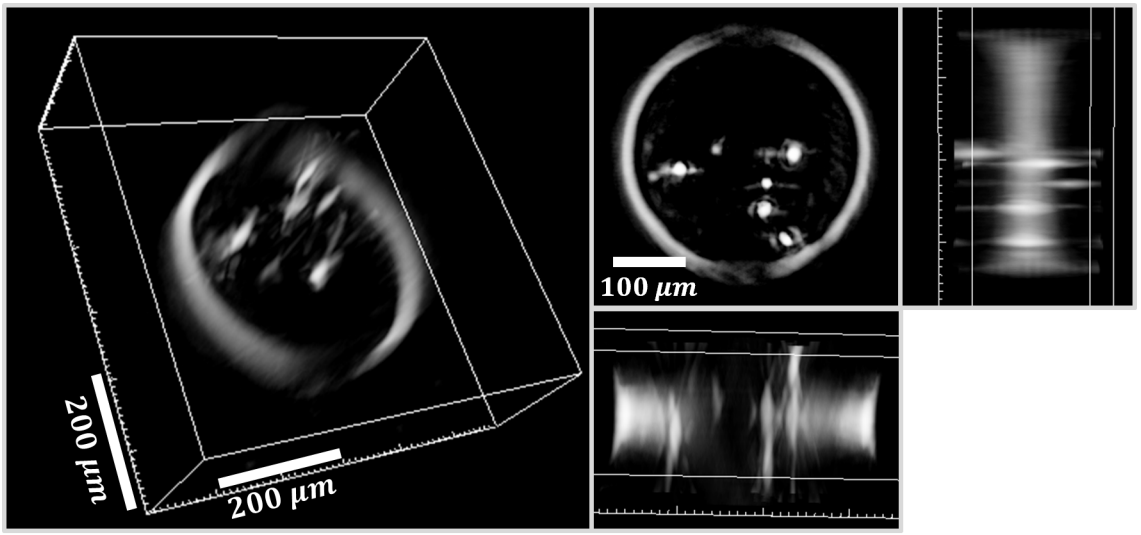

Figure III.19: Reconstruction of the dataset introduced in figure III.12. The dataset is composed of the three angles $\varphi \in \{-15°, 0°, 15°\}$ in the three RGB channel, aligned by LSM on the raw data. The reconstructed volume is $\sim 585\times \sim 585\times \sim 214\ \mu m^3 \simeq 0.07\ mm^3$.

No constraint on f is applied and the sparsity hyperparameter is set to $\mu_{L_1} = 250$. The reconstructed volume is composed of $350 \times 350 \times 128$ voxels, with a side of $1.67\ \mu m$. The distribution of the objects on different planes is visible. As previously noted in figure III.12, the capsule is not uniformly reconstructed because of the limited angular coverage and the orientation of the rotation axis.

4 A third method based on the Fourier diffraction theorem

This section is mainly based on the content of the article published in the Biomedical Optics Express journal [80] and uses the formalism developed in chapter II, section 3.

4.1 Overview of the method: a Fourier mapping

As mentioned in chapter II, section 2, the Fourier diffraction theorem can either be used to go from the object f toward the diffracted wave U_{dif} for simulation purposes, or from the diffracted wave to the object for reconstructions (see figure II.3). The latter is used in this section.

Let's assume that one has a dataset of N acquisitions recorded under different illumination situations[24] $\left\{\overrightarrow{k_0'^j} = k_0'^j \left(p_0^j, q_0^j, m_0^j\right)\right\}_{j\in[\![1,N]\!]}$.

The discrete formulation of the Fourier diffraction theorem (II.51) introduced in chapter II, section 3, can be reversed to map the Fourier domain of the object f for a given illumination j from a hologram pattern centered on $\left(x_0^j, y_0^j\right)$ on the corresponding cap cap^j:

$$\begin{aligned}\mathrm{FFT}_{3D}\left[pad\left(f\right)\right]|_{cap^j} = interp^{-1}\Big(H_{z_s}^j.M_U^j.\mathrm{FFT}_{2D}\left[pad\left(M_{\hat{f}}^j.U_{dif}^j\right)\right], \cdots \\ \left(u_{2D}^{pad}, v_{2D}^{pad}, w\left(u_{2D}^{pad}+u_0^j, v_{2D}^{pad}+v_0^j\right)-w_0^j\right)\Big)\frac{ds}{dv}\end{aligned} \tag{III.21}$$

keeping the notations $\left(u_0^j, v_0^j, w_0^j\right) = \left(\frac{n_0.p_0^j}{\lambda_0^j}, \frac{n_0.q_0^j}{\lambda_0^j}, \frac{n_0.m_0^j}{\lambda_0^j}\right)$, and where:

$$H_{z_s}^j = \frac{4\pi}{ik_0'^2} w\left(u_{2D}^{pad}+u_0^j, v_{2D}^{pad}+v_0^j\right) e^{-2i\pi w\left(u_{2D}^{pad}+u_0^j, v_{2D}^{pad}+v_0^j\right)z_s} \tag{III.22}$$

is a matrix which can be considered as a filter in the Fourier domain, characteristic of the distance of propagation z_s,

$$M_U^j = e^{-2i\pi\left(x_0^j u_{2D}^{pad}+y_0^j v_{2D}^{pad}\right)} \tag{III.23}$$

is a modulation matrix in the Fourier domain to translate U_{dif} in the spatial domain to $\left(x_0^j, y_0^j\right)$,

$$M_{\hat{f}}^j = e^{-2i\pi\left(\left(x_{2D}+x_0^j\right)u_0^j+\left(y_{2D}+y_0^j\right)v_0^j\right)} \tag{III.24}$$

is a modulation matrix in the spatial domain to translate the spherical cap cap^j in the Fourier domain of $\hat{f}$ according to the lighting illumination j.

[24] Let's remember here that the information of the illumination wavelength is in the wave number (the norm of the wave vector): $\left\|\overrightarrow{k_0'^j}\right\| = k_0'^j = \frac{2\pi n_0}{\lambda_0^j}$

"$interp^{-1}$" is the inverse function of the function "$interp$" for the nearest neighbor technique: it consists in reversing the orientation of the blue arrows in figure II.7.

Let's note here that a voxel can consequently be mapped twice or more (for example $\left(u_{i_p-1}, w_{k_v}\right)$ in the figure). Several strategies can be applied here such as an averaging. For the simplicity and the rapidity of the code, we decided in this chapter to only keep one value[25], not taking into account the others. Thus, each illumination j allows mapping the Fourier domain of the object on a spherical cap.

Noting $interp_j^{-1}(M) = interp^{-1}\left(M, \left(u_{2D}^{pad}, v_{2D}^{pad}, w\left(u_{2D}^{pad}+u_0^j, v_{2D}^{pad}+v_0^j\right)-w_0^j\right)\right)$, an approximation of the 3D object to retrieve is finally given by:

$$\boxed{f \simeq pad^{-1}\left[\mathrm{FFT}_{3D}^{-1}\left(interp_{j\in[\![1,N]\!]}^{-1}\left(H_{z_s}^j.M_U^j.\mathrm{FFT}_{2D}\left[pad\left(M_{\hat{f}}^j.U_{dif}^j\right)\right]\right)\frac{ds}{dv}\right)\right]} \tag{III.25}$$

Let's note here that this method only gives a very sparse estimation of the Fourier transform of the object as one can see in figure III.20. The coefficients which are not mapped are set to zero and one can expect numerous artifacts in the reconstructions.

This sparsity is due to the finite number of acquisition angles but also to the limitations of the angular coverage of the φ-mode. One can indeed notice that this mode strongly limits the access to the part surrounding the vertical axis and the rotation axis in the Fourier domain (along γ and α).

Some interpolation methods could be applied to generate a fully filled 3D frequency support but this is not in the scope of this section.

4.2 A phase ramp to compensate the lack of phase

One may have noticed that the introduced method is based on the knowledge of the diffracted wave U_{dif}. Nevertheless only the intensity of the total transmitted wave $I_{tot}^j = \left|U_{tot}^j\right|^2 = \left|U_{inc}^j + U_{dif}^j\right|^2$ is recorded by the sensor.

Hence one needs to approximate the diffracted wave U_{dif}^j from I_{tot}^j. To do so, I_{tot}^j is normalized so that the background value, corresponding to the unperturbed incident wave, is equal to 1. Let's note this normalized projection $\tilde{I}_{tot}^j$.

The square root of $\tilde{I}_{tot}^j$ is multiplied by a phase ramp $e^{i\overrightarrow{k_0'^j}.\vec{r}}$ to take into account the non-uniform phase shift induced by the tilted incidence of $\overrightarrow{k_0'^j}$ relative to the sensor plane. Then the theoretical incident plane wave $U_{inc}^j = e^{i\overrightarrow{k_0'^j}.\vec{r}}$ is subtracted:

$$U_{dif}^j \simeq \sqrt{\tilde{I}_{tot}^j}.e^{i\overrightarrow{k_0'^j}.\vec{r}} - U_{inc}^j \tag{III.26}$$

This formula is schematically represented in figure III.21. This is a needed step in the presented method. Indeed, the phase is very important since, *inter alia*, it contains the inclination of the wave front. Without this information, the mapping of the Fourier space with equation (III.25) cannot work because the computed 2D

[25] As mentioned later in chapter IV, this is a critical choice. Averaging can greatly change the reconstruction quality.

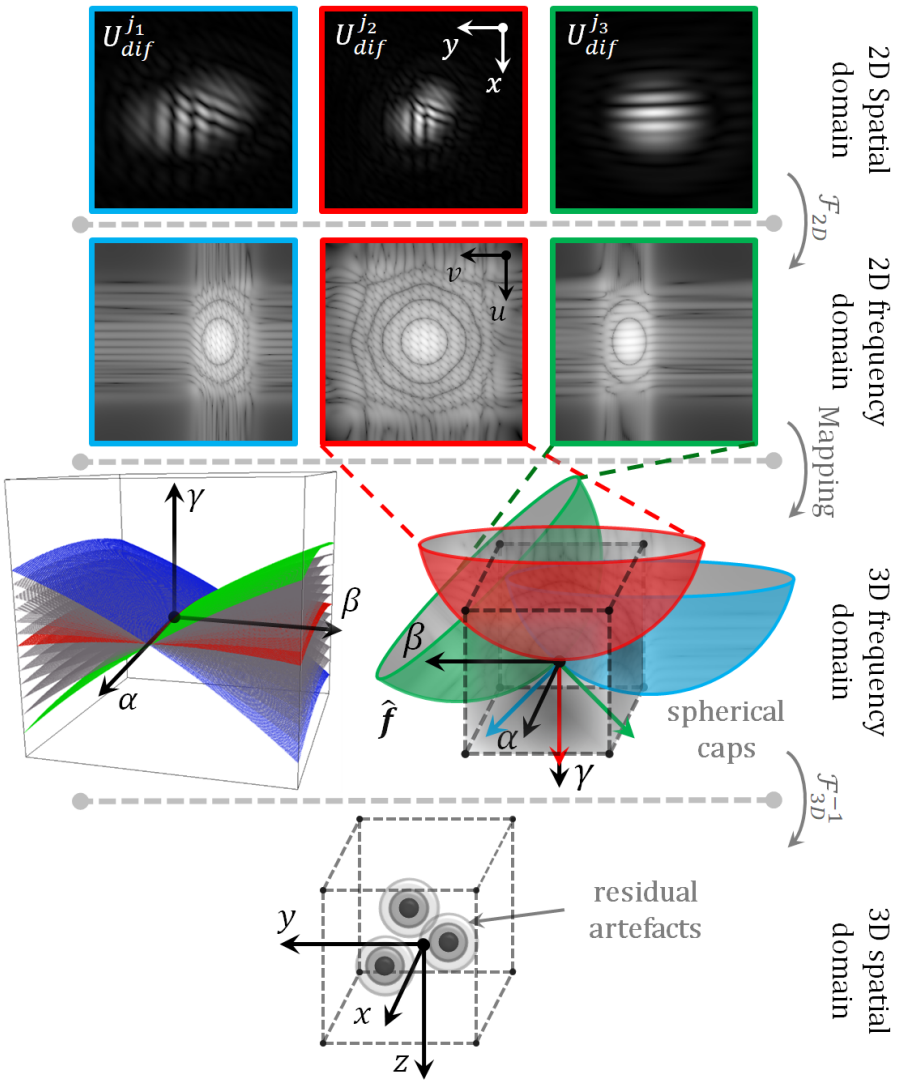

Figure III.20: Illustration of the method of the Fourier mapping with the notations of figure II.3. The 3D frequency space of the object of interest f is mapped with the 2D Fourier transform of the projections $U_{dif}^{j_1}$, $U_{dif}^{j_2}$ and $U_{dif}^{j_3}$. An example of a Fourier region which is actually filled by the algorithm in the φ-mode configuration is given in the medallion in the 3D frequency domain part of the figure. It is the mapped region for a volume of $512\times512\times512$ voxels with a voxel size of $1.67\times1.67\times1.67$ μm^3 at $\lambda_0 = 520$ nm with an illumination angle varying from -30° (blue) to 30° (green) with a step of 5° at a distance of $z_s = 2.5$ mm. The red cap corresponds to the region mapped with the normal illumination.

spectra will be shifted in the Fourier space. Equation (III.26) allows reintroducing the information of the illumination angle in the data even if the simulated phase is just an approximation of the real one.

This calculation does not totally compensate the lack of phase information at the sensor plane. In particular, the phase distortion introduced by the object is

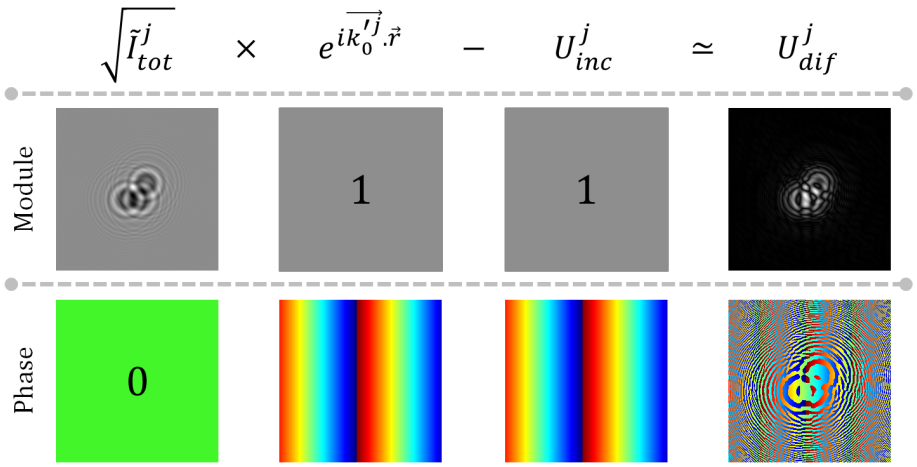

Figure III.21: Illustration of the steps to get an approximation of U^j_{dif} for a given j.

not taken into account and could be approximated by means of a phase retrieval algorithm in order to diminish the artifactual twin-image [59] but is not in the scope of this section and once again, one can expect artifacts in the reconstructions.

4.3 3D reconstruction and comments

In this section, only reconstructions on the RWPE1 cell network data introduced previously in figure III.4 are presented[26].

The chosen angular coverage varies from -30° to 30° with an angular pitch of 1° (for a total of 61 angles) and the reconstructed volume is $4 \times 4 \times 1.34\ mm^3$, using the data in the green channel: $\lambda_0 = 520\ nm$. Presented in figure III.22, it shows that the cells interestingly tend to form a structured network as it is deduced from figure III.11.

Such a large volume is reconstructed by pieces of $1.34 \times 1.34 \times 1.34\ mm^3$, *i.e.* nine reconstructions. The data are divided into nine adjacent regions of interest of size $1.34 \times 1.34\ mm^2$ (800×800 pixels), as illustrated in figure III.23. The centering of each projection is done with the least squares minimization method on the raw data, applied relative to the central region of interest (red dashed in figure III.23). This central region of interest is also used by the focusing algorithm to estimate the distance z_s between the sensor plane and the cell culture. The eight other regions of interest remain adjacent to this one whatever the angle of view, to ensure the continuity in the 3D reconstruction. Each reconstructed 3D image has a size of $800 \times 800 \times 400$ voxels with the sampling rate $1.67 \times 1.67 \times 3.34\ \mu m^3$. Owing to this decoupling task, the reconstruction of a single region of interest has a size of two gigabytes in double precision which can be handled on a desktop computer. As

[26]Let's put the stress on the fact that in the current section, the reconstruction are done as if everything is in the air: $n_0 = 1$. As presented in the next section 5, taking in account the refraction in the illumination direction is essential to prevent any scaling factor along the z-axis. This means that all the distances and positioning in z are not absolute but only relative in this section.

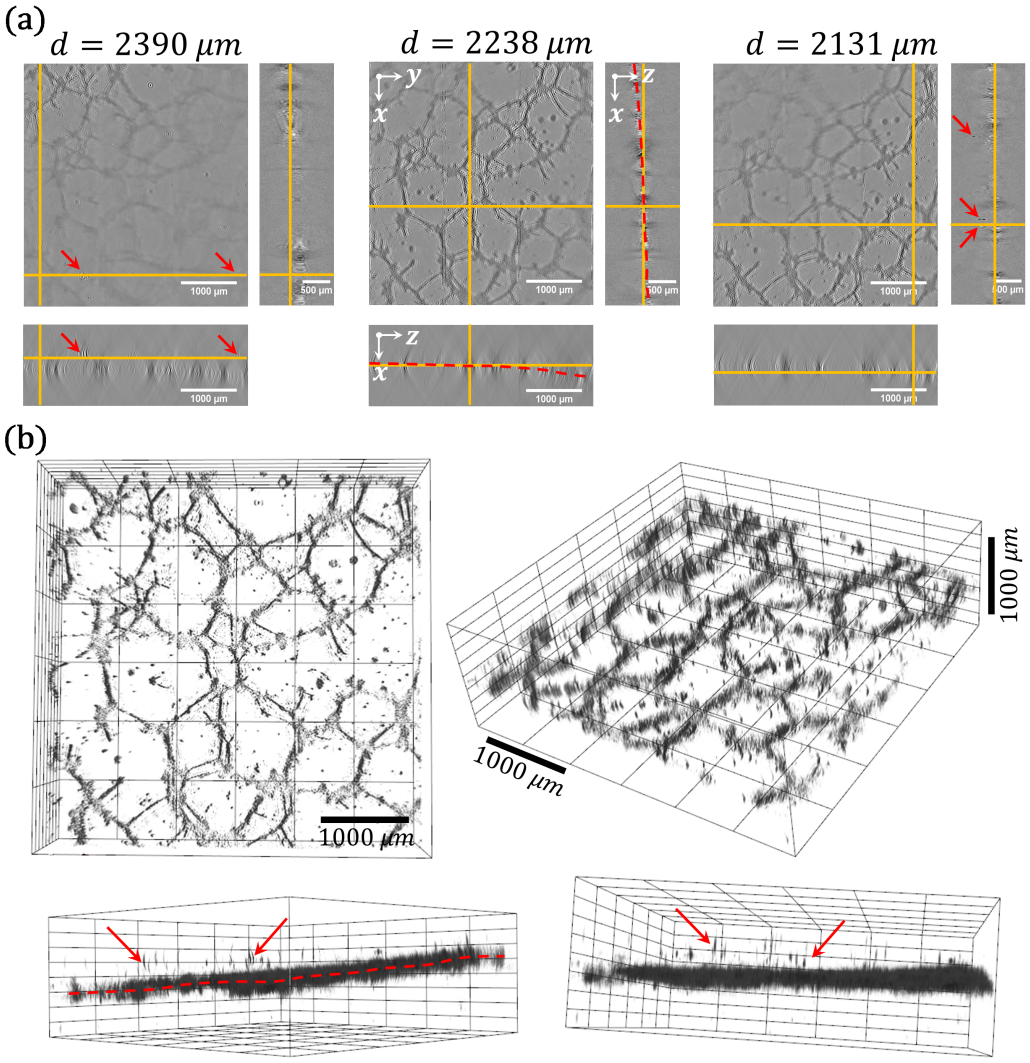

Figure III.22: Piecewise 3D reconstruction (imaginary part of f) of a large volume ($4\times4\times1.34\ mm^3$) of the culture of RWPE1 prostate cells. (a) 3 orthogonal sectional views are shown, each one extracted at a given distance $d = z_s - z$ from the sensor. (b) 3D views of the reconstruction from different observation points. The dash red curves indicate the tilt of the network relative to the horizontal plane. The red arrows point out isolated objects that are not focused at the same altitude as the network.

a result the global 3D image has a size of $2400 \times 2400 \times 400$ voxels and with the same sampling rate, this whole image has a size close to 20 gigabytes.

The whole reconstructed volume f is shown in figure III.22. Let's note here that the reconstructed scattering potential f is a complex number. Only its imaginary part which gives the most observable information is presented in this section. Three different sectional views - xy (center), xz (right) and yz (bottom) - show that the network formed by the cells is well focused at precise altitudes in the volume. The network fits a surface which is not horizontal. That demonstrates that the recon-

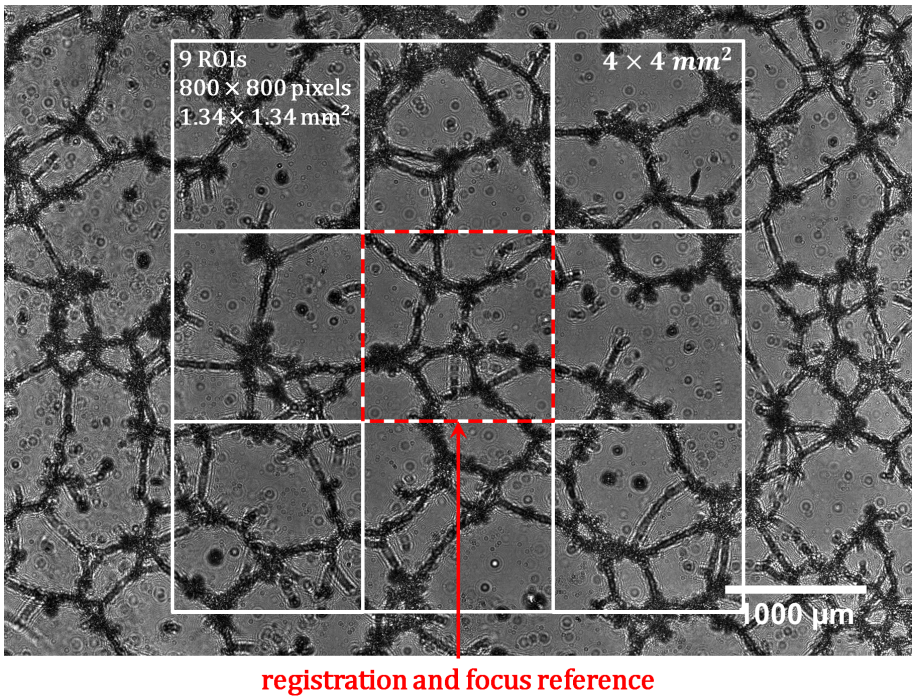

Figure III.23: Extraction of 9 regions of interest of size $1.34 \times 1.34\ mm^2$ (800×800 pixels) for the piecewise 3D reconstruction of the 3D culture of RWPE1 prostate cells presented in figure III.4.

struction algorithm effectively operates in 3D. Isolated objects are also focused apart from the network at independent altitudes. Some of them are pointed out by red arrows.

The central and top-right regions of the reconstructed volume of figure III.22 are detailed in figures III.24 and III.25. They correspond respectively to the central and bottom-right regions of interest on the raw data in figure III.23. Each of these figures represents the three sectional views - xy (center), xz (right) and yz (bottom) - and a 3D view of the region of interest and two specific patterns such as a cell or a cluster of cells which are pointed by arrows in the regions of interest. The rings around the focused objects on the xy views are artifactual: this is the phenomenon of twin-image, induced by the lack of absolute phase information in the data.

To analyze the performances of the setup and the 3D reconstruction algorithm to recover unambiguously biological objects, a comparative study with 2D reconstructions from 2D lens-free data acquired at the normal illumination ($\varphi = 0°$) in the RGB channels is conducted[27]. The algorithm used to perform the 2D reconstructions has already shown, as a 2D lens-free imaging application, its ability to recover single cells and clusters while removing the twin-images.

Figure III.26 shows the 2D reconstruction of a region of the studied field of view. One can observe the efficiency of the reconstruction algorithm to recover the biological scene showing branching networks, isolated clusters and cells. To

[27]Such algorithms are mentioned in chapter I section 3.2

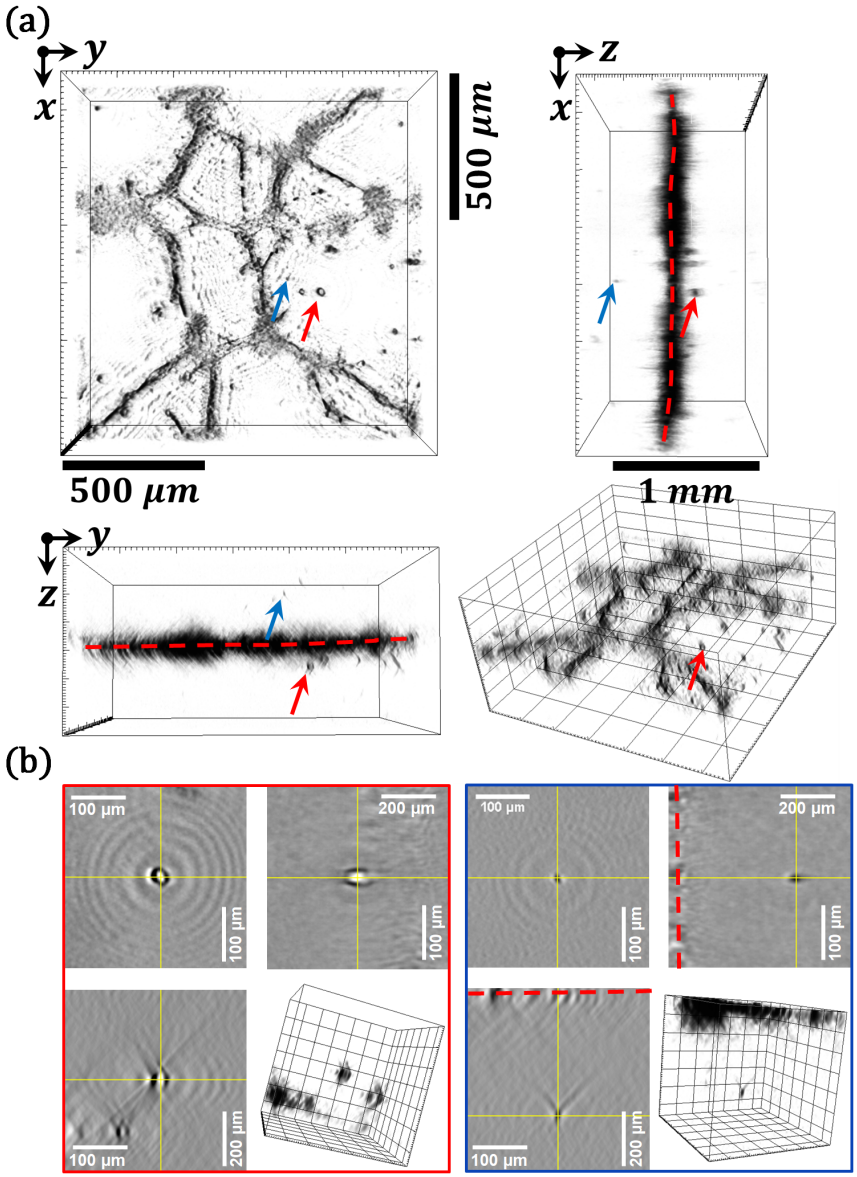

Figure III.24: Region of interest at the center of the piecewise 3D reconstruction of the volume III.22. (a) Orthogonal views and 3D rendering of the region of interest. (b) Orthogonal sectional views and 3D rendering on two specific clusters at the full resolution of the reconstruction. These are pointed by arrows on the global view. The dashed-line indicates the network plane. The red arrow points toward a $33 \times 38 \times 42$ μm^3 object and the blue arrow toward a $16 \times 17 \times 40$ μm^3 object.

perform the comparison with the 3D reconstruction, three objects are selected from the objects highlighted figures III.24 and III.25: two cells (see regions of interest 1 and 2 in figure III.26) and one cluster (see region of interest 3 in figure III.26). Two axial cut profiles respectively in x and y-directions are taken for both the 2D and 3D reconstructions, and one cut profile in the z-direction for the 3D reconstruction. These cut profiles are illustrated on the three graphs in figure III.26.

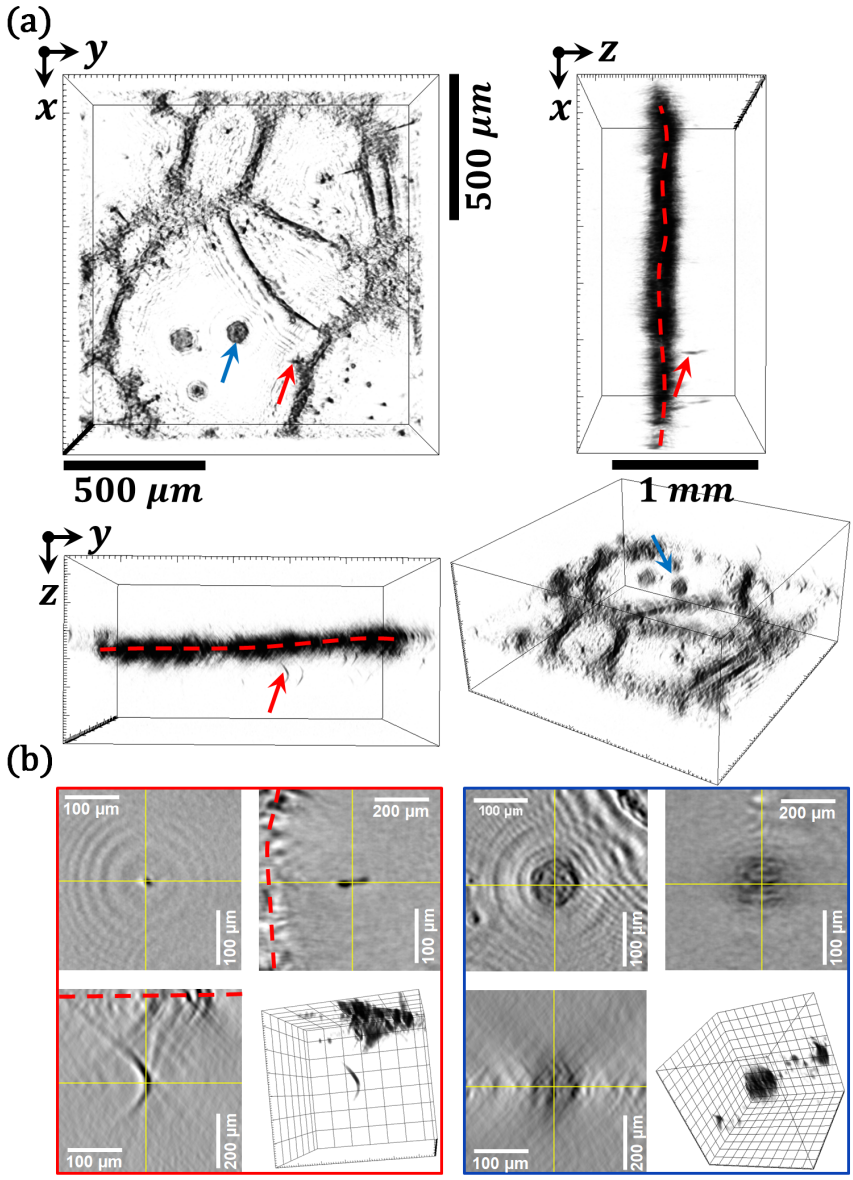

Figure III.25: Region of interest at the right corner of the piecewise 3D reconstruction of the volume III.22. (a) Orthogonal views and 3D rendering of the region of interest. (b) Orthogonal sectional views and 3D rendering on two specific clusters at the full resolution of the reconstruction. These are pointed by arrows on the global view. The dashed-line indicates the network plane. The red arrow points toward a $12 \times 43 \times 96$ μm^3 object and the blue arrow toward a $80 \times 80 \times 100$ μm^3 object.

As a first observation, one can see that axial profiles are globally equivalent in 2D and 3D, allowing to measure approximatively cell sizes of ~ 15 μm for the region of interest 2 and ~ 30 μm for the region of interest 1 considering the width of the central lobe of the profiles (the secondary lobes are known to be twin-image artifacts), which is consistent with typical cell sizes. For the cluster, the profiles are more erratic but we can distinguish a kind of a plateau curve, the width of

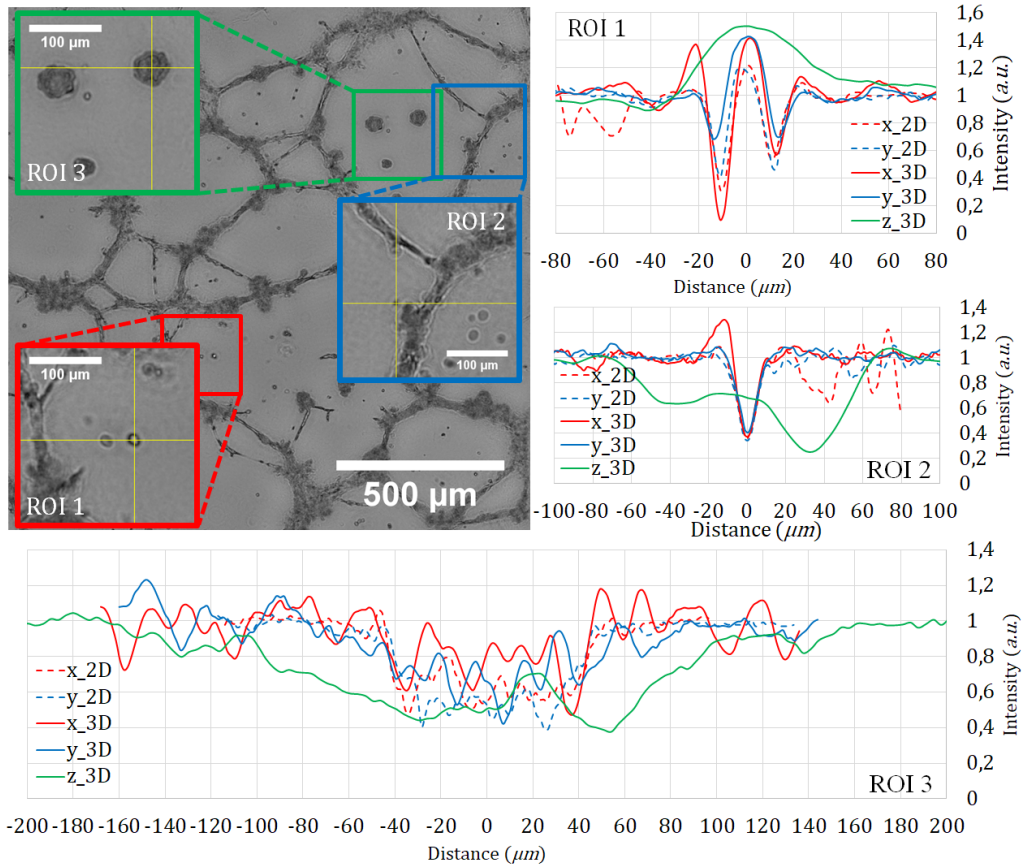

Figure III.26: 2D reconstruction from 2D lens-free data acquired on the 3D culture of RWPE1 prostate cells presented in figure III.23. Comparisons of two axial cut profiles respectively in x and y directions taken on both 2D and 3D reconstructions, and one cut profile in the z direction taken on the 3D reconstruction, for three biological objects: two cells, one identified in figure III.24 (region of interest 1 in red) and one identified in figure III.25 (region of interest 2 in blue) and one cluster identified in figure III.25 (region of interest 3 in green). The dashed and solid curves correspond respectively to the 2D and 3D reconstruction cut profiles.

which is measured at $\sim 90\ \mu m$. As expected, the observations are different in the z direction and the resolution is clearly degraded: whereas the objects must have a global isotropic behavior in terms of size in 3D, our measurements give $\sim 80\ \mu m$ for the cell in the region of interest 1, $\sim 115\ \mu m$ for the cell in the region of interest 2 and $\sim 200\ \mu m$ for the cluster in the region of interest 3. Moreover, the disparities of the measurements for the cells tend to show that the apparent resolution highly depends on the position of the object in the field of view: the more one goes away from the center (from the regions of interest 1 and 2), the worse is the resolution in the z-direction. Note that the term of "resolution" used here has not to be confused with the strict definition of optical resolution. These are empirical measurements that allow concluding that single biological objects are effectively and unambiguously identified in the 3D reconstruction.

Uncertainties in the calibration of the setup and the projection model can explain some artifacts in the image and the previous quantifications of figure III.26. For example the stretching of holograms is not taken into account in the registration of the projections whereas it depends of the lighting direction. Thus some misalignment can be present after the registration step. Moreover uncertainties remain on these lighting directions, due to the multiple refractions in between the different propagating media (air, culture medium, sensor glass, etc.) which change the illumination orientations[28]. The induced artifacts then get worse as the distance from the center increases since the errors on the objects positioning grow with this distance. That is maybe why the artifactual bow shape around the single objects get worse on the side, as one can see comparing figure III.24 and III.25 and the profiles in figure III.26.

As a conclusion, one can see that as for the method based on the Radon transform[29] this method can deal with large volumes in reasonably short time[30]. But the former can work directly on the volume slices whereas the latter must work piecewise.

On the other side, the lack of absolute phase in the data leads to numerous artifacts. Moreover, as for the reconstructions obtained with the inversion of the Radon transform, the artifacts are highly anisotropic between the directions parallel and orthogonal to the sensor, but also between the directions aligned or orthogonal to the rotation axis. Indeed, the bow-shaped structures can once again be attributed to the setup design[31].

5 A few thoughts on the lighting angles...

As mentioned in the previous section, some artifacts could be explained by some uncertainties on the lighting angles. Indeed, the refraction effect at the different interfaces is not taken in account and all the reconstruction parameters are set as if everything is in the air: $n_{air} = 1$.

But all the biological samples are embedded in a specific medium of refractive index n_0 (generally water with a refractive index of $n_{H_2O} = 1.33$). The index jump is not negligible and as presented in figure III.27.a it should lead to a difference between the design angle θ_{air} of the light source position and the angle in the medium θ_0 because of the Snell's law:

$$\boxed{n_{air}.\sin\theta_{air} = n_0.\sin\theta_0} \tag{III.27}$$

To check if the holograms are indeed characteristic of the illumination angle θ_0 given by equation (III.27) a specific experiment is designed. Micro-beads are put

[28] See section 5 for more details.

[29] See section 2.

[30] The longest parts are the 3D FFTs computations which remain limited, leading to a reconstruction time in the order of one minute.

[31] Otherwise these artifacts would present a symmetry on the x and y-axes.

in water and their holograms are recorded for different lighting angle θ_{air} in the air ranging from 20° to 50° (see figure III.27.b).

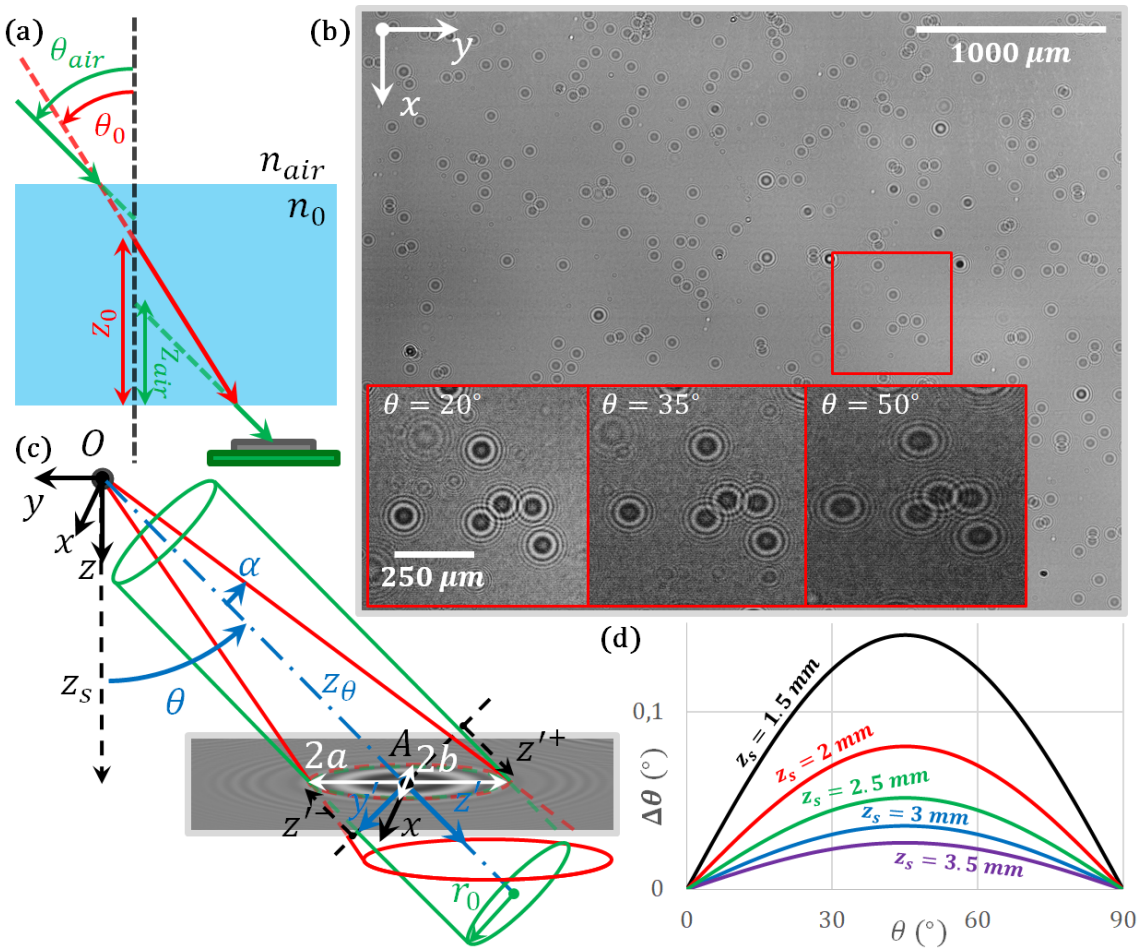

Figure III.27: (a) Optical scheme of the Snell's law: due to the difference in refractive index between the air and the culture medium, the lighting angle is changed in the medium. (b) Holograms of micro-beads in water for $\theta_{air} = 20°$. The red medallions are zooms on a given region of interest for different angle $\theta \in \{20°, 35°, 50°\}$ (c) To retrieve the lighting angle θ from a given hologram, the diffraction pattern is supposed to be cylindrical (green) with a radius of $r_0 = b$ instead of conical (red). a and b are the semi-axes of the ellipse. (d) Curves of the differences between the measured angles within the cylindrical approximation and the real angle for a radius of $r_0 = 150$ μm and for different distances z_s between the sensor and the sample.

5.1 Method and experiment

To retrieve the effective illumination angle θ_0 for each hologram, the conical hologram pattern is approximated by a cylinder of radius r_0, cut with an angle θ_0 by a plane rotated around the x-axis. In the rotated frame $(A; x' = x, y', z')$, using

the notation in figure III.27.c, the equations of the plane, the cone and the cylinder are:

$$\boxed{z' = -y' \tan\theta \text{ and } r = \sqrt{x^2 + y'^2} = r_0 \left(1 + \frac{z'}{z_\theta}\right) \text{ and } r_0^2 = x^2 + y'^2} \tag{III.28}$$

This cylindrical approximation holds as far as the cone can be approximated by a cylinder in the spatial extension of its intersection with the tilted plane, *i.e.* in the range $z' \in [-z^-, z^+]$ where $-z'^-$ and z'^+ are computed at the extreme two intersections for $x = 0$.

Assuming this cylindrical approximation, it is possible to retrieve the illumination angle θ from the characteristics of the ellipses shaped by the holograms. Indeed, its semi-minor axis is directly $b = r_0$ while its semi-major axis a is obtained in the plane $x = 0$ where $|y\prime| = r_0$. From equation (III.28), one gets:

$$a = \sqrt{y'^2 + z'^2} = r_0\sqrt{1 + \tan^2\theta} = \frac{r_0}{\cos\theta} \tag{III.29}$$

and then:

$$\boxed{\cos\theta = \frac{b}{a} = \sqrt{1 - e^2}} \tag{III.30}$$

where e is the ellipse eccentricity.

This must be compared with the theoretical value obtained with the intersection with the cone[32]. In the frame $(A; x, y, z)$, the expression of the coordinates (y', z') are:

$$y' = y\cos\theta + z\sin\theta \text{ and } z' = z\cos\theta - y\sin\theta \tag{III.31}$$

and in this frame, the equation of the plane is $z = 0$. From equation (III.28), the equation of the ellipse is:

$$x^2 + y^2\cos^2\theta = r_0^2\left(1 - \frac{y\sin\theta}{z_\theta}\right)^2 \tag{III.32}$$

and with $\tan\alpha = r_0/z_\theta$

$$x^2 + 2z_\theta y\tan^2\alpha\sin\theta + y^2\left(\cos^2\theta - \tan^2\alpha\sin^2\theta\right) = r_0^2 \tag{III.33}$$

The eccentricity of such an ellipse is then given by [85]:

$$\begin{aligned} e &= \sqrt{\frac{2\left|1 - \cos^2\theta + \tan^2\alpha\sin^2\theta\right|}{1 + \cos^2\theta - \tan^2\alpha\sin^2\theta + \left|1 - \cos^2\theta + \tan^2\alpha\sin^2\theta\right|}} \\ &= \sqrt{\frac{2\sin^2\theta\left(1 + \tan^2\alpha\right)}{2 - \sin^2\theta - \tan^2\alpha\sin^2\theta + \sin^2\theta\left(1 + \tan^2\alpha\right)}} \\ &= \frac{\sin\theta}{\cos\alpha} \end{aligned} \tag{III.34}$$

[32]Let's thanks "gb" who gave some clues on a forum: `http://www.les-mathematiques.net/phorum/read.php?8,512589,512687`.

and with $z_\theta = z_s / \cos\theta$

$$\begin{aligned}\frac{b}{a} = \sqrt{1-e^2} &= \sqrt{1-\left(1+\frac{r_0^2}{z_\theta^2}\right)\sin^2\theta} \\ &= \sqrt{\cos^2\theta - \frac{r_0^2}{z_\theta^2}\sin^2\theta} \\ &= \cos\theta\sqrt{1-\frac{r_0^2}{z_s^2}\sin^2\theta}\end{aligned} \tag{III.35}$$

This result (III.35) must be compared with equation (III.30). To get an overview of the error made with the cylindrical approximation, figure III.27.d presents the difference between the real angle θ_r and the angle θ_m measured within the cylindrical approximation for different distances z_s between the sample and the sensor and for a radius of $r_0 = 150\ \mu m$. This radius is in the order of magnitude of the diffraction pattern of the beads on the x-axis for all the recorded angles:

$$\Delta\theta = \theta_m - \theta_r = \text{acos}\left(\cos\theta_r\sqrt{1-\frac{r_0^2}{z_s^2}\sin^2\theta_r}\right) - \theta_r \tag{III.36}$$

The figure shows that the difference is negligible ($< 0.15°$ for the worst case of $z_s = 1500\ \mu m$). For the purpose of this section, the approximation gives a sufficient precision.

To retrieve θ from the numerous holograms present in the field of view and to take into account that some of them may be overlapping, a special algorithm is implemented. Presented in figure III.28, it works as follows:

- Step 1 (a→b): 2D Fourier transform of the field of view. In order to average all the holograms, the phase of the Fourier transform is removed by taking its absolute value.
- Step 2 (b→c): An inverse Fourier transform brings back the information in the 2D real space. To minimize the influence of the noise, the obtained pattern is oversampled by a factor of two using a bilinear interpolation and a blurring Gaussian filter is applied.
- Step 3 (c→d): Computation of the gradient of the pattern to detect the edge of the interference rings.
- Step 4 (d→e): Thresholding to select only the minimal values of the gradient (dark and light rings of the pattern).
- Step 5 (e→f): First automatic guess[33] of the illumination tilt θ as well as its rotation φ around the z-axis.
- Step 6 (f→g,h): Refinement[34] of the illumination parameters (θ, φ) by fitting

[33] Using `regionprops(..., 'Centroid', 'Area', 'MajorAxisLength', 'MinorAxisLength', 'Eccentricity', 'Orientation')` in Matlab®.

[34] Using `fminsearch` in Matlab®.

ellipses in the dark regions of the threshold picture.

The robustness of the algorithm is tested on simulated data for different values of θ and ϕ. Table [III.1] shows a good agreement between the input values and the values measured by the algorithm for high values of θ despite it is tested in the worst scenario of figure III.27.d with $z_s = 1.5\ mm$. For low values, because of the lack of specificity of the cosine function, the errors are bigger. On the contrary, for high values of θ, the assumption of the cylindrical approximation provides very good results.

$\theta_{th}\,(^\circ)$	5	10	15	20	25	30	35	40	45
$\theta_m\,(^\circ)$	8.9	11.7	14.0	19.9	24.5	30.2	34.8	40.2	44.4
$\varphi_{th}\,(^\circ)$	0	25	15	45	5	10	35	20	40
$\varphi_m\,(^\circ)$	-8.4	24.9	17.3	45.8	5.42	10.6	34.9	19.6	39.0

Table III.1: Test of the algorithm of figure III.28 on simulated pictures. $z_s = 1.5\ mm$, $nb_x = nb_y = 1024$, $nb_z = 32$, $dx = dy = dz = 1.67\ \mu m$, 40 beads with a diameter of 20 μm with a normal dispersion of $\sigma = 2\ \mu m$ and a refractive index of $\delta n = 0.005i$ with a normal dispersion of $\sigma = 5.10^{-5}i$.

5.2 Results

This algorithm is slightly changed before its application on the real data. Indeed, because of the noise in the threshold images, the automatic step 5 fails. This step is replaced by a manual guess of the parameters which are initialized to the awaited values. The found ellipses are kept from one angle to the next and scaled according to these awaited values to initialize the matching of step 6. The algorithm is used to check if the theoretical values are in the order of magnitude of the ones actually measured.

The angle determination is done on the 31 recorded angles $\theta_{air} \in [20^\circ, 50^\circ]$ using 8 ellipses with width of 1.5 pixel. Figure III.29 presents the results for three angles. For the last angles $\theta_{air} \in \{49^\circ, 50^\circ\}$, the matching of the fourth ellipse failed and it merged with another one, giving the impression that only 7 ellipses are matched. This does not change the interpretation of the results.

All the results[35] are synthesized on the curves of figure III.30.

Figure III.30.a shows that the measured $\sin\theta_m$ lie on a line in terms of $\sin\theta_{air}$. It is in accordance with Snell's law (III.27). A linear regression $y = s.x$ gives a slope of $s = 0.758$ with a coefficient of determination of $R^2 = 0.995$. With $n_{air} \simeq 1$, the refractive index of the medium is given according to the Snell's law (III.27) by:

$$\boxed{n_0 = \frac{1}{a} \simeq 1.32} \tag{III.37}$$

[35]The angle φ are not presented as they do not provide any interesting information in this section.

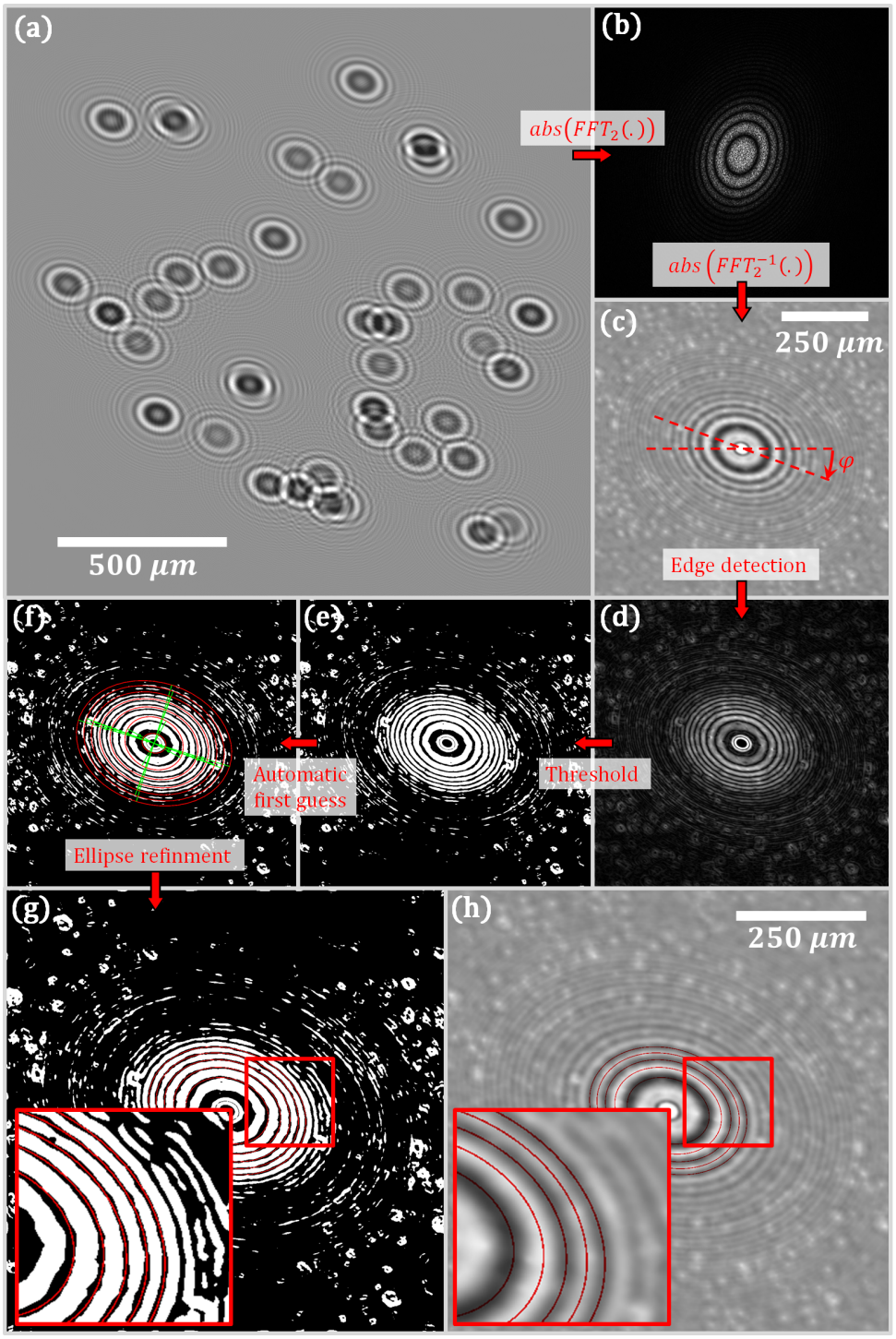

Figure III.28: Illustration of the algorithm to retrieve the illumination parameters (θ, φ) on simulated data (a) with parameters $(\theta = 40°, \varphi = 20°)$. (b) Absolute value of 2D Fourier transform of (a). (c) Absolute value of 2D Fourier transform of (b), scaled by a factor of 2 and blurred with a Gaussian filter. (d) Edges of (c). (e) Thresholding of (d). (f) Automatic detection of the ellipse patterns in (e). (g-h) Results of the fitted ellipses on the threshold (f) and overlaid on (c).

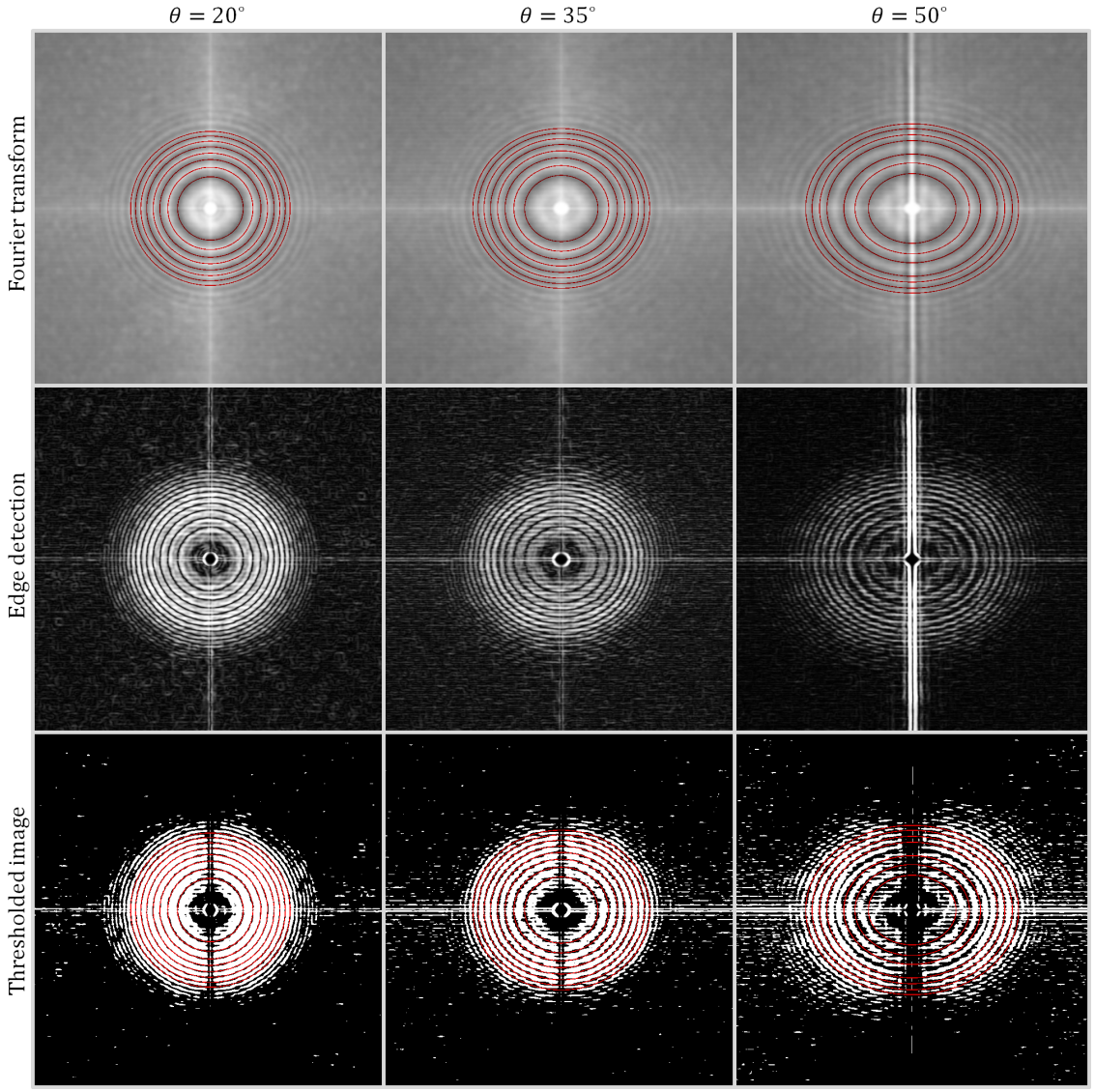

Figure III.29: Results of the algorithm for three different input angles $\theta_{air} \in \{20°, 35°, 50°\}$.

This is close from the value of the refractive index of water $n_{H_20} = 1.33$. This is confirmed in figure III.30.b where the ratio $\sin\theta_{air}/\sin\theta_m$ is plotted for different values of θ_{air}. Excepted for the high angles where the noise degrades the ellipse matching, the curve is in good agreement with a constant value of refractive index of $n_0 = 1.33$.

5.3 Conclusion and discussion

First, it is proven that, as expected, the angle of the lighting source θ_{air} is not the one that should be used in the reconstruction algorithm. The holograms have the characteristics of holograms created under a different angle of illumination θ_0.

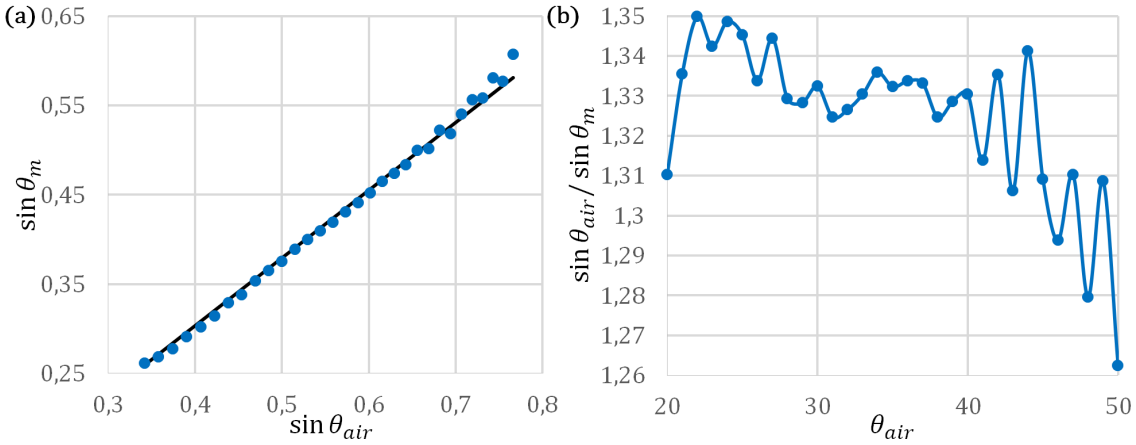

Figure III.30: (a) Plot of $\sin\theta_m$ (blue) as a function of $\sin\theta_{air}$ and the associated linear regression (black). (b) Plot of $\sin\theta_{air}/\sin\theta_m$ as a function of θ_{air}.

Then, the results show that even if the holograms are recorded in the air and after the sensor glass, these layers do not change the holograms properties which match the ones of the medium in which they are originating. Everything acts as if the sample was illuminated by a source tilted at an angle θ_0 corrected from the angle in the air θ_{air} with Snell's law (III.27).

It exists two ways to take into account this refraction effect in the numerical reconstructions.

The first one is straightforward and consists in replacing all the angles θ_{air} in the algorithm by their corrected value θ_0.

The second can be seen as an *a posteriori* correction and consists in a scaling factor along the z-axis, all the reconstruction being done as if everything was in the air. Indeed, looking back at the figure III.27.a, it is possible to express the ratio of the position z_{air} in the sample measured in the reconstruction with the wrong angle with its real position z_0. From $z_{air}\tan\theta_{air} = z_0\tan\theta_0$ and Snell's law (III.27), it comes:

$$\begin{aligned}\frac{z_0}{z_{air}} &= \frac{\tan\theta_{air}}{\tan\theta_0} = \frac{\sin\theta_{air}}{\sin\theta_0}\frac{\cos\theta_0}{\cos\theta_{air}} \\ &= \frac{n_0}{n_{air}}\frac{\sqrt{1-\sin^2\theta_0}}{\sqrt{1-\sin^2\theta_{air}}} \\ &= \frac{n_0}{n_{air}}\sqrt{\frac{n_0^2/n_{air}^2 - n_0^2\sin^2\theta_0/n_{air}^2}{1-\sin^2\theta_{air}}}\end{aligned} \tag{III.38}$$

$$\boxed{\frac{z_0}{z_{air}} = \sqrt{\frac{n_0^2/n_{air}^2 - \sin^2\theta_{air}}{1-\sin^2\theta_{air}}}} \tag{III.39}$$

This solution is also implemented to correct the 3D acquisitions in standard microscopy when the refractive index of the sample medium n_1 does not match with the refractive index n_2 of the air or the immersion oil used in the optics [86, 87]. It

is interesting to notice the similarity of the corrective scaling factor:

$$\boxed{\frac{z_2}{z_1} = \sqrt{\frac{n_2^2 - NA^2}{n_1^2 - NA^2}}} \tag{III.40}$$

where NA is the numerical aperture of the objective.

These two methods are numerically equivalent to reconstruct a 3D sample. Both of them give the same reconstructed volume.

Note here that the second solution cannot be implemented to correct the reconstructions of the previous section 4. Indeed several different angles θ_{air} are used in the reconstructions and a common scaling factor to simultaneously correct them does not exist. This confirms that a part of the identified artifacts are due to a non-rigorous use of the angles.

Chapter IV

A second design and new reconstruction methods

This chapter represents mainly the work done at the end of the first year and during the second year of the PhD program. From the experience and the conclusions of the previous chapter, a new prototype is built from a rethought design adapted for standard culture protocols in Petri dishes. New reconstruction techniques are implemented and tested on more complex 3D biological samples and first comparisons with microscope views are made. They are all based on the Fourier diffraction introduced in chapter II, section 2.

This work has led to a second publication in the Applied Optics journal [88] and an oral participation at BiOS 2017 [89].

1 Overview of the experimental bench

1.1 Design motivations

It has been seen in the previous chapter that the θ-mode is hardly adaptable to cell culture conditions and the reconstructions on biological sample are focused on the φ-mode, a mode in which the sample is fixed and the sensor remains parallel to the Petri dish. This solution has the advantage of being completely adapted to standard culture protocols. No sample preparation is needed and the Petri dish can directly be put on the lens-free microscope. This solution is consequently kept to design the new prototype.

Moreover, as noticed in section 4, lots of artifacts in the reconstructions seem linked with the geometry of the acquisitions, the lighting positions being constrained to a single plane on the rotating arm. The artifacts surrounding the isolated objects are not isotropic but rather gathered in this rotation plane. A better angular coverage had to be designed for the new prototype.

To choose among different possibilities, several solutions are numerically tested. To do so, a 10 μm diameter bead is simulated in a volume of 301^3 voxels of 1.67^3 μm^3 with a difference of refractive index of $\delta n = 0.005i$. For different designs, its holo-

grams are computed using the model developed in chapter II, section 3 in three different wavelengths $\lambda \in \{640\ nm, 520\ nm, 450\ nm\}$ and $z_s = 1.5\ mm$. Both the 2D plane and the 3D volume are zero-padded.

These theoretical holograms are then used to reconstruct the bead with the Fourier mapping method developed in chapter III, section 4. A noticeable difference is that contrary to the previous chapter, when a voxel in the Fourier space is filled with different information due to the mapping method and the different lighting positions and wavelengths, the Fourier coefficients are computed as an average of this overlapping information[1]. As in the previous chapter and contrary to the simulations, no padding is applied in the 2D and 3D spaces.

Figures IV.1, IV.2 and IV.3 present the results of the reconstructions for different design choices for one wavelength $\lambda = 450\ nm$. Each design uses 32 lighting positions, equally distributed along different patterns.

Two noiseless reconstructions are performed in a comparison purpose. In the first case, only the simulated intensities of the diffracted waves are used to reconstruct the bead. As in standard in-line holography, the phase information is lost and is compensated by a phase ramp, as presented in chapter III, section 4. Artifacts are awaited in the reconstruction (red frame in the figures). In the second case, the importance of the phase information is highlighted by using directly the complex diffracted waves to map the Fourier domain and shows the importance to perform a phase retrieval step in the reconstruction algorithms (green frames in the figures). The figures also indicate the position of the Fourier coefficients which are mapped during the reconstruction (blue frames) and can be interpreted as the frequency response of the lens-free microscope for a given design. The red and green frames are only extracted parts of the reconstructed volumes of 101^3 voxels centered on the bead and can be interpreted as the point spread function of the prototype.

These reconstructions must be compared with the reconstructions of real 10 μm beads presented in the last chapter, section 3.

Figure IV.1 compares the two acquisition modes of the first prototype. It supports the fact that a complete angular coverage with the θ-mode will always give better results than the information available using the φ-mode. The filling of the Fourier space appears more homogeneous and even without the phase of the diffracted wave, the reconstruction in the θ-mode gives a good result on the bead[2].

In the φ-mode, the Fourier filling is strongly anisotropic and this can be seen in the 3D reconstructions which are not symmetrical. The reconstruction presents the bow-shaped artifacts identified in the reconstructions of chapter III, section 4.

Some tests (not presented here) showed that the quality of the reconstruction is more linked with the opening angle φ_{max} than with the number of lighting positions between $-\varphi_{max}$ and φ_{max}. The parallax effect consequently appears to be the most important factor.

[1] And not forced to be equal to the first information filling the voxel as previously.

[2] Note here that the 3D rendering view is more representative of the reconstruction quality than the average intensity projections which squeeze the dynamics of the reconstructions by dividing the high value of the reconstructed bead by the number of voxel along the projection axis.

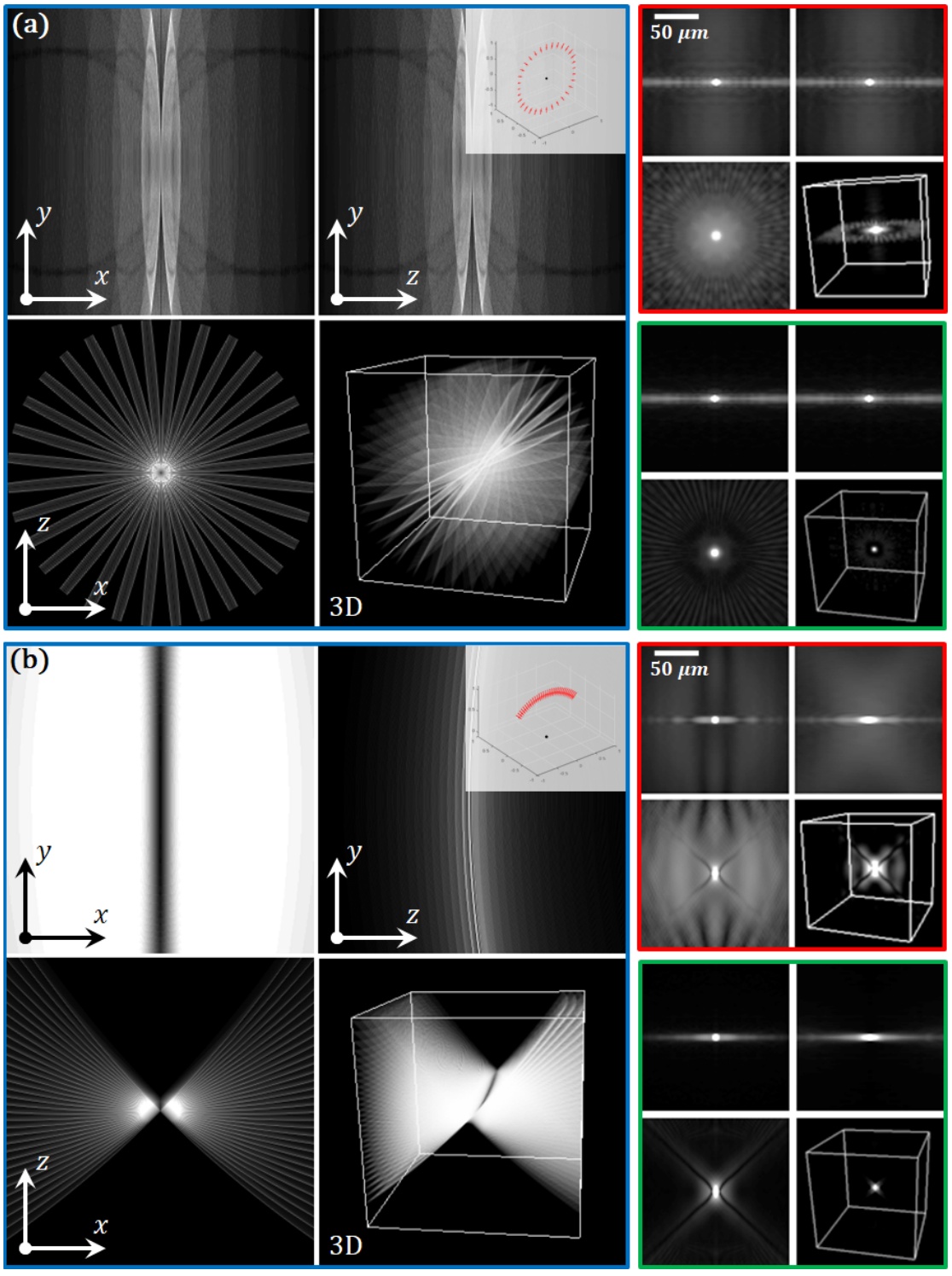

Figure IV.1: Comparison of the two designs for 32 lighting positions of the first prototype (white medallions). (a) θ-mode. (b) φ-mode, $\varphi \in [-45°, 45°]$. Average intensity orthogonal projections and 3D rendering of the accessible Fourier coefficients (blue) and the numerical reconstructions of a simulated 10 μm bead without (red) and with (green) the knowledge of the phase of the diffracted wave.

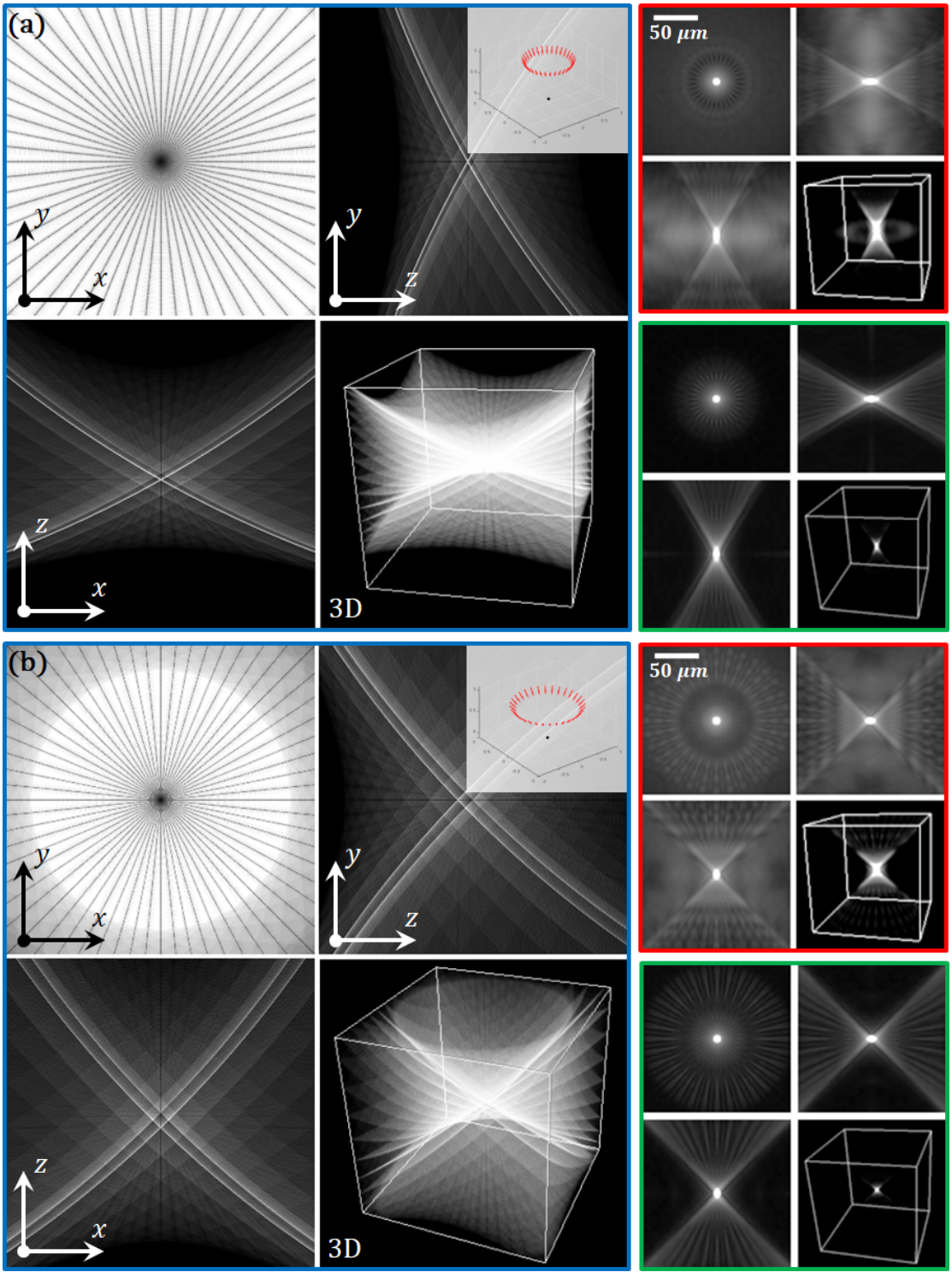

Figure IV.2: Comparison of two designs for 32 lighting positions (white medallions). (a) Crown with an opening angle $\theta = 30°$. (b) Crown with an opening angle $\theta = 45°$. Average intensity orthogonal projections and 3D rendering of the accessible Fourier coefficients (blue) and the numerical reconstructions of a simulated 10 μm bead without (red) and with (green) the knowledge of the phase of the diffracted wave.

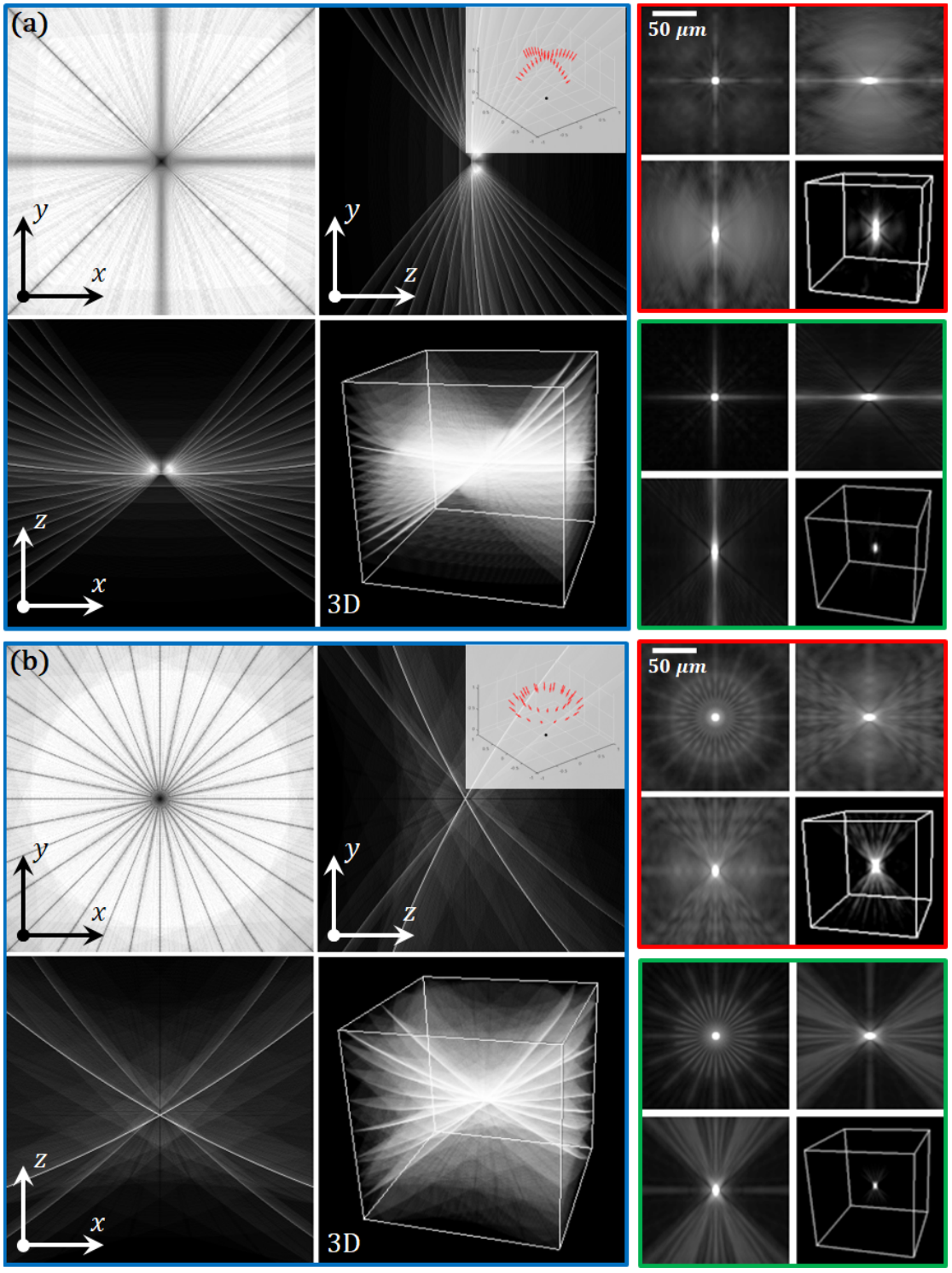

Figure IV.3: Comparison of two designs for 32 lighting positions (white medallions). (a) Orthogonal cross ($\theta_{max} = 45°$). (b) Double crown ($\theta \in \{30°, 45°\}$). Average intensity orthogonal projections and 3D rendering of the accessible Fourier coefficients (blue) and the numerical reconstructions of a simulated 10 μm bead without (red) and with (green) the knowledge of the phase of the diffracted wave.

This remark leads to the new kind of designs presented in figure IV.2 based on a crown, similar to the one used in the 3D Cell Explorer (Nanolive [42]). Using the notations of figure IV.6 for the new definition of the angles θ and φ, this crown is composed of lightings tilted by an angle of $\theta = 30°$ (a) or $\theta = 45°$ (b) compared to the sensor plane and are equally spread on $\varphi \in [0°, 360°]$ ($\Delta\varphi = 11.25°$). It appears that this solution provides a better and more homogeneous coverage of the Fourier domain of the object than the previous design constraining the positions on the plane $\varphi = 0°$. The artifacts are localized on a cone whose opening angle is directly θ and produce a lower unwanted signal. The reconstruction of the bead is better and as expected, the wider the crown is open, the better the reconstruction is. As the parallax effect increases, the spatial extension of the bead along the z-axis diminishes.

To confirm that this choice is the most adapted to the needs, two other intermediate designs are tested. A cross with 16 positions along $\varphi = 0°$ and 16 positions along $\varphi = 90°$ with theta equally spread in $\theta \in [-45°, 45°]$ ($\Delta\theta \simeq 2.8°$, figure IV.3.a) and a double crown with 16 angles spread at $\theta = 30°$ and 16 other at $\theta = 45°$ ($\Delta\varphi = 22.5°$, figure IV.3.b). To maximize the coverage, the two crowns present on offset of $\varphi_0 = 11.25°$ to intercalate the upper crown between the positions of the lower crown.

The cross design leads to a double bow-shaped artifact around the bead, similar to the one seen in figure IV.1.a but in the two orthogonal planes of the cross and with a reduced amplitude. The results remain better with the crown solution, even with an opening angle $\theta = 30°$.

The results given by the double-crown design are better but present both the artifacts of the single crown design at the two angles in figure IV.2. Two cone shapes are interlaced and the upper crown degrades the reconstruction on the z-axis.

This confirms that a single crown with a high opening angle remains the best tested solution. This can also be intuited by the fact that, as the opening angle increases, this design tends toward the θ-mode which is proven to be the best in figure IV.1.a.

These different designs are also tested on a more complex numerical sample and reconstruct with the inverse problem approach developed in chapter III, section 3. The volume presented in figure IV.4.a is composed of composed of 128^3 voxels of 1.67^3 μm^3 for a volume of $214^3 = 9.8\ 10^6$ μm^3 and is composed of cells of radius 10 μm and refractive index difference of $\delta n = 0.005i$ with a normal dispersion of $\delta n/10$. These cells are randomly spread in two clusters of 50 cells and two trains of 250 cells crossing the volume.

The figure presents the average intensity orthogonal projections colored according to the depth of each view as well as the 3D rendering of the reconstructed for different lighting designs composed of 16 positions. The simulated datasets are simulated in the blue channel $\lambda = 450\ nm$. The 2D and 3D spaces are zero-padded for the reconstructions. The hyperparameter value is kept to $\mu_r = 250$ for $nb_{it} = 30$ iterations. The φ-mode with $\theta \in [-45°, 45°], \varphi = 0°$ (b), the cross with $\theta \in [-45°, 45°], \varphi \in \{0°, 90°\}$ (c) as well as two crowns with $\theta = 30°$ (d) and $\theta = 45°$

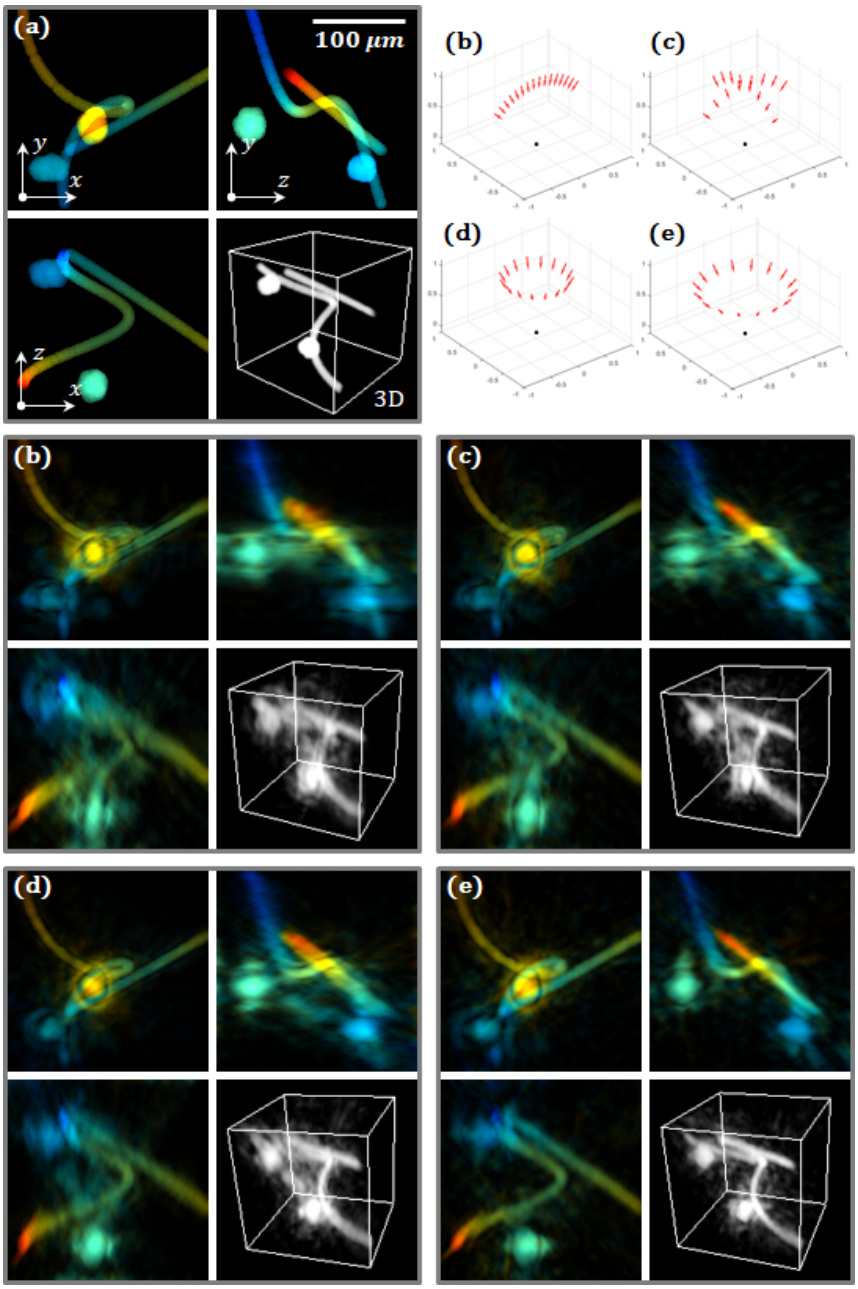

Figure IV.4: Comparison of different designs on a simulated complex object and its holograms reconstructed with the inverse problem approach developed in chapter III, section 3. Average intensity orthogonal projections and 3D rendering of the initial object (a) and the reconstructions for the design (b) $\theta \in [-45°, 45°], \varphi = 0°$, (c) $\theta \in [-45°, 45°], \varphi \in \{0°, 90°\}$ (d) $\theta = 30°, \varphi \in [0°, 360°]$ and (e) $\theta = 45°, \varphi \in [0°, 360°]$. The color codes for the depth in each view: the shallowest in blue, the deepest in red.

(e) with $\varphi \in [0°, 360°]$ are presented.

Similar conclusions concerning the design can be driven from these reconstruc-

tions. Comparing (b) and (c), the clusters are better reconstructed with the cross design with artifacts which appear similar on the xz and yz-views whereas they seem better determined on the yz-view for the φ-mode reconstruction.

But the best results are given by the crown design. Even if at $\theta = 30°$ (d) the maximal angular coverage is less important than for the cross (c) for example, the reconstruction quality is better and allows to separate the two trains of cells and reduces their spatial extension along the z-axis. And as expected, the best results are given by the last design (e) where the lighting angle is set at $\theta = 45°$.

Finally, the effect of multi-wavelength acquisitions is tested on the numerical object introduced in chapter II, section 3 and composed of three spheres. Data are simulated for the blue channel $\lambda = 450\ nm$ and for a RGB illumination $\lambda \in \{640, 520, 450\}$ and reconstructed by Fourier mapping as presented in chapter III, section 4.

The results are presented in figure IV.5. In the absence of phase information, the simulation shows the presence of the twin-image artifact on the xy-views when only one wavelength is used for the reconstruction, as previously seen in the previous chapter, section 4 in the reconstructions of biological data. As for the 2D reconstruction, the use of a RGB lighting slightly reduces this artifact which remains nevertheless present.

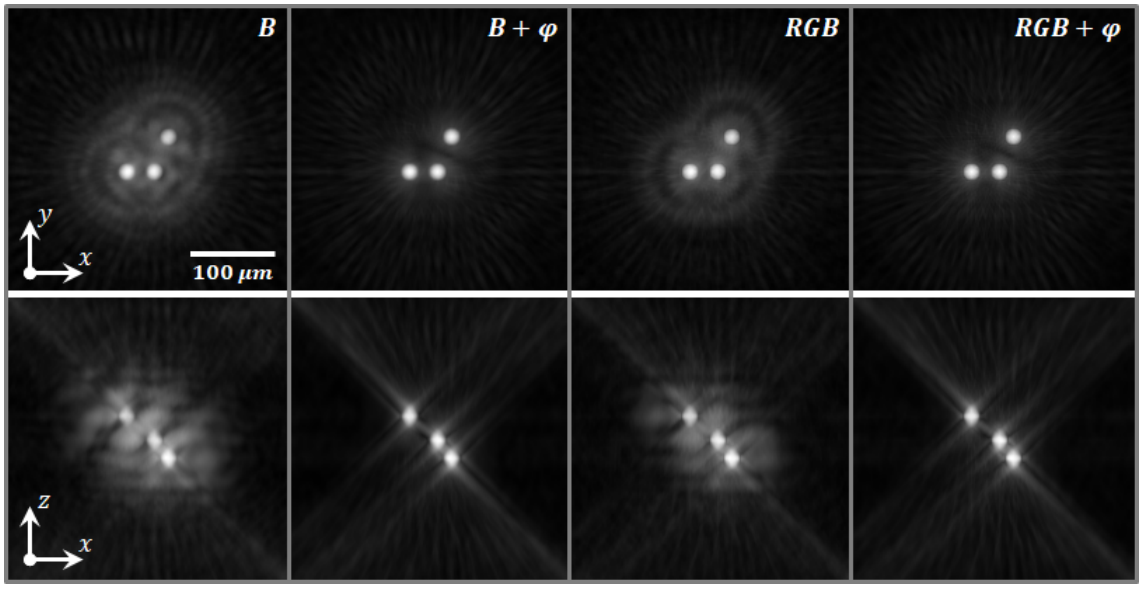

Figure IV.5: (a) Numerical tests of the chosen design on the three beads introduced in chapter II, section 3. Comparison of the reconstructions with only the blue wavelength (B) $\lambda = 450\ nm$ or the three available wavelengths (RGB) $\lambda \in \{640\ nm, 520\ nm, 450\ nm\}$ and with and without the knowledge of the phase of the diffracted wave (φ).

But the best mean to completely erase this artifact is to use the phase information. The effect is so effective that no difference clearly appears between the one lambda or the RGB reconstructions.

This simulation emphasizes the important role of the phase information in the reconstruction and the necessity to perform efficient phase retrieval in the reconstruction algorithms.

1.2 First acquisitions and reconstructions

Following the conclusions of the previous section, the crown design giving the best results on simulations in terms of reconstruction, a new prototype is built. Presented in figure IV.6, it uses the same sensor[3] and LED[4] used in the first experimental bench.

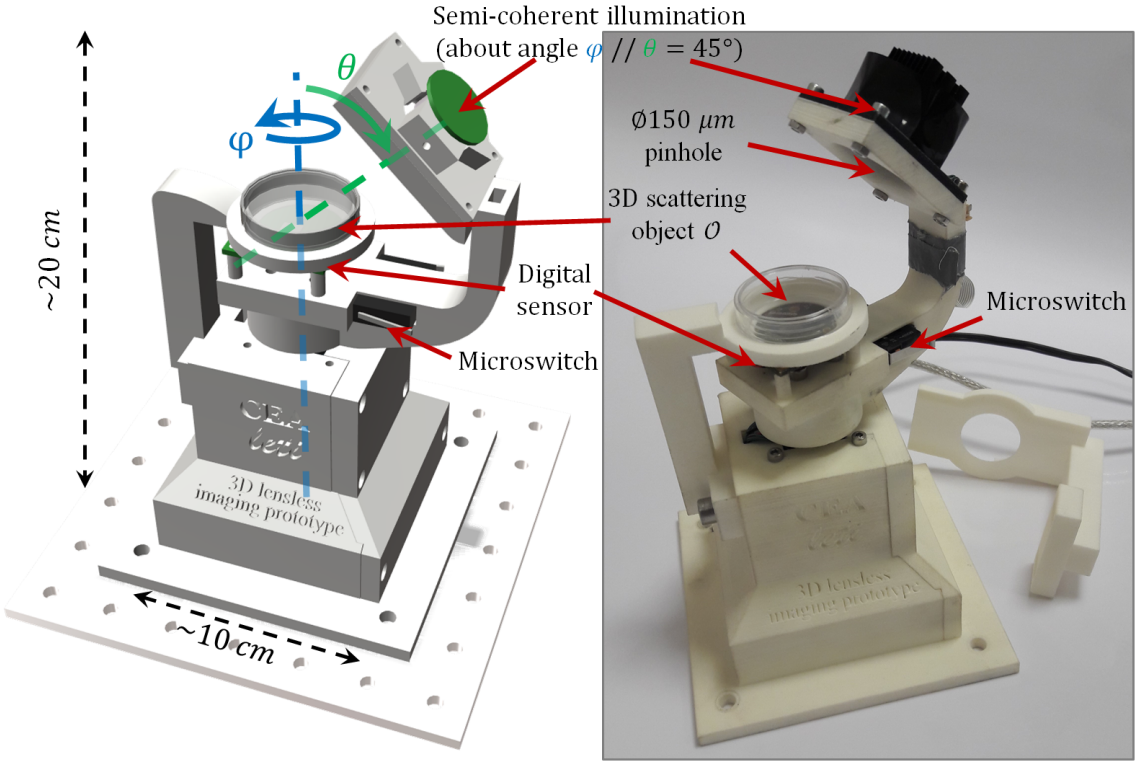

Figure IV.6: Proposed design for the second prototype. It introduces a new definition for the angles θ and φ, the inclination angle of the lighting compared to the sensor plane and its rotation angle around the fixed sample.

The sample is hold above the sensor. The height of the sample holder can be adjusted by screws. The sensor and the lighting are fixed on a stepper motor[5] and rotate according to the angle φ around the sample. The angle θ between the normal to the sensor and the lighting position is fixed at $\theta = 45°$.

The drawback of this design is to keep a moving part in the device via the stepper motor. Nevertheless, this solution allow shifting the sensor so that the hologram of

[3] IDS - 29.4 mm^2, 3840 × 2748 monochromatic pixels, pixel pitch 1.67 μm - *ref.* UI-1492LE-M

[4] LED CREE RGB, $\lambda_R = 640\ nm$, $\lambda_G = 520\ nm$, $\lambda_B = 450\ nm$ - *ref.* XLamp MC-E RGBW MCE4CT

[5] *ref.* RS-535-0401, 0.9°, 44 Ncm, 2.8 V, 1.68 A, 4 Wires

the biological sample remains centered in its field of view whatever the value of φ. This solution consequently maximizes the available field of view and the 3D volume which can be reconstructed. With a fixed sensor and the use of an array of LEDs such as in [70], the field of view is indeed reduced. Moreover, more angles can be acquired around φ instead of the limited discrete number of positions available in an array.

Microswitches[6] are used to detect the sample holder in order to stop the stepper motor before hitting its arm.

Figure IV.7 presents the first data (a) and reconstructions on bubbles and dust lying at the bottom of a Petri dish (b-h). The reconstruction parameters are $\varphi \in \{0°, 282°\}$, $\Delta\varphi = 18.8°$, $\theta = 45°$, $\lambda \in \{630, 520, 450\ nm\}$, $z_s = 2.8\ mm$, $512 \times 512 \times 256$ voxels of $3.34 \times 3.34 \times 5.32\ \mu m^3$ for a final volume of $1.7 \times 1.7 \times 1.4\ mm^3 \simeq 4\ mm^3$.

As mentioned at the end of the previous chapter in section 5, a scaling factor is applied on the z-axis using equation (III.39) as the data are reconstructed for an angle $\theta = \theta_{air} = 45°$: $z_0/z_{air} = 1.5930$.

The 1024×1024 pixels data of $1.67 \times 1.67\ \mu m^2$ are aligned using the least mean squares minimization algorithm on the raw data, using the central bubble hologram as alignment pattern.

The reconstructions are performed via the Fourier mapping method. Contrary to chapter III, section 4, the overlapping information in a given voxel during the mapping are averaged.

Compared to the results presented in this former section, the reconstruction quality is greatly improved. The artifacts seem homogeneous on the whole field of view and with a reduced spatial extension on the z-axis for the small objects. On the big bubbles, limits of the design appear with shadowing effects which create the straight artefactual sides on the bubbles. They are inclined by the angle $\theta_0 \simeq 32.1°$, corrected from $\theta_{air} = 45°$ in the medium of refractive index $n_0 = n_{H_2O} = 1.33$ according to the Snell's law (III.27).

The twin image artifact is present, especially around the big objects

A zoom on a reconstructed particles of dust (h) shows that the artifacts surrounding small objects are coherent with the reconstructions of the numerical bead for the choice of the design in figure IV.2.

A closer look at the artifacts shows that their shape (g) is characteristic to the lighting positions. Out of focus, they shape a ring of small artifacts, spread according to the lighting positions and merge with the focus on the object. On this artefactual ring, it is possible to identify the missing angles in the angular coverage due to the sample holder which limits the available range for φ to $\varphi \in [0°, 285°]$.

Different padding situations on the 2D data and the 3D volume are tested and plotted using maximum intensity projections to limit the influence of the noise and artifacts in the projected views.

As seen qualitatively in figures (b-e), the padding operation does not dramatically change the reconstruction quality.

[6] *ref.* RS-686-6840, SPDT-NO/NC Simulated Roller Lever Microswitch, 5 A, 125 V ac

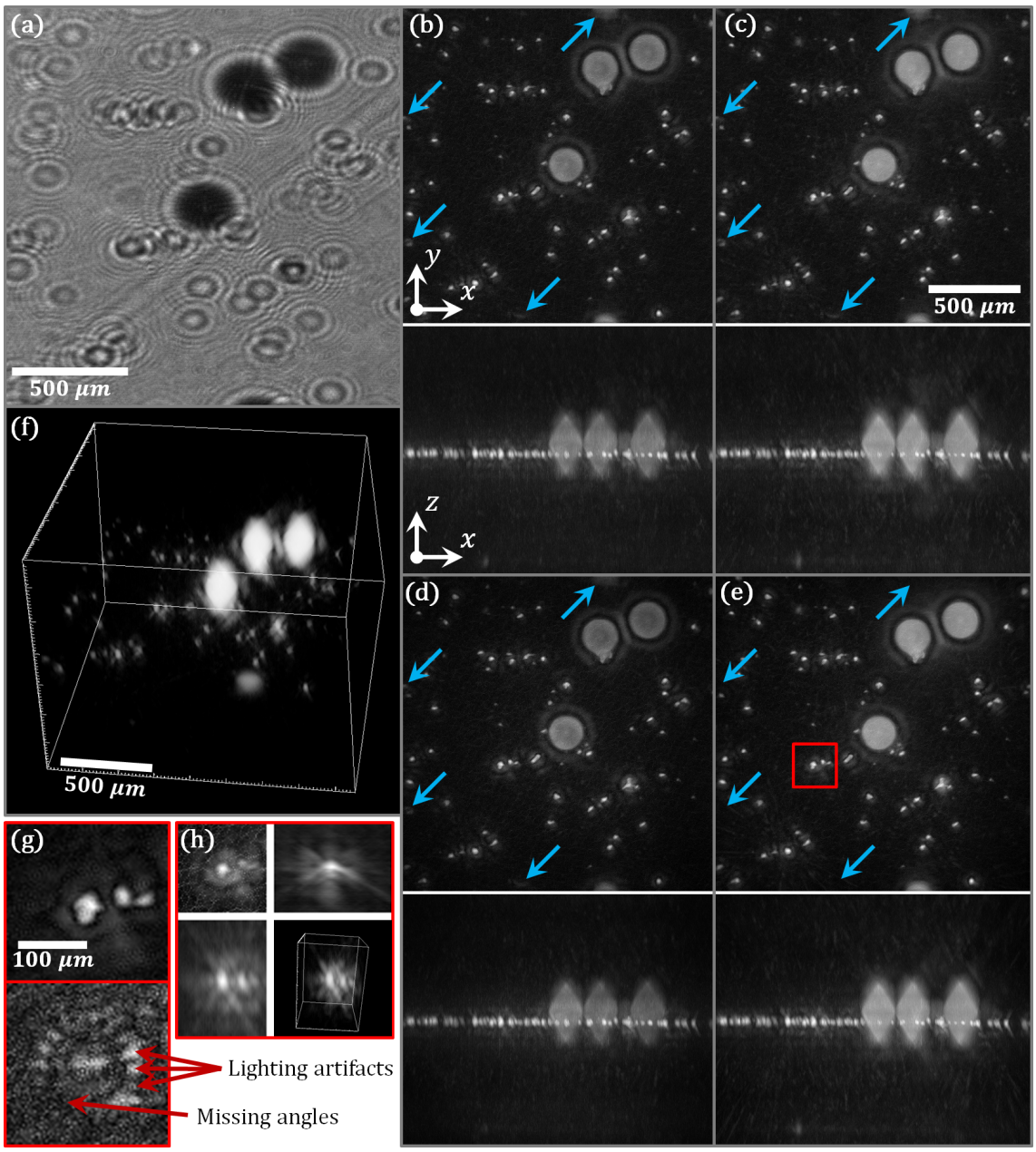

Figure IV.7: First data and reconstruction with the second prototype on bubbles and dust at the bottom of a Petri dish filled with water. (a) Raw data in the red channel for $\varphi = 0°$. (b-e) Comparison of the influence of the padding on the reconstructions on the xy and xz-maximum intensity projections. (b) No padding. (c) Padding on the 3D volume. (d) Padding on the 2D data. (e) Padding on the 2D data and the 3D volume. The blue arrows point at the aliasing artifacts due to a periodization of the objects if no padding is applied. (f) 3D rendering of (e). (g) Zoom on a region of interest framed in red on (e) in the dust particle plane and in plane with a defocus of 117 μm. (h) Average intensity orthogonal projections and 3D rendering of the region of interest (g).

Nonetheless, if one of the spaces is not padded (2D or 3D), the periodization of the data and/or the volume leads to "ghost" reconstructions of objects which should be outside the field of view on the opposite side. These are emphasized by the blue arrows. A striking example is the bubble at the lower edge of the xy-view which overflows at the top of the view, excepted if a padding is applied on both the 2D and the 3D spaces.

Another effect which cannot be directly driven from the figures is the contrast of the reconstructions. Indeed, the value of the scattering potential at the center of the central bubble in the different volumes changes according to the padding situation as shown in table [IV.1].

	No padding	3D padding	2D padding	2D and 3D padding
$\|f\|$	$2.9\ 10^{-4}$	$6.3\ 10^{-5}$	$3.1\ 10^{-4}$	$2.5\ 10^{-4}$

Table IV.1: Table of the measured intensities of the scattering potential f at the center of the bubble of figure IV.7 for the different padding possibilities.

The zero-padding on the 3D appears to have a "dilution" effect which diminishes the intensity of the reconstructed volume. This effect is compensated by the zero-padding of the 2D space. Padding both of the spaces gives similar results than no padding at all.

These padding operations will nevertheless be part of a trade-off between the wanted quality and the reconstruction time or even the capability of the computer to deal with large padded-matrices. In extreme cases, even the absence of padding can provide an acceptable result if one remembers that ghost effect can appear on the edges of the reconstructed volumes.

2 Iterative phase retrieval

As mentioned in chapter I, section 3 and chapter II, section 3, in the context of 2D lens-free imaging the absence of phase information in the sensor plane leads to "twin-image" artifacts in the 2D back-propagations. As seen in chapter III, section 4 and in the previous section 1 of this chapter, similar artifacts are present in the 3D reconstructions.

As presented in [70], performing an iterative phase retrieval allows finding a better estimate of the unknown phase in the sensor plane than the phase ramp introduced in the Fourier mapping method developed in chapter III, section 4. To this end, for each 2D picture I^j_{tot} of the dataset $j \in [\![1, N]\!]$, the 3D object to retrieve is approximated by an average median plane t^j_{2D} as previously presented in chapter III, section 2.2 in figure III.7. In this section, the final aim is not to retrieve this 2D transmissive plane but to use this mathematical artifice in a phase retrieval algorithm to get the phase at the sensor plane for this given illumination j. Alternatively to the method exposed in [70], the presented phase retrieval technique is based on an inverse problem approach.

2.1 Inverse problem formulation

For low scattering objects, the 2D complex transmission can be rewritten: $t_{2D} = 1 + \delta t$ and the Rayleigh-Sommerfeld equation (I.1) can be expressed in terms of incident and scattered complex waves:

$$U_{tot}\left(\overrightarrow{r'}\right) = U_{inc}\left(\overrightarrow{r'}\right) + U_{dif}\left(\overrightarrow{r'}\right) = U_{inc}\left(\overrightarrow{r'}\right) + \left(U_{inc}.\delta t\right) \star \left(\frac{z_s}{i\lambda}\frac{e^{ik'_0 r}}{r^2}\right) \tag{IV.1}$$

To take into account the limited coherence length l_{coh} of the illumination and to reduce aliasing effects due to the high frequencies of the convolution kernel, a pyramidal mask is added in the kernel:

$$M_{l_{coh}}(x,y) = \begin{cases} \frac{l_{coh}-r_{2D}}{l_{coh}} \text{ if } r_{2D} < l_{coh} \\ 0 \text{ if } r_{2D} > l_{coh} \end{cases}, \; r_{2D} = \sqrt{x^2+y^2} \tag{IV.2}$$

Then for any δt, it exists a direct model giving the complex diffracted wave $U_{dif}(\delta t)$ at the sensor plane:

$$\boxed{U_{dif}(\delta t) = (\delta t.U_{inc}) \star \left(M_{l_{coh}}\frac{z_s}{i\lambda}\frac{e^{ik'_0 r}}{r^2}\right)} \tag{IV.3}$$

The inverse problem of retrieving δt from the measurements I_d is ill-posed due, among other reasons, to the lack of phase measurement on the detector plane. Moreover this model (IV.3) does not provide an analytic inverse formula to go from the knowledge of the diffracted wave to t_{2D} and the Gerchberg-Saxton algorithm presented in I, section 3 cannot be used.

The reconstruction problem is solved via an inverse problem approach by minimizing the following data-fidelity term[7]:

$$\tilde{\delta t} = \underset{\delta t}{\operatorname{argmin}} \left\| I_d - \left|U_{inc} + U_{dif}(\delta t)\right|^2 \right\|^2 \tag{IV.4}$$

The initial parameters of the experiment (here δt) are retrieved from the knowledge of the experimental data (here I_d) and the direct model allowing to simulate numerical data for a given set of parameters. This inverse approach models the non-linear direct process of image formation without requiring an inversion formula.

Nonetheless, minimizing directly equation (IV.4) will not be sufficient to retrieve the phase of U_{dif} since an infinite number of phase can match the recorded intensities I_d. One needs to add some constraints and regularizations to the minimization problem (IV.4). Using the formalism introduced in chapter III, section 3.3 an inverse

[7]Here it matches the definition given in appendix D for $W = 1$. As mentioned in the appendix, it is possible to weight each pixel for example to minimize the influence of hot or dead pixels.

approach allows to perform this by minimizing the following cost function:

$$\boxed{\begin{aligned} J(\delta t) = & \underbrace{\frac{1}{nb_x^p nb_y^p nb_\lambda}\sum_{j=1}^{nb_\lambda}\left\| I_d^j - \left| U_{inc}^j + U_{dif}^j(\delta t)\right|^2\right\|^2}_{\text{data fidelity } J_d(\delta t)} + \cdots \\ & \mu_{L_1} \underbrace{\frac{1}{nb_x^p nb_y^p}\left\|\delta t\right\|_{L_1,\epsilon}}_{\text{sparsity constraint } J_{L_1,\epsilon}(\delta t)} + \mu_\nabla \underbrace{\frac{1}{nb_x^p nb_y^p}\left\|\nabla\delta t\right\|_{L_1,\epsilon}}_{\text{gradient sparsity constraint } J_{\nabla,\epsilon}(\delta t)} \end{aligned}} \tag{IV.5}$$

to retrieve the 2D transmissive plane:

$$\boxed{\tilde{\delta t} = \underset{C(\delta t)}{\operatorname{argmin}} J(\delta f) = \underset{C(\delta t)}{\operatorname{argmin}} J_d(\delta t) + \mu_{L_1} J_{L_1,\epsilon}(\delta t) + \mu_\nabla J_{\nabla,\epsilon}(\delta t)} \tag{IV.6}$$

$\frac{1}{nb_x^p nb_y^p nb_\lambda}$ and $\frac{1}{nb_x^p nb_y^p}$ are normalization factors, nb_x^p, nb_y^p still being the pixel numbers in each direction of the 2D planes[8]. nb_λ is the number of wavelength used for the iterative reconstruction. As mentioned earlier for the 3D scattering potential in chapter II, section 1, the effective 2D transmissive plane δt is supposed to be independent of the illumination wavelength.

As previously, $C(\delta t)$ stands for the constraint given on the domain of definition of δt. As defined in appendix D the central term is a sparsity prior numerically given by:

$$\left\|\delta t\right\|_{L_1,\epsilon} = \sum_{pixels_{k,l}} \sqrt{\left|\delta t_{k,l}\right|^2 + \epsilon^2} \tag{IV.7}$$

where the indices (k,l) stand for the $nb_x^p \times nb_y^p$ pixels locations on the image grid respectively on the x and y-axes.

As defined in appendix D the right-hand term of equation (IV.5) is a sparsity prior on the gradient of δt to enforce an edge-preserving regularization. It is numerically computed as follows:

$$\begin{aligned} \left|\nabla\delta t_{k,l}\right|^2 = \frac{1}{2}\Big[& \left|\delta t_{k+1,l} - \delta t_{k,l}\right|^2 + \left|\delta t_{k,l+1} - \delta t_{k,l}\right|^2 + \cdots \\ & \left|\delta t_{k+1,l+1} - \delta t_{k,l+1}\right|^2 + \left|\delta t_{k+1,l+1} - \delta t_{k+1,l}\right|^2\Big] \end{aligned} \tag{IV.8}$$

In order to tune an appropriate trade-off between data-fidelity and *a priori* information, the regularization terms are respectively weighted by two hyperparameters μ_{L_1} and μ_∇.

Appendix D presents how to numerically compute $J_{L_1,\epsilon}$ and $J_{\nabla,\epsilon}$ as well as their gradient. It remains to find a numerical expression for J_d. The convolution $\star$ of equation (IV.3) is computed in the padded Fourier domain. To avoid the computation of the Fourier transform of $\delta t.U_{inc}$ for each wavelength at each iteration, the same trick for incident plane wave than for equation (II.40) is used to convert the

[8]In this section both the planes of sensor and the 2D object are composed of $nb_x^p \times nb_y^p$ pixels

spatial modulation introduced by U_{inc} into a translation in the Fourier domain of the convolution kernel.

Using the notation introduced in chapter II, section 3.1, from equation IV.3, the hologram centered on (x_0, y_0, z_s) can be numerically computed as follows:

$$\boxed{\begin{aligned} U_{dif} = \frac{z_s}{i\lambda} e^{i\overrightarrow{k_0'}.(x_{2D},y_{2D},0)}.pad^{-1}\Bigg(\mathrm{FFT}_{2D}^{-1}\Bigg(\mathrm{FFT}_{2D}\left(pad\left(\delta t\right)\right).\cdots \\ \mathrm{FFT}_{2D}\Bigg(e^{-i\overrightarrow{k_0'}.\left(x_{2D}^{pad},y_{2D}^{pad},0\right)}.M_{l_{coh}}\left(x_{2D}^{pad},y_{2D}^{pad},0\right).\cdots \\ \frac{e^{ik_0'\sqrt{\left(x_{2D}^{pad}+x_0\right)^2+\left(y_{2D}^{pad}+y_0\right)^2+z_s^2}}}{\left(x_{2D}^{pad}+x_0\right)^2+\left(y_{2D}^{pad}+y_0\right)^2+z_s^2}\Bigg)\Bigg)\Bigg)dx.dy \end{aligned}} \tag{IV.9}$$

Noting $\hat{H_{z_s}^j}$ the matrix:

$$\begin{aligned} \hat{H_{z_s}^j} = dx.dy.\mathrm{FFT}_{2D}\Bigg(\frac{z_s}{i\lambda^j}e^{-i\overrightarrow{k_0^j}.\left(x_{2D}^{pad},y_{2D}^{pad},0\right)}.M_{l_{coh}}\left(x_{2D}^{pad},y_{2D}^{pad},0\right).\cdots \\ \frac{e^{ik_0'^j\sqrt{\left(x_{2D}^{pad}+x_0^j\right)^2+\left(y_{2D}^{pad}+y_0^j\right)^2+z_s^2}}}{\left(x_{2D}^{pad}+x_0^j\right)^2+\left(y_{2D}^{pad}+y_0^j\right)^2+z_s^2}\Bigg) \end{aligned} \tag{IV.10}$$

equation (IV.9) becomes:

$$U_{dif}^j = U_{inc}^j.pad^{-1}\left(\mathrm{FFT}_{2D}^{-1}\left(\hat{H_{z_s}^j}.\mathrm{FFT}_{2D}\left(pad\left(\delta t\right)\right)\right)\right) \tag{IV.11}$$

All these operations are linear. Keeping the notations previously defined in chapter III, section 3.3 but for 2D matrices, δt being decomposed on its real and imaginary parts, this equation (IV.11) becomes:

$$\begin{aligned} \overrightarrow{U}_{dif}^j &= diag\left(\overrightarrow{U}_{inc}^j\right) \times P^i \times F^i \times diag\left(\overrightarrow{\hat{H_{z_s}^j}}\right) \times F \times P \times R2C \times \overrightarrow{\delta t} \\ &= O \times \overrightarrow{\delta t} \end{aligned} \tag{IV.12}$$

It comes from appendix D:

$$\nabla J_d\left(\overrightarrow{\delta t}\right) = \frac{1}{nb_x^p nb_y^p nb_\lambda}\sum_{j=1}^{nb_\lambda} 4\mathcal{R}\left[O^\star \times \left[\overrightarrow{U}_{tot}^j\left(\overrightarrow{\delta t}\right).\left(\left|\overrightarrow{U}_{tot}^j\left(\overrightarrow{\delta t}\right)\right|^2 - \overrightarrow{I}_d^j\right)\right]\right] \tag{IV.13}$$

with:

$$O^\star = R2C^\star \times P^\star \times F^\star \times diag\left(\overrightarrow{\hat{H_{z_s}^j}}\right)^\star \times F^{i\star} \times P^{i\star} \times diag\left(\overrightarrow{U}_{inc}^j\right)^\star \tag{IV.14}$$

From the analysis done in chapter III, section 3.3 it is possible to express the gradient of the data fidelity in terms of the complex transmissive plane δf from

equations (IV.13) and (IV.14):

$$\nabla J_d(\delta t) = \frac{1}{nb_x^p nb_y^p nb_\lambda} \sum_{j=1}^{nb_\lambda} 4.pad^{-1}\Big(\mathrm{FFT}_{2D}^{-1}\Big(\bar{\hat{H}}_{z_s}^j.\mathrm{FFT}_{2D}\Big(\cdots pad\left(\bar{U}_{inc}^j.U_{tot}^j(\delta t).\left(\left|U_{tot}^j(\delta t)\right|^2 - I_d^j\right)\right)\Big)\Big)\Big) \tag{IV.15}$$

Finally, the numerical expression of the gradient of the cost function (IV.5) at a given δt is:

$$\nabla J(\delta t) = \nabla J_d(\delta t) + \mu_{L_1} \nabla J_{L_1,\epsilon}(\delta t) + \mu_\nabla \nabla J_{\nabla,\epsilon}(\delta t) \tag{IV.16}$$

One can now iteratively solve the minimization problem (IV.6) using a descent gradient algorithm, which is performed by the VMLM-B algorithm [90], a modified limited memory quasi-Newton convex optimization method with BFGS updates and bound constraints[9].

Once δt is estimated for a given illumination j, the corresponding diffracted wave U_{dif}^j can be computed via equation (IV.9). When the 2D phase information of all the different acquisitions is retrieved, a 3D Fourier mapping is performed as previously exposed in chapter III, section 4 via equation (III.25) to obtain the final fully 3D reconstructed volume.

This method solves one pitfall of the Fourier mapping method: the phase information introduced in the reconstruction is more realistic and should reduce some artifacts. Nevertheless, it does not solve the problem of the Fourier mapping limitations: only the same coefficients on the spherical caps are accessible.

2.2 Numerical simulations

To test the efficiency of the proposed phase retrieval algorithm, total wave fronts I_{sim}^{RGB} are simulated for a known numerical object presented in figure IV.8.a. It is composed of composed of 512^3 voxels of 1.67^3 μm^3 for a volume of $855^3 = 6.25\ 10^8$ μm^3 and is composed of cells of radius 10 μm and refractive index difference of $\delta n = 0.005i$ with a normal dispersion of $\delta n/10$. These cells are randomly spread in five clusters of 50 cells and five trains of 250 cells crossing the volume.

Holograms are simulated with the Fourier diffraction theorem by padding the 2D and the 3D spaces and using the nearest-neighbor interpolation method, for an illumination direction of $\theta = 30°$ and $\varphi = 112.5°$, for the three RGB wavelengths $\lambda \in \{630\ nm, 520\ nm, 450\ nm\}$, in the air $n_0 = 1$ and for a sensor distance of $z_s = 2\ mm$. To test the robustness of the iterative phase retrieval algorithm, a Gaussian noise is added to the intensity with $\sigma = 0.2$ (see figure IV.8.b). The simulated phase[10] of figure IV.8.c represents the goal of the phase retrieval algorithm.

[9]It was implemented in C by Eric Thiébaut in his OptimPack library [91] and Hervé Carfantan provided an interface [92] of this library running under Matlab® which was adapted by Fabien Momey.

[10]Note here that in this section, for the sake of clarity, all the displayed phase are corrected by a phase ramp characteristic of the given illumination direction.

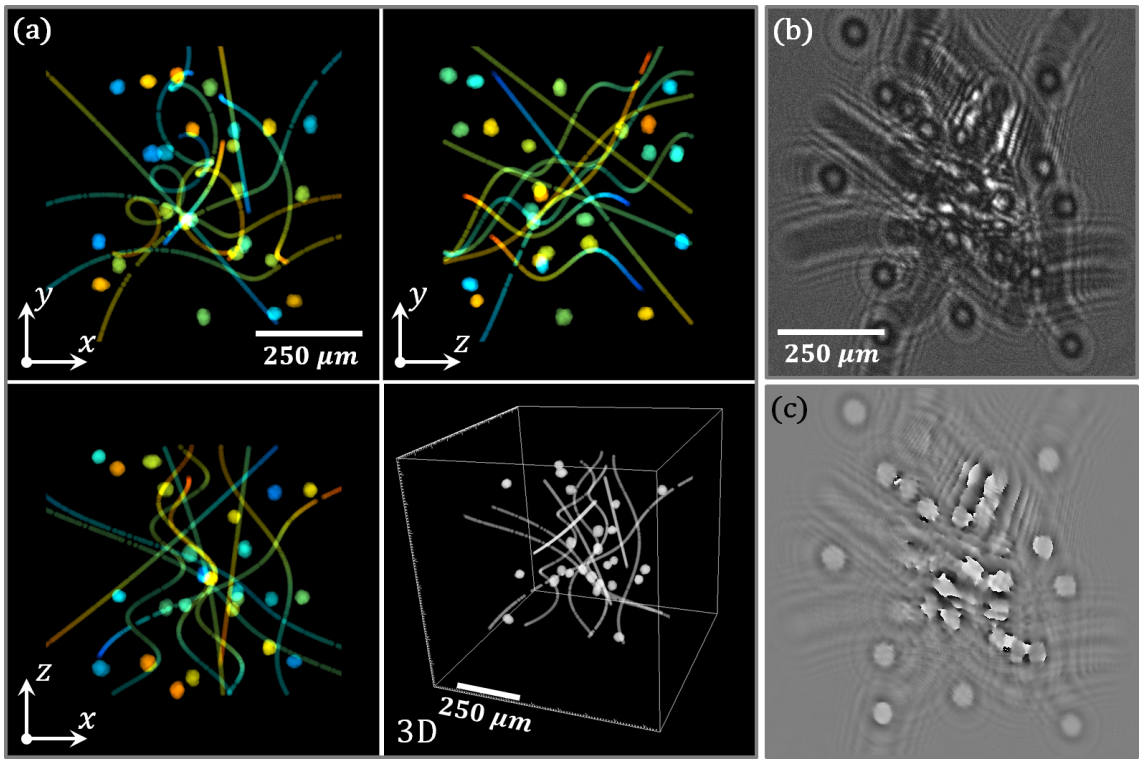

Figure IV.8: (a) Average intensity orthogonal projections and 3D rendering of a numerical object used to simulate a hologram on which both the intensity I_{sim} (b) and the phase φ_{sim} (c) are known (here in the green channel) for an illumination direction of $\theta = 30°$ and $\varphi = 112.5°$. To test the robustness of the iterative phase retrieval algorithm, a Gaussian noise with $\sigma = 0.2$ is added to the intensity. The color codes for the depth in each view: the shallowest in blue, the deepest in red.

Different configurations for the iterative parameters are tested to find the best set. All the tests are run with $nb_{it}^{PR} = 100$ iterations, by padding the 2D space and with $l_{coh} = 500\ \mu m$.

Figure IV.9 compares the effects of a strong sparsity regularization alone with the effects of a regularization on the gradient alone for different value of μ_{∇}. Looking at the modulus of the reconstructed transmissive planes t_{2D} and at the cell branches, it appears that the ∇-regularization is the most efficient to reduce the noise in the reconstructions but fails at removing the twin-image artifacts. For high values, it even increases its amplitude. On the other side, the L_1-regularization efficiently cleans the twin-image around these small objects.

Looking at the phase differences, it appears that the two regularizations fail at retrieving the phase. The ∇-regularization seems to work better on the big clusters whereas the L_1-regularization succeeds in retrieving the phase of some cell branches.

From the reconstructed modulus of figure IV.9, it appears that the twin-image is bright: this means that its modulus is higher than the background modulus whose value is 1: a perfectly transparent plane. Values higher than 1 are then interpreted as emissive objects. In the present case, this in not physical as the objects do not

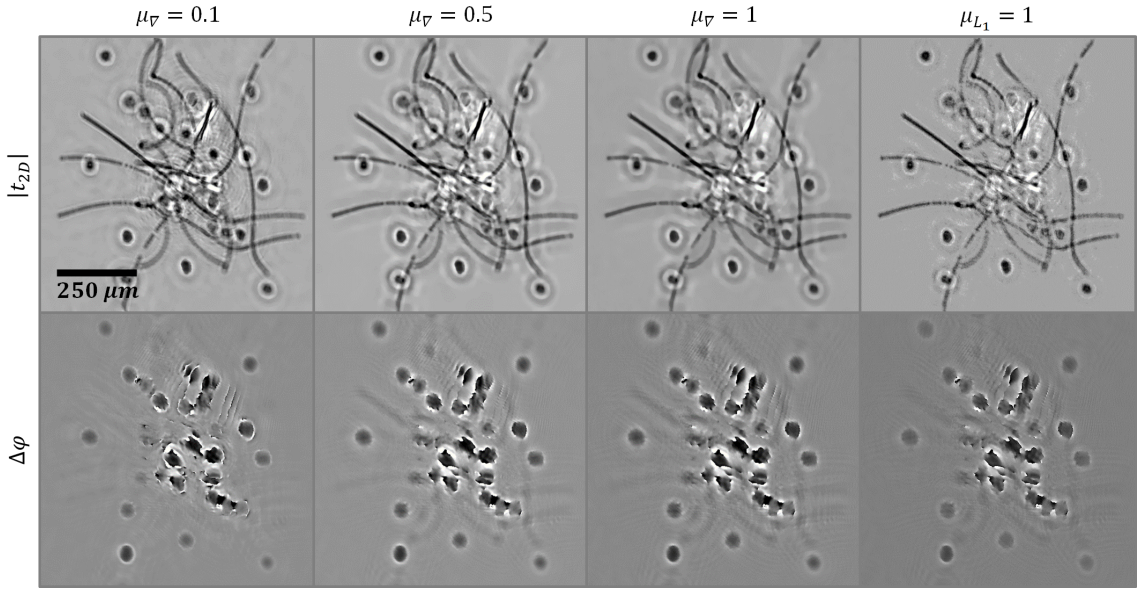

Figure IV.9: Comparison of the modulus $|t_{2D}|$ of the reconstructed transmissive plane t_{2D} and the difference $\Delta\varphi = \varphi_{PR} - \varphi_{sim}$ between the retrieved phase on the sensor plane with the numerical simulation of figure IV.8.c for different values of the hyperparameters μ_{L_1} and μ_∇ after $nb_{it}^{PR} = 100$ iterations.

emit any light but only scatter or absorb the incident wave front. The use of an adapted constraint $C(\delta t)$ can help to enforce this physical property.

Technically, a non-emissive object is characterized by a modulus of less than one: $|t_{2D}| \leq 1$. But this constraint cannot be directly applied in the present algorithm as the object δt is decomposed on its real and imaginary parts. Nonetheless, it can give a necessary constraint on δt. Indeed:

$$\begin{aligned} |t_{2D}| = |1 + \delta t| \leq 1 &\Leftrightarrow (1 + \mathcal{R}(\delta t))^2 + \mathcal{I}(\delta t)^2 \leq 1 \\ &\Rightarrow -1 \leq 1 + \mathcal{R}(\delta t) \leq 1 \\ &\Rightarrow \mathcal{R}(\delta t) \leq 0 \end{aligned} \tag{IV.17}$$

This condition is necessary but not sufficient. Indeed, for $\mathcal{R}(\delta t) = 0$, any δt with $\mathcal{I}(\delta t) \neq 0$ will break the constraint $|t_{2D}| \leq 1$.

This condition is tested in figure IV.10 as well as combinations of the different regularizations.

Using both the L_1 and the ∇-regularization combines the good performances mentioned above by erasing the twin-image around the small objects while efficiently retrieving their phase as well as on some bigger objects.

The constraint $\mathcal{R}(\delta t) \leq 0$ is the most effective to reduce the twin-image artifacts around the small objects and most of the big clusters.

Only combined with the ∇-regularization, the phase on the small objects is not well retrieved. The effect on the clusters is more important with some phase reversed compared to figure IV.9 for $\mu_\nabla = 0.1$.

Combining the 3 solutions gives the best results. The twin-image artifacts are

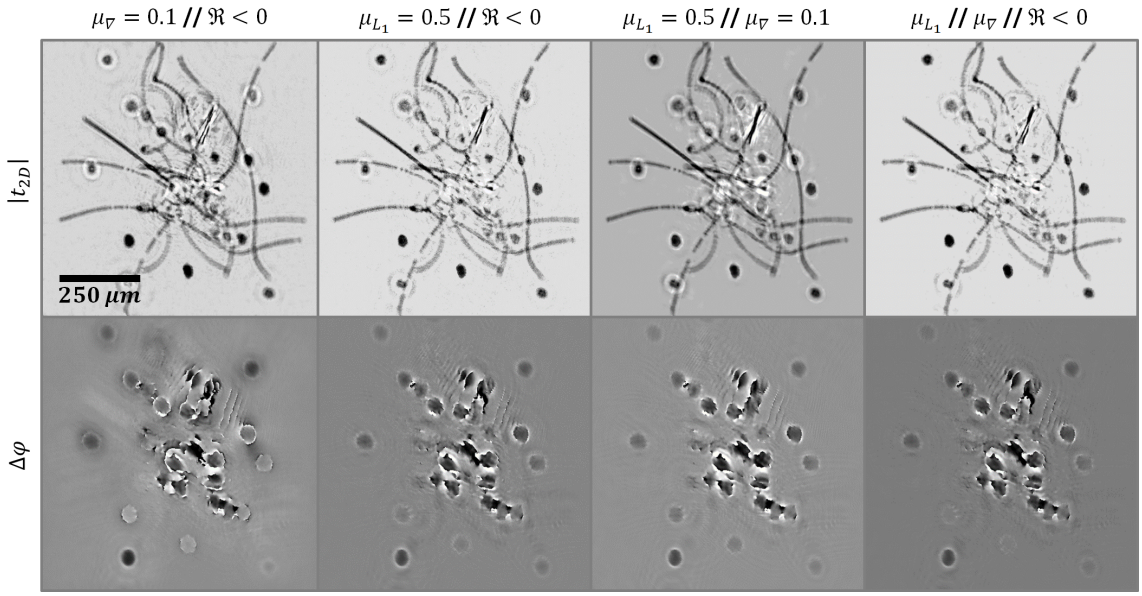

Figure IV.10: Comparison of the modulus $|t_{2D}|$ of the reconstructed transmissive plane t_{2D} and the difference $\Delta\varphi = \varphi_{PR} - \varphi_{sim}$ between the retrieved phase on the sensor plane with the numerical simulation of figure IV.8.c for different combinations of the hyperparameters μ_{L_1} and μ_∇ with a constraint on the domain of δt: $\mathcal{R}(\delta t) \leq 0$ after $nb_{it}^{PR} = 100$ iterations.

erased around almost all the objects, even the clusters. The phase on the small objects is retrieved as well as on some of the clusters. Nonetheless, none of the combination succeeds in retrieving the phase at the center of the field which is denser and where lots of objects at different heights are overlapping.

Finally, figure IV.11 shows the normalized value of the cost function (IV.5) during the iterations of the phase retrieval algorithm for the simulated data as well as the experimental data presented in the next section. Excepted for a small bump in the first 40 iterations, the two curves have a similar convergence rate which becomes very slow after the 80^{th} iterations.

2.3 3D reconstructions on experimental data

The phase retrieval algorithm is tested on the experimental data introduced in the previous section 1 in figure IV.7.

For the phase retrieval algorithm, the 2D spaces of $nb_x^p = nb_y^p = 1024$ are padded, $l_{coh} = 500\ \mu m$ and $nb_{it}^{PR} = 100$. The hyperparameters are set to $\mu_{L_1} = 0.5$, $\mu_\nabla = 0.1$ and $C(\delta t) = \{\delta t / \mathcal{R}(\delta t) \leq 0\}$.

The lighting parameters are $\varphi \in \{0°, 282°\}$, $\Delta\varphi = 18.8°$, $\theta = 45°$, $\lambda \in \{630, 520, 450\ nm\}$, $z_s = 2.8\ mm$. These three wavelengths are used both for the 2D phase retrieval and the 3D reconstruction.

A scaling factor is applied on the z-axis using equation (III.39) as the data are reconstructed for an angle $\theta = \theta_{air} = 45°$: $z_0/z_{air} = 1.5930$. For the 3D reconstruc-

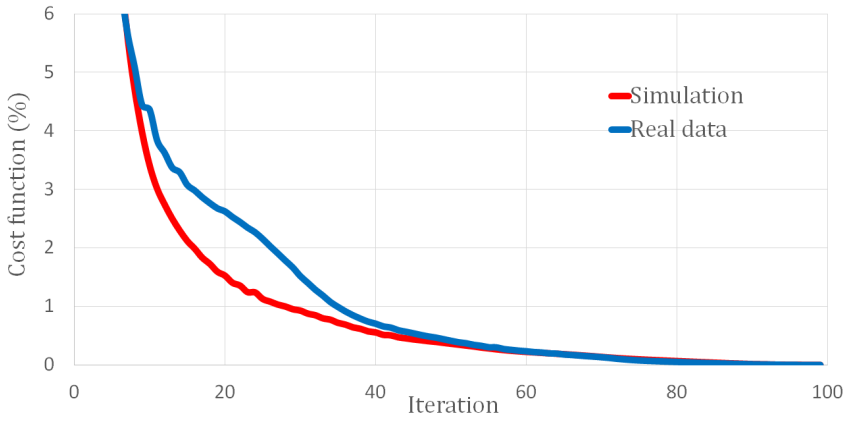

Figure IV.11: Convergence curves of the iterative RGB phase retrieval for the simulated data of figure IV.8 and the experimental data of figure IV.12 with $\mu_{L_1} = 0.5$, $\mu_{\nabla} = 0.1$ and $\mathcal{I}(\delta t) \leq 0$. The curves are normalized to their minimal and maximal values.

tion, the volume[11] is composed of $512 \times 512 \times 256$ voxels of $3.34 \times 3.34 \times 5.32\ \mu m^3$ for a final volume of $1.7 \times 1.7 \times 1.4\ mm^3 \simeq 4\ mm^3$. The 2D and the 3D spaces are both zero-padded. The simulated total wave fronts I^j_{sim} and φ^j_{sim} are used for the reconstruction with the Fourier mapping method.

Figure IV.12 presents the results of the phase retrieval procedure for the lighting position $\theta = 45°$ and $\varphi = 0°$.

The simulated intensities are in agreement with the experimental data. All the holograms are well simulated for the bubbles, the dust particles and the scratch at the bottom of the dish. One another side, the regularization efficiently cleaned the noise and the background heterogeneities mainly due to the surfaces of the Petri dish and the plastic cap.

Figure IV.12.d is a simple back-propagation of the experimental intensity and is obtained by reversing the convolution in equation (IV.9) by a division in the Fourier domain and using a phase ramp approximation for the unknown phase[12]. As for the simulation, a comparison with the modulus of the retrieved δt in figure IV.12.e shows that the phase retrieval procedure removes all the twin-image artifacts and produces sharper objects with a clean background. Looking also at the reconstructed phase in figure IV.12.f, it appears that excepted for their edge, the bubbles are seen as absorbent objects. The dust particles share an absorbent part and a dephasing part whereas the scratch is only seen in the phase picture.

The 3D reconstruction obtained once the 2D RGB phase retrieval algorithm has been performed on the 16 lighting positions is presented in figure IV.13 and has to be compared with the results given in figure IV.7. As expected, the twin-images artifacts have been removed around all the objects and the background is darker (or in an equivalent way one can say that the signal is stronger).

[11] $512 \times 512 \times 256$ voxels of $3.34 \times 3.34 \times 3.34\ \mu m^3$ before scaling.

[12] A similar artifice is implemented in chapter III, section 4.

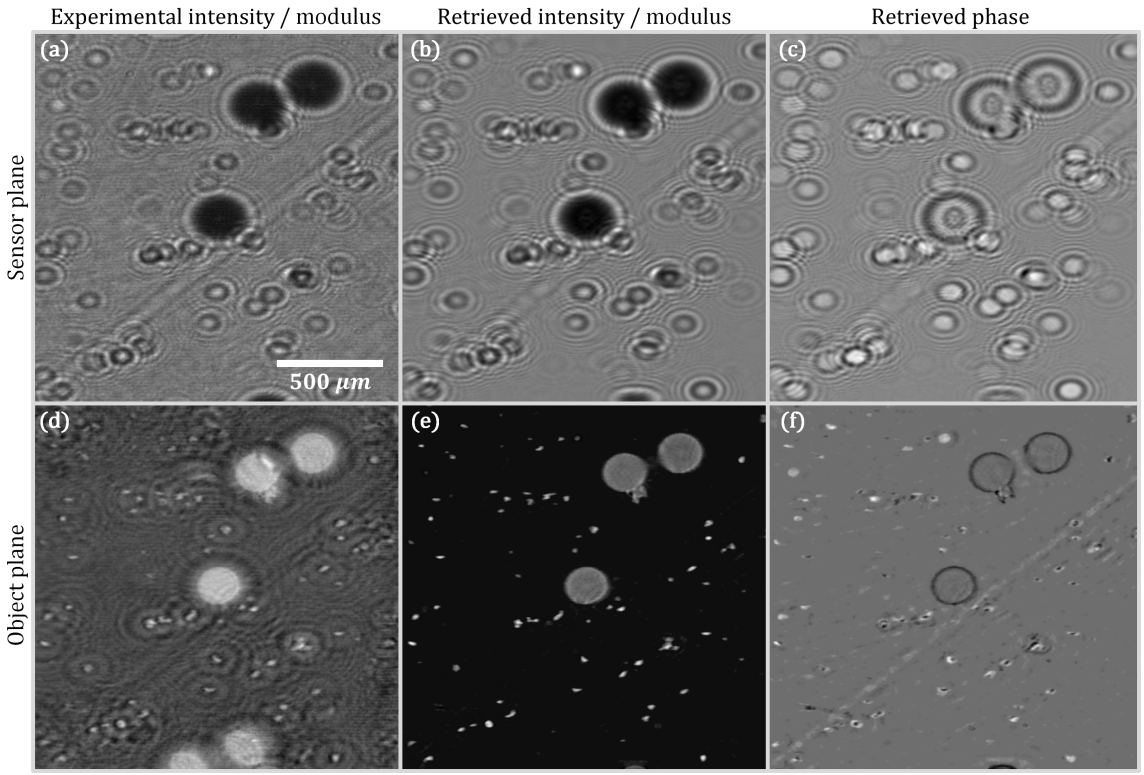

Figure IV.12: Results of the *RGB* phase retrieval algorithm on the experimental data in the green channel (a) introduced in figure IV.7 after 100 iterations. (b) Simulated intensity on the sensor plane for the retrieved 2D object t_{2D}. (c) Retrieved phase on the sensor plane for the retrieved 2D object t_{2D}. (d) Modulus of the simple back-propagation of the experimental data. (e) Modulus of the retrieved 2D object t_{2D}. (d-e) The gray scale has been reversed to facilitate the interpretation and the comparison with the 3D reconstructions. (f) Phase of the retrieved 2D object t_{2D}.

Comparing figure IV.7.h and figure IV.13.d with the simulations in figure IV.2, one can see that the reconstructions are close from the simulation when the phase is known in the Fourier mapping method with a contrasted hourglass shape. The remaining artifacts are consequently due to the limited angular coverage.

These artifacts are spread around the reconstructed objects in accordance with the lighting positions and can be seen on the maximum intensity projection of figure IV.13.a. They are emphasized in figure IV.13.f where the contrast is enhanced. They appear more contrasted than in figure IV.7.g in which they are blurred in the noise and background signal.

Figures IV.13.a-f are made from the 3D reconstructed volume using the total simulated wave fronts I^j_{sim} and φ^j_{sim}. Figures IV.13.g-i compare on an extracted slice at the focus of the dust particles the effect of choosing only the experimental data I^j_d, combining them with the retrieved phase information φ^j_{PR} or using the full simulated wave fronts I^j_{PR} and φ^j_{PR}.

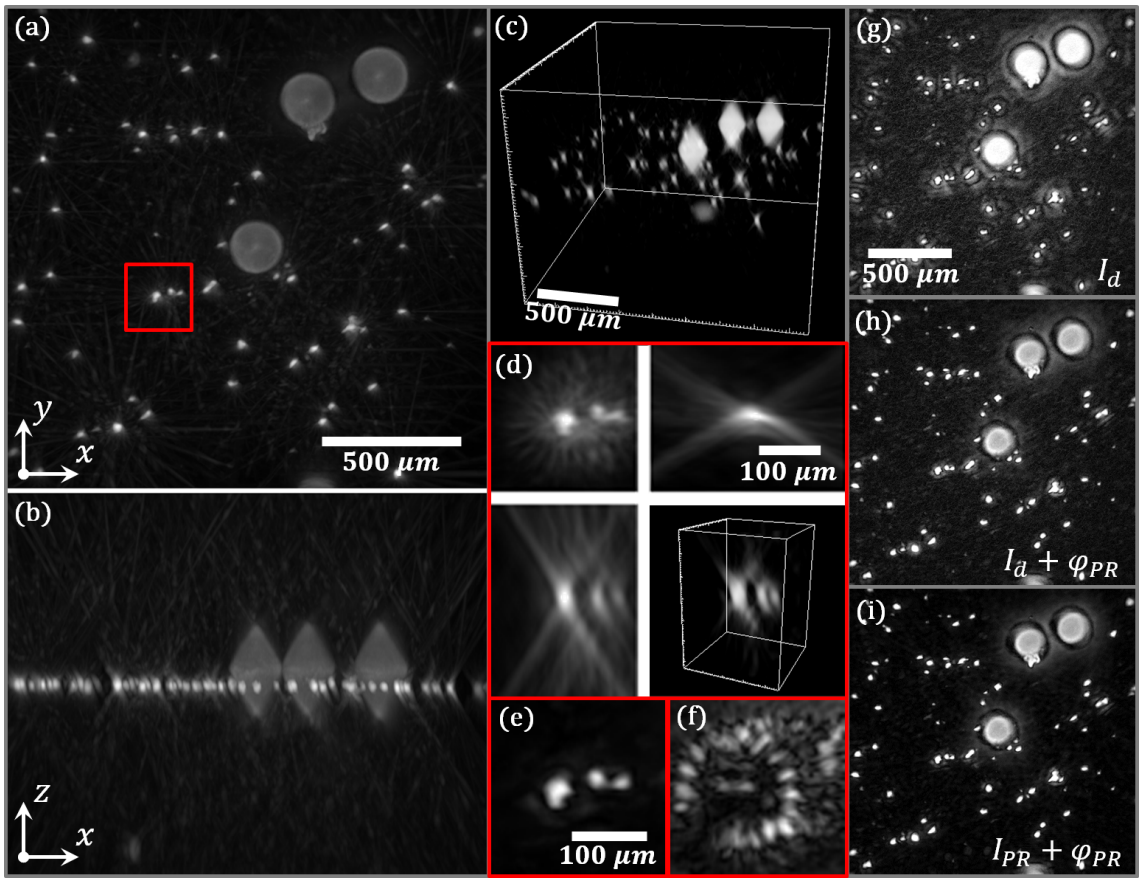

Figure IV.13: Modulus of the reconstructed scattering potential f of bubbles and dust at the bottom of a Petri dish filled with water after an iterative RGB phase retrieval for each lighting position and the use of the simulated wave fronts in the Fourier mapping process. (a-b) xy and xz-maximum intensity projections of the reconstructed volume. (c) 3D rendering of the 3D volume. (d) Average intensity orthogonal projections and 3D rendering of the region of interest framed in red on (a). (e-f) Zoom on the region of interest at the focal plane of the dust particle (e) and with a defocus of 117 μm (f). (g-i) Comparison of a slice of the reconstructed volumes on the plane of the dust particles if only the experimental intensities I_d^j are used (g), if the experimental intensities I_d are combined with the retrieved phase information φ_{PR}^j (h) or if the full simulated wave fronts I_{PR}^j and φ_{PR}^j are used (i).

Using the retrieved phase information erases the twin-image artifacts in figure IV.13.h but the background remains noisy. Using the simulated intensities cleans the background and produces sharper objects in figure IV.13.i.

3 3D inverse problem approach

In the previous section 2, the remaining artifacts are attributed to the lack of angular coverage by the lens-free microscope around the sample. Even if the phase

is retrieved, only the coefficients lying on the spherical caps covered by the dataset are mapped in the Fourier domain. A huge part of the Fourier domain is then left at its initialization value: 0.

Besides, it was mentioned that the reconstructed volumes are beyond of the validity domain of the Fourier diffraction theorem. This means that the model cannot perfectly fit the data even using the phase retrieval algorithm. Consequently, to improve the reconstructions quality this constraint on the data fidelity must be relaxed.

In the method developed in this section, the Fourier diffraction theorem (II.18) is used as a simulation tool for a direct model to simulate the holograms of a given object f as explained in chapter II, section 2 from figure II.3. This direct model is at the base of an inverse problem approach implemented to iteratively retrieve the 3D object f.

Working directly on the full volume f theoretically allows to retrieve more Fourier coefficients than the previous methods via an extrapolation of the missing frequencies which lie outside spherical caps thanks to *a priori* information.

Moreover, such an approach appropriately deals with the lack of phase information to reduce artifacts as no assumption on the phase on the sensor plane is needed.

Finally, the simulated data are compared with the experimental measurements but are not forced to perfectly match them. This can partially take into account that the model of the Fourier diffraction theorem, only valid for low scattering objects, cannot perfectly simulate the experimental data for big objects.

3.1 Inverse problem formulation

It has been seen in chapter II, section 3 that it exists an expression to compute the diffracted wave U^j_{dif} scattered by a given potential f via equation (II.48) for a given wavelength and lighting direction $\overrightarrow{k_0^{'j}}$.

This direct model is used to define a new cost function:

$$J(f) = \underbrace{\frac{1}{nb_x^p nb_y^p N}\sum_{j=1}^{N}\left\| I_d^j - \left|U_{inc}^j + U_{dif}^j(f)\right|^2\right\|^2}_{\text{data fidelity } J_d(f)} + \cdots$$
$$\mu_{L_1}\underbrace{\frac{1}{nb_x^v nb_y^v nb_z^v}\|f\|_{L_1,\epsilon}}_{\text{sparsity constraint } J_{L_1,\epsilon}(f)} + \mu_\nabla \underbrace{\frac{1}{nb_x^v nb_y^v nb_z^v}\|\nabla f\|_{L_1,\epsilon}}_{\text{gradient sparsity constraint } J_{\nabla,\epsilon}(f)} \tag{IV.18}$$

and a new minimization problem:

$$\tilde{f} = \underset{C(f)}{\operatorname{argmin}} J(f) = \underset{C(f)}{\operatorname{argmin}} J_d(f) + \mu_{L_1} J_{L_1,\epsilon}(f) + \mu_\nabla J_{\nabla,\epsilon}(f) \tag{IV.19}$$

$\frac{1}{nb_x^p nb_y^p N}$ and $\frac{1}{nb_x^v nb_y^v nb_z^v}$ are normalizing factors, nb_x^p, nb_y^p still being the pixels number in each direction of the 2D planes and nb_x^v, nb_y^v, nb_z^v the voxels number in each direction

of the 3D reconstructed volume f. N is the number of acquisitions recorded under different lighting situations (both in terms of wavelength and direction $\overrightarrow{k_0'^j}$).

As in the previous section 2, $C(f)$ stands for the constraints given on the domain of definition of f. The central term is still a sparsity prior, but on a 3D object, numerically given by:

$$\|f\|_{L_1,\epsilon} = \sum_{pixels_{k,l,m}} \sqrt{|f_{k,l,m}|^2 + \epsilon^2} \tag{IV.20}$$

where the indices (k,l,m) stand for the $nb_x^v \times nb_y^v \times nb_z^v$ voxels locations on the volume grid respectively on the x, y and z-axes. The right-hand term is the 3D sparsity prior on the gradient of f and is numerically computed as follows:

$$\begin{aligned}|\nabla f_{k,l,m}|^2 = \frac{1}{4}\Big[&q_x\,|f_{k+1,l,m} - f_{k,l,m}|^2 + q_x\,|f_{k+1,l+1,m} - f_{k,l+1,m}|^2 + \cdots\\ &q_x\,|f_{k+1,l,m+1} - f_{k,l,m+1}|^2 + q_x\,|f_{k+1,l+1,m+1} - f_{k,l+1,m+1}|^2 + \cdots\\ &q_y\,|f_{k,l+1,m} - f_{k,l,m}|^2 + q_y\,|f_{k+1,l+1,m} - f_{k+1,l,m}|^2 + \cdots\\ &q_y\,|f_{k,l+1,m+1} - f_{k,l,m+1}|^2 + q_y\,|f_{k+1,l+1,m+1} - f_{k+1,l,m+1}|^2 + \cdots\\ &q_z\,|f_{k,l,m+1} - f_{k,l,m}|^2 + q_z\,|f_{k+1,l,m+1} - f_{k+1,l,m}|^2 + \cdots\\ &q_z\,|f_{k,l+1,m+1} - f_{k,l+1,m}|^2 + q_z\,|f_{k+1,l+1,m+1} - f_{k+1,l+1,m}|^2\Big]\end{aligned} \tag{IV.21}$$

As explained in appendix D, (q_x, q_y, q_z) are weighting coefficients to take into account that the grid can be not orthonormal and are set to $q_x = 1$, $q_y = dx/dy$ and $q_z = dx/dz$.

As previously, the two hyperparameters μ_{L_1} and μ_∇ weight the two regularization terms of the cost function (IV.18).

The gradient of the two regularization terms being given by appendix D, it remains to find a numerical expression for J_d and its gradient. These expressions are based on the direct numerical formulation (II.51) developed in chapter II, section 3.

With the notations introduced in chapter III, section 3.3 and noting P_{2D}, P_{2D}^i, P_{3D}, P_{3D}^i, F_{2D}, F_{2D}^i, F_{3D}, F_{3D}^i and I^j and the matrix representations of pad, pad^{-1} in the 2D and 3D spaces, FFT_{2D}, FFT_{2D}^{-1}, FFT_{3D}, FFT_{3D}^{-1} and $interp\left[.,\left(u_{2D}^{pad}, v_{2D}^{pad}, w\left(u_{2D}^{pad}+u_0^j, v_{2D}^{pad}+v_0^j\right)-w_0^j\right)\right]$ which are all linear operators and defining:

$$M_S^j = e^{2i\pi\left(\left(x_{2D}+x_0^j\right)u_0^j+\left(y_{2D}+y_0^j\right)v_0^j\right)}\frac{dv}{ds} \tag{IV.22}$$

$$M_F^j = \frac{ik_0'^{2j}e^{2i\pi\left[x_0^j u_{2D}^{pad}+y_0^j v_{2D}^{pad}+z_s w\left(u_{2D}^{pad}+u_0^j, v_{2D}^{pad}+v_0^j\right)\right]}}{4\pi w\left(u_{2D}^{pad}+u_0^j, v_{2D}^{pad}+v_0^j\right)} \tag{IV.23}$$

with $w(u,v) = \sqrt{\frac{n_0^2}{\lambda_0^2} - u^2 - v^2}$, $\left(u_0^j, v_0^j, w_0^j\right) = \left(\frac{n_0.p_0^j}{\lambda_0^j}, \frac{n_0.q_0^j}{\lambda_0^j}, \frac{n_0.m_0^j}{\lambda_0^j}\right)$, $ds = dx^p.dy^p$ the elementary pixel surface and $dv = dx^v.dy^v.dz^v$ the elementary voxel volume,

equation (II.51) can be rewritten:

$$\begin{aligned}\overrightarrow{U}^{j}_{dif} &= diag\left(\overrightarrow{M}^{j}_{S}\right) \times P^{i}_{2D} \times F^{i}_{2D} \times diag\left(\overrightarrow{M}^{j}_{F}\right) \times I^{j} \times F_{3D} \times P_{3D} \times R2C \times \overrightarrow{f} \\ &= O \times \overrightarrow{f}\end{aligned} \tag{IV.24}$$

It comes from appendix D:

$$\nabla J_d\left(\overrightarrow{f}\right) = \frac{1}{nb^p_x nb^p_y N} \sum_{j=1}^{N} 4\mathcal{R}\left[O^{\star} \times \left[\overrightarrow{U}^{j}_{tot}\left(\overrightarrow{f}\right).\left(\left|\overrightarrow{U}^{j}_{tot}\left(\overrightarrow{f}\right)\right|^2 - \overrightarrow{I}^{j}_{d}\right)\right]\right] \tag{IV.25}$$

with:

$$O^{\star} = R2C^{\star} \times P^{\star}_{3D} \times F^{\star}_{3D} \times I^{j\star} \times diag\left(\overrightarrow{M}^{j}_{F}\right)^{\star} \times F^{i\star}_{2D} \times P^{i\star}_{2D} \times diag\left(\overrightarrow{M}^{j}_{S}\right)^{\star} \tag{IV.26}$$

From the analysis done in chapter III, section 3.3, the Hermitian adjoint of all the matrices are already known excepted for I^j. Its matrix shape is:

$$I^{j} = \begin{pmatrix} & \cdots & & \cdots & \\ 0\cdots0 & w^{j}_{l,1} & 0\cdots0 & w^{j}_{l,n} & 0\cdots0 \\ & \cdots & & \cdots & \\ & c^{j}_{l,1} & & c^{j}_{l,n} & \end{pmatrix} \begin{array}{l} \\ l \leftarrow \text{index of the interpolated} \\ \text{coefficient on the spherical cap} \\ \\ \\ \\ \end{array}$$

$$\begin{array}{c} \\ \\ \\ \uparrow \\ \text{indices of the neighboring} \\ \text{coefficients in the 3D volume} \end{array} \begin{array}{c} \\ \\ \\ \uparrow \\ \\ \\ \end{array} \tag{IV.27}$$

where:

- l is a line in I^j corresponding to a given coefficient on the 2D j^{th} spherical cap[13] which is interpolated in the 3D volume,
- $\left\{c^{j}_{l,k}\right\}_{k\in[\![1,n]\!]}$ are the columns in I^j corresponding to the position of the neighboring coefficients[14] in the 3D volume,
- $\left\{w^{j}_{l,k}\right\}_{k\in[\![1,n]\!]}$ are the weights to apply on the neighboring coefficients in the 3D volume,
- n is the number of neighboring coefficients. For a nearest-neighbor interpolation, $n = 1$. In the case of a linear interpolation, if the grids overlap on the x and y-directions[15], $n = 2$; if the grids overlap only on the x or the y-direction [16], $n = 4$; and if none the grids overlap[17], $n = 8$.

[13]This coefficient is consequently placed at the l^{th} position in the vector shape of this spherical cap.

[14]These coefficients are consequently placed at the $\left\{c^{j\ th}_{l,k}\right\}_{k\in[\![1,n]\!]}$ positions in the vector shape of the 3D volume.

[15]The interpolation is on a line between two known coefficients on the z-axis.

[16]The interpolation is in a rectangle of four known coefficients on the y or the x-axis and the z-axis.

[17]The interpolation is in a parallelepiped of eight known coefficients on the x, y and the z-axes.

Thus, the Hermitian adjoint $I^{j\star}$ of I^j is:

$$I^{j\star} = \begin{pmatrix} & \vdots & \\ & w^j_{l,1} & \\ \vdots & \vdots & \vdots \\ & w^j_{l,n} & \\ & \vdots & \end{pmatrix} \tag{IV.28}$$

From this matrix, it appears that the Hermitian adjoint $interp^\star$ of $interp$ consists in summing back the interpolated 2D coefficients on their neighboring 3D coefficients weighted by the same weights.

It is now possible to express the gradient of the data fidelity in terms for a given scattering potential f from equations (IV.25) and (IV.26):

$$\begin{aligned} \nabla J_d(f) = \frac{1}{nb_x^p nb_y^p N} \sum_{j=1}^{N} 4.pad^{-1} \Big[[\mathrm{FFT}_{3D}^{-1} \Big[interp^\star \Big[\bar{M}_F^j . \cdots \\ \mathrm{FFT}_{2D} \Big[pad \left(\bar{M}_S^j . U_{tot}^j(f) . \left(\left| U_{tot}^j(f) \right|^2 - I_d^j \right) \right) \Big], \cdots \\ \left(u_{2D}^{pad}, v_{2D}^{pad}, w\left(u_{2D}^{pad} + u_0^j, v_{2D}^{pad} + v_0^j \right) - w_0^j \right) \Big] \Big] \Big] \end{aligned} \tag{IV.29}$$

$$\begin{aligned} \nabla J_d(f) = \frac{1}{nb_x^p nb_y^p N} \sum_{j=1}^{N} 4.pad^{-1} \Big[[\mathrm{FFT}_{3D}^{-1} \Big[interp^\star \Big[\cdots \\ \frac{-ik_0'^2 j e^{-2i\pi \left[x_0^j u_{2D}^{pad} + y_0^j v_{2D}^{pad} + z_s w\left(u_{2D}^{pad} + u_0^j, v_{2D}^{pad} + v_0^j \right) \right]}}{4\pi w\left(u_{2D}^{pad} + u_0^j, v_{2D}^{pad} + v_0^j \right)} . \cdots \\ \mathrm{FFT}_{2D} \Big[pad \Big(e^{-2i\pi \left((x_{2D} + x_0^J) u_0^j + (y_{2D} + y_0^j) v_0^j \right)} . \cdots \\ U_{tot}^j(f) . \left(\left| U_{tot}^j(f) \right|^2 - I_d^j \right) \Big) \Big], \cdots \\ \left(u_{2D}^{pad}, v_{2D}^{pad}, w\left(u_{2D}^{pad} + u_0^j, v_{2D}^{pad} + v_0^j \right) - w_0^j \right) \Big] \Big] \Big] \frac{dv}{ds} \end{aligned} \tag{IV.30}$$

Finally, the numerical expression[18] of the gradient of the cost function (IV.18) at a given f is:

$$\nabla J(f) = \nabla J_d(f) + \mu_{L_1} \nabla J_{L_1,\epsilon}(f) + \mu_\nabla \nabla J_{\nabla,\epsilon}(f) \tag{IV.31}$$

The resolution of the minimization problem (IV.19) is performed with the same convex optimization algorithm [90] introduced in the previous method, in section 2

[18]Let's mention here that all the conclusions on the impact of the hyperparameter values in this chapter IV with the inverse problem approach are subject to caution. Indeed, it was found afterwards that the implementation of the gradient of the ∇-regularization was wrong. The normalization factor $\frac{1}{nb_x^v nb_y^v nb_z^v}$ was replaced by $\frac{1}{nb_x^p nb_y^{vp}}$ for the gradient but not for the cost $J_{\nabla,\epsilon}$. Some tests tend to show that the results are close from the ones that can be obtained with $\tilde{\mu}_\nabla = \mu_\nabla \frac{nb_x^v nb_y^v nb_z^v}{nb_x^p nb_y^{vp}}$. All the values presented in this thesis are corrected accordingly.

of this chapter[19].

This inverse problem approach is schemed in figure IV.14.a: at each iteration of the algorithm, the object $f_{i^{th}}$ at the i^{th} iteration is forced to satisfy the constraints $C(f_{i^{th}})$. It is then used to simulate holograms I_s^j for the N different lighting situations j. They are compared with the experimental data I_d^j in the data fidelity term J_d. In parallel, the sparsity constraints on f and its gradient are computed. In blue, the medallions show the effect of the two implemented regularizations. The L_1-regularization favors spatially limited objects in a sparse environment. The ∇-regularization produces sharp and homogeneous objects. With these two terms $J_{L_1,\epsilon}$ and J_∇, ϵ, one gets the global cost function J. Its gradient gives the direction of the next step $f_{i^{th}+1}$ of the iterative loop.

The loop is run nb_{it}^{IP} times.

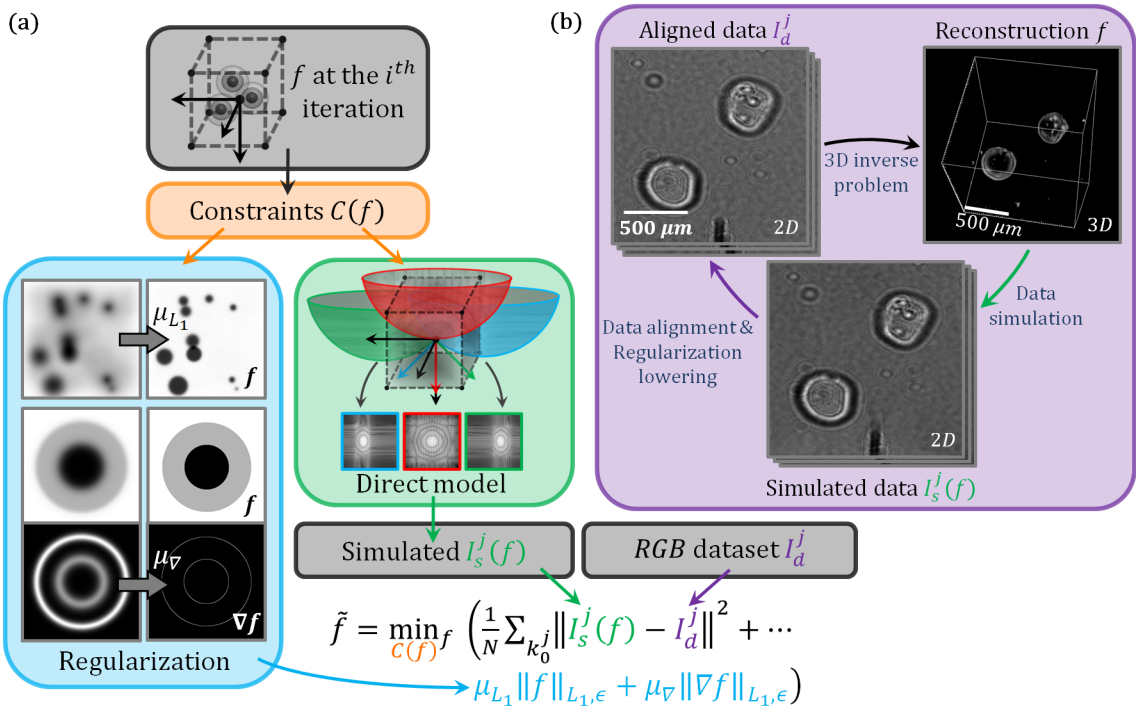

Figure IV.14: (a) Schematic view of the inverse problem approach: the domain of definition of the scattering potential $f_{i^{th}}$ at the i^{th} iteration is limited by the constraints $C(f)$ (orange). The regularization term is computed (blue) and a set of intensities I_s^j is simulated (green) and compared with the experimental data I_d^j (purple) to compute the data fidelity term. The summation of these three terms gives the global cost function whose gradient at $f_{i^{th}}$ determines the new value for $f_{i^{th}+1}$. (b) After a given number of iteration nb_{it}^{IP}, the regularized simulated intensities I_s^j can be used as references to refine the alignment of the experimental data I_d^j before a new batch of iterations of the algorithm.

[19]Thanks to Eric Thiébaut who shared his implementation in C code for the computation of the regularization term $\|\nabla.\|_{L_1,\epsilon}$ for 3D objects and Fabien Momey who adapted it for complex variables and provided its interfacing with Matlab®.

But besides addressing the lacking phase and estimating the global Fourier transform of f, this method also allows improving the data alignment. Indeed, after having performed a first estimation of f, one can use the direct model (IV.24) to simulate a numerical dataset $\tilde{I}_s^j = |U_{inc}^j + U_{dif}^j(f)|^2$, $j \in [\![1, N]\!]$. By construction, this set of simulated intensities $\tilde{I}_s^j$ is aligned with the numerical 3D object f. It can consequently be used as a reference to refine the registration[20] of the experimental data I_s^j.

Performing anew a 3D reconstruction of this dataset via a new batch of iterations increases the quality of the retrieved object. One can iterate these steps alternating between 3D reconstruction and data alignment as schemed in figure IV.14.b. This refinement cannot be performed with the methods developed previously.

In addition, one must notice that this method is the only one developed during this PhD which can correctly take into account a linear interpolation in the Fourier space via the function $interp^\star$ in a reconstruction algorithm. Indeed, as mentioned in the conclusion of chapter II, section 3, algorithms using the Fourier diffraction theorem (II.18) as a reconstruction tool cannot reverse the linear interpolation and are constrained to use a nearest-neighbor interpolation. In the proposed algorithm, the Fourier diffraction theorem is only used as a direct model in which the linear interpolation can be properly taken into account.

Finally, all the reconstructions are done on the scattering potential f of the 3D object. In some situations, it may be more interesting to work directly on the complex refractive index $\delta n = n - n_0$. The cost function (IV.18) is expressed in terms of δn:

$$J(\delta n) = \underbrace{\frac{1}{nb_x^p nb_y^p N}\sum_{j=1}^{N}\left\| I_d^j - \left| U_{inc}^j + U_{dif}^j\left(f\left(\delta n, n_0\right)\right)\right|^2\right\|^2}_{\text{data fidelity } J_d(\delta n)} + \cdots$$
$$\mu_{L_1}\underbrace{\frac{1}{nb_x^v nb_y^v nb_z^v}\left\|\delta n\right\|_{L_1,\epsilon}}_{\text{sparsity constraint } J_{L_1,\epsilon}(\delta n)} + \mu_\nabla \underbrace{\frac{1}{nb_x^v nb_y^v nb_z^v}\left\|\nabla\delta n\right\|_{L_1,\epsilon}}_{\text{gradient sparsity constraint } J_{\nabla,\epsilon}(\delta n)} \tag{IV.32}$$

with:

$$f(\delta n, n_0) = (1 + \delta n/n_0)^2 - 1 \tag{IV.33}$$

Nevertheless, $f(., n_0)$ is not a linear operator and it consequently does not exist a matrix representation similar to equation (IV.24) which is nevertheless needed to compute the gradient of the data fidelity term $J_d(\delta n)$. The solution is to locally linearize $U_{dif}(\delta n)$ around δn with a Taylor expansion for a small dn:

$$f(\delta n + dn, n_0) \simeq f(\delta n, n_0) + \frac{2}{n_0^2}(n_0 + \delta n)\, dn \tag{IV.34}$$

[20]The experimental data are aligned with the simulated intensities via a least squares minimization of the difference between the simulated intensities and the interpolation of the experimental data for a given shift and a given rotation as presented in appendix C

Then:

$$\left|U_{inc}^{j}+U_{dif}^{j}\left(f\left(\delta n+dn,n_0\right)\right)\right|^2 \simeq \left|U_{tot}^{j}\left(f\left(\delta n,n_0\right)\right)+U_{dif}^{j}\left(\frac{2}{n_0^2}\left(n_0+\delta n\right)dn\right)\right|^2 \tag{IV.35}$$

with $U_{dif}^{j}\left(\frac{2}{n_0^2}\left(n_0+\delta n\right)dn\right)$ which is linear in terms of dn for a given δn. Noting $M_{\delta n}$ the 3D matrix:

$$M_{\delta n}=\frac{2}{n_0^2}\left(n_0+\delta n\right) \tag{IV.36}$$

one gets a new linear operator from (IV.24):

$$O_{\delta n}=diag\left(\overrightarrow{M}_S^j\right)\times P_{2D}^{i}\times F_{2D}^{i}\times diag\left(\overrightarrow{M}_F^j\right)\times I^j\times F_{3D}\times P_{3D}\times diag\left(\overrightarrow{M}_{\delta n}\right)\times R2C \tag{IV.37}$$

With the same reasoning than in appendix D the gradient for $J_d\left(\delta n\right)$ is:

$$\begin{aligned}\nabla J_d\left(\delta n\right)=\frac{1}{nb_x^p nb_y^p N}\sum_{j=1}^{N}\frac{8}{n_0^2}\left(n_0+\bar{\delta n}\right)pad^{-1}\Big[\big[\mathrm{FFT}_{3D}^{-1}\Big[interp^{\star}\Big[\cdots\\ \frac{-ik_0'^2 j e^{-2i\pi\left[x_0^j u_{2D}^{pad}+y_0^j v_{2D}^{pad}+z_s w\left(u_{2D}^{pad}+u_0^j,v_{2D}^{pad}+v_0^j\right)\right]}}{4\pi w\left(u_{2D}^{pad}+u_0^j,v_{2D}^{pad}+v_0^j\right)}\cdot\cdots\\ \mathrm{FFT}_{2D}\Big[pad\Big(e^{-2i\pi\left(\left(x_{2D}+x_0^J\right)u_0^j+\left(y_{2D}+y_0^j\right)v_0^j\right)}\cdot\cdots\\ U_{tot}^{j}\left(f\left(\delta n,n_0\right)\right).\left(\left|U_{tot}^{j}\left(f\left(\delta n,n_0\right)\right)\right|^2-I_d^j\right)\Big)\Big],\cdots\\ \left(u_{2D}^{pad},v_{2D}^{pad},w\left(u_{2D}^{pad}+u_0^j,v_{2D}^{pad}+v_0^j\right)-w_0^j\right)\Big]\Big]\Big]\frac{dv}{ds}\end{aligned} \tag{IV.38}$$

It is now possible to work and apply constraints and regularizations directly on δn to reconstruct the sample 3D complex refractive index .

3.2 Numerical simulations

To evaluate the efficiency of the 3D inverse problem approach, different configurations of the parameters are tested on the numerical volume introduced in the previous section 2.

The holograms are simulated with the Fourier diffraction theorem by padding the 2D and the 3D spaces and using the nearest-neighbor interpolation, for 16 lighting directions of $\theta = 30°$ and $\varphi \in [0°, 359°]$ ($\Delta\varphi = 22.5°$), for the red channel $\lambda = 630\ nm$, in the air $n_0 = 1$ and for a sensor distance of $z_s = 2\ mm$. Figure IV.15 presents the central slice as well as the xy-average intensity projection of the volume and an example of hologram for $\varphi = 112.5°$. This hologram is the target of the data fidelity term J_d of the cost function (IV.18).

Excepted if mentioned, all the reconstructions are based on the scattering potential f with $nb_x^p = nb_y^p = 512$, $dx^p = dy^p = 1.67\ \mu m$, $nb_x^v = nb_y^v = nb_z^v = 256$, $dx^v = dy^v = dy^v = 3.34\ \mu m$, $z_s = 2\ mm$, $n_0 = 1$ and without any constraint on the domain of definition of f. No padding is applied. All the tests are run with $nb_{it}^{IP} = 20$ iterations.

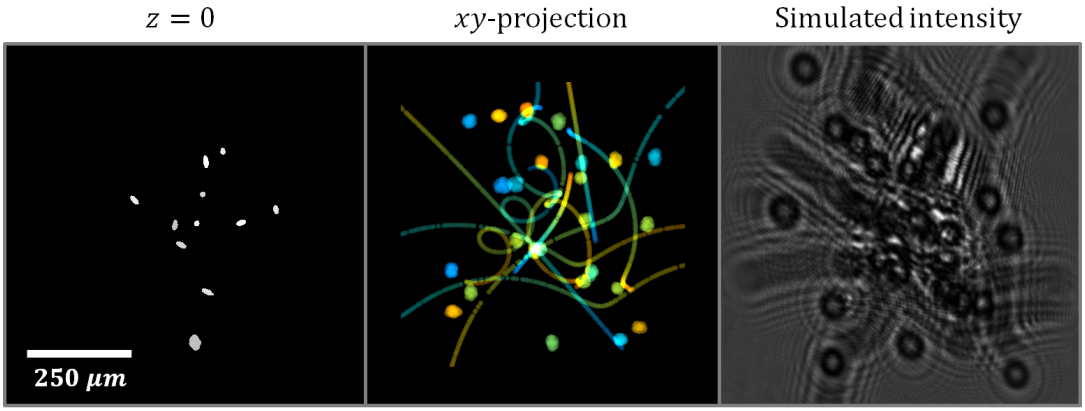

Figure IV.15: Numerical object and simulations on which the inverse problem approach is tested. The slice $z = 0$ and the xy-average intensity projection of the 3D scattering potential f are presented. The color codes for the depth: the shallowest in blue, the deepest in red. The hologram in the red channel $\lambda = 630\ nm$ with a lighting direction $\theta = 30°$ and $\varphi = 112.5°$ is given as reference.

Different configurations for the iterative parameters are tested.

Figure IV.16 compares the effect of the regularization on the sparsity of the object for different values of μ_{L_1}. Without any regularization the algorithm manages to reconstruct the volume but gives a noisy result with twin-image around big objects (see the $z = 0$ slice which as to be compared with the one in figure IV.15). Increasing the L_1-regularization reduces this artifacts around the big objects. The center of the volume is also cleaner with a darker background.

Figure IV.16 compares the effect of the regularization on the sparsity of the object gradient for different values of μ_∇. Looking at the noisy background for $\mu_\nabla = 64$ and $\mu_\nabla = 640$, the smoothing effect of such a regularization is clearly visible with the apparition of some "speckle"-type patterns. This smoothing with the dark background helps to reduce the noise but is not as effective as the L_1-regularization and it does not help to erase the twin-image artifacts. The fact that this regularization favors homogeneous objects helps to better reconstruct the branches which are more contrasted than with the L_1-regularization, especially at the center of the volume. If the regularization is too high as for $\mu_\nabla = 6400$, the crowded areas tend to be more homogeneous and the background noise is enhanced counterbalancing the previous advantages.

As for the previous method introduced in section 2, combining the L_1 and the ∇-regularization gives the best results as one can see in figure IV.18 in which the two first situations are run with a bigger number of iterations: $nb_{it}^{IP} = 150$. The twin-image around the big objects is largely removed and the branches are well identified. The influence of the padding does not seem to have a significant influence on the reconstruction quality. The contrast is even slightly better if no-padding is applied.

The choice of the interpolation method appears to be more important. Indeed, even if the last reconstruction is also done with $nb_{it}^{IP} = 25$ and cannot be directly compared with the two others, it can be compared with the previous figures. And

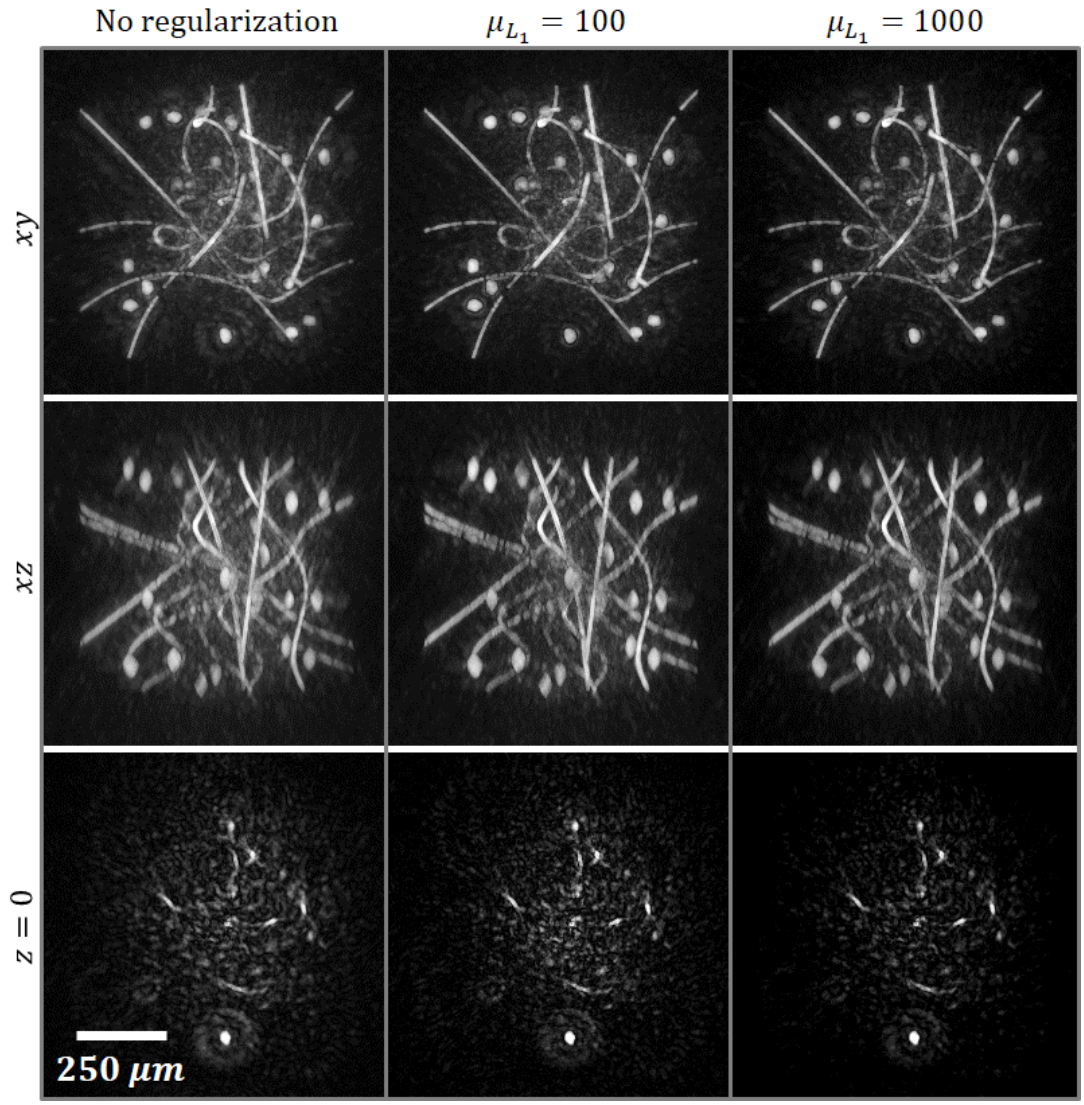

Figure IV.16: Comparison of the xy and xz-maximum intensity projections and slices $z = 0$ of the reconstructed 3D scattering potential f for different values of the hyperparameter μ_{L_1}.

even if the data are simulated using the nearest-neighbor interpolation, the best reconstructions are obtained with the linear interpolation as one can see comparing the background of the reconstruction with the backgrounds with $\mu_{L_1} = 1000$ in figure IV.16 or with $\mu_{L\nabla} = 640$ in figure IV.17. This shows the potential of this inverse problem approach where more coefficients are available in the Fourier domain than previously and better taken into account.

Figure IV.19 presents the residuals of the data fidelity term for the different situations tested in figure IV.18. It compares the intensities simulated from the retrieved 3D volumes with the theoretical simulation of figure IV.15 and table [IV.2] compares the gray value scales of the figures.

It appears that on all the situations, the data fidelity is not strictly enforced.

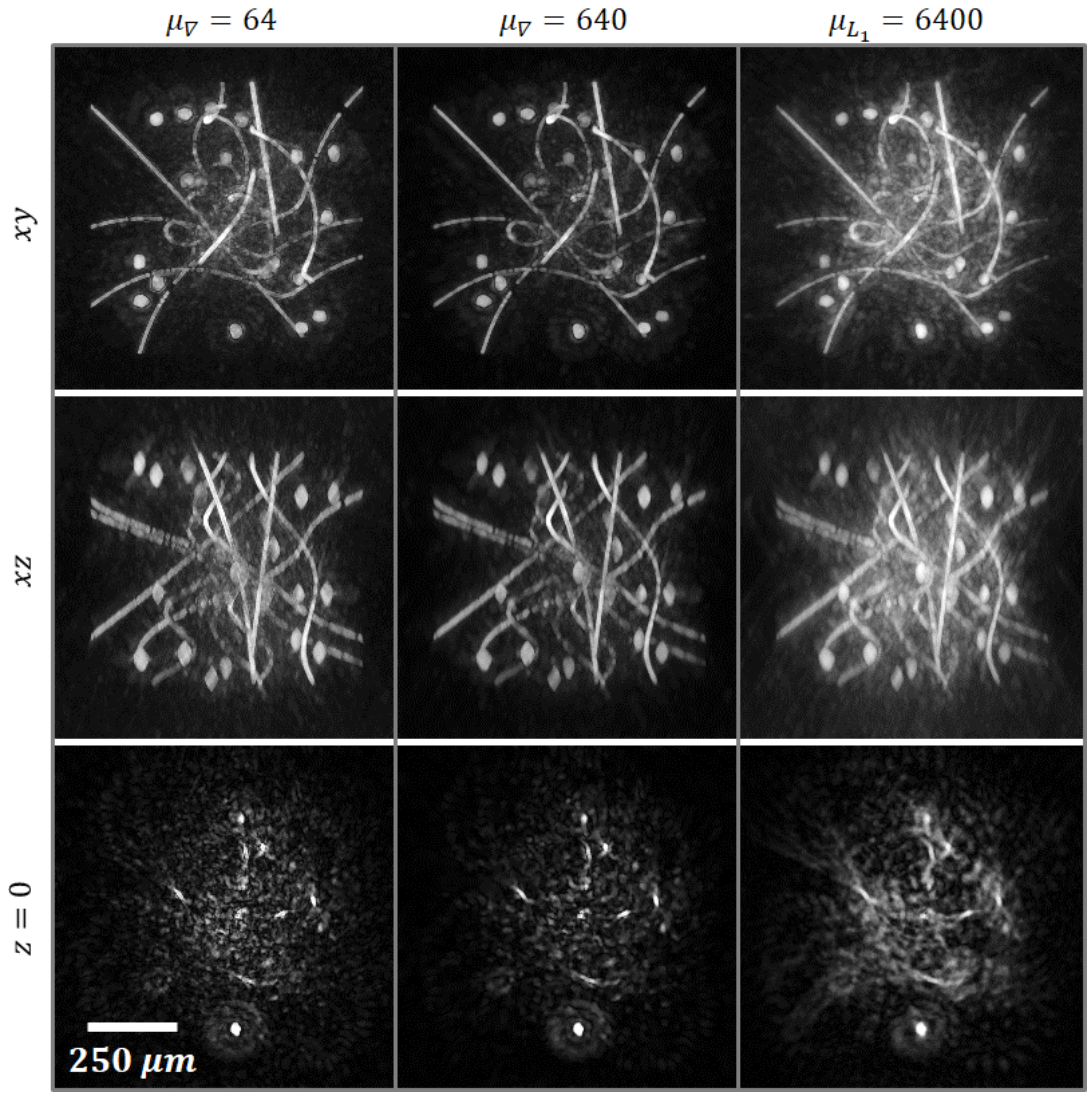

Figure IV.17: Comparison of the xy and xz-maximum intensity projections and slices $z = 0$ of the reconstructed 3D scattering potential f for different values of the hyperparameter μ_∇.

	No padding	2D&3D padding	Nearest-neighbor
min	−1.75	−1.63	−1.87
max	0.82	0.83	0.85

Table IV.2: Table of the minimal and maximal gray values of the differences of the simulated holograms for different reconstruction parameters (no padding applied, padding of the 2D and 3D spaces and padding with the nearest-neighbor interpolation) with the reference hologram (see figures IV.15 and IV.19).

One may argue that the number of iterations may be too low to achieve a good

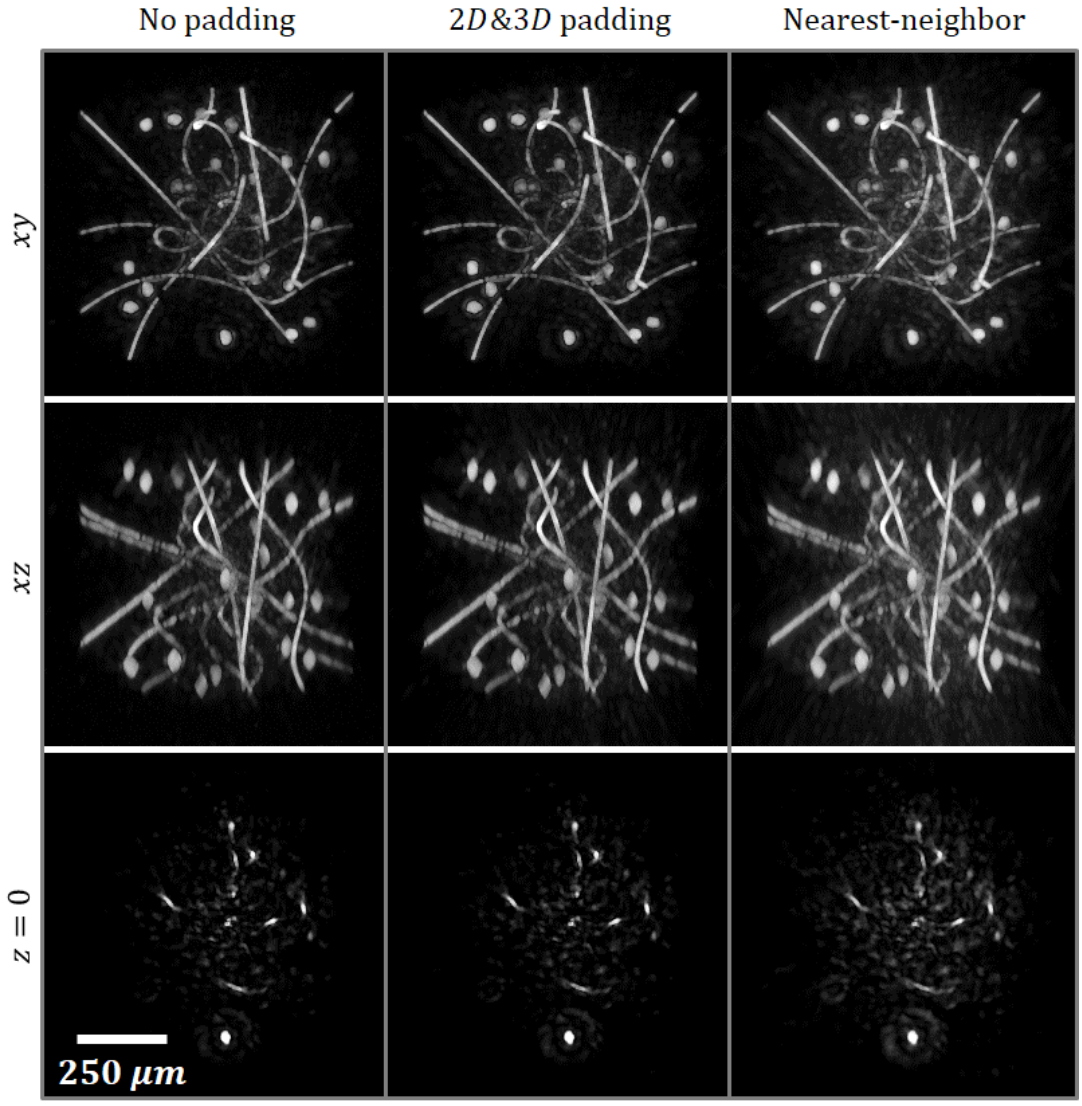

Figure IV.18: Comparison of the xy and xz-maximum intensity projections and slices $z = 0$ of the reconstructed 3D scattering potential f for a combination of the hyperparameters $\mu_{L_1} = 1000$ and $\mu_{\nabla} = 640$ without and with a zero-padding of the 2D and the 3D spaces. The nearest-neighbor interpolation with a zero-padding of the 2D and the 3D spaces is also presented.

convergence (and consequently a good agreement with the data). But looking at the convergence curves in figure IV.20, the convergence rate strongly decreases after the 50^{th} iterations. Moreover, from the figure and the values of table [IV.2] the residues are in the same order of magnitude at $it = 25$ or $it = 150$ whereas the blue curve has not yet reached a plateau. This also suggests that the iterative process mainly acts on the two regularizations, the data fidelity being enforced quite rapidly and then presents a small evolution.

Note here that in this section, no test is done on reconstructions based on the refractive index δn of the sample. Some tests are needed to check the validity of

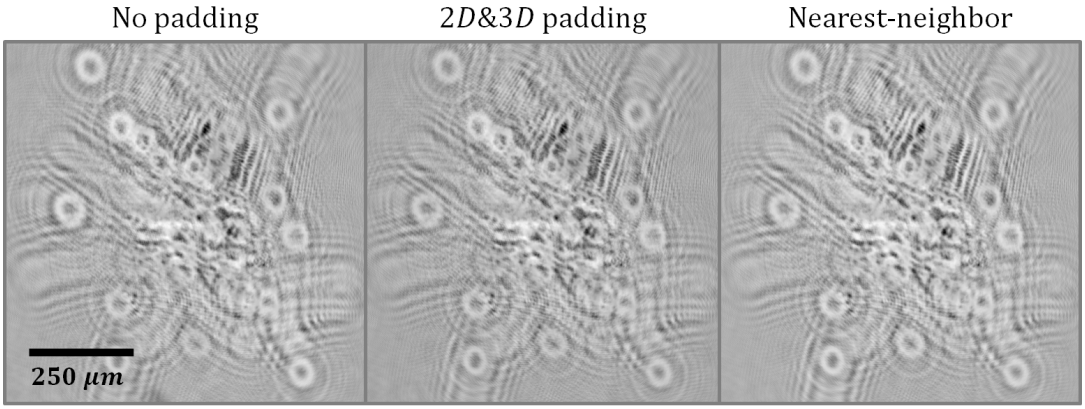

Figure IV.19: Residuals of the simulated intensities given by the reconstructions of figure IV.18 compared to the reference of figure IV.15 when the iterative algorithm is run without and with a zero-padding of the 2D and the 3D spaces. The nearest-neighbor interpolation with a zero-padding of the 2D and the 3D spaces is also presented. The gray value scales are given in table [IV.2].

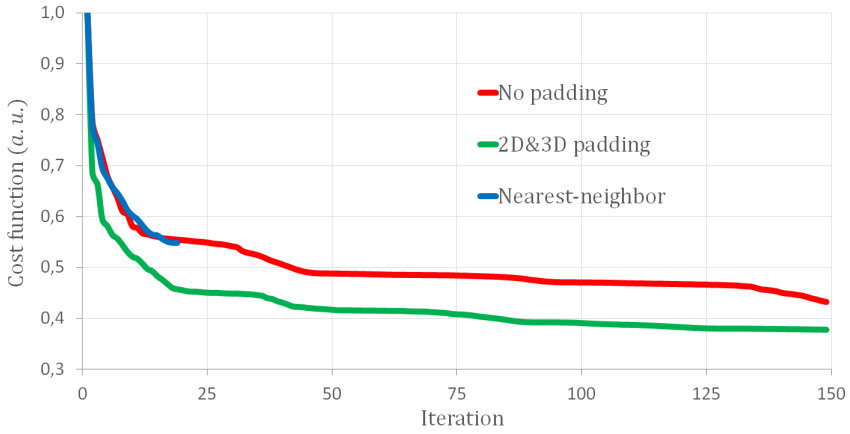

Figure IV.20: Evolution of the cost functions $J(f)$ during the iterations for the situations tested in figure IV.18. The curves are normalized by their first value.

the Taylor expansion (IV.34) and the efficiency of such an approach compared to a reconstruction based on the scattering potential f.

In addition, a better choice of hyperparameters could be found by a brute force test of a larger set of μ_{L_1} and μ_{∇} and comparing the reconstruction with the theoretical initial volume[21].

Finally, no reconstruction with constraints $C(f)$ on the domain of definition of f has been presented whereas it can help to reduce the twin-image artifacts. Indeed, as in the previous section 2, these artifacts present opposite sign compared to the real signal (not presented here), such as a negative real part for the refractive index,

[21]For example in this section, the reconstructed 3D volumes are not directly compared with the initial volume. With an adapted norm such as the L_2-norm, such a comparison would provide a more quantitative criterion to discriminate the different values of the hyperparemeters.

and can consequently be treated with an appropriate domain constraint.

3.3 3D reconstructions on experimental data

This section presents the test of the 3D inverse problem approach on new experimental data acquired on empty capsules[22] of Matrigel® in which some droplets of oil are trapped during the capsule formation process.

The reconstructed dataset is composed of 31 holograms in the green channel $\lambda = 520\ nm$ of $nb_x^p = nb_y^p = 512$, $dx^p = dy^p = 3.34\ \mu m$ aligned using the least mean squares minimization algorithm on the raw data[23], using a capsule hologram as alignment pattern.

The reconstruction parameters for the 3D volume are $\varphi \in \{0°, 285°\}$, $\Delta\varphi = 9.4°$, $\theta = 45°$, $\lambda = 520\ nm$, $z_s = 2.7\ mm$. As mentioned at the end of the previous chapter in section 5, a scaling factor is applied on the z-axis using equation (III.39) as the data are reconstructed for an angle $\theta = \theta_{air} = 45°$: $z_0/z_{air} = 1.5930$. The reconstructed volume[24] is composed $340 \times 340 \times 200$ voxels of $5.01 \times 5.01 \times 7.98\ \mu m^3$ for a final volume of $1.7 \times 1.7 \times 1.6\ mm^3 \simeq 4.6\ mm^3$.

The reconstruction is based on the scattering potential f on which no constraint on the domain of definition is applied. The 2D and 3D spaces are zero-padded. The iterative process is split in 9 batches of $nb_{it}^{IP} = 10$ iterations. In between each of the batches a refinement of the data alignment is performed as explained in figure IV.14.b.

Something which is also tested in this reconstruction procedure is to change the weight of the hyperparameters along this iterative process. Indeed, especially for complex samples, one can start with a problem strongly regularized in terms of localization with high values for μ_∇: the data fidelity is degraded, but the over-regularization forces the reconstructed object to be localized, and consequently the simulated data to be well aligned, bettering the registration step. Once the alignment of the experimental data is more accurate, the hyper-parameter μ_∇ can be set to lower values, increasing the data fidelity relative weight in the cost function. μ_∇ is consequently set to vary from 450 to 90 ($[440, 350, 260, 180, 90, 90, 90, 90, 90]$).

The results are presented in figure IV.21.

Comparing the reconstructions after the first and the last batch of iteration, it appears that the regularization is very effective to remove the artifacts due to the limited angular coverage: the conical shape around the capsules is strongly diminished. This result can be compared with the reconstructions of chapter III, section 3.3. In both cases, the lack of angular coverage is not sufficient to fully reconstruct the capsules surface. Nonetheless a full ring is reconstructed. This supports the choice of a crown design as presented in section 1 of this chapter.

The effect of the regularization can also be seen on the objects which are sharper and better localized in the 3D reconstruction after $it = 9$ batches.

[22] See next section 5.1 for more details on the culture protocol to produce Matrigel® capsules.
[23] See appendix C for more details.
[24] $340 \times 340 \times 200$ voxels of $5.01 \times 5.01 \times 5.01\ \mu m^3$ before scaling.

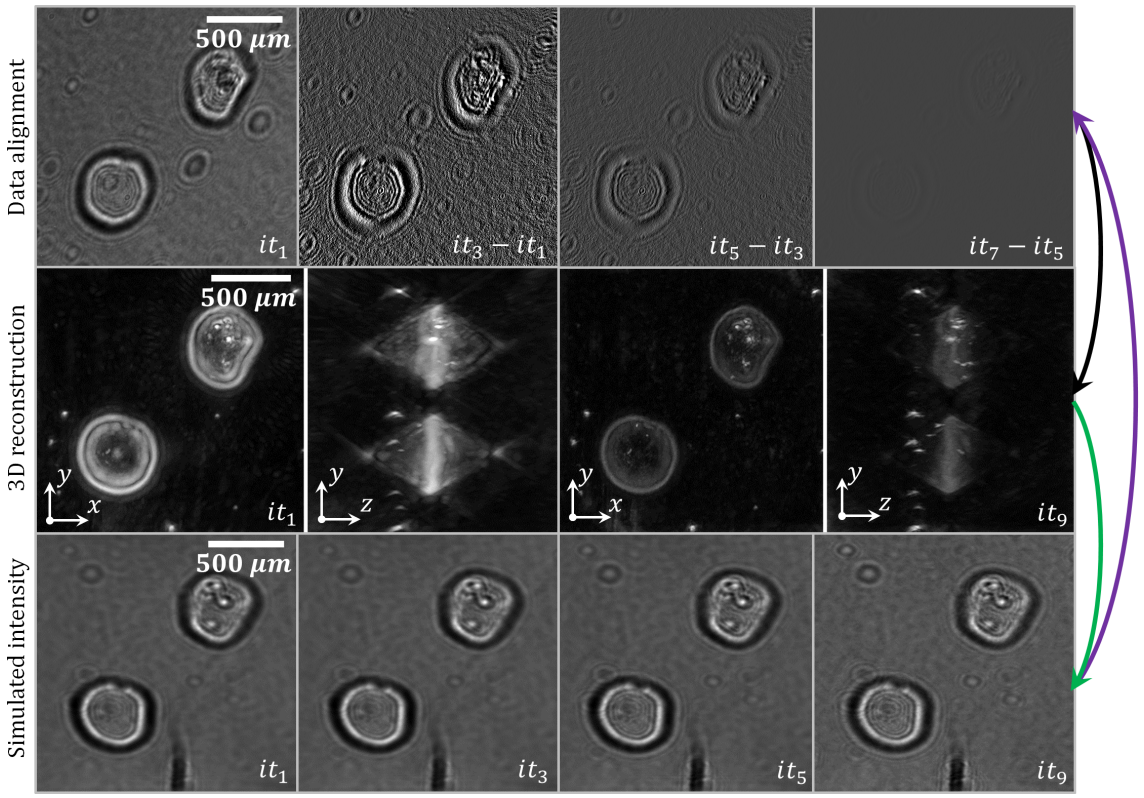

Figure IV.21: Results of the inverse problem approach on Matrigel® capsules. *First line* - Results of the refinement of the data alignment. The first batch of iteration it_1 of the inverse problem is run based on the first picture (here for $\varphi = 235°$). After each batch, the data alignment is refined. The other figure gives the difference of the extracted data for two different alignments separated by two batches of iterations with the same gray value scales. *Second line* - Comparison of the xy and yz-maximum intensities projections of the reconstructed scattering potential after the first and the last batch of iterations. *Last line* - Comparison of the simulated intensities (here for $\varphi = 0°$) after different batches of iterations. The color code of the arrows is the same than in figure IV.14.

This conclusion can also be observed on the simulated intensities during the iterations. As expected, the strong regularization at the beginning produces over-regularized holograms whose background and interference fringes are smoothed. As the regularization diminishes, the data fidelity is better enforced and the simulations give sharper and more detailed holograms.

Finally, figure IV.21 shows the potential and the efficiency of this approach to refine the data alignment. The gray value indicates the importance of the difference between two data alignments. A high value means that the correction in the alignment is important. As the iterations progress, this correction is less and less visible: the extracted data converge toward a better alignment. Thus, the alignment refinement and the regularization create a virtuous circle in which they mutually improve each other as well as the overall reconstruction quality.

4 Regularized Gerchberg–Saxton algorithm

The algorithm developed in the previous section 3 has a very long runtime. Indeed, in each iteration, a 3D FFT and N 2D FFTs must be computed twice. Once for the simulation of the diffracted wave in the data fidelity term and once for the computation of its gradient. With the addition of the computation of the regularization terms and their gradient in 3D, each iteration can be very long.

In the previous section 3, the inverse problem approach is initialized by a constant matrix equal to 0. Finding a better first guess of the reconstructed volume to initialize the loop can reduce the time needed to achieve convergence.

A new algorithm is implemented whose base comes from a discussion with Volker Jaedicke from the University of California, Berkeley about standard algorithms in digital holography microscopy and optical diffractive tomography that he presented during his talk at BiOS 2017. They are based on a Gerchberg-Saxton algorithm similar to the one presented in chapter I, section 3.

Such a structure has been modified in this PhD work to integrate regularization on the reconstructed object. A similar idea was also independently implemented in the context of the 2D lens-free microscopy [61] in which a 2D propagations and back-propagations loop alternates with a regularization step.

4.1 A modified Gerchberg–Saxton algorithm

This algorithm is based on the possibilities given by the Fourier diffraction theorem (II.18) to be used as a simulation or a reconstruction tool, as explained in chapter II, section 2.2.

This can be used in a back and forth loop between the recorded holograms and the reconstructed object as presented in the context of 2D lens-free microscopy in figure I.9.a. Once again the combination of the three wavelengths is a constraint on the object to close the loop.

But stronger constraints can be derived for the domain of definition of the object.

Indeed, it has been mentioned in chapter II, section 1 that the refractive index can be interpreted as the absorption (the imaginary part) and the desaphing property (the real part) of the sample. For absorbent and transparent objects, they cannot physically be negative[25]. This leads to the positivity constraint: $C(\delta n) = \{\delta n / \mathcal{R}(\delta n) \geq 0, \mathcal{I}(\delta n) \geq 0\}$.

If the object is described by its scattering potential f, remembering that the models and algorithms are developed for low scattering objects, the approximation (II.54) leads to a similar constraint $C(f) = \{f / \mathcal{R}(f) \geq 0, \mathcal{I}(f) \geq 0\}$.

The Fourier diffraction theorem and these constraints are the bricks of the Gerchberg-Saxton algorithm used in digital holography microscopy and optical diffractive tomography[44] which iteratively loops over the following steps:

[25]Excepted for air bubbles for example, it is indeed expected that the reconstructed objects are more dephasing than their surrounding aqueous medium implying that $\mathcal{R}(\delta n) \geq 0$.

- Step 1: At the first iteration $it = 0$ of the algorithm, the complex waves on the sensor at the different illumination $j \in [\![1, N]\!]$ are initialized with moduli corresponding to the recorded intensities and a phase set to 0: $U^j_{tot,0} = \sqrt{I^j_d}$. In the next iterations, step 1 insures the data fidelity. The complex waves simulated in step 4 are updated to match the recorded dataset: $U^j_{tot,it} = \frac{\sqrt{I^j_d}}{\left|U^j_{tot,it-1}\right|} U^j_{tot,it-1}$.
- Step 2: The 3D Fourier domain $\hat{f}$ is mapped with the corresponding diffracted waves $U^j_{dif,it}$ according to the Fourier diffraction theorem (II.18).
- Step 3: Constraints C are applied on the real and imaginary parts of the updated retrieved object.
- Step 4: Using the Fourier diffraction theorem (II.18) as a direct model, a new set of complex waves $U^j_{tot,it}$ is simulated.

This iterative loop is schemed in figure IV.22. Its number of iteration is noted nb^{GS}_{it}. As explained in chapter II, section 3, the interpolation in the Fourier domain cannot be linear. Consequently, for the direct model and the reconstruction algorithm, the interpolations in the Fourier domain are based on the nearest-neighbor technique.

Given the microscope geometry, the angular coverage of the lighting positions is very limited. This algorithm is not efficient to properly compensate this lack of information in the dataset. It is consequently only used on a few iterations to initialize the reconstruction. Then, a new step is added in the loop, between steps 3 and 4, leading to the blue loop in figure IV.22. This step 3.2 consists in regularizing the object. To do so, a minimization problem is defined as:

$$\boxed{J(O) = \mu_{L_1} \underbrace{\frac{1}{nb^v_x nb^v_y nb^v_z} \|O\|_{L_{1,\epsilon}}}_{\text{sparsity constraint } J_{L_1,\epsilon}(O)} + \mu_\nabla \underbrace{\frac{1}{nb^v_x nb^v_y nb^v_z} \|\nabla O\|_{L_{1,\epsilon}}}_{\text{gradient sparsity constraint } J_{\nabla,\epsilon}(O)}} \tag{IV.39}$$

and new minimization problem:

$$\boxed{\tilde{O} = \underset{C(O)}{\operatorname{argmin}} J(O) = \underset{C(O)}{\operatorname{argmin}} \mu_{L_1} J_{L_1,\epsilon}(O) + \mu_\nabla J_{\nabla,\epsilon}(O)} \tag{IV.40}$$

where O can either be the refractive index δn or the scattering potential f. The L_1 norm and the 3D gradient ∇. have the same definition than in the previous section 3. Their gradient is given by appendix D. $C(O)$ are the constraints on the domain of definition of O previously defined for the Gerchberg-Saxton loop.

The resolution of the minimization problem (IV.40) is performed with the same convex optimization algorithm [90] introduced in the previous methods, in sections 2 and 3 of this chapter.

The aim of this regularization is to reduce the artifacts of the reconstructions due to the limited angular coverage and the lack of phase information in the dataset

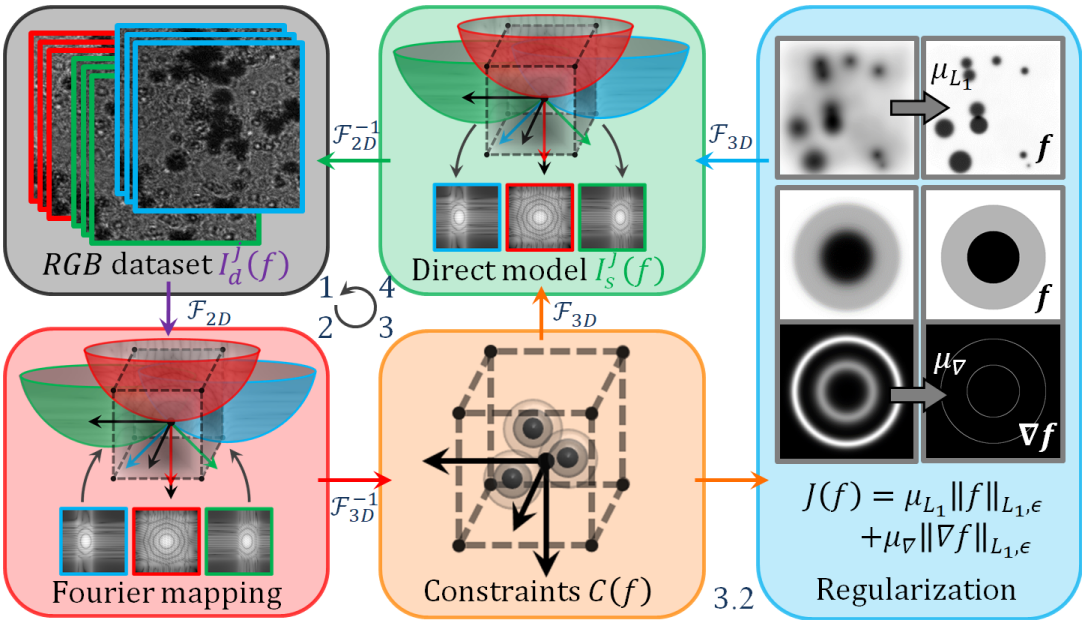

Figure IV.22: Scheme of the Gerchberg-Saxton algorithm. Step 1: The algorithm is initialized with a set of complex waves. Their modulus is directly the square root of the recorded intensities. Their unknown phase is initialized to 0. Step 2: These waves are used to map the 3D Fourier domain of the object $\hat{f}$ using the Fourier diffraction theorem. Step 3: Domain constraints are applied on the simulated object f. Step 4: The new object is used to simulate a new set of complex waves using the Fourier diffraction theorem as a direct model. Step 1: The algorithm loops to start a new iteration. Data fidelity is performed by keeping the simulated phase and replacing the simulated modulus by the recorded dataset. In between the steps 3 and 4, an additional step can be added: step 3.2. After applying the constraints, the object is regularized with a sparsity constraint on the object and its gradient.

recorded by the sensor. To accelerate the cleaning of the artifacts, there is no data fidelity term in the cost function (IV.39). The data fidelity is only ensured later in the loop by step 4. As a consequence, the solution of the minimization problem (IV.40) is the volume $O = 0$. Thus, a limited number of iterations nb_{reg}^{GS} is performed, on which the sparsity prior efficiently cleans the noise and artifacts with low values while the edge-preserving regularization maintains high the signal on the objects limiting their convergence toward the trivial solution 0.

Let's mention here that to directly reconstruct the refractive index δn, an inversion formula for equation (II.7) is needed to get δn from the scattering potential f. Mathematically, this inversion is not possible because of the squaring and it exists two solutions:

$$\delta n\left(f, n_0\right) = n_0\left(\left|1+f\right|^{0.5} e^{i\varphi(1+f)/2+s\pi} - 1\right) \tag{IV.41}$$

where s can be equal to 0 or 1 and $\varphi(c)$ gives the argument of a complex number in the range $[0, 2\pi]$. Nevertheless, as stated above, δn cannot have a negative imaginary

part[26]. It implies that:

$$\varphi\,(1+f)\,/2 + s\pi \in [0,\pi] \Rightarrow s = 0 \tag{IV.42}$$

Hence, the inverse formula can be defined as:

$$\boxed{\delta n\,(f, n_0) = n_0\left(|1+f|^{0.5}\,e^{i\varphi(1+f)/2} - 1\right)} \tag{IV.43}$$

Finally with this algorithm, when the step 4 is reached, the data fidelity of the simulated complex waves can be strongly degraded. Indeed, the regularization step forces the objects to be localized and cleans the noise. As in the previous method, section 3, this new set of simulated waves can consequently be used to refine the alignment of the experimental data. This improves the overall reconstruction of the object. To do so, between step 4 and step 1, the experimental data are aligned with the simulated intensities via a least squares minimization of the difference between the latter and the former as detailed in appendix C.

This alignment step is time consuming and is not performed at each iteration of the loop.

In the following, the number of regularized loops of the Gerchberg-Saxton algorithm is noted $nb_{it}^{GS,r}$.

4.2 Numerical simulations

To test the efficiency of the proposed algorithm, total wave fronts are simulated for a known numerical object presented in figure IV.23.a. It is composed of $256 \times 256 \times 200$ voxels of $1.67^3\ \mu m^3$ for a volume of $427 \times 427 \times 344 = 6.1\ 10^7\ \mu m^3$ with cells of refractive index difference of $\delta n = 0.005i$ with a normal dispersion of $\delta n/10$. These cells are randomly spread in ten clusters of three cells of identical refractive index and radius $r_c = 10\ \mu m$ and four trains of 200 cells of identical refractive index and radius $r_c/3$ crossing the volume.

32 holograms of 256×256 pixels are simulated with the Fourier diffraction theorem by padding the 2D and the 3D spaces and using a linear interpolation, for an illumination direction of $\theta = 45°$ and $\varphi \in [0°, 285]$ ($\Delta\varphi = 9.1°$), for the three RGB wavelengths $\lambda \in \{640\ nm, 520\ nm, 450\ nm\}$, in water[27] $n_0 = 1.33$ and for a sensor distance of $z_s = 1\ mm$. To test the robustness of the iterative phase retrieval algorithm, a Gaussian noise is added to the intensities with $\sigma = 0.1$ (see figure IV.23.b).

Different values are tested for μ_{L_1} and μ_∇. It is also tested to only apply the L_1 regularization or the ∇-regularization. In the first case, the regularization tends homogeneously toward zero in a few iterations and the regularization step is useless. In the second case, the background noise and the twin-image artifacts in the 3D reconstructions are neither cleaned nor reduced and then get amplified in the Gerchberg-Saxton loop.

[26]This is physically impossible. Otherwise the object would behave as a light emitter.

[27]The effective angle for the reconstruction is then $\theta_0 \simeq 32.1°$ according to the analysis done in chapter III, section 5.

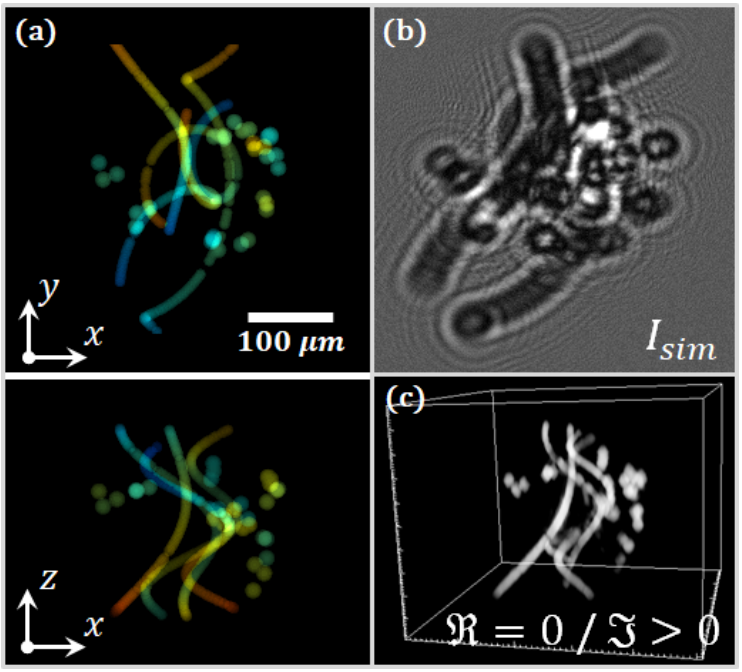

Figure IV.23: (a) xy and xz-average intensity projections of the simulated object. On each view, the colors codes for the depth: the shallowest in blue, the deepest in red. (b) Example of a simulated noisy hologram in the green channel for $\varphi = 0°$. (c) 3D rendering of the reconstructed volume with the regularized Gerchberg-Saxton algorithm under the constraints $\mathcal{R}(f) = 0$ and $\mathcal{I}(f) \geq 0$.

These studies are not presented here. In all the reconstructions presented in this thesis, a fixed ratio of $\mu_\nabla/\mu_{L_1} = 1.25$ is used.

Several values for nb_{reg}^{GS} are tested (also not presented here). $nb_{reg}^{GS} = 10$ appeared to be a good compromise between a too low and a too high number of iterations. If the number of iterations is too low the cleaning of the artifacts is not efficient and the Gerchberg-Saxton loop puts more artifacts in the reconstructions than the regularization step is capable of processing. If the number of iterations is too high, as mentioned above, the minimization (IV.40) rapidly converges toward 0 and the small objects are erased and consequently not reconstructed.

The reconstructions presented here are based on the scattering potential f with $nb_x^p = nb_y^p = 512$, $dx^p = dy^p = 1.67\ \mu m$, $nb_x^v = nb_y^v = 256$, $nb_z^v = 200$, $dx^v = dy^v = dy^v = 1.67\ \mu m$, $z_s = 2\ mm$, $n_0 = 1$ with two different constraints on the domain of definition of f: $C(f) = \{f/\mathcal{R}(f) \geq 0, \mathcal{I}(f) \geq 0\}$ and $C(f) = \{f/\mathcal{R}(f) = 0, \mathcal{I}(f) \geq 0\}$.

The two reconstructions are run on 15 iterations with $nb_{it}^{GS} = 6$ and $nb_{it}^{GS,r} = 9$ (see figure IV.22). The results are presented in figure IV.24.

The role of the different elements of the algorithms can be well identified.

The first iteration $it = 1$ is equivalent to the Fourier mapping method introduced in chapter III, section 4 just adding a projection of the results on the constraints $C(f)$. As previously, the twin-image artifacts are presented around the

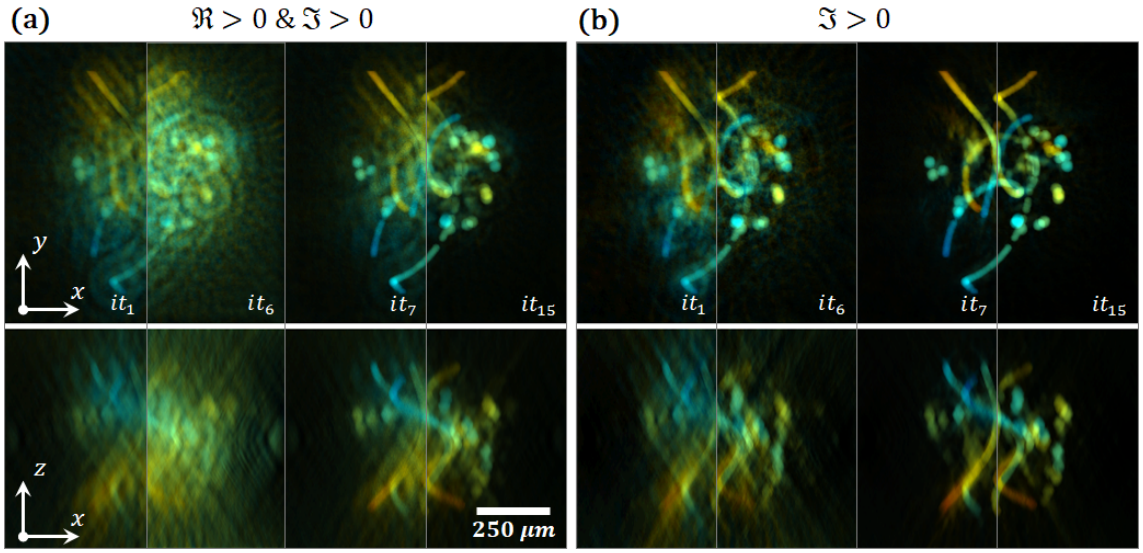

Figure IV.24: xy and xz-average intensity projections of the reconstructed volume at different iterations $it \in \{1, 6, 7, 15\}$ of the Gerchberg-Saxton loop for two different domain of definitions: $C(f) = \{f/\mathcal{R}(f) \geq 0, \mathcal{I}(f) \geq 0\}$ and $C(f) = \{f/\mathcal{R}(f) = 0, \mathcal{I}(f) \geq 0\}$.

objects and the background is blurred and noisy.

After a few step of the Gerchberg-Saxton algorithm at $it = 6$, the choice of the constraints on the domain of definition appears to be critical. If the constraint is not strong enough, as in figure IV.24.a, the only effect of the algorithm is to enhance the amplitude of the reconstruction. But the artifacts are also proportionally enhanced. In figure IV.24.b, a more limiting constraint is applied and even if the background is still noisy, the twin-image artifacts completely disappear[28].

Even after just one regularized loop[29] at $it = 7$ the effect of the regularization can be seen: a huge part of the noise in the background is erased or is at least smoothed to a negligible value. On the contrary, as expected, the objects are more localized with sharper edges and an enhanced contrast. In figure IV.24.a the twin-image, more spread and consequently more sensitive to the L_1-regularization than the ∇-regularization, tends also to be smoothed with the background rather than being enhanced with the object signal.

The following iterations continues this cleaning effect and at the end, at $it = 15$, a huge part of the artifacts has been removed. In figure IV.24.a some noise remains at the center of the volume in the crowded area. The strong regularization in figure IV.24.b gives an almost perfect result compared with the initial volume in figure IV.23.a, even in this difficult area. A 3D rendering of this reconstruction is shown in figure IV.23.b. The main remaining artifact is directly the shadowing effect

[28] One could draw a parallel with the results obtained in chapter IV, section2 for the 2D phase retrieval algorithm. The twin-image is contained in the bright/positive parts of the transmissive plane. In 3D they seem to be contained in the real part of the scattering potential.

[29] That is to say after a regularization via step 3.2 of figure IV.22 and a Fourier mapping.

due to the limited opening angle θ which prevents from reconstructing the simulated cells as spheres but rather as a double conical shape elongated along the z-axis.

More tests should be done combining objects with purely real or purely imaginary or combined refractive index δn to test the efficiency of the constraints $C(f)$ in the different cases.

4.3 3D reconstructions on experimental data

This section presents some tests of the regularized Gerchberg-Saxton algorithm on experimental data acquired on two different cell cultures: prostate epithelial cells (RWPE1) grown in Matrigel® capsules and murine epithelial cells encapsulated and grown in alginate shells with tubular shape.

RWPE1 cell culture The reconstructed dataset[30] is composed of 31 holograms in the three RGB channel $\lambda \in \{640\ nm, 520\ nm, 450\ nm\}$ of 1024^2 pixels of $1.67^2\ \mu m^2$. Their alignment is provided by the inverse problem approach on the full resolution reconstruction introduced in the next section 5.3.

The reconstruction parameters for the 3D volume are $\varphi \in \{0°, 285°\}$, $\Delta\varphi = 9.4°$, $\theta = 45°$, $\lambda = 520\ nm$, $z_s = 3.52\ mm$. As mentioned at the end of the previous chapter in section 5, a scaling factor is applied on the z-axis using equation (III.39) as the data are reconstructed for an angle $\theta = \theta_{air} = 45°$: $z_0/z_{air} = 1.5930$. The reconstructed volumes[31] is composed $512 \times 512 \times 300$ voxels of $3.34 \times 3.34 \times 3.34\ \mu m^3$ for a final volume of $1.7 \times 1.7 \times 1.6\ mm^3 \simeq 4.7\ mm^3$.

The reconstruction is based on the scattering potential f with a positivity constraint on the domain of definition: $C(f) = \{f / \mathcal{R}(f) \geq 0, \mathcal{I}(f) \geq 0\}$. The 2D and 3D spaces are zero-padded. The reconstruction is run on 100 iterations with $nb_{it}^{GS} = 11$ and $nb_{it}^{GS,r} = 89$ (see figure IV.22). The results are presented in figure IV.25. For the sake of visibility, only a part of the volume along the z-axis is pictured, the rest of the volume being mainly empty.

Looking at figure IV.25.b, especially at the center of the field of view, the algorithm shows its capability to work on big objects which are strongly overlapping. The small objects are well localized and contrasted with a clean and dark background. Their spatial elongation along the z-axis seems limited and in the same order of magnitude than their xy-extension. On the xy-projection the objects have sharp edges and there is no evident sign of twin-image artifact. It is possible to identify the edges of the capsules which are completely invisible on the raw holograms of figure IV.25.a. They shape a honeycomb structure on the xy-projection.

Comparing the figures IV.25.b-e, the same features than in the simulations previously analyzed can be identified. Between $it = 1$ and $it = 11$, the simple Gerchberg-Saxton loop increases the reconstructed amplitude and the background appears very noisy with twin-image around the big objects. After the first regularized loop,

[30] The cells conditioning and the culture protocol of this experiment are given in the next section 5.1.

[31] $512 \times 512 \times 300$ voxels of $3.34^3\ \mu m^3$ before scaling.

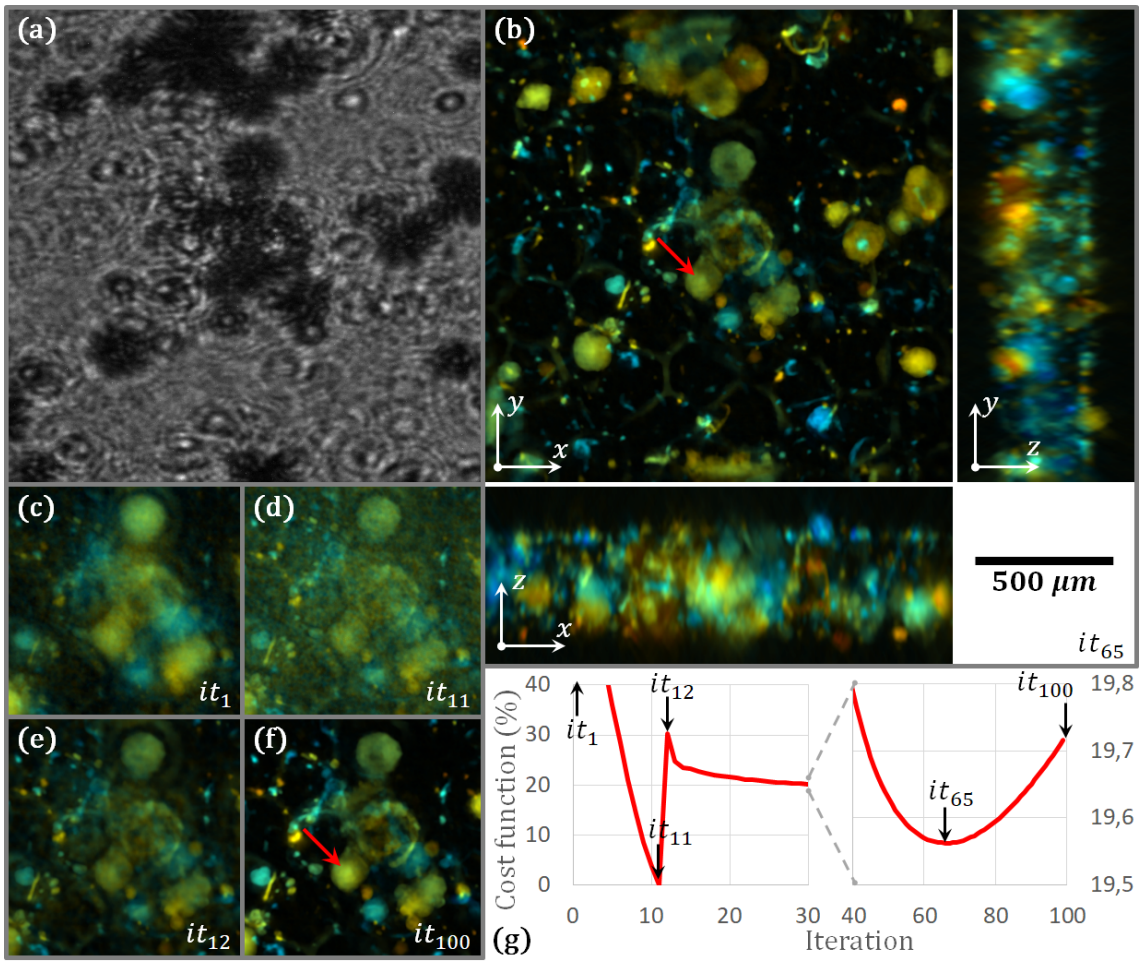

Figure IV.25: Reconstructed scattering potential of a RWPE1 cell culture in Matrigel® capsules. (a) Raw data in the green channel $\lambda = 520\ nm$. (b) Orthogonal average intensity projections of the reconstructed volume at iteration $it = 65$. (c-f) xy-average intensity projections at the center of the reconstructed volume at different iterations $it \in \{1, 11, 12, 100\}$. The red arrow points at a diverging area. On each view, the colors codes for the depth: the shallowest in blue, the deepest in red. (g) Evolution of the data fidelity term $J_d(f)$ during the iterations normalized to its minimum and maximum values. Black arrows point at the iterations shown on (b-f).

at $it = 12$, a large part of the background has seen its noise diminish but the twin-image is still present. During the iterations, the contrast of the reconstructed signal continues to increase as the twin-image disappears to reach the results of figure IV.25.b at $it = 65$.

The effects of the regularization can also be seen on the data fidelity term[32] $J_d(f)$ computed at each iteration. Between $it = 11$ and $it = 12$ the first application of the regularization strongly degrades the data fidelity whose cost function starts again

[32]Introduced in the previous section 3 in equation (IV.18).

to diminish afterward but with a lower convergence rate.

Something unexpected happens at $it = 65$. The convergence curve reaches a local minimum and then starts to diverge. This is due to the regularization step which begins to degrades the reconstruction and its data fidelity more than the Fourier mapping is able to compensate. This can be seen in figures IV.25.b,f where red arrows point at a large cluster of cells whose reconstructed amplitude starts to diverge.

Murine epithelial cell culture In this cell culture[33], epithelial cells (EpH4 J3B1A, murine mammary gland derived cells) are encapsulated and grown in alginate shells with tubular shape. These alginate tubes are obtained with a protocol adapted from [93]. Briefly, a coaxial flow device is obtained by 3D printing (Micro Plus Hi-Res, EnvisionTEC) and is used to generate a multi-layered jet. This method leads to the formation of an external alginate hydrogel shell, coated internally with a layer of Matrigel® matrix (Corning, #354248, New York, USA) in order to reconstitute the extracellular matrix. A Matrigel® concentration of 40% v/v is used to completely cover the inner wall of the alginate tube.

The principle of the microfluidic device is represented in [94]: the solution containing both the cells and the Matrigel® is injected in an inner channel, an insulating layer is made by injection of a 300 mM solution of sorbitol (Merck) in an intermediate channel and a 2.5% w/v solution of sodium alginate (Protanal LF200S; FMC) is injected in an external channel. The final multi-layered jet at the exit of the microfluidic device is directed in contact with a gelation bath containing 100 mM calcium chloride $CaCl_2$ (VWR International).

Once alginate tubes are formed, they are washed with DMEM medium (Dulbecco's Modified Eagle's medium - Invitrogen) supplemented with 10% v/v FBS (Fetal Serum Bovin - Invitrogen), 1% NEAA (MEM Non-Essential Amino Acids - Invitrogen) and 1% antibiotics (penicillin-streptomycin 10000 $U.mL^{-1}$ - Invitrogen) in order to remove the calcium chloride. They are then maintained in DMEM medium supplemented with 10% v/v CS (Calf Serum - Invitrogen) and 1% antibiotics (penicillin-streptomycin 10000 $U.mL^{-1}$ - Invitrogen) in humidified atmosphere containing 5% CO_2 at 37°C.

Two acquisitions sets are captured on two different Petri dishes with the new prototype that is presented in the next chapter V, section 1. The reconstructed datasets are composed of 3×32 holograms of 1024^2 pixels of 3.34^2 μm^2 acquired with $\varphi \in \{0°, 305°\}$, $\Delta\varphi = 9.8°$ in the three RGB channels $\lambda \in \{640\ nm, 520\ nm, 450\ nm\}$. The final 3D grids are made of $512 \times 512 \times 256$ voxels of 6.68^3 μm^3 for a final volume of $3.4 \times 3.4 \times 1.7$ $mm^3 \simeq 20$ mm^3.

The data alignment is done in the green channel by the least mean squares minimization algorithm on the raw data using a cell hologram as reference. This alignment is then refined using the three wavelengths available with manual supervision.

[33]Kindly given by Caterina Tomba from Aurélien Roux's Lab at the University of Geneva.

The first acquisition is also reconstructed at higher resolution with extracted regions of interest of 1024^2 pixels of $1.67^2\ \mu m^2$ for a final 3D grid of $512 \times 512 \times 256$ voxels of $3.34^3\ \mu m^3$ and a final volume of $1.7 \times 1.7 \times 0.85\ mm^3 \simeq 2.5\ mm^3$.

For the three reconstructions, only a padding on the z-axis $nb_z^{pad} = 2 \times nb_z$ is applied. The iterations started with a batch of 6 not regularized iterations. Then, all the iterations are regularized and a refinement of the data alignment is performed every 3 iterations[34].

Concerning the reconstruction parameters, the angle $\theta = 45°$ is corrected to get the effective angle[35] in water $\theta_0 \simeq 32.1°$. A similar constraint $C(f) = \{f/\mathcal{R}(f) \geq 0, \mathcal{I}(f) \geq 0\}$ on the domain of definition of the scattering potential f is applied for the three reconstructions. Finally, for the first set of acquisitions, $z_s = 2.95\ mm$ and for the second, $z_s = 2.875\ mm$.

As previously, for the sake of visibility, only a part of the volume along the z-axis is pictured, the rest of the volume being mainly empty.

Figure IV.26 shows the results of the reconstruction of the first data set whose number of iterations is pushed to $it = 551$. Figure IV.26 shows the reconstruction at higher resolution of the center of the volume. The iterations are stopped at $it = 69$. Figure IV.28 shows the results of the reconstruction of the second data set whose number of iterations is pushed to $it = 298$.

Once again, it appears in all the figures that between $it = 1$ and $it = 6$, the simple Gerchberg-Saxton loop increases the reconstructed amplitude and the background noise without any influence on the reduction of the twin-image artifacts. The first regularized loop smooths the noise but is inefficient in removing the artifacts due to the lack of phase information in the data. The following regularized loops efficiently clean this artificial signal without erasing the small objects and isolated cells.

All these effects are very marked on the blue areas (the shallowest) in the empty spaces which are only cleaned during the regularized loops.

Another effect of the ∇-regularization is to fill the signal of the tube wall (see figure IV.26.a). At first, at iterations 6 and 7, the tube wall and its twin-image have similar intensities. At $it = 83$, the twin-image is removed but not the tube whose intensity is nevertheless low. At $it = 551$, the tube signal has increased.

The usefulness of the regularization and the refinement of the data alignment steps is also seen in the xz-projections of figures IV.26 and IV.27. First of all the global background noise is removed and secondly, the spatial elongation of the objects along the z-axis is reduced. But once again, it is not sufficient to reconstruct the full section of the tube. As previously for the Matrigel® capsules, it is only visible in the central xy-plane.

One can note that the influence on the reconstruction edges of the absence of padding is very limited, especially in the two reconstructions at very low resolution. This comes from the limited spatial coherence of the incident wave front. The interferences have a spatially limited impact outside the field of view.

[34]Excepted for the first set of acquisitions reconstructed at low resolution. The refinement step is stopped after $it = 75$.

[35]According to the analysis done in chapter III, section 5.

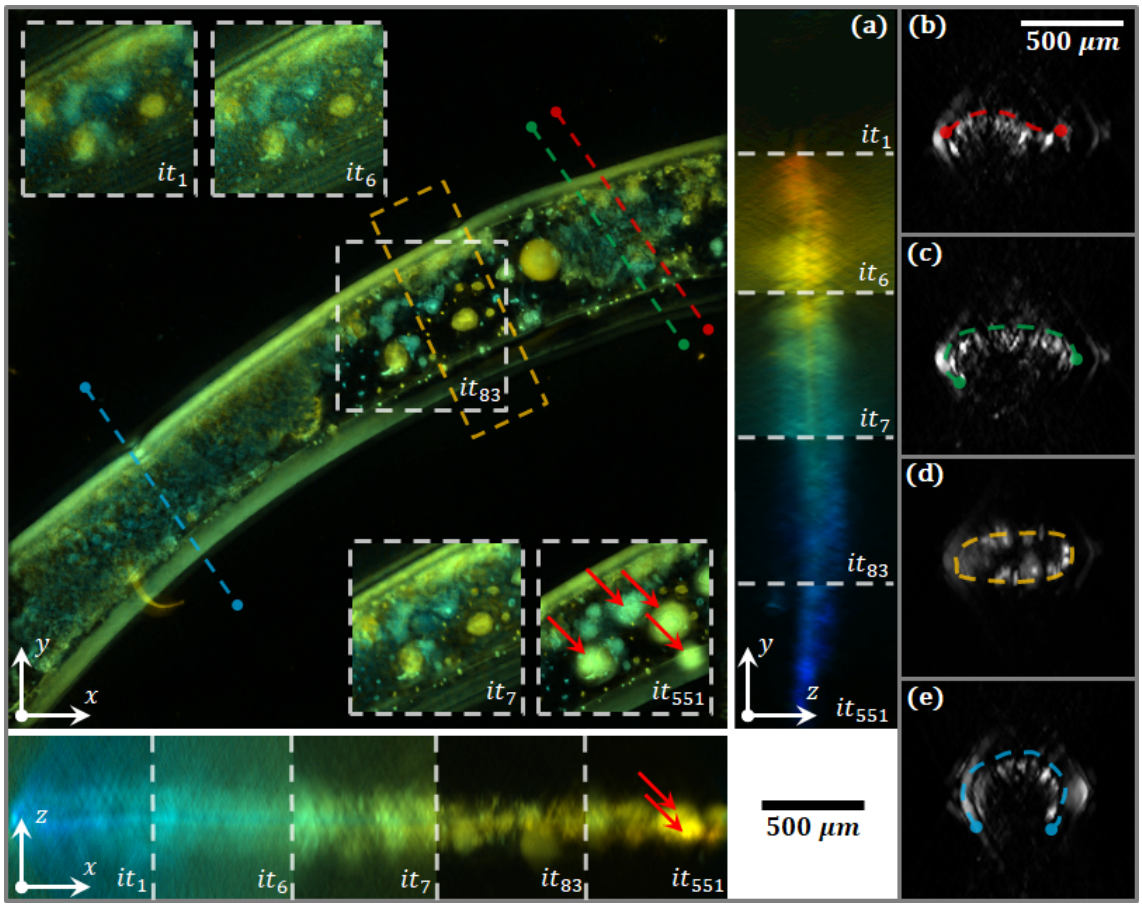

Figure IV.26: Reconstructed scattering potential of murine epithelial cells encapsulated and grown in alginate shells with tubular shape. (a) Orthogonal average intensity projections of the reconstructed volume at iteration $it = 83$. On the xy-view, the medallions present a given region of interest at different iterations $it \in \{1, 6, 7, 83, 551\}$. On the xz and yz-views, the medallions present the reconstructions at different iterations on different parts of the projections. (b-e) Transversal views of the 3D volume along their corresponding colored lines on (a). (b), (c) and (e) are slices. (d) is a maximum intensity projection of an extracted volume, cored along the orange rectangle in (a).

Looking at the transversal slices (b-e) in figure IV.26, the lens-free microscope shows all its potential to study large scale structures[36]. Despite the elongation of the objects on the z-axis and the fact that the tube section is not reconstructed, the tubular shape is clearly visible when scattering objects are lying on the tube surface. The tube section can either be circular as expected (e) or squeezed (c-d). In (b), the red curve follows a bump which can be interpreted as a detachment of the cell layer from the tube wall[37]. Figures IV.26.d-e shows the possibility to reconstruct

[36]Let's remind here that the field of view is $3.4 \times 3.4 \times 1.7\ mm^3 \simeq 20\ mm^3$.

[37]A phenomenon observed by Caterina Tomba and her colleagues and that they would like to study with more details on large scales.

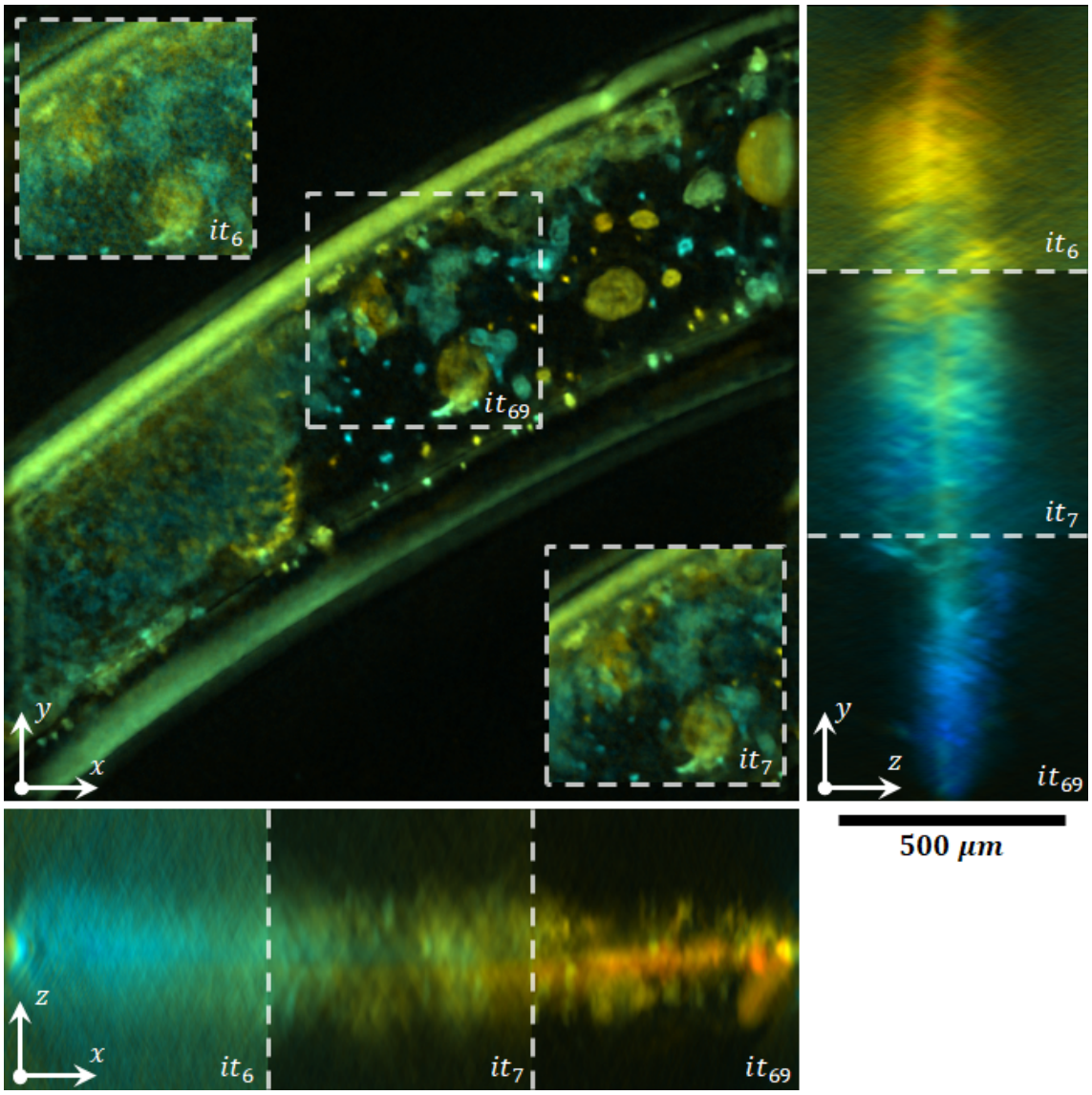

Figure IV.27: Orthogonal average intensity projections of the cell culture presented in figure IV.26 reconstructed at higher resolution at iteration $it = 69$. On the xy-view, the medallions present a given region of interest at different iterations $it \in \{1, 6, 69\}$. On the xz and yz-views, the medallions present the reconstructions at different iterations on different parts of the projections.

the layer even if the objects are slightly overlapping.

In figure IV.29, the data fidelity terms show a small bump when the first regularized loop is run which degrades the data fidelity similar to that observed in figure IV.25.g. But more noticeable, the two low resolution reconstructions also show a divergence after a given number of iterations stressed by the black arrows.

The effect mentioned earlier about the amplitude divergences on extended objects is even more visible in these two figures where all the big objects "expand" and diverge as seen in the medallions of the last iterations. The red arrows point at some of

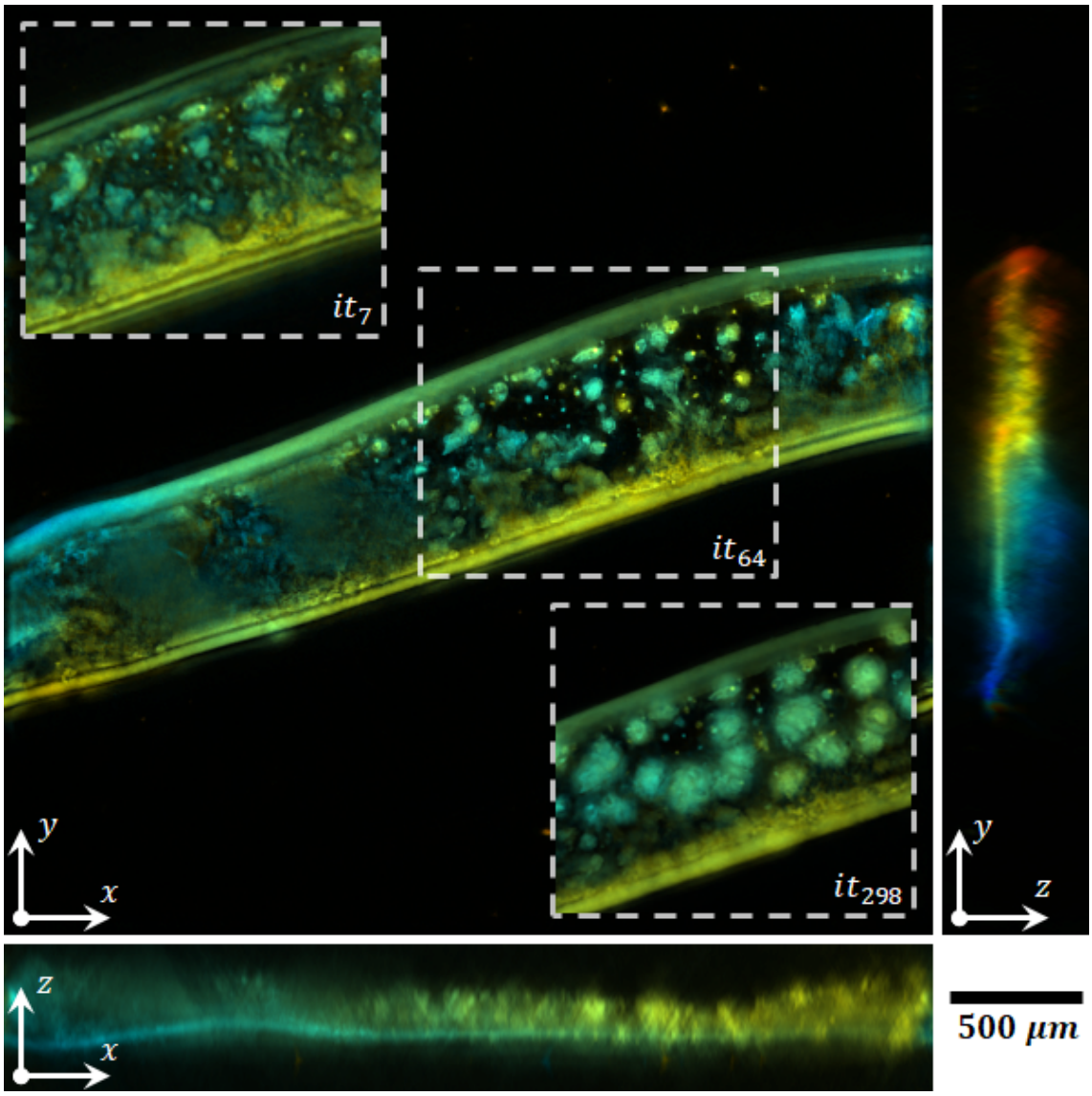

Figure IV.28: Orthogonal average intensity projections of a cell culture similar the one presented in figure IV.26 at iteration $it = 64$. On the xy-view, the medallions present a given region of interest at different iterations $it \in \{7, 64, 298\}$.

them in the xy and xz-projections in figure IV.26.a.

Once again, it appears that it is not useful to execute a too large number of iterations. At a given iteration, the reconstruction starts to diverge.

5 Comparison of the algorithms

The objective of this section is to compare the main algorithms which are developed in this thesis.

To summarize, four algorithms are implemented to overcome the two main pit-

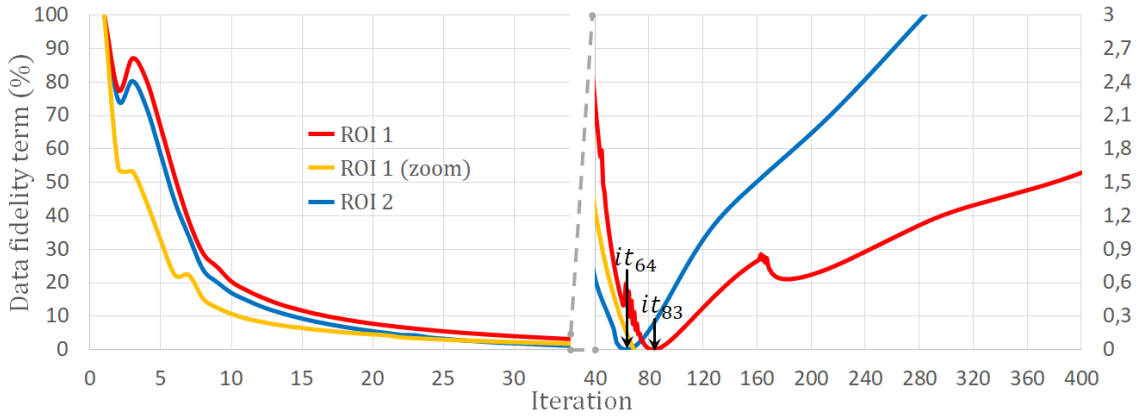

Figure IV.29: Evolution of the data fidelity term $J_d(f)$ during the iterations of the reconstructions presented in figures IV.26 (ROI 1), IV.27 (ROI 1 (zoom)) and IV.28 (ROI 2). The curves are normalized by their first value.

falls of lens-free tomographic acquisitions: the lack of phase information in the in-line holographic configuration and the limited angular coverage. The four designed fully 3D reconstruction algorithms are all based on the Fourier diffraction (II.18) theorem as used in standard diffractive tomography [44, 45, 46, 71]. They lead to an increasing reconstruction quality at the cost of an increased complexity. For the sake of clarity, in the following, they are referenced as:

- **Method III.4: the Fourier mapping method** - Introduced in chapter III, section 4, it reintroduces an approximation of the unmeasured phase by a phase ramp in the dataset.
- **Method IV.2: the 2D phase retrieval method** - Introduced in chapter IV, section 2, it performs an iterative phase retrieval based on a regularized inverse problem approach on each 2D acquisition. In comparison to the former method, this algorithm handles better the lack of phase information in the data acquisition process by estimating a realistic guess for it.
- **Method IV.3: the 3D inverse problem approach** - Introduced in chapter IV, section 3, it also uses the regularized inverse problem formalism, but directly applied on the whole dataset and the unknown 3D object, the Fourier diffraction theorem providing the direct model. Doing so, at the cost of an increased computation time, it overcomes the limited number of acquisitions and admissible angles around the sample by directly adding constraints on the 3D object.
- **Method IV.4: the regularized Gerchberg-Saxton algorithm** - Introduced in chapter IV, section 4, it is a hybrid algorithm alternating a Gerchberg-Saxton type loop between the experimental holograms and the reconstructed object and a step dedicated to the regularization of the object. This method also provides a solution for the unknown phase on the sensor and limited angular coverage.

To compare the reconstruction methods in terms of artifact reduction, signal-to-noise ratio and computation time, they are tested on two experimental datasets: a HUVEC endothelial cell culture and a RWPE1 prostate cell culture grown in a 3D extracellular matrix of Matrigel®. The first one presents a planar geometry and the second one is a complex fully 3D structure.

In the following, the cell cultures experiments are introduced. Then, reconstructions with the four algorithms are analyzed and compared. The best algorithms are finally compared with phase contrast and fluorescence microscopy.

This section is mainly inspired from the published paper in the Applied Optics journal [88]. Nonetheless, some of the results and conclusions differ. Indeed, the paper only compares the first three algorithms. This section introduces also the regularized Gerchberg-Saxton algorithm. Furthermore, in the paper, for the first two methods, when several coefficients are falling into the same voxel in the Fourier mapping step, only the first one is considered. As mentioned above, it has been seen later that taking into account all these coefficients by averaging them[38] change a lot the quality of the reconstructed background and consequently of the global reconstruction[39].

5.1 Biological samples

The different 3D reconstruction approaches are tested and compared on two types of cell models which lead to different morphologies when grown in 3D scaffolds.

Human Umbilical Vein Endothelial Cells (HUVEC)

HUVEC cells (Millipore) are primary cells extracted from human neonatal umbilical cords used for many vascular biology research applications, such as inflammation, angiogenesis and blood clotting. The culture is maintained in a subconfluent state in culture Petri Dish (113 cm^2) coated with fibronectin at 37°C. HUVEC cells are grown in EndoGro basal medium (Millipore) supplemented with 5 ng/mL of rhVEGF, rhEGF, rhFGFb respectively, 15 ng/mL rh IGF-1, 10 mM L-glutamine, 0.75 U/mL heparin sulfate, 1 $\mu g/mL$ hyroscortisone hemisucinate, 50 $\mu g/mL$ ascorbic acid, and 10% FBS.

For the final cell culture, the cells are grown in Matrigel® (BD Biosciences) according to a no top coat protocol: the cells are directly seeded on the top of a Matrigel® bed, laid down in the Petri dish and can freely move on this 3D surface. For polymerization, Matrigel® is incubated for 30 minutes at 37°C and 4000 to 10000 cells are seeded and allowed adhering for approximately 45 minutes. Then their complete medium is slowly poured over the attached cells with 4 to 5% of Matrigel®.

All cells are routinely cultured in a humidified atmosphere with 5% CO_2 at 37°C for a day.

[38] As done in this chapter.

[39] The interested reader can compare the results with methods III.4 and IV.2 presented in [88] and in this section.

Prostate Epithelial Cells (RWPE1)

RWPE1 cell line is obtained from ATCC (ATCC CRL-11609). This cell line is derived from non-neoplastic human prostate epithelial cells by immortalization with human papillomavirus. RWPE1 cells are used as a model for normal prostate epithelial cell behavior as characterized by a polarized acinar morphology in 3D cultures. RWPE1 cells are maintained in KSFM (Life Technologies) supplemented with 5 ng/mL Epidermal Growth Factor (Life Technologies), 50 $\mu g/mL$ Bovine Pituitary Extract (Life Technologies) and 1% Penicillin-Streptomycin (Life Technologies). Cells are passaged upon 70% confluence and seeded at 20000 cells/mL density. All cells are routinely cultured in a humidified atmosphere with 5% CO_2 at 37°C.

Cell number and viability is measured by trypan blue dye exclusion staining using an EVE™ Automatic Cell Counter (NanoEnTek).

For the final 3D cell culture, Matrigel® (BD Biosciences) capsules are produced using a microfluidic chip with flow focusing geometry as described in [52, 95]. For the acinar morphogenesis assay, RWPE1 cells in Matrigel® capsules are allowed developing into clusters by clonal division for 7 days in KSFM (Life Technologies) supplemented with 50 ng/mL Epidermal Growth Factor (Life Technologies), 2% Foetal Bovine Serum (Life Technologies), 1% Matrigel® and 1% Penicillin-Streptomycin (Life Technologies) in multiwell plates. Cell culture medium is changed every two days.

Finally, capsules are washed twice with medium and are then embedded in Matrigel® deposited at the center of Greiner petri dishes (Sigma-Aldrich) and allowed polymerizing for 30 minutes at 37°C. Culture medium is subsequently added.

Acquisitions of the microscope views (RWPE1)

For comparison purpose, microscope acquisitions are performed on the RWPE1 cell culture. The clusters in capsules are labelled with 10 μM CellTracker™ Orange CMTMR dye (Thermo Fisher Scientific) in media for 30 minutes at 37°C. Finally, the RWPE1 culture is fixed using 2% paraformaldehyde 1% glutaraldehyde for 20 min.

During these steps, the cell culture could have been slightly modified and some structures washed away. As the aim is to compare the z-positioning and the shape of some objects, it is however deemed sufficient.

z-stacks of phase and fluorescence images are acquired using an AxioObserver.Z1 inverted microscope (Zeiss) with a N-Achroplan 5x/0.13 Ph0 air objective mounted with an AxioCam 503 monochrome digital camera. Acquisitions are performed on 150 slices equally spread[40] on $\Delta z = 300\ \mu m$.

[40] In the air, not in the culture medium.

5.2 3D reconstructions

Reconstruction parameters

The two 3D cell cultures are similarly processed, working directly on their scattering potential f.

Acquisitions - Both datasets are composed of 3×16 acquisitions done at 16 different angles $\varphi \in \{0°, 282°\}$, $\Delta\varphi = 18.8°$ in the three available wavelengths of the RGB LED $\lambda \in \{630\,nm, 520\,nm, 450\,nm\}$. In each dataset, a region of interest of 1024×1024 pixels of $1.67^2\ \mu m^2$ is selected[41]. The only limitation in this selection is that the observed region must be in all the pictures of the dataset. A representative region of each dataset is chosen by encompassing several typical structures, *i.e.* branches for the HUVEC network, and capsules and clusters for the RWPE1 culture.

Reconstruction volume - To reduce the computing time and the memory consumption, the final reconstruction[42] is composed of $512 \times 512 \times 300$ voxels of $3.34 \times 3.34 \times 5.32\ \mu m^3$ for a global volume of $1.7 \times 1.7 \times 1.6\ mm^3 = 4.7\ mm^3$. Knowing that the reconstruction angle is $\theta = 45°$ in the air, the voxels are not orthonormal to take into account the distortion on the z-axis induced by the refraction between the air of refractive index $n_{air} = 1$ and the culture medium[43] of refractive index $n_0 = n_{H_20} = 1.33$. For the HUVEC cell culture, $z_s = 3.3\ mm$ and for the RWPE1 cell culture, $z_s = 3.32\ mm$. For the sake of visibility, only a part of the volumes along the z-axis are displayed, the rest of the volume being mainly empty.

Data alignment - The initial data alignment is done by the least mean squares minimization algorithm on 2D reconstructed data. This alignment is used to initialize method IV.3. The results of the alignment refinement steps of this method are then used to initialize the three other methods.

Method IV.2 - The three available wavelengths are used together to improve the 2D phase retrieval via the minimization problem (IV.6). As mentioned earlier the effective 2D transmissive plane δt is supposed to be independent of the illumination wavelength. To insure non-emissive objects, the constraint $C(\delta t)$ is chosen to force δt to have a negative real part: $\mathcal{R}(\delta t) \leq 0$ as explained earlier for method IV.2. l_{coh} is set to 500 μm and the hyperparameters to $\mu_{L_1} = 0.5$ and $\mu_\nabla = 0.1$. The number of iterations is fixed to $nb_{it}^{PR} = 100$.

Method IV.3 - For the 3D inverse problem approach, the iterative process is split in seven batches of $nb_{it}^{IP} = 10$ iterations in between which a data alignment refinement is performed. As explained earlier, the constraints are set to $\mathcal{R}(f) \geq 0$ and $\mathcal{I}(f) \geq 0$. It is also mentioned that the values of the hyperparameters can be changed during the iterations to first favor the alignment step and then the reconstruction quality. For example, one can start with a small regularization on

[41] $1.7^2\ mm^2$

[42] $512 \times 512 \times 300$ voxels of $3.34^3\ \mu m^3$ before scaling.

[43] See chapter III, section 5.

sparsity and increase the hyperparameter μ_{L_1} afterwards to enforce the constraint. To do so, μ_{L_1} is set to vary from 0 to 100 ($[0, 0, 0, 10, 10, 100, 100]$ for the HUVEC dataset and $[0, 0, 0, 0, 10, 10, 100]$ for the RWPE1 dataset). On the other hand, especially for complex samples, one can start with a problem strongly regularized in terms of localization with high values for μ_{∇}. It is consequently set to vary from 225 to 75 for the HUVEC dataset ($[225, 75, 75, 75, 75, 75, 75]$) and from 375 to 75 for the RWPE1 dataset ($[375, 375, 225, 75, 75, 75, 75, 75, 75]$). The 2D and the 3D spaces are padded. For the sake of reconstruction time, the nearest-neighbor interpolation in the Fourier domain is chosen.

Method IV.4 - The reconstructions are run on 106 iterations with $nb_{it}^{GS} = 6$ and $nb_{it}^{GS,r} = 100$. No data alignment refinement is done. As above, the constraints are set to $\mathcal{R}(f) \geq 0$ and $\mathcal{I}(f) \geq 0$, keeping a ratio of $\mu_{\nabla}/\mu_{L_1} = 1.25$. For the sake of reconstruction time, only the z-axis is zero-padded $nb_z^{pad} = 2 \times nb_z$.

Performances of the different methods

Method IV.2 - As expected, the iterative RGB 2D phase retrieval algorithm developed reduces the numerous artefacts introduced by the lack of phase information (see figure IV.30). The sparsity constraint efficiently cleans the noise and the twin-image signal present in the background of figure IV.30.b: the background in figure IV.30.c is homogeneous with overlying sharp and contrasting objects.

After a rapid drop in the first 20 iterations for each dataset (see figure IV.31.a), the cost function (IV.5) barely decreases after the 50^{th} iteration.

Method IV.3 - The convergence curves for the 3D inverse problem (see figure IV.31.b) are less intuitive as they are not strictly decreasing. This is due to the fact that all 10 iterations, a data alignment refinement occurs and the values of the hyperparameters may change. Both of these effects are visible on the curves.

If the registration step does not have a visible effect on the HUVEC convergence curve, its effect is noticeable between the first and the second batch of the RWPE1 dataset reconstruction. Indeed, between these two batches, at the 10^{th} iteration, the values of the hyperparameters are unchanged ($\mu_{L_1} = 0$ and $\mu_{\nabla} = 375$) and so are the values of the last two terms of the cost function (IV.18). The change in the cost function from more than 16 % to less than 14 % can therefore only be attributed to the diminution of the data fidelity term because of a better agreement between the experimental and simulated data.

The noticeable upward jumps are linked with the change of the value of the hyperparameter μ_{L_1}. It gains a factor 10 at the 30^{th} and the 50^{th} iterations for the HUVEC reconstruction and at the 40^{th} and the 60^{th} iterations for the RWPE1 reconstruction.

Method IV.4 - As previously seen, the convergence curves for method IV.4 present a bump when the regularization begins to be applied. The number of iterations is nevertheless too low to observe the divergences previously seen. Nevertheless, a new behavior can be identified on the RWPE1 curve: small oscillations whose origin remains unknown.

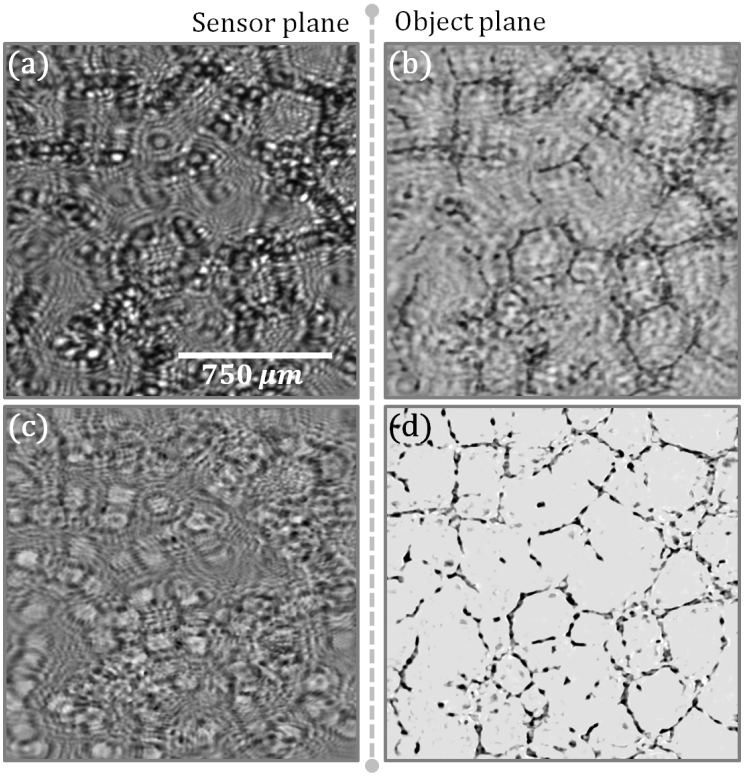

Figure IV.30: Example of a *RGB* phase retrieval performed on the first illumination position in the HUVEC dataset. (a) Raw acquisition by the sensor with the green illumination. (b) Modulus of a simple 2D back-propagation of the green intensity to the object plane. The classical twin-image effect is clearly visible around the isolated cells and the branches of the HUVEC network. (c) Recovered phase information in the sensor plane for the green illumination after the iterative *RGB* retrieval. (d) Modulus of the retrieved 2D object. Most of the artifacts are erased by the regularized inverse problem approach.

Reconstruction time - Table [IV.3] compares the running times of the reconstruction methods. With the phase ramp method III.4, it is directly the time of the Fourier mapping operation and is quite fast ($\sim mins$)

As expected, most of the reconstruction time with method IV.2 is spent in the 2D phase retrieval: several minutes for each of the 16 lighting positions. In details, the final reconstruction times for the HUVEC and RWPE1 datasets are $\sim 16\times5+2\ min$ and $\sim 16\times7+2\ min$. The last 2 minutes correspond to the final Fourier mapping operation.

Unsurprisingly, the 3D inverse problem approach IV.3 is slower. The running time being composed of roughly 60% for the minimization of the problem (IV.18) and 40% for the data registration refinement.

The last method IV.4 appears to be the slowest one. Nevertheless this statement must be nuanced. Indeed, during the 106 main iterations, $nb_{reg}^{GS} \times nb_{it}^{GS,r} = 1000$ regularized steps have been performed. This number must be compared with the

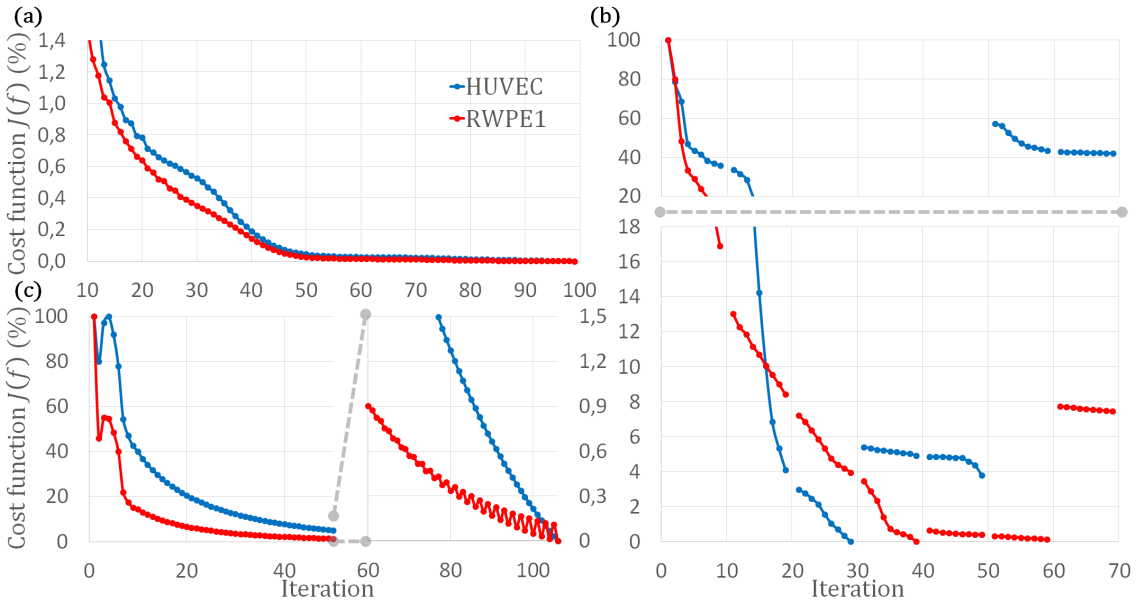

Figure IV.31: Convergence curves of the reconstruction of the HUVEC and RWPE1 datasets. (a) *RGB* phase retrieval IV.2 performed on the first illumination position in the HUVEC (see figure IV.30) and RWPE1 datasets. (b) Iterative 3D inverse problem IV.3. For each dataset, the batches of 10 iterations are separated by a blank in the curve to emphasize the iterations where the alignment of the data is refined and where a change in the hyperparameters can occur. (c) Regularized Gerchberg-Saxton algorithm IV.4. A zoom on the second part of the iterations is shown. All the curves are normalized to their values at the first and the last iterations.

	Method III.4	Method IV.2	Method IV.3	Method IV.4
HUVEC	$\sim 1\ min$	$\sim 1\ h\ 20\ min$	$\sim 7\ h$	$\sim 14\ h\ 20\ min$
RWPE1	$\sim 1\ min$	$\sim 2\ h$	$\sim 10\ h$	$\sim 15\ h$

Table IV.3: Comparison of the reconstruction times with the different methods. The increase in the complexity of the reconstruction method significantly lengthens the computation time. They are obtained with a Matlab® code running on an Intel(R) Xeon(R) CPU E5-2620 v3 @ 2.40 GHz processor. The code is not fully optimized, thus the given times must be considered as an order of magnitude for comparison purposes.

regularized 70 iterations of the inverse problem approach IV.3 which took roughly 6 h for the RWPE1 dataset for example[44]. The same number of iterations[45] is done in 1 h by the regularized Gerchberg-Saxton algorithm IV.4.

[44] 60% 10 h
[45] 15 $h \times 70/1000$

3D reconstructions

In this section, the 3D reconstructions on the two experimental datasets are compared for the four methods.

HUVEC reconstruction - Figure IV.32 presents 3D views of the reconstructed volume. The solution of the inverse problem approach IV.3, which gives the sharpest 3D view is kept for the 3D rendering whereas the result of the Gerchberg-Saxton algorithm IV.4, which gives the most contrasted reconstruction, is kept for the orthogonal projections. Figure IV.33 compares the different methods.

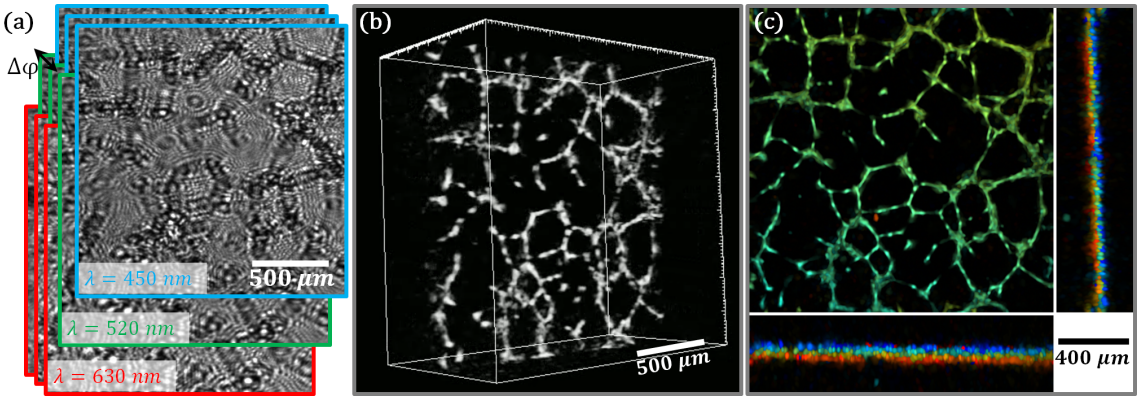

Figure IV.32: 3D reconstruction of the HUVEC dataset. The cells spread on the Matrigel® surface and the final network is overall planar. (a) Raw data at the three wavelengths and at different angles. (b) 3D visualization of the reconstructed volume with the 3D inverse problem method IV.3. (c) Orthogonal maximum intensity projections of the constructed volume with the regularized Gerchberg-Saxton algorithm IV.4. On each view, the colors codes for the depth: the shallowest in blue, the deepest in red.

It clearly appears on the volume slices in figures IV.33.a-d that methods IV.2, IV.3 and IV.4 strongly diminish the artifacts of the phase ramp solution III.4 by cleaning the twin-image from the background (see the red arrows in the profiles of figure IV.33.i). One can nevertheless see on the orthogonal views in figures IV.33.e-h that strong artifacts remain in the reconstructions performed with method IV.2. They are due to the limited angular coverage: the cone shapes around the contrasted objects are characteristic of the angle θ at which the sample is illuminated.

On a qualitative point of view, method IV.4 provides the best results in term of contrast and artifact reduction. The objects are well contrasted and the background is homogeneously black in both the xy and xz-views. With method IV.3, the background is darker than with methods III.4 and IV.2 but some "speckle"-like artifacts remain.

For morphological and positioning analysis, method IV.2 appears to be sufficient compared to the two last methods IV.3 and IV.4 (see figures IV.33.b-d). The gain of contrast in the plotted profiles in figure IV.33.i does not justify the high calculation

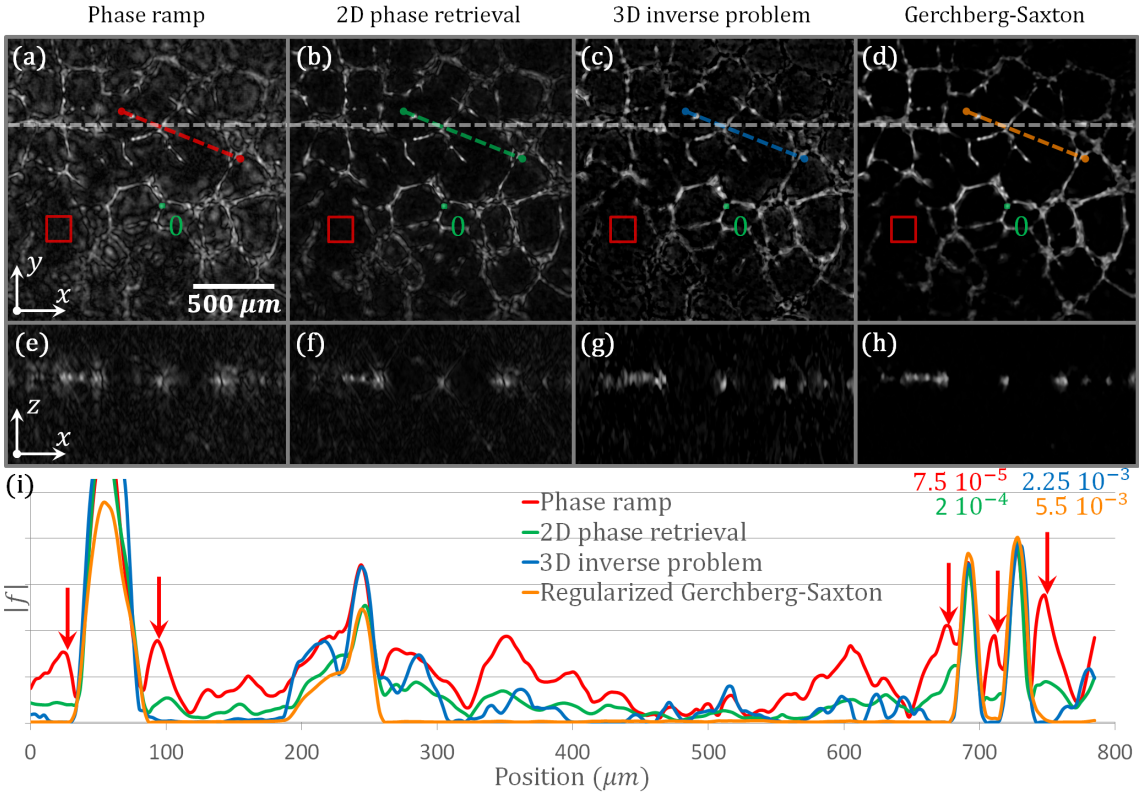

Figure IV.33: Comparison of the reconstruction methods on the HUVEC network. (a-d) Slice of the volume at $z = 0$ μm. The red square and the green spot (0) represent respectively the areas on which the background and the signal are estimated. (e-h) Orthogonal xz-slices to the white dashed lines. (i) Profiles drawn along the colored dashed lines in (a-d). The red arrows point at the twin-image artifacts left by the phase ramp method III.4 in the reconstruction.

time of methods IV.3 and IV.4, since the three methods give similar results in terms of segmentation capabilities.

RWPE1 reconstruction - Figure IV.34 presents 3D views of the reconstructed volume. The solution of the inverse problem approach IV.3, which gives the sharpest 3D view is kept for the 3D rendering whereas the result of the Gerchberg-Saxton algorithm IV.4, which gives the most contrasted reconstruction, is kept for the orthogonal projections. Figure IV.35 compares the different methods.

The HUVEC network is overall planar compared to the RWPE1 cell culture which is more complex with overlapping structures spread on a large scale along the z-axis (see figures IV.34.b-c). It appears that the previous remarks on the artifacts reduction still holds (see figures IV.35.a-h).

Besides, some 3D structures only contrast from the background with methods IV.3 and IV.4. This is particularly visible on the profiles in figure IV.35.i in which the signal of small individual objects strongly peaks (such as the one pointed by the green arrows) in all the reconstructions, whereas some bigger objects have

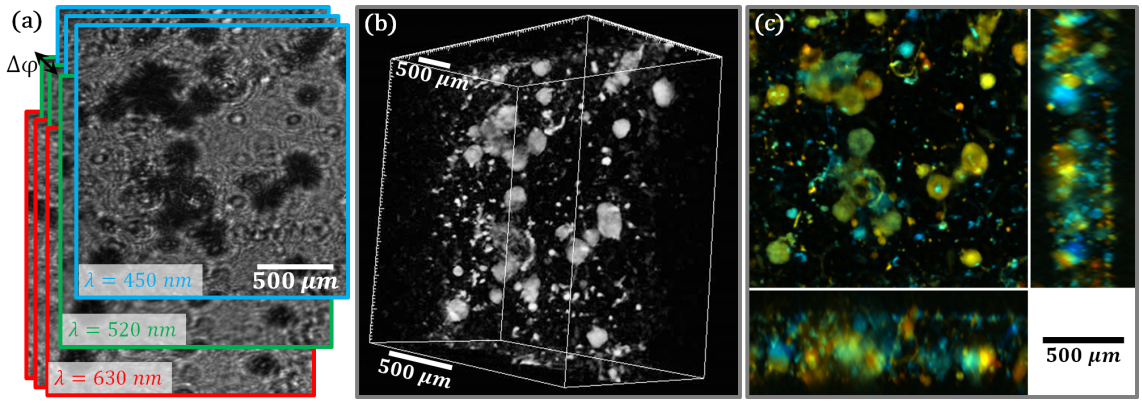

Figure IV.34: 3D reconstruction of the RWPE1 cell culture. The cells tend to form clusters when embedded in Matrigel®. (a) Raw data at the three wavelengths and at different angles. (b) 3D visualization of the reconstructed volume with the 3D inverse problem method IV.3. (c) Orthogonal maximum intensity projections of the constructed volume with the regularized Gerchberg-Saxton algorithm IV.4. On each view, the colors codes for the depth: the shallowest in blue, the deepest in red.

a very low contrast with the background artifacts for the first two methods III.4 and IV.2 (such as the one pointed by the red arrows). In addition, the segmentation between the three structures between the blue brackets along the dashed lines appears possible only with methods IV.3 and IV.4 (blue arrows in figure IV.35.i).

As for the HUVEC reconstructions, method IV.4 gives the best reconstruction in terms of background cleaning and contrast on the reconstructed objects. Method IV.3 is efficient to retrieve the objects and separate them but the previously identified "speckles" are once again present.

In order to better quantify these differences in the reconstructions quality, a contrast to noise ratio R is estimated on specific regions of interest and compared for the four methods. A region of 45×45 pixels is selected in a region seemingly without any reconstructed object to compute the mean value m_b and the standard deviation σ_b of the background signal. Then spots of 3×3 pixels are selected to estimate their mean intensity m_s. The contrast to noise ratio is then computed as follows:

$$R = \frac{m_s - m_b}{\sigma_b} \tag{IV.44}$$

This does not pretend to be a rigorous signal to noise ratio estimation. Indeed, the real signal, which should actually be compared with the reconstructions, is not known. Moreover, these ratios do not reflect the efficiency of the different methods to reduce the artifacts: the background is estimated in a region where they seem to appear minimal, whereas these regions can peak rather high (see the twin-image in the phase ramp reconstructions in figures IV.33.a and IV.35.a). These ratios consequently give only an idea on how the different algorithms increase the signal intensity compared to the background.

First of all, the different contrasts in table [IV.4] confirm that isolated objects

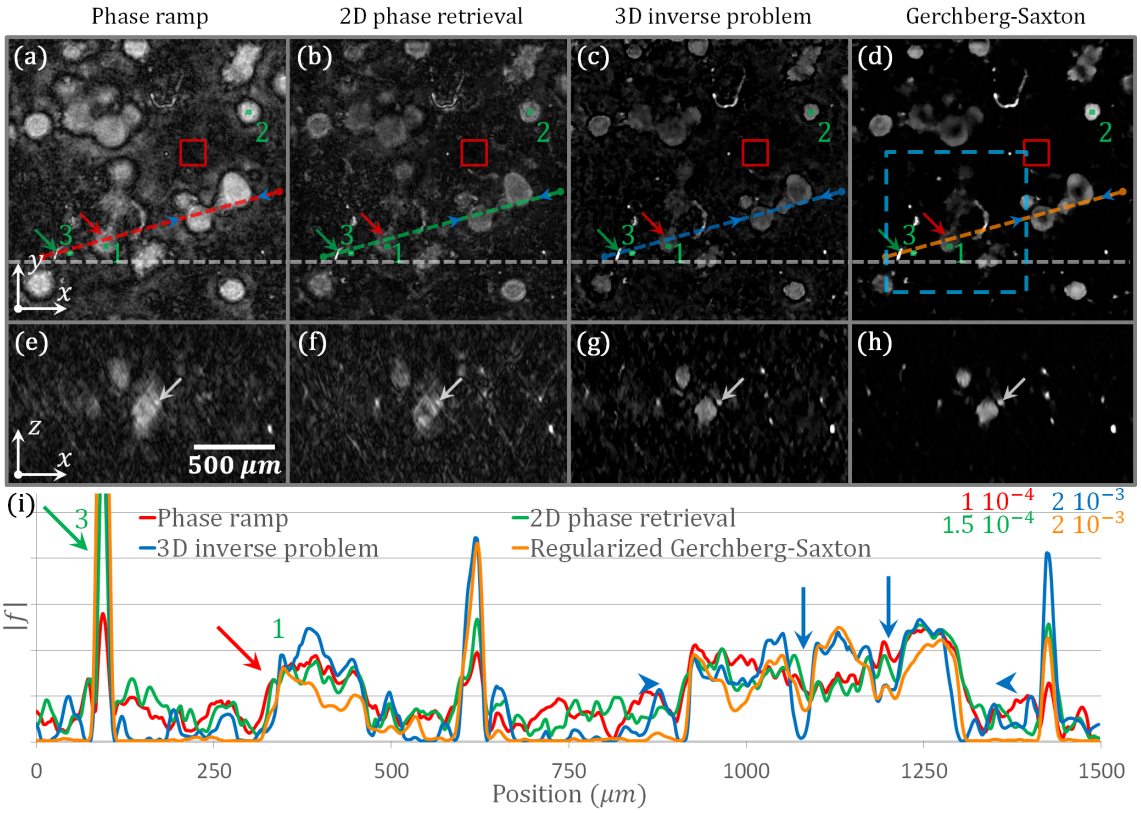

Figure IV.35: Comparison of the reconstruction methods on the RWPE1 cell culture. (a-d) Slice of the volume at $z = -48\ \mu m$. The red square and the green spots $(1, 2, 3)$ represent respectively the areas on which the background and the signal are estimated. The blue square is the zone which is reconstructed with a higher resolution for comparison with a standard microscope. (e-h) Orthogonal xz-slices to the white dashed lines. The white arrows point at a small object close to a large cluster of cells. (i) Profiles drawn along the colored dashed lines in (a-d). The green and the red arrows point at an isolated object and a cluster. The blue arrows point at noticeable regions in between big structures where the background noise is hard to erase.

are well reconstructed with a contrast higher than 26 compared to the background (R_0 and R_3) for all the reconstruction techniques. The value R_1 confirms that some structures such as the spot 1 (red arrows in figures IV.35.a-d) have a very low contrast to the background with the 2D phase retrieval IV.2 (b), even less than with the phase ramp III.4 (a). One needs the 3D inverse problem approach IV.3 (c) or the regularized Gerchberg-Saxton algorithmIV.4 (d) to correctly extract these structures from the background intensity.

The contrast to noise ratio is higher with method IV.3. One could have nevertheless expected a better contrast based on the scales of the profiles in figures IV.33.i and IV.35.i. This comes from the standard deviation of the background which gains a factor of ~ 21 with this method compared to methods III.4 and IV.2.

		Phase ramp III.4	2D phase retrieval IV.2	3D inverse problem IV.3	Gerchberg-Saxton IV.4
HUVEC	$m_b\,(10^{-6})$	8.68	10.2	83.5	10.1
	$\sigma_b\,(10^{-6})$	3.22	3.79	79.8	11.1
	$m_s\,(10^{-4})$	1.02	2.57	26.2	55.9
	R_0	29	65	32	500
RWPE1	$m_b\,(10^{-6})$	5.32	8.04	54.5	5.26
	$\sigma_b\,(10^{-6})$	2.36	4.08	53.6	5.55
	$m_s^1\,(10^{-5})$	2.64	2.18	70.6	55.1
	$m_s^2\,(10^{-5})$	5.40	8.07	114	172
	$m_s^3\,(10^{-5})$	6.68	15.1	356	327
	R_1	9.0	3.4	12	98
	R_2	21	18	20	310
	R_3	26	35	65	588

Table IV.4: Details of the estimation of the contrast R for the different areas spotted in figures IV.33.a-d and IV.35.a-d. The exponents are coherent with the numbering of these spots in these figures.

The regularized Gerchberg-Saxton technique IV.4 achieves the best contrasts on all the spotted objects. This comes from its good efficiency in cleaning the background artifacts as one can see on the profiles in figures IV.33.i and IV.35.i, where the low values of the orange curves are squeezed by the high dynamics of the reconstruction.

Concerning the sectioning on the z-direction, the 3D view of figure IV.34.b shows that objects are widely spread in the three dimensions and artifacts on this direction seem limited. Looking more closely at the orthogonal views in figures IV.35.e-h, it appears once again that only the 3D regularized approaches IV.3 and IV.4 are able to clean the artifacts to correctly retrieve the objects.

Indeed, one can see that the isolated and small objects that are blurred by the twin-image with the simple phase ramp method III.4 are well reconstructed by the 2D phase retrieval algorithm IV.2 (see figures IV.35.e-f). Added to methods III.4 and IV.2, methods IV.3 and IV.4 efficiently clean the remaining artifacts due to the lack of angular coverage. Objects in the vicinity of the big clusters of cells are now visible and well separated (see white arrows in figures IV.35.e-h). Nonetheless, their shape normally spherical appears rather straight with the inverse problem approach IV.3. This is once again due to the impossibility of acquiring widely distributed polar angles (θ-angle in figure IV.6): the algorithm cannot recover the information which is in the zones of shadow of the clusters. Method IV.4 seems to slightly correct this effect but provides less sharp edges.

To conclude this analysis, figure IV.34.c must be compared with the reconstructions of the previous section 4.3 where 31 φ angles are used. This shows that the number of lighting positions plays a role in the reconstruction quality. As expected,

its gets better with a higher number of angles: the objects are more contrasted with sharper edges. With only 16 angles, some of the capsules edges are not reconstructed and the others are barely visible.

5.3 Comparison with a standard microscope

To further study the sectioning capabilities of the device and the algorithms on the z-axis, a comparison is made with the acquisitions previously obtained with the AxioObserver.Z1 inverted microscope (Zeiss).

To do so, a fully 3D reconstruction is performed with a higher resolution on the RWPE1 cell culture with the 3D inverse problem approach IV.3 and the Gerchberg-Saxton algorithm IV.4. The region of interest is framed by a blue dashed square on figure IV.35.d.

Reconstruction parameters

Acquisitions - The dataset is composed of 3×31 acquisitions done at 31 different angles $\varphi \in \{0°, 282°\}$, $\Delta\varphi = 9.4°$ in the three available wavelengths of the RGB LED $\lambda \in \{630\ nm, 520\ nm, 450\ nm\}$. The selected region of interest is composed of 512×512 pixels[46] of $1.67^2\ \mu m^2$.

Reconstruction volume - The final reconstruction[47] is composed of $512\times512\times300$ voxels of $1.67 \times 1.67 \times 2.66\ \mu m^3$ for a global volume of $855 \times 855 \times 800\ \mu m^3 = 0.584\ mm^3$. As previously, the voxels are not orthonormal to take into account the distortion on the z-axis induced by the refraction between the air of refractive index $n_{air} = 1$ and the culture medium, the reconstruction being performed for an angle $\theta = 45°$ in the air. The sensor distance is $z_s = 3.52\ mm$. For the two methods, the 2D and the 3D spaces are zero-padded. The constraints on the reconstructed scattering potential are set to $\mathcal{R}(f) \geq 0$ and $\mathcal{I}(f) \geq 0$. For the sake of visibility, only a part of the volumes along the z-axis are displayed, the rest of the volume being mainly empty.

Data alignment - The initial data alignment is done by the least mean squares minimization algorithm on 2D reconstructed data. This alignment is used to initialize method IV.3. The results of the alignment refinement steps of this method are then used to initialize method IV.4.

Method IV.3 - The iterative process is split in twenty batches of $nb_{it}^{IP} = 10$ iterations in between which data alignment refinement are performed for the first fourteen batches (for a total of 13 refinements). For the sake of reconstruction time, the nearest-neighbor interpolation in the Fourier domain is chosen and the hyperparameters are varying from 0 to 1000 for μ_{L_1} and varying from 375 to 32.5 for μ_{∇}.

[46] $855 \times 855\ \mu m^2$

[47] $512 \times 512 \times 300$ voxels of $1.67^3\ \mu m^3$ before scaling.

Method IV.4 - The reconstructions are run on 46 iterations with $nb_{it}^{GS} = 6$ and $nb_{it}^{GS,r} = 40$, keeping a ratio of $\mu_{\nabla}/\mu_{L_1} = 1.25$.

3D reconstructions

Comparison of methods IV.3 and IV.4 - For method IV.3, the total reconstruction time is $\sim 30\ h$ whose $\sim 12\ h$ are dedicated to the data registration refinement. In comparison, method IV.4 ran for $\sim 7\ h$. With the same reasoning than above, method IV.3 performed 200 regularized steps in $\sim 18\ h$ and method IV.4 400 in almost three times less time[48] As predicted in sections 3 and 4 of this chapter, method IV.3 is the slowest method.

For the two methods, the reconstruction quality is degraded on the z-direction on the final reconstructed scattering potentials (see figure IV.36). This is due to the acquisition geometry: it is impossible to rotate the sample to acquire more specific data on the z-direction. This loss of information leads to a limited number of coefficients accessible in the Fourier domain of the object as mentioned above. Nevertheless, the 3D regularization compensates this lack of viewing angles. Even if all the information is not retrieved, these two algorithms allow cleaning and reducing artefacts which appear in classical tomographic algorithms with limited angular coverage [96].

Interestingly, contrary to the previous results, method IV.3 gives the best results. In figures IV.36.a-b, method IV.4 reconstructs objects which are less contrasted. Color clarity is better with method IV.3 and color changes (that is to say, dispersion in heights) in some objects are well visible. In figures IV.36.c-d, even if some capsule edges reconstructed with method IV.4 are erased, the background quality is higher: it is darker and homogeneous.

The shape of the clusters can be reconstructed as well as some contrast changes inside the structures (see figure IV.36.c-d). Let's insist here again that this is not quantitative as already mentioned in this work. What seems to be a bridge is visible between two planes at different z in the yz-slices in figures IV.36.c-d.

Comparison of method IV.3 with microscope views - Figure IV.37.a compares the xy-projections of the lens-free volumes and the phase contrast and fluorescence acquisitions. The main structures are common to all the views. Nevertheless, as mentioned earlier, in the reconstructed volume, single objects (red arrows) artificially contrast more than extended structures (blue arrows).

The green arrows in figure IV.37.b point at objects of interest in xz-slices. The positions of these objects in the lens-free reconstruction are coherent with the microscope acquisitions.

Figure IV.38 presents the comparison of different slices of the fully 3D reconstructed volume with their microscope counterparts. Despite a non-quantitative

[48] It means that the following comparison between the two algorithms is fairer than the previous one, the numbers of regularized steps being in the same order of magnitude (200/400 compared to 70/1000 before).

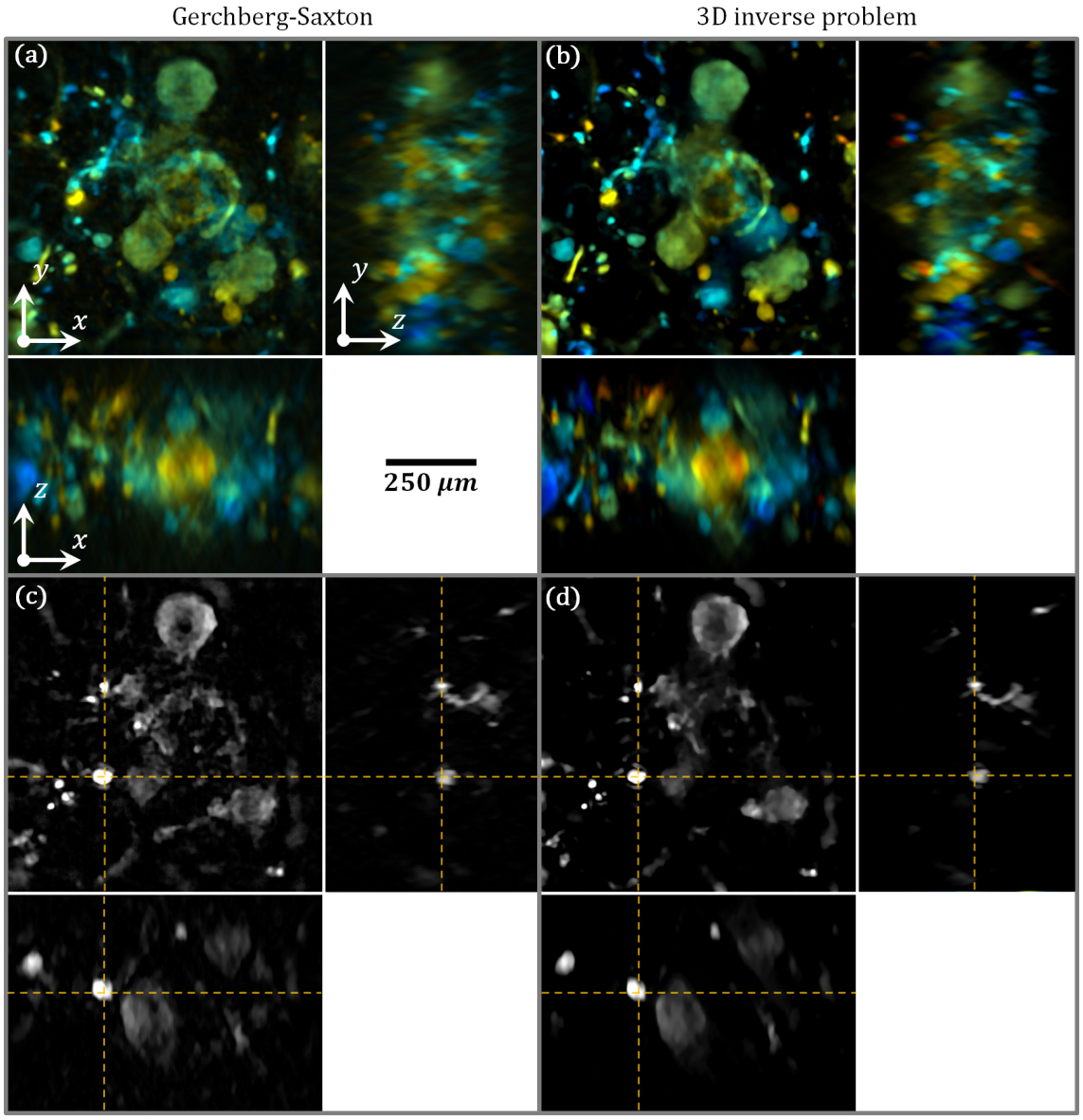

Figure IV.36: Visualizations of the reconstructed volume of the RWPE1 dataset at full resolution with the Gerchberg-Saxton algorithm IV.4 (a,c) and the 3D inverse problem approach IV.3 (b,d). (a-b) Orthogonal average intensity projections. On each view, the colors codes for the depth: the shallowest in blue, the deepest in red. (c-d) Orthogonal slices: xy-slice at $z = 48$ μm, xz-slice at $y = -117$ μm, yz-slice at $x = -164$ μm.

contrast, one can see that the main structures are accurately reconstructed both in terms of positioning and morphology[49].

[49]Let's mention here that the lens-free and microscope volumes are globally matching along the z-axis before the scaling of the lens-free volume to take into account the refraction effect between the air and the medium. This is coherent with the fact that the first one is reconstructed as if the holograms are obtained in the air and that the second ones are acquired by moving the

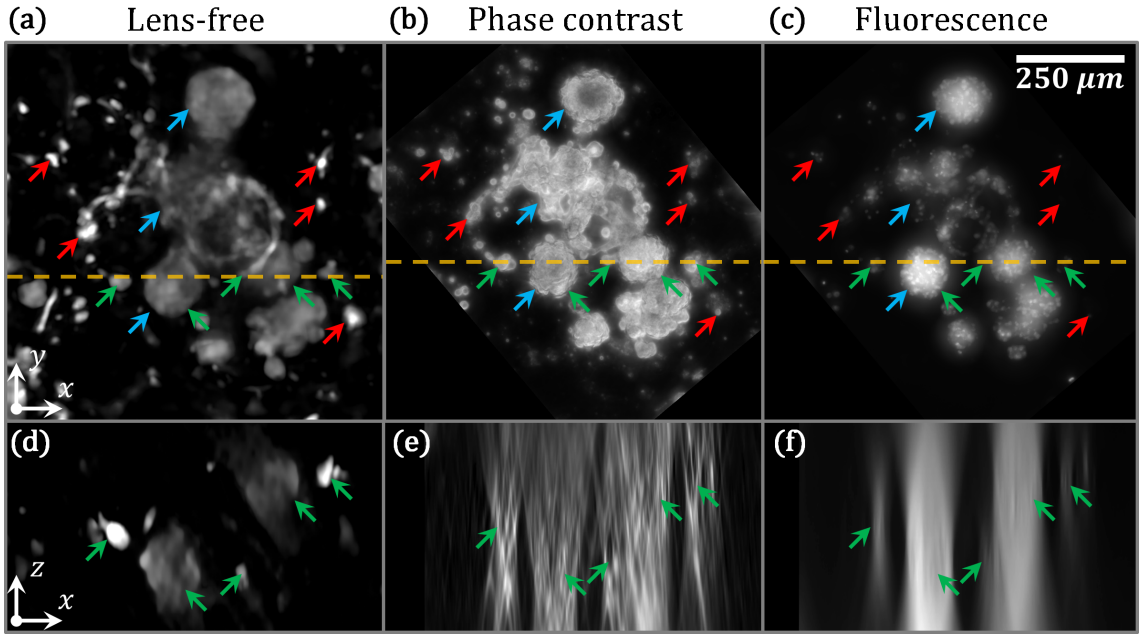

Figure IV.37: (a-c) Comparison of the xy-projections of the fully 3D reconstructed volumes (a - average intensity), the phase contrast (b - average intensity) and the CellTracker™ visualization (c - maximum intensity). Red arrows point at small isolated objects. Blue arrows point at big cell clusters. The green arrows point at different objects of interest. (d-f) Orthogonal slices of the different volumes on the xz-plane along the corresponding yellow dashed lines. The green arrows point at different objects of interest. For the phase contrast and fluorescence imaging, the arrows are placed are the objects seem at their best focus on the xy-plane.

The z-sectioning also appears more selective compared with the focused/unfocused criterion and is able to separate extended overlapping structures (figures IV.37.d-f and IV.38). For example, the cluster in the $z = 193$ μm slice is well set apart from the cellular branch at $z = -33$ μm without any bridging artifact in the $z = 105$ μm slice. Another example is the structure at the bottom right of the $z = -33$ μm slice: it appears separated from the underlying slightly unfocused small cluster visible on the microscope view. This small structure is actually reconstructed at $z = -84$ μm (not presented here).

In the slice $z = -126$ μm, some structures are still visible despite the fact that this slice is the deepest one into the object and consequently largely beyond the limits of the model (II.12) developed under the Born approximation since the incident wave front crossed the entire sample.

With the fully 3D reconstruction, one can also see that the two cellular branches at $z = 193$ μm and $z = 105$ μm are actually bridged in the third dimension: this is the branch mentioned above, in the yz-slices in figures IV.36.c-d.

translation stage in the air. On both volumes, a scaling factor must be applied to get the distances in the aqueous culture medium. The same scaling factor than for the lens-free reconstruction is consequently applied on the microscope acquisitions.

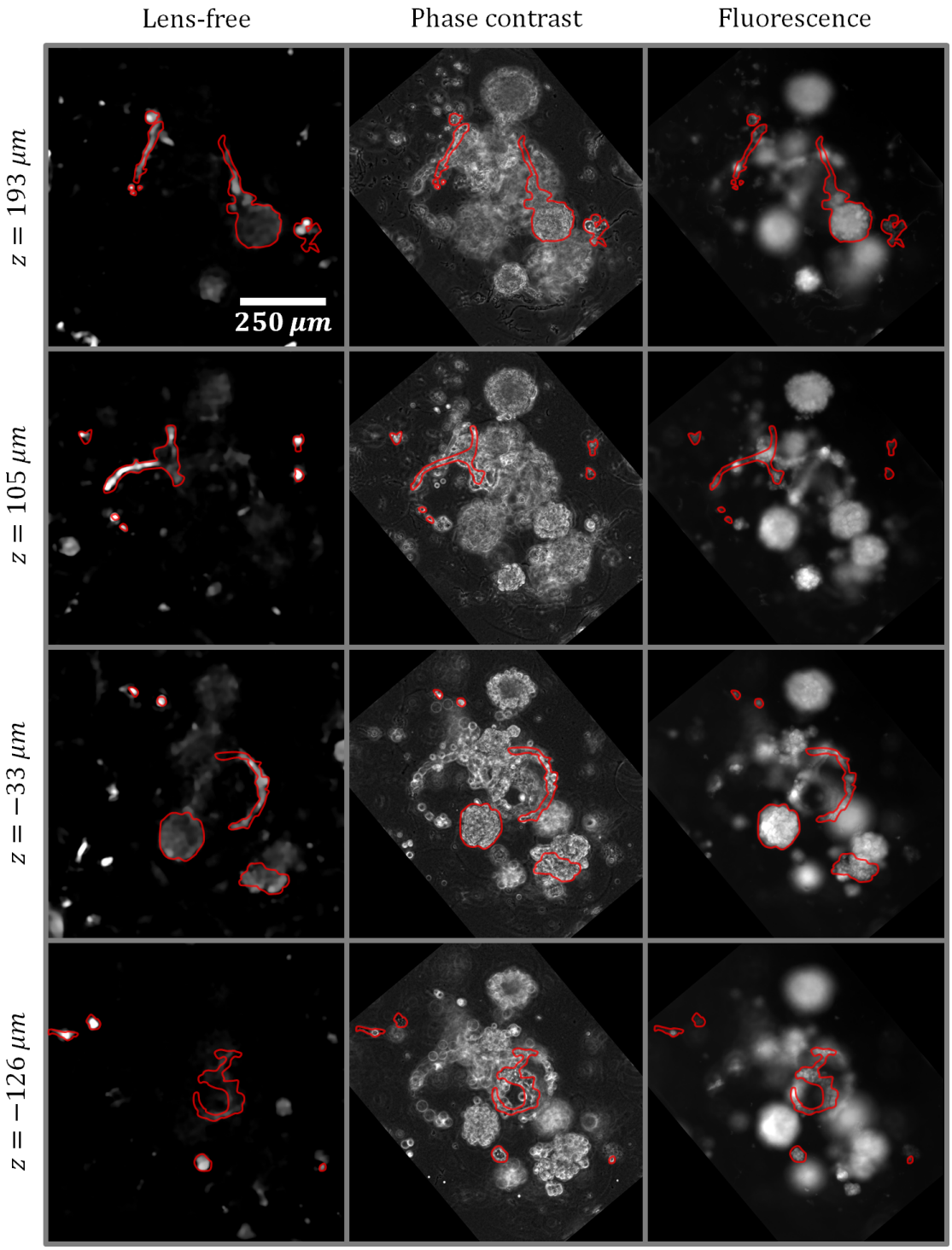

Figure IV.38: Comparison of the fully 3D reconstructed volume (*left*) with the microscope views of phase contrast imaging (*middle*) and CellTracker™ visualization (*right*). Different slices at different depths are presented. At each focusing distance, the main characteristic structures that are in focus on the phase contrast images are manually segmented. The red outlines are superimposed on the reconstructed slices and on the CellTracker™ visualization.

5.4 Conclusion, discussion and perspectives

The four algorithms are able to overcome the limitations raised by the lens-free microscope - that is to say the lack of phase information on the data and the limited angular coverage - in order to retrieve the 3D object but with different qualities in terms of contrast to noise ratio and computational time. Giving the result in a single pass, the algorithm based on a phase ramp is fast but leads to a signal which can be hard to distinguish from the artifacts and the noise. Providing the best contrast, the algorithms based on the 3D inverse problem approach or a regularized Gerchberg-Saxton loop can nevertheless be extremely time consuming.

It appears then that the choice to use either an algorithm or another will depend on the targeted application. To identify isolated single cells in a 3D volume, which produce a strong signal, the first algorithms III.4 or IV.2 can be sufficient. On the other hand if one aims at reconstructing complex overlapping structures, a 3D regularized method is needed. At high resolution, the 3D regularized iterative approach IV.3 provides a more pertinent result at the cost of a long runtime. For low resolution reconstruction, the modified Gerchberg-Saxton loop IV.4 gives the best results with an equivalent runtime in terms of regularized iterations which is faster.

Comparisons with standard microscope views show that the fully 3D reconstructions are accurate in terms of morphology and positioning. The proposed lens-free device provides a cheap and easy to use tool with a good sectioning in the z-direction on large volumes. Nonetheless, it has been shown that the reconstructions are not quantitative in terms of contrast (figure IV.37). The small objects will appear highlighted compared to larger structures. This is a limitation of the method and makes the image prone to interpretation errors.

Beyond this proof of concept, some work remains to be done, especially in terms of computational time.

As mentioned for method IV.2, the decreasing rate of the cost function sharply diminishes after the 50^{th} iteration. It would have been possible to stop the algorithm at that point without degrading the reconstruction quality, leading to a reconstruction time divided by 2. Moreover, all the lighting positions are processed sequentially, slowing down the all process. Indeed, different lighting positions giving independent results in this method, the phase retrieval process could be run in a parallel loop instead of a sequential loop.

The computational time of the regularized approaches IV.3 and IV.4 are their main pitfall. It is mainly divided between the data refinement and the 3D iterative problem.

Concerning the first part, the alignment steps are performed sequentially. Since then, a multi-threaded solution aligning the data by batches in parallel has been implemented. In this case, the registration process is directly divided by the number of cores of the machine: 12 with the computed used during this PhD work. In the case of the full resolution RWPE1 reconstruction, the time dedicated to the alignment process would decrease from $\sim 12\ h$ to $\sim 1\ h$. Furthermore, the alignment method is based on the minimization of the least mean squares between the simulated data

and the experimental intensities. This solution has the advantage to work out the relative angle but can be very time consuming. In the refinement step, the simulated and experimental data are already relatively close and other faster alignment techniques may be implemented.

For the second part, as regards the iterative codes themselves, the bottleneck of methods IV.3 and IV.4 is the computation of the data fidelity term[50]. The L_1-regularization is indeed fast to be computed. The ∇-regularization can be quite long but is already optimized anyway[51].

At each iteration the computation of the data fidelity term (and its gradient for method IV.3) can take several minutes since it requires 3D and 2D Fourier transforms and extraction/mapping of spherical caps in the Fourier domain. In the realm of tomographic diffractive microscopy, some works have shown that an intelligent use of GPU programming can dramatically reduce this step to just a few seconds [97]. In the case of the full resolution RWPE1 reconstruction with method IV.3, this would represent a gain of ~ 10 h on the ~ 18 h dedicated to the iterative process. for a remaining time of ~ 8 h, comparable with the runtime of ~ 7 h for a similar reconstruction with method IV.4.

Another track for improvement concerns the choice of the hyperparameters. In this work, they are empirically chosen for methods IV.2, IV.3 and IV.4 to provide reasonable results. A more thorough study of their effects and an optimized choice, based on simulations, could also improve the quality of the reconstruction. Indeed during the simulations for the tests of the different methods in the previous sections, none of the obtained reconstructions is directly compared with the initial numerical volume to quantify their efficiency on a known example. Doing so by testing different hyperparameters for the different methods would give an objective criterion to choose the best hyperparameters.

A better choice of hyperparameters may also influence the large standard deviation of the background signal mentioned above for the inverse problem approach IV.3: further studies are necessary to determine if it comes from the method and if a better choice for the hyperparameters would solve the issue or if the area is not as empty as it seems. Indeed the presented cultures are grown in Matrigel®. It presents good optical properties for standard microscopy [23, 98] but can be a very heterogeneous structure with a possible formation of fibrils or agglomerates, not adapted to diffractive microscopy. Some other extracellular matrices could be tested [99]. The optimization of the hyperparameters and the extracellular matrix represents an in-depth study that is not pursued during this thesis.

Moreover, more tests are needed to really compare methods IV.3 and IV.4. Indeed, it is surprising that the method identified as the best changes for low and high resolutions. Especially knowing that method IV.3 is expected to be the most

[50]Which corresponds for method IV.4 to the standard step 1 to 4 of the Gerchberg-Saxton loop without including the eventual regularization step. In terms of computation needs, it is the same than for the data fidelity term and its gradient in method IV.3: 2 3D FFTs and $2N$ 2D FFTs.

[51]Thanks to its implementation in C code gently shared by Eric Thiébaut and thanks to Fabien Momey who adapted it in C code for complex variables and provided its interfacing with Matlab®.

complete formulation and should unequivocally lead to the best reconstructions. As mentioned above, their comparison are not completely fair as method IV.4 is iterated an order of magnitude more than method IV.3 for the low resolution reconstructions. Nevertheless, method IV.4 achieves its convergence faster that method IV.3. Thus, the results at high resolution consequently tend to support the fact that with well tuned hyperparameters method IV.3 has the best potential as the reconstructions given with this method are better than the ones obtained with method IV.4 which cannot provide better results on this dataset.

It has been seen on the RWPE1 experiment that the number of angles changes the reconstruction quality as well as the sensitivity on the objects which can be reconstructed. More in-depth studies are needed to test the influence of the number of lighting positions and the number of wavelengths on experimental data. For a given number of lighting situations, is better to multiply the number viewing angles with fewer wavelengths or to multiply the number of wavelengths with less viewing angles?

Concerning the method themselves, different improvements can be consider for each of the methods.

Concerning method IV.2, a similar variable change than the one done in the inverse problem approach IV.3 to go from the scattering potential f to the refractive index δn can be implement to rather directly work on the amplitude and phase of the transmissive plane[52]. To do so, the new variable is $\phi \in \mathbb{C}$ the complex argument of the complex transmission t_{2D}:

$$t_{2D}(\phi) = e^{i\phi} \Rightarrow \delta t(\phi) = e^{i\phi} - 1 \tag{IV.45}$$

Doing so, the phase of the transmissive plane is directly $\mathcal{R}(\phi)$ and its amplitude is $|t_{2D}| = e^{-\mathcal{I}(\phi)}$. Following the same reasoning detailed in section 3 of this chapter:

$$\begin{aligned} \delta t(\phi + d\phi) &= e^{i\phi}e^{id\phi} - 1 \simeq e^{i\phi}(1 + id\phi) - 1 \\ &\simeq \delta t(\phi) + ie^{i\phi}d\phi \simeq \delta t(\phi) + i(1 + \delta t(\phi))\, d\phi \end{aligned} \tag{IV.46}$$

and the gradient of the data fidelity term (IV.15) expressed in terms of ϕ becomes:

$$\begin{aligned} \nabla J_d(\phi) = \frac{1}{nb_x^p nb_y^p nb_\lambda} \sum_{j=1}^{nb_\lambda} -4i.\left(1 + \bar{\delta t}(\phi)\right) pad^{-1}\Big(\mathrm{FFT}_{2D}^{-1}\Big(\bar{\hat{H}}_{z_s}^j.\mathrm{FFT}_{2D}\Big(\cdots \\ pad\left(\bar{U}_{inc}^j.U_{tot}^j(\delta t(\phi)).\left(\left|U_{tot}^j(\delta t(\phi))\right|^2 - I_d^j\right)\right)\Big)\Big)\Big) \end{aligned} \tag{IV.47}$$

More than the complex transmission, some results in the lab concerning 2D lens-free imaging by Lionel Hervé tend to show that the optical length $l = \phi\lambda/2\pi$ of the 2D plane is a grandeur more relevant to be reconstructed to correctly take into

[52]This implementation is done for some tests in parallel of this PhD work in the context of 2D reconstructions simultaneously performed on planes at different distances to clean artifacts, for example dust particles on different sides of a coverslip. It is nevertheless not tested in the context of 3D reconstructions and is consequently not presented here.

account the wavelength diversity and the fact the transmissive plane should not be the same for all the wavelengths:

$$t_{2D}(l) = e^{2i\pi l/\lambda} \tag{IV.48}$$

In addition, more tests should be done on the coherence length l_{coh}: pertinence compared with experimental data with a tilted lighting, optimization of its value or finding a better mask $M_{l_{coh}}$ or a better model.

Concerning method IV.3, the fact that the "speckle"-like effects disappeared between the low and the high resolution reconstructions tend to imply that this is due to a wrong choice of hyperparameters. As mentioned earlier in section 3 of this section, a mistake is made in the implementation of the gradient of the ∇-regularization and may influence the conclusions concerning this method. For sure, the error in the normalization factor means that the values of μ_∇ are not independent of the grid parameters nb_x^p, nb_y^p, nb_x^v, nb_y^v, nb_z^v as thought when they are tuned during simulations. New tests need to be run to optimize the reconstruction.

In addition, deeper tests of the linear interpolation compared to the nearest-neighbor interpolation should be done to check the influence and the efficiency of each of the method.

Then, it is mentioned that the inverse problem approach IV.3 (as well as the regularized Gerchberg-Saxton algorithm IV.4) can work directly on the refractive index of the sample to reconstruct. This possibility and its implication on the physical interpretation of the reconstructions[53] are not studied.

Finally, in a more distant future, the inverse problem approach could be fully used to refine the reconstruction parameters. Similarly to the data alignment refinement step, this approach can be used to optimize the variables which are manually set and consequently not optimal. For example, in order of importance: the distance z_s, the wavelengths λ, the angle θ, the angles φ.

Concerning method IV.4, some ideas could be tested to deal with the divergence observed in the cost function curves during iterations. Indeed, it is seen than even when the divergence starts on some parts of the reconstruction, others can continue to be well reconstructed (see the tube wall in figure IV.26.a in section 4 of this chapter).

The divergence is attributed to the ∇-regularization. To limit its effect, once the quality of the reconstruction is "good enough"[54], the value of the ratio μ_∇/μ_{L_1} could be changed and lowered.

On another level, new techniques to better enforce the data fidelity could be implemented. For example, it could be interesting to mix methods IV.2 and IV.4, replacing the experimental amplitudes in the data fidelity of step 1 of method IV.4 by the simulated complex waves via method IV.2.

It is even possible to replace the simple Fourier mapping III.4 in step 1 by a 2D phase retrieval algorithm directly performed on all the 2D holograms simultaneously as in [48]. Contrary to method IV.2 in which the 2D phases are sequentially

[53] In terms of absorption and dephasing properties.

[54] According to a criterion which remains to be found.

retrieved, each hologram being considered independently from the others, in this technique all the phases are simultaneously retrieved by a back and forth mapping of the Fourier domain with all the holograms until the simulated intensities converge to the experimental intensities. This technique does not need time consuming 3D FFTs. Only one is performed at the end to go back to the object. This technique nevertheless assumes that the number and the positions of the spherical cap in the Fourier domain are important enough to have a non-negligible overlapping[55]. Replacing step 1 of method IV.4 by this algorithm would enforce a far more constraining data fidelity.

[55]Otherwise the algorithm would not have any effect, nothing changing the coefficients on a given spherical cap during the iterations.

Chapter V

Towards 3D time-lapse microscopy in incubator

This chapter focuses on the last year efforts to adapt the 3D lens-free microscopy developed in the previous chapters to incubator conditions. Such an adaptation would open the field of time-lapse microscopy to large volumes analysis of overall sparse 3D cell cultures, dedicated to screening assays for example.

To do so, a new lens-free prototype is designed and built with an increased number of functionalities to facilitate its use and adapted to incubator while being cell-friendly. An new experiment dedicated to the microscope characterization is also run to check the validity of the reconstructions, especially in terms of three dimensional positioning and scales.

This work was presented in an oral participation at ECBO 2017 [100].

1 Toward an improved and incubator-proofed prototype

At first, it is tried to adapt the prototype introduced in the previous chapter IV, section 1 to perform acquisitions directly into incubators.

Nevertheless, its lack of flexibility in the adjustment of the alignment of the light source, the sample and the sensor makes it hard to use it routinely for acquisitions on numerous samples. Indeed, it is designed with a fixed relative position of the light source and the sensor. The center of rotation of the object is geometrically aligned with them only for a given position. This is only adjustable with the sample holder height, leading to a rough precision. Moreover, the further is the sample from the sensor, the worse are the recorded holograms because of the limited spatial and temporal coherence of the light source.

On another point, the electronics has not been prepared to high levels of humidity during the conception and lots of short-circuit or welding issues come out.

And finally, nothing is done to deal with the sensor heating. Source of evaporation of the culture medium, it leads to condensation on the container's cap,

preventing any acquisition. Working with an open container for short periods of time is not an option neither as the reached temperatures, up to $50°C$, are lethal for cells.

As a conclusion it appears easier to build a new adapted lens-free prototype to correct these points as soon as the conception step, keeping the same electronics but changing the design. The resulting prototype shown in figure V.1 presents new functionalities.

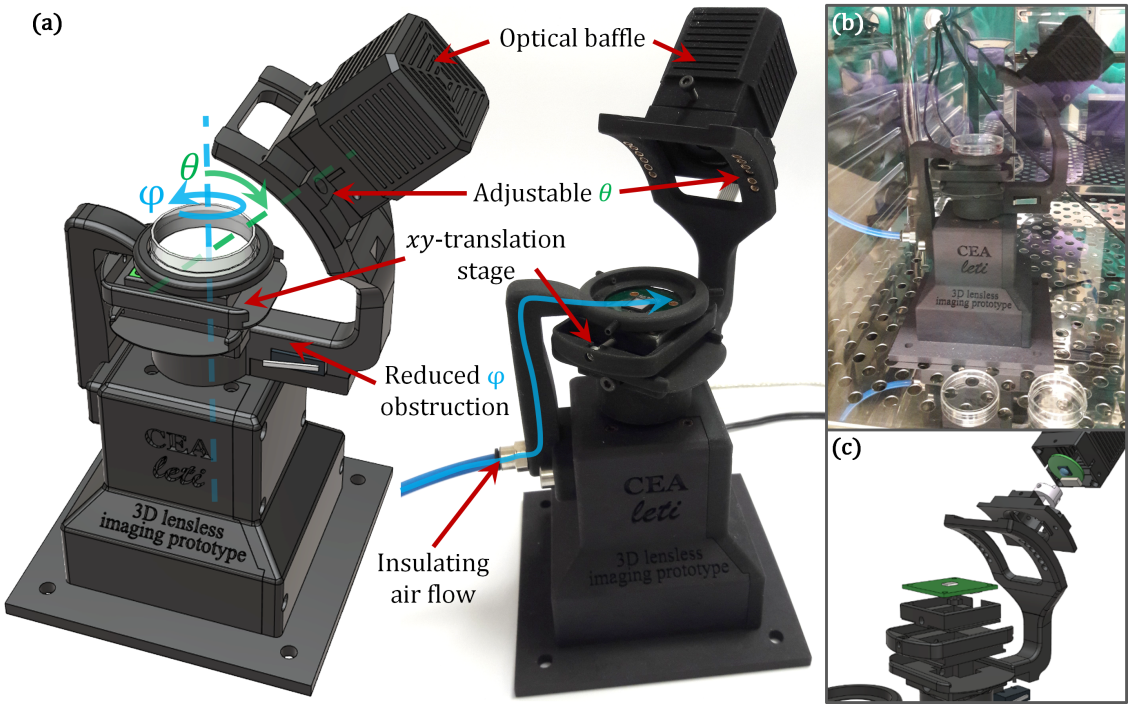

Figure V.1: (a) New lens-free prototype built to resist to incubator conditions. New features are added such as a cooling system via an air flow and the possibility to adjust the sensor position or the polar angle θ of the lighting. (b) Picture of the prototype inside an incubator. (c) Exploded view of the light source (the pinhole and the radiator are not pictured) and the xy-translation stage designed for the sensor positioning.

First of all, all the 3D printed pieces are manufactured to be easily removable in order to ease the possible need to fix the prototype. The previous design needed to be entirely disassembled to have access to the electronics in case of breakage. The position of the microswitches is changed to optimize the angular coverage from $\varphi \in \{0, 282°\}$ to $\varphi \in \{0, 305°\}$. Then, the electronics is coated with an insulation layer to be protected from the incubator humidity. The light source and its radiator are hidden behind on optical baffle allowing ventilating the heat emitted by the LED while preventing parasitic reflection on the incubator wall.

In terms of new functionalities, a rail allows changing the polar angle θ of the light source in the range of $\theta \in [30°, 55°]$. Thanks to a xy-translation stage which permits to adjust the alignment of the sensor with the sample and the light source,

the sample holder can be placed as close as possible to the sensor, improving the holograms quality. The holder is equipped which three screws which gives little room for maneuver to select a given area of the 3D sample to acquire. But their main role is to hold and prevent any movement of the culture dish due to the vibrations produced when the stepper motor is rotating.

In order to acquire data on large periods of time without killing the cells, a cooling system is added. Indeed, as mentioned above, when the sensor is on, the CMOS warms up to 50 $°C$ whereas the cell culture must be stabilized at 37 $°C$. The thermal insulation from the sensor is performed with an air knife flowing in between the sensor and the Petri dish from a vein carved in the sample holder as schemed in Fig.V.2.a.

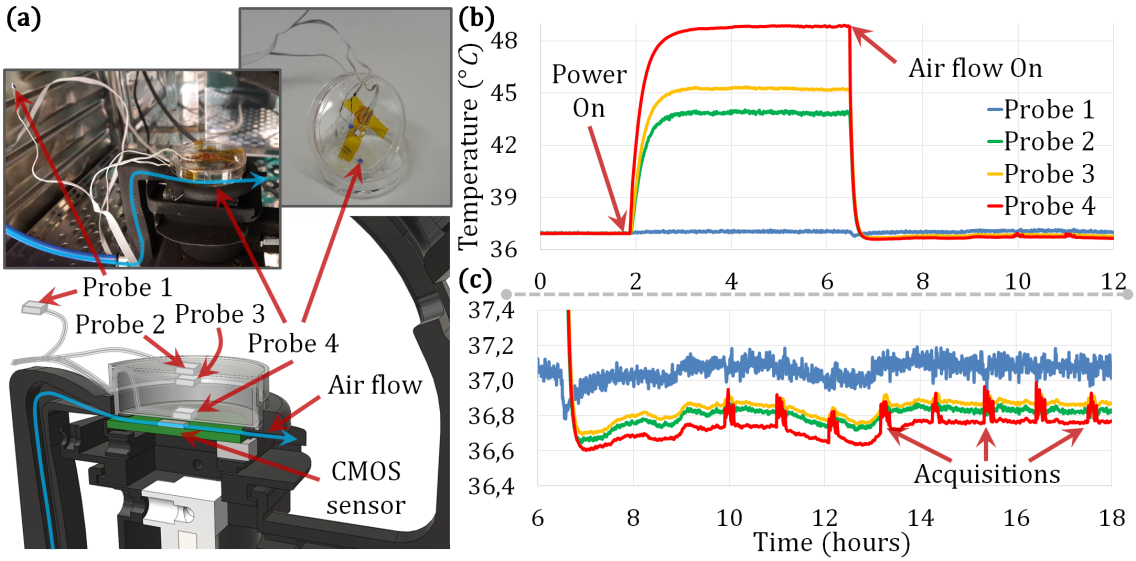

Figure V.2: (a) Scheme of the cooling system: an air flow is brought through the sample holder to create a thermal insulation of the cell culture with an air knife between the sensor and the Petri dish. To test the efficiency of the system, thermal probes are placed on a mock Petri dish ($\varnothing$ 35 mm) at different places: probe 1 in the incubator, probe 2 at the top of the cap, probe 3 in the dish at the bottom of the cap and probe 4 at the bottom of the dish. (b) Temperature curves of the four probes during the mock experiment: the system is placed into the incubator and at $t \simeq 2\ h$ the power is turned on. As the sensor warms up, the temperature in the Petri dish increases rapidly. At $t \simeq 6.5\ h$, the cooling air flow is triggered and the temperatures drop to standard culture values. (c) Focus on temperature curves during the acquisition process: starting at $t \simeq 10\ h$ a dataset is recorded every hour.

Figure V.2.b shows the temperature with and without the cooling system in a mock Petri dish. Four thermal probes are placed to measure the temperature in the incubator, at the bottom of the Petri where normally lies the cell culture and on the two sides of the cap.

As soon as the sensor is turned on, within 4 min, the temperature inside the dish goes higher than 40 $°C$. The difference of temperature with the outside creates con-

densation on the cap preventing any acquisition. If nothing is done, the temperature stabilizes above 48 $°C$ in less than 45 min in the cell culture and around 44 $°C$ in all the Petri dish. When the cooling system in activated with an adequate pressure, the temperature quickly drops to its initial value in less than 15 min.

When acquisitions are performed, as the sensor rotates, the geometry of the air knife changes, lowering the efficiency of the cooling system. This leads to small bumps in the temperature curves. They nevertheless remain confined within a 0.2 $°C$ range, which is adapted for cell culture.

2 3D+t reconstructions

2.1 Access to 3D large scale phenomena

Few tests are run outside the incubator on yeasts which can grow at room temperature and conditions and in incubator on 2D cell culture in Petri dishes to validate the air cooling system on living samples.

Once the prototype is proven to be robust and cell-friendly, a first experiment is designed to perform time-lapse reconstructions on large scale 3D samples.

Cell culture

This RWPE1 cell line[1] is prepared according to the no top coat protocol introduced in chapter IV, section 5 for the HUVEC cells, replacing the Matrigel® bed by a small Matrigel® drop on which the cells can freely move.

This drop is consequently deposited at the center of a Greiner petri dish (Sigma-Aldrich) and allows polymerizing for 30 minutes at 37°C. RWPE1 cells are then added at the surface of Matrigel and allow to attach for 1 hour at 37°C. KSFM (Life Technologies) supplemented with 50 ng/mL Epidermal Growth Factor (Life Technologies), 2% Fetal Bovine Serum (Life Technologies) and 1% Penicillin-Streptomycin (Life Technologies) is subsequently added.

The culture is monitored during two weeks.

Reconstruction parameters

Acquisitions - Every 68 min a dataset is acquired, composed of 3×32 acquisitions done at 32 different angles $\varphi \in \{0°, 305°\}$, $\Delta\varphi = 9.8°$ in the three available wavelengths of the RGB LED $\lambda \in \{640\,nm, 520\,nm, 450\,nm\}$. These data are first aligned via the least mean squares minimization algorithm on 2D reconstructed data and then used to reconstruct three different time-lapse views of the experiment. They are all based on the scattering potential on which positivity constraints are applied: $C(f) = \{f / \mathcal{R}(f) \geq 0, \mathcal{I}(f) \geq 0\}$.

[1] See chapter IV, section 5.1 for more details on the cells conditioning

Low resolution reconstruction - The first time-lapse is composed of low resolution reconstructions, based on a region of interest of 800×800 pixels of 3.34^2 μm^2 selected[2] at the center of the sensor field of view.

To reduce the computing time and the memory consumption, the final reconstructions are composed of $800 \times 800 \times 128$ voxels of $3.34 \times 3.34 \times 5.32$ μm^3 for a global volume of $2.67 \times 2.67 \times 0.68 = 4.86$ mm^3. With $\theta_{air} = 45°$, the effective angle for the reconstruction in water[3] is 32.1°. The reconstruction distance is $z_s = 1.66$ mm. None of the 2D and the 3D spaces is padded.

The volumes are reconstructed with the regularized Gerchberg-Saxton method run on 20 iterations with $nb_{it}^{GS} = 5$ and $nb_{it}^{GS,r} = 15$ iterations. The data alignment is refined every 3 regularized step for the first acquisition time and then the same alignment parameters are used for all the other acquisition times.

The obtained volumes are used in figures V.3 and V.5.

Full resolution reconstruction - The second time-lapse is composed of reconstructions with a voxel size given by the sensor pixel pitch and based on a region of interest of 800×800 pixels of 1.67^2 μm^2 selected[4] at the center of the sensor field of view.

The final reconstructions are composed of $800 \times 800 \times 200$ voxels of $1.67 \times 1.67 \times 2.66$ μm^3 for a global volume of $1.34 \times 1.34 \times 0.530 = 1$ mm^3. With $\theta_0 = 32.1°$. The reconstruction distance is $z_s = 1.67$ mm. Only the z-axis of the 3D volume is padded.

The volumes are reconstructed with the regularized Gerchberg-Saxton method run on 10 iterations with $nb_{it}^{GS} = 6$ and $nb_{it}^{GS,r} = 4$ iterations followed by 2 batches of 10 iterations[5] of the inverse problem approach IV.3 with $\mu_{L_1} = 1000$ and $\mu_{\nabla} = 75$. The interpolation in the Fourier domain is linear. For all the acquisition times, the data are aligned twice: once after 2 regularized iterations of method IV.4.

The obtained volumes are used in figure V.4 for the clusters 2 and 3 and in figure V.6.

Cluster reconstruction - The third time-lapse aims at reconstruct a cluster of cell which is at the lower limit of the previous reconstructed time-lapse. The region of interest[6] of 256×256 pixels of 1.67^2 μm^2 is centered on the holograms of this cluster of cells whose positions are computed relatively to the alignment parameters given by the previous time-lapse reconstruction. Indeed, their holograms are mixed with the ones of the overlying layer of cells and cannot be identified and extracted easily.

To reduce the computing time and the memory consumption, the final reconstructions are composed of $256 \times 256 \times 128$ voxels of 1.67×1.67^3 μm^3 for a global

[2] 2.67^2 mm^2

[3] See chapter III, section 5

[4] 1.34^2 mm^2

[5] In this chapter, the problem on the normalization factor for the ∇-regularization in the inverse problem approach is corrected.

[6] 428^2 μm^2

volume of $427 \times 427 \times 214 = 3.9\ 10^7\ \mu m^3$. With $\theta_0 = 32.1°$. The reconstruction distance is $z_s = 1.4\ mm$. Only the z-axis of the 3D volume is padded.

The volumes are reconstructed with the regularized Gerchberg-Saxton method run on 20 iterations with $nb_{it}^{GS} = 10$ and $nb_{it}^{GS,r} = 10$ iterations followed by 4 batches of 10 iterations of the inverse problem approach IV.3 with $\mu_{L_1} = 1000$ and $\mu_\nabla = 75$. For all the acquisition times, the data alignment is computed from the results of the previous time-lapse.

The obtained volumes are used in figure V.4 for cluster 1[7].

Results

This experiment shows the potential of 3D lens-free microscopy to acquire pertinent data on four domains of cell culture:

- 3D cell motility and large scale migrations
- Cell(s)-cell(s) interactions
- Developmental biology
- Extracellular matrix-cell(s)- interactions

3D cell motility - Figure V.3.a shows a snapshot of the 3D time-lapse reconstructions at low resolution. The reconstructed volume is as large as 4.86 mm^3 ($2.67\ mm \times 2.67\ mm \times 0.68\ mm$) and it is possible to image simultaneously hundreds of cellular objects.

This large field of view allows tracking cells on long distances. It is emphasized on figure V.3.b where the maximal values of the temporal stack are kept. The cells displacements leave tracks on such a visualization. It can be seen that the cells do not follow a random movement but are moving along extended organized trajectories.

A first analysis consists in counting the number of cell clusters present in the 3D reconstructed volume as a function of time (figure V.3.c) and measuring their size in terms of projected area (figure V.3.d) in the xy-projection.

At first, with the first cell divisions, the number of clusters reaches a maximum of 496 at $t_0 + 90\ h$. But then, via cell divisions and successive merging, this number drops to 383 at $t_0 + 210\ h$. In parallel, the average projected area of the clusters increases while the occupied area of the field of view reaches a plateau. This implies that the cells stop multiplying (otherwise the occupied area would increase) and favor global movements and merging.

Developmental biology - Examples of clusters growth due to cellular division are presented in figure V.4. Three clusters (identified with numbers in figure V.6) are blocked in the Matrigel®and grow inside the extracellular matrix (ECM). It is consequently possible to follow their development during the two weeks monitoring.

[7]The fact that the reconstructions of the different clusters 1, 2 and 3 are similar tend to show that the problem in the normalization of the ∇-regularization is effectively corrected as the same values for the hyperparameters are used but on volumes of different sizes.

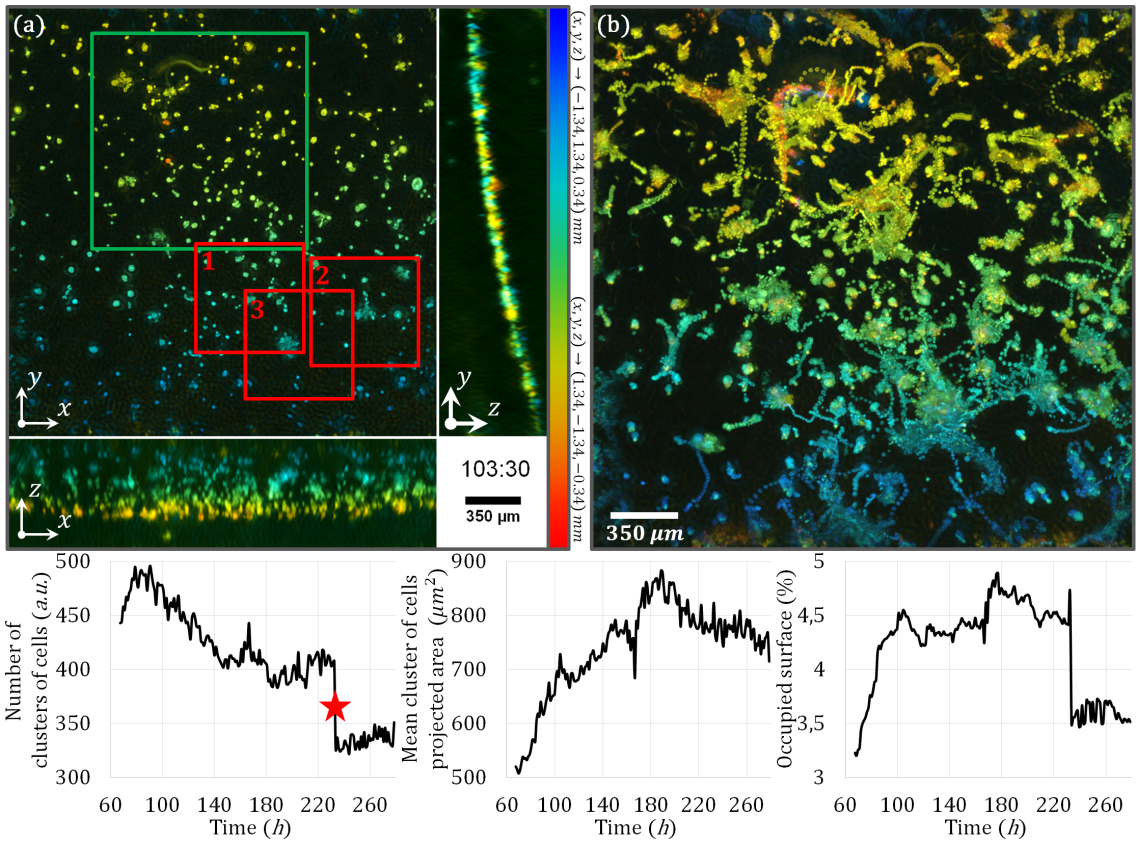

Figure V.3: (a) Orthogonal average intensity projections of the reconstructed volume at $t_0 + 103\ h\ 30\ min$. The RWPE1 cell culture is followed during two weeks on the 3D lens-free microscope. The color bar gives the depth in the volume for each views. The blue color encodes for the highest positions ($z = 0.34\ mm$ for the xy-view, $x = -1.34\ mm$ for the yz-view, $y = 1.34\ mm$ for the xz-view) and the red color encodes for the deepest positions ($z = -0.34\ mm$ for the xy-view, $x = 1.34\ mm$ for the yz-view, $y = -1.34\ mm$ for the xz-view). The green square is the region of interest which is reconstructed at high resolution (see figure V.6). The red regions of interest emphasize noticeable cell behaviors (see figure V.5). (b) Maximum intensity projection of the temporal stack for each pixel of the xy-view. The trajectory of isolated cells on large scales can be identified. (c) Number of detected objects as a function of the experiment time. The red star indicates a change of culture media at $t_0 + 234\ h$ in which several clusters of cells have detached. This has biased the measurement (d) Mean projected area on the xy-plane of the detected objects as a function of the experiment time. (e) Percentage of the occupied area on the overall xy-plane of the field of view.

Cluster 1 time-lapse reconstruction is specially reconstructed to study it. Clusters 2 and 3 time-lapse reconstruction is extracted from the high resolution time-lapse reconstruction. The volume are estimated according to a 3D segmentation performed using a simple thresholding algorithm.

Cluster 1 extends by ejecting some cells on its sides.

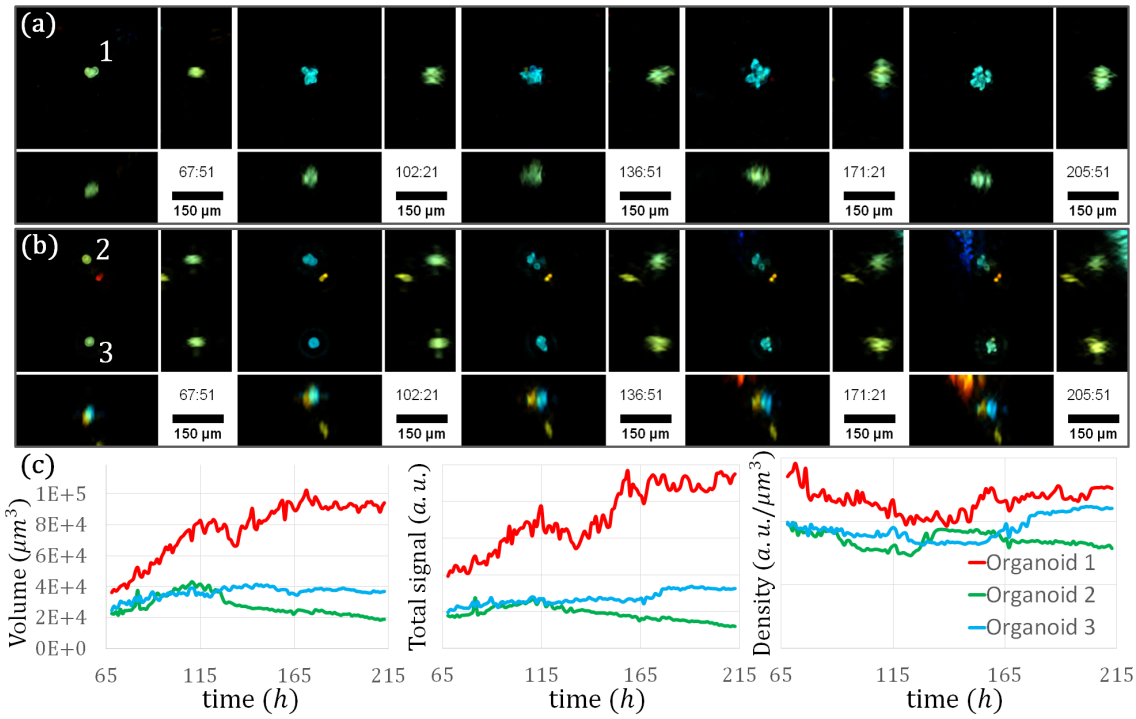

Figure V.4: (a-b) Time series of the reconstructed volume of three different clusters of cells highlighted in figure. V.6 at 34 h 30 min time intervals. The volume is 430 μm × 430 μm × 210 μm. Time is indicated in hours: minutes. On each view, the colors codes for the depth: the shallowest in blue, the deepest in red. The clusters mainly spread on two dimensions. (c) The volume, the integrated signal on the volume and the resulting density of the three clusters are plotted over time.

Monitoring their volume in figure V.4.b, it appears that they grow before reaching a plateau and even retracting for the cluster 2. Cluster 1 volume grows linearly from 40 10^3 to 225 $10^3 \mu m^3$, reaching a plateau at $t_0 + 165$ h. In comparison, the initial growth of clusters 2 and 3 is negligible with a volume oscillating around 30 $10^3 \mu m^3$.

Even if the reconstruction methods are not proven to be quantitative, it is interesting to draw the overall reconstructed signal on the volume as well as the cluster density (the integrated signal divided by the volume). Their density remains overall constant.

As stated above, the decreasing number of clusters of cells is due to merging of such clusters at the surface of the Matrigel® drop. This also participates to the overall growth of the clusters mean projected area.

Cells-cells interactions - This merging between clusters implies large scale interaction that can be observed thank to the large field of view provided by the lens-free microscope. It allows finding rare phenomena which can hardly be found or monitored with classical imaging techniques.

Figure V.5 presents three montages extracted from the regions of interest intro-

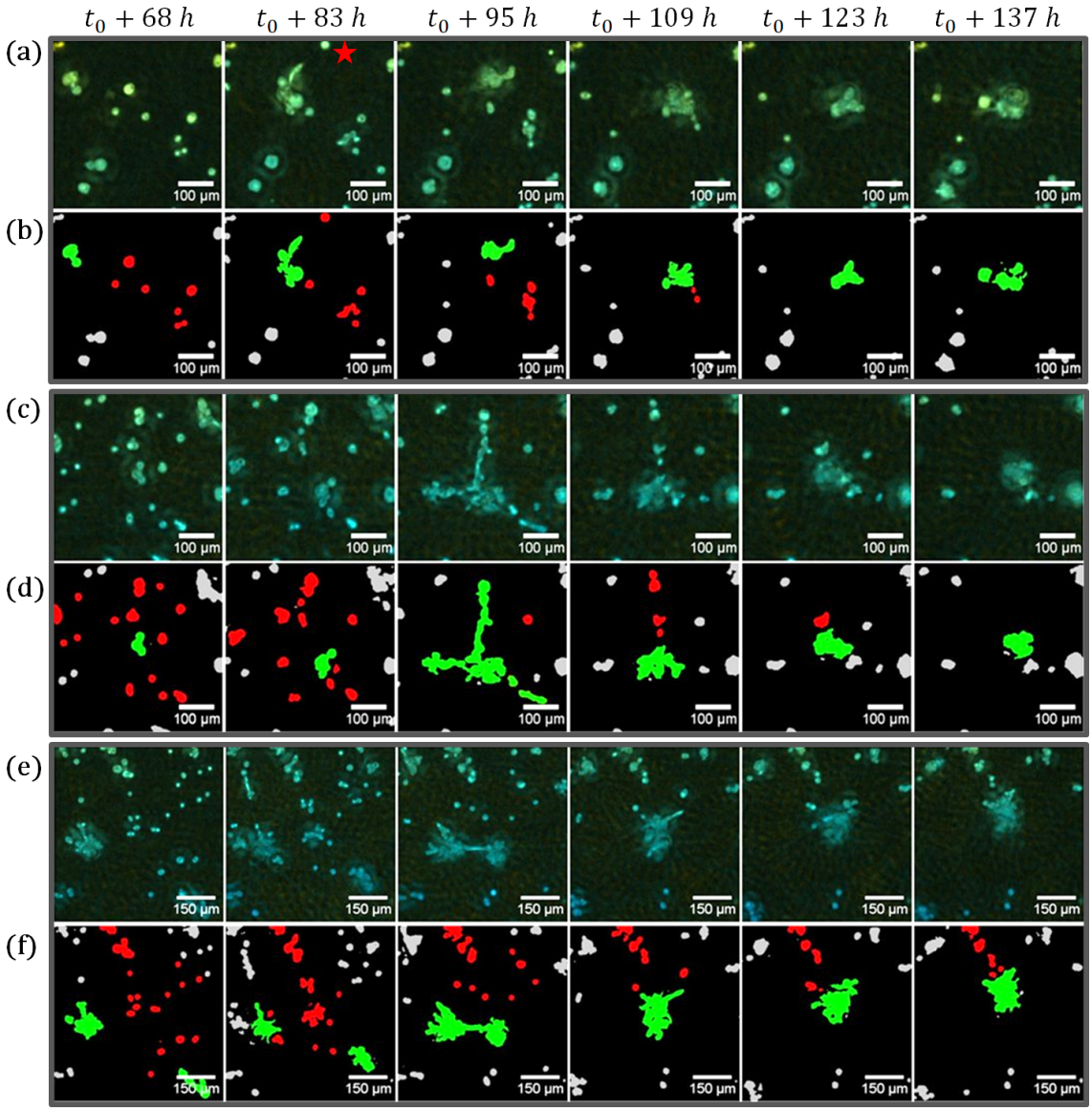

Figure V.5: Time series of region of interests showing cell migration patterns resulting in the growth of large aggregates of cells. (a,c,e) 3D time-lapse reconstructions of three different regions of interest taken from the full-field reconstruction framed in red in figure V.3.a. On each view, the colors codes for the depth: the shallowest in blue, the deepest in red. (b),(d) and (f) The xy-projections depicted in respectively (a),(c) and (e) are segmented and a color code is given to the different clusters of cells: green for the cluster of interest and red for the cells that will be aggregated into this cluster. Other cells that are not aggregated to this cluster are depicted in gray. (a-b) The organoid (green) moves into the field of view and grabs the surrounding cells (red). (c-d) The organoid (green) pulls cells (red) before their merging. (e-f) Two organoids (green) exchange cells before creating a branch and merging. Some other cells (red) are then pulled before their merging.

duced in figure V.3. These montages emphasize some cells-cells behaviors.

Figures V.5.a-b show the growth of a cluster of cells initially 25 μm in diameter (in the xy-projection). The growth is initiated when the cluster starts moving in its surrounding and merges with other cells. The cluster moves by 250 μm in 38 hours with an average speed of 14 $\mu m.h^{-1}$ and during its course it aggregates around himself 7 small clusters of cells of 15 to 30 μm in diameter to form a larger cell aggregate. At one point, at $t_0 + 83$ h, the aggregate forms a 150 μm long cell branching initiated by the dispersal of a 25 μm diameter cell cluster (see red star in figure V.5.a). In the following 20 hours this cell branching is however re-absorbed to the aggregate. At the end of its course, the aggregate is about 70 μm in diameter and there are no more cells present within a circle of 390 μm in diameter. In the following 140 hours, one can observe that this newly formed aggregate is unstable. It wiggled and its size oscillated between 60 and 90 μm in diameter as it dispersed and re-absorbed small cell clusters of 5 to 20 μm in diameter (not presented here). The distance of the dispersions ranges between 5 and 75 μm and it appears that the larger the dispersed clusters of cells, the larger the distance of dispersal.

Figures V.5.c-d show another particular cell aggregate growth. In this case the growth is apparently initiated from the merging of three single cells that are first orbiting around each other. At $t_0 + 95$ h, suddenly, this newly formed cluster of cells generated three extensions of 70 μm, 220 μm and 190 μm in length respectively. These branches are finally re-absorbed and, doing so, the cluster attracts to itself a large number of cells present in its neighboring. In sum, this cluster grows through the merging of 15 other clusters that are initially present within a circle of 450 μm. This cell aggregate is also unstable. By three times it ejected clusters of cells in the direction of another cell aggregate located at a distance of 250 μm (not presented here).

Figures V.5.e-f show the merging of two cell aggregates consecutive to pairwise attraction. At $t_0 + 68$ h, the two aggregates are about 55 μm in diameter and they are separated by a distance of 450 μm. They first move towards each other, accumulating cells from the surroundings. When the distance between the two aggregates is about 100 μm, branching cells emerge and connect the two aggregates that finally merge together in the time of four hours. The resulting aggregate continue to move a little, by 150 μm and accumulated more neighboring cells. At $t_0 + 280$ h this aggregate is as large as 140 μm in diameter and the number of cells present in its neighboring becomes very low.

These observations take place on more than four days and demonstrate thus that small amounts of localized cell migrations are able to strongly affect the growth of cell aggregate.

Extracellular matrix-cells interactions - A region of figure V.3 is selected to be reconstructed at full resolution (the green square). Figure V.6.a presents the 3D reconstruction at $t = 193$ h 12 min.

Figure V.6.b emphasizes a more striking example of clusters merging. It concerns the accumulation of 25 clusters of cells into one very large aggregate. The latter still manages to move as a cohesive group at a speed in the range of 5 to 10 $\mu m.h^{-1}$. The

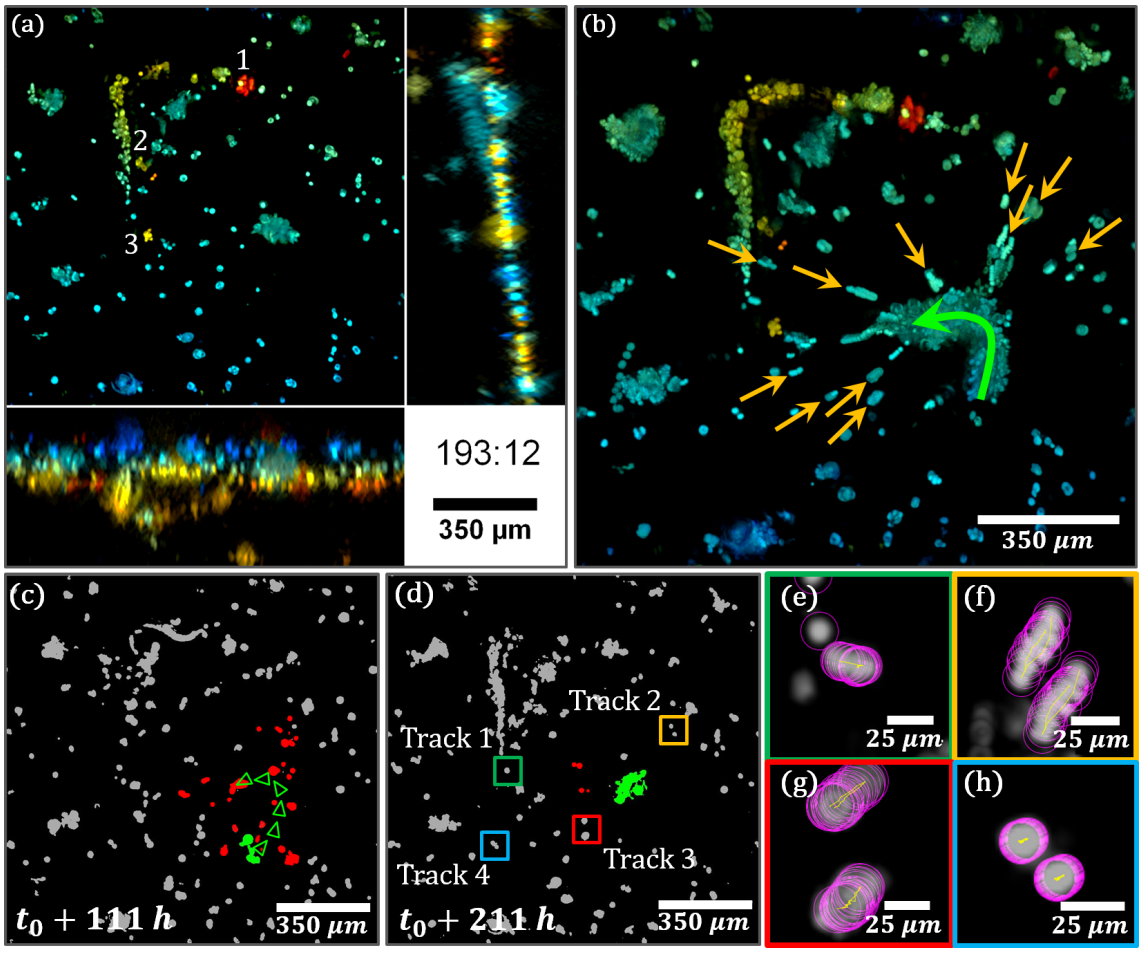

Figure V.6: (a) Reconstruction of the region of interest highlighted in green in figure V.3 at $t_0+193\ h\ 12\ min$ at higher resolution. It shows the merging of cells aggregates into a very large aggregate. Three clusters which grew inside the Matrigel® are numbered (see figure V.4). On each view, the colors codes for the depth: the shallowest in blue, the deepest in red. (b) Maximal value of the temporal stack for each pixel of the xy-view between $t_0 + 176\ h\ 39\ min$ and $t_0 + 208\ h\ 23\ min$. The yellow arrows point at cells fixed in the Matrigel® which highlight its deformation as the cluster of cells moves along the green arrow. (c-d) xy-snapshots at $t_0 + 111\ h$ and $t_0 + 211\ h$. The projections images are segmented and a color code is given to the different objects: green for the cluster of interest and red for the cells that will be aggregated into this cluster. Other cells that are not aggregated to this cluster are depicted in gray. Green arrows show the displacement of the cluster of interest. (e-h) Visualizations of cell displacements resulting from the traction forces created by the large aggregate of cells onto the Matrigel®. The initial positions of the clusters of cells are shown in (d). The cell tracking has been performed with the `trackmate` plug-in in `ImageJ` [79] on the 2D projections. The figure shows the sum of the temporal tracks from $t_0 + 176\ h\ 39\ min$ to $t_0 + 208\ h\ 23\ min$. The cell cluster detection is shown in purple, the track in yellow and the initial starting point in red.

measured speed presents also local maxima of about 30 $\mu m.h^{-1}$ which, correspond to sequences of expansion/contraction of the aggregate. These local maxima of speed are observed at $t_0 + 120\ h$ and between $t_0 + 180\ h$ and $t_0 + 210\ h$ (see figure V.7.a-b).

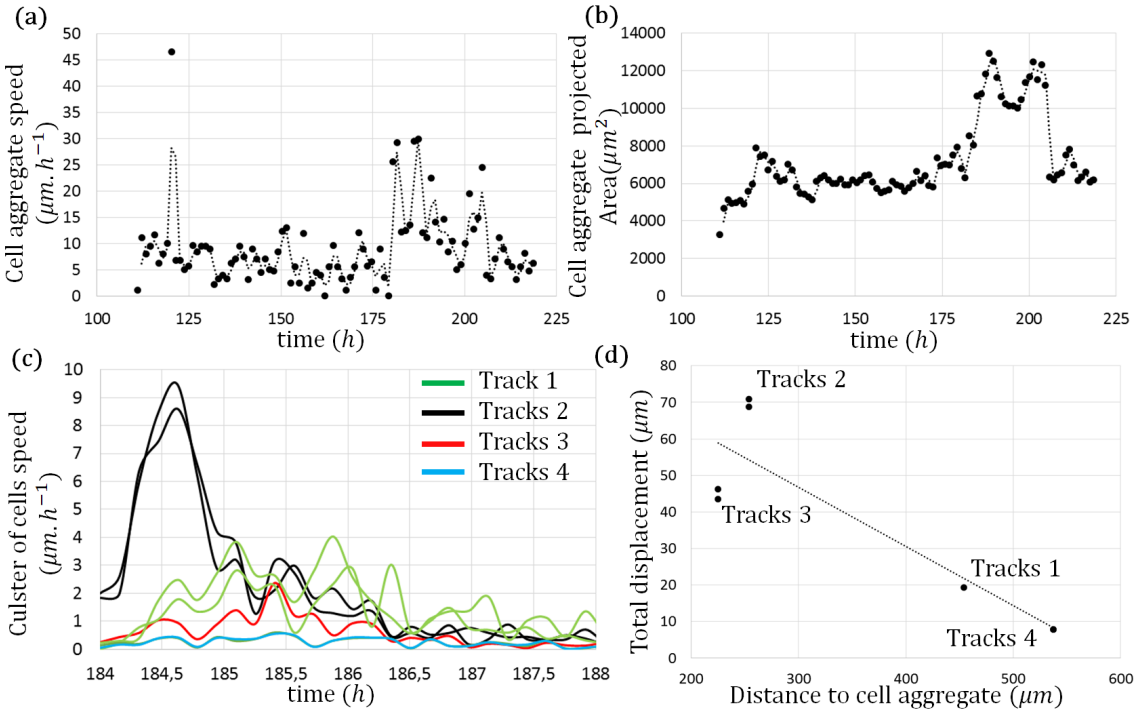

Figure V.7: (a) Speed of the large aggregate of cells in figure V.6 as a function of time. (b) Total projected area of the large aggregate of cells as a function of time. (c) Speed of the clusters of cells depicted in figure V.6.c-f as a function of time. (d) Total displacement of the clusters of cells depicted in figure V.6.c-f as a function of the distance to the large aggregate of cells.

During the latest sequence of expansion/contraction, the large aggregate clearly created traction forces onto the ECM over large distances, from tens to hundreds of micrometers. At $t_0 + 184\ h$ hours, following a large expansion of the cell aggregate, a traction force is generated onto the ECM. It is indirectly observed through the displacement of several clusters of cells towards the large aggregate (figures V.6.e-h). These traction forces disappear as the aggregate releases the tensions applied to the ECM and the clusters move back to their initial positions. Figures V.7.c-d show that the traction forces are isotropic and that they can be observed up to a distance of 550 μm.

2.2 Study of the extracellular matrix

This observation of an ECM modification due to cell traction led to a second experiment to better visualize these 3D deformations.

The protocol is the same than for the previous experiment excepted that fluorescent beads with a diameter of 10 μm (Sigma-Aldrich) are mixed with the

Matrigel®before its deposition at the center of the dish. It is monitored by lens-free imaging for 7 days. Cell culture medium is changed every two days.

This method is usually performed at the microscopic scale to monitor and quantify single cell traction forces [101]. Here it is used to show the long scale deformations of the ECM.

Acquisitions - Every hour a dataset is acquired, composed of 3×32 acquisitions done at 32 different angles $\varphi \in \{0°, 305°\}$, $\Delta\varphi = 9.8°$ in the three available wavelengths of the RGB LED $\lambda \in \{640\ nm, 520\ nm, 450\ nm\}$. These data are first aligned via the least mean squares minimization algorithm on 2D reconstructed data.

Scattering potential reconstruction - This is composed of low resolution reconstructions, based on a region of interest of 800×800 pixels of $3.34^2\ \mu m^2$ selected[8] at the center of the sensor field of view.

To reduce the computing time and the memory consumption, the final reconstructions are composed of $800 \times 800 \times 128$ voxels of $3.34 \times 3.34 \times 6.10\ \mu m^3$ for a global volume of $2.67 \times 2.67 \times 0.78 = 5.57\ mm^3$. With $\theta_{air} = 55°$, the effective angle for the reconstruction in water[9] is 38°. The reconstruction distance is $z_s = 3.435\ mm$. Only the z-axis of the 3D volume is padded.

The volumes are reconstructed with the regularized Gerchberg-Saxton method run on 12 iterations with $nb_{it}^{GS} = 6$ and $nb_{it}^{GS,r} = 6$ iterations followed by 4 batches of 10 iterations of the inverse problem approach IV.3 with $\mu_{L_1} = [1000, 1000, 2000, 2000]$ and $\mu_{\nabla} = 75$. For all the acquisition times, the data are aligned three times: once after 2 regularized iterations of method IV.4 and once after the two first batches of iterations with method IV.3.

As described in the previous chapter, positivity constraints are applied on the reconstructed scattering potential: $C(f) = \{f / \mathcal{R}(f) \geq 0, \mathcal{I}(f) \geq 0\}$.

The obtained volumes are used in figures V.9, V.10 and V.11.

Refractive index reconstruction - As seen later, the previous time-lapse shows a global drift along the z-direction and the reconstructed beads and cells slowly go out of the reconstructed field of view. Moreover, at the end of the experiment, when the field of view is crowded, a lot of twin-image remains and degrades the reconstruction quality. Some tests on these acquisitions (not presented here) showed that reconstructions based on the refractive index are more robust to this situation.

The second time-lapse is composed of the same acquisitions than previously and uses the alignment parameters produced by the previous time-lapse but modified to take into account the z-drift and keep the initial region of interested centered in the reconstructed field of view.

The final reconstructions are also composed of $800 \times 800 \times 128$ voxels of $3.34 \times 3.34 \times 6.10\ \mu m^3$ for a global volume of $2.67 \times 2.67 \times 0.78 = 5.57\ mm^3$, with $\theta_{air} = 55°$. The reconstruction distance varies around $z_s = 3.435\ mm$. Only the z-axis of the 3D volume is padded.

[8] $2.67^2\ mm^2$

[9] See chapter III, section 5

The volumes are reconstructed with the regularized Gerchberg-Saxton method run on 10 iterations with $nb_{it}^{GS} = 5$ and $nb_{it}^{GS,r} = 1$.

Positivity constraints are applied on the reconstructed refractive index: $C(n) = \{n/\mathcal{R}(n) = 0, \mathcal{I}(n) \geq 0\}$.

Some of the obtained volumes compose the figure V.8.

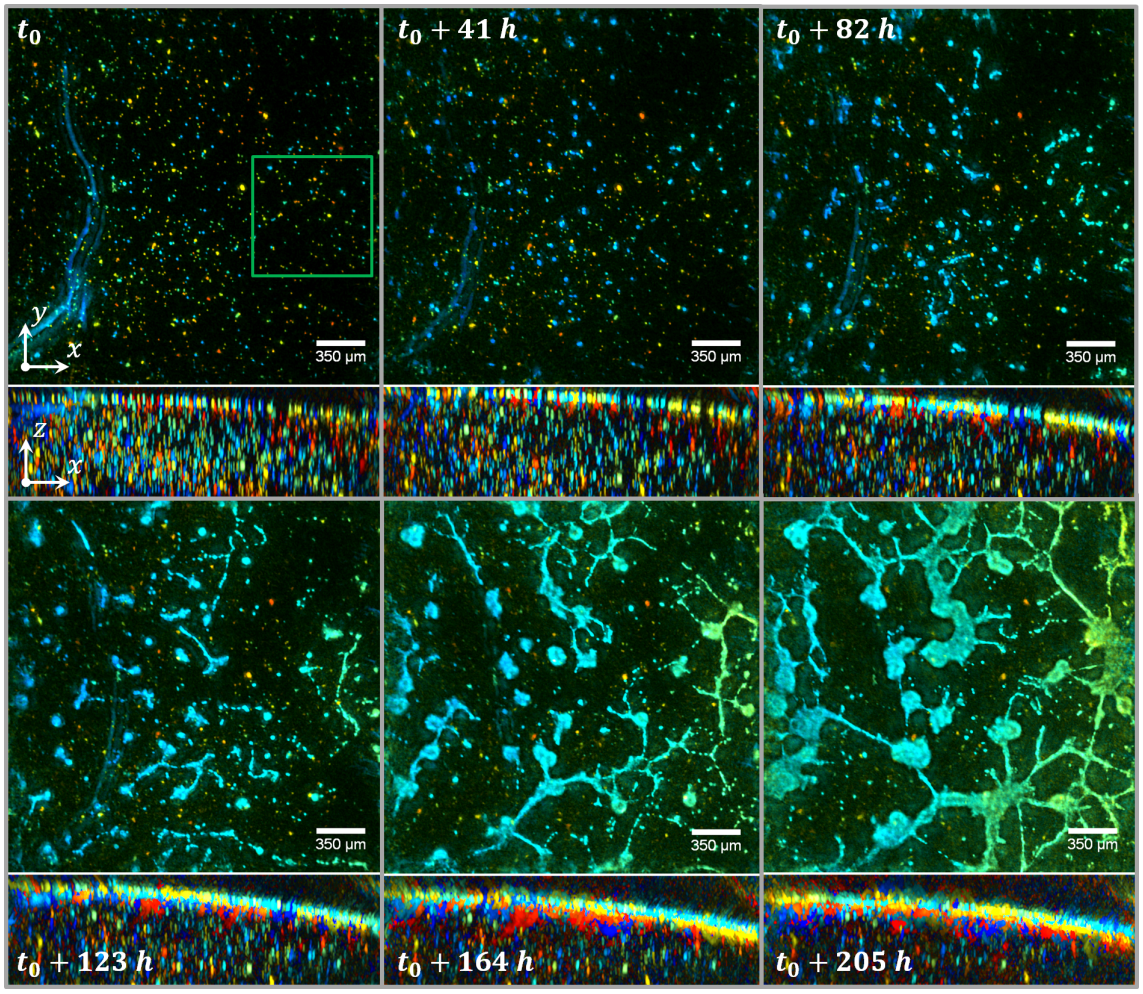

Figure V.8: (a) Orthogonal average (xy) and maximum (xz) intensity projection of reconstructed volumes of a 3D culture of RWPE1 cells with 10 μm beads embedded into the ECM monitored during 10 days in incubator conditions. Final volume: 2.67 mm × 2.67 mm × 0.78 mm = 5.57 mm^3. On each view, the colors codes for the depth: the shallowest in blue, the deepest in red. The xz-projections show clearly the presence of the 10 μm beads embedded into the ECM. The green square is the region of interest presented in figure V.9.

At first sight, this second 3D time-lapse acquisition performed over eight consecutive days, shows a striking evolution of the RWPE1 3D cell culture, namely the construction of a cellular network.

In contrast to the first experiment where the cell aggregates are moving, deforming and merging, here another interesting phenomena can be observed. A small

population of cells clusters (15 out of 140 clusters) start to eject cells and in some case dissociate into batches of single cells.

As previously, large scale cell movements can be identified. Figure V.9 shows the total dissociation of four clusters together with the tracks of the dispersed cells that further migrate on the Matrigel® at a speed of about 30 $\mu m.h^{-1}$. These cells migrate along linear paths, they follow each other, sometimes turning back. Importantly they form trains of cells moving as cohesive groups (see red stars in figures V.9.b-d). In a second phase these paths taken by the single cells become gradually branches of cells connecting larger cellular structures. After six days of cell culture, one can observe about 30 cells aggregates in the range of 50 to 100 μm in diameter. They are separated by distances of about 250 μm and most of them are interconnected with each other (see figure V.8).

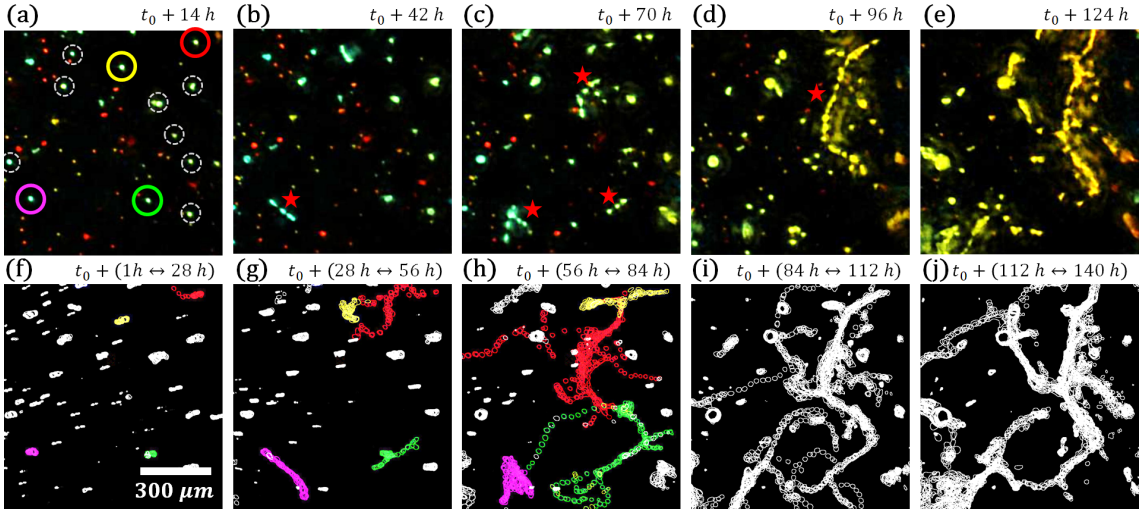

Figure V.9: Visualization of a region of interest of figure V.8 showing migrations of single cells. The snapshots are details of xy projections of the 3D reconstructions taken at time intervals of 28 hours. In (a), four cell clusters of interest are pointed with different colored circles. These are clusters that will next decompose into single cells. Other clusters that remain solid are pointed with dashed white circles. The red stars in (b-d) point at different "train of cells". (f-j) Time series of the dissociation of the four clusters of cells and the tracks of the dispersed single cells. The cell tracks are presented in a temporal window of 28 h with the color code given in (a). The tracking is performed manually up $t_0+84\ h$. After this frame, it is no longer possible to conduct the cell tracking owing to the large number of cells and the relatively large frame rate of 1 acquisition every hour.

Finally, in a third and final phase, the cellular network collapses, branches of cells merge, closed structures collapse and cell islands merge together. Despite this collapse, the cellular network does not vanish completely. After eight days of culture, there are still branches of cells connecting very large cellular structures, some of them as long as 500 μm.

In sum, three distinct phases in this RWPE1 3D cell culture can be distinguished:

a first phase of single cell migration, a second phase of interconnection between cell aggregates, and a final phase where the cellular network collapses partially. These three phases are accompanied by deformations of the ECM which can be visualized thanks to the presence of the introduced microbeads.

In the third phase in particular, the collapses of the network reveals significant pulling forces that distort the ECM. But at first sight, in the first hours of the experiment, the presence of the microbeads allows observing the intrinsic 3D deformations of the ECM made of Matrigel®. Their positions are monitored in the three dimensions using an algorithm similar to the one developed in the next section 3 of this chapter.

During the first 140 hours of the experiment, the ECM expands radially in the xy-plan. All the beads move away from a central point at a speed increasing with the distance to this point (red star in figure V.10.a). The speed of the beads is under 1 $\mu m.h^{-1}$ close to the center of expansion ($\sim 0.8\ \mu m.h^{-1}$) and about 2 $\mu m.h^{-1}$ at a distance of approximately 2.5 mm (see figuresV.10.a-b). At $t_0 + 90\ h$, the expansion stops and the ECM remains stable at least in the xy-projection.

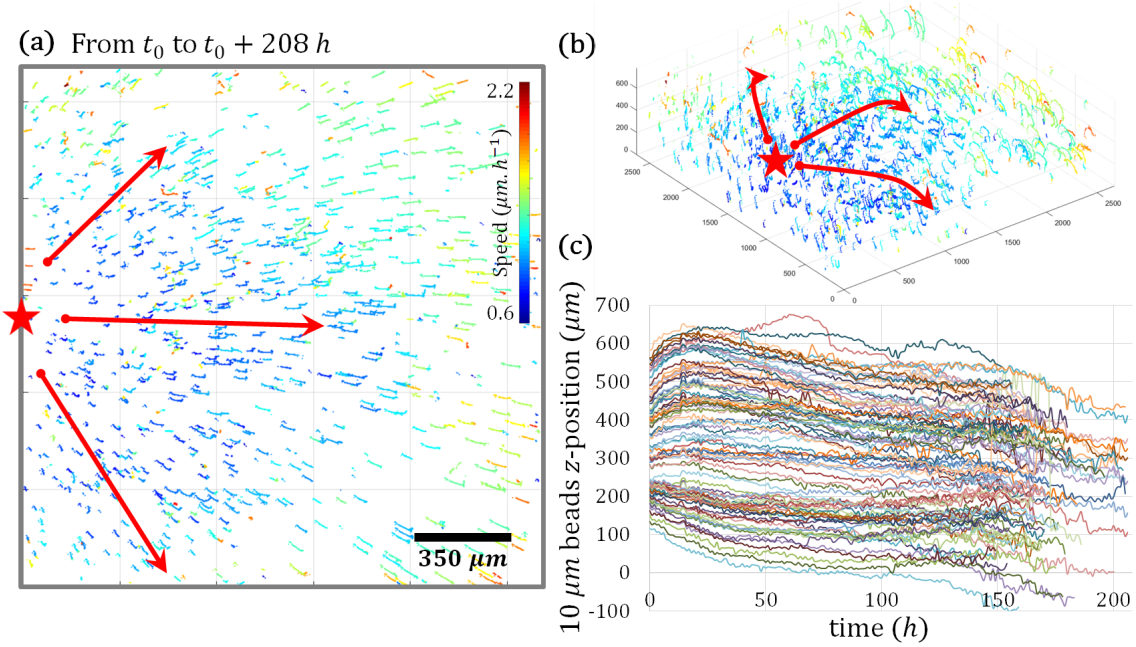

Figure V.10: (a-b) 3D particle tracking of the beads in the xy-projection (a) and the 3D volume (b). The figure shows the tracks of the 10 μm beads over 208 hours, with a color code corresponding to their median speed. The red arrows show the overall direction of the tracks. The red star shows the center of the ECM radial dilation. (c) Plot of the tracks of 250 beads along the z-direction as a function of time.

In the z-direction, in the first 24 hours of the time-lapse acquisition, there is an important ECM dilation of about 125 μm (see figures V.10.b-c) followed by a slow drift which lasts until the end of the experiment.

ECM deformation resulting from traction forces generated by cell aggregate can be clearly seen at $t_0 + 136\ h$ in figure V.11. At a distance of 350 μm to one large cell aggregate, a traction force is detected that move the 10 μm beads by 100 μm (speed of 12 $\mu m.h^{-1}$) and at a depth of several tens of microns below the Matrigel® surface (see figure V.11.c). This traction force is still visible through beads displacement at a large of distance of 1200 μm (see figure V.11.b). Thus, these observations show the long-scale effects of the traction forces generated by cell aggregate onto ECM.

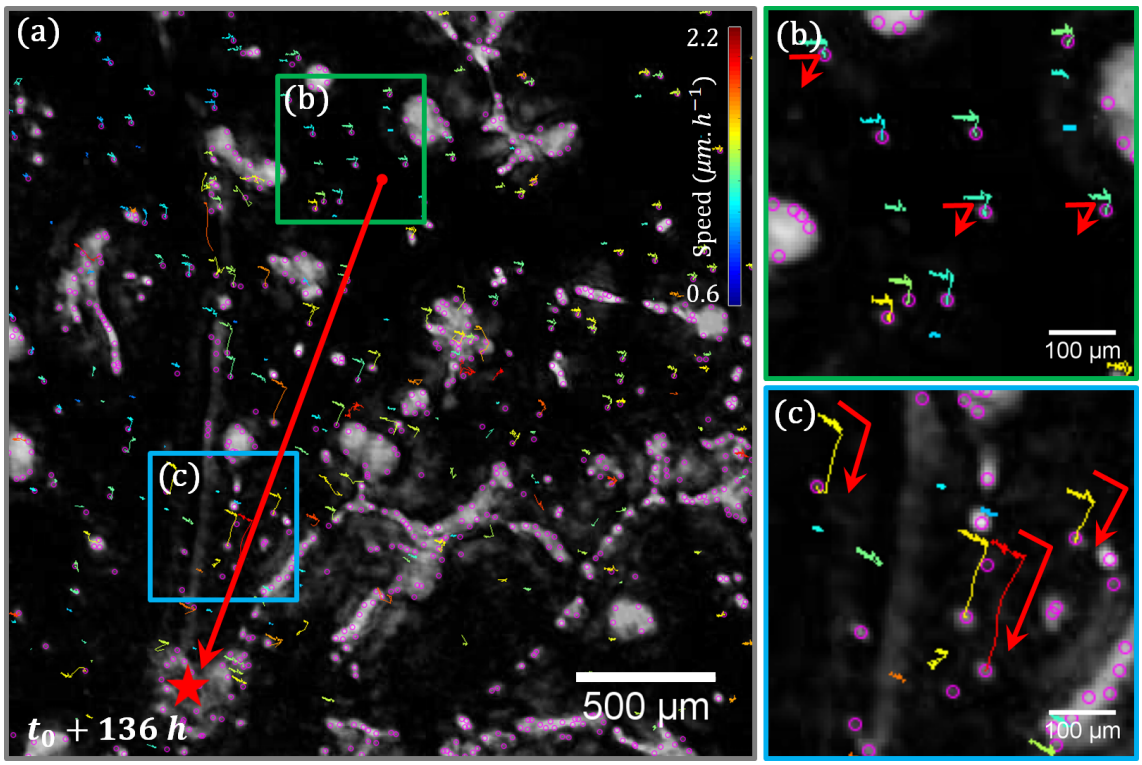

Figure V.11: (a) Snapshot of a region of interest at $t_0 + 136\ h$ showing a long-scale deformation of the ECM consecutive to traction forces generated by a cell aggregate (red star) slightly deeper below the Matrigel® surface. The direction of the traction forces is shown with a red arrow in. (b-c) Details of (a) showing the displacement of the beads towards the cell aggregate at distances of 1200 μm and 350 μm respectively. The red arrows highlight the change in direction of the 10 μm beads tracks consecutive to the generation of traction forces onto the ECM. The tracking is performed with the `trackmate` plug-in in `ImageJ` [79].

3 Characterization

The previous section 2 proves that the lens-free microscope is robust to incubator conditions and able to routinely monitor large 3D cell cultures. Moreover, the reconstruction quality is good enough to be able to analyze the reconstructed

volumes and retrieve quantitative information on the biological objects: position, shape, volume, speed, and so on.

These features need a quantitative analysis of the reconstructed volumes. In order to validate the figures given in the analysis of the previous section, it is necessary to characterize the lens-free microscope and the associated reconstruction codes both in terms of accuracy and resolution on a known object.

It is shown in the previous chapter IV, section 5.3 that the sectioning capabilities of the lens-free microscope outclasses the focused/unfocused estimation of 2D standard microscopes. But to better quantify the resolution on the z-axis, comparisons with classical optical 3D microscopes such as confocal or light-sheet microscopes are needed with simpler objects.

The idea for an adequate reference object comes from the results of the previous section in which the beads position in 3D is easy to extract with a good accuracy.

As a consequence, a new experiment dedicated to the lens-free microscope calibration is run and specific codes are implemented to compare the 3D reconstruction of a reference object from lens-free acquisitions with acquisitions through a standard microscope.

3.1 Experiment and data processing

The 3D reference object is directly inspired from the experiment presented in the previous section 2. At the center of Greiner petri dishes (Sigma-Aldrich), a small drop of Matrigel® is deposited to serve as a bed of another small layer of Matrigel® in which fluorescent microbeads with a diameter of 10 μm (Sigma-Aldrich) are mixed. It is then allowed to polymerize for 30 minutes at $37°C$ before addition of cell culture medium. As seen in the previous section 2, Matrigel® deforms along time. To limit this effect, the dish is put in incubator for three days before the acquisitions.

The final volume is consequently composed of fluorescent microbeads randomly spread in the three dimensions.

The reference for the positions is obtained by fluorescence microscopy: z-stacks fluorescent images are then acquired using an AxioObserver.Z1 inverted microscope (Zeiss) with a N-Achroplan 5x/0.13 Ph0 air objective mounted with an AxioCam 503 monochrome digital camera. In this configuration, the effective pixel size given by the microscope is 0.9080 μm on 1936×1460 pixels ($\sim 1.76 \times 1.33 \simeq 2.33\ mm^2$). 856 slices are imaged with a scanning pitch of: $\delta z = 1\ \mu m$. Let's note here that no immersion oil is used and that the translation stage moves in the air. The axial distances given by the microscope correspond to distances in the air.

Trying to get the best signal and to study its influence, lens-free acquisitions with and without the Petri dish cap are done. As shown in figure V.12.a, the cap produces a non-uniform background signal and blurs the beads holograms.

To analyze the effect of the illumination angle θ, different sets of acquisitions are acquired with the lens-free microscopes. Indeed, it is shown in chapter IV, section 1 that the higher the angle is, the better the results should be. Three angles are tested: $\theta \in \{35°, 45°, 55°\}$. As seen in figure V.12.b, a high angle leads to a

degraded signal.

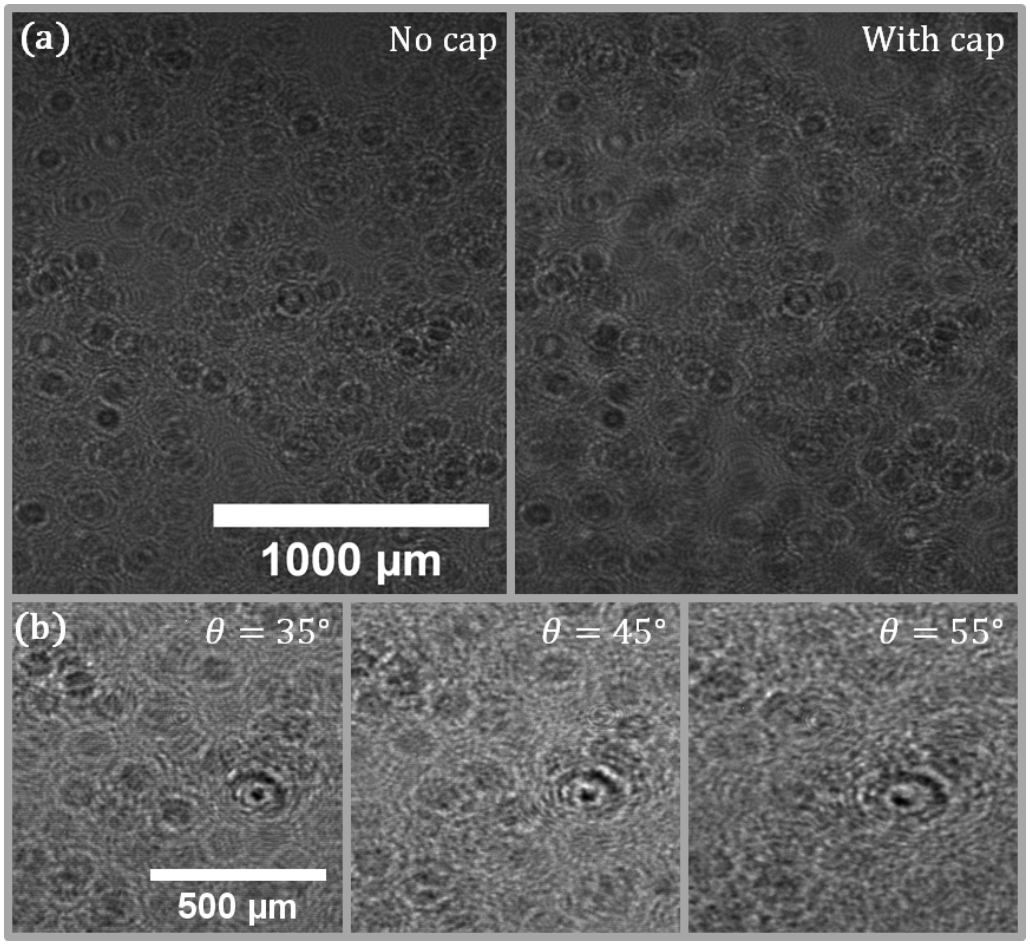

Figure V.12: (a) Comparison of a region of interest in the red channel with and without the cap on the Petri dish at $\theta = 35°$. (b) Comparison of a region of interest for different values of the angle θ in the red channel.

All the datasets are composed of 3×32 acquisitions done at 32 different angles $\varphi \in \{0°, 305°\}$, $\Delta\varphi = 9.8°$ in the three available wavelengths of the RGB LED $\lambda \in \{450, 520, 640\ nm\}$. In each dataset, a region of interest of 1024×1024 pixels ($\sim 1.7^2 \simeq 2.9\ mm^2$) is selected and aligned.

Both the fluorescence and lens-free acquisitions are performed outside the incubator. The air flow is activated to prevent the sensor from warming the dish and to avoid any condensation on the Petri dish cap during the lens-free acquisitions.

As the objects to reconstruct are simple, the regularized Gerchberg-Saxton algorithm presented in chapter IV section 4 is sufficient. The reconstructed volumes are composed of $512 \times 512 \times 400$ voxels of $3.34^3 \mu m^3$ for a global volume of $1.7 \times 1.7 \times 1.3\ mm^3 = 3.9\ mm^3$. The angles θ are corrected to take into account the refraction effect as presented in chapter III, section 5. Constraints of positivity $\mathcal{R}(f) \geq 0$ and $\mathcal{I}(f) \geq 0$ are enforced and the reconstructions are initialized by $nb_{it}^{GS} = 6$ loops without regularization. Then $nb_{it}^{GS,r} = 46$ regularized loops are

performed with a hyperparameters ratio of $\mu_\nabla/\mu_{L_1} = 1.25$. The data alignment is refined every 3 iterations.

Figure V.13 shows a comparison between the fluorescence acquisition and the lens-free reconstruction without cap and at $\theta = 35°$. On the fluorescence view, one can see the elongated signal around the beads due to out-of-focus fluorescence. The axial resolution appears better in the lens-free reconstruction.

To characterize the lens-free reconstructions, the position of the beads must first be extracted from the fluorescence z-stack and the reconstructed volumes. The same method is applied to the two volumes. First, a top view of the xy-plane is computed by selecting the maximal value of the volumes along the z axis to perform a maximum intensity projection (see figures V.13.c-d). These views are used to determine the positions of the beads on the xy-plane.

A homemade algorithm refines these 2D xy-positions and determines the altitude z of each bead. Presented in figure V.14, it consists in extracting a coring of the volume around each bead over the whole height of the volume. For each bead, one gets a volume similar to the one in the white medallions in figures V.14.a,c,e. The coring is extracted inside the blue perimeters. In each coring a specific pattern (presented in the white medallions in figures V.14.b,d,f) is matched by a 3D cross-correlation performed in the Fourier space to extract the 3D position. The chosen matching pattern is an ellipsoid of characteristic dimensions of $r_x = r_y = r_{rad}$ and r_z. The base of the extracted coring is a square of side r_{rad}^{ext}. These dimensions depend on the resolution of the pixel and the dimensions of the beads pattern in each volume.

- Fluorescence z-stack: $r_{rad} = 5\ pix$, $r_z = 45\ pix$ and $r_{rad}^{ext} = 8\ pix$
- Lens-free reconstruction ($\theta = 35°$): $r_{rad} = 2\ pix$, $r_z = 7\ pix$ and $r_{rad}^{ext} = 4\ pix$
- Lens-free reconstruction ($\theta = 45°$): $r_{rad} = 2\ pix$, $r_z = 9\ pix$ and $r_{rad}^{ext} = 4\ pix$
- Lens-free reconstruction ($\theta = 55°$): $r_{rad} = 2\ pix$, $r_z = 10\ pix$ and $r_{rad}^{ext} = 4\ pix$

For a checking purpose, the volumes are synthesized using the found 3D position and the chosen matching pattern. Comparisons between the original volume and the extracted position show a good agreement for both the fluorescence (figures V.14.a,c,e,g,i versus b,d,f,h,j)) and the lens-free volumes (not presented).

Once the 3D positions of the beads are known in the different volumes in terms of voxel, they must be paired.

For each reconstructed lens-free volume, the positions of the beads $\vec{r}_1^{\,b_i} = \left(x_1^{b_i}, y_1^{b_i}, z_1^{b_i}\right)$ extracted from the fluorescence z-stack are considered as the reference. These positions must be paired with the position $\vec{r}_2^{\,b_i} = \left(x_2^{b_i}, y_2^{b_i}, z_2^{b_i}\right)$ extracted from each of the lens-free reconstructions. To do so, the parameters of a transformation $pos_{1\to2}$ between the coordinates of two given volumes must be determined. These parameters take in account different effects:

- s_{2D}: a scaling factor on the 2D xy-plane to deal with the difference in effective pixel size between the fluorescence acquisitions and the lens-free reconstructions.

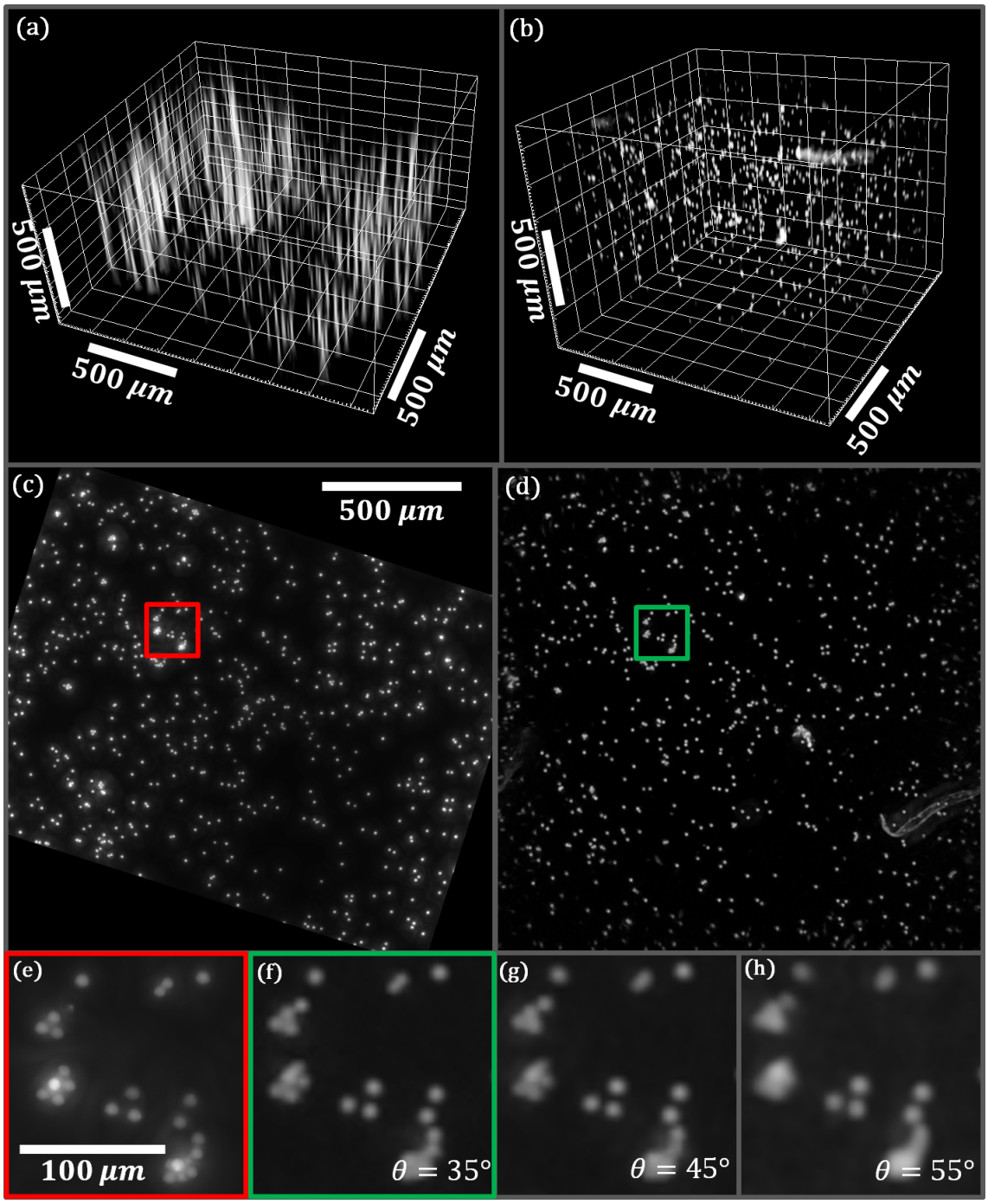

Figure V.13: (a) Visualization of the z-stack acquired with the fluorescence microscope. (b) 3D view of the reconstructed scattering potential of the volume at $\theta = 35°$ without the cap. (c) Maximum intensity projection of the volume presented in (a). (d) Maximum intensity projection of the volume presented in (b). (e) Zoom on a selected region of interest in the fluorescence view (c). (f) Zoom on the same region of interest in the lens-free view (d). (g-h) Zoom on the same region of interest but in the reconstructed volumes acquired with $\theta = 45°$ and $55°$.

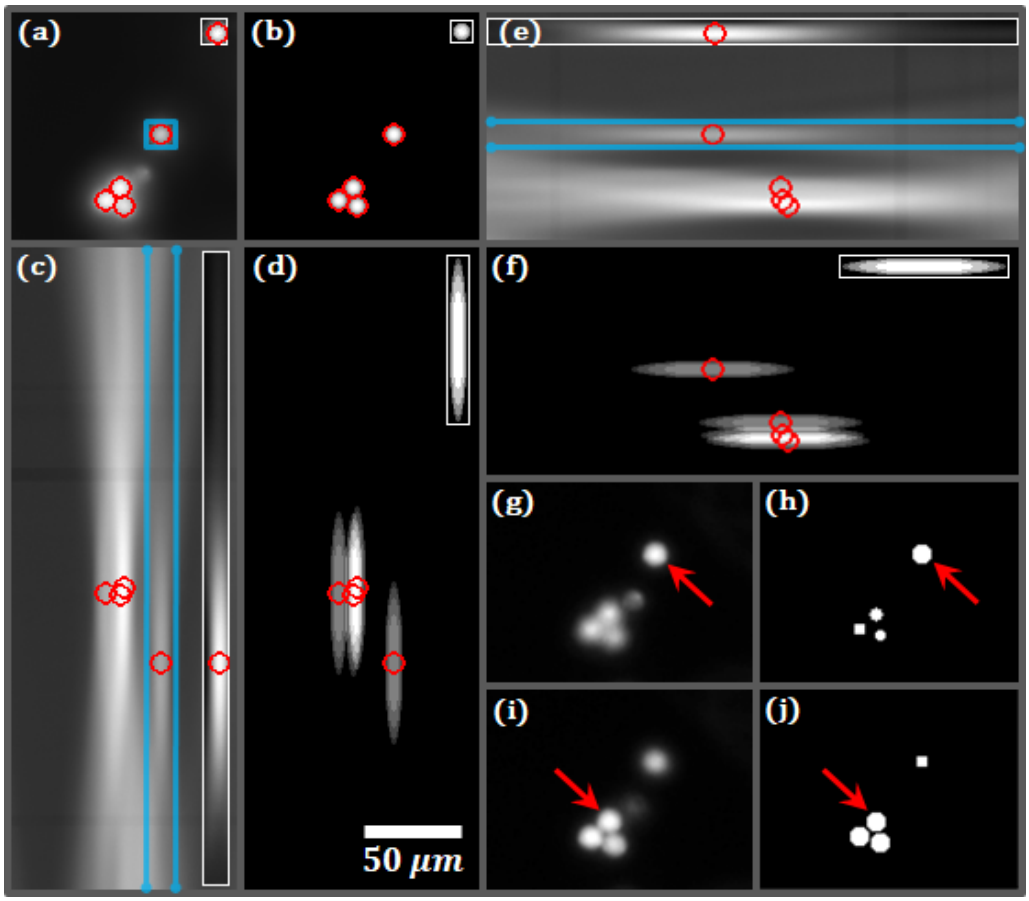

Figure V.14: (a,c,e) Orthogonal views of a region of interest of the fluorescence z-stack. Each view is an average intensity projection. The blue frames correspond to the side of the cored volume for a given bead. Its position (the red circles) is searched in this extracted volume (in the white medallions). (b,d,f) Orthogonal views of the region of interest synthesized with the found positions of the identified beads. The matching pattern is presented in the white medallions. (g-j) Comparison of the fluorescence z-stack (g,i) with the synthesized volume (h,j) at two different acquisition planes spaced $\Delta z = 28\ \mu m$ apart. The red arrows point at beads which are in focus in a given plane.

- s_z: a scaling factor along the z axis to deal with the difference between the sampling δz along the z-axis of the fluorescence acquisitions and the effective voxel size of the lens-free reconstructions.

- α: the angle of rotation on the 2D xy-plane between the two volumes to deal with the 2D rotation of the sample between its position on the fluorescence and lens-free microscopes.

- (x_0, y_0): the translation on the 2D xy-plane between the two volumes to deal with the 2D translation of the sample between its position on the fluorescence and lens-free microscopes.

- z_0: an offset on the z-axis to deal with a possible difference between the center of the volume acquired with the fluorescence microscope and the center of the reconstructed lens-free volumes.

In terms of 3D positions, this transformation works as follows:

$$\begin{aligned}\begin{pmatrix} x_2^{b_i} \\ y_2^{b_i} \\ z_2^{b_i} \end{pmatrix} &= pos_{1\to 2}\left([s_{2D}, s_z, \alpha, x_0, y_0, z_0]\,; \begin{pmatrix} x_1^{b_i} \\ y_1^{b_i} \\ z_1^{b_i} \end{pmatrix} \right) \\ &= \begin{pmatrix} s_{2D} \\ s_{2D} \\ s_z \end{pmatrix} . \begin{pmatrix} \cos\alpha & -\sin\alpha & 0 \\ \sin\alpha & \cos\alpha & 0 \\ 0 & 0 & 1 \end{pmatrix} \times \begin{pmatrix} x_1^{b_i} - x_0 \\ y_1^{b_i} - y_0 \\ z_1^{b_i} - z_0 \end{pmatrix}\end{aligned} \tag{V.1}$$

Let's note here that the transformation (V.1) between the positions of the beads expressed in the reference frame of the first volume and their expression in the reference frame of the second volume does not take in account a possible tilt of the volume compared to the axial direction. This consequently assumes that for all the acquisitions, the sample remained strictly parallel to the sensor. Over the dimensions on the xy-axes larger than a few hundreds of microns, even a small tilt can lead to a difference of several tens of microns on the z-axis. This effect consequently degrades the expected lens-free accuracy found along the z-axis.

To initialize the set of parameters, at least $nb_b = 6$ matching pairs $\{b_1, \cdots, b_{nb_b}\}$ are selected by the user. The set of parameters $\widetilde{par} = [\widetilde{s_{2D}}, \widetilde{s_z}, \widetilde{\alpha}, \widetilde{x_0}, \widetilde{y_0}, \widetilde{z_0}]$ is then estimated by minimizing[10] the distance between the transformed positions and the extracted positions in the second volume:

$$\widetilde{par} = \underset{par}{\operatorname{argmin}} \frac{1}{nb_b} \sum_{i=1}^{nb_b} \left\| \vec{r}_2^{\,b_i} - pos_{1\to 2}\left(par; \vec{r}_1^{\,b_i}\right) \right\|_2 \tag{V.2}$$

Using this set of parameters, a second homemade program automatically proposes new matching pairs that the user can choose to keep or not. It is possible also to refine the set of parameters running the minimization problem (V.2) again on the new set of matching pairs. As soon as the user estimates that enough pairs have been chosen and that the automatic matching is satisfactory, a last refinement of the parameters is done before an automatic matching of all the beads.

For each bead identified in the first volume, the automatic matching consists in computing their corresponding positions in the second volume from their position in the first volume via equation (V.1) and finding the closest identified bead in the second volume. If the distance between this closest bead and the computed position falls within a tolerance of 20 voxels, the two beads are paired. Otherwise, the bead is put apart. If the bead in the second volume is already paired, the bead in the first volume giving the closest computed position in the second volume is kept.

Figure V.15 presents the result for the pairing algorithm on the fluorescence z-stack and the lens-free reconstruction at $\theta = 35°$.

[10] Command "`fminsearch`" in Matlab®.

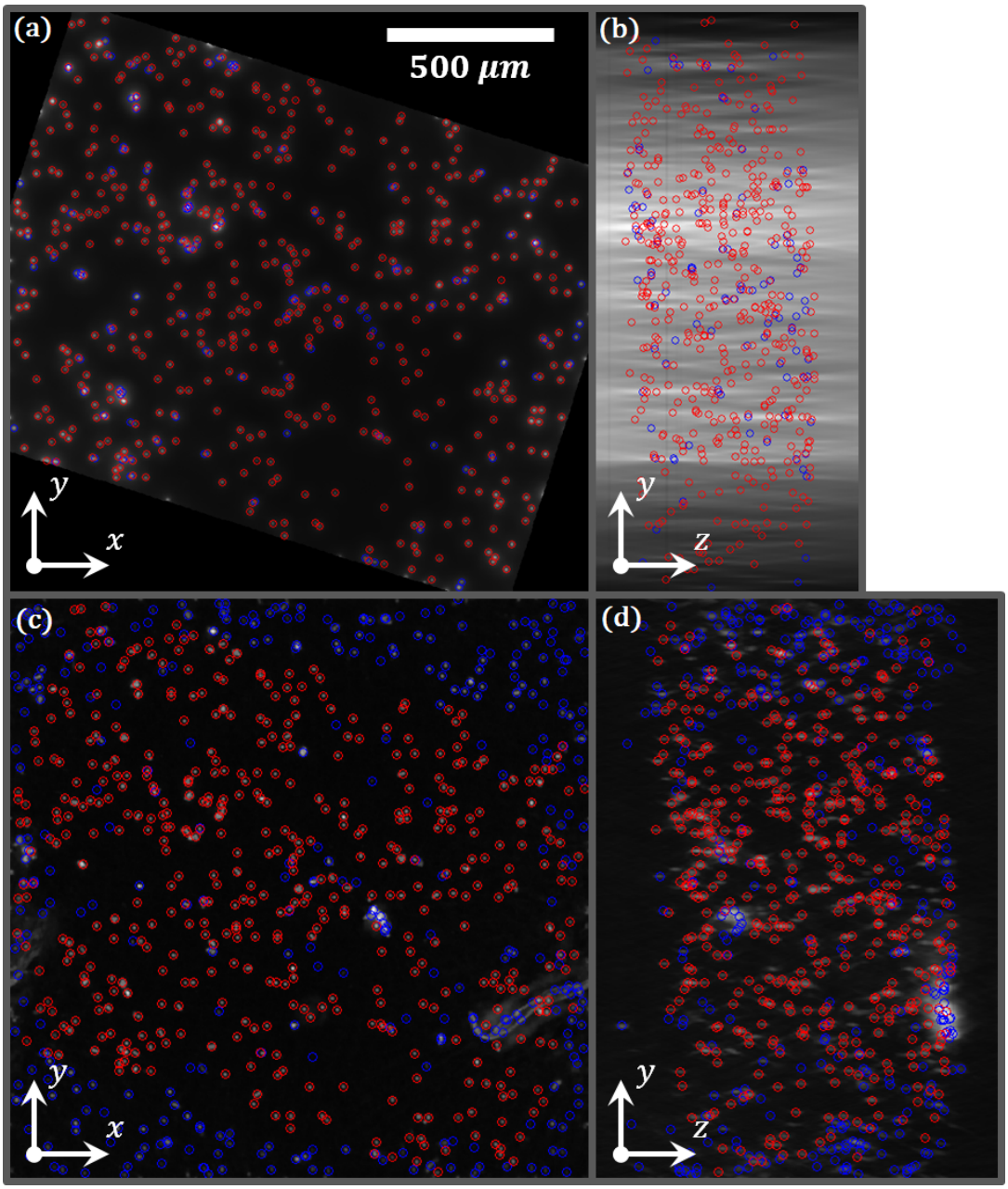

Figure V.15: (a,b) Average intensity orthogonal projection of the fluorescence z-stack. (c,d) Average intensity orthogonal projection of the lens-free reconstruction ($\theta = 35°$). The blue circles indicate the unpaired identified beads and the red circles the paired beads.

3.2 Accuracy

Figure V.16 presents the results on the beads which are paired between the fluorescence z-stack and the 3 lens-free volumes with $\theta \in \{35°, 45°, 55°\}$ without cap on the Petri dish.

On the xy-plane, the data are not scaled but only rotated and translated to give

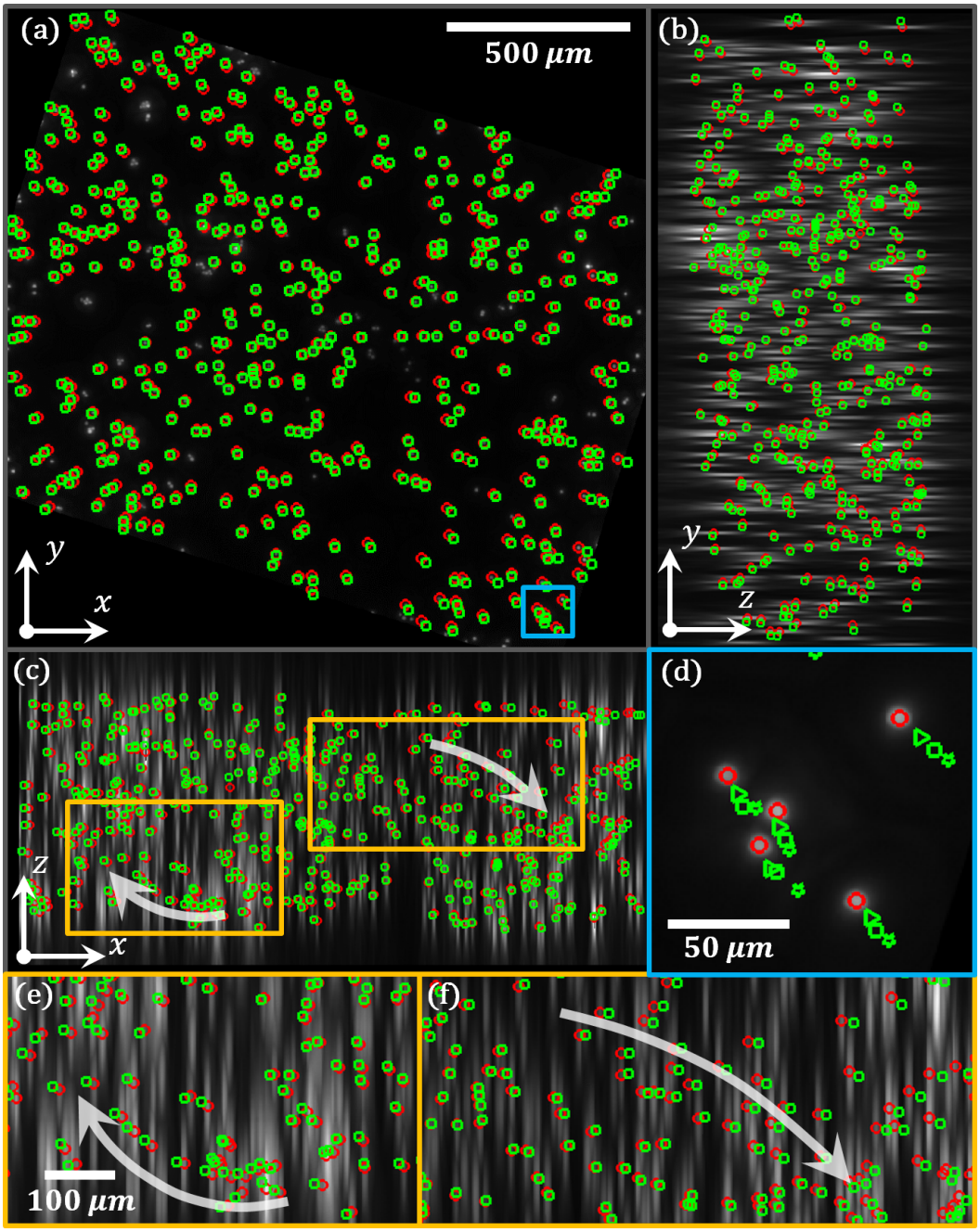

Figure V.16: (a,b,c) Maximum intensity orthogonal projections of the fluorescence z-stack. Red circles: the beads positions identified in the fluorescence z-stack. Green squares: the beads positions identified in the lens-free volume ($\theta = 45°$) (d) Zoom on the blue square on (a). Red circles: the xy-positions in the fluorescence z-stack. Green markers: the xy-positions in the lens-free reconstructed volumes at $\theta = 35°$ (triangles), $45°$ (squares) and $55°$ (pentagons). (e-f) Zooms on the orange rectangles on the xz-view (c). The gray arrows emphasize a tilt angle of the Petri dish between the acquisitions on the fluorescence microscope and the lens-free microscope.

the best matching[11] between the clouds of points[12]. The distances to the rotation center are directly given by the effective pixel size of the different volumes[13].

Looking at the xy-view in figure V.16.a, the lens-free reconstruction seems dilated. A zoom on the bottom-right corner in figure V.16.d shows that this effect happens for the three tested angles but with a different coefficient. The higher is the angle, the bigger is the coefficient.

On the z-axis the positions of the lens-free reconstructions are translated but also scaled to match the fluorescence positions. It seems to be a very good agreement between the paired positions.

The zooms on the xz-view in figures V.16.e,f show that the sample is tilted clockwise around the y-axis. As mentioned in the previous section, this transformation is not taken in account by equation (V.1) and will lead to a bias in the determination of the z-accuracy which will be underestimated.

To better quantify these effects, the distribution of the positions of the beads in the reconstructed volumes without cap as a function of the positions in the fluorescence z-stack is fitted on the xy-plane and along the axial direction. The results are presented in figure V.17 and table [V.1]. They are linear regressions $y = s.x$ which compare the extracted positions in the reconstructed volume with their reference positions in the fluorescence z-stack which lie on the line $y = x$. On the xy-plane, to analyze the dilation, the distances $d^{b_i} = \left\|\vec{r}_{1,2}^{\,b_i}\right\|_2$ are used rather than the xy-positions $x_{1,2}^{b_i}$ and $y_{1,2}^{b_i}$.

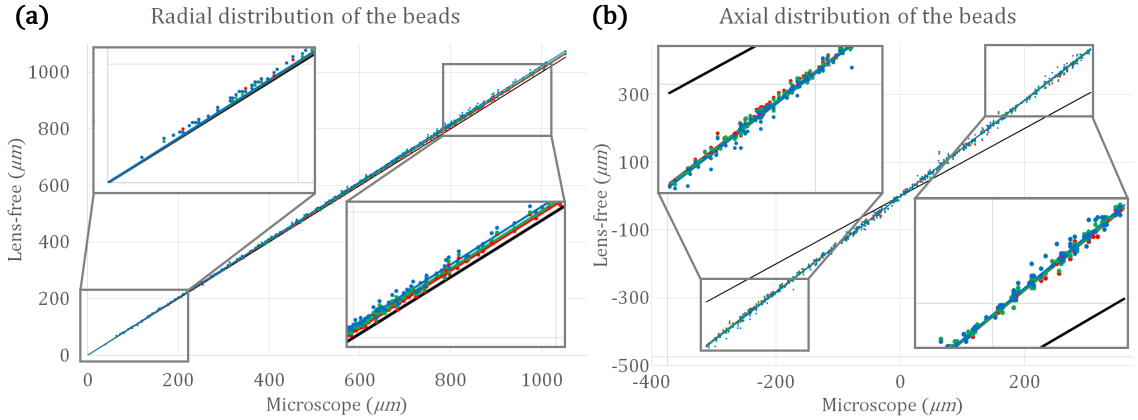

Figure V.17: Comparison between the positions determined in the fluorescence z-stack (black) and the lens-free reconstructed volumes (red $\rightarrow \theta = 35°$, green $\rightarrow \theta = 45°$ and blue $\rightarrow \theta = 55°$). (a) Comparison of the radial positions (on the xy-plane). (b) Comparison of the axial positions (along the z-axis).

Both for the radial and axial distributions, the data lie precisely as expected on lines with coefficients of determination higher than $R^2 > 0.999$.

[11] Using a minimization problem similar to the problem (V.2) but with only θ, x_0 and y_0 as parameters. The positions of the beads are directly given in terms of microns and not pixels.

[12] The fluorescence z-stack remains the reference.

[13] 0.9080 μm for the fluorescence and 3.34 μm for the lens-free.

$nb_b = 409$	Radial distributions			Axial distributions		
	$\theta = 35°$	$\theta = 45°$	$\theta = 55°$	$\theta = 35°$	$\theta = 45°$	$\theta = 55°$
s	1.0113	1.0155	1.0221	1.4046	1.4114	1.4237
R^2	0.9997	0.9997	0.9997	0.9992	0.9993	0.9991
σ (μm)	3.6835	3.7599	3.9926	6.6085	6.4412	7.4261

Table V.1: Results of the linear regression performed on the $nb_b = 409$ beads matched in the fluorescence z-stack and the three reconstructed volumes without the cap on the Petri dish. For $\theta \in \{35°, 45°, 55°\}$, the slope s, the coefficient of determination R^2 and the standard deviation σ of the linear regressions are given both for the radial (on the xy-plane) and the axial (along the z-axis) distributions.

For the radial distribution, the dilation effect noticed in figure V.16.a is visible on the linear regressions and their slope s which increases with the angle as seen above. At the highest distortion ($\theta = 55°$ and $s = 1.0221$), this effect remains nevertheless under 2.5 % with a low standard deviation $\sigma < 4\ \mu m$.

The increase of the dilation factor with the angle θ is also observed on the z-axis. The standard deviation is worse than on the radial plane with values around $\sigma \simeq 7\ \mu m$. But the most interesting parameter is the value of the slopes $s \simeq 1.41$, similar for all the angles but far from the ideal value of $s = 1$ if the reconstructions perfectly matched the fluorescence acquisitions. Actually this is the coefficient mentioned in chapter III, section 5: a scaling factor (III.40) must be applied in the microscope acquisitions along the z-axis because of the refractive index mismatch between the sample in the water and the moving objective in the air [86]. With $NA = 0.13$, $n_2 = n_{H_2O} = 1.33$ and $n_1 = n_{air}$ in equation (III.40), it comes:

$$\frac{z_{H_2O}}{z_{air}} = \sqrt{\frac{n_{H_2O}^2 - NA^2}{n_{air}^2 - NA^2}} \simeq 1.335 \tag{V.3}$$

which is closer of the found slopes s even if it is shown that this formula has some limitations [87]. The fact that the slopes are identical for the three angles supports the validity of the choices proposed in chapter III, section 5 to correct the illumination properties in order to take into account this refractive index mismatch. This also means that the lens-free reconstructions give the absolute position[14] on the z-axis without the need for any other scaling factor.

3.3 Resolution and xyz-sizing

To get an estimation of the resolution and the sizing capabilities of the lens-free microscope and the associated reconstructions, a region of interest is selected and an isolated bead is chosen.

[14] In the sense that the distances measured in the volume are actual distances in microns and not relative heights between the objects.

The datasets without the cap are also reconstructed at full resolution using the same reconstruction parameters concerning the hyperparameters, the positivity constraints and the number of iterations and alignments. The region of interest is a square of 256×256 pixels (428^2 μm^2) and the reconstructed volumes are composed of $256 \times 256 \times 256$ voxels of $1.67^3 \mu m^3$.

Figure V.18 shows this region of interest as well as the bead by comparing the xy and xz-average intensity projections of the fluorescence z-stack and the lens-free reconstruction without cap at full resolution for $\theta = 35°$.

On the xy-projections, isolated beads are perfectly identifiable and in the clusters of beads, the resolution appears sufficient enough to resolve the beads which lie in a same plane. For the rightmost cluster, the beads are agglutinated in the three directions and it becomes more difficult to separate the different beads.

On the xz-projections it clearly appears that the lens-free reconstructions have a better sectioning capability than the fluorescence microscope[15]. Nevertheless, the resolution is worse than on the xy-plane: the beads are elongated along z.

The undersampling of the reconstruction, the presence of the cap or the value of the angle θ can influence the quality of the reconstructions and the resulting resolution. Figures V.19 and V.20 compare the effects of these parameters.

The cap on the Petri dish does not seem to influence the quality of the reconstruction. There is no noticeable difference between the low resolution projections.

The voxel resolution 1.67 μm *v.s.* 3.34 μm does not influence the reconstruction resolution neither. Indeed, if the pixelization is visible on the low resolution projections, the full resolution projections do not provide better information. These projections are blurred and the edges of the beads are not sharper as it could be expected. Some tests (not presented here) showed that these projections are very similar with a scaling by a factor of 2 of the low resolution pictures with a bilinear interpolation.

The voxel resolution has nevertheless an effect on the noise: the background in the low resolution reconstruction is darker and cleaner. An explanation for this effect is that no matter what is the voxel resolution, the pixel resolution in the dataset remains 1.67 μm. This means that there is four times more redundant data in the low resolution reconstructions per voxel than for the full resolution reconstruction. This averages the noise in the data.

The influence of the angle θ is much stronger. On the xy-views, the resolution slightly degrades as θ increases. This effect is particularly visible on the clusters where the resolution at $\theta = 55°$ is not sufficient anymore to dissociate the beads. But it is along the z-axis that this effect is the most visible: the elongation of the beads strongly deteriorates with the angle.

To better quantify these effects, profiles are drawn along the x and the z-axis for the bead pointed in figures V.18, V.19 and V.20. For the visualization in figures V.21

[15]Let's recall here that the fluorescence microscope is not a confocal microscope. Such a microscope would provide a better sectioning capability. Acquisitions have been attempted on a spinning disk confocal microscope but the amplitude of the translation stage along the z-axis is too short to acquire large volumes and perform a comparison on a large statistic of beads.

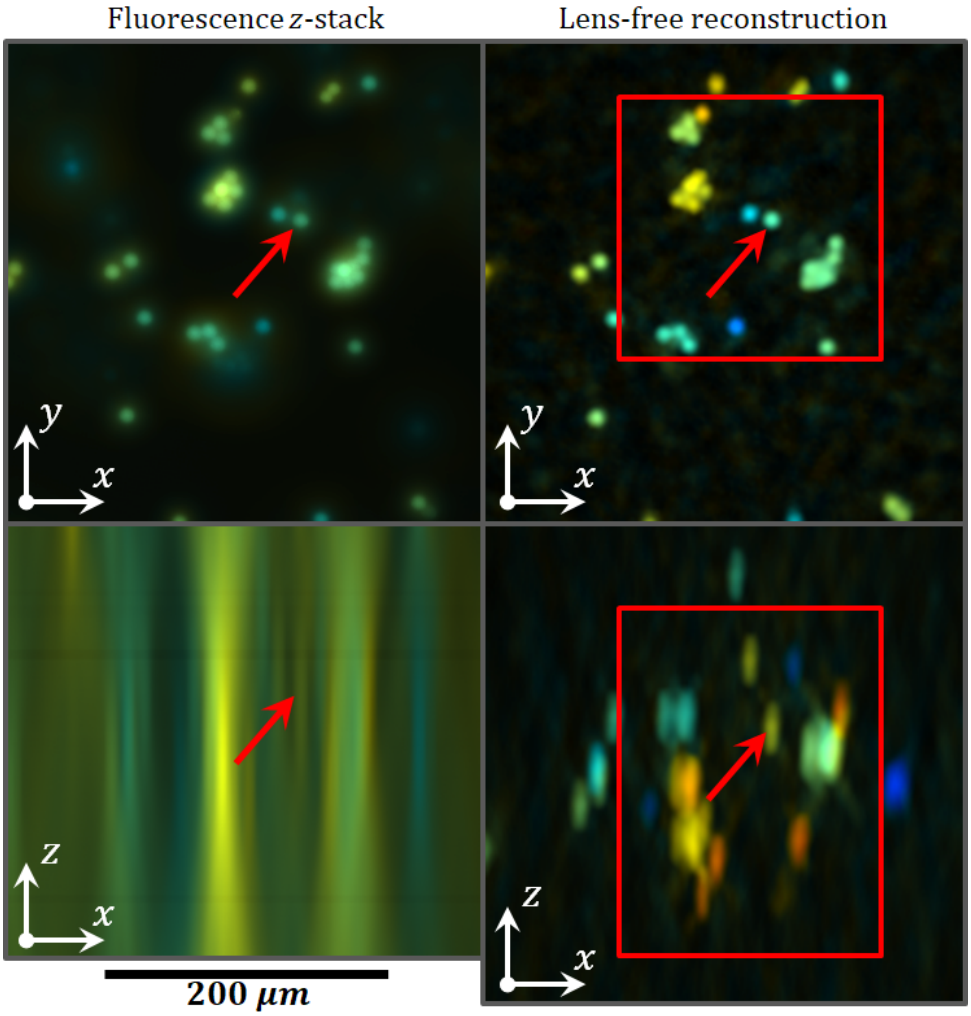

Figure V.18: xy and xz-average intensity projections of a region of interest of the fluorescence z-stack (*left*) and its counterpart in the lens-free reconstruction at full resolution (*right*, $\theta = 35°$, without cap). The red arrow points at the bead which is investigated. The red rectangles frame the regions which are compared in figures V.19 and V.20. On each view, the colors codes for the depth: the shallowest in blue, the deepest in red.

and V.22, the profiles are all normalized and centered.

For each profiles, its full width at half maximum (FWHM) is manually measured along the z-axis. For the xy-plane, Gaussian distributions are fitted with parameters x_0 (the translation of the curve), σ (the standard deviation), A (the amplitude) and off (the offset):

$$f(x) = A.e^{-\frac{(x-x_0)^2}{2\sigma^2}} + off \tag{V.4}$$

The FWHM is then given by [102]:

$$\text{FWHM}(\sigma) = 2\sqrt{2\ln 2}\sigma \tag{V.5}$$

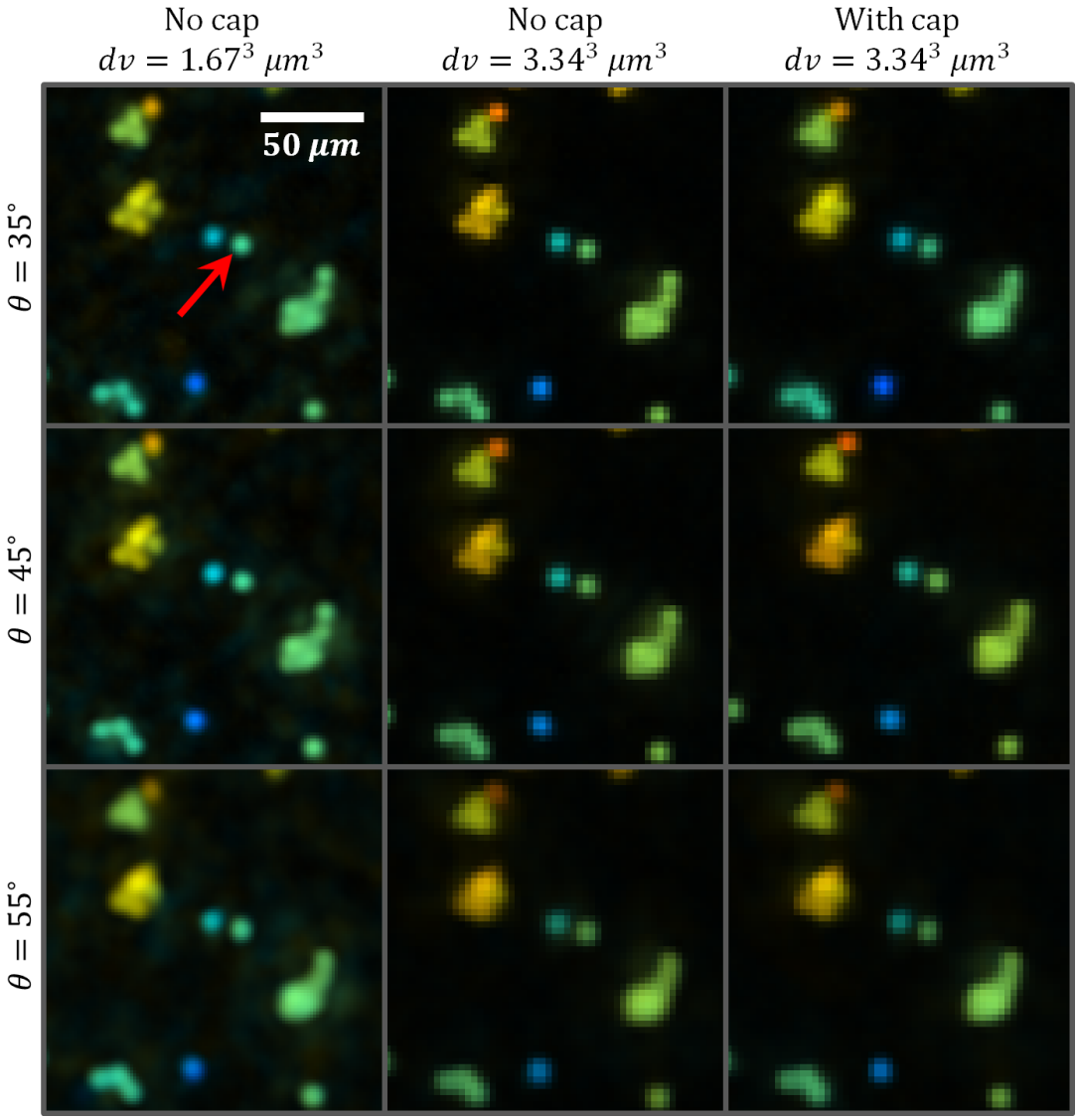

Figure V.19: xy-average intensity projections of a region of interest of the reconstructed volumes for different angles and reconstruction resolutions, with and without the cap on the Petri dish. The red arrow points at the bead which is investigated. On each view, the colors codes for the depth: the shallowest in blue, the deepest in red.

The results are presented in the table [V.2]. As they are done on a single isolated bead these results cannot be used to quantify the resolution but they give an idea of the sizing capabilities of the system.

On the radial plane, figure V.21 confirms some of the previous qualitative observations. Excepted a more pronounced pixelization effect between the full resolution reconstruction (solid lines) and the undersampled reconstructions (dotted and dashed lines), the curves present a similar FWHM around $9 \sim 10\ \mu m$ which is in a good agreement with the fluorescence measurements. Let's note here that x

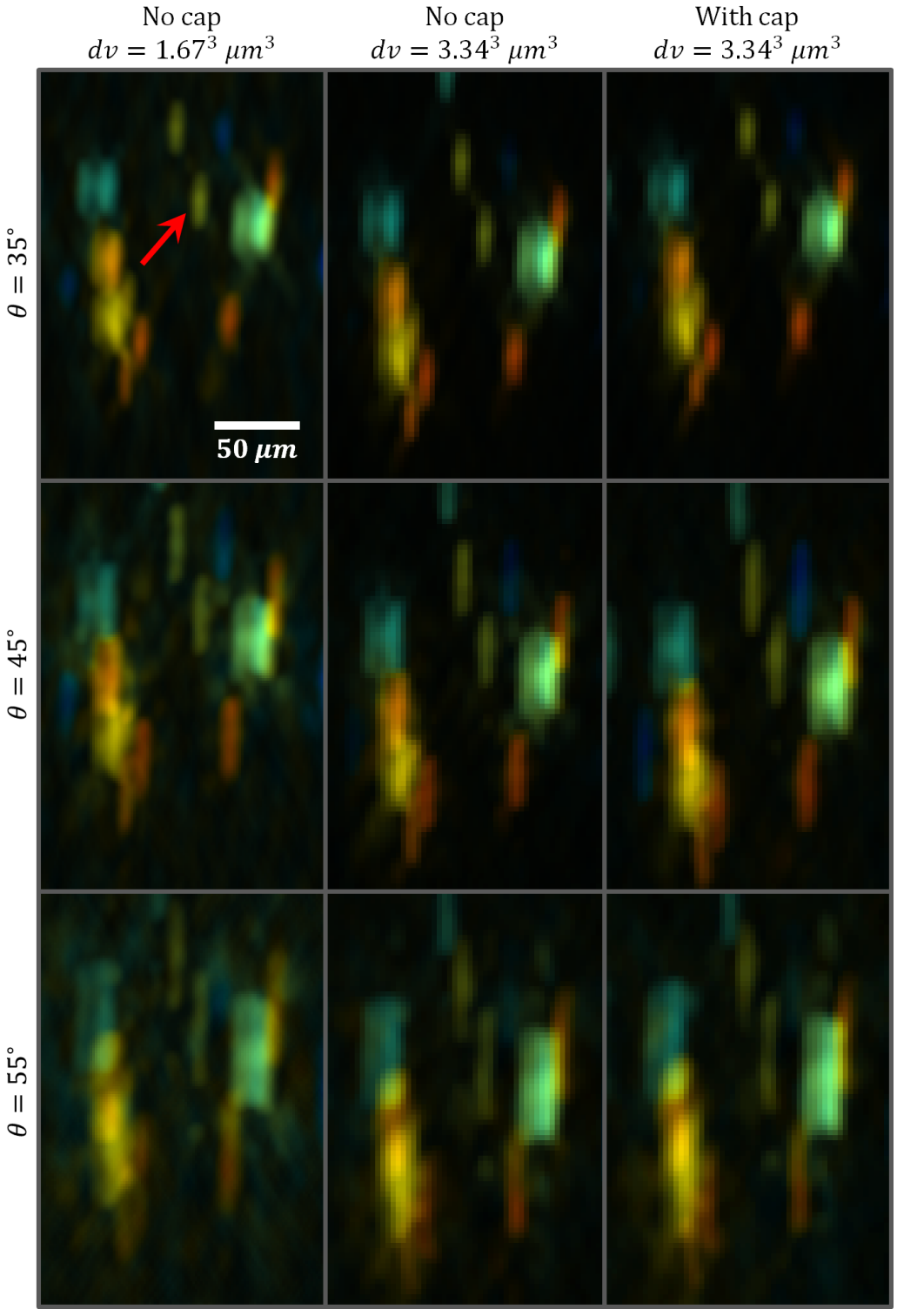

Figure V.20: xz-average intensity projections of a region of interest of the reconstructed volumes for different angles and reconstruction resolutions, with and without the cap on the Petri dish. The red arrow points at the bead which is investigated. On each view, the colors codes for the depth: the shallowest in blue, the deepest in red.

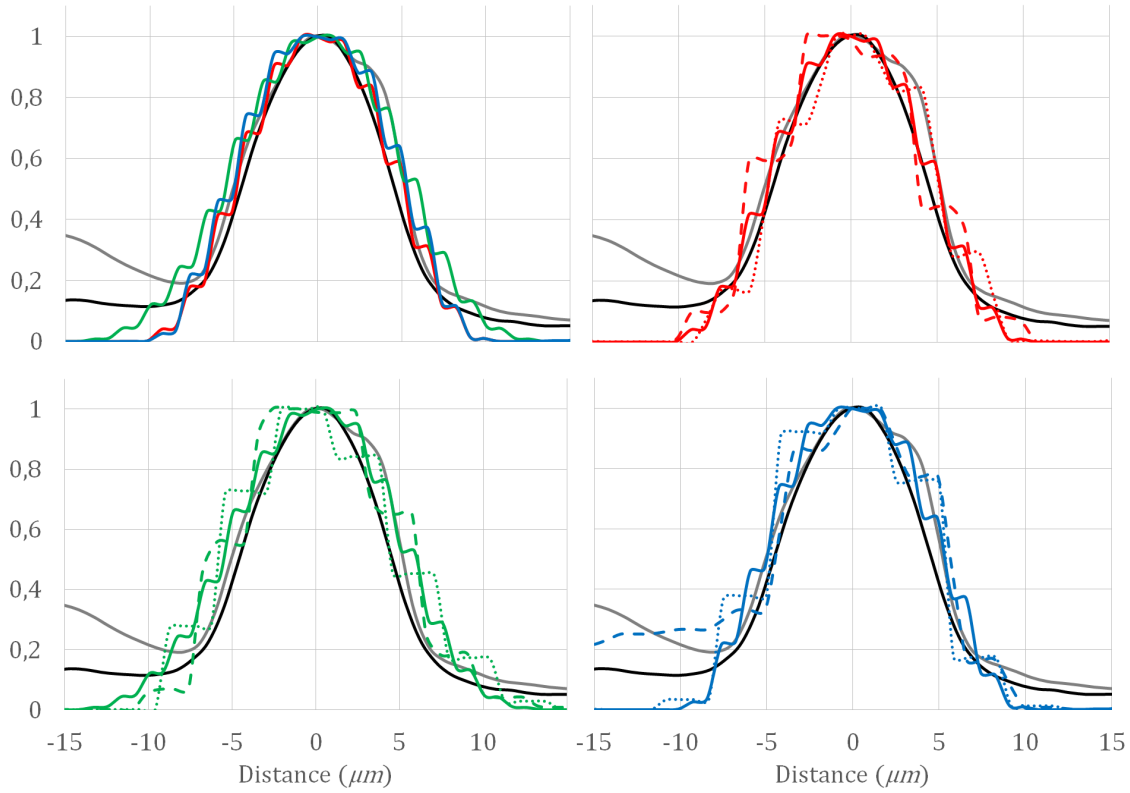

Figure V.21: Comparison of xy-profiles drawn at the center of the bead pointed in figure V.18 in the fluorescence z-stack (gray line along the x-direction, black line along the y-direction) and the reconstructed volumes for $\theta = 35°$ (red), $\theta = 45°$ (green) and $\theta = 55°$ (blue) at full resolution (solid line) and low resolution with (dotted line) and without (dashed line) the cap on the Petri dish.

	Fluo	Full resolution			No cap			With cap		
θ	0°	35°	45°	55°	35°	45°	55°	35°	45°	55°
x (y)	9.1 (8.3)	9.1	10.5	9.5	9.0	11	9.7	9.2	10.0	10.6
z	134	32	49	75	34	44	70	28	51	74

Table V.2: Table of the measured full widths at half maximum in the different situations. The values are given in microns.

and y-profiles are drawn for the fluorescence plane because unfocused fluorescence of a bead on the left of the bead of interest is degrading the signal along the x-axis (bump on the left of the gray curves)[16]. The oversampling does not degrade the sizing capability, the edge of the beads decreases in the same manner. This is in line with the previous qualitative remark on the spatial resolution on the xy-plane.

[16]Let's also note that the found FHMWs of 9.1 and 8.3 μm do not match the theoretical value of 10 μm diameter. This may be due to the choice to fit a Gaussian curve to get the FHWM.

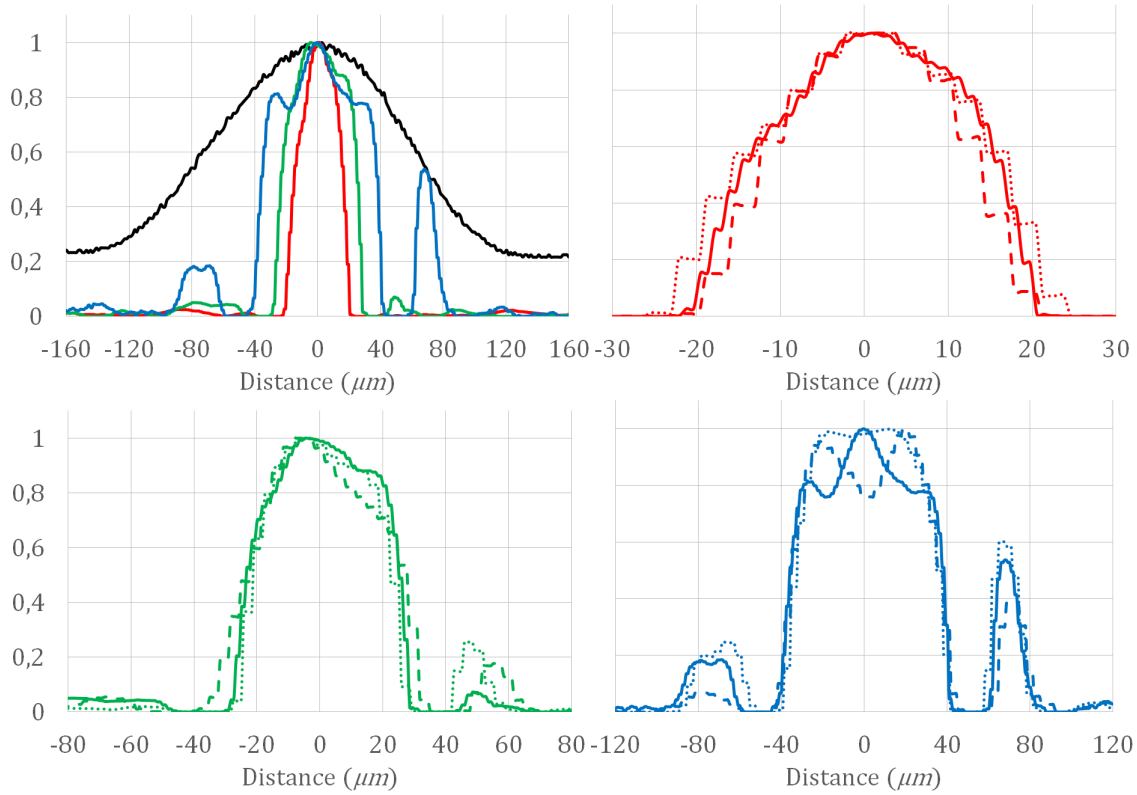

Figure V.22: Comparison of z-profiles drawn at the center of the bead pointed in figure V.18 in the fluorescence z-stack (black) and the reconstructed volumes for $\theta = 35°$ (red), $\theta = 45°$ (green) and $\theta = 55°$ (blue) at full resolution (solid line) and low resolution with (dotted line) and without (dashed line) the cap on the Petri dish.

Similarly, the presence or the absence of the cap on the Petri dish does not significantly change the measured FWHMs. The reconstruction conserves its quality. This means that the regularization is efficient to get rid of the structured background added by the presence of the cap in the signal.

But the FWHMs are not influenced by the value of the angle θ. This is in contradiction with the previous qualitative observation of a loss of resolution in the clusters. This may be due to the fact that this is an isolated bead on which the regularization is efficient compared to the clusters where a lack of resolution will be enhanced by the regularization which fosters an extended homogeneous object.

The curves of figure V.22 confirm the conclusions of the analysis of figure V.20. The resolution of the reconstruction and the presence of the cap on the Petri dish do not have much influence, giving similar FWHMs.

The effect of the angle θ is much more impressive. If all the reconstructions are better than the z-profile in the fluorescence z-stack, there is a strong disparity in the three cases with an elongation shifting from ~ 30 μm for $\theta = 35°$ to ~ 70 μm for $\theta = 55°$. They are several times bigger than the 10 μm theoretical diameter

of the beads. The sizing capabilities are consequently strongly diminished along the z-axis with an overestimation of at least[17] $\sim 20\ \mu m$. These FWHMs give also the low limit of the axial resolution which cannot be expected to be better than these values.

Another remark concerns the shape of the profiles. The nice dome at $\theta = 35°$ on which it is simple to identify the position of the bead is replaced by a plateau at $\theta = 45°$ and $55°$ on which the position is less obvious.

Let's also mention the two bumps in the z-profiles surrounding the central peak for $\theta = 55°$. These are artefactual as they are not present in the other reconstructions curves.

Interestingly, these artifacts are not present for all the beads in the volume. It only concerns isolated beads (not presented here).

3.4 Conclusion and discussion

As a conclusion, the lens-free microscope provides its best results at $\theta = 35°$ and the presence or the absence of the cap on the Petri dish does not significantly change the reconstructions quality.

Apart from a dilation factor under 2.5 %, it can achieve a very good accuracy on the xy-plane with a low standard deviation $\sigma < 4\ \mu m$ for all the tested angles θ. It is proven that contrary to an uncorrected fluorescence acquisition, the lens-free reconstructions provide quantitative information on the z-axis in terms of positioning with an accuracy slightly degraded (standard deviation around $\simeq \sigma < 7.5\ \mu m$ for $\theta = 55°$ and $\sigma \lesssim 6.5\ \mu m$ otherwise).

The study of the resolution is only qualitative, looking at the average intensity projections. A low limit is nevertheless found on the z-axis via a sizing capability study. It cannot be better than $\sim 30\ \mu m$ for $\theta = 35°$ and $\sim 70\ \mu m$ for $\theta = 55°$. On the contrary good sizing capability is performed on the xy-plane for objects of at least $10\ \mu m$ in diameter.

These results seem in contradiction with the simulations presented in the previous chapter, section 1. It has been seen that the wider the angle θ is open, the better the resolution on the z-axis should be. In this section, wider opening angle are linked with a degradation of the reconstructions along the z-axis. Several factors may play a role in this difference of results.

First, the simulation are performed on perfect simulated data, whereas the noise strongly increases in the real data (see figure V.12.b) and participates to degrade the reconstructions quality.

Then, the model reaches its limits at high angle. Indeed, all the simulations and reconstructions are based on the Fourier diffraction theorem which assumes a monochromatic incident plane wave with infinite spatial and time coherence, whereas the real lighting is only semi-coherent with an extended spatial source. As the holograms spread and overlap each other at high angle, this effect degrades the interferences of the holograms.

[17] The best FWHM $\sim 30\ \mu m$ minus the theoretical size of the beads $10\ \mu m$

And finally, the sensor response is neither modeled nor even known at high angle. The sensors efficiency and light acceptance are known to degrade with the angle [103]. A characterization of the sensor may be needed to model these effects and take them into account in the reconstruction algorithms.

Let's also give some limitations of the proposed method.

First of all, no oversampling is used. This means that the cross-correlation cannot perform sub-pixel positioning. This degrades the position determination as it is constrained to be an entire multiple of the pixel size. As a first approximation, this is nonetheless considered sufficient. But looking at the standard deviations of table [V.1] on the radial distributions, it appears that they are of the same order of magnitude than the voxel size[18]. It implies that the limitation in the accuracy presented here is not the reconstruction algorithm nor the reconstruction quality but the algorithm to extract the beads positions.

Then the 3D position determination depends on the matching pattern designed by the user and the size of the extracted coring. For each volume, different parameters are tested and an "average" set of parameters around which the results are not significantly different is chosen. Deeper studies are necessary to quantify this effect, especially concerning the pattern shape in the fluorescence z-stack. An ellipsoid may not be the optimal shape.

As mentioned, transformation (V.1) does not work out the tilt of the 3D sample which appears non negligible in figures V.16.e,f. This increases the dispersion of the clouds of points in figure V.17.b and thus decreases the estimated accuracy on the z-axis (see table [V.1]). It could be interesting to include a tilt parameter in the transformation (V.1). This is nevertheless a subtle work as it must take in account that the voxels are not normed in the three directions because of the scaling factor introduced on z-axis.

It is also shown that the reconstructed volumes present a dilation on the xy-plane. Constrained between 1.1 % and 2.3 % depending on the angle θ, these scaling factor are in the order of magnitude of the scaling factors found in chapter II, section 3 which are due to the approximation of the incident spherical wave by a plane wave.

Nevertheless the light source is forced to move on a circle centered on the sample and whose radius is 7 cm. The scaling factor should consequently not present the observed variations according to the angle θ. To investigate if they are due to the acquisition angle or a dilation/contraction of the Matrigel® along time as observed in section 2 of this chapter, lens-free reconstructions with and without cap which are done at the same angles but different timings are compared in figure V.23.

The curve in figure V.23.b is not conclusive. Indeed on the one hand, the scaling factors appear to follow a coherent temporal evolution with a decreasing value along time. Nevertheless on the other hand, it is not as marked as it should be, the scaling factor also forming clusters according to the angle θ.

A closer look in figure V.23.a does not provide better interpretation as on some trails, the dilation appears coherent with an temporal evolution (green arrows) whereas on some other this clustering effect is also visible (red arrows).

[18] $dx_v = dy_v = 3.34\ \mu m \sim 3.683\ \mu m \leq \sigma \leq 3.993\ \mu m$

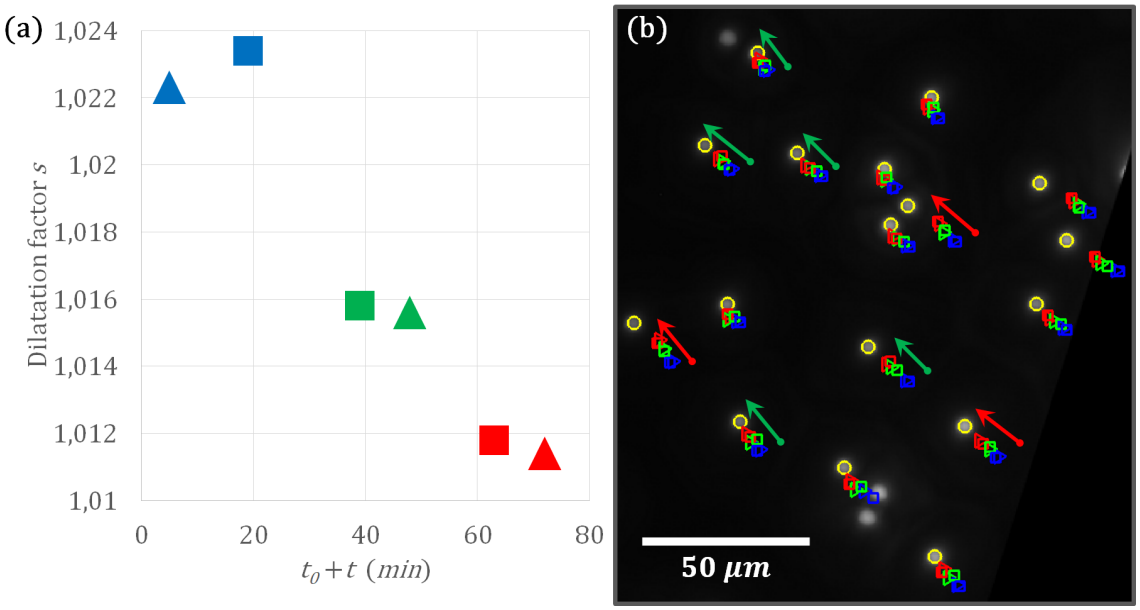

Figure V.23: Comparison of the scaling factor s on the radial plane for the lens-free reconstruction with (squares) and without (triangles) the cap on the Petri dish at the different angles $\theta = 35°$ (red), $45°$ (green) and $55°$ (blue). (a) Temporal evolution of the scaling factor s. (b) Zoom on the bottom right corner of the xy-view of figure V.16.a. The yellow circles are the positions of the beads identified with the fluorescence microscope. The green arrows follow the beads which seem to have a temporal contraction whereas the red arrows follow the beads where a clustering effect with the angle seems to prevail.

$nb_b = 389$	Without cap			With cap		
	$\theta = 35°$	$\theta = 45°$	$\theta = 55°$	$\theta = 35°$	$\theta = 45°$	$\theta = 55°$
s	1.0114	1.0156	1.0223	1.0118	1.0158	1.0234
R^2	0.9997	0.9997	0.9997	0.9997	0.9997	0.9997
σ (μm)	3.6759	3.7641	3.9852	3.6384	3.9474	4.0110
$t_0 + t$ (min)	72	48	5	63	39	19

Table V.3: Results of the linear regression performed on the radial distribution for the $nb_b = 389$ beads matched in the fluorescence z-stack and the six reconstructed volumes with and without the cap on the Petri dish. For $\theta \in \{35°, 45°, 55°\}$, the slope s, the coefficient of determination R^2, the standard deviation σ of the linear regressions and the time of acquisition are given.

As a conclusion, if the value of the scaling factor seems mainly due to the plane wave approximation of the incident spherical wave front, it is not possible to give a certain explanation of the variation of the dilation with the angle θ observed in figure V.16.a. The experiment depends on too many factors. The sample is indeed in incubator for 3 days before its imaging at the ambient air on the fluorescence

microscope. Let at room temperature it is imaged half a day later on the lens-free microscope at $\theta = 55°$ with a large dilation factor with the cooling air flow activated. Because of the formation of mist during the first acquisition with a cap, the pressure of the air flow is augmented. For the higher angles, a contraction of the Matrigel® is observed concomitant with the change of θ. It is hard to conclude on a change in the dilation factor due to a temperature or a geometrical effect.

To discriminate the effects, it is needed to perform again the experiments with either another reference object which does not evolve along time or with a more controlled environment in terms of temperature and with longer periods of time in between the acquisitions.

Concerning the accuracy, only the reconstructions obtained with the regularized Gerchberg-Saxton algorithm IV.4 are investigated. It would be an interesting result to also reconstruct the data with the regularized inverse problem approach IV.3. If a gain in resolution on the xy-plane is not expected, maybe that the regularization could improve the resolution along the z-axis.

Conclusion and perspectives

As a conclusion, this thesis shows the possibility to adapt the lens-free microscopy to the imaging of 3D biological samples over large fields of view and extended periods of time in incubator conditions as well as the possibility to adapt the algorithms to perform tomographic reconstructions.

Concerning the prototypes, several solutions are tested whose designs depend on the potential applications. A first design is more adapted to standard tomographic acquisitions with a sensor and a light rotating relatively to the sample. But it implies strong constraints on the sample preparation because of limitations on the container size or geometry and because of refractive index matching issues.

A second design finally converges to a scheme combining two conditions. The first requirement is the choice of simplicity of use with a cell culture in standard Petri dish and requiring no specific preparation or change of container. The second condition is to find the best possible angular coverage of lighting angles in regards of the geometric constraints imposed by the first requirement.

Finally, an incubator-proof version of this design is successfully built and tested.

Regarding the dedicated tomographic reconstruction algorithms, all the developed methods aim to correct two inherent problems of a lens-free in-line holographic microscope: the absence of phase information, the sensor being sensitive only to the intensity of the incident wave, and the limited angular coverage.

Different pragmatic solutions are tested using techniques previously developed in the context of X-rays tomography and 2D lens-free tomography.

A solution using z-stack acquisitions and the diffraction physics under the Born approximation does not appear conclusive but paves the way to reconstructions based on 3D diffraction physics.

The work on the algorithm mainly focuses on four major solutions, all based on the Fourier diffraction theorem, conventionally used in optical diffractive tomography and with an increasing complexity. The first algorithm simply replaces the unknown phase with that of an incident plane wave. If this method is fast, it is however the source of many artifacts. The second solution tries to estimate the missing phase by approximating the unknown object by an average plane and uses the tools of the 2D lens-free microscopy to recover the missing phase in an inverse problem approach. The third solution consists in implementing a regularized inverse problem approach on the 3D object to reconstruct. It is the most effective method to deal with the two problems mentioned above but it is very slow. The fourth and last solution is based on a modified Gerchberg-Saxton algorithm with a regularized

step on the object and can be used to initialize the third algorithm.

The use of an algorithm more than another is directly linked with the sample characteristics and the wanted reconstruction quality.

All these methods are compared and tested successfully on numerical simulations as well as on experimental biological data, fixed and living. Comparisons with conventional microscope acquisitions show the validity of the reconstructions in terms of shape and location of the retrieved objects as well as the accuracy of their three-dimensional positioning. Biological samples are reconstructed with volumes of several tens of cubic millimeters, inaccessible in standard microscopy.

Moreover, 3D time-lapse data successfully obtained in incubators show the relevance of this type of imaging by highlighting large-scale interactions between cells or between cells and their three-dimensional environment.

Thus, as synthesized in the following table, this thesis demonstrates the capability of a 3D lens-free microscope to acquire and gather relevant information on different kinds of 3D cell culture.

3D model	**Relevant information**	**Experiment**
Culture substrate	Large volumes, cell-cell interactions, cluster development and migration, 3D network formation	Chapter III, sections 2, 4 Chapter IV, section 5 Chapter V, section 2
Capsules	3D distribution of single cells, cluster development and escape from the capsule	Chapter III, sections 2, 3 Chapter IV, sections 3, 4, 5
Tubes	Angiogenesis, tubular processes	Chapter IV, section 4
Extracellular matrix	Passive evolution, dynamic remodeling	Chapter V, section 2

In terms of perspectives, this work paves the way to new experiments in biology with temporal statistics on large volumes and opens new possibilities in terms of design and prototype conception and reconstruction algorithms development.

In 3D biology - Chapter V, section 2 demonstrates for the first time the capability of a lens-free tomographic microscopy to perform 3D+t acquisitions of 3D cell culture in incubator. Being able to monitor large volumes over a period of time covering several days allows observing within the same experiment a large number of phenomena dealing with cell migration in 3D environment: single cell migration, collective migrations of cells, displacement of cell aggregates, dispersal of cells, aggregation of tens of cells into one single aggregate, interactions with the ECM, ECM remodeling and so on. These kinds of observation can help to validate biophysical models develop in different branches of 3D biology.

For example, the cell migration and merging observations are very much in line with the broad spectrum of migration and invasion mechanisms discussed in [104, 105] and [106].

The sprouting of cells observed around the clusters, that is to say short-range dispersal of cells, echoes the mechanisms described in [107] to explain faster rate of tumor growth.

The observations are also in line with the model introduced in [108] which describes the possible migration of very large aggregates of cells. The cohesive migration of an aggregate of cells of 6000 to 10000 μm^2 (projected area) confirms their prediction that an isolated cells monolayer may acquire a global polarity and consequently performs persistent random walks. Overall, all these observations demonstrate that 3D lens-free microscopy is an interesting technique to capture and study the complex multicellular dynamics and remodeling that are supported by collective cell migration processes [109].

In addition to the observation of cell migrations in 3D environment, the intrinsic deformations of the ECM can be measured. The speed of these deformations are in the range of 1 to 2 $\mu m.h^{-1}$ which is not negligible. Hence they should be systematically taken into account when measuring for example the speed of single cells in 3D cell culture.

More importantly isolate ECM deformations resulting from traction forces generated by large cell aggregates are observed. It means that lens-free microscopy allows capturing in time the dynamic interplay between cell growth in 3D and ECM remodeling. It is an important observation since ECM is a key active event in the embryonic development or tissue homeostasis. And any dysregulation affecting ECM may contribute to pathologies such as inflammation [110], age-related diseases [111] or cancer [112, 113]. Thus the capability of 3D lens-free microscopy to monitor the process of ECM modifications could provide a mean to measure this dynamic signature.

One can question whether 2D lens-free microscopy would have allowed all these observations. Indeed, it has been shown that 2D holographic reconstruction algorithm can be successfully used to monitor 3D cell culture [52]. But in this context of a no top coat culture, the objects are mainly lying on a 2D surface and do not have a large distribution in terms of z-positions. Moreover, all the contextual information, such as the 3D positions of the clusters of cells and the deformation of the ECM are lost with a 2D lens-free microscopy setup. The contribution of the lens-free 3D reconstruction is proven to be particularly important for the tracking of beads embedded within the ECM at different depths. It provides a unique tool to observe 3D deformation of the ECM and judge the long-range effect of the traction forces created by cells aggregates onto the ECM.

Concerning large biological reconstruction, future works can focus to test the 3D lens-free microscope on standard objects such as C. Elegans. It has also been recently proven the possibility to acquire pertinent data on cleared samples [114] which would be good objects to test the limit of the model and the reconstruction algorithms.

Something which is also investigated in this PhD work, but not presented in this thesis because of the lack of in-depth studies, is the possibility to use 3D lens-free microscopy to discriminate acini (hollow cell cluster) from spheroids (full cell

cluster) in RWPE1 prostate epithelial cell cultures. These cells form polarized acini with lumen under standard 3D culture conditions while the first event in epithelial carcinogenesis is a loss of polarity, followed by uncontrolled proliferation leading to metastasis and the filling of the lumen and thus to spheroid formation [52]. They represent difficult objects to reconstruct because of their important cell density but on which 3D information is essential in terms of biological applications. They constitute a pertinent sample to test the limit of the models and reconstruction methods on large and dense objects

To conclude in terms of biological applications, it would be interesting to test the limitations of the proposed tool with stained or pigmented cells. Indeed, the reconstruction algorithms are based on the assumption that the sample is transparent. Nonetheless staining is often used in biology to label specific cells or structures. Some works have shown the possibility to use lens-free devices to image such 2D samples [115], a need which will also appear in 3D samples.

Reconstruction algorithms - This thesis introduces new algorithms dedicated to reconstruction of lens-free tomographic data and more in-depth studies are needed to improve and complete them. Some perspectives are already given at the end of chapter IV, section 5.

Concerning the proposed codes themselves, let's remind here the need to optimize the choice of the hyperparameters especially for the inverse problem approach IV.3 and test their validity for different volume sizes and voxel pitches. The effect of the numbers of acquisition angles and wavelengths as well as their combination should be more studied to optimize the number of lighting situations needed to achieve good reconstruction quality while limiting the acquisition time.

Most of the reconstructions with the inverse problem approach IV.3 uses the nearest-neighbor interpolation technique whereas it is shown in chapter II, section 3 that a linear interpolation should lead to better reconstruction. This should be tested.

Still concerning the inverse problem approach, a similar step than the alignment refinement could be dedicated to refine the other reconstruction parameters such as the reconstruction distance z_s and the illuminations wavelengths which are critical or the lighting positions via the values of φ and θ.

Through its characterization, especially in terms of admissible angles, the sensor behavior could also be modeled and integrated in the direct model used in the inverse problem approach. The same could be done with the LED spectra which are assumed to be monochromatic in this entire thesis. A model adding incoherent holograms of different wavelengths around the emission peak of each LED could simulate this limited temporal coherence.

For the regularized approaches IV.3 and IV.4, only two regularization are tested: a sparsity prior on the object and on its gradient. The main limitation of the lens-free microscope is its limited angular coverage. It leads to the elongated artifacts on the z-axis observed in all the reconstructions of this thesis, the missing information being hardly retrieved by the implemented regularizations. New regularizations adapted to the reconstructed objects could be tried. For instance, it could expected that the

reconstructed objects present similar properties in the three directions since in a first approximation, a cell can be considered as spherical. Enforcing this characteristic in a constraint, as proposed in [116], could improve the reconstruction quality.

Some ideas for new algorithms based from the ones already developed are also given. For example methods IV.2 and IV.4 or methods IV.2 and IV.3 could be combined to force the retrieved phase by method IV.2 in the data fidelity enforcement step. Method IV.2 could also be replaced by a completely new phase retrieval algorithm presented in [48] to perform the data fidelity in the Gerchberg-Saxton loop of method IV.4. By enforcing stronger data fidelity, it should accelerate the convergence with a minimal extra cost in terms of computation needs both, in memory and time.

But it is also possible to think about new algorithms based on different techniques such as presented in [49] which combines incoherent illuminations and z-stack acquisition or in [117] which trains a neural network for a machine learning approach.

In a more pragmatic point of view, none of the algorithms developed in this thesis which takes into account the 3D diffraction physics is tested for θ-mode acquisitions with the first prototype. Nevertheless, the simulations on a bead of the chapter IV, sectio, 1 show a strong reduction of the reconstruction artifacts and simulations on cells embedded in a capsule (not presented here) lead to a complete reconstruction of the encapsulating envelope and not only a ring in the plane parallel to the sensor as in chapter III, section 3 or chapter IV, section 3. As a consequence, if a lens-free device is built to implement the θ-mode on real data, tremendous improvements in the reconstructions quality are awaited.

Reconstruction time - As often in tomographic reconstruction, the bottleneck of the presented methods is their computation time, up to several hours (or days) for a given volume. The acquisition of systematic temporal data, as in chapter V, section 2, raises the concern of the global reconstruction of the 3D time-lapse video of an experiment monitored during several days which can take several weeks. This leads to the impossibility to acquire data on several experiments and reconstruct and compare them in a reasonable period of time.

Some ideas to shorten the reconstruction time are given in chapter IV, section 5 and some of them are tested during this PhD work but not presented in this thesis because the overall gain in computation time is not convincing.

For example an algorithm is implemented to perform the extraction/mapping of the coefficients of the spherical caps in the Fourier domain for method IV.3 in parallel in terms of lighting situations. Nevertheless, its multi-threading faces the impossibility to share large matrices of the master thread to the slaves in Matlab®. Getting around this issue compensates the gain of time of the method. C-code or GPU programming have already demonstrated to correct these issues [97] in the case of method III.4. Adapting these solutions to the algorithms presented in this thesis would be beneficial.

The alignment refinement remains also a time consuming step. It can take up to tens of minutes for large fields of view to align all the angles and wavelengths. Faster alignment techniques would decrease the reconstruction time or improve the

reconstruction quality as they could be run more times.

Pre-processing steps - As presented in appendix C, the pre-processing steps of data alignment and z_s determination are essential to achieve good reconstruction quality. They are complex steps which need the user's supervision or manual intervention. This can be a strong impediment to the development of 3D lens-free microscopy because of this implication of a degraded ease of use compared to a 2D lens-free in which even the focusing step can be done automatically [118].

Testing similar criterion of finding new metrics to qualify the focus automatically would provide more objective reconstruction distances and remove a step which is currently manual in the reconstruction.

The bottleneck remains the data alignment. A new algorithm must be invented to be able to align the data independently or all together in the same time to avoid the error propagation mentioned in appendix C. This new algorithm also needs to be robust to complex fields of view where a specific pattern present and isolated on all the acquisitions is hard to find.

In order not to diminish the ease of use, such an algorithm would also gain to be automatic.

3D diffraction model - In this thesis, all the reconstruction methods are based on the Born approximation with strong limitations in terms of domain of validity. These conditions are generally not met by the large 3D samples observed in lens-free microscopy.

It may be an explanation for the unexplained inversion in the interpretation of the complex refractive index mentioned in II, section 3 for the absorption and dephasing properties of the reconstructed objects. This incomprehension is the reason why refractive index representations are barely used in this thesis. Nevertheless, this possibility given by the different algorithms to directly reconstruct the scattering potential should be tested and compared with scattering potential reconstructions to determine which is the one giving the best results and if it depends on the sample nature. These reconstructions should also be compared with the expected complex refractive index in order to identify where this problem may come from.

The Born approximation prevents any quantitative interpretation of the reconstructed volumes and there is a need of a more adapted model. More in-depth studies are needed to determine if this refractive index problem can be directly attributable to the 3D diffraction model and the Born approximation or some gaps in the overall modeling of the system, for example with the effect of the temporal and spatial coherence of the LEDs which should be studied more into details.

Concerning the Born approximation, the Rytov formulation mentioned in II, section 1.2 is supposed to have a greater validity domain and should be tested and compared with reconstructions based on the Born formulation.

Some recent works solve this issue by completely changing the propagation technique by moving to multislice models [47, 119]. Only based on 2D propagations, they run faster with an increased domain of validity. They could be adapted to an inverse problem approach similar to method IV.3.

In any case, much work remains to be done before having quantitative reconstructions.

Device conception - But in the short term, efforts must focus on the prototype to provide a really effective and easy to use 3D lens-free microscope for long term use in incubator conditions.

Before the acquisitions, there is a long procedure of adjustment of the positions of the sensor and the sample using small screws. This procedure aims to insure that the center of rotation of the projected holograms of the object of interest is centered and to maximize the field of view which can be reconstructed. The screw system allows precise and easy positioning of the sensor and a similar solution should be implemented for the sample. Moreover, this system is not always intuitive.

For the acquisitions, the stepper motor should be replaced by a smoother and faster solution. Indeed, the sample needs to be maintained to prevent any displacement because of the vibrations induced by the rotation of the light source and the sensor. To prevent any blurring effect during the hologram recording, a preventive waiting time is performed after each movement before the first acquisition. This leads to a very slow acquisition procedure: up to 10 min for 32 lighting positions and 3 wavelengths. This can be greatly improved (with a similar geometry with optimized components, the 3D Cell Explorer from Nanolive performs the full acquisitions within less a second [42]).

Moreover this moving part is source of lots of breakages and problem of welding in the wires linking the fixed structure of the microscope with the moving sensor and light source. More adapted solutions must be found to insure the robustness of the prototype in long period of time without premature wear using electronics pieces dedicated to wiring of rotation stages.

A solution could also be to move to a fixed strip of LEDs laid on a crown similar to the solution implemented in [49, 70]. With the sensor fixed on the axis of symmetry, there is no moving part anymore. A prototype with this solution is built but not presented in this thesis. This nevertheless implies that the sample is put as close as possible to the sensor to insure that its holograms are projected on the sensor field of view. It also leads to an overall reduced field of view.

The long acquisition time is also partly due to the low power of the LEDs. Combined with the not normal illumination, only a small part of the emitted light reaches the sensor. This degrades the signal over noise ratio and forces to use the maximal exposure time available of the sensor model.

A more powerful LED could be used. Laser diodes with higher temporal coherence and emitting power should be tested as they would increase the interference quality and provide an illumination more adapted to the models used in the different reconstruction algorithms which assume monochromatic fully coherent plane wave. They would also increase the signal over noise ratio.

Using the recent results of the 2D lens-free microscopy, the size of the pinhole ($\varnothing 150\ \mu m$) should also be reduced (to $\varnothing 50\ \mu m$ for example) to increase the spatial coherence.

Still concerning the light source, it is shown in this thesis that the spherical wave

produced by the LED is at the origin of a dilation effect of a few percent on the reconstructed objects. The use of a more powerful source could allow increasing its distance to the sample, limiting this effect. Some works also demonstrate the possibility to use holographic plates to create a rigorous plane wave illumination in a compact system as well as controlling the lighting direction without the need of any moving part [120, 121]. This direction could also be investigated.

The air cooling system is also a compulsory need in the lens-free microscope functioning. It relies on an external air supply and is very sensitive to the input pressure. It could be interesting to test less heating sensors or to actively monitor and cool the sensor temperature.

Concerning the θ-mode, this thesis shows the difficulties to handle large scale 3D objects acquisitions which cannot be put in a glass capillary or fixed on a rotating spike. Nevertheless, simulations show all the potential of such a mode in terms of reconstruction quality. Reducing the size of the studied samples to aggregates of a few cells, different techniques could be tested in a standard 2D lens-free microscope to manipulate and rotate the sample in 3D to acquire holograms at different angles, such as acoustic [122, 123] or optical [124] tweezers or dielectrophoresis [125].

Finally, this PhD work focuses on designs directly inspired from the 2D lens-free microscopes only composed of a semi-coherent light source behind a pinhole and a fixed sensor. But one could try to modify other designs in which lenses are mainly used as magnification tool to turn them into 3D lens-free microscopes. For example, in chapter III, section 3 the method base on a z-stack acquisition is said to be a dead end with the chosen designs and models. But some works have shown that an adapted light source and specific LED patterns can lead to tomography algorithms needing only normal illuminations to simulate bright-field and phase contrast images and a translation stage to multiply the acquisitions distances [49, 126], perfectly adapted to multiwell plates. It opens new perspectives in terms of design.

Communications

Posters

- **Gresti 2015** - Groupement de Recherche En Traitement du Signal et de l'Image, "Lensless diffractive tomography applied to 3D cell culture", September 2015, Lyon, France

- **JIONC 2016** - Journées Imagerie Optique Non-Conventionnelle, "Lens-free diffractive tomography for the imaging of 3D cell cultures", March 2016, Paris, France

Orals

- **FINYS 2016** - French Imaging Network of Young Scientist, "3D lens-free imaging for 3D cell cultures", June 2016, Dourdan, France

- **NaMiSCeB workshop 2016** - Nano and Micro Systems for molecular and Cellular Biology, "3D lens-free imaging for 3D cell cultures", October 2016, Grenoble, France

- **Holoφ 2016** - Rencontre francophone d'holographie numérique, "3D lens-free imaging for 3D cell cultures", November 2016, Lille, France

- **BiOS 2017** - Biomedical Optics Conference / Three-Dimensional and Multi-dimensional Microscopy: Image Acquisition and Processing XXIV, "Lens-free diffractive tomography for the imaging of 3D cell cultures", January 2017, San Francisco, United States of America [89]

- **JIONC 2017** - Journées Imagerie Optique Non-Conventionnelle, "3D lens-free time-lapse microscopy for 3D cell culture", March 2017, Paris, France

- **ECBO 2017** - European Conferences on Biomedical Optics / Advances in Microscopic Imaging, Novel Techniques, "3D lens-free time-lapse microscopy for 3D cell culture", June 2017, Munich, Germany [100]

Publications

- **Biomedical Optics Express** - "Lens-free diffractive tomography for the imaging of 3D cell cultures", March 2016 [80]
- **Applied Optics** - "Comparative study of fully three-dimensional reconstruction algorithms for lens-free microscopy", May 2017 [88]

Appendix A

Green's functions to solve linear differential equations

The aim of this Appendix is to give a brief overview of the definition and the use of the Green's function to solve linear equations. It gives a more consistent framework for the results stated in chapter II, section 1 by detailing some of the main steps to solve equation (II.5). It does not intend at being mathematically rigorous.

1 Overview

The reader willing for a more rigorous frame is encouraged to refer to [74], entry "Green's function".

Let's consider a linear differential operator $\mathcal{L}$ acting on a function u according to the variable x in Ω. The present problem is to solve the following equation[1]:

$$\boxed{\mathcal{L}u\left(x\right) = f\left(x\right)} \tag{A.1}$$

where f is another function called the forcing term since it forces the value of $\mathcal{L}u$ according to x.

Let's now consider that for any given y in Ω, it exists a function g depending on (x, y) such as:

$$\boxed{\mathcal{L}g\left(x,y\right) = \delta\left(x-y\right)} \tag{A.2}$$

where δ is the classical notation for the Dirac delta function. g is the so-called Green's function.

It is now possible to express a solution u for the equation (A.2). Indeed, f can be expressed in terms of distribution:

$$f\left(x\right) = \int_{y\in\Omega} f\left(y\right)\delta\left(x-y\right)dy \tag{A.3}$$

[1]To be well-posed, the problem also needs boundary conditions. For example, for the wave equation, the Sommerfeld radiation condition is generally chosen (see [74], entry "Radiation conditions"). It states that the energy must scatter to infinity and is radiated from the source and not toward the source from infinity.

Then, from equation (A.2), it comes:

$$\int_{y\in\Omega} f(y)\,\mathcal{L}g(x,y)\,dy = \int_{y\in\Omega} f(y)\,\delta(y-x)\,dy \tag{A.4}$$

Knowing that $\mathcal{L}$ is linear and acting on the variable x, it is possible under certain circumstances to invert the integration on y and the derivation on x. One then gets from equations (A.1) and (A.3):

$$\mathcal{L}\int_{y\in\Omega} f(y)\,g(x,y)\,dy = f(x) = \mathcal{L}u(x) \tag{A.5}$$

It is then tempting to speculate that:

$$\boxed{u(x) = \int_{y\in\Omega} f(y)\,g(x,y)\,dy} \tag{A.6}$$

This assumption is true under certain circumstances, at least in term of distributions. Generally in physical sciences, one considers that all the needed conditions are met to use the mathematical properties encountered in this section, and a solution of equation (A.1) is actually given by the expression (A.6).

It appears then that the solution is a weighting in space of the Green's function g by the forcing function f.

This formulation (A.6) is used to obtain equation (II.9) from equations (II.5) and (II.8).

2 Solution of the wave equation

Let's now deal with the wave equation (II.5) met in chapter II section 1:

$$\Delta U_{dif}(\overrightarrow{r}) + k_0'^2 U_{dif}(\overrightarrow{r}) = f_0(\overrightarrow{r})\,U_{tot}(\overrightarrow{r})$$

And more specifically the equation (II.8) expressed according to the associated Green's function:

$$\Delta g(\overrightarrow{r_1},\overrightarrow{r_2}) + k_0'^2 g(\overrightarrow{r_1},\overrightarrow{r_2}) = \delta(\overrightarrow{r_1}-\overrightarrow{r_2})$$

Let's have a glimpse on how the solution for g can be worked out. Let's insist again that the following calculations are not meant to be rigorous and aim at highlighting the main steps.

Noticing that there is no spatial dependence in equation (II.8), it can be written in a new reference frame centered on $\overrightarrow{r_2}$. Posing $\overrightarrow{r} = \overrightarrow{r_1} - \overrightarrow{r_2}$, the equation is now written as:

$$\Delta g\left(\overrightarrow{r},\overrightarrow{0}\right) + k_0'^2 g\left(\overrightarrow{r},\overrightarrow{0}\right) = \delta(\overrightarrow{r}) \tag{A.7}$$

The first idea is to get inspired from the physics underlying behind this equation: this is a wave equation with a forcing term (the Dirac delta function δ) associated

with a point inhomogeneity placed at the origin of the reference frame. The problem has a spherical symmetry and as a consequence, g only depends on $r = \| \overrightarrow{r} \|$:

$$\boxed{\Delta g(r) + k_0'^2 g(r) = \delta(r)} \tag{A.8}$$

Moreover, one may expect from a point inhomogeneity that the resulting wave is a spherical wave diverging from this point. Its amplitude must then decrease according to $1/r$, so that the global intensity $G = |g|^2$ lying on a sphere of radius r remains constant[2]. The phase of the field is expected to grow with the distance r. This leads to a first guess for the Green's function:

$$g(r) = g_0 \frac{e^{ikr}}{r} \tag{A.9}$$

Let's check this is actually a solution for equation (A.8). Knowing the expression of the Laplacian in spherical coordinates[3]:

$$\Delta f(r,\theta,\varphi) = \frac{1}{r^2}\frac{\partial}{\partial r}\left(r^2 \frac{\partial f}{\partial r}\right) + \frac{1}{r^2 \sin\varphi}\left(\frac{\partial}{\partial r}\left(\sin\varphi \frac{\partial f}{\partial \varphi}\right) + \frac{\partial^2 f}{\partial \theta^2}\right) \tag{A.10}$$

and from the fact that g only depends on r, one gets $\forall r \neq 0$:

$$\Delta g(r) = \frac{1}{r^2}\frac{\partial}{\partial r}\left(r^2 \frac{\partial g}{\partial r}\right) = \frac{1}{r^2}\frac{\partial}{\partial r}\left(g_0 e^{ikr}(ikr - 1)\right) = -k^2 g_0 \frac{e^{ikr}}{r} \tag{A.11}$$

Then, from equation (A.8), it comes $\forall r \neq 0$:

$$-k^2 g_0 \frac{e^{ikr}}{r} + k_0'^2 g_0 \frac{e^{ikr}}{r} = 0 \tag{A.12}$$

This is true if $k = \pm k_0'$. As only the waves outgoing from the point inhomogeneity should be kept, only $k = k_0'$ remains. To find the value of g_0, let's suppose that the solution (A.9) stays valid when $k_0' \to 0$ in equation (A.8), meaning that $g(r) = g_0/r$ satisfies the Poisson's equation:

$$\Delta g(r) = \delta(r) \tag{A.13}$$

Using the divergence theorem[4] on a spherical cap $\mathcal{S}$ of radius r_0 for the vector $\overrightarrow{\nabla} g(r)$, one gets:

$$\iint_{\mathcal{S}} \overrightarrow{\nabla} g(r) . \overrightarrow{ds} = \iiint_{\mathcal{V}_\mathcal{S}} \overrightarrow{\nabla} . \overrightarrow{\nabla} g(r)\, dv = \iiint_{\mathcal{V}_\mathcal{S}} \Delta g(r)\, dv = \iiint_{\mathcal{V}_\mathcal{S}} \delta(r)\, dv = 1 \tag{A.14}$$

Knowing the expression of the gradient in spherical coordinates[5]:

$$\overrightarrow{\nabla} f(r,\theta,\varphi) = \frac{\partial f}{\partial r}\overrightarrow{u_r} + \frac{1}{r\sin\theta}\frac{\partial f}{\partial \varphi}\overrightarrow{u_\varphi} + \frac{1}{r}\frac{\partial f}{\partial \theta}\overrightarrow{u_\theta} \tag{A.15}$$

[2] If there is no loss during the propagation, the quantity $4\pi r^2 G$ is constant.
[3] See[74], entry "Spherical coordinates".
[4] See[74], entry "Divergence theorem".
[5] See[74], entry "Spherical coordinates".

and using again the fact that g only depends on r, and that on the spherical cap $\mathcal{S}$ $\overrightarrow{ds} = r_0^2 \sin\theta d\theta d\varphi \overrightarrow{u_r}$ one gets :

$$\overrightarrow{\nabla} g(r) . \overrightarrow{ds} = \frac{\partial}{\partial r}\left(\frac{g_0}{r}\right)\Big|_{r=r_0} r_0^2 \sin\theta d\theta d\varphi = -g_0 \sin\theta d\theta d\varphi \tag{A.16}$$

Hence:

$$\iint_{\mathcal{S}} \overrightarrow{\nabla} g(r) . \overrightarrow{ds} = \int_{\theta=0}^{\pi} \int_{\varphi=0}^{2\pi} -g_0 \sin\theta d\theta d\varphi = -4\pi g_0 \tag{A.17}$$

From equality (A.14), one finally has:

$$g_0 = \frac{-1}{4\pi} \tag{A.18}$$

and finally finds back the solution used in chapter II, section 1 as a solution for the wave equation (II.8) in terms of Green's function:

$$\boxed{g(r) = \frac{-1}{4\pi}\frac{e^{ik_0' r}}{r}} \tag{A.19}$$

Appendix B

Weyl's integral for harmonic spherical waves

The aim of this appendix is to demonstrate the relation (II.22) used in chapter II, section 2 to state the Fourier diffraction theorem:

$$\boxed{\frac{e^{ikr}}{r} = \frac{ik}{2\pi}\iint_{-\infty}^{\infty}\frac{1}{m}e^{ik(px+qy+m|z|)}dpdq}$$

with $k > 0$, $r = \sqrt{x^2+y^2+z^2}$ and $m = (1-p^2-q^2)^{1/2}$, m being complex if $p^2 + q^2 > 1$.

This formulation and its proof are attributed to Weyl who published them almost a century ago in [127]. As the author does not understand the proof in this paper, another proof is introduced here, developed by the author and based on holomorphic functions and the residue theorem.

1 Reformulation of the problem

Let's begin by expressing $\frac{e^{ikr}}{r}$ in terms of its Fourier transform[1], using the definitions introduced in chapter II:

$$\begin{aligned}\frac{e^{ikr}}{r} &= \mathcal{F}_{3D}^{-1}\left[\mathcal{F}_{3D}\left[\left(\frac{e^{ikr}}{r}\right)\right]\left(\overrightarrow{\xi}\right)\right](\overrightarrow{r'}) \\ &= \iiint_{-\infty}^{+\infty}\left[\mathcal{F}_{3D}\left(\frac{e^{ikr}}{r}\right)\right]\left(\overrightarrow{\xi}\right)e^{2i\pi(xu+yv+zw)}d^3\overrightarrow{\xi} \\ &= \iiint_{-\infty}^{+\infty}\left[\mathcal{F}_{3D}\left(\frac{e^{ikr}}{r}\right)\right]\left(\overrightarrow{\xi}\right)e^{2i\pi\,\overrightarrow{r'}.\overrightarrow{\xi}}d^3\overrightarrow{\xi}\end{aligned} \tag{B.1}$$

[1]Thanks to "kennytm" who gives the steps presented here on a forum: `http://physics.stackexchange.com/questions/1524/spherical-wave-as-sum-of-plane-waves`.

where $\overrightarrow{r} = (x, y, z)$ and $\overrightarrow{\xi} = (u, v, w)$ are the coordinates in the spatial and frequencies spaces. It comes:

$$\begin{aligned}\mathcal{F}_{3D}\left[\left(\frac{e^{ikr}}{r}\right)\right]\left(\overrightarrow{\xi}\right) &= \iiint_{-\infty}^{+\infty} \frac{e^{ikr}}{r} e^{-2i\pi(ux+vy+wz)} d^3\overrightarrow{r} \\ &= \iiint_{-\infty}^{+\infty} \frac{e^{ikr}}{r} e^{-2i\pi\,\overrightarrow{\xi}.\overrightarrow{r}} d^3\overrightarrow{r}\end{aligned} \tag{B.2}$$

One must notice that the problem has a spherical symmetry and without loss of generality, it can be considered that $\overrightarrow{\xi}$ is aligned with the z-axis. If not, it is possible to perform a change of variables to align the new z'-axis with the unit vector $\overrightarrow{u_{z'}} = \overrightarrow{\xi}/\xi = (u, v, w)/\xi$. Let's also express the integration in terms of spherical coordinates (r, θ, φ):

$$\begin{aligned}\mathcal{F}_{3D}\left[\left(\frac{e^{ikr}}{r}\right)\right](\xi\overrightarrow{u_{z'}}) &= \iiint_{-\infty}^{+\infty} \frac{e^{ikr}}{r} e^{-2i\pi\xi z'} d^3\overrightarrow{r} \\ &= \int_{r=0}^{+\infty}\int_{\theta=0}^{\pi}\int_{\varphi=0}^{2\pi} \frac{e^{ikr}}{r} e^{-2i\pi\xi r\cos\theta} r^2\sin\theta dr d\theta d\varphi \\ &= 2\pi\int_{r=0}^{+\infty}\int_{\theta=0}^{\pi} e^{ikr} r\sin\theta e^{-2i\pi\xi r\cos\theta} dr d\theta \\ &= 2\pi\int_{r=0}^{+\infty} e^{ikr}\left[\frac{e^{-2i\pi\xi r\cos\theta}}{2i\pi\xi}\right]_{\theta=0}^{\pi} dr \\ &= \frac{1}{i\xi}\int_{r=0}^{+\infty}\left(e^{i(k+2\pi\xi)r} - e^{i(k-2\pi\xi)r}\right) dr \\ &= \frac{1}{i\xi}\left[\frac{e^{i(k+2\pi\xi)r}}{i\,(k+2\pi\xi)} - \frac{e^{i(k-2\pi\xi)r}}{i\,(k-2\pi\xi)}\right]_{r=0}^{+\infty} \\ &= \frac{1}{\xi}\left(\frac{1}{(k+2\pi\xi)} - \frac{1}{(k-2\pi\xi)}\right) \\ &= \frac{4\pi}{4\pi^2\xi^2 - k^2}\end{aligned} \tag{B.3}$$

Let's note that the last integration converges for $r \to \infty$ only if k has a strictly positive imaginary part. As mentioned, the previous calculations hold for any $\overrightarrow{\xi}$ and then:

$$\boxed{\mathcal{F}_{3D}\left[\left(\frac{e^{ikr}}{r}\right)\right]\left(\overrightarrow{\xi}\right) = \frac{4\pi}{4\pi^2\xi^2 - k^2}} \tag{B.4}$$

From equations (B.1) and (B.4), one gets:

$$\begin{aligned}\frac{e^{ikr}}{r} &= \lim_{\epsilon\to 0^+} \frac{e^{i(k+i\epsilon)r}}{r} \\ &= \lim_{\epsilon\to 0^+} \iiint_{-\infty}^{+\infty} \frac{4\pi}{4\pi^2\xi^2 - (k+i\epsilon)^2} e^{2i\pi\,\overrightarrow{r}.\overrightarrow{\xi}} d^3\overrightarrow{\xi} \\ &= \lim_{\epsilon\to 0^+} \iiint_{-\infty}^{+\infty} \frac{4\pi e^{2i\pi(xu+yv+zw)}}{4\pi^2\left(u^2+v^2+w^2\right) - (k+i\epsilon)^2} du dv dw\end{aligned} \tag{B.5}$$

Performing the change of variables $2\pi\left(u,v,w\right)\longleftrightarrow k\left(p,q,s\right)$ and supposing that the limit and the integral can be inverted, one gets:

$$\begin{aligned}\frac{e^{ikr}}{r} &= \lim_{\epsilon\to 0^+}\iiint_{-\infty}^{+\infty}\frac{4\pi e^{2i\pi(xp+yq+zs)}}{k^2\left(p^2+q^2+s^2-\left(1+i\frac{\epsilon}{k}\right)^2\right)}\left(\frac{k}{2\pi}\right)^3 dpdqds \\ &= \iint_{-\infty}^{+\infty}e^{ik(xp+yq)}\lim_{\epsilon\to 0^+}\left(\int_{-\infty}^{+\infty}\frac{k}{2\pi^2}\frac{e^{ikzs}}{p^2+q^2+s^2-\left(1+i\frac{\epsilon}{k}\right)^2}ds\right)dpdq \\ &= \frac{k}{2\pi^2}\iint_{-\infty}^{+\infty}e^{ik(xp+yq)}\lim_{\epsilon\to 0^+}\left(\int_{-\infty}^{+\infty}\frac{e^{ikzs}}{p^2+q^2+s^2-\left(1+i\epsilon\right)^2}ds\right)dpdq\end{aligned} \tag{B.6}$$

where it is used that $\epsilon\to 0^+\Leftrightarrow\frac{\epsilon}{k}\to 0^+$.

Let's find a way to compute:

$$\boxed{I_\epsilon=\int_{-\infty}^{+\infty}\frac{e^{ikzs}}{p^2+q^2+s^2-\left(1+i\epsilon\right)^2}ds} \tag{B.7}$$

2 Holomorphic functions and residue theorem to calculate integrals

Such integrals as equation (B.7) can be estimated with the use of their corresponding holomorphic function $f\left(z\right)$ where z is a complex variable and the residue theorem[2]. It states that a holomorphic function f on $U\backslash\left\{a_1,\cdots,a_n\right\}$ a simply connected open subset of the complex plane U, the integral of f along a closed rectifiable curve γ in U which does not meet $\left\{a_1,\cdots,a_n\right\}$ equals to:

$$\boxed{\oint_\gamma f\left(z\right)dz=2\pi i\sum_{k=1}^{n}\mathrm{Ind}_\gamma\left(a_k\right)\mathrm{Res}\left(f,a_k\right)} \tag{B.8}$$

where the winding number $\mathrm{Ind}_\gamma\left(a_k\right)$ of the curve γ about the point a_k counts the number of times the curve winds counter-clockwise around the point a_k and where $\mathrm{Res}\left(f,a_k\right)$ is the residue of f at the singularity a_k. For a simple pole c, its value is given by:

$$\boxed{\mathrm{Res}\left(f,c\right)=\lim_{z\to c}\left(z-c\right)f\left(z\right)} \tag{B.9}$$

Let's now suppose that f is a holomorphic function on $\mathbb{C}$, excepted on purely complex singularities z_j and that:

$$\exists\left(M,R\right)>0,\alpha>1/\forall z,\left|z\right|>R\text{ and }\mathcal{I}\left(z\right)>0,\left|f\left(z\right)\right|<\frac{M}{\left|z\right|^\alpha} \tag{B.10}$$

[2]See[74], entry "Analytic function". This section is also strongly inspired from [128] and [129].

Let's use the holomorphic properties of f to compute[3]:

$$I_f = \int_{\infty}^{+\infty} f(x)\, dx \tag{B.11}$$

First of all, let's define an integration contour γ_R in the complex plane as presented in figure B.1.

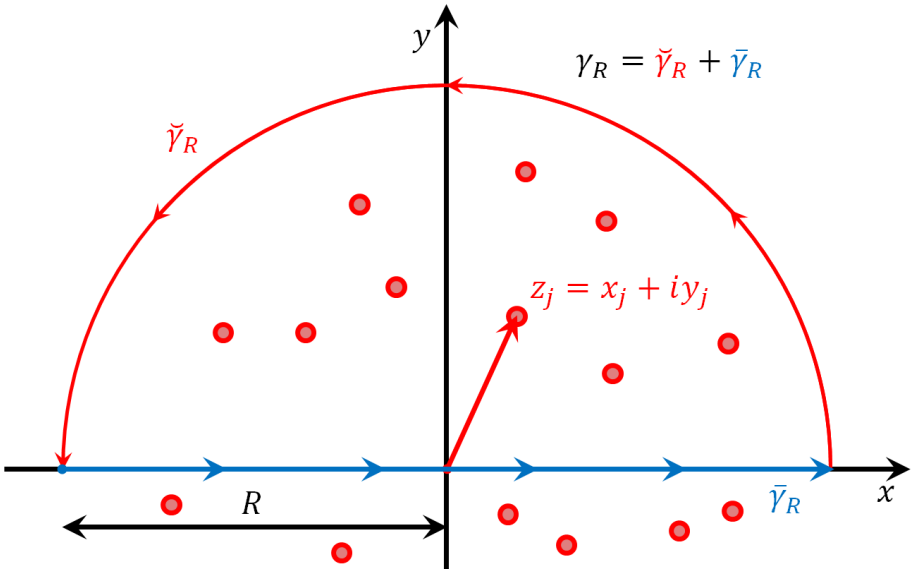

Figure B.1: Illustration of an integration contour γ_R. It is drawn counter-clockwise around the complex singularities z_j and is composed of a semicircle $\breve{\gamma}_R$ of radius R and the remaining $\bar{\gamma}_R$ segment $[-R, R]$ on the real axis.

With this definition, one can notice that:

$$\boxed{\int_{-\infty}^{+\infty} f(x)\, dx = \lim_{R\to+\infty} \oint_{\bar{\gamma}_R} f(z)\, dz} \tag{B.12}$$

Moreover, it comes:

$$\boxed{\oint_{\bar{\gamma}_R} f(z)\, dz = \oint_{\gamma_R} f(z)\, dz - \oint_{\breve{\gamma}_R} f(z)\, dz} \tag{B.13}$$

Firstly, according to the residue theorem (B.8) when R is large enough[4], γ_R winds counter-clockwise around all the purely complex singularities z_j with a strictly positive imaginary part once[5] and one gets:

$$\boxed{\lim_{R\to+\infty} \oint_{\gamma_R} f(z)\, dz = 2\pi i \sum_{\mathcal{I}(z_j)>0} (f, z_j)} \tag{B.14}$$

[3]Note that this integral can be improper, only converging according to the Cauchy principal value definition(see [130]). It is this definition which is used here.

[4]Understood as when $R \to +\infty$ all the complex singularities z_j with a strictly positive imaginary part $\mathcal{I}(z_j) > 0$ lie within the contour γ_R.

[5]$\mathrm{Ind}_{\gamma_{R,\epsilon}}(z_j) = +1$

Secondly, according to the conditions (B.10) listed above, when R is large enough:

$$\left|\oint_{\breve{\gamma}_R} f(z)\,dz\right| \leq \oint_{\breve{\gamma}_R} |f(z)|\,dz \leq \oint_{\breve{\gamma}_R} \frac{M}{|z|^\alpha} dz = \oint_{\breve{\gamma}_R} \frac{M}{R^\alpha} dz = \frac{\pi M}{R^{\alpha-1}} \tag{B.15}$$

And consequently, as $\alpha > 1$:

$$\boxed{\oint_{\breve{\gamma}_R} f(z)\,dz \xrightarrow[R\to+\infty]{} 0} \tag{B.16}$$

Finally, from the previously computed limits (B.14) and (B.16) one gets the global limit from (B.12) and (B.13):

$$\boxed{\int_{-\infty}^{+\infty} f(x)\,dx = 2i\pi \sum_{\mathcal{I}(z_j)>0} \mathrm{Res}(f, z_j)} \tag{B.17}$$

Let's note here that if the conditions (B.10) are not satisfied on the positive imaginary part of the complex plane $\mathcal{I}(z) > 0$ but on the negative part $\mathcal{I}(z) < 0$:

$$\exists (M, R) > 0, \alpha > 1 / \forall z, |z| > R \text{ and } \mathcal{I}(z) < 0, |f(z)| < \frac{M}{|z|^\alpha} \tag{B.18}$$

the same demonstration holds with an integral contour in the negative part of the complex plane drawn clockwise symmetrically to the one presented in figure B.1. In this situation the winding number is negative[6] and:

$$\boxed{\int_{-\infty}^{+\infty} f(x)\,dx = -2i\pi \sum_{\mathcal{I}(z_j)<0} \mathrm{Res}(f, z_j)} \tag{B.19}$$

3 Proof of Weyl's integral

The function introduced in equation (B.7) $f(s) = \frac{e^{ikzs}}{p^2+q^2+s^2-(1+i\epsilon)^2}$ has the following asymptotic behavior:

$$|f(s)| \underset{|s|\to+\infty}{\sim} \frac{e^{-kz\mathcal{I}(s)}}{|s|^2} \tag{B.20}$$

Thus, according to the sign of z on which depends the divergence of the exponential part, $f(s)$ satisfies either the conditions (B.10) ($z > 0$) or (B.18) ($z < 0$)

Let's manipulate the integrand of I_ϵ to find its residue:

$$\begin{aligned} f(s) &= \frac{e^{ikzs}}{p^2+q^2+s^2-(1+i\epsilon)^2} \\ &= \frac{e^{ikzs}}{s^2-\left((1+i\epsilon)^2-p^2-q^2\right)} \\ &= \frac{e^{ikzs}}{\left(s+\left((1+i\epsilon)^2-p^2-q^2\right)^{1/2}\right)\left(s-\left((1+i\epsilon)^2-p^2-q^2\right)^{1/2}\right)} \end{aligned} \tag{B.21}$$

[6] $\mathrm{Ind}_{\gamma_{R,\epsilon}}(z_j) = -1$

The integrand has consequently two simple poles:

$$\begin{aligned} s_\pm &= \pm\left((1+i\epsilon)^2 - p^2 - q^2\right)^{1/2} \\ &= \left(1-p^2-q^2\right)^{1/2}\left(1+\frac{2i\epsilon}{1-p^2-q^2}+\mathcal{O}\left(\epsilon^2\right)\right)^{1/2} \\ &= \left(1-p^2-q^2\right)^{1/2}\left(1+\frac{i\epsilon}{1-p^2-q^2}+\mathcal{O}\left(\epsilon^2\right)\right) \end{aligned} \tag{B.22}$$

whose residues are according to the formula (B.9):

$$\mathrm{Res}\left(f, s_\pm\right) = \frac{\pm e^{\pm ikz\left((1+i\epsilon)^2-p^2-q^2\right)^{1/2}}}{2\left((1+i\epsilon)^2-p^2-q^2\right)^{1/2}} \tag{B.23}$$

We can then use the results found in the previous section to calculate the integral I_ϵ. There are two cases.

Case 1: $p^2+q^2<1$

Then $1-p^2-q^2 \geq 0$ and the two poles are:

$$s_\pm = \pm\sqrt{1-p^2-q^2}\left(1+\frac{i\epsilon}{|1-p^2-q^2|}+\mathcal{O}\left(\epsilon^2\right)\right) \tag{B.24}$$

with $\mathcal{I}\left(s_\pm\right) = \pm\frac{\epsilon}{\sqrt{1-p^2-q^2}}+\mathcal{O}\left(\epsilon^2\right)$.

As $\epsilon \to 0^+$, $\mathcal{I}\left(s_+\right) > 0$ and $\mathcal{I}\left(s_-\right) < 0$. Using the relations (B.17) or (B.19) according to the sign of z, one gets:

$$I_\epsilon = \begin{cases} 2i\pi\mathrm{Res}\left(f, s_+\right) = \frac{i\pi e^{ikz\left((1+i\epsilon)^2-p^2-q^2\right)^{1/2}}}{\left((1+i\epsilon)^2-p^2-q^2\right)^{1/2}} & \text{if } z>0 \\ -2i\pi\mathrm{Res}\left(f, s_-\right) = \frac{i\pi e^{-ikz\left((1+i\epsilon)^2-p^2-q^2\right)^{1/2}}}{\left((1+i\epsilon)^2-p^2-q^2\right)^{1/2}} & \text{if } z<0 \end{cases} \tag{B.25}$$

That is to say:

$$I_\epsilon = \frac{i\pi e^{ik|z|\left((1+i\epsilon)^2-p^2-q^2\right)^{1/2}}}{\left((1+i\epsilon)^2-p^2-q^2\right)^{1/2}} \xrightarrow[\epsilon\to 0]{} \frac{i\pi e^{ikm|z|}}{m} \text{ with } m=\sqrt{1-p^2-q^2} \tag{B.26}$$

Case 2: $p^2+q^2>1$

Then $1-p^2-q^2 \leq 0$ and the two poles are:

$$s_\pm = \pm i\sqrt{p^2+q^2-1}\left(1-\frac{i\epsilon}{|p^2+q^2-1|}+\mathcal{O}\left(\epsilon^2\right)\right) \tag{B.27}$$

with $\mathcal{I}\left(s_\pm\right) = \pm\sqrt{p^2+q^2-1}+\mathcal{O}\left(\epsilon^2\right)$.

As $\epsilon \to 0^+$, $\mathcal{I}(s_+) > 0$ and $\mathcal{I}(s_-) < 0$. Using the relations (B.17) or (B.19) according to the sign of z, one gets:

$$I_\epsilon = \begin{cases} 2i\pi \mathrm{Res}(f, s_+) = \frac{i\pi e^{ikzi\left(p^2+q^2-(1+i\epsilon)^2\right)^{1/2}}}{i\left(p^2+q^2-(1+i\epsilon)^2\right)^{1/2}} & \text{if } z > 0 \\ -2i\pi \mathrm{Res}(f, s_-) = \frac{i\pi e^{-ikzi\left(p^2+q^2-(1+i\epsilon)^2\right)^{1/2}}}{i\left(p^2+q^2-(1+i\epsilon)^2\right)^{1/2}} & \text{if } z < 0 \end{cases} \tag{B.28}$$

That is to say:

$$I_\epsilon = \frac{i\pi e^{ik|z|i\left(p^2+q^2-(1+i\epsilon)^2\right)^{1/2}}}{i\left(p^2+q^2-(1+i\epsilon)^2\right)^{1/2}} \xrightarrow[\epsilon\to 0]{} \frac{i\pi e^{ikm|z|}}{m} \text{ with } m = i\sqrt{p^2+q^2-1} \tag{B.29}$$

Finally, with the formulations (B.6) and (B.7) and the results (B.26) and (B.29) one gets the wanted relation (II.22) for the spherical waves:

$$\frac{e^{ikr}}{r} = \frac{ik}{2\pi} \iint_{-\infty}^{\infty} \frac{1}{m} e^{ik(px+qy+m|z|)} dpdq$$

with:

$$m = \begin{cases} \sqrt{1-p^2-q^2} & \text{if } p^2+q^2 < 1 \\ i\sqrt{p^2+q^2-1} & \text{if } p^2+q^2 > 1 \end{cases}$$

Appendix C

Data registration methods and z_S estimation

This appendix gives some details about some pre-processing steps needed prior any 3D reconstruction which are not detailed in the main text:

- **the data registration** - the different algorithms introduced in this thesis assume that the datasets are centered on the projected holograms of the samples to reconstruct.
- **the estimation of z_s** - in lens-free imaging, the focus is performed numerically and the reconstruction algorithms take as an input this distance z_s between the sensor plane and the sample to reconstruct.

1 Data registration methods

Excepted for the θ-mode of the first design where the holograms are aligned by construction[1], the different proposed microscope designs acquire non-aligned data.

In the case of the first design of chapter III, for the φ-mode, the lighting rotation leads to a translation of the holograms in the sensor field of view.

In the case of the second design of chapter IV, excepted if an object is perfectly on the intersection of the stepper motor rotation axis and the axis connecting the sensor and the light source, its projected hologram center moves along a circle in the sensor field. And in all the cases, the holograms rotate on themselves because the sensor orientation changes with the angle φ.

As a consequence, the data need to be aligned. This is a critical step as it is known that in tomography algorithms, the reconstruction quality is highly sensitive to the data registration [131].

Two techniques are used in this PhD: an autocorrelation and a least mean squares optimization. According to the situation, they are used on the raw holograms or their reconstructions.

[1] And only if the adjustments of the different pieces are correct.

1.1 Registration algorithms

The pre-processing registration step is based on a simple idea schemed in figure C.1. For a given frame f_i , a characteristic pattern p_i is identified and then used frame by frame to register the different lighting situation. The pattern p_i identified in picture f_i is matched in picture f_{i+1}. As the pattern may change according to the lighting angle, the pictures are aligned according to consecutive angles and the identified pattern p_{i+1} in frame f_{i+1} becomes the reference pattern for picture f_{i+2}. And so on...

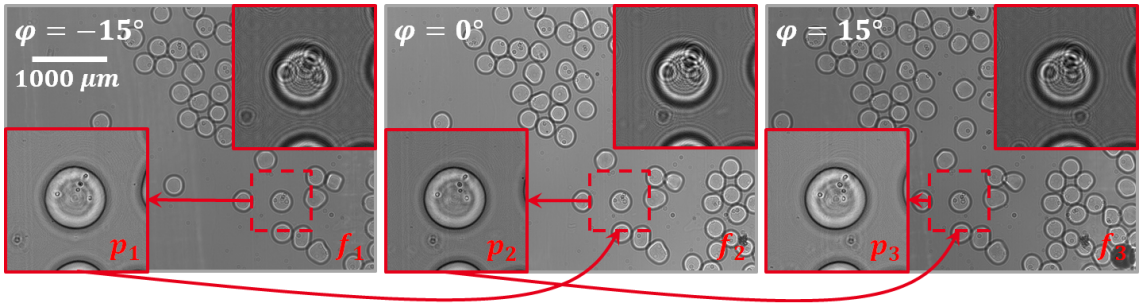

Figure C.1: Illustration of the alignment technique on the example of the Matrigel® capsules reconstructed in chapter III, section 3. For the three angles $\varphi \in \{-15°, 0°, 15°\}$, a capsule is chosen as a reference pattern p_i to align the frame f_{i+1} of the neighboring angle. In that case, the alignment is performed on the 2D back-propagated data. The raw holograms are given for information in the medallions.

The main feature of this alignment technique remains the matching algorithm used to identify the position of the pattern p_i in the frame f_i. First of all, the matching algorithm can be initialized with a position closed to the expected position. Indeed, the position of the pattern p_{i+1} can be estimated for the two situations.

For the φ-mode of the first prototype, the shift Δx_i of the projection i compared to the projection with a normal illumination should directly be $\Delta x_i = z_s . \tan \varphi_i$.

For the second design, from the knowledge of the alignment of the two first patterns, knowing $\varphi_{i+1} - \varphi_i$, a center of rotation and the associated radius can be determined and used to predict the position of the other patterns[2].

Concerning the matching itself, two techniques are used.

Maximum of the cross-correlation - In this technique, the cross-correlation of the pattern p_i with an extracted region of f_{i+1} around the expected position is computed [132]. Supposing that p_i is effectively in f_{i+1}, the operation is similar to the computation of the autocorrelation [133] whose maximum gives the relative translation of the pattern p_i in the frame f_{i+1} and consequently the position of the new pattern p_{i+1} and the relative alignment of the two frames.

This technique gives good results for patterns with a high specificity and is very fast to run. It is nevertheless very sensitive the change of the pattern shape according

[2]This center of rotation and radius can be refined when new patterns are identified.

to the angle, especially if the raw holograms are used to aligned the data. Indeed, nothing looks like more a hologram of a cell (circles into other circles) than another hologram of a cell, misleading the algorithm if the extracted frame to perform the cross-correlation is too big and contains many holograms.

This alignment technique is used until chapter III, section 2.

Iterative registration by least mean squares minimization - This technique aims at being more robust by taking in account that the pattern evolves from one angle to another. For a given frame d_{i+1}, it finds the area which "looks like the most" to the pattern p_i.

This estimation is performed by computing the L_2-norm of the difference between the pattern p_i to identify and the possible pattern in f_{i+1} defined as:

$$\|f\|_{L_2} = \sqrt{\sum_l |f_l|^2} \tag{C.1}$$

Finding the best parameters consists in the least mean squares minimization [134] of the following problem:

$$\boxed{\left(\tilde{dx}, \tilde{dy}, \tilde{d\theta}\right) = \underset{(dx,dy,d\theta)}{\operatorname{argmin}} \|\text{interp}_{2D}\left(f_{i+1}, dx, dy, d\theta\right) - p_i\|_{L_2}^2} \tag{C.2}$$

where $\text{interp}_{2D}\left(f_{i+1}; (dx, dy, d\theta)\right)$ is the 2D linear interpolation of f_{i+1} on a 2D mesh - which matches the characteristics of the one of p_i in terms of pixel number nb_x and nb_y and pixel pitch - translated of dx and dy and rotated of $d\theta$. As this technique is initialized with the forecast position of the pattern to find, it is less likely to diverge far away from this position on another pattern looking alike the target as a cross-correlation on the full area could do. It rather reaches the closest surrounding pattern.

Contrary to the previous algorithm, this technique can perform sub-pixel alignment and can find the relative angle of the frame whereas the cross-correlation can only find a relative translation. It is also more robust to hologram deformation.

It is nevertheless longer to run as it is solved by an iterative gradient descent method[3].

It is this technique which is implemented in the steps dedicated to alignment refinement in methods IV.3 and IV.4.

This alignment technique is used from chapter III, section 3 in the main text.

1.2 Raw *versus* reconstructed holograms

For the first reconstructions of this PhD work, the alignment is done via the cross-correlation technique on the raw holograms. For isolated objects or big characteristic areas, it works well enough.

But as stated above, a hologram changes according to the wavelength and is not a very specific pattern as interference rings interference with their neighbors,

[3]Using "`fminsearch`" in Matlab®.

depending on the angles. For example, looking at the holograms in figure C.1, it is impossible to do a precise alignment directly on a specific object inside the capsule, its hologram interfering with other objects holograms or the capsule edge. In contrary, on the presented 2D back-propagated frames, the individual objects are clearly separated and a precise alignment on one of them is possible.

Once 2D back-propagation model are developed, it is possible to provide better pictures to feed the algorithms.

For the first prototype, 2D reconstructions are done on the stretched holograms as described in chapter III, section 2.2 using the 2D back-propagation and phase retrieval algorithms introduced in chapter I, section 3 to remove the twin-image.

For the second design, once a more realistic model has been developed to take in account the 2D tilted wave propagation, simple back-propagations[4] as presented in chapter IV, sections 2 and 5 are used to focus the patterns p_i.

1.3 Discussion

A question which has not been raised so far concerns the different wavelengths and how they should be taken into account in the alignment procedures.

At first, the alignment is assumed to be the same for all the three wavelengths $\lambda \in RGB$. Consequently the results of the three wavelengths are averaged to extract one position in the field of view to extract the aligned data.

But this assumption is wrong. It is observed that the three wavelengths are slightly shifted, for example because of the relative position of their corresponding LEDs behind the pinhole or refraction effects which depends on the wavelength, and should be aligned independently. To do so, the green channel, whose wavelength is in between the two others (blue and red) is used as a reference to align the two other wavelengths. This means that the algorithms align the green channel and then, the red and blue channel are aligned on the green extracted patterns.

This works with the raw holograms, but is very well adapted to an alignment on the 2D back-propagated planes.

On another point, these algorithms are based on a strong assumption: that the holograms or their reconstruction patterns are coherent angle after angle, which is wrong. This means that the alignment cannot be perfectly made with these techniques. Moreover, the alignment being performed angle after angle, the errors made during these alignment accumulate. To minimize this effect, the central angle φ_c can be used to separate the angles in two equal set, one the "left" and the other on the "right" of φ_c. Then the errors accumulate on half of the angles instead of on the whole dataset.

This shows the importance of the alignment refinement steps in methods IV.3 and IV.4 where the holograms are aligned independently from one another.

In addition, it was mentioned in the conclusion of chapter IV, section 5 that the alignment step can be very long. In tomography problems, registration is a recurrent issue [131] and it surely exists faster alignment techniques than the one

[4] Figures IV.12.d and IV.30.b.

implemented in this thesis, especially if estimating the relative angle is not necessary. It is something that is not deepened during this PhD work.

Finally, these algorithms imply the existence of a specific pattern or object isolated enough to produced isolated holograms in the field of view for all the angles. If it is not isolated enough its hologram will overlap with holograms of other objects depending of the lighting situation and the relative positions of the objects.

This means that it can be very hard or even impossible to align data acquired on too complex samples in the pre-processing steps using these techniques. When this happens, it is still possible to use the alignment parameters of a previous experience hoping that they will be close enough to those sought and that the refinement steps in methods IV.3 and IV.4 will be sufficient to correct the errors.

2 z_s estimation

The other determinant parameter in the 3D reconstruction quality is the distance z_s between the sensor and the object. For all the reconstructions of this thesis, it is manually estimated.

The reconstruction quality may benefit of an objective criterion automatically optimized. It nevertheless implies more in-depth studies and is not treated in this PhD work.

2.1 Simple 2D back-propagation

Until chapter IV, section 3 and for section 5, z_s is estimated through simple 2D back-propagation, using a 2D propagation model adapted to the situation.

In the case of the first prototype, the z_s is computed using the hologram acquired with a normal angle $\varphi = 0°$ for which standard 2D back-propagation algorithm developed for standard 2D lens-free microscopy can be used. Small objects holograms are chosen in the field of view and back-propagated using $h^{\lambda_0}_{-z_s}$ until their reconstruction appears to be the sharpest.

In the case of the second design, there is no acquisition performed with a normal angle because θ is fixed to a given value. The adapted tilted model developed in chapter IV, section 2 is used as a simple back-propagation tool. It is nevertheless trickier as taking in account the angle is subtle (see III, section 5). One needs to be careful to use the same angle θ_{air} or θ_0 for the 2D and the 3D reconstructions. Moreover, lots of artifacts remain and make it harder to identify the focal plane based on the sharpness of the reconstructed objects.

The problem of the simple 2D back-propagation method is that the focus is adjust using a single object in the field of view whose height may strongly differ from the one of the reconstructed volume. If this object does not belong to the plane $z = 0$ of this volume, the overall focus will be wrong.

This problem is handled correctly by the following method.

2.2 Simple 3D back-propagation

This method is based on a brute force approach in which 3D reconstructions using a simple Fourier mapping III.4 are computed for different distances z_s on a small region of the dataset. Without any regularization, the reconstructions are noisy with many artifacts. But as shown in chapter IV, section 5, single isolated objects can be easily identified and have a strong peaked signal.

Working directly on one of the reconstructed particles or on the xy-maximum intensity projection of the whole volume, the distance z_s giving the sharpest signal is chosen to feed the 3D reconstruction algorithm on the full dataset.

This technique, used for chapter IV, section 4 and chapter V, is more accurate as it gives a 3D criterion on the focus parameter. But it is longer to run.

Appendix D

Gradient of $J(f)$

The aim of this appendix is to give on overview of the computation of the gradient of the cost functions introduced in this thesis.

1 Data fidelity

This section focuses on the data fidelity term of the cost functions:

$$\boxed{J_d(f) = \left\| |U_{tot}(f)|^2 - I_d \right\|^2} \tag{D.1}$$

I_d symbolizes an intensity data measured by the sensor and U_{tot} the total complex wave front on the sensor for a given diffracting object f.

With the canonical scalar product and its associated norm, equation (D.1) gives a data fidelity term for gradient descent methods, leading to a minimization of the least squares between the data and the simulated intensities. These numerical methods generally need the expression of the gradient at a given f. Finding such a formulation is the objective of this appendix.

The following formalism applies for vectors, not matrices. Thus, for example if I_d is the 2D matrix of the measures on the sensor, it will be unfolded toward a vector shape. The same applies for f which can either be a 2D or a 3D complex matrix, unfolded on its real and imaginary parts[1]:

$$\begin{aligned} f_{2D} \in \mathcal{M}_{nb_x,nb_y}(\mathbb{C}) \Rightarrow f = (\mathcal{R}(f_{2D}(:)); \mathcal{I}(f_{2D}(:))) \in \mathbb{R}^{2nb_x nb_y} \\ f_{3D} \in \mathcal{M}_{nb_x,nb_y,nb_z}(\mathbb{C}) \Rightarrow f = (\mathcal{R}(f_{3D}(:)); \mathcal{I}(f_{3D}(:))) \in \mathbb{R}^{2nb_x nb_y nb_z} \end{aligned} \tag{D.2}$$

Furthermore, one can introduced a weighting factor W to weight the data fidelity pixel by pixel[2]. This can be used to avoid taking in account defective pixels such as hot pixels or dead pixels. The definition of the scalar product and the associated

[1] Using Matlab® notations.

[2] Which is generally set uniformly to 1 in this thesis, giving the canonical scalar products $\langle .,. \rangle_{\mathbb{R}}$ and $\langle .,. \rangle_{\mathbb{C}}$.

norm becomes:

$$\begin{array}{c} \forall (x,y) \in \mathbb{R}^n \times \mathbb{R}^n, \langle x,y \rangle_{W,\mathbb{R}} = \sum_{k=1}^n w_k x_k y_k \\ \forall (x,y) \in \mathbb{C}^n \times \mathbb{C}^n, \langle x,y \rangle_{W,\mathbb{C}} = \sum_{k=1}^n w_k \overline{x_k} y_k \\ \|.\|_W^2 = \langle .,. \rangle_{W,\mathbb{R}} \end{array} \tag{D.3}$$

Let's suppose that U_{dif} is linearly dependent on f. This is consistent with the models developed in chapter II, sections 1.2 and 2 for low scattering objects. Thus it exists a linear operator of matrix representation O such that:

$$\boxed{U_{tot}(f) = U_{inc} + U_{dif}(f) = U_{inc} + O \times f} \tag{D.4}$$

where all the complex fields are unfolded as mentioned above[3].

Let's now find the first order development of $J(f+\delta f)$ according to δf:

$$\begin{aligned} J_d(f+\delta f) &= \left\| |U_{inc} + O \times (f+\delta f)|^2 - I_d \right\|_W^2 \\ &= \left\| |U_{inc} + O \times f + O \times \delta f|^2 - I_d \right\|_W^2 \\ &= \left\| |U_{tot}(f) + O \times \delta f|^2 - I_d \right\|_W^2 \\ &= \left\| |U_{tot}(f)|^2 + |O \times \delta f|^2 + 2\mathcal{R}\left(\overline{U_{tot}}(f).(O \times \delta f)\right) - I_d \right\|_W^2 \\ &= \left\| |U_{tot}(f)|^2 - I_d \right\|_W^2 + \cdots \\ &\qquad 2\left\langle |U_{tot}(f)|^2 - I_d, 2\mathcal{R}\left(\overline{U_{tot}}(f).(O \times \delta f)\right)\right\rangle_{W,\mathbb{R}} + o(\|\delta f\|) \\ &= J(f) + \cdots \\ &\qquad 4\mathcal{R}\left\langle |U_{tot}(f)|^2 - I_d, \overline{U_{tot}}(f).(O \times \delta f)\right\rangle_{W,\mathbb{C}} + o(\|\delta f\|) \\ &= J(f) + \cdots \\ &\qquad 4\mathcal{R}\left\langle W.U_{tot}(f).\left(|U_{tot}(f)|^2 - I_d\right), O \times \delta f\right\rangle_{\mathbb{C}} + o(\|\delta f\|) \\ &= J(f) + \cdots \\ &\qquad 4\mathcal{R}\left\langle O^\star \times \left[W.U_{tot}(f).\left(|U_{tot}(f)|^2 - I_d\right)\right], \delta f\right\rangle_{\mathbb{C}} + o(\|\delta f\|) \\ &= J(f) + \cdots \\ &\qquad \left\langle 4\mathcal{R}\left[O^\star \times \left[W.U_{tot}(f).\left(|U_{tot}(f)|^2 - I_d\right)\right]\right], \delta f\right\rangle_{\mathbb{R}} + o(\|\delta f\|) \end{aligned} \tag{D.5}$$

using that $|U_{tot}(f)|^2 - I_d$ and δf are real vectors to reverse the scalar products $\langle .,. \rangle_{\mathbb{R}}$ and $\langle .,. \rangle_{\mathbb{C}}$ and the projection on the real part $\mathcal{R}$. $\overline{U_{tot}}$ stands for the complex conjugate of U_{tot} and $O^\star$ is the Hermitian adjoint[4] of O.

It finally comes the gradient expression of the cost function (D.1) at a given point f:

$$\boxed{\nabla J_d(f) = 4\mathcal{R}\left[O^\star \times \left[W.U_{tot}(f).\left(|U_{tot}(f)|^2 - I_d\right)\right]\right]} \tag{D.6}$$

[3] $\times$, the matrix multiplication sign, is the only matrix operator. The modulus $|.|$, square ^{2} and multiplication . operators are applied term by terms on the vectors.

[4] For a matrix, $O^\star = {}^t\overline{O}$.

2 L_1-norm

This section focuses on the L_1-norm term of the cost functions whose minimization favors a sparse solution:

$$\boxed{J_{L_1}(f) = \|f\|_{L_1}} \tag{D.7}$$

If one works with overall sparse objects, this aims at enforcing the fact that the expected reconstruction is mainly composed of isolated "particles" [135, 136].

The L_1-norm of f is defined as the sum of the absolute value of its coefficients. Using a vector shape, indexed by k, the expression is:

$$\|f\|_{L_1} = \sum_k |f_k| \tag{D.8}$$

One may note that such an expression is not differentiable on 0, which can be problematic for gradient descent resolution. It is numerically implemented by the following convex approximation:

$$\boxed{\|f\|_{L_{1,\epsilon}} = \sum_k \sqrt{|f_k|^2 + \epsilon^2}} \tag{D.9}$$

where ϵ is a small number[5].

Consequently, the gradient of the expression (D.9) at a given point f is:

$$\boxed{\nabla J_{L_{1,\epsilon}}(f) = \left(\frac{f_k}{\sqrt{|f_k|^2 + \epsilon^2}} \right)_k} \tag{D.10}$$

3 ∇-norm

This section focuses on the ∇-norm term of the cost functions whose minimization enforces an edge-preserving regularization [137, 138] by favoring a sparse gradient of the reconstructed object:

$$\boxed{J_{\nabla}(f) = \|\nabla f\|_{L_1}} \tag{D.11}$$

This *a priori* hypothesis is based on the expectation that the "particles" in the reconstructions have almost uniform values inside their support. As a result, the gradient of the objects has to be almost sparse. Another interpretation is that the reconstructed image has to be smooth while preserving sharp edges at the locations of the particles.

The gradient of the object is computed on its "inner" coefficients. Indeed, the gradient is estimated in between the pixels for 2D objects or in between the voxels for 3D objects using the surrounding neighbors (see figure D.1). It cannot be

[5] $\epsilon = 10^{-7}$ in all this PhD work.

computed on the edges. Thus, defining $I_{2D} = [\![1, nb_x - 1]\!] \times [\![1, nb_y - 1]\!]$ and $I_{3D} = [\![1, nb_x - 1]\!] \times [\![1, nb_y - 1]\!] \times [\![1, nb_z - 1]\!]$ it comes for the 2D objects $\forall (k,l) \in I_{2D}$:

$$\begin{aligned} |\nabla f_{k,l}|^2 = \frac{1}{2}\Big[& q_x \left| f_{k+1,l} - f_{k,l} \right|^2 + q_y \left| f_{k,l+1} - f_{k,l} \right|^2 + \cdots \\ & q_x \left| f_{k+1,l+1} - f_{k,l+1} \right|^2 + q_y \left| f_{k+1,l+1} - f_{k+1,l} \right|^2 \Big] \end{aligned} \tag{D.12}$$

and for the 3D objects $\forall (k,l,m) \in I_{3D}$:

$$\begin{aligned} |\nabla f_{k,l,m}|^2 = \frac{1}{4}\Big[& q_x \left| f_{k+1,l,m} - f_{k,l,m} \right|^2 + q_x \left| f_{k+1,l+1,m} - f_{k,l+1,m} \right|^2 + \cdots \\ & q_x \left| f_{k+1,l,m+1} - f_{k,l,m+1} \right|^2 + q_x \left| f_{k+1,l+1,m+1} - f_{k,l+1,m+1} \right|^2 + \cdots \\ & q_y \left| f_{k,l+1,m} - f_{k,l,m} \right|^2 + q_y \left| f_{k+1,l+1,m} - f_{k+1,l,m} \right|^2 + \cdots \\ & q_y \left| f_{k,l+1,m+1} - f_{k,l,m+1} \right|^2 + q_y \left| f_{k+1,l+1,m+1} - f_{k+1,l,m+1} \right|^2 + \cdots \\ & q_z \left| f_{k,l,m+1} - f_{k,l,m} \right|^2 + q_z \left| f_{k+1,l,m+1} - f_{k+1,l,m} \right|^2 + \cdots \\ & q_z \left| f_{k,l+1,m+1} - f_{k,l+1,m} \right|^2 + q_z \left| f_{k+1,l+1,m+1} - f_{k+1,l+1,m} \right|^2 \Big] \end{aligned} \tag{D.13}$$

(q_x, q_y, q_z) are weighting coefficients to take into account that the grid can be not orthonormal. They are set to $q_x = 1$, $q_y = dx/dy$ and $q_z = dx/dz$.

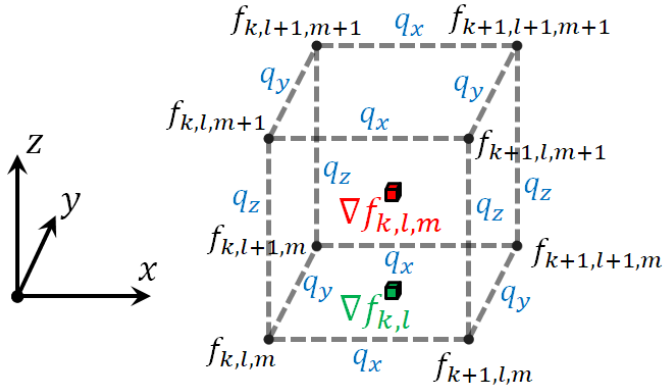

Figure D.1: Illustration of the coefficients used to compute the gradients $\nabla f_{k,l}$ and $\nabla f_{k,l,m}$ in two (green) and three (red) dimensions using the neighboring elements.

The ∇-norm of f is defined as the sum of the absolute value of the coefficients of its gradient:

$$\boxed{\|\nabla f\|_{L_1,\epsilon} = \begin{cases} \sum_{(k,l)\in I_{2D}} \sqrt{|\nabla f_{k,l}|^2 + \epsilon^2}, \text{ for 2D objects} \\ \sum_{(k,l,m)\in I_{3D}} \sqrt{|\nabla f_{k,l,m}|^2 + \epsilon^2}, \text{ for 3D objects} \end{cases}} \tag{D.14}$$

The parameter ϵ is again used to avoid the singularity when $\nabla f = 0$. It has also the property of relaxing the strong constraint put by the L_1-norm on the sharpness of edges by acting like a threshold on the gradient. Below this threshold, regularization

smooths the solution (behaving like a L_2-norm) while above this threshold, the contrast is preserved (behaving like a L_1-norm).

From equation (D.14), it appears that a given coefficient $f_{k,l}$ in 2D ($f_{k,l,m}$ in 3D) have multiple participation in the gradient: two for each pixel surrounding $f_{k,l}$ (or three for each voxel surrounding $f_{k,l,m}$). This means that for inner elements, the gradient will be composed of a summation of $2 \times 4 = 8$ terms, $2 \times 2 = 4$ for the elements on the side of the surface and $2 \times 1 = 2$ in the corner (and in 3D, $3 \times 8 = 24$ for the inner coefficients, $3 \times 4 = 12$ for the faces of the volume, $3 \times 2 = 6$ for the sides and $3 \times 1 = 3$ for the eight corners).

Noting N the surrounding neighbors[6] of (k,l) (or (k,l,m) for 3D objects) and $E(N_i)_{k,l}$ (or $E(N_i)_{k,l,m}$) the two elements participating in the gradient[7] for each neighbor N_i, the gradient of the expression (D.14) at a given point f is:

$$\nabla J_{L_1,\epsilon}(f) = \begin{cases} \left(\sum_{N_i \in N(k,l)} \sum_{E_i \in (N_I)_{k,l}} \frac{q(k,l;E_i)}{2} \frac{f_{k,l} - f_{E_i}}{\sqrt{\left|\nabla f_{N_i}\right|^2 + \epsilon^2}} \right)_{k,l} & \text{, in 2D} \\ \left(\sum_{N_i \in N(k,l,m)} \sum_{E_i \in (N_I)_{k,l,m}} \frac{q(k,l,m;E_i)}{4} \frac{f_{k,l,m} - f_{E_i}}{\sqrt{\left|\nabla f_{N_i}\right|^2 + \epsilon^2}} \right)_{k,l,m} & \text{, in 3D} \end{cases} \tag{D.15}$$

where $q(.,.)$ is defined to equal q_x, q_y or q_z depending on the given situation.

[6] For example, for an inner coefficients $f_{k+1,l+1}$ in 2D and $f_{k+1,l+1,m+1}$ in 3D, one gets:

- in 2D: $N(k+1,l+1) = \{(k,l),(k+1,l),(k,l+1),(k+1,l+1)\}$
- in 3D: $N(k+1,l+1,m+1) = \{(k,l,m),(k+1,l,m),(k,l+1,m),(k+1,l+1,m),\cdots (k,l,m+1),(k+1,l,m+1),(k,l+1,m+1),(k+1,l+1,m+1)\}$

[7] For example, for an inner coefficients $(k+1,l+1)$ in 2D and $(k+1,l+1,m+1)$ in 3D, and a given $N_i = (k,l)$ in 2D and $N_i = (k,l,m)$ in 3D, one gets:

- for 2D objects: $E(k,l)_{k+1,l+1} = \{(k+1,l),(k,l+1)\}$
- for 3D objects: $E(k,l,m)_{k+1,l+1,m+1} = \{(k+1,l,m+1),(k,l+1,m+1)\}$

Appendix E

3D chemotaxis simulations

The aim of this appendix is to give some examples of 3D cell culture applications in biological research and how the knowledge of the 3D cells distribution could improve the tested models.

The main objective is to give an idea of the potential use of the 3D information available via a large field of view given by a 3D lens-free microscope as an input for biophysical models.

The results in this appendix are preliminary and do not pretend to provide the explanation of the underlying biology of the presented experiments.

Both of the examples given in this appendix are based on chemotaxis: the cells are able to sense the surrounding concentration of molecules and move accordingly. The experiments focus on the cells displacement in their culture medium to shape ordered structure. They were done before the PhD work using a 2D lens-free microscope.

1 Experiments

In these experiments, the cells are seeded on a Matrigel® bed according to the no top coat protocol previously described in the main document, in chapter IV, section 5. This section also presents the two cell lines that are used in this appendix. Contrary to 2D Petri dishes, in which the cells can only develop bidimensionally, this extracellular matrix allows them shaping 3D structures.

1.1 RWPE1: Prostate Epithelial Cells

Figure E.1 emphasizes the temporal evolution over 35 hours of two regions of interest in a RWPE1 cells culture[1].

The RMPE1 cells are tumorous cells from the human prostate. Cultivated prostate cells grow into acini, empty spheres of cells in which are produced hormones. In Matrigel®, RMPE1 cells tend to form spheroids, which are acini, filled with tumorous cells. Besides, on a Matrigel® bed coated with liquid culture medium,

[1]Non published data.

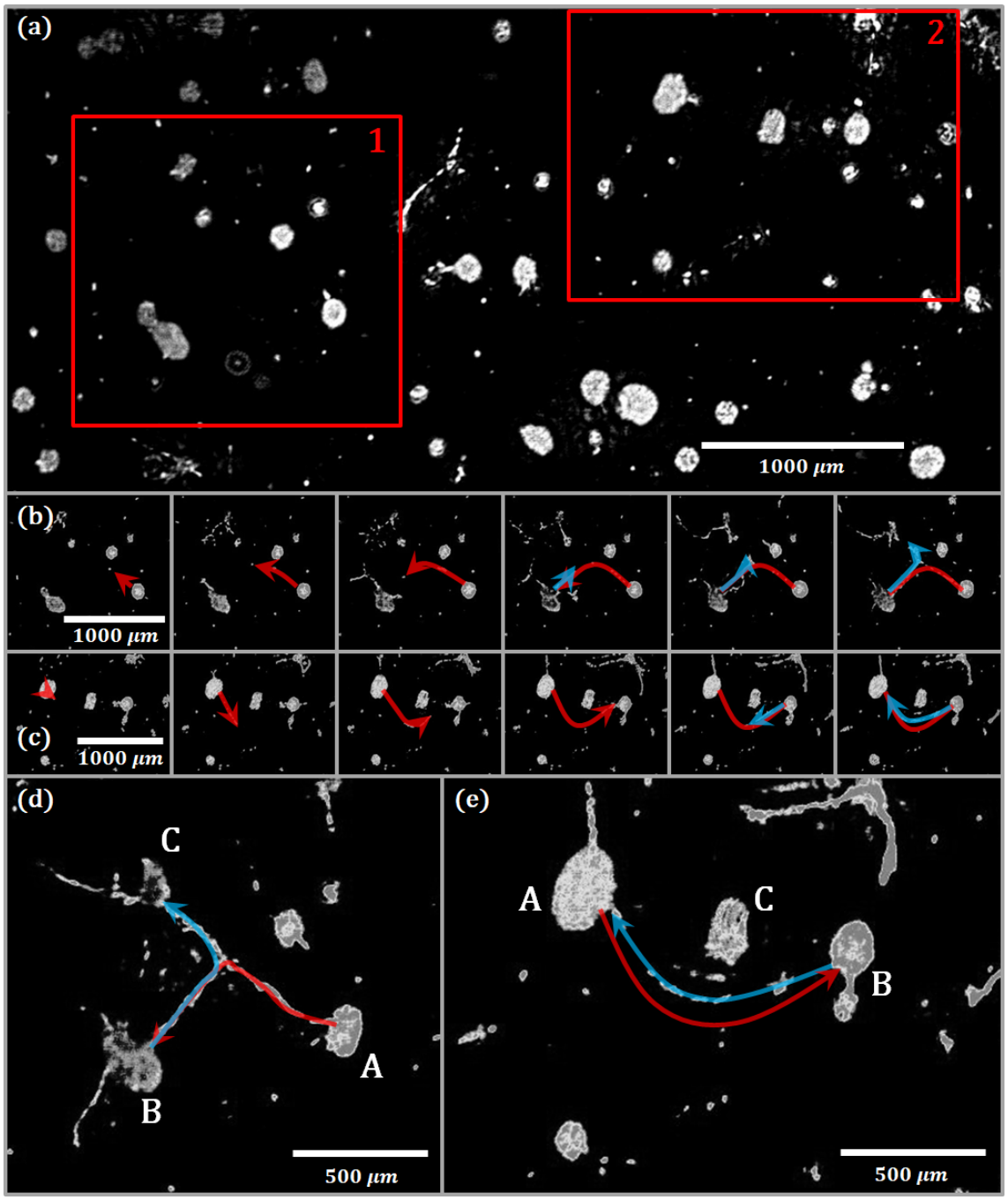

Figure E.1: Time-lapse on a RWPE1 culture. Two regions of interests, 1 and 2, are enlightened on (a). The evolution of 1 (resp. 2), is detailed on (b) (resp. (c)), with a 5 hours step between each frame. Its final configuration is shown on (d) (resp. (e)). On each region of interest, a cell stream seems to be ejected from one acinus and migrates to another one, on a specific path. Once it reaches this second acinus, the stream cell moves backward. In 2, it goes back to its original acinus whereas in 1 it moves towards another neighbor.

cells are free to move on the interface between the gel and the liquid and tend to create networks between acini. It is the early stage of this phenomenon which can be seen in figure E.1.

Contrary to what one may think, the experiment shows that cell migration between acini does not appear to be random. Cells follow specific tracks. On each region of interest, cells move from the spheroid A to B, on a curved path, specifically targeting B. On the region labeled 2, the path avoids carefully C. In the two cases, the cells seem to turn back once they have reached B. If in 2 they just go back to A, a shift happens in 1 where the cells begin to follow their track before turning towards C.

Hence, it appears that studying such 3D cells cultures can help understanding fundamental biological phenomena in the realms of morphogenesis and tumorigenesis.

This experiment in particular has initiated a work to explain the trajectories thanks to a mathematical model.

1.2 HUVEC: Human Umbilical Vein Endothelial Cells

In figure E.2, one can see the early stages of vascular network assembly in an endothelial cells culture. This experiment shows several steps from the first layout of the cells shaping the future structure to their division and strengthening of the network.

Figure E.3 focuses on the first part of the network assembly. Randomly spread, the cells first begin to migrate to form the shape of the future network. As the cells do not touch their neighbors yet, chemotaxis can be an explanation of their migration to one another.

Once again, understanding such a phenomenon can lead to better knowledge of fundamental biological phenomena in the realms of vasculogenesis and angiogenesis.

2 Mathematical model

This section focuses on the mathematical model developed to simulate the two previous experiments. Some works already exist on chemotaxis simulation and this work is mainly based on [17] in which the authors simulate the 2D early stages of vascular network assembly. It has the advantages to both take into account the diffusion of proteins[2] released by the cells in the culture medium and the displacements of cells, that is to say the diffuser themselves.

The aim here is to develop a 3D model. Nonetheless, no information is known about the z-distribution of cells in the given experiments. As a consequence, all the objects are placed in the same plane.

In the first place, the diffusion model is introduced for static diffusers, before focusing in a second part on the situations in which the cells producing proteins are

[2]Or any other chemoattractant that will also be mentioned as "proteins" in this appendix.

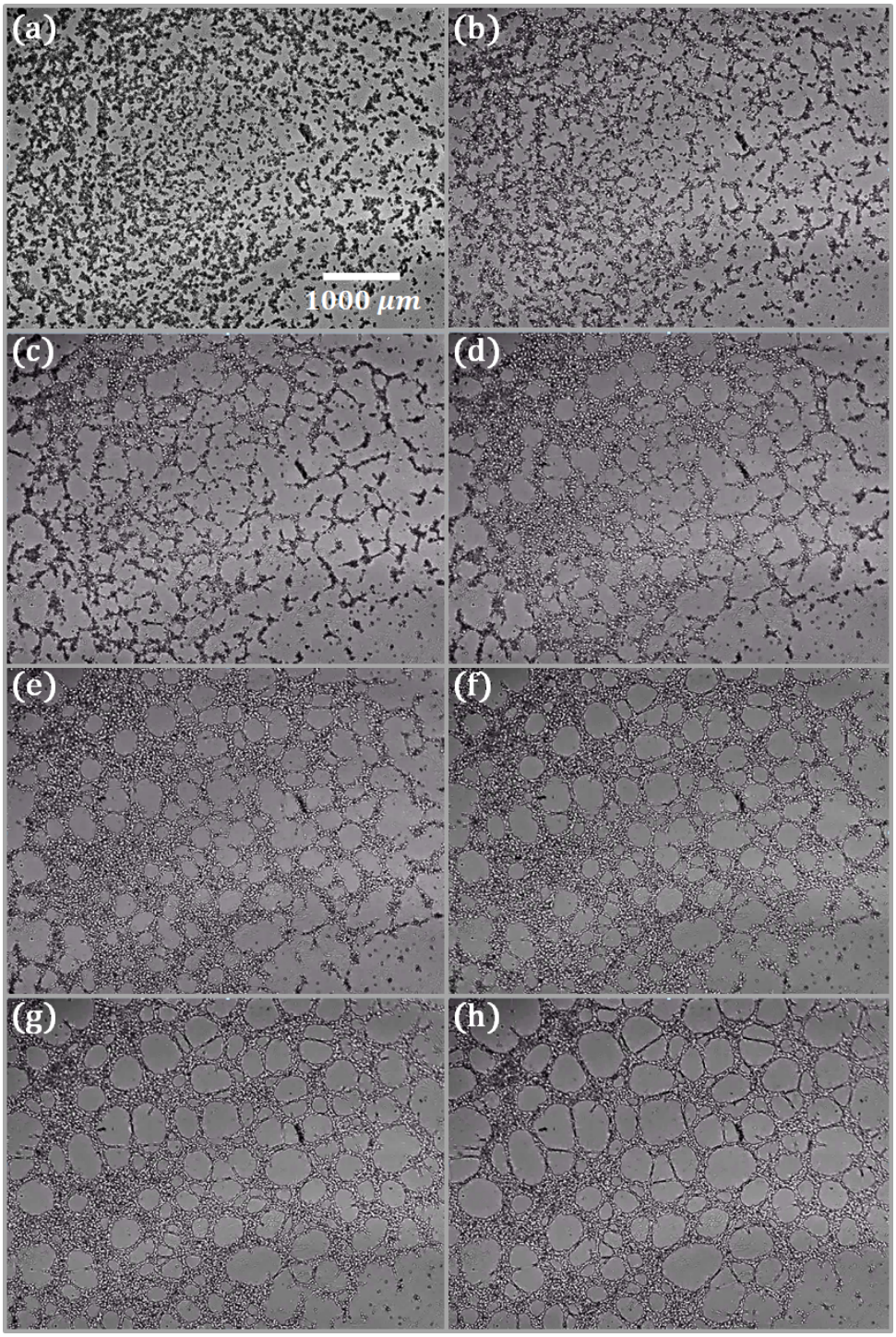

Figure E.2: Time-lapse on HUVEC culture. On these frames, spaced every three hours, randomly spread cells agglutinate to form the early stages of a vascular network assembly (a-c). After a phase of contraction, once the network shape is formed, cells begin to divide (d) and expand their occupation on the Matrigel® surface (e-g) before stabilizing in a vast network (h).

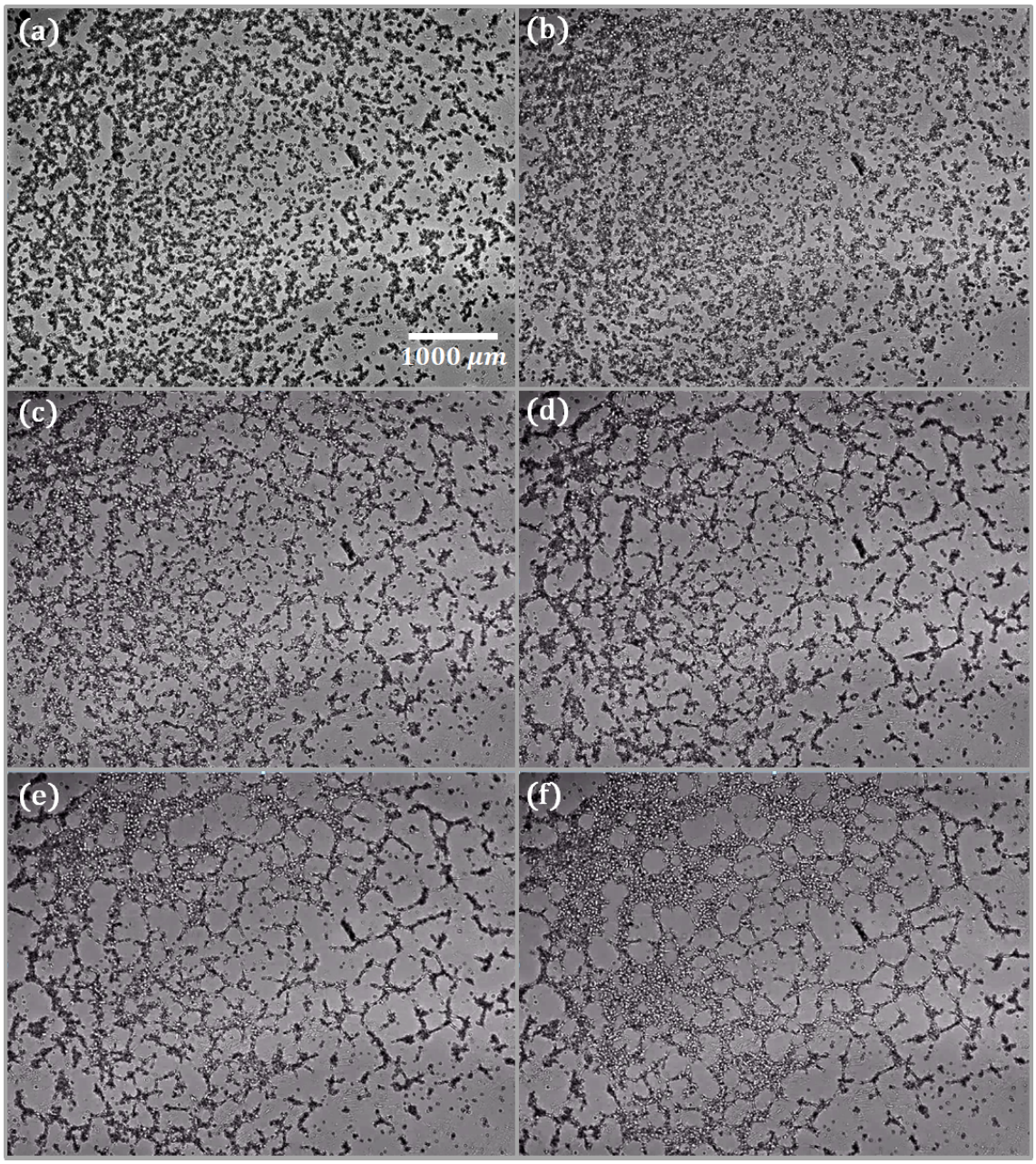

Figure E.3: Focusing on the first four frames of the figure E.2 (a-d). On these frames, spaced every 1.5 hours, one can see the initially randomly spread cells agglutinating to form the early stages of the future network before the phase of cells division (f).

also moving in the sample.

It should be noted that all the equations are written for continuous variable. The 3D mesh and the temporal evolution are discrete in the simulation and a direct equivalence between the continuous and discrete formulae is implied.

2.1 The model

The model of chemotaxis chosen for these simulations is based on the fact that cells are sensitive to their surrounding proteins concentrations and move accordingly along their gradients. Thus, the cells velocity is here supposed[3] to be proportional to this gradient:

$$\overrightarrow{v} = \frac{d\overrightarrow{pos}}{dt} = k.\overrightarrow{grad}\, c \tag{E.1}$$

where $\overrightarrow{v}$ is the velocity of the cells and $\overrightarrow{pos}$ their position, c the concentration of the proteins and k a coefficient of proportionality.

Then one needs to know the proteins distribution in the culture medium to work out its gradient. The temporal evolution in the mesh is led by the following equation:

$$\frac{\partial c}{\partial t} = D\Delta c + \alpha n - \tau^{-1} c \tag{E.2}$$

where D is the diffusion coefficient, α the rate of release and τ the decay rate of the proteins. n is the diffuser density. D represents the ability of the chemoattractant to spread in the culture medium. αn is the source term of the proteins. And τ is the characteristic degradation time of these proteins.

These steps are shown schematically in figure E.4.

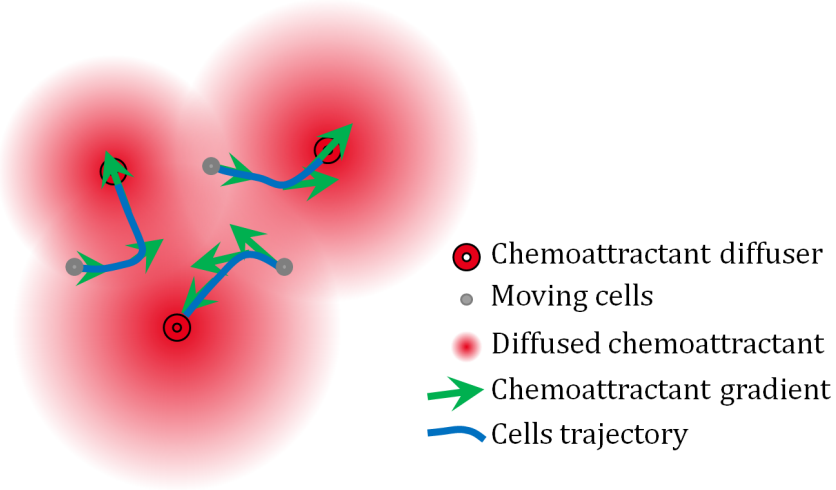

Figure E.4: Scheme of the algorithm: after the diffusers have released their chemoattractant (on red color), the cells move along its concentration gradient (the green arrows) on specific streamlines (the blue curves).

For the discrete problem, the spatial derivative is computed thanks to second order symmetric finite difference method and once the grid is known for the time t_n, the time evolution is updated with the Euler method [139] for the discrete evolution δt:

$$\overrightarrow{pos_{n+1}} = \overrightarrow{pos_n} + \delta t.k.\overrightarrow{grad}\, c \tag{E.3}$$

[3]Whereas in [17], the acceleration $\overrightarrow{a}$ is supposed to be proportionally linked to the gradient.

$$c\left(t_{n+1}\right) = c\left(t_n\right) + \delta t \times \left(D\Delta c + \alpha n - \tau^{-1} c\right)\left(t_n\right) \tag{E.4}$$

Contrary to [17], the migrating cells are not modeled by a field but remain here discrete points, moving freely in the discrete mesh. The field n is then computed by counting the cells in each elementary volume, the voxels, of the mesh.

2.2 Static diffusers

For the simulation of chemotaxis with acini, the previous model is slightly different. Indeed, the diffusers are static and the source term is accordingly changed. In this situation, the hypothesis that the concentration in the diffusers is supposed to be constant.

Thus, at each time step, the concentration in the diffusers' voxels is forced to be kept constant and c is led by :

$$\frac{\partial c}{\partial t} = D\Delta c - \tau^{-1} c \tag{E.5}$$

Each time step is then composed of two sub-steps:

- Sub-step 1: evolution of c according to (E.5)
- Sub-step 2: update in the mesh of c forced to be constant in the diffusers voxels.

In this situation, c reaches an equilibrium in which all the proteins released by the diffusers are compensated by their degradation through the term "$-\tau^{-1}c$" (see figure E.5).

Once the concentration is known, one can work out directly the trajectory of the cells, given by the streamlines in the gradient according to equation (E.1) (see figure E.6).

2.3 Mobile diffusers

If one now wants to simulate the network assembly experiment, the complete model described in 2.1 must be used. Thus, the times steps are now composed of three sub-steps:

- Sub-step 1: computation of "αn" $= \alpha . \frac{nb_{cells\,per\,voxels}}{Vol_{voxel}}$, the discrete source term.
- Sub-step 2: evolution of c according to equation (E.4).
- Sub-step 3: update of the cells positions $\overrightarrow{pos}$ according to equation (E.3).

If nothing is added to this model, as one can see on figure E.8, the cells agglomerate in a non-physical manner: the cellular pressure, preventing the cells from overlapping is indeed not modeled.

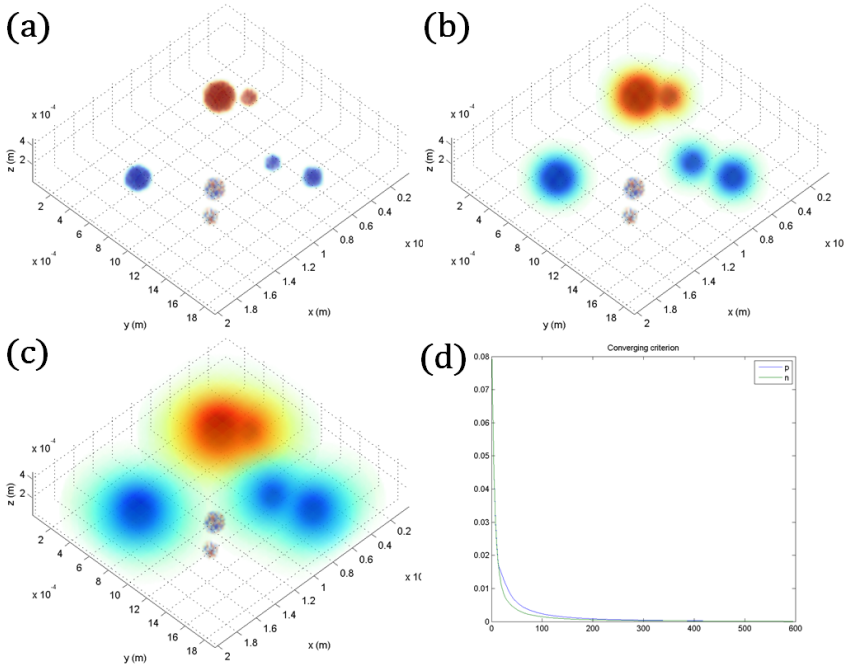

Figure E.5: These figures show the evolution of the proteins concentration in the 3D mesh at different time steps (a-c). (a) is the initial situation. (d) represents the convergence curve: it is for each step n the l^2-norm of the difference of the concentration field at t_n and t_{n+1}

Thus a pressure term p depending on the density must be added. $p \sim 0$ for $n \sim 0$ and for $n \sim Vol_{cells}$, p must rapidly increase.

Equation (E.1) then becomes:

$$\overrightarrow{v} = k.\overrightarrow{grad}\, c + k_p.\overrightarrow{grad}\, p \tag{E.6}$$

This is this new expression which must be used in the previous sub-step 3. If the pressure term p is well chosen, it will prevent the non-physical agglomerations while allowing the network formation.

2.4 Boundary conditions

Before running the model, another important issue must be addressed: what are the correct boundary conditions? Indeed, to apply the finite differences formulae on the 3D mesh, one must define the properties of the boundaries.

Different boundary condition are implemented and summed up in figure E.6. To simplify the coming expressions, the mesh is supposed to be mono-dimensional, from index $n = 1$ to $n = N$. One must then define c_0 and c_{N+1}. We will focus on c_{N+1}, c_0 being symmetrically defined.

Periodic: $c_{N+1} = c_1$ - The mesh is supposed to be periodic. As one can see on figure E.6, it is a strong condition leading to very bent streamlines because of diffuser out of the field of view due to the volume periodization.

Extrapolation: $c_{N+1} - c_N = c_N - c_{N-1}$ - The derivative on the boundary is supposed to be constant. This leads to a boundary which seems to absorb too much of the proteins, curving the streamlines towards the outside of the volume.

Neumann condition: $c_{N+1} = c_N$ - This leads to a null flux on the boundaries: $\frac{\partial c}{\partial x} = 0$. Contrary to the previous situation, the proteins are trapped in the medium and the streamlines are curved towards the inside.

Zero padding: $c_{N+1} = 0$ - As for the extrapolation, the boundaries seem to absorb too much of the medium proteins, but the effect is less marked than with the previous conditions. This solution is then kept for following analysis.

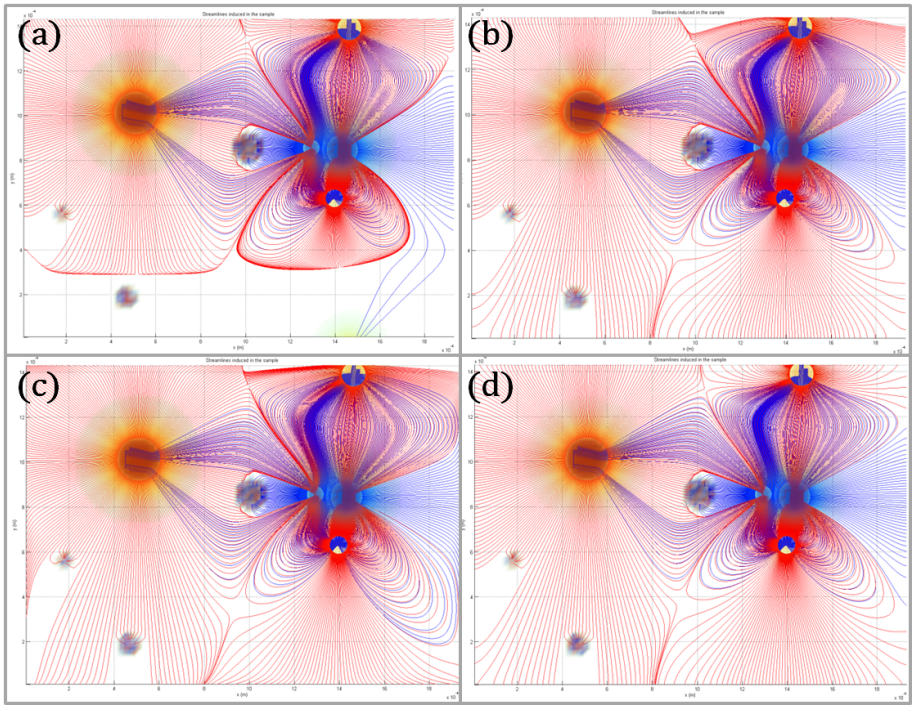

Figure E.6: This figure shows the streamlines in the concentration gradient once the convergence is reached for static diffuser according to different boundary conditions: periodic (a), extrapolation (b), Neumann condition (c) and zero padding (d).

3 Results and discussion

This section introduces preliminary results of the previous models and their confrontation with the real data.

As mentioned earlier, the static diffusers model 2.2 is used for the acini experiment and the network assembly with HUVEC cells uses the mobile diffusers model 2.3.

3.1 RWPE1: tumorous prostatic cells

The aim of this section is to simulate the experiment presented in section 1.1. To do so, two sets of chemoattractants[4] are introduced, let's say A and B, that can be released by the acini. On a given cell, these two sets will have opposite effects. For example, the cell will be attracted by A and rejected by B. It will be noted $A_{yes}//B_{no}$.

This leads to two proteins field c_A and c_B. They can both have their specific characteristics, such as D and τ and are both diffused thanks to equation (E.2). The streamlines are then computed thanks an upgraded expression of $\overrightarrow{v}$:

$$\overrightarrow{v} = k_A.\overrightarrow{grad}\, c_A + k_B.\overrightarrow{grad}\, c_B \tag{E.7}$$

The sign of the k coefficients will determine if the cell is attracted or rejected by the given type. For example, for a $A_{yes}//B_{no}$ cell, $k_A > 0$ and $k_B < 0$.

In the context of the model developed for this appendix, having at least two sets of proteins is mandatory in such a simulation. Indeed, if one keeps only one set of proteins A, only radial trajectories from (A_{no}) [or towards (A_{yes})] an acinus can be modeled. To be able to visualize an exchange between two structures, at least two sets, one being *yes*, the other one being *no* must be present.

For the different experiments, a type is given to each acinus: A, B or neutral[5].

The simulations on the two regions of interest in figure E.1 are run with the following parameters:

$$\begin{cases} D = 10^{-11}\ m^2.s^{-1} \\ \tau = 64 \times 60\ s \\ |k_A| = |k_B| = 1\ a.u. \end{cases} \tag{E.8}$$

where *a.u.* stands for *arbitrary unit*. Moreover, the concentration in the acini is also fixed to $|c_A| = |c_B| = 1$ *a.u.* and the discrete time δt is computed thanks the Courant-Freidrich-Levy condition [140]: $\delta t = 0.95 \times \frac{dl^2}{6.\max(|k_A|,|k_B|)}$.

The results of the simulation can be seen on the figure E.7. In both cases, even if the streamlines do not strictly overlap the real trajectory, some global features can be noticed.

On the first region of interest, the acini 1 and 2 are modeled as being of type A, 3, 4 and 7 of type B and 5 and 6 are neutral. The fact that the two acini 4 and 7 produce the same kind of chemoattractant B prevents the cells from directly making a bridge in between. Indeed, the meeting of the two released proteins sets creates a sort of wall[6], forcing a cell being $A_{yes}//B_{no}$ to have a right angle shift in its direction of propagation. This behavior corresponds to the one observed in the real data set during the first 20 hours of the experiment.

[4] It can be a specific protein, or a set of proteins leading to a specific effect.

[5] Note that the neutral acini do not affect the simulation and the proteins diffusion. The corresponding voxels are artificially set to zero at the end of the iterations. A better model taking into account the proteins diffusion around such acini has still to be developed. So far, the proteins cross these acini during the iterative process as they did not exist.

[6] It is actually a valley in the proteins concentration of B.

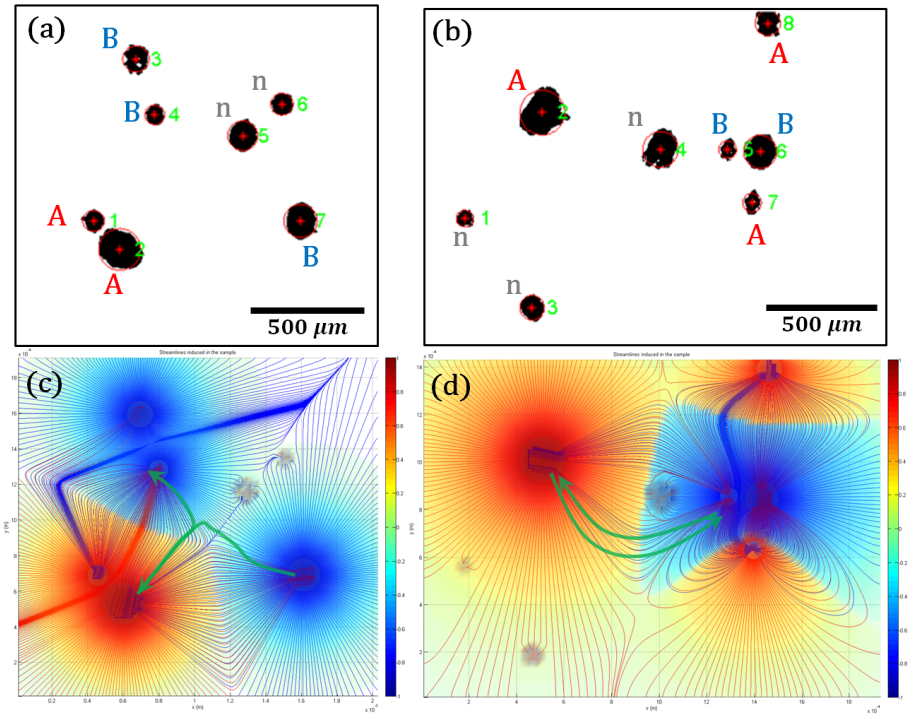

Figure E.7: (a,b) Initial acini identification and type of the two regions of interest enlightened in figure E.1. (b,d) Streamlines at the end of the simulation . The set of proteins A (resp. B) is in red (resp. blue) color while the red (resp. blue) streamlines represent the $A_{no}//B_{yes}$ (resp. $A_{yes}//B_{no}$) cells trajectories. The actual path of the cells identified on the figure E.1 are in green color.

On the other hand, if a cell being $A_{no}//B_{yes}$ is released by the acinus 2 close to this wall, can either turn left toward the acinus 4 or right toward the acinus 7 according to the side of the wall it lays on. A slight shift in the release position can affect the "choice" between 4 and 7.

Thus, the first experiment could be explained as following through the interpretation of our model: a train of cells being $A_{yes}//B_{no}$ is released from the acinus 7. Reaching the previously mentioned wall and sensing the proteins A, it turns toward the acinus 2. Once it reaches it, it gets a chemical signal from 2 turning it from $A_{yes}//B_{no}$ to $A_{no}//B_{yes}$. The train of cells then goes back on its track. But having slightly moved to the left side of the wall, it turns left to the acinus 4, creating the three branched bridge one can see on the final state of the experiment.

On the second region of interest, the acini 2, 7 and 8 are modeled as being of type A, 5 and 6 of type B and 1, 3 and 4 are neutral. The same interpretation can be led: a train of cells being $A_{no}//B_{yes}$ is released from the acinus 2, following one of the curved streamlines avoiding the acinus 4. Once it reaches the acinus 5, it gets a chemical signal turning it from $A_{no}//B_{yes}$ to $A_{yes}//B_{no}$. It goes back to 2 on a slightly different streamline. It appears indeed that two streamlines can have very close release points on 2 and 5 while having a noticeable difference at the apogee of the trajectory.

3.2 HUVEC: Epithelial cells

This section aims at simulating the experiment presented in section 1.2, using the model developed in section 2.3. As mentioned in this section, different pressure terms are tested to prevent cells agglutination on discrete points.

Two forms of pressure are used:

$$p = \left| \frac{x}{1-x} \right|^{\beta} \tag{E.9}$$

and:

$$p = (x.e^{x})^{\beta} \tag{E.10}$$

where $x = n.Vol_{cell}$. Both of the expression tend to zero for a density close to zero[7]. But when the density is closed to the cells volume ($x \sim 1$), the first one quickly diverge to infinity while the other one increases exponentially. The results are presented in figure E.8. The simulations are run with this set of parameters:

$$\begin{cases} D = 10^{-11}\ m^2.s^{-1} \\ \tau = 64 \times 60\ s \\ |k| = |k_p| = 0.5.10^{-12}\ m^2.s^{-1}a.u.^{-1} \\ \alpha = 10^{-16}\ a.u.s^{-1} \\ \beta = 2 \\ r_{cell} = 10\ \mu m \end{cases} \tag{E.11}$$

where $a.u.$ is an arbitrary concentration scale.

For the three tested pressures, the early stages of the simulation shows the shaping of a global structure closed to the one observed in the real data. But without any pressure, it quickly collapses before a network can be shaped. It enlightens the fact that adding a pressure term is not an option if one wants to see the network assembly.

With the pressure term (E.9), the collapse is restrained at the beginning of the simulation and a network begins to appear. But once more, the pressure cannot resist enough to the collapse of the structure. It can be explained by the fact that the pressure can get higher than $x \sim 1$ without diverging: indeed, once the limit $x = 1$ is crossed, the expression of p quickly decreases again. This expression can then not really prevent the collapse.

Finally, the pressure term (E.10) is the best to retain the agglutination. Indeed, once the limit $x \sim 1$ is crossed, p continues to diverge and the pressure term plays its role. In this simulation, after the shaping of the network, this latter stabilizes and the system stops evolving. Nonetheless, the branches of the network appear to be a bit too wide.

[7] As the cells are laid on a bidimensional surface, for the simulation it is more interesting to focus on preventing the discs overlapping. n is replaced by $n.dl$ where dl is the side of the elementary volume and Vol_{cell} is replaced by $Vol_{cell}/\left(4/3.r_{cell}\right)$

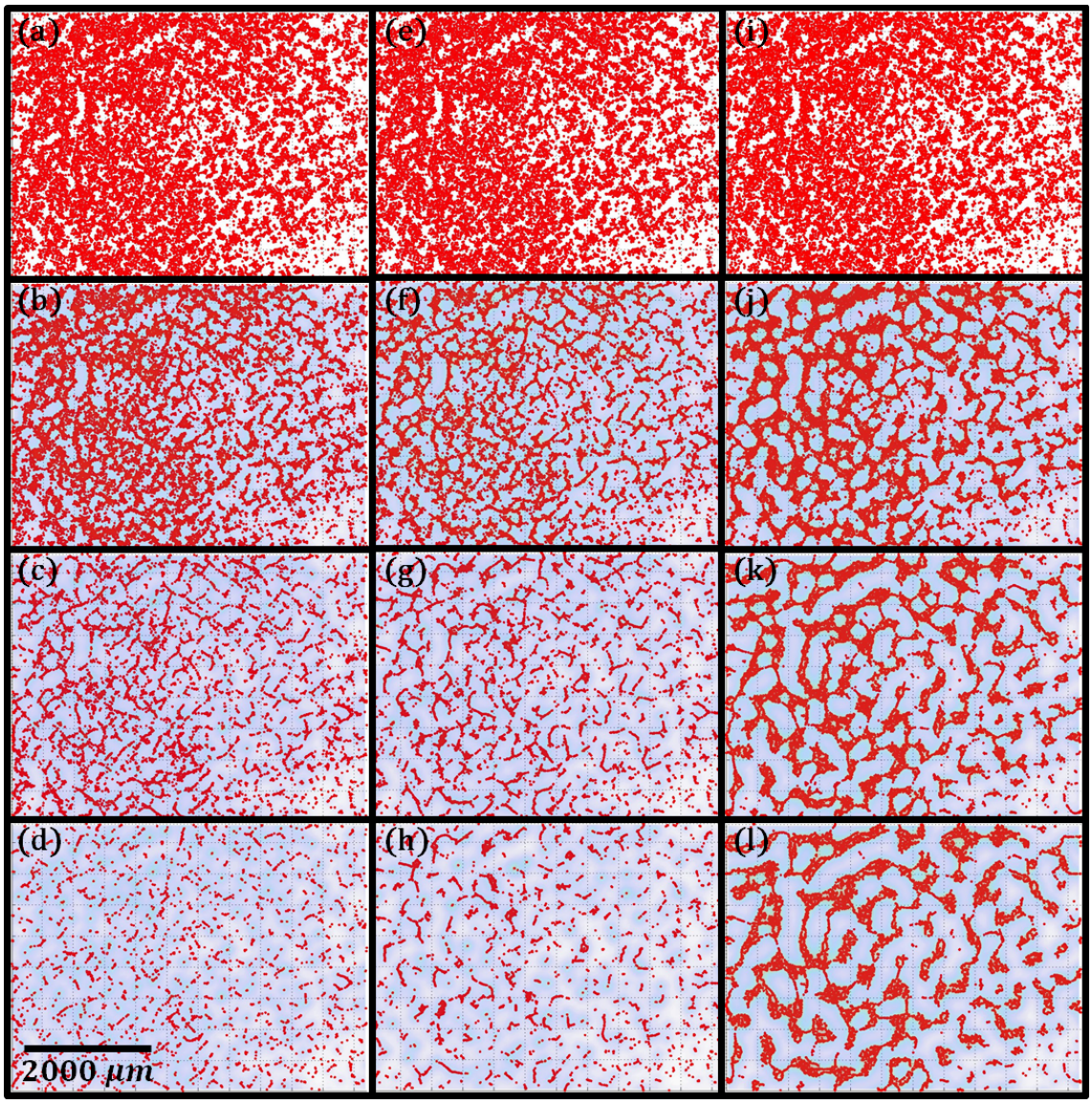

Figure E.8: This figure shows the evolution of the simulated network assembly according to different pressure terms. (a-d) No pressure: cells agglutinate towards points. This is not physical. (e-h) p is defined by equation (E.9). One can see the assembly of a network before its agglutination. (i-l) p is defined by equation (E.10). One can see the assembly of a network and the pressure term is enough to prevent cells agglutination.

3.3 Discussion

Concerning the RMPE1 experiment (section 3.1), even if the computed streamlines do not strictly coincide with the real trajectories, in both of the cases the global behavior is well simulated. Moreover the back and forth movements of cells can be interpreted with a change in the cells sensitivity to the chemoattractants. To go deeper in the model, one could change the characteristics of A and B and the

associated cells sensibility (so far they are the same for both of the proteins sets). Moreover different choices for the acini type could be tested, as well as the rate of release for each acinus. Even so, the model can be considered as promising as it gives results comparable to the experiments.

On the HUVEC simulation (see section 3.2), the chemotaxis model is successfully used to get a network shaping and stabilization. Nevertheless some works remain to be done to improve the pressure term to get more realistic network. Moreover as previously mentioned, different parameters could be tested such as the influence of the protein rate or the cells sensitivity. On another point, this model cannot render the second step observed in the data: the strengthening of the network with the cells multiplication. A step further in the simulation could consist in adding a cell division once the cell density reaches a threshold value.

Finally, all the simulations are performed with molecules diffusing in a 3D matrix. Nonetheless, as the culture is grown via a no top coat protocol, only the underlying half-space should be taken into account. Indeed, the overlying liquid culture media in the superior half-space quickly mixes the molecules, erasing the local effects of gradient concentrations.

Appendix F

Résumé en Français

Cette thèse étant rédigée en anglais, cette annexe en fournit un résumé détaillé en français, chapitre par chapitre.

Introduction

En biologie, la culture cellulaire en deux dimensions a pendant longtemps été le standard dans les laboratoires. Toutefois la nature est par essence tridimensionnelle et ce modèle de culture finit par atteindre ses limites en introduisant de nombreux biais dans les observations biologiques. Depuis le début des années 2000, de nouveaux protocoles pour cultiver les cellules en trois dimensions sont apparus, ouvrant de nouveaux champs d'étude en oncologie, médecine régénérative ou biologie fondamentale par exemple. Ce nouveau type de culture a entraîné un besoin pour de nouveaux types de microscopies adaptés à ces conditions spécifiques.

En microscopie, d'autre part, les microscopes optiques restent le standard en termes de technique d'imagerie depuis leur introduction en biologie au XVII^{ième} siècle par Leeuwenhoek. Malgré une complexité toujours croissante dans le but d'atteindre de meilleures résolutions, des contrastes plus élevés ou des grossissements plus importants, le principe de base reste le même, celui de l'utilisation d'une source de lumière et de multiples lentilles pour focaliser sur l'échantillon à observer. Cet accroissement en complexité est lié à un accroissement du coût des microscopes et de leur difficulté de mise en œuvre, ainsi que de leur adaptation aux conditions d'incubateur pour pouvoir suivre les cultures cellulaires au cours du temps sans endommager les cellules. De récents travaux se concentrent sur l'introduction d'une nouvelle physique dans le contexte de la microscopie biologique dans le but de concevoir de nouvelles techniques d'imagerie qui soient à la fois peu chères, faciles d'utilisation et robustes. L'imagerie sans lentille, basée sur le principe de l'holographie en ligne introduit par Gabor en 1948 répond à ces besoins dans le cadre de la culture cellulaire en 2D, fournissant des acquisitions non photo-toxiques et sans marquage sur de grands champs de vue.

Cette thèse se situe à l'interface de ces deux domaines. Son but est de montrer la possibilité d'adapter cette technologie sans lentille à l'imagerie des cultures cellu-

laires en 3D tout en préservant ses nombreux avantages. De nouveaux prototypes de microscopes sans lentille sont conçus en parallèle du développement d'algorithmes de reconstructions tomographiques dédiés.

Concernant les prototypes, plusieurs solutions sont testées pour converger vers un microscope sans lentille conciliant d'une part la simplicité d'utilisation avec une culture cellulaire en boîte de Petri standard et ne nécessitant aucune préparation spécifique ou aucun changement de contenant et d'autre part une couverture angulaire des positions d'éclairage suffisante pour obtenir des reconstructions pertinentes en termes d'observables biologiques. Enfin, une version adaptée aux conditions en incubateur est développée et testée avec succès.

Concernant les algorithmes développés, ils se doivent de corriger deux problèmes inhérents au microscope sans lentille : l'absence de l'information de phase, le capteur n'étant sensible qu'à l'intensité de l'onde reçue, et la couverture angulaire limitée. Différentes solutions sont proposées dans cette thèse. Toutes ces méthodes sont comparées et testées avec succès sur des simulations numériques et des données expérimentales. Des comparaisons avec des acquisitions au microscope classique montrent la validité des reconstructions en matière de tailles et de formes des objets reconstruits ainsi que la précision de leur positionnement tridimensionnel. Elles permettent de reconstruire des volumes de plusieurs dizaines de millimètres cubes de cultures cellulaires 3D, inaccessibles en microscopie standard.

Enfin les données spatio-temporelles obtenues avec succès en incubateur montrent aussi la pertinence de ce type d'imagerie en mettant en évidence des interactions dynamiques sur de grandes échelles des cellules entres elles ainsi qu'avec leur environnement tridimensionnel.

Chapitre I : Contexte et état de l'art

Ce chapitre donne un aperçu général du contexte biologique de la culture cellulaire 3D et des techniques d'imagerie conventionnellement mises en œuvre pour leur étude. Il introduit aussi la technique de l'imagerie sans lentille dans le cadre de la culture 2D ainsi que les travaux réalisés par d'autres équipes dans le but de l'adapter aux cultures 3D.

Développement de la culture cellulaire 3D

En ce qui concerne la biologie 3D, il est communément admis de nos jours que la culture 2D introduit de nombreux biais observationnels et cache ou modifie de nombreux phénomènes biologiques. Pendant longtemps, la seule alternative pour concevoir des cultures cellulaires en 3D fut le modèle sur petit animal, qui soulève de nombreuses questions éthiques et pratiques concernant la répétabilité.

La culture cellulaire 3D apparaît donc un outil intermédiaire entre la culture cellulaire 2D et le modèle animal. Elle est rendue possible par le développement récent de gels organiques dans lesquels les cellules peuvent se nourrir et croître dans les trois directions de l'espace.

Les applications potentielles sont nombreuses, ne serait-ce qu'en termes de biologie fondamentale ou de recherches pharmaceutiques, avec de nombreuses avancées récentes, en autres en : motilité cellulaire, chimiotaxie et adhésion cellulaire ; expression génétique ; morphogénèses épithéliale et endothéliale ; embryogénèse et organogénèse ; oncologie ; toxicologie et dépistage de nouveaux principes actifs.

Développement de la culture cellulaire 3D

Ces nouveaux types de culture cellulaire ont déclenché un besoin en nouveaux types d'imagerie adaptés, répartis en trois grandes catégories.

Les microscopes classiques peuvent être utilisés sur des échantillons fixés et transparents après avoir été adaptés à l'acquisition de plusieurs angles pour faire de la tomographie par projection optique.

La microscopie par fluorescence reste la technologie dominante en ce qui concerne l'imagerie 3D, répartie en trois grandes techniques : la microscopie confocale, la microscopie à feuille de lumière et la microscopie multi-photons. Ces techniques tirent profit du marquage des échantillons avec des protéines spécifiques qui fluorescent sous certaines conditions d'illumination. Toutefois, sauf cas particuliers, elles nécessitent une longue préparation de l'échantillon avec une étape de marquage qui peut se révéler toxique. Au final, l'échantillon est rarement étudié dans son état naturel et son suivi au cours du temps peut se révéler difficile.

Le développement de la microscopie par imagerie cohérente cherche à s'affranchir de cette étape de marquage en étant directement sensible à l'indice de réfraction de l'objet à étudier. La tomographie en cohérence optique est une technique déjà largement répandue pour l'étude de la rétine ou de la peau par exemple. La tomographie optique diffractive se développe quant à elle sur les bases de la microscopie holographique digitale et produit sans marquage des images très résolues de petits échantillons, apportant des informations complémentaires à l'imagerie par fluorescence. Les microscopes sans lentille appartiennent à ce type de microscopie.

Développement de vidéo-microscopie sans lentille

La microscopie sans lentille se base sur le principe de l'holographie en ligne proposée par Gabor en 1948 : une illumination cohérente est diffractée par un échantillon. Les taches d'interférences produites sont ensuite enregistrées : il s'agit de l'hologramme de l'objet. Connaissant la physique de la propagation de la lumière, tout le jeu de ce type de microscopes est de « remonter le temps » à partir de l'hologramme pour focaliser l'image et retrouver l'objet recherché. Le rôle des lentilles dans un microscope classique est ici remplacé par des algorithmes informatiques de rétro-propagation.

Un microscope sans lentille utilisant ce principe d'holographie en ligne est donc minimaliste, seulement composé d'un éclairage semi-cohérent à quelques centimètres d'un capteur, l'échantillon étant placé au plus proche du capteur. Il s'agit donc d'une technologie facile d'utilisation (il n'y pas besoin de faire de mise au point, ni

de préparer l'échantillon), robuste et peu chère (car sans partie mobile ou fragile) et facilement adaptable aux conditions de culture régnant dans un incubateur (et permet donc de suivre des cultures cellulaires sur de longues périodes de temps). Le champ de vue, directement de la taille du capteur utilisé, est plus grand que par microscopie conventionnelle.

Cette technologie présente toutefois des inconvénients telles qu'une résolution limitée par la taille du pixel et les modèles physiques utilisés ainsi que l'absence de bras de référence dans le montage optique qui permettrait de connaître la phase de l'onde incidente. Ce défaut majeur doit être compensé par les algorithmes de reconstructions développés.

Plusieurs équipes ont déjà proposé des solutions de microscopes sans lentille pour des échantillons 3D. Toutefois, aucune n'a présenté de résultats à la fois basés sur des modèles physiques en 3D de la diffraction et sur des échantillons biologiques 3D.

Chapitre II : Physique de la diffraction 3D

L'objectif de ce chapitre est de donner un aperçu de la physique de la diffraction 3D en partant des équations de propagation des ondes. A proprement parlé, il n'introduit pas de nouveaux résultats comparés à la littérature mais en condense les résultats pour présenter toutes les étapes menant à la démonstration du théorème de diffraction de Fourier. Pendant du théorème de Radon dans le cadre de la diffraction, il est utilisé dans la plupart des algorithmes de reconstruction tomographique en optique diffractive.

Modèle de la diffraction 3D pour les objets faiblement diffusants

L'objectif de cette partie est de trouver l'expression mathématique de l'onde lumineuse sur le capteur en fonction de l'onde incidente et de l'objet diffusant qu'elle croise sur son chemin. Ce modèle est indispensable pour espérer construire un algorithme de reconstruction qui va dans l'autre sens, du capteur vers l'objet.

Une solution analytique explicite ne pouvant être dérivée des modèles, il est nécessaire d'introduire des approximations dans le but de simplifier les équations.

L'approximation de Born consiste à supposer que l'onde lumineuse après l'échantillon est composée de deux sous-parties : l'onde incidente initiale qui a traversé l'objet sans être modifiée et une onde diffractée par l'objet. Le capteur enregistre l'interférence de ces deux ondes.

L'expression de l'onde diffractée est directement l'équivalent 3D du principe de Huygens-Fresnel : elle est constituée de la somme d'ondes sphériques réémises en chaque point de l'objet 3D et dont l'amplitude dépend de l'indice de réfraction local et de l'onde incidente en ce point.

Théorème de diffraction de Fourier

Cette partie donne les étapes essentielles de la démonstration du théorème de diffraction de Fourier et en donne une interprétation géométrique.

L'objectif principal du chapitre et des modèles présentés est de trouver un lien entre les hologrammes 2D accessibles par la mesure avec un capteur et l'objet 3D à reconstruire. Ce lien existe en fait entre leurs transformées de Fourier respectives. Le théorème de diffraction de Fourier énonce que la surface 2D de la transformée de Fourier 2D de l'onde diffractée se trouve sur une calotte sphérique de la transformée 3D de l'objet étudié.

Ce théorème peut donc être utilisé à la fois comme méthode de reconstruction ou comme outil de simulation. Dans le premier cas, la multiplication des angles d'éclairages et donc d'ondes diffractées permet en effet de remplir au fur et à mesure l'espace de Fourier 3D de l'objet par cartographies successives de différentes calottes sphériques. Dans le second cas, la simulation d'un hologramme à partir d'un objet numérique se fait par l'extraction d'une calotte sphérique dans cet espace de Fourier 3D.

Ce théorème est le pendant diffractif du théorème de Radon utilisé dans les algorithmes de reconstruction en tomographie par rayons X. La diffraction est négligeable à cause des longueurs d'onde en jeu et les rayons vont droit. Dans le théorème de Radon, les calottes sphériques sont remplacées par des plans dans l'espace de Fourier de l'objet à reconstruire.

Simulations numériques 3D

Cette partie se concentre sur une formulation numérique des modèles physiques développés dans le chapitre dans le but de les appliquer numériquement dans des algorithmes de simulation ou de reconstruction.

Une fois mises en place, ces méthodes numériques sont utilisées pour comparer l'approximation de Born et le théorème de diffraction de Fourier qui en découle. La cohérence des hologrammes simulés à l'aide des modèles 3D avec les modèles 2D développés dans le cadre de l'imagerie sans lentille 2D est aussi testée.

Les tests montrent une bonne cohérence des modèles 3D entre eux et avec les modèles 2D. Mais le résultat principal reste un problème quant à l'interprétation physique des indices de réfraction complexes mis en jeu avec une inversion des propriétés absorbantes et déphasantes des objets simulés entre la 2D et la 3D.

Chapitre III : Un prototype polyvalent et premiers algorithmes de reconstruction

Ce chapitre condense les travaux préliminaires effectués en termes de prototypage et d'algorithmes pour se familiariser avec les problèmes de l'imagerie sans lentille en 3D d'une part et des contraintes posées par les cultures cellulaires en 3D d'autre part. Travailler sur les deux sujets de front permet de faire évoluer les plans du microscope

et la structure des algorithmes en prenant en considération les contraintes de ces deux domaines.

Différentes directions sont testées dont beaucoup sont abandonnées par absence de résultat. Toutefois, leur présentation est nécessaire pour la bonne compréhension du déroulé des pensées et de la réflexion tout au long de ce travail de thèse.

Premier banc expérimental

Un microscope sans lentille dédié à la culture cellulaire 3D reprend les caractéristiques d'un microscope sans lentille 2D, à savoir un capteur CMOS et une LED derrière un sténopé pour produire un éclairage semi-cohérent. Toutefois, la première intuition est que pour reconstruire un objet en trois dimensions, il faut pouvoir l'observer sous différents angles.

Ainsi, un moteur rotatif vient s'ajouter dans la liste des composants d'un microscope sans lentille. Deux modalités sont testées :

- Le mode-θ dans lequel l'éclairage et le capteur sont fixes, l'éclairage étant normal au plan capteur. C'est l'objet qui tourne sur lui-même au-dessus du capteur.
- Le mode-φ dans lequel le capteur et l'échantillon sont fixes, l'éclairage étant sur fixé au bout d'un bras tournant autour d'un axe dans le plan capteur, ce qui permet de changer l'angle d'éclairage.

Le mode-θ est le plus intuitif et permet d'accéder à n'importe quel angle de rotation de l'objet sur lui-même. Toutefois, c'est aussi le plus compliqué à mettre en œuvre en pratique. En effet, il est très difficile de fixer un échantillon biologique au bout d'une tige pour le faire tourner, le tout dans l'eau pour éviter un trop gros saut d'indice de réfraction entre l'objet et le milieu environnant. Une piscine adaptée est conçue pour gérer ce problème. Des tests sont aussi réalisés en capillaire en verre mais s'avèrent non concluants à cause de la différence d'indice entre l'eau et le verre.

Le mode-φ est le plus simple à mettre en œuvre puisqu'il suffit de poser l'échantillon en boîte de Petri directement sur le système sans avoir besoin d'une préparation au préalable. Toutefois, la couverture angulaire est extrêmement limitée. C'est ce mode qui est ensuite gardé tout au long de la thèse.

Un premier algorithme de reconstruction 3D basé sur la transformée de Radon

Le premier algorithme développé au cours de cette thèse se base sur les techniques de reconstruction utilisées en tomographie axiale calculée par ordinateur où les acquisitions à différents angles d'un objet sont des projections de cet objet le long d'une direction donnée. L'objet est alors reconstruit à partir de ces différentes projections grâce à l'inversion de la transformée de Radon précédemment évoquée.

Dans le cas de l'imagerie sans lentille, l'approximation est faite que les hologrammes des objets étudiés soient directement cette projection, sans prendre en

compte la diffraction. Cette méthode a l'avantage de pouvoir travailler rapidement, coupe 2D par coupe 2D, sur de très gros volumes avec des algorithmes déjà optimisés, dédiés à la tomographie axiale calculée par ordinateur.

Dans le but de partiellement prendre en compte la diffraction, une étape de focalisation des hologrammes 3D sur un plan moyen 2D via les algorithmes de rétropropagation classiques développés pour la microscopie sans lentille 2D est implémentée.

Les résultats sont convaincants malgré la présence d'artefacts dans les reconstructions dus à la mauvaise prise en compte du phénomène de diffraction 3D.

Une seconde méthode basée sur un empilement en z

Cette méthode s'inspire de la formulation numérique de l'approximation de Born introduite plus haut. En effet, le calcul par transformée de Fourier 3D d'un objet mène numériquement à la connaissance de l'onde diffractée sur tout un volume.

La question à se poser alors est de savoir si réciproquement, la connaissance de l'onde diffractée sur tout un volume est suffisante pour reconstruire l'objet.

Les simulations montrent que la déconvolution de ce problème est difficile et que le nombre d'acquisitions à différentes distances z est beaucoup moins déterminant que la diversité angulaire dans les acquisitions.

Cette idée est donc abandonnée même si elle permet d'introduire la notion de problème inverse dans ce travail de thèse.

Une troisième méthode basée sur le théorème de diffraction de Fourier

Cette méthode implémente la possibilité donnée par le théorème de diffraction de Fourier d'être utilisé comme un outil de reconstruction.

Toutefois, elle doit résoudre un problème soulevé par l'holographie en ligne. Un tel système n'enregistre que le module de l'onde totale arrivant sur le capteur alors que le théorème de diffraction de Fourier n'utilise que la partie de cette onde complexe correspondant à l'onde diffractée. Il faut donc extraire cette onde diffractée à partir de l'unique connaissance du module de l'onde totale. Il manque la phase de l'onde complexe au niveau du capteur.

Dans cette méthode, cette phase inconnue est approximée par une rampe de phase caractéristique de l'angle d'éclairage avec lequel est acquis chaque hologramme. Une fois les ondes diffractées extraites pour chaque position de l'éclairage, ces informations sont cartographiées sur leur calotte respective dans l'espace de Fourier 3D de l'objet.

Cette méthode permet de reconstruire les objets 3D en prenant en compte la diffraction en une passe. Mais l'approximation de la phase réelle inconnue par une rampe de phase produit de nombreux artéfacts dans les reconstructions qui s'apparentent au problème des « images jumelles » en reconstruction holographique 2D.

Quelques réflexions sur les angles d'éclairage...

Durant tout le chapitre, les reconstructions sont réalisées en prenant en compte l'angle d'éclairage dans l'air dans les algorithmes. Toutefois, de nombreux artefacts dans les reconstructions sont attribués à des problèmes d'angle dans les sections précédentes. En effet, les objets biologiques sont dans l'eau et donc l'angle dans le milieu doit varier selon les lois de la réfraction de Snell-Descartes.

Dans le but de déterminer si les hologrammes finalement enregistrés par le capteur sont caractéristiques d'un éclairage dans l'eau ou dans l'air, une expérience est menée. Des billes sont placées dans l'eau et leurs hologrammes sont enregistrés pour différents angles d'éclairage.

Ces hologrammes forment donc des ellipses dont l'excentricité peut être reliée à l'angle d'éclairage. L'extraction de cette information pour les différents angles d'acquisitions montre que ces hologrammes, bien qu'acquis dans l'air, sont effectivement caractéristiques d'un angle dans l'eau.

Ainsi, deux solutions sont proposées pour prendre en compte ce phénomène dans les reconstructions : soit de directement corriger les angles de reconstruction dans les algorithmes par les angles dans le milieu de culture via la loi de Snell-Descartes, soit d'appliquer un facteur d'échelle le long de l'axe z *a posteriori*.

Chapitre IV : Un second choix de conception et nouvelles méthodes de reconstruction

Fort de l'expérience acquise au cours des travaux du chapitre précédent, un nouveau prototype est conçu et testé et de meilleurs codes de reconstruction sont implémentés pour résoudre les problèmes soulevés par les premières reconstructions 3D.

Ce chapitre constitue le cœur des travaux de thèse.

Deuxième banc expérimental

Tout d'abord, les codes du chapitre précédent sont utilisés pour simuler différentes configurations possibles pour un nouveau prototype de microscope sans lentille. Les nouveaux plans se concentrent sur une contrainte déduite des expériences du chapitre précédent sur des échantillons biologiques : ce nouveau prototype doit être en « mode-φ » pour faciliter son utilisation, avec donc un capteur sous la culture cellulaire qui reste parallèle au fond de la boîte de Petri.

Les différentes simulations convergent vers une solution où l'éclairage tourne sur une couronne avec un angle zénithal d'ouverture constant. Le capteur est aussi légèrement déporté pour tourner avec le support de l'éclairage, ce qui permet de garder l'hologramme projeté de l'objet d'étude au centre du champ de vue et donc de maximiser la taille du volume reconstructible. Comme le prototype précédent, la LED possède trois longueurs d'onde : rouge, verte et bleue.

Le prototype est construit et testé sur données inertes avec des résultats prometteurs.

Estimation itérative de la phase manquante

Cette méthode vise à corriger le défaut principal de la méthode proposée en fin du chapitre précédent, à savoir l'approximation de la phase manquante, alors remplacée par une rampe de phase.

Tout d'abord, un modèle 2D de propagation en biais de la diffraction produite par un objet 2D est développé. Ensuite, comme pour l'algorithme implémenté avec l'inversion de la transformée de Radon, à chaque angle d'éclairage, l'objet est approximé par un plan 2D. Cet artifice mathématique permet de trouver une approximation de la phase par une approche inverse.

Le modèle direct est donné par le modèle 2D de propagation en biais, l'attache aux données est faite sur l'intensité de l'onde complexe au niveau du plan capteur et les contraintes sont appliquées sur l'approximation 2D de l'objet. Une contrainte de domaine est implémentée en fonction des propriétés physiques de l'objet et deux régularisations sont mises en œuvre : une imposant que l'objet soit parcimonieux, ce qui favorise des objets localisés et nettoie le bruit de fond et l'autre imposant que son gradient soit parcimonieux, ce qui favorise des objets homogènes à bord franc et lisse le fond. L'utilisation des trois longueurs d'onde de la LED à chaque angle de vue améliore les résultats de l'algorithme. La résolution de ce problème est faite itérativement par descente de gradient.

Une fois la phase estimée pour toutes les acquisitions à tous les angles d'éclairage, l'espace de Fourier 3D de l'objet est cartographié comme précédemment, calotte par calotte.

Problème inverse 3D

Cette méthode est similaire à la méthode précédente, sauf que c'est directement l'objet 3D qui est l'inconnue sur laquelle s'appliquent les contraintes de domaine et de régularisation. Le modèle direct est donné par le théorème de diffraction de Fourier, comme précédemment expliqué dans le chapitre II et l'attache aux données est effectuée sur toutes les intensités mesurées à la fois. La résolution de ce problème est faite itérativement par descente de gradient.

Avec cette méthode, la diffraction 3D est prise en compte, contrairement à la méthode précédente où l'objet était approximé par un plan à chaque angle d'éclairage.

De plus, dans la méthode précédente, seuls les coefficients de l'espace de Fourier de l'objet qui se trouvent sur l'une des calottes sphériques cartographiées sont estimés. Cette méthode, via les termes de régularisations travaille sur tout l'espace de Fourier de l'objet et estime donc tous les coefficients.

Enfin, cette méthode permet de raffiner l'alignement des données, étape cruciale des algorithmes de reconstruction tomographique. En effet, au cours des itérations

de l'algorithme, l'attache aux données étant relaxée, il est possible de simuler des données qui sont légèrement différentes des données expérimentales et qui sont, par construction, alignés avec l'objet reconstruit. Ces données simulées peuvent servir de référence pour réaligner les données expérimentales. Cela améliore grandement la qualité finale des reconstructions 3D.

Un algorithme de Gerchberg-Saxton modifié

L'algorithme précédent peut être très long à faire tourner à cause des multiples transformées de Fourier 3D qu'il engendre.

Dans le but de l'initialiser avec une meilleure valeur de départ un algorithme de type Gerchberg-Saxton est implémenté.

La base de ce type d'algorithme est d'alterner entre l'objet à reconstruire et les acquisitions des phases de reconstructions et de simulations. A chaque itération de la boucle, l'attache aux données est forcée dans les simulations au niveau des acquisitions et des contraintes sont appliquées dans les reconstructions au niveau de l'objet.

Avec la faible couverture angulaire du prototype proposé, inhérente à la culture en boîte de Petri, cet algorithme n'est pas suffisant pour corriger les artefacts de reconstruction. Il est donc modifié avec l'ajout d'une étape de régularisation sur l'objet avec l'application des contraintes de parcimonies précédemment évoquées sur l'objet et son gradient.

Comme l'algorithme précédent, celui-ci traite les deux problèmes du prototype de microscope sans lentille en estimant les phases manquantes au niveau du capteur et en travaillant directement sur l'ensemble des coefficients de l'espace de Fourier.

Comparaison des algorithmes

Le chapitre se termine sur une comparaison des algorithmes sur deux cultures de références. La première est composée de cellules endothéliales cultivées sur une couche de matrice extracellulaire, les menant à la formation d'un réseau cellulaire. La deuxième est constituée de cellules épithéliales, encapsulées dans des sphères de matrice extracellulaire dans lesquelles elles vont former des amas de cellules et éventuellement s'échapper des capsules.

Ces deux cultures sont reconstruites avec les quatre algorithmes précédemment décrits utilisant le théorème de diffraction de Fourier sur des volumes de 5 mm^3. Les résultats sont nets. Si les deux premiers ont des temps d'exécution courts, seuls les deux derniers, régularisés, sont en mesure d'efficacement nettoyer les artefacts de reconstruction au prix d'un temps de reconstruction qui peut s'avérer rédhibitoire.

Ensuite, une zone reconstruite à plus haute résolution avec les deux derniers algorithmes est comparées avec des acquisitions faites au microscope. Cette zone présente une large distribution en z des objets et constitue donc un bon moyen de tester les algorithmes sur des objets avec de forts recouvrements en z ainsi que leur capacité de sectionnement axial des volumes.

La comparaison montre que les reconstructions sont fidèles à l'objet biologique observé avec un sectionnement en z bien meilleur que le critère « focalisé/défocalisé » du microscope.

Enfin, différentes pistes sont proposées pour tenter de répondre aux problèmes soulevés par les conclusions de cette comparaison de ces quatre méthodes.

Chapitre V : Vers la vidéo-microscopie 3D en incubateur

Après avoir testé les performances des différents algorithmes en termes de temps et de qualité de reconstruction, les derniers efforts de la thèse se focalisent sur l'adaptation du prototype sans lentille aux conditions d'incubateur pour pouvoir suivre des cultures cellulaires 3D au cours du temps.

Une caractérisation des reconstructions est aussi effectuée sur un objet de référence pour quantifier la précision des positionnements en 3D obtenus avec le microscope sans lentille.

Vers un prototype résistant aux conditions d'incubateur

Il est d'abord essayé d'adapter l'ancien prototype aux conditions d'incubateur. Toutefois, sa conception n'est pas optimisée en conséquence et il apparaît plus simple d'en reconstruire un autre avec de nouvelles fonctionnalités.

Tout d'abord une platine de translation sur le plan xy est intégrée dans le support du capteur pour pouvoir affiner sa position sous l'échantillon placé au plus près. Un rail est aussi ajouté sous l'éclairage pour pouvoir changer l'angle zénithal de l'illumination.

Mais la principale nouvelle fonctionnalité consiste en l'ajout d'un système de refroidissement. En effet, en fonctionnement, le capteur chauffe à une température pouvant atteindre les $50°C$, létal pour les cellules. Dans le but d'isoler la culture cellulaire du capteur, une lame d'air est injectée entre celui-ci et le dessous de la boîte de Petri.

Des tests avec une boîte de Petri monitorée avec des sondes de température montrent l'efficacité de ce dispositif pour stabiliser la température dans le milieu biologique de la culture cellulaire.

Reconstruction 3D+t

Deux cultures cellulaires sont suivies pendant plus d'une semaine avec le prototype en incubateur, montrant sa capacité à résister aux conditions d'humidité et de température le tout sans tuer les cellules. Il s'agit de cellules épithéliales cultivées à la surface d'une matrice extracellulaire.

Les résultats de la première expérience démontrent la capacité d'un microscope sans lentille d'acquérir des données pertinentes sur de larges volumes grâce à

l'observation de quatre grands types de phénomènes :

- Le déplacements de cellules sur de longues distances avec une trajectoire qui ne semble pas aléatoire mais au contraire structurée sur de grandes échelles.
- Les interactions entre cellules ou amas de cellules sur de larges distances avec fusions successives.
- Le développement et la croissance d'amas de cellules bloquées dans la matrice extracellulaire.
- Le déplacement sur de grandes distances d'amas de plusieurs dizaines de cellules ainsi que les forces de tractions engendrées sur la matrice extracellulaire.

Ce dernier point mène à la conception de la deuxième expérience dans laquelle des microbilles sont intégrées directement dans la matrice extracellulaire dans le but d'étudier ses déformations. Comme précédemment, des mouvements de la matrice dus aux déplacements des amas cellulaires sont mis en évidence jusqu'à des distances dépassant le millimètre. Mais la présence des billes dans la matrice permet aussi d'étudier sa dilatation radiale au cours du temps avec un suivi précis des billes dans les trois dimensions de l'espace.

Caractérisation

Cette dernière expérience a servi de base à la conception d'un objet de référence pour caractériser le microscope sans lentille proposé.

Des billes sont mélangées à de la matrice extracellulaire qui est ensuite laissée à polymériser. L'objet obtenu, sans cellule et uniquement composé de billes, est reconstruit à l'aide de l'imagerie sans lentille pour différents angles zénithaux pour l'éclairage et comparé avec une acquisition par fluorescence au microscope.

Des algorithmes dédiés sont développés pour identifier et appareiller les billes dans les différents volumes reconstruits. La comparaison des positions extraites montre un excellent positionnement obtenu par l'imagerie sans lentille sur le plan xy. Un léger facteur de dilatation est attribué à l'approximation faite sur l'onde d'éclairage, supposée être plane alors qu'elle est sphérique. Les positionnements en z montrent que les algorithmes de reconstruction en imagerie sans lentille prennent bien en compte les différents effets de réfraction sur les angles et que les positions sont bien absolues et non relatives le long de l'axe z, contrairement à la microscopie classique où un facteur d'échelle dépendant de l'objectif et de l'indice de réfraction de l'huile à immersion (ou de l'air si aucune huile n'est utilisée) doit être pris en compte.

En terme de résolution, il apparaît naturellement qu'elle est dégradée le long de l'axe z. De manière surprenante, contrairement à l'intuition, les reconstructions apparaissent d'autant plus dégradées que l'angle zénithal de l'éclairage est élevé alors qu'il est légitime de s'attendre à ce qu'une parallaxe plus élevée améliore les reconstructions, comme le laissaient entendre les simulations.

Conclusions et perspectives

En conclusion, cette thèse montre la possibilité d'adapter l'imagerie sans lentille à l'imagerie d'échantillons biologiques 3D. Différents prototypes et algorithmes sont construits et implémentés.

Le prototype converge vers un schéma réunissant deux conditions : la facilité d'utilisation avec un microscope devant fonctionner sur des boîtes de Petri et une couverture angulaire optimisée à la vue de la première contrainte. Un prototype adapté à la culture cellulaire en incubateur est construit et testé avec succès.

Concernant les codes de reconstruction, ils se concentrent sur quatre grandes méthodes, toutes basées sur le théorème de diffraction de Fourier. Chacune propose une solution pour traiter les deux problèmes liés à l'holographie en ligne : l'absence de mesure de la phase de l'onde arrivant sur le capteur et la couverture angulaire limitée. L'amélioration de la qualité des reconstructions se fait au prix d'une complexité croissante.

Les différents prototypes et algorithmes sont testés avec succès sur des simulations et des données expérimentales, avec des volumes reconstruits de plusieurs dizaines de millimètres cubes. Les premiers résultats en incubateur montrent les capacités de la microscopie sans lentille 3D de rassembler des données pertinentes sur les cultures 3D par exemple via l'observation à grande échelle d'interaction cellulaire avec la matrice extracellulaire environnement.

En ce qui concerne les perspectives, plusieurs pistes sont envisagées dans différents domaines.

En biologie, les résultats obtenus en incubateur ouvrent la voie vers de nouvelles expériences pour observer le remodelage dynamique de la matrice extracellulaire, au cœur de nombreux sujets de biologie, tels que les cancers ou les inflammations par exemple. Il pourrait aussi être intéressant d'étudier des objets classiques de la biologie en 3D tels que le C. Elegans ou de tenter de discriminer les objets pleins des objets creux, fonction utile pour identifier les phénomènes de cancérogénèse.

Concernant les algorithmes de reconstruction, les travaux suivants devront surtout s'orienter vers l'optimisation des hyperparamètres dans les approches inverses ainsi qu'au développement de nouvelles régularisations plus pertinentes. D'autres algorithmes récemment développés par d'autres équipes dans le cadre de la microscopie diffractive optique avec lentille peuvent aussi être adpatés.

Un travail doit aussi être effectué sur l'optimisation des temps de calcul. En effet, les algorithmes régularisés présentés dans cette thèse peuvent s'avérer particulièrement longs, rendant impossible l'étude de plusieurs cultures cellulaires au cours du temps dans un temps raisonnable. Ceci consiste donc un frein puissant à la démocratisation de la technologie.

L'alignement des données ainsi que la détermination de la distance de reconstruction restent aussi des points qui n'ont pas été automatisés durant ces travaux et qui se doivent d'être traités pour une utilisation de l'imagerie sans lentille 3D par un utilisateur non initié.

Le modèle utilisé durant cette thèse n'est pas valide pour les objets étudiés. Il

est toutefois gardé pour sa simplicité de mise en œuvre. Pour améliorer les reconstructions ou si devenir quantitatif est un objectif, de nouveaux modèles doivent être implémentés. Différents travaux indiquent par exemple qu'un modèle multi-couches peut constituer une alternative pertinente.

Enfin, en termes de conception, beaucoup de travail reste à faire sur le prototype pour le rendre résistant à long terme aux conditions d'incubateur et robuste à l'usure mécanique. Plus d'études se doivent d'être réalisées pour optimiser l'éclairage, par exemple à l'aide de diodes lasers, plus puissantes et plus cohérentes ce qui améliorerait le rapport signal à bruit ou même la validité du modèle qui suppose une onde parfaitement cohérente. L'utilisation d'un meilleur moteur permettrait aussi d'accélérer les temps d'acquisition qui peuvent être limitants pour certaines applications. De plus, d'autres types de microscopes pourraient être adaptés à une technologie sans lentille en changeant le type d'éclairage par exemple.

Annexes

En plus de ce résumé en français, cette thèse présente plusieurs annexes.

Les deux premières sont des annexes mathématiques qui introduisent les outils nécessaires à la démonstration du théorème de diffraction de Fourier et qu'il n'était pas pertinent d'intégrer dans le texte principal sous peine d'alourdir le discours.

La troisième annexe est consacrée aux étapes de prétraitements nécessaires dans cette thèse à toute reconstruction tomographique: l'alignement des données et la détermination de la distance de propagation entre l'objet et le plan capteur. Elle présente les différentes méthodes mises en œuvre pour déterminer ces différents paramètres.

La quatrième annexe donne les outils nécessaires au calcul du gradient des différentes fonctions coût introduites au cours de cette thèse dans la formulation des approches par problèmes inverses.

Enfin, la cinquième annexe est consacrée à un travail de modélisation biophysique réalisé en parallèle de la thèse. Il s'agit de modéliser le phénomène de chimiotaxie sur deux expériences réalisées avec des cellules épithéliales et endothéliales. Son objectif est de démontrer la pertinence d'avoir des acquisitions 3D sur larges champs de vue pour contraindre ce genre de modèle.

Bibliography

[1] S. Ringer, "Concerning the Influence exerted by each of the Constituents of the Blood on the Contraction of the Ventricle," *Journal of Physiology (London)*, vol. 3, pp. 380–393, Aug 1882. Cited on page 1.

[2] A. Nair, *Principles of Biochemistry and Genetic Engineering*. Laxmi Publications Pvt Limited, 2010. Cited on page 1.

[3] R. Edmondson, J. J. Broglie, A. F. Adcock, and L. Yang, "Three-dimensional cell culture systems and their applications in drug discovery and cell-based biosensors," *Assay and Drug Development Technologies*, vol. 12, pp. 207–218, May 2014. 4 citations on pages 1, 5, 6, and 7.

[4] F. Pampaloni, E. G. Reynaud, and E. H. K. Stelzer, "The third dimension bridges the gap between cell culture and live tissue," *Nature Publishing Group*, vol. 8, no. 10, pp. 839–845, 2007. 3 citations on pages 1, 5, and 6.

[5] S. Breslin and L. O'Driscoll, "Three-dimensional cell culture: the missing link in drug discovery," *Drug Discovery Today*, vol. 18, pp. 240–249, Mar 2013. 3 citations on pages 1, 6, and 7.

[6] D. Huh, G. A. Hamilton, and D. E. Ingber, "From 3D cell culture to organs-on-chips," *Trends in Cell Biology*, vol. 21, no. 12, pp. 745 – 754, 2011. 2 citations on pages 1 and 5.

[7] E. R. Shamir and A. J. Ewald, "Three-dimensional organotypic culture: experimental models of mammalian biology and disease," *Nature Reviews Molecular Cell Biology*, vol. 15, pp. 647–664, Oct 2014. 2 citations on pages 1 and 6.

[8] M. Ravi, V. Paramesh, S. Kaviya, E. Anuradha, and F. P. Solomon, "3D cell culture systems: Advantages and applications," *Journal of Cellular Physiology*, vol. 230, no. 1, pp. 16–26, 2015. 3 citations on pages 1, 5, and 6.

[9] N. Scherf and J. J. Huisken, "The smart and gentle microscope," *Nature Biotechnology*, 2015. 3 citations on pages 1, 5, and 14.

[10] Wikipedia, "Optical microscope — Wikipedia, The Free Encyclopedia," 2017. [Click to open link] [Online; accessed 19-July-2017]. Cited on page 1.

[11] C. Dobell, "A protozoological bicentenary: Antony van leeuwenhoek (1632–-1723) and louis joblot (1645–1723)," *Parasitology*, vol. 15, no. 3, p. 308–319, 1923. Cited on page 1.

[12] Wikipedia, "Timeline of microscope technology — Wikipedia, The Free Encyclopedia," 2017. [Click to open link] [Online; accessed 19-July-2017]. Cited on page 1.

[13] Z. Zheng, S. A. Lee, Y. Antebi, M. B. Elowitz, and C. Yang, "The ePetri dish, an on-chip cell imaging platform based on subpixel perspective sweeping microscopy (SPSM)," *Proceedings of the National Academy of Sciences of the United States of America*, vol. 108, no. 18, pp. 16889–16894, 2011. 2 citations on pages 2 and 14.

[14] I. Pushkarsky, Y. Liu, W. Weaver, T. W. Su, O. Mudanyali, A. Ozcan, and D. Di Carlo, "Automated single-cell motility analysis on a chip using lensfree microscopy," *Scientific Reports*, vol. 4, Apr. 2014. 2 citations on pages 2 and 14.

[15] D. Gabor, "A new microscopic principle," *Nature*, pp. 777–778, May 1948. 2 citations on pages 2 and 14.

[16] Wikipedia, "Matrigel — Wikipedia, The Free Encyclopedia," 2017. [Click to open link] [Online; accessed 10-September-2017]. Cited on page 5.

[17] G. Serini, D. Ambrosi, E. Giraudo, A. Gamba, L. Preziosi, and F. Bussolino, "Modeling the early stages of vascular network assembly," *The EMBO Journal*, 2003. 4 citations on pages 6, 249, 252, and 253.

[18] F. Pampaloni, E. H. K. Stelzer, and A. Masotti, "Three-dimensional tissue models for drug discovery and toxicology," *Recent Patents on Biotechnology*, vol. 3, no. 2, pp. 103–117, 2009. Cited on page 7.

[19] J. Sharpe, U. Ahlgren, P. Perry, B. Hill, A. Ross, J. Hecksher-Sørensen, R. Baldock, and D. Davidson, "Optical projection tomography as a tool for 3d microscopy and gene expression studies," *Science*, vol. 296, no. 5567, pp. 541–545, 2002. 2 citations on pages 7 and 8.

[20] A. Kak and M. Slaney, *Principles of computerized tomographic imaging*. IEEE press, 1988. 7 citations on pages 7, 13, 21, 25, 26, 30, and 63.

[21] D. Zhu, K. V. Larin, Q. Luo, and V. V. Tuchin, "Recent progress in tissue optical clearing," *Laser & Photonics Reviews*, vol. 7, pp. 732–757, Sep 2013. Cited on page 7.

[22] J. F. Colas and J. Sharpe, "Live optical projection tomography," *Organogenesis*, vol. 5, pp. 211–216, Oct 2009. Cited on page 7.

[23] B. W. Graf and S. A. Boppart, "Imaging and analysis of three-dimensional cell culture models," *Methods in Molecular Biology*, vol. 591, pp. 211–227, 2010. 3 citations on pages 7, 12, and 170.

[24] The Nikon MicroscopyU Reference Library, "Introduction to Fluorescence Microscopy," 2017. [Click to open link] [Online; accessed 9-June-2017]. Cited on page 7.

[25] The Nikon MicroscopyU Reference Library, "Introductory Confocal Concepts," 2017. [Click to open link] [Online; accessed 9-June-2017]. Cited on page 8.

[26] The Nikon MicroscopyU Reference Library, "Light Sheet Fluorescence Microscopy," 2017. [Click to open link] [Online; accessed 9-June-2017]. Cited on page 8.

[27] The Nikon MicroscopyU Reference Library, "Multiphoton Microscopy – Fundamentals and Applications in Multiphoton Excitation Microscopy," 2017. [Click to open link] [Online; accessed 12-June-2017]. Cited on page 8.

[28] J. M. Bueno, F. J. Ávila, and P. Artal, "Second harmonic generation microscopy: A tool for quantitative analysis of tissues," in *Microscopy and Analysis* (S. G. Stanciu, ed.), ch. 05, Rijeka: InTech, 2016. 2 citations on pages 10 and 11.

[29] B. Weigelin, G. J. Bakker, and P. Friedl, "Third harmonic generation microscopy of cells and tissue organization," *Journal of Cell Science*, vol. 129, pp. 245–255, Jan 2016. Cited on page 10.

[30] R. Genthial, E. Beaurepaire, M. C. Schanne-Klein, F. Peyrin, D. Farlay, C. Olivier, Y. Bala, G. Boivin, J. C. Vial, D. Debarre, and A. Gourrier, "Label-free imaging of bone multiscale porosity and interfaces using third-harmonic generation microscopy," *Scientific Reports*, vol. 7, p. 3419, Jun 2017. Cited on page 10.

[31] S. T. Hess, T. P. Girirajan, and M. D. Mason, "Ultra-high resolution imaging by fluorescence photoactivation localization microscopy," *Biophysical Journal*, vol. 91, pp. 4258–4272, Dec 2006. Cited on page 10.

[32] M. J. Rust, M. Bates, and X. Zhuang, "Sub-diffraction-limit imaging by stochastic optical reconstruction microscopy (STORM)," *Nature Methods*, vol. 3, pp. 793–796, Aug. 2006. Cited on page 10.

[33] S. W. Hell and J. Wichmann, "Breaking the diffraction resolution limit by stimulated emission: stimulated-emission-depletion fluorescence microscopy," *Optics Letters*, vol. 19, pp. 780–782, Jun 1994. Cited on page 10.

[34] N. Ramanujam, "Fluorescence spectroscopy of neoplastic and non-neoplastic tissues," *Neoplasia*, vol. 2, no. 1-2, pp. 89–117, 2000. Cited on page 11.

[35] F. Pampaloni, B.-J. Chang, and E. H. K. Stelzer, "Light sheet-based fluorescence microscopy (lsfm) for the quantitative imaging of cells and tissues," *Cell and Tissue Research*, vol. 360, pp. 129–141, Apr 2015. Cited on page 11.

[36] P. Y. Liu, L. K. Chin, W. Ser, H. F. Chen, C. M. Hsieh, C. H. Lee, K. B. Sung, T. C. Ayi, P. H. Yap, B. Liedberg, K. Wang, T. Bourouina, and Y. Leprince-Wang, "Cell refractive index for cell biology and disease diagnosis: past, present and future," *Lab on a Chip*, vol. 16, pp. 634–644, Feb 2016. Cited on page 12.

[37] C. Apelian, F. Harms, O. Thouvenin, and A. C. Boccara, "Dynamic full field optical coherence tomography: subcellular metabolic contrast revealed in tissues by interferometric signals temporal analysis," *Biomedical Optics Express*, vol. 7, pp. 1511–1524, Apr 2016. Cited on page 12.

[38] O. Thouvenin, C. Apelian, A. Nahas, M. Fink, and C. Boccara, "Full-field optical coherence tomography as a diagnosis tool: Recent progress with multimodal imaging," *Applied Sciences*, vol. 7, no. 3, 2017. Cited on page 12.

[39] M. Kim, "Principles and techniques of digital holographic microscopy," *Journal of Photonics for Energy*, pp. 018005–018005–50, 2010. Cited on page 12.

[40] M. Debailleul, B. Simon, V. Georges, O. Haeberlé, and V. Lauer, "Holographic microscopy and diffractive microtomography of transparent samples," *Measurement Science and Technology*, vol. 19, no. 7, p. 074009, 2008. 2 citations on pages 13 and 25.

[41] B. Simon, M. Debailleul, A. Beghin, Y. Tourneur, and O. Haeberlé, "High-resolution tomographic diffractive microscopy of biological samples," *Journal of Biophotonics*, vol. 3, no. 7, pp. 462–467, 2010. 2 citations on pages 13 and 25.

[42] A. Ali, Y. Abouleila, S. Amer, R. Furushima, S. Emara, S. Equis, Y. Cotte, and T. Masujima, "Quantitative Live Single-cell Mass Spectrometry with Spatial Evaluation by Three-Dimensional Holographic and Tomographic Laser Microscopy," *Analytical Sciences*, vol. 32, no. 2, pp. 125–127, 2016. 3 citations on pages 13, 108, and 219.

[43] W. Choi, C. Fang-Yen, K. Badizadegan, S. Oh, N. Lue, R. R. Dasari, and M. S. Feld, "Tomographic phase microscopy," *Nature Methods*, vol. 4, pp. 717–719, Sep 2007. 2 citations on pages 13 and 21.

[44] Y. Sung, W. Choi, C. Fang-Yen, K. Badizadegan, R. Dasari, and M. Feld, "Optical diffraction tomography for high resolution live cell imaging," *Optics*

Express, vol. 17, pp. 266–277, Jan 2009. 6 citations on pages 13, 21, 25, 30, 139, and 152.

[45] O. Haeberlé, K. Belkebir, H. Giovaninni, and A. Sentenac, "Tomographic diffractive microscopy: basics, techniques and perspectives," *Journal of Modern Optics*, vol. 57, no. 9, pp. 686–699, 2010. 2 citations on pages 13 and 152.

[46] Y. Cotte, F. Toy, P. Jourdain, N. Pavillon, D. Boss, P. Magistretti, P. Marquet, and C. Depeursinge, "Marker-free phase nanoscopy," *Nature Photonics*, vol. 7, no. 2, pp. 113–117, 2013. 3 citations on pages 13, 77, and 152.

[47] L. Tian and L. Waller, "3D intensity and phase imaging from light field measurements in an led array microscope," *Optica*, vol. 2, pp. 104–111, Feb 2015. 3 citations on pages 13, 14, and 218.

[48] R. Horstmeyer, J. Chung, X. Ou, G. Zheng, and C. Yang, "Diffraction tomography with fourier ptychography," *Optica*, vol. 3, pp. 827–835, Aug 2016. 3 citations on pages 14, 172, and 217.

[49] M. Chen, L. Tian, and L. Waller, "3D differential phase contrast microscopy," *Biomedical Optics Express*, vol. 7, pp. 3940–3950, Oct 2016. 4 citations on pages 14, 217, 219, and 220.

[50] S. Chowdhury, W. J. Eldridge, A. Wax, and J. A. Izatt, "Structured illumination multimodal 3D-resolved quantitative phase and fluorescence sub-diffraction microscopy," *Biomedical Optics Express*, vol. 8, pp. 2496–2518, May 2017. Cited on page 14.

[51] K. Lee, K. Kim, G. Kim, S. Shin, and Y. Park, "Time-multiplexed structured illumination using a dmd for optical diffraction tomography," *Optics Letters*, vol. 42, pp. 999–1002, Mar 2017. Cited on page 14.

[52] M. E. Dolega, C. Allier, S. V. Kesavan, S. Gerbaud, F. Kermarrec, P. Marcoux, J.-M. Dinten, X. Gidrol, and N. Picollet-D'Hahan, "Label-free analysis of prostate acini-like 3D structures by lensfree imaging," *Biosensors and Bioelectronics*, vol. 49, pp. 176 – 183, 2013. 4 citations on pages 14, 154, 215, and 216.

[53] S. V. Kesavan, M. Momey, O. Cioni, B. David-Watine, N. Dubrulle, S. Shorte, E. Sulpice, D. Freida, B. Chalmond, J. M. Dinten, X. Gidrol, and C. Allier, "High-throughput monitoring of major cell functions by means of lensfree video microscopy," *Scientific Reports*, vol. 4, Aug. 2014. Cited on page 14.

[54] L. Denis, C. Fournier, T. Fournel, and C. Ducottet, "Twin-image noise reduction by phase retrieval in in-line digital holography," in *Wavelets XI, SPIE's Symposium on Optical Science and Technology* (M. A. U. Manos Papadakis, Andrew F. Laine, ed.), vol. 5914 of *Proceedings of SPIE – Volume 5914*, (San

Diego, United States), p. 59140J, Aug. 2005. 14 pages. 2 citations on pages 17 and 19.

[55] S. V. Kesavan, F. P. Navarro, M. Menneteau, F. Mittler, B. David-Watine, N. Dubrulle, S. L. Shorte, B. Chalmond, J.-M. Dinten, and C. P. Allier, "Real-time label-free detection of dividing cells by means of lensfree videomicroscopy," *Journal of Biomedical Optics*, vol. 19, no. 3, p. 036004, 2014. Cited on page 17.

[56] J. W. Goodman, *Introduction to Fourier optics*. Englewood (Colorado): Roberts, 2005. 2 citations on pages 17 and 18.

[57] S. N. A. Morel, *Imagerie grand champ en anatomo-pathologie*. PhD thesis, under the supervision of Antoine Delon (Physics), Université Grenoble Alpes, 2017. 3 citations on pages 18, 20, and 66.

[58] R. W. Gerchberg and W. O. Saxton, "A practical algorithm for the determination of the phase from image and diffraction plane pictures," *Optik*, vol. 35, pp. 237–246, 1972. 2 citations on pages 19 and 20.

[59] J. R. Fienup, "Phase retrieval algorithms: a comparison," *Applied Optics*, vol. 21, pp. 2758–2769, Aug 1982. 2 citations on pages 19 and 88.

[60] J. R. Fienup, "Reconstruction of an object from the modulus of its fourier transform," *Optics Letters*, vol. 3, pp. 27–29, Jul 1978. Cited on page 19.

[61] Y. Rivenson, Y. Wu, H. Wang, Y. Zhang, A. Feizi, and A. Ozcan, "Sparsity-based multi-height phase recovery in holographic microscopy," *Scientific Reports*, vol. 6, p. 37862, Nov 2016. 2 citations on pages 19 and 139.

[62] A. Greenbaum and A. Ozcan, "Maskless imaging of dense samples using pixel super-resolution based multi-height lensfree on-chip microscopy," *Optics Express*, vol. 20, pp. 3129–3143, Jan 2012. Cited on page 19.

[63] W. Bishara, T.-W. Su, A. F. Coskun, and A. Ozcan, "Lensfree on-chip microscopy over a wide field-of-view using pixel super-resolution," *Optics Express*, vol. 18, pp. 11181–11191, May 2010. Cited on page 19.

[64] J. P. Ryle, S. McDonnell, and J. T. Sheridan, "Lensless multispectral digital in-line holographic microscope," *Journal of Biomedical Optics*, vol. 16, no. 12, pp. 126004–126004–17, 2011. Cited on page 19.

[65] D. W. Noom, D. E. B. Flaes, E. Labordus, K. S. Eikema, and S. Witte, "High-speed multi-wavelength fresnel diffraction imaging," *Optics Express*, vol. 22, pp. 30504–30511, Dec 2014. Cited on page 19.

[66] S. N. A. Morel, L. Hervé, T. Bordy, O. Cioni, A. Delon, C. Fromentin, J.-M. Dinten, and C. Allier, "Whole slide imaging of unstained tissue using

lensfree microscopy," in *Proceedings SPIE*, vol. 9711, pp. 97111L–97111L–5, 2016. Cited on page 19.

[67] C. Allier, S. Morel, R. Vincent, L. Ghenim, F. Navarro, M. Menneteau, T. Bordy, L. HervÉ, O. Cioni, X. Gidrol, Y. Usson, and J.-M. Dinten, "Imaging of dense cell cultures by multiwavelength lens-free video microscopy," *Cytometry Part A*, Feb. 2017. Cited on page 19.

[68] S. O. Isikman, W. Bishara, S. Mavandadi, F. W. Yu, S. Feng, R. Lau, and A. Ozcan, "Lens-free optical tomographic microscope with a large imaging volume on a chip," *Proceedings of the National Academy of Sciences of the United States of America*, vol. 108, no. 18, pp. 7296–7301, 2011. 3 citations on pages 21, 22, and 63.

[69] S. O. Isikman, A. Greenbaum, W. Luo, A. F. Coskun, and A. Ozcan, "Giga-pixel lensfree holographic microscopy and tomography using color image sensors," *PLoS ONE*, vol. 7, p. e45044, Sept. 2012. 2 citations on pages 21 and 63.

[70] C. Zuo, J. Sun, J. Zhang, Y. Hu, and Q. Chen, "Lensless phase microscopy and diffraction tomography with multi-angle and multi-wavelength illuminations using a led matrix," *Optics Express*, vol. 23, pp. 14314–14328, Jun 2015. 5 citations on pages 21, 23, 112, 114, and 219.

[71] E. Wolf, "Three-dimensional structure determination of semi-transparent objects from holographic data," *Optics Communications*, vol. 1, no. 4, pp. 153–156, 1969. 3 citations on pages 25, 30, and 152.

[72] A. J. Devaney, "Inverse-scattering theory within the Rytov approximation," *Optical Letters*, vol. 6, pp. 374–376, Aug 1981. Cited on page 30.

[73] X. J. Liang, A. Q. Liu, C. S. Lim, T. C. Ayi, and P. H. Yap, "Determining refractive index of single living cell using an integrated microchip," *Sensors and Actuators A: Physical*, vol. 133, no. 2, pp. 349 – 354, 2007. Cited on page 30.

[74] M. Hazewinkel, *Encyclopedia of Mathematics*. Springer, 2001. 4 citations on pages 35, 223, 225, and 229.

[75] Wikipedia, "Radon transform — Wikipedia, The Free Encyclopedia," 2017. [Click to open link] [Online; accessed 4-September-2017]. Cited on page 35.

[76] Wikipedia, "Projection-slice theorem — Wikipedia, The Free Encyclopedia," 2017. [Click to open link] [Online; accessed 4-September-2017]. Cited on page 35.

[77] W. Xu, M. H. Jericho, I. A. Meinertzhagen, and H. J. Kreuzer, "Digital in-line holography for biological applications," *Proceedings of the National Academy of Sciences of the United States of America*, vol. 98, pp. 11301–11305, Sep 2001. Cited on page 48.

[78] P. Bon, N. Bourg, S. Lecart, S. Monneret, E. Fort, J. Wenger, and S. Leveque-Fort, "Three-dimensional nanometre localization of nanoparticles to enhance super-resolution microscopy," *Nature Communications*, vol. 6, p. 7764, Jul 2015. Cited on page 50.

[79] J. Y. Tinevez, N. Perry, J. Schindelin, G. M. Hoopes, G. D. Reynolds, E. Laplantine, S. Y. Bednarek, S. L. Shorte, and K. W. Eliceiri, "TrackMate: An open and extensible platform for single-particle tracking," *Methods*, vol. 115, pp. 80–90, Feb 2017. 3 citations on pages 51, 185, and 191.

[80] F. Momey, A. Berdeu, T. Bordy, J.-M. Dinten, F. K. Marcel, N. Picollet-D'hahan, X. Gidrol, and C. Allier, "Lensfree diffractive tomography for the imaging of 3D cell cultures," *Biomedical Optics Express*, vol. 7, pp. 949–962, Mar 2016. 3 citations on pages 57, 85, and 222.

[81] Wikipedia, "Wiener deconvolution — Wikipedia, The Free Encyclopedia," 2016. [Click to open link] [Online; accessed 5-September-2017]. Cited on page 76.

[82] Wikipedia, "Fourier transform — Wikipedia, The Free Encyclopedia," 2017. [Click to open link] [Online; accessed 22-August-2017]. Cited on page 81.

[83] M. Schmidt, "Limited-memory bfgs," 2012. [Click to open link] [Online; accessed 22-August-2017]. Cited on page 81.

[84] Wikipedia, "Broyden–Fletcher–Goldfarb–Shanno algorithm — Wikipedia, The Free Encyclopedia," 2017. [Online; accessed 6-September-2017]. Cited on page 81.

[85] Wikipedia, "Conic section — Wikipedia, The Free Encyclopedia," 2017. [Click to open link] [Online; accessed 25-July-2017]. Cited on page 96.

[86] T. Visser, J. Oud, and G. Brakenhoff, "Refractive index and axial distance measurements in 3-d microscopy," *Optik*, vol. 90, no. 1, pp. 17–19, 1992. 2 citations on pages 101 and 201.

[87] T. H. Besseling, J. Jose, and A. Van Blaaderen, "Methods to calibrate and scale axial distances in confocal microscopy as a function of refractive index," *Journal of Microscopy*, vol. 257, pp. 142–150, Feb 2015. 2 citations on pages 101 and 201.

[88] A. Berdeu, F. Momey, B. Laperrousaz, T. Bordy, X. Gidrol, J.-M. Dinten, N. Picollet-D'hahan, and C. Allier, "Comparative study of fully three-dimensional reconstruction algorithms for lens-free microscopy," *Applied Optics*, vol. 56, pp. 3939–3951, May 2017. 3 citations on pages 103, 153, and 222.

[89] A. Berdeu, F. Momey, J.-M. Dinten, X. Gidrol, N. Picollet-D'hahan, and C. Allier, "Lensfree diffractive tomography for the imaging of 3D cell cultures,"

in *Biomedical optics, and imaging conference*, vol. 10070, pp. 10070 – 10070 – 7, 2017. 2 citations on pages 103 and 221.

[90] J. Nocedal, "Updating quasi-newton matrices with limited storage," *Mathematics of Computation*, vol. 35, pp. 773–782, 7 1980. 3 citations on pages 118, 128, and 140.

[91] E. Thiébaut, "Optimpack library," 2017. [Click to open link] [Online; accessed 22-August-2017]. Cited on page 118.

[92] H. Carfantan, "Optimpack library interface," 2017. [Click to open link] [Online; accessed 22-August-2017]. Cited on page 118.

[93] K. Alessandri, M. Feyeux, B. Gurchenkov, C. Delgado, A. Trushko, K. H. Krause, D. Vignjevi?, P. Nassoy, and A. Roux, "A 3D printed microfluidic device for production of functionalized hydrogel microcapsules for culture and differentiation of human Neuronal Stem Cells (hNSC)," *Lab on a Chip*, vol. 16, pp. 1593–1604, April 2016. Cited on page 147.

[94] K. Alessandri, B. R. Sarangi, V. V. Gurchenkov, B. Sinha, T. R. Kiessling, L. Fetler, F. Rico, S. Scheuring, C. Lamaze, A. Simon, S. Geraldo, D. Vignjevic, H. Domejean, L. Rolland, A. Funfak, J. Bibette, N. Bremond, and P. Nassoy, "Cellular capsules as a tool for multicellular spheroid production and for investigating the mechanics of tumor progression in vitro," *Proceedings of the National Academy of Sciences of the United States of America*, vol. 110, pp. 14843–14848, September 2013. Cited on page 147.

[95] M. E. Dolega, F. Abeille, N. Picollet-D'hahan, and X. Gidrol, "Controlled 3D culture in matrigel microbeads to analyze clonal acinar development," *Biomaterials*, vol. 52, pp. 347 – 357, 2015. Cited on page 154.

[96] G.-H. Chen, J. Tang, and S. Leng, "Prior image constrained compressed sensing (piccs): A method to accurately reconstruct dynamic ct images from highly undersampled projection data sets," *Medical Physics*, vol. 35, no. 2, pp. 660–663, 2008. Cited on page 165.

[97] J. Bailleul, B. Simon, M. Debailleul, H. Liu, and O. Haeberlé, "GPU acceleration towards real-time image reconstruction in 3d tomographic diffractive microscopy," in *Real-Time Image and Video Processing 2012, Brussels, Belgium, April 19, 2012*, p. 843707, 2012. 2 citations on pages 170 and 217.

[98] X. Liang, B. W. Graf, and S. A. Boppart, "Imaging engineered tissues using structural and functional optical coherence tomography," *Journal of Biophotonics*, vol. 2, pp. 643–655, Nov 2009. Cited on page 170.

[99] S. C. Neves, D. B. Gomes, A. Sousa, S. J. Bidarra, P. Petrini, L. Moroni, C. C. Barrias, and P. L. Granja, "Biofunctionalized pectin hydrogels as 3d cellular

microenvironments," *Journal of Materials Chemistry B*, vol. 3, pp. 2096–2108, 2015. Cited on page 170.

[100] A. Berdeu, F. Momey, B. Laperrousaz, T. Bordy, X. Gidrol, J.-M. Dinten, N. Picollet-D'hahan, and C. Allier, "3D lens-free time-lapse microscopy for 3D cell culture," in *European Conferences on Biomedical Optics*, vol. 10414, pp. 10414 – 10414 – 7, 2017. 2 citations on pages 175 and 221.

[101] M. L. Gardel, B. Sabass, L. Ji, G. Danuser, U. S. Schwarz, and C. M. Waterman, "Traction stress in focal adhesions correlates biphasically with actin retrograde flow speed," *Journal of Cell Biology*, vol. 183, pp. 999–1005, Dec 2008. Cited on page 187.

[102] Wikipedia, "Full width at half maximum — Wikipedia, The Free Encyclopedia," 2016. [Click to open link] [Online; accessed 19-July-2017]. Cited on page 203.

[103] E. Optics, "Sensor Relative Illumination, Roll Off and Vignetting," 2017. [Click to open link] [Online; accessed 01-August-2017]. Cited on page 209.

[104] P. Friedl and K. Wolf, "Tumour-cell invasion and migration: Diversity and escape mechanisms," *Nature Reviews Cancer*, vol. 3, pp. 362–374, 5 2003. Cited on page 214.

[105] P. Friedl and D. Gilmour, "Collective cell migration in morphogenesis, regeneration and cancer," *Nature Reviews Molecular Cell Biology*, vol. 10, pp. 445–457, Jul 2009. Cited on page 214.

[106] O. Ilina and P. Friedl, "Mechanisms of collective cell migration at a glance," *Journal of Cell Science*, vol. 122, no. 18, pp. 3203–3208, 2009. Cited on page 214.

[107] B. Waclaw, I. Bozic, M. E. Pittman, R. H. Hruban, B. Vogelstein, and M. A. Nowak, "A spatial model predicts that dispersal and cell turnover limit intratumour heterogeneity," *Nature*, vol. 525, pp. 261–264, Sep 2015. Cited on page 215.

[108] B. Smeets, R. Alert, J. Pe?ek, I. Pagonabarraga, H. Ramon, and R. Vincent, "Emergent structures and dynamics of cell colonies by contact inhibition of locomotion," *Proceedings of the National Academy of Sciences of the United States of America*, vol. 113, pp. 14621–14626, Dec 2016. Cited on page 215.

[109] P. Friedl, J. Locker, E. Sahai, and J. E. Segall, "Classifying collective cancer cell invasion," *Nature Cell Biology*, vol. 14, pp. 777–783, Aug 2012. Cited on page 215.

[110] A. C. Petrey and C. A. de la Motte, "The extracellular matrix in IBD: a dynamic mediator of inflammation," *Current Opinion in Gastroenterology*, vol. 33, pp. 234–238, Jul 2017. Cited on page 215.

[111] S. Freitas-Rodriguez, A. R. Folgueras, and C. Lopez-Otin, "The role of matrix metalloproteinases in aging: Tissue remodeling and beyond," *Biochimica et Biophysica Acta*, May 2017. Cited on page 215.

[112] R. L. Blackmon, R. Sandhu, B. S. Chapman, P. Casbas-Hernandez, J. B. Tracy, M. A. Troester, and A. L. Oldenburg, "Imaging extracellular matrix remodeling in vitro by diffusion-sensitive optical coherence tomography," *Biophysical Journal*, vol. 110, no. 8, pp. 1858 – 1868, 2016. Cited on page 215.

[113] B. Lee, J. Konen, S. Wilkinson, A. I. Marcus, and Y. Jiang, "Local alignment vectors reveal cancer cell-induced ECM fiber remodeling dynamics," *Scientific Reports*, vol. 7, p. 39498, Jan 2017. Cited on page 215.

[114] Y. Zhang, Y. Shin, K. Sung, S. Yang, H. Chen, H. Wang, D. Teng, Y. Rivenson, R. P. Kulkarni, and A. Ozcan, "3d imaging of optically cleared tissue using a simplified clarity method and on-chip microscopy," *Science Advances*, vol. 3, no. 8, 2017. Cited on page 215.

[115] A. Greenbaum, Y. Zhang, A. Feizi, P.-L. Chung, W. Luo, S. R. Kandukuri, and A. Ozcan, "Wide-field computational imaging of pathology slides using lens-free on-chip microscopy," *Science Translational Medicine*, vol. 6, no. 267, pp. 267–175, 2014. Cited on page 216.

[116] F. Soulez, "A "learn 2D, apply 3D" method for 3D deconvolution microscopy," in *2014 IEEE 11th International Symposium on Biomedical Imaging (ISBI)*, pp. 1075–1078, Apr 2014. Cited on page 217.

[117] U. S. Kamilov, I. N. Papadopoulos, M. H. Shoreh, A. Goy, C. Vonesch, M. Unser, and D. Psaltis, "Learning approach to optical tomography," *Optica*, vol. 2, pp. 517–522, Jun 2015. Cited on page 217.

[118] O. Mudanyali, C. Oztoprak, D. Tseng, A. Erlinger, and A. Ozcan, "Detection of waterborne parasites using field-portable and cost-effective lensfree microscopy," *Lab on a Chip*, vol. 10, pp. 2419–2423, Sep 2010. Cited on page 218.

[119] R. Eckert, N. Repina, M. Chen, Y. Liang, R. Ng, and L. Waller, "Modeling light propagation in 3d phase objects," in *Imaging and Applied Optics 2017 (3D, AIO, COSI, IS, MATH, pcAOP)*, p. DW2F.2, Optical Society of America, 2017. Cited on page 218.

[120] M. Rostykus and C. Moser, "Flat Lensless Phase Imager," in *Imaging and Applied Optics 2016*, p. DM3E.3, Optical Society of America, 2016. Cited on page 220.

[121] M. Rostykus, "High resolution flat lensfree phase imager," in *Digital Holography and Three-Dimensional Imaging*, p. M2A.2, Optical Society of America, 2017. Cited on page 220.

[122] F. Guo, Z. Mao, Y. Chen, Z. Xie, J. P. Lata, P. Li, L. Ren, J. Liu, J. Yang, M. Dao, S. Suresh, and T. J. Huang, "Three-dimensional manipulation of single cells using surface acoustic waves," *Proceedings of the National Academy of Sciences of the United States of America*, vol. 113, no. 6, pp. 1522–1527, 2016. Cited on page 220.

[123] V. Aubert, R. Wunenburger, T. Valier-Brasier, D. Rabaud, J.-P. Kleman, and C. Poulain, "A simple acoustofluidic chip for microscale manipulation using evanescent scholte waves," *Lab on a Chip*, vol. 16, pp. 2532–2539, 2016. Cited on page 220.

[124] K. Kim and Y. Park, "Tomographic active optical trapping of arbitrarily shaped objects by exploiting 3D refractive index maps," *Nature Communications*, vol. 8, p. 15340, May 2017. Cited on page 220.

[125] M. Habaza, M. Kirschbaum, C. Guernth-Marschner, G. Dardikman, I. Barnea, R. Korenstein, C. Duschl, and N. T. Shaked, "Rapid 3D Refractive-Index Imaging of Live Cells in Suspension without Labeling Using Dielectrophoretic Cell Rotation," *Advanced Science*, vol. 4, p. 1600205, Feb 2017. Cited on page 220.

[126] J. M. Soto, J. A. Rodrigo, and T. Alieva, "Label-free quantitative 3D tomographic imaging for partially coherent light microscopy," *Optics Express*, vol. 25, pp. 15699–15712, Jul 2017. Cited on page 220.

[127] H. Weyl, "Ausbreitung elektromagnetischer Wellen über einem ebenen Leiter," *Annalen der Physik*, vol. 365, no. 21, pp. 481–500, 1919. Cited on page 227.

[128] Wikipedia, "Residue theorem — Wikipedia, The Free Encyclopedia," 2017. [Click to open link] [Online; accessed 9-September-2017]. Cited on page 229.

[129] Wikipedia, "Théorème des résidus — Wikipedia, The Free Encyclopedia," 2017. [Online; accessed 9-September-2017]. Cited on page 229.

[130] Wikipedia, "Cauchy principal value — Wikipedia, The Free Encyclopedia," 2017. [Click to open link] [Online; accessed 9-September-2017]. Cited on page 230.

[131] L. Houben and M. B. Sadan, "Refinement procedure for the image alignment in high-resolution electron tomography," *Ultramicroscopy*, vol. 111, no. 9, pp. 1512 – 1520, 2011. 2 citations on pages 235 and 238.

[132] Wikipedia, "Cross-correlation — Wikipedia, The Free Encyclopedia," 2017. [Click to open link] [Online; accessed 1-September-2017]. Cited on page 236.

[133] Wikipedia, "Autocorrelation — Wikipedia, The Free Encyclopedia," 2017. [Click to open link] [Online; accessed 1-September-2017]. Cited on page 236.

[134] Wikipedia, "Least mean squares filter — Wikipedia, The Free Encyclopedia," 2017. [Click to open link] [Online; accessed 1-September-2017]. Cited on page 237.

[135] D. L. Donoho, "Compressed sensing," *EEE Transactions on Information Theory*, vol. 52, pp. 1289–1306, Apr. 2006. Cited on page 243.

[136] L. Denis, D. Lorenz, E. Thiébaut, C. Fournier, and D. Trede, "Inline hologram reconstruction with sparsity constraints," *Optics Letters*, vol. 34, pp. 3475–3477, Nov 2009. Cited on page 243.

[137] L. I. Rudin, S. Osher, and E. Fatemi, "Nonlinear total variation based noise removal algorithms," *Journal of Physics D*, vol. 60, pp. 259–268, Nov. 1992. Cited on page 243.

[138] P. Charbonnier, L. Blanc-Feraud, G. Aubert, and M. Barlaud, "Deterministic edge-preserving regularization in computed imaging," *Transactions on Image Processing*, vol. 6, pp. 298–311, Feb. 1997. Cited on page 243.

[139] Wikipedia, "Euler method — Wikipedia, The Free Encyclopedia," 2017. [Click to open link] [Online; accessed 1-September-2017]. Cited on page 252.

[140] Wikipedia, "Courant–Friedrichs–Lewy condition — Wikipedia, The Free Encyclopedia," 2017. [Online; accessed 1-September-2017]. Cited on page 256.

Résumé - Ce travail de thèse se situe à l'interface de deux domaines : la culture cellulaire en trois dimensions et l'imagerie sans lentille.

Fournissant un protocole de culture cellulaire plus réaliste sur le plan physiologique, le passage des cultures monocouches (2D) à des cultures tridimensionnelles (3D) - via l'utilisation de gels extracellulaires dans lesquels les cellules peuvent se développer dans les trois dimensions - permet de faire de grandes avancées dans de nombreux domaines en biologie tels que l'organogénèse, l'oncologie et la médecine régénérative. Ces nouveaux objets à étudier créent un besoin en matière d'imagerie 3D.

De son côté, l'imagerie sans lentille 2D fournit un moyen robuste, peu cher, sans marquage et non toxique, d'étudier les cultures cellulaires en deux dimensions sur de grandes échelles et sur de longues périodes. Ce type de microscopie enregistre l'image des interférences produites par l'échantillon biologique traversé par une lumière cohérente. Connaissant la physique de la propagation de la lumière, ces hologrammes sont rétro-propagés numériquement pour reconstruire l'objet recherché. L'algorithme de reconstruction remplace les lentilles absentes dans le rôle de la formation de l'image.

Le but de cette thèse est de montrer la possibilité d'adapter cette technologie sans lentille à l'imagerie des cultures cellulaires en 3D. De nouveaux prototypes de microscopes sans lentille sont conçus en parallèle du développement d'algorithmes de reconstructions tomographiques dédiés.

Concernant les prototypes, plusieurs solutions sont testées pour converger vers un schéma alliant deux conditions. La première est le choix de la simplicité d'utilisation avec une culture cellulaire en boîte de Petri standard et ne nécessitant aucune préparation spécifique ou aucun changement de contenant. Cette condition entraînant de fortes contraintes géométriques sur l'architecture, la deuxième est de trouver la meilleure couverture angulaire possible des angles d'éclairage. Enfin, une version adaptée aux conditions en incubateur est développée et testée avec succès.

Concernant les algorithmes, quatre types de solutions sont proposés, basées sur le théorème de diffraction de Fourier classiquement utilisé en tomographie diffractive optique. Toutes cherchent à corriger deux problèmes inhérents au microscope sans lentille : l'absence de l'information de phase, le capteur n'étant sensible qu'à l'intensité de l'onde reçue, et la couverture angulaire limitée. Le premier algorithme se limite à remplacer la phase inconnue par celle d'une onde incidente plane. Rapide, cette méthode est néanmoins source de nombreux artefacts. La deuxième solution, en approximant l'objet 3D inconnu par un plan moyen, utilise les outils de la microscopie sans lentille 2D pour retrouver cette phase manquante via une approche inverse. La troisième solution consiste à implémenter une approche inverse régularisée sur l'objet 3D à reconstruire. C'est la méthode la plus efficace pour compenser les deux problèmes mentionnés, mais elle est très lente. La quatrième et dernière solution est basée sur un algorithme de type Gerchberg-Saxton modifié avec une étape de régularisation sur l'objet.

Toutes ces méthodes sont comparées et testées avec succès sur des simulations numériques et des données expérimentales. Des comparaisons avec des acquisitions au microscope classique montrent la validité des reconstructions en matière de tailles et de formes des objets reconstruits ainsi que la précision de leur positionnement tridimensionnel. Elles permettent de reconstruire des volumes de plusieurs dizaines de millimètres cubes de cultures cellulaires 3D, inaccessibles en microscopie standard.

Par ailleurs, les données spatio-temporelles obtenues avec succès en incubateur montrent aussi la pertinence de ce type d'imagerie en mettant en évidence des interactions dynamiques sur de grandes échelles des cellules entres elles ainsi qu'avec leur environnement tridimensionnel.

Abstract - This PhD work is at the interface of two fields: 3D cell culture and lens-free imaging.

Providing a more realistic cell culture protocol on the physiological level, switching from single-layer (2D) cultures to three-dimensional (3D) cultures - via the use of extracellular gel in which cells can grow in three dimensions - is at the origin of several breakthroughs in several fields such as developmental biology, oncology and regenerative medicine. The study of these new 3D structures creates a need in terms of 3D imaging.

On another side, 2D lens-free imaging provides a robust, inexpensive, non-labeling and non-toxic tool to study cell cultures in two dimensions over large scales and over long periods of time. This type of microscopy records the interferences produced by a coherent light scattered by the biological sample. Knowing the physics of light propagation, these holograms are retro-propagated numerically to reconstruct the unknown object. The reconstruction algorithm replaces the absent lenses in the role of image formation.

The aim of this PhD is to show the possibility of adapting this lens-free technology for imaging 3D cell culture. New lens-free microscopes are designed and built along with the development of dedicated tomographic reconstruction algorithms.

Concerning the prototypes, the tested solutions converge to a scheme combining two conditions. The first requirement is the choice of simplicity of use with a cell culture in standard Petri dish and requiring no specific preparation or change of container. The second condition is to find the best possible angular coverage of lighting angles in regards of the geometric constraint imposed by the first requirement. Finally, an incubator-proof version is successfully built and tested.

Regarding the algorithms, four major types of solutions are implemented, all based on the Fourier diffraction theorem, conventionally used in optical diffractive tomography. All methods aim to correct two inherent problems of a lens-free microscope: the absence of phase information, the sensor being sensitive only to the intensity of the incident wave, and the limited angular coverage. The first algorithm simply replaces the unknown phase with that of an incident plane wave. However, this method is fast but it is the source of many artifacts. The second solution tries to estimate the missing phase by approximating the unknown object by an average plane and uses the tools of the 2D lens-free microscopy to recover the missing phase in an inverse problem approach. The third solution consists in implementing a regularized inverse problem approach on the 3D object to reconstruct. This is the most effective method to deal with the two problems mentioned above but it is very slow. The fourth and last solution is based on a modified Gerchberg-Saxton algorithm with a regularization step on the object.

All these methods are compared and tested successfully on numerical simulations and experimental data. Comparisons with conventional microscope acquisitions show the validity of the reconstructions in terms of shape and positioning of the retrieved objects as well as the accuracy of their three-dimensional positioning. Biological samples are reconstructed with volumes of several tens of cubic millimeters, inaccessible in standard microscopy.

Moreover, 3D time-lapse data successfully obtained in incubators show the relevance of this type of imaging by highlighting large-scale interactions between cells or between cells and their three-dimensional environment.